

Springer Transactions in Civil
and Environmental Engineering

Harald Drück
Jyotirmay Mathur
Varghese Panthalookaran
V. M. Sreekumar *Editors*

Green Buildings and Sustainable Engineering

Proceedings of GBSE 2019

 Springer

Springer Transactions in Civil and Environmental Engineering

Editor-in-Chief

T. G. Sitharam, Department of Civil Engineering, Indian Institute of Science,
Bangalore, Karnataka, India

Springer Transactions in Civil and Environmental Engineering (STICEE) publishes the latest developments in Civil and Environmental Engineering. The intent is to cover all the main branches of Civil and Environmental Engineering, both theoretical and applied, including, but not limited to: Structural Mechanics, Steel Structures, Concrete Structures, Reinforced Cement Concrete, Civil Engineering Materials, Soil Mechanics, Ground Improvement, Geotechnical Engineering, Foundation Engineering, Earthquake Engineering, Structural Health and Monitoring, Water Resources Engineering, Engineering Hydrology, Solid Waste Engineering, Environmental Engineering, Wastewater Management, Transportation Engineering, Sustainable Civil Infrastructure, Fluid Mechanics, Pavement Engineering, Soil Dynamics, Rock Mechanics, Timber Engineering, Hazardous Waste Disposal Instrumentation and Monitoring, Construction Management, Civil Engineering Construction, Surveying and GIS Strength of Materials (Mechanics of Materials), Environmental Geotechnics, Concrete Engineering, Timber Structures.

Within the scopes of the series are monographs, professional books, graduate and undergraduate textbooks, edited volumes and handbooks devoted to the above subject areas.

More information about this series at <http://www.springer.com/series/13593>

Harald Drück · Jyotirmay Mathur ·
Varghese Panthalookaran · V. M. Sreekumar
Editors

Green Buildings and Sustainable Engineering

Proceedings of GBSE 2019

 Springer

Editors

Harald Drück
Institute of Building Energetics
Thermotechnology and Energy
Storage (IGTE)
Stuttgart University
Stuttgart, Germany

Varghese Panthaloorkaran
Department of Basic Sciences
and Humanities
Rajagiri School of Engineering
& Technology
Kochi, Kerala, India

Jyotirmay Mathur
Centre for Energy and Environment
Malaviya National Institute of Technology
Jaipur, Rajasthan, India

V. M. Sreekumar
Department of Mechanical Engineering
Rajagiri School of Engineering
& Technology
Kochi, Kerala, India

ISSN 2363-7633

ISSN 2363-7641 (electronic)

Springer Transactions in Civil and Environmental Engineering

ISBN 978-981-15-1062-5

ISBN 978-981-15-1063-2 (eBook)

<https://doi.org/10.1007/978-981-15-1063-2>

© Springer Nature Singapore Pte Ltd. 2020

This work is subject to copyright. All rights are reserved by the Publisher, whether the whole or part of the material is concerned, specifically the rights of translation, reprinting, reuse of illustrations, recitation, broadcasting, reproduction on microfilms or in any other physical way, and transmission or information storage and retrieval, electronic adaptation, computer software, or by similar or dissimilar methodology now known or hereafter developed.

The use of general descriptive names, registered names, trademarks, service marks, etc. in this publication does not imply, even in the absence of a specific statement, that such names are exempt from the relevant protective laws and regulations and therefore free for general use.

The publisher, the authors and the editors are safe to assume that the advice and information in this book are believed to be true and accurate at the date of publication. Neither the publisher nor the authors or the editors give a warranty, expressed or implied, with respect to the material contained herein or for any errors or omissions that may have been made. The publisher remains neutral with regard to jurisdictional claims in published maps and institutional affiliations.

This Springer imprint is published by the registered company Springer Nature Singapore Pte Ltd. The registered company address is: 152 Beach Road, #21-01/04 Gateway East, Singapore 189721, Singapore

Conference Organizers and Boards

Rajagiri School of Engineering and Technology

Indo-German Dialogue and International Conference on Green Building and Sustainable Engineering (GBSE2019)

Theme: “Ecotechnological and Digital Solutions for Smart Cities”

Patron

Rev. Dr. Mathew Vattathara, CMI, Director, RSET

General Chair

Dr. A. Unnikrishnan, RSET, India

Program Chairs

Dr.-Ing. Harald Drück, University of Stuttgart, Germany

Dr.-Ing. Varghese Panthaloorkaran, RSET, India

Organizing Chair

Dr. Manoj G. Tharian (Chief Coordinator)

Mr. Jithin P. N. (Associate Coordinator)

Mr. BibinHezakiel V. (Associate Coordinator)

I. Pre-conference Workshop Coordinators

Dr. Nivish George

Ms. Caroline Ann Sam

II. Conference Coordinators

Dr. V. M. Sreekumar

Dr. Asha Vishwanath

(i) Publication Chairs

Dr.-Ing. Harald Drück, University of Stuttgart, Germany

Dr. Jyotimay Mathur, MNIT Jaipur

Dr.-Ing. Varghese Panthalookaran

Dr. V. M. Sreekumar

(ii) Steering Committee

Dr. Benny Mathews Abraham, CUSAT, India

Dr. Benny Raphel, IITM, India

Prof. C. G. Nandakumar, CUSAT, India

Prof. Eldho T. I., IITB, India

Prof. Frank Spate, Amberg-Weiden University, Germany

Prof. Ganesh L. S., IITM, India

Prof. Dr.-Ing. Gerhard Seelmann, Hochschule Aalen, Germany

Prof. Dr.-Ing. Harald Mandel, Duale Hochschule Baden-Württemberg, Germany

Dr.-Ing. Henner Kerskes, Universität Stuttgart, Germany

Dr. John Jose, IITG, India

Dr. John M. George, RSET, India

Prof. Dr.-Ing. Jürgen Trost, Hochschule Aalen, Germany

Dr. Lakshman Nandagiri, NITK, India

Prof. Dr. sc. techn. Michael Pfeffer, Ravensburg University, Germany

Dr. Ramesh Rayudu, Victoria University of Wellington, New Zealand

Prof. Rupen Goswami, IIT Madras

Dr. Santosh G. Thampi, NIT Calicut, India

Prof. Simon Furbo, Technical University of Denmark

Dr. V. M. Sreekumar, RSET, India

Dr. Thankachan T. Pullan, RSET, India

Mr. Werner Weiss, Director, AEE—Institute for Sustainable Technologies, Austria

Prof. Zinian He, Beijing Solar Energy Research Institute, China

Dr. Aysha Zeneeb Majeed, RSET, India

Prof. K. A. Ouseph, RSET, India
Dr. Unnikrishnan P. C.
Dr. Ajith Kumar A., RSET, India
Dr. Asha, RSET, India

(iii) **Technical Program Committee**

Dr. A. Veeraragavan, IIT Madras, India
Dr. Amba Shetty, NIT Surathkal, India
Dr. Benny Mathews Abraham, CUSAT, India
Dr. Bino I. Koshy, RIT, India
Dr. Daniel Mugnier, TECSOL, Perpignan, France
Mr. David Kaufman, National Solar Institute, Energy Solutions, USA
Dr.-Ing. Elke Malleier, Sustainability and Green Building Consultant, Singapore
Dr. Glory Joseph, CUSAT, India
Dr. Honey John, Department of Polymer Science and Rubber Technology, CUSAT, India.
Prof. Jean-Christophe Hadorn, EPFL, Switzerland
Dr. Job Thomas, CUSAT, India
Prof. Dr.-Ing. Jörg Londong, Faculty of Civil Engineering, Bauhaus-Universität Weimar, Germany
Mr. Ken Guthrie, Director of Sustainable Energy Transformation Pty Ltd, Australia
Dr. Kim Augustin, Hamburg Wasser, Hamburg, Germany
Dr. Lakshman Nandagiri, NIT Surathkal, India
Mr. Lex Bosselaar, The Netherlands
Prof. Luisa F. Cabeza, University of Lleida, Spain
Dr. M. Satyakumar, Mar Baselios College of Engineering and Technology, India
Dr. M. V. L. R. Anjaneyulu, NIT Calicut, India
Dr. Manju V. S., Government College of Engineering, TVM, India
Dr. Nisa Salim, Deakin University, Australia
Dr. Nishar Hameed, University of Swinburne, Australia
Dr. Padmakumar R., College Of Engineering, TVM, India
Mr. Qingtai Jiao, Jiangsu Sunrain Solar Energy Co., Ltd, China
Dr. Rakesh J. Pillai, NIT Warangal, India
Dr. Ruby Abraham, Marian Engineering College, India
Prof. S. Shrihari, NITK, India
Dr. Santhosh Thampi, NIT Calicut, India
Dr. Sobha Cyrus, CUSAT, India
Dr. Suja R., GEC, Barton Hill, India
Mr. Thomas Giese, Hamburg Wasser, Hamburg, Germany
Prof. Dr. Ursula Eicker, University of Applied Sciences Stuttgart, Stuttgart

III. Indo-German Dialogue Coordinators

Dr. Elizabeth Rita Samuel
Ms. Anu Mathew

IV. GBSE Expo Coordinators

Mr. Arun B.
Mr. Thomas K. P.

V. Rajagiri Grand Challenge

Mr. Jebin Francis
Mr. Vishnu Sankar

VI. Post-conference Technical and Heritage Tours

Mr. Vineeth Krishna P.
Mr. Jibin Joseph

Finance Chairs

Mr. Sidheek P. A. (Coordinator)
Ms. Jayasri R. Nair
Ms. Aswathy G.

Invitation Committee/Publicity Committee

Ms. Elsa Paul (Coordinator)
Fr. Mejopaul
Mr. Tony Chacko
Mr. Jeffin Johnson
Ms. NimishaReji
Ms. Deepthi I. Gopinath
Ms. Renu George
Ms. Sreepriya R.
Ms. Caroline Ann Sam
Ms. Tressa Kurian
Mr. Mathew Baby

Sponsorship Committee

Mr. Rathish T. R. (Coordinator)
Dr. Joseph Babu K.
Mr. Jibin Noble
Mr. Jithin K. Francis
Ms. Anna Mathew
Mr. Krishnaraj P. P.
Mr. Unnikrishnan L.
Ms. Ragam Rajagopal
Ms. Anitha Varghese
Mr. Vineeth Krishna P.
Ms. Nimisha Reji
Mr. Abinson Paul
Mr. Arun T. Moonjely
Mr. James Mathew

Preface

The program on Green Buildings and Sustainable Engineering (GBSE2019) organized by Rajagiri School of Engineering & Technology (RSET), Kochi, India, together with Institute for Building Energetics, Thermotechnology and Energy Storage (IGTE), University of Stuttgart, Germany, was held during February 19–20, 2019, at RSET. GBSE2019 under the theme “Ecotechnological and Digital Solutions for Smart Cities” is an important step toward fulfilling the dream that one day we can live in a clean, healthy, and high-quality environment, where cities, townships, and communities are built on the fundamentals of Green Buildings and Sustainable Engineering.

The program was inaugurated by Mr. Prasad Panicker, Executive Director, Bharat Petroleum Corporation Limited, Kochi. Mission Director of Smart Cities Mission, Government of India, Mr. Kunal Kumar IAS delivered the keynote address through Skype at the inaugural session of GBSE2019. Program Chairs, Dr.-Ing. Harald Drück, the Head of TZS, Technical University of Stuttgart, and Dr.-Ing. Varghese Panthaloorkaran, Professor, RSET, introduced GBSE2019 to the august gathering.

Forty-eight technical papers were presented in the conference from institutions ranging from IISc and NITs to other engineering colleges from India after review of 73 submissions. The review panel included eminent academicians and experts in the field of Green Building and Sustainable Engineering from India and abroad including Germany, USA, and China. The papers were presented in eight sessions, namely Digitization of Energy Sector, Renewable Energy Solutions for Smart Cities, Energy Efficient Buildings, Green Manufacturing, Intelligent Technologies for Smart Cities, Environmental Technologies, E-mobility and Sustainable Transportation systems, and Green Materials.

The Indo-German Summit was one of the highlights of GBSE2019, where delegates from some of the renowned industries, academic institutions, and start-ups from India as well as Germany shared their experience on governance, smart solutions, and innovative strategies for smart cities.

As part of GBSE2019, pre-conference workshop held on February 18, 2019, had two sessions. Forenoon session was on the topic “Green Mobility for Smart Cities”

conducted by Mr. Renji V. Chacko, Associate Director, Power Electronics Group, CDAC, Thiruvananthapuram. Afternoon session was on the topic “Laurie Baker Approach” delivered by Ar. R. D. Padma Kumar, Member Secretary, Laurie Baker Centre for Habitat Studies, Thiruvananthapuram.

GBSE2019 included Rajagiri Grand Challenge 2019 based on All Terrain Remote Controlled Car Race. The participants were expected to design remotely operable vehicles that should traverse the tracks with different obstacles and challenges. A total of 114 teams participated in Rajagiri Grand Challenge during GBSE2019.

GBSE2019 Expo had major participation from finishing schools and research centers doing researches on smart technologies and electric vehicles.

We would like to thank all the Steering Committee Members, Technical Committee Members, and Reviewers for their hard work in reviewing papers carefully and rigorously. In addition, we thank all the sponsors of GBSE 2018, especially STEAG Energy Services (India) Pvt. Ltd, NeST Technologies, CIAL Ltd., and Zuari Cement Pvt. Ltd.

We hope that you will find these proceedings to be a valuable resource in your professional, research, and educational activities.

Stuttgart, Germany
Kochi, India
Jaipur, India
Kochi, India

Harald Drück
Varghese Panthaloorkaran
Jyotirmay Mathur
V. M. Sreekumar

Contents

Part I Renewable Energy Solutions for Smart Cities

1	Feasibility Study of Liquid-Based Spectral Beam Splitting Technique for Solar Panel Cooling	3
	Richu Zachariah and V. N. Amalnath	
2	Estimation of Daily Global Solar Radiation (DGSR) in Different Cities of Tamil Nadu	19
	Vishnupriyan Jegadeesan, Arunkumar Jayakumar and K. S. Srinivasan	
3	Solar-Fed Hybrid Modular Multilevel Converter for Motor Drives	35
	Lakshmi Krishnakumar and Elizabeth Rita Samuel	
4	Pine Needles Biomass Gasification Based Electricity Generation for Indian Himalayan Region: Drivers and Barriers	47
	Arvind Singh Bisht and N. S. Thakur	
5	Enhancement of Biofuel Quality Through Sustainable In-bed Additives	61
	Joel George, P. Arun and C. Muraleedharan	
6	Development of a Systematic Design Procedure for Circulating Fluidized Bed Gasifier	71
	P. Suraj, P. Arun and C. Muraleedharan	
7	Analysis of Dynamic Behavior of Fluidized Bed Gasifier Using CFD	85
	Nadeem Abdul Hameed, P. Arun and C. Muraleedharan	
8	Efficiency Improvement of Canal Top Solar Photovoltaic Power Plant with Reflectors	97
	Rani Chacko and Asha Sajimon	

9	Load Frequency Control of Microgrid: A Technical Review	115
	K. S. Rajesh, S. S. Dash and Ragam Rajagopal	
Part II Energy Efficient Buildings and Intelligent Technologies for Smart Cities		
10	ICT as a Tool for the Structured Management of Urban Sprawl	141
	K. S. Krishnaveni and P. P. Anilkumar	
11	Modelling and Simulating the Thermal Comfort Aspects of Natural Ventilated Classrooms in Hot-Humid Climates	161
	P. V. Sasidhar, Kratika Shrivastava and M. Ramgopal	
12	Green Building Rating Systems and Energy Efficiency of a Building from the Building Lifecycle Perspective	173
	Nina Lazar and K. Chithra	
13	Recent Trends in Use of Phase Change Materials for Sustainable Thermal Management of Buildings: A Review	191
	Rohini Sibi, Rajesh Baby and Bennet Kuriakose	
14	Energy Analysis, Simulation, and Comparison of a Commercial Building Using Standard Approach and AECOSim	197
	Geon Clinton, Akshayakumar V. Hanagodimath and Shrihari K. Naik	
15	Effect of Column Configuration on the Behaviour of Stone Column Supported Ground	207
	M. P. Vibhoosha, Anjana Bhasi and Sitaram Nayak	
16	A Novel Machine Learning System to Improve Heart Failure Patients Support	215
	J. Dheebea and J. Jebe Sonia	
17	Study of Air Distribution in Operating Room	227
	M. A. Rinjesh, C. Muraleedharan and V. K. Vikas	
18	Building-Integrated Photovoltaics (BIPV) in India: A Framework for TRIZ-Based Parametric Design	237
	Avantika Srivastava, Tarun Kumar, Kriti Bhalla and Vishal Mishra	
Part III Green Materials and Green Manufacturing		
19	Production of Semi-lightweight Concrete Using Calcite Powder Pellets as Coarse Aggregates	249
	P. Parthiban and J. Karthikeyan	
20	Solar Desalination Using Modified Parabolic Trough Concentrator	257
	D. Deebhesh, B. Sreejith and O. Arjun	

21 Thermal Performance of Loop Heat Pipes Using Nanofluids	273
Jobin Jose and Rajesh Baby	
22 Life Cycle Assessment of Traditional Handloom Silk as Against Power-loom Silks: A Comparison of Socio-economic and Environmental Impacts	283
Kriti Bhalla, Tarun Kumar, Jananee Rangaswamy, Ranjana Siva and Vishal Mishra	
23 Nano Lithium Grease (NLG): Tribological Property Evaluation of Coconut Oil-Based Lithium Grease Added with Ceria Nanoparticles	295
Jibin T. Philip, Chacko Preno Koshy, C. M. Shajahan and Basil Kuriachen	
24 Exploiting the Potentials of Graphene Nano-platelets for the Development of Energy-Efficient Lubricants for Refrigeration Systems	303
S. S. Sanukrishna and M. Jose Prakash	
25 Experimental Study on Mechanical Properties of Areca Nut Fibre-Reinforced Self-compacting Concrete	313
L. Divakar, Abhishek Pulgur Venkatesha Babu, R. K. Chethan Gowda and S. Nithin Kumar	
26 Development of Eco-friendly Geopolymer Concrete Using M-Sand	323
Dhavamani Doss Sakthidoss and Thirugnanasambandam Senniappan	
27 Mechanical and Durability Study of Steel Fiber-Reinforced Geopolymer Concrete	337
Abhishek Pulgur Venkatesha Babu, R. K. Chethan Gowda, L. Divakar, C. Vachan, Rajath Raj, C. H. Sri Karan and R. D. Sayabanna	
28 Performance of Plantain Fibre in Nutmeg Shell Concrete.	343
Elsa Paul, Eami Eldhose, Anju Anna Thomas, Chrismica M. Thomas and Jeena T. Wilson	
29 Performance Evaluation of Composite Shear Wall	353
S. Sariganath and Milu Mary Jacob	
30 Condensation and Associated Microbial Growth in Air-Conditioned Healthcare Facilities in Tropical Climate—A Case Study	371
V. K. Vikas, C. Muraleedharan and B. Hariprasad	
31 Numerical Evaluation of Composite Slabs	381
Ajma Mohan and Milu Mary Jacob	

Part IV Environmental Technologies

- 32 Numerical Investigation on the Temperature Distribution of a Steel Reactor with Copper Bottom Surface for Pyrolysis of Polyethylene Terephthalate Waste Plastics** 397
Anandhu Vijayakumar and Jilse Sebastian
- 33 Soil Organic Carbon Estimation Using Remote Sensing Technique** 405
Akhil Francis, R. Kevin, Girigan Gopi and Rajesh Baby
- 34 Assessment of Water Pollution Using GIS: A Case Study in Periyar River at Eloor Region** 413
K. V. Anjusha, Amala Mareena James, Feby Ann Thankachan, John Benny and V. Bibin Hezakiel
- 35 Scale Control on Pipe Materials: A Review** 421
Namitha Joshy and V. Meera
- 36 Smart and Sustainable Urine-Powered Microbial Fuel Cells Eco-Technology** 431
S. Azhar Mohammed Pillai, N. Madhavan and Arun K. Sundaram
- 37 Gasification of Sawdust in Bubbling Fluidised Bed Gasifier** 441
Jerald Joseph, John Raphael, R. Kevin, Joel George and Vishnu Sankar

Part V Digitization of Energy Sector, E-Mobility and Sustainable Transportation Systems

- 38 Numerical Simulation and Performance Analysis of MLI During Reentry of Hypersonic Vehicles** 453
P. M. Suteesh and Alex Chollackal
- 39 Detachable Module for Semi-automating a Conventional Wheelchair** 463
Ahmed Harris, Allwyn Francis, Amritha Behanan, Arnold Fernandez, Vishnu Sankar and John M. George
- 40 Brainwave-Assisted Drive for Electric Vehicles** 473
Jeffin Francis, Anupama Johnson, N. Aby Biju, Jeswant Mathew, Alan Jones Ukken, P. Jegil Jerson and Vishnu Sankar
- 41 Suitability of an LRT Connecting Thoppumpady and Goshree** 481
Hridya Mary Joseph, Megha Jose Kandappassery, K. R. Malavika, Prinu Varkey and Deepthi I. Gopinath

42 Parameter Study of Electric Vehicle (EV), Hybrid EV and Fuel Cell EV Using Advanced Vehicle Simulator (ADVISOR) for Different Driving Cycles 491
P. K. Prathibha, Elizabeth Rita Samuel and A. Unnikrishnan

43 Pre-feasibility Study on Light Rail Transit Connecting Kakkanad and Padma Junction 505
Lalichan Nithya, A. Aathira, B. Abhilash, John Thomas Joel, Joseph Joseena and Sebastian Angel

About the Editors



Dr.-Ing. Harald Drück is a Mechanical Engineer who has been working at the Institute for Thermodynamics and Thermal Engineering (ITW), today Institute for Building Energetics Thermotechnology and Energy Storage (IGTE), University of Stuttgart for more than 20 years. Since 1999 he has been the Head of the Research and Testing Centre for Solar Thermal Systems (TZS). His main research interests lie in the field of solar thermal technology, focusing on advanced heating and cooling systems, thermal energy storage and the development of performance testing methods as well as energy efficient solar buildings. Harald Drück has authored or co-authored around 300 publications in the field of solar thermal energy and heat storage. He is convener of several German and European working groups related to the standardisation and testing of solar thermal systems and components, such as the Solar Keymark Network, the Global Solar Certification Network and the Solar Certification Fund. He acts as an advisor to several high-level international organisations, is chairman or member of the scientific board of several conferences and workshops and teaches a highly successful postgraduate course on solar thermal energy at the University of Stuttgart. Furthermore he was one of the initiators of the German and European Solar Thermal Technology Platforms and is currently a member of the steering committees of both platforms. In addition to his activities at the University, he is the

Director of SWT – Solar- und Wärmetechnik Stuttgart. SWT is a spin-off company of ITW and is a service provider in the field of solar thermal energy.



Dr. Jyotirmay Mathur is working as Professor in Mechanical Engineering, and Centre for Energy and Environment in Malaviya National Institute of Technology, Jaipur (India). Dr. Mathur works in the field of energy planning and modeling, building energy simulation, energy conservation in buildings, and life cycle assessment of renewable energy systems. He has 70 journal papers, more than 150 talks, several research projects including 5 international collaborative projects besides having supervised 11 Ph.D. scholars in his credit. He is an active member in several professional bodies related to energy management in buildings. Current activities include studies on adaptive thermal comfort, modeling of passive and low energy cooling systems, development of standards and codes for energy efficiency, long term energy system modeling penetration of renewable energy. His research areas include energy efficiency in buildings, passive cooling systems, renewable energy and energy policy modelling, development of codes and standards, low energy cooling.



Dr.-Ing. Varghese Panthalookaran, MSc Professor and Coordinator of Rajagiri Research and Consultancy Center (RRCC) at Rajagiri School of Engineering & Technology (RSET). He acquired a doctoral degree in Mechanical Engineering (Dr.-Ing.) in 2007 from the University of Stuttgart, Germany, where he was also employed as research assistant. He holds a Master degree in Physics from Cochin University of Science and Technology (CUSAT). He has worked as a guest-lecturer in Physics at Sacred Heart College, Thevara. He is a recognized research adviser of Birla Institute of Technology (BIT), Mesra/India. He is also a reviewer for international journals and conferences. He has written three books in three languages. His drama book in Malayalam titled: “Buddhan Veendum Chirikkunnu” (translated: Buddha Laughs Again” has won him the Endowment Award of Kerala Sahitya Academy in 2000. He also have a German book “Die Lehre Jesu als Schluessel zur Lebensfreude” to his credit. He is member of professional bodies like

American Society of Mechanical Engineering (ASME), Institute of Electrical and Electronics Engineers (IEEE) and Indian Society of Technical Education (ISTE). Currently, he also serves as the member of General Department Council for Education and Communication Media of the congregation of the Carmelites of Mary Immaculate (CMI).



Dr. V. M. Sreekumar is currently working as Assistant Professor in the Mechanical Engineering Department, Rajagiri School of Engineering & Technology (RSET), Kochi, India. He completed B.E. in Metallurgical Engineering from National Institute of Technology Durgapur in 2001 and Ph.D in Metallurgical and Materials Engineering from Indian Institute of Technology Kharagpur in 2008. He worked as Post Doctoral Fellow in Deakin University Australia from 2008 to 2011 and Brunel University UK from 2012 to 2015. He has 25 technical publications in National and International Journals and Conference proceedings and reviewed papers in several international Journals. He received life membership from Indian Institute of Metals and Materials Research Society of India and Chartered Engineer certificate from Institution of Engineers India.

Part I
Renewable Energy Solutions for Smart
Cities

Chapter 1

Feasibility Study of Liquid-Based Spectral Beam Splitting Technique for Solar Panel Cooling



Richu Zachariah and V. N. Amalnath

1.1 Introduction

The fossil fuel crisis is an imminent threat to the human race. It can only be tackled with the effective utilization of renewable sources of energy, especially solar. Solar photovoltaic is one of the commonly used techniques for electricity generation from solar energy. A typical polycrystalline PV panel will have the conversion efficiency in the range of 12–17% (Solanki 2015). The performance of the solar PV systems depends on different parameters such as irradiation, dust, clouds, relative humidity, and heat developed in the panels. Power output of PV module is linearly dependent on the cell operating temperature. For each 1 °C rise in temperature, the efficiency of the PV panel decreases by 0.04%. Various correlations of cell temperature for various PV module topologies have been reviewed (Dubey et al. 2013). It includes basic environmental variables for both the system and the parameters such as ambient temperature, local wind speed, solar irradiation, glass cover transmittance, and plate absorbance. The application of these correlations must be put in use only after confirming the system topology and material properties. PV cell temperature is highly sensitive to wind speed, slightly to wind direction, and extremely dependent on solar insolation (Mekhtoub 2014). So, practically it is insensitive to the ambient temperature.

The PV module efficiency is sensitive to the module temperature and the addition of surface cooling resulted in an increase in the module efficiency by 9.2% (Sharma et al. 2015). Research is going on in the back-panel cooling techniques

R. Zachariah (✉)

Department of Mechanical Engineering, Amal Jyothi College of Engineering, Kanjirappally, Kottayam 686518, Kerala, India
e-mail: richuzachariah@gmail.com

V. N. Amalnath

Department of Electrical and Electronics Engineering, Amal Jyothi College of Engineering, Kanjirappally, Kottayam 686518, Kerala, India

(Joy et al. 2016). But, the actual source of this heat generation is the infrared radiations that are there in the sunlight. From the terrestrial solar radiation, PV cell converts only the radiations equivalent to its energy bandgap into electricity, and the rest is lost in the form of heat. Terrestrial solar radiations consist of 43% infrared (IR), 48% visible light (VIS), and remaining are ultraviolet (UV) rays (Solanki 2015). These radiations are in the wavelength range of 250–2500 nm and are not monochromatic (Sukhatme and Naik 2014). The single junction c-Si solar cell has a bandgap of 1.1 eV which corresponds to a wavelength of 1120 nm in the terrestrial solar spectrum. These solar cells perform better when exposed to the solar range of 750–1125 nm (PV band).

The incident radiations, other than the portion used for electricity conversion, will cause heating of the PV module (Heat Generation in PV Modules 2017). The factors which contribute to the heat generation are the reflection from the top surface of the module, its electrical operating point, sunlight absorption by the solar cell and the regions not covered by the cells, absorption of infrared (low energy) light, and the packing density of the solar cells. The infrared radiations having wavelength above 1125 nm in the solar spectrum is the primary cause for the heating of PV modules.

Water is observed as the best absorber with 13% absorption compared to Ethylene Glycol (EG), Propylene Glycol (PG), and Therminol VP-1 heat transfer fluids for thicknesses 0.1, 2, and 10 mm, but still a weak absorber (Otanicar et al. 2009). Propylene glycol (PG) exhibits better properties for spectral splitting applications over various heat transfer fluids as per different studies conducted. It transmits about 77% of light in the wavelength range 700–1100 nm (Mojiri et al. 2016). It has higher refractive indices over water. It is comparatively nontoxic to ethylene glycol and has better thermal conductivity and specific heat. The higher density and viscosity of PG introduces additional requirements for a stronger hydraulic system (Looser et al. 2014). It is observed that there is a 3.46% reduction in performance for a 3-month-old aged PG than a new PG (Stanley et al. 2016). The thermophysical properties of fluids can be increased by suspending nanoparticles in it. Addition of nanoparticles such as carbon nanotube, graphite, and silver with the base fluids are tested for various particle sizes and a fraction of volumes exhibits a collector efficiency improvement up to 5% (Otanicar et al. 2010). An optimization study revealed that, at the most, a volume fraction of 0.0011% of nanofluid is required to achieve optimum filters for PV/T applications (Taylor et al. 2012) and has an advantage that magnetic/electric fields can easily control them, making them ideal for applications during its operation.

The electrical performance of a c-Si solar PV cell with tap water, coconut oil, and transformer oil filters is better than using Ethylene glycol (EG), Glycerin (GL), Rice bran oil (RB), Coconut oil (CO), and Al_2O_3 nanofluid with spectrum beam splitting approach (Joshi et al. 2016). The extended study (Joshi and Dhoble 2017) on a 10 W PV panel with fluid filters like coconut oil, water, and silicone oil under natural daylight exhibits an increase in its total efficiency considering both the electrical and thermal performance. But, the electrical efficiency is reduced after

adding the filter. Coconut oil shows better performance as a fluid filter considering both electrical and thermal output.

Spectral band splitting employed for a non-tracking hybrid PV/T collector for building applications (Ulavi et al. 2014) provides 20% more total energy conversion efficiency than an independent PV and solar thermal module of equivalent area. Wavelength selective film is coated with a compound parabolic concentrator. This hybrid system exhibits lower individual PV electrical (35% drop) and thermal efficiency.

A new concept of PV/T collector called Thermal Electrical Solar Photovoltaic Integration (TESPI) panel in which a fluid cabin is having a fluid thickness of 2.5 cm is placed on top of the PV module without any air gap between the module and fluid cabin is developed (Colangelo et al. 2015). Higher gain in efficiency of the system is obtained for lower wind speed and overall vertical position.

1.2 Conceptual System

A schematic diagram of the conceptual PV/T system is shown in Fig. 1.1. A layer of a suitable liquid filled in a cabin (glass or acrylic) is placed over the top surface of the module for beam splitting application. The fluid is expected to have circulation from and to the storage tank by a mechanism of thermosyphon. In the cabin, there will be a cold fluid inlet at the bottom end and a hot fluid outlet at the top end. The fluid filter placed on top of the module will transmit radiation in the PV band and absorb the IR part of radiation for reducing the PV temperature. The absorbed radiation can be used for thermal applications such as water heating. Selection of best fluid, the optimum fluid thickness as well as the air gap length will be based on

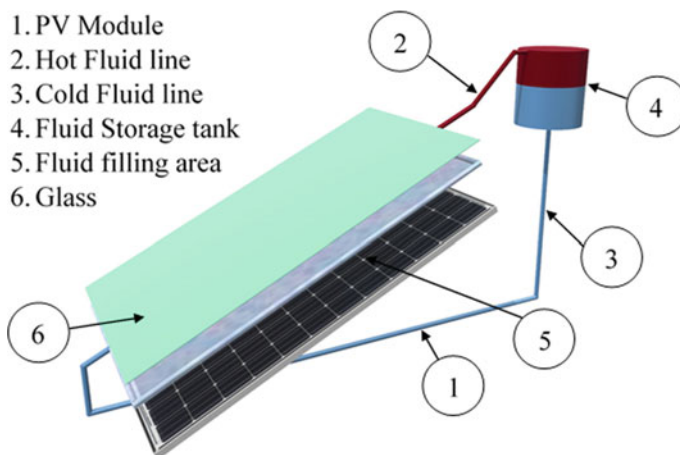


Fig. 1.1 Schematic of the conceptual PV/T system

the experimental analysis to be carried out. The initial evaluation for making the conceptual system is carried out by this analysis.

1.3 Experimental Setup and Measurements

This study involves the analysis of various temperature values in a PV module, report of the optical property of multiple fluids, analysis of the effect of the fluid filter on PV modules. The studies are done on a solar PV cell simulator (Fig. 1.5) and modules under ambient conditions. c-Si PV cell, 10 and 100 W polycrystalline modules are used for the study. Specifications of the PV modules are shown in Table 1.1.

To study the effect of different temperatures on a module, PV top temperature, bottom temperature along with the ambient temperature are measured. The top surface and the bottom surface temperatures of the module with the loaded and unloaded condition, with and without glass cabin (Fig. 1.2) are measured.

The fluids having a better optical property such as tap water, coconut oil, transformer oil, mineral oil, and propylene glycol (PG) are selected for analyzing its optical property (transmission and absorption), using a spectrophotometer, for a fluid thickness of 1 cm in the wavelength 250–2500 nm. Transmission and absorption are calculated as per Eqs. (1.1) and (1.2) (Spectrophotometry 2017).

$$T = \left(\frac{I}{I_0} \right) \times 100 \quad (1.1)$$

$$\text{Abs} = -\log_{10} \left(\frac{T}{100} \right) \quad (1.2)$$

Table 1.1 Specifications of modules used for experimentation

Specification	Values	
	Waaree	Sunsolar
Maximum power (P_{MP})	10 W	100 W
Voltage at P_{MP} (V_{MP})	17.03 V	17.2 V
Current at P_{MP} (I_{MP})	0.59 A	5.81 A
Open circuit voltage (V_{OC})	21.07 V	21.6 V
Short circuit current (I_{SC})	0.63 A	6.52 A
Module efficiency	9.52%	15.15%
Temperature coefficient of voltage	-0.2941%/°C	-0.361%/°C
Temperature coefficient of current	0.0681%/°C	0.102%/°C
Temperature coefficient of power	-0.3845%/°C	-0.48%/°C

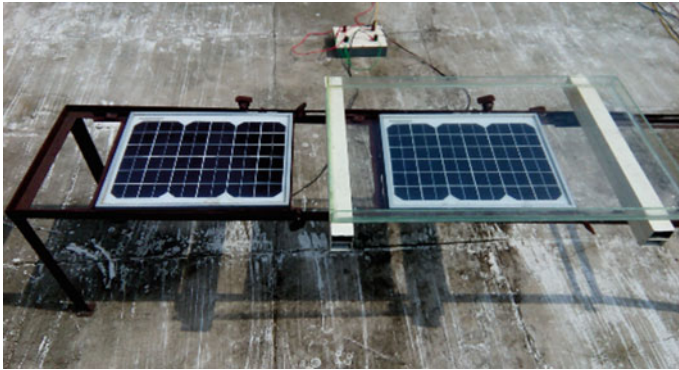


Fig. 1.2 Experimental setup to find the effect of temperature on PV with empty glass cabin

where I is the amount of light transmitted through the filter and I_0 is the amount of light transmitted through the reference medium.

The power output of PV is analyzed for different PV cell/module and filter arrangements. The schematic explanation of the study on PV cell/module with fluid filter is shown in Fig. 1.3. The radiation (G_1) incident on top of the liquid filter with a thickness FT is transmitted (G_2) to the PV top surface. An air gap (AG) is provided between the filter and PV.

The experimental arrangement of the PV module and the liquid filter for different observations are shown in Fig. 1.4b. The mode of study includes the following: PV cell power output for various fluid filters using solar cell simulator; 10 W PV power output with different selected fluid filters; 10 W PV power output with the best fluid filter having fluid at various thicknesses; 10 W PV power output and temperature measurement with the best fluid filter at various air gap length; and observing the performance of a 100 W PV using the best fluid filter with optimum thickness and air gap length. The power and efficiency of the PV panel are calculated based on Eqs. (1.3) and (1.4).

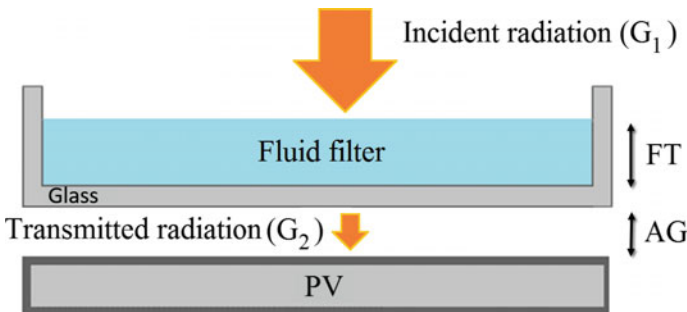


Fig. 1.3 Schematic view of filter study on solar PV

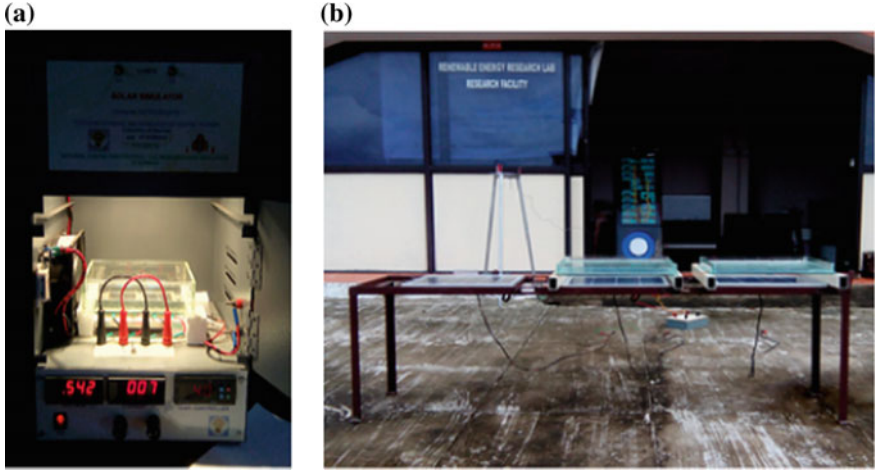


Fig. 1.4 **a** Solar cell simulator, **b** filter arrangement on PV module

$$P_{mp} = V_{mp} \times I_{mp} \quad (1.3)$$

$$\eta_{PV} = \frac{P_{mp}}{G \times A_{PV}} \times 100 \quad (1.4)$$

where V_{mp} and I_{mp} are the voltage and current at maximum power point P_{mp} for particular irradiation. A_{PV} is the area of the PV module.

1.3.1 Uncertainty Analysis

The uncertainty of the PV module power is calculated using Eq. (1.5) and that of its efficiency is calculated using Eq. (1.6). An uncertainty of 0.49 W is attained for PV module power and 0.15% for its efficiency.

$$U_{Power} = P_{mp} \sqrt{\left(\frac{\Delta V_{mp}}{V_{mp}}\right)^2 + \left(\frac{\Delta I_{mp}}{I_{mp}}\right)^2} \quad (1.5)$$

$$U_{Efficiency} = \eta_{PV} \sqrt{\left(\frac{V_{mp}}{V_{mp}}\right)^2 + \left(\frac{I_{mp}}{I_{mp}}\right)^2 + \left(\frac{\Delta G}{G}\right)^2 + \left(\frac{\Delta A_{PV}}{A_{PV}}\right)^2} \quad (1.6)$$

1.4 Results and Discussion

To aid the construction of the proposed prototype, the results from the above experiments are analyzed.

1.4.1 Effect of Temperature on the PV Module

The temperature at the top and bottom part of the PV panel is analyzed for the ambient temperature in Fig. 1.5. PV top temperature is higher than the ambient temperature with a maximum difference of 13 °C. Similarly, bottom temperature is higher than the top temperature with a maximum difference of 15 °C. The higher temperature in the bottom surface might be due to the presence of electrical cell contacts, PV material property, reduced air movement, etc.

There may be variations in PV temperature due to variation in load and addition of a filter. To study the effect of load on PV temperature, top and bottom temperatures of a 100 W PV are observed for a day for both the loaded and unloaded conditions. The observations are shown in Fig. 1.6. For the open-circuited PV, both the top and bottom temperature values are the same because the heat generation is happening only due to the absorption of radiation by the PV material. But an

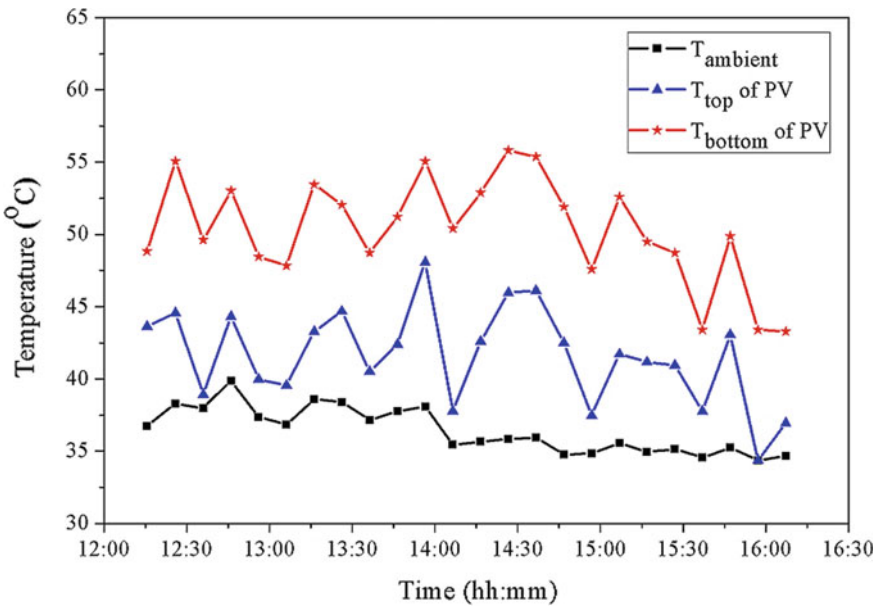


Fig. 1.5 The ambient, top surface, and bottom surface temperature of the 100 W PV

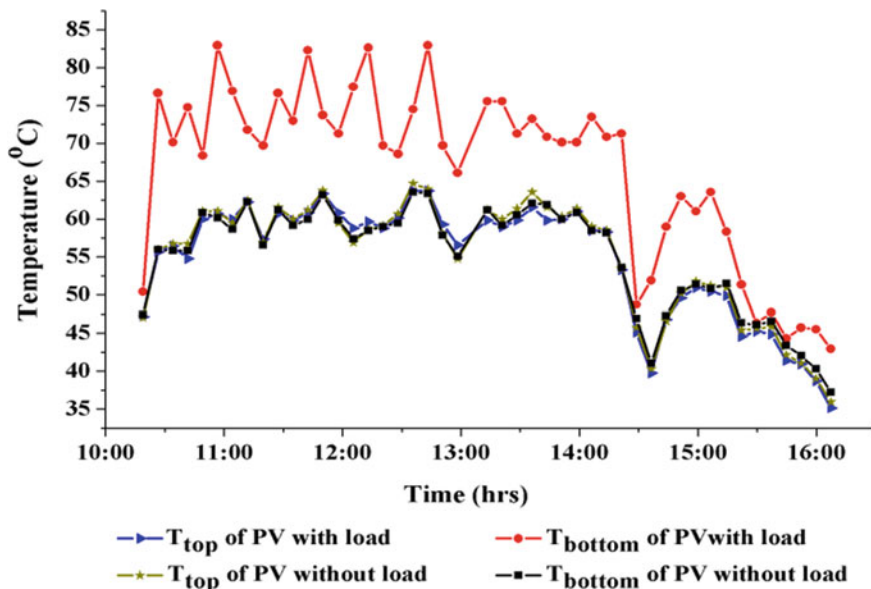


Fig. 1.6 Top surface temperature and the bottom surface temperature of the 100 W PV on loaded and unloaded condition

increase of 30 °C is observed in the bottom temperature as compared to the top when the PV is loaded.

Effect of glass on PV performance as a filter is analyzed by studying the temperature variations and the power output. It is observed that there is no change in the panel top temperature while using the filter as shown in Fig. 1.7a. This may be due to the reduced air movement at its top surface and increased the temperature in the medium between the glass and module, generated by continuous internal

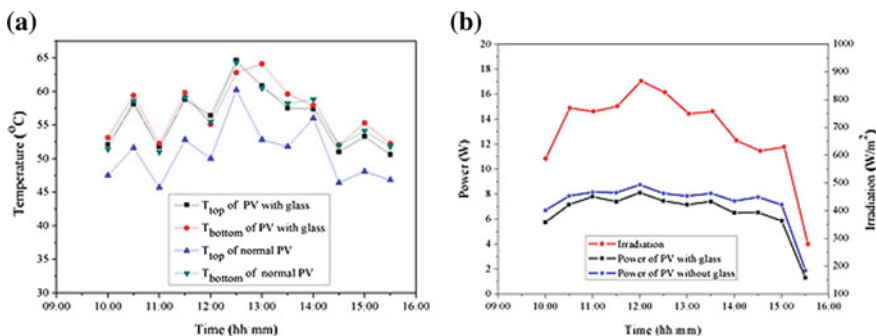


Fig. 1.7 a Top and bottom surface temperature, b irradiation and power output for a 10 W PV with and without empty glass cabin

reflections. For uniformly loaded modules with and without glass filter, power output is higher for the normal module as shown in Fig. 1.7b. This might be due to the reflection and reduced transmission of light through the glass.

1.4.2 Study of Fluids

To choose a suitable fluid for the beam splitting application which is to be employed on the suggested PV/T system, a fluid feasibility test is carried out. Analyzing the optical property of the fluids is the initial study. Transmission and absorption of light in the wavelength range of 250–2500 nm were observed for the selected fluids with a thickness of 1 cm using a spectrophotometer, having 1 nm precision. Ideal fluid should transmit radiation within the PV band (750–1125) and should absorb the infrared radiation, for spectral beam splitting application.

The absorption characteristics of fluids in the total solar spectrum and the infrared region are shown in Fig. 1.8. Transmission characteristics of fluids in the total solar spectrum and the PV band are shown in Fig. 1.9. Since UV rays do not contribute to the heating up of PV, they are not taken into consideration.

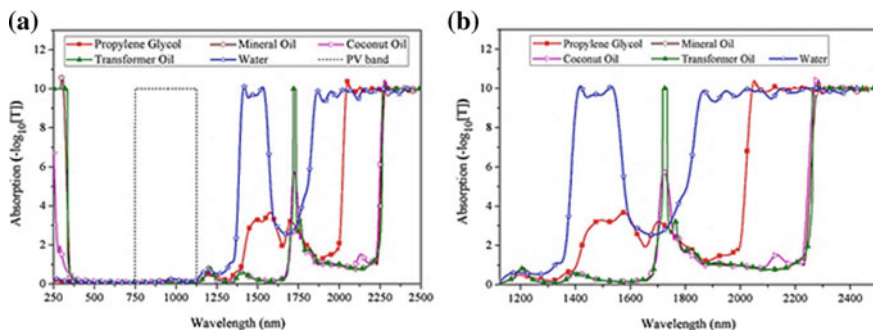


Fig. 1.8 Absorption of the selected fluids tested on a spectrophotometer

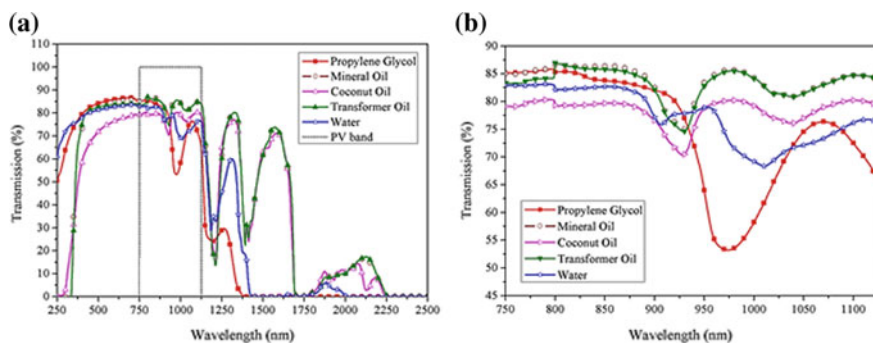


Fig. 1.9 Transmission of fluids in the PV band

Table 1.2 Cost of the fluids

Fluids	Rs/Liter
Propylene glycol (industrial grade)	900
Mineral oil	250
Coconut oil	150
Transformer oil	120
Water (bottled)	20

From the test results, it is observed that transformer oil has a better transmission in the PV band. Transformer oil and mineral oil have almost the same characteristics. So, mineral oil is not taken for the PV studies. In the absorption part of the IR region, water and propylene glycol (PG) show better absorption. PG is the costliest and water is the cheapest among the selected fluids. Usage of PG, as a heat transfer fluid, will increase the system cost by 45% so an additional cost will be needed for installing a separate heat exchanger if the fluid is not water. The cost of the fluids per liter is given in Table 1.2.

1.4.3 Effect of Fluid Filter on PV

PV characteristics of the solar cell providing halogen light irradiation of 800 W/m^2 and maintaining constant cell temperature of 40°C for a solar cell with and without fluid filters are shown in Fig. 1.10.

It can be seen that the solar cell with an empty glass cabin on top, reduces its power output to 79%. This is due to the reflection of radiation by the glass material. Usage of the antireflective coating can improve the performance further, but they are expensive. It is observed that the water filter is having better performance for the solar cell. So, water is selected as a filter for further studies.

The performance of a solar cell with a water filter is studied for various thicknesses as shown in Fig. 1.11. As can be seen, water at 1 cm exhibits a better power output of 85% to that of a normal cell. The power output of the cell with the different filter configurations is shown in Table 1.3 where the power output of a normal solar cell is taken as 100%.

Further studies were carried out on a 10 W PV module under natural sunlight. Filter configurations are tested for 1 cm fluid thickness and 2.5 cm air gap (AG). Propylene glycol is not taken for the present study considering its poor optical performance and non-feasibility due to higher cost. The performance of 10 W modules is tested for a day with different fluid filters (water, coconut oil, and transformer oil) and compared with a 10 W solar module without the filter. As shown in Fig. 1.12, the module with water filter is giving better performance compared to the other configurations. Modules are placed at 0° tilting and with no mechanical tracking. Hence the readings taken from 11.30 AM to 1.30 PM are used to evaluate the performance.

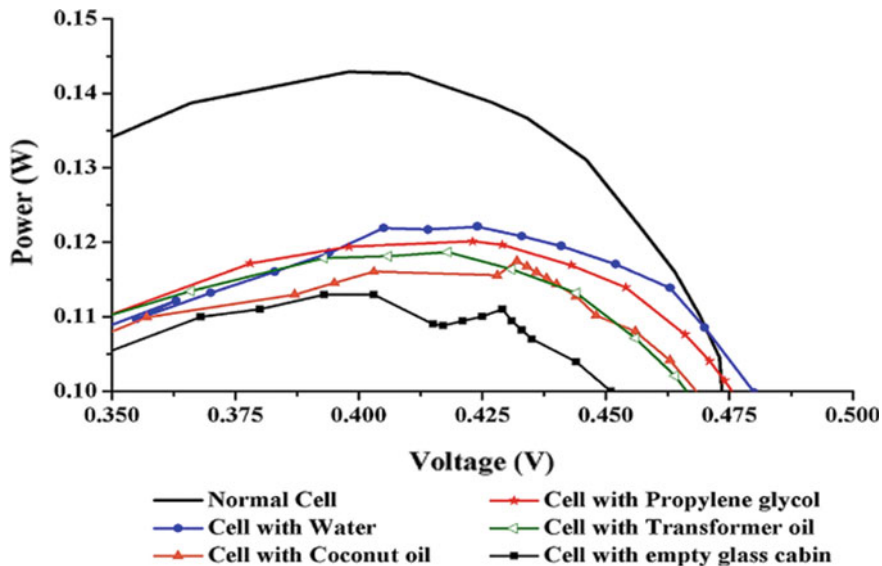


Fig. 1.10 PV characteristics of normal solar cell and cell with different fluid filters

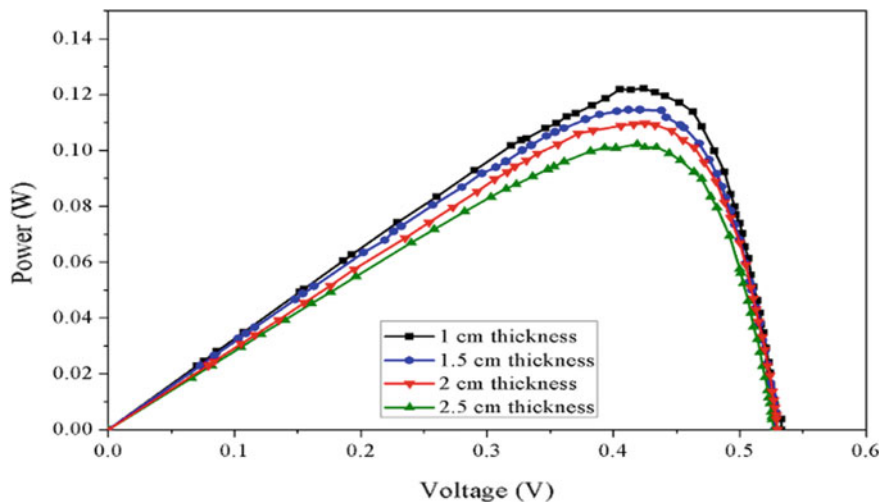


Fig. 1.11 Solar cell PV characteristics with water filter for various thicknesses

To study the effect of glass cabin on the performance of the PV module, a 10 W cabin is tested with an empty glass cabin and compared with the normal PV module of the same specifications. It is found that with the introduction of a glass layer on top of the PV module, the power output is reduced to 92% to that of a normal one.

Table 1.3 The power output of solar cell tested on the simulator with various filters

Filter configuration	Power output (W)	Percentage output (%)
Normal cell	0.143	100
Water at 1 cm thickness	0.122	85
Propylene glycol at 1 cm thickness	0.120	84
Transformer oil at 1 cm thickness	0.119	83
Coconut oil at 1 cm thickness	0.116	81
Water at 1.5 cm thickness	0.115	80
Empty glass cabin	0.113	79
Water at 2 cm thickness	0.110	77
Water at 2.5 cm thickness	0.102	71

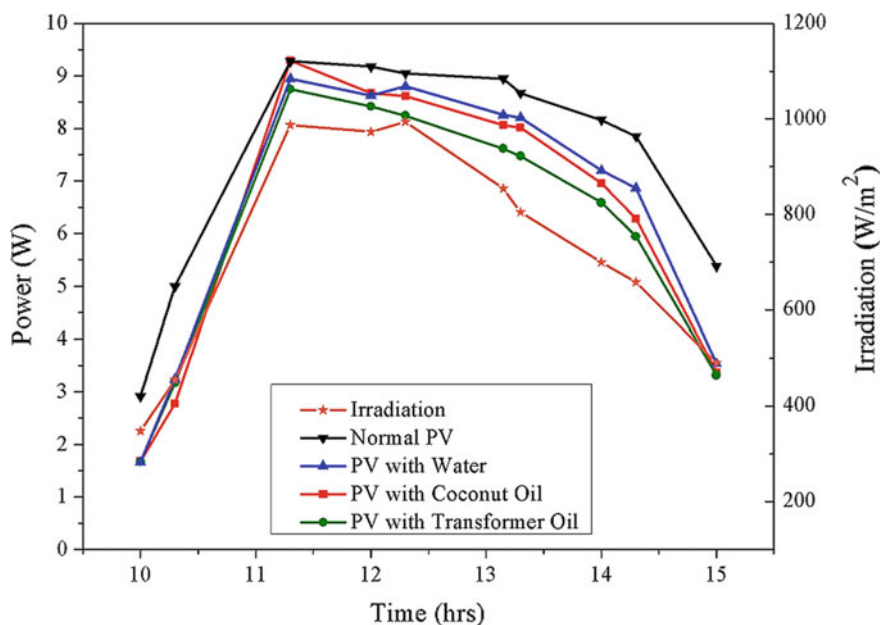


Fig. 1.12 The power output of the normal 10 W module and module with different fluid filters

From the preliminary studies, it is found that water is giving better performance as a fluid filter. So, it is again tested for varying air gap, and fluid thickness and the results are shown in Fig. 1.13. Efficiency-1 represents the efficiency of the module for the normal incident radiation. Efficiency-2 is the efficiency of the module with the filter concerning the transmitted radiation incident on the top of the filter. Efficiency-1 is higher for the normal module and reduced after adding the filter. This can be due to the introduction of a glass layer into the radiation path. As can be seen, the efficiency is reducing as the fluid thickness and air gap increases. So, the

fluid thickness of the fluid layer should be optimum. A thickness of 1 cm is showing better performance in the present study. From Fig. 1.13, it is observed that the air gap should be kept minimum for good results. But the minimum air gap possible in the given scenario was restricted to 2.5 cm due to the insertion of lux meter for getting filtered radiation. Also, as the air gap is increased beyond a limit, there may be a chance for shading the PV panel by the filter cabin, which will reduce the performance further by during the morning and evening hours of the day.

As per the study conducted on PV cell and 10 W PV modules, further analysis was carried out on a 100 W panel with water as a filter. The performance of a 100 W panel is observed with a water filter of fluid thickness 1 cm and an air gap of 2.5 cm in comparison with a normal PV panel. The variations in the temperature on the top and the bottom side of the PV panel with filter and that of the normal PV are shown in Fig. 1.14a. Top temperature of both the panels with and without a filter is almost the same, but there is a difference of 10–20 °C in bottom temperatures. Bottom temperature of the panel with filter is lower than that of the normal one. The water filter absorbs or filters the IR radiations which cause a reduction in the bottom temperature of the PV system.

Figure 1.14c shows the power output from a 100 W panel with and without the water filter. The power output of the normal panel is higher than that of the panel with the filter. This is because the amount of filtered radiation is only 80–87% of incident radiation without the filter. So, the power output of the panel with filter is also reduced by 80–87% to that of the normal panel.

The Efficiency-2 (the efficiency of PV panel with a filter for the incident radiation on top of the filter) of the panel is reduced by 80–87% to the Efficiency-1 (the efficiency of normal PV panel for the incident radiation) which is equivalent to the percentile reduction in transmitted radiation. Efficiency-3 (the efficiency of the PV panel with a filter for the radiation transmitted by the screen) is improved by 5%

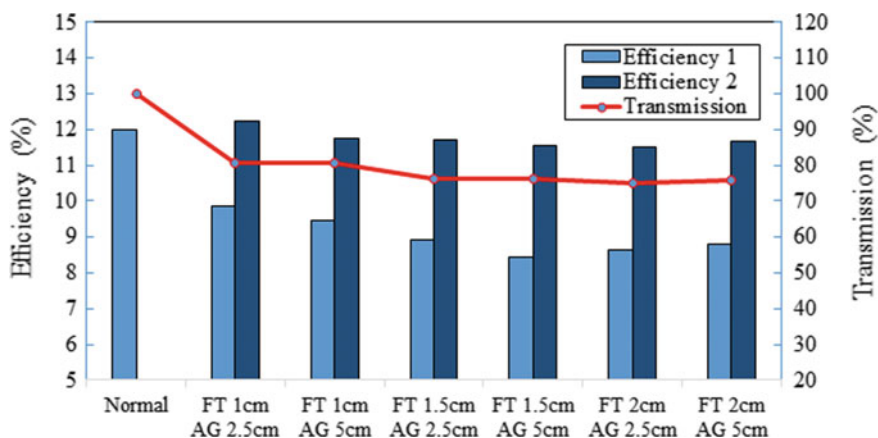


Fig. 1.13 Efficiency and the percentage transmittance of radiation for a 10 W PV tested under sunlight with a water filter for various thickness and air gap

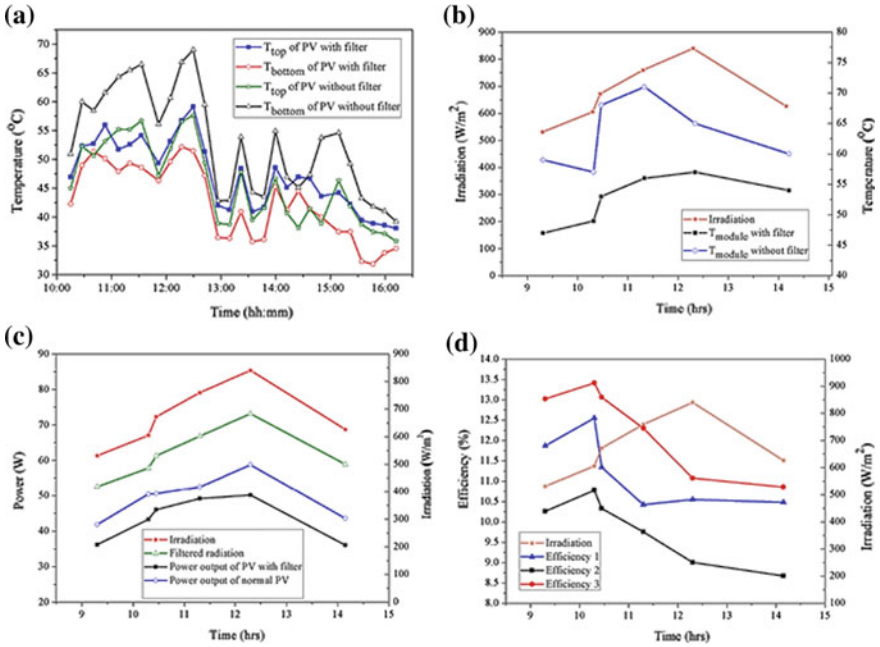


Fig. 1.14 100 W PV experimental results **a** top and bottom surfaces temperature, **b** irradiation and module temperature, **c** irradiation and power output, **d** irradiation and different efficiencies

compared to Efficiency-1. This system will become feasible if the thermal output also is considered. The water used as a filter can be used as preheated water for meeting the hot water requirements in the building. Figure 1.14b–d shows the variations in temperature, power output, and efficiency, respectively, for 100 W panels with and without a filter. It can be noted that as the radiation increases, the power output is more but the temperature buildup is there. For the panel with a filter, this temperature buildup is less as compared to that without the filter. The temperature of the module with filter is reduced by 8 °C with 81% of incident radiation; the power output is 86% to that of the standard panel output. The reduction in power output is due to the filtering of useful radiations by the glass layer. This can be avoided if the glass layer is removed and the water layer is integrated with the PV panel as suggested in the conceptual system.

1.5 Conclusions

The feasibility of using fluid filters for improving the performance of PV systems is investigated. Among the selected fluids, water exhibits better performance for PV cells. From the studies conducted on PV systems, it is noticed that the PV bottom

temperature is higher than the top temperature due to decreased convection rate and the resistive loss occurring at the bottom surface with a maximum difference of 13 °C. Bottom temperature of loaded PV is higher than that of unloaded PV due to the resistive losses at the bottom with a maximum deviation of 30 °C. Top temperature of PV with glass cabin is higher than that of a standard PV due to the greenhouse effect with a maximum difference of 7.5 °C and its power output is reduced by 7–15% due to the optical property of glass. As the water thickness increase or air gap increases, transmitted radiation is reduced to 87–80% of incident radiation and thus the power output is reduced to 85–80% of normal module power. Bottom temperature of 100 W PV with a water filter for FT 1 cm and AG 2.5 cm is lower than normal PV with a maximum difference of 30 °C due to the absorption of IR radiation by water while the top temperature for both the modules is the same. The efficiency of PV with the filter for transmitted radiation is increased by 5% and the temperature is reduced to a maximum of 30 °C than normal PV. Still, there is a reduction in power output up to 86%, which can be reduced by removing the glass layer and integrating filter into the panel as suggested in this paper. Reduction in PV temperature improves the power output and life period of the PV module. Considering the thermal output also from the system, it stands a viable option for future applications.

Acknowledgements The authors wish to thank the Principal, Amal Jyothi College of Engineering and the Management of the college for their support.

References

- Colangelo G, Romano D, Marco Tina G (2015) Performance evaluation of a new type of combined photovoltaic–thermal solar collector. *J Sol Energy Eng* 137
- Dubey S, Sarvaiya JN, Seshadri B (2013) Temp dependent photovoltaic (PV) efficiency and its effect on PV production in the world—a review. *Energy Procedia* 33:311–321
- Heat Generation in PV Modules (2017). <http://pveducation.org/pvcdrom/modules/heat-generation-in-pv-modules>. Last accessed 20 May 2017
- Joshi SS, Dhoble AS (2017) Experimental investigation of solar photovoltaic thermal system using water, coconut oil and silicone oil as spectrum filters. *J Brazilian Soc Mech Sci Eng*
- Joshi SS, Dhoble AS, Jiwanapurkar PR (2016) Investigations of different liquid based spectrum beam splitters for combined solar photovoltaic thermal systems. *J Sol Energy Eng* 138
- Joy B, Philip J, Zachariah R (2016) Investigations on serpentine tube type solar photovoltaic/thermal collector with different heat transfer fluids: experiment and numerical analysis. *Sol Energy* 140:12–20
- Looser R, Vivar M, Everett V (2014) Spectral characterisation and long-term performance analysis of various commercial heat transfer fluids (HTF) as direct-absorption filters for CPV-T beam-splitting applications. *Appl Energy* 113:1496–1511
- Mekhtoub FBS (2014) PV cell temperature/PV power output relationships homer methodology calculation. *Ipcos* 2:1–12
- Mojiri A, Stanley C, Rodriguez-Sanchez D, Everett V, Blakers A, Rosengarten G (2016) A spectral-splitting PV-thermal volumetric solar receiver. *Appl Energy* 169:63–71
- Otanicar TP, Phelan PE, Golden JS (2009) Optical properties of liquids for direct absorption solar thermal energy systems. *Sol Energy* 83:969–977

- Otanicar TP, Phelan PE, Prasher RS, Rosengarten G, Taylor RA (2010) Nanofluid-based direct absorption solar collector. *J Renew Sustain Energy* 2
- Sharma M, Bansal K, Buddhi D (2015) Operating temperature of PV module modified with surface cooling unit in real time condition. In: India international conference on power electronics, IICPE 2015
- Solanki CS (2015) *Solar photovoltaics: fundamental, technologies and applications*, 3rd edn. PHI Learning Private Limited, Delhi
- Spectrophotometry. http://web.mst.edu/~gbert/Color_Lg/spec/Aspec.html. Last accessed 12 Jan 2017
- Stanley C, Mojiri A, Rahat M, Blakers A, Rosengarten G (2016) Performance testing of a spectral beam splitting hybrid PVT solar receiver for linear concentrators. *Appl Energy* 168:303–313
- Sukhatme SP, Naik JK (2014) *Solar energy principles of thermal collection and storage*. Mc Graw Hill
- Taylor RA, Otanicar T, Rosengarten G (2012) Nanofluid-based optical filter optimization for PV/T systems. *Light Sci Appl* 1:e34
- Ulavi TU, Davidson JH, Hebrink T (2014) Analysis of a hybrid PV/T concept based on wavelength selective mirror films. *J Sol Energy Eng* 136

Chapter 2

Estimation of Daily Global Solar Radiation (DGSR) in Different Cities of Tamil Nadu



Vishnupriyan Jegadeesan, Arunkumar Jayakumar
and K. S. Srinivasan

2.1 Introduction

Energy and the environment are mutually dependent in many aspects, specifically in relation to sustainability (Arunkumar et al. 2017). Solar based PV is a prospective energy system that can lead to sustainability in an economical manner. Daily Global Solar Radiation (DGSR) estimation for a selected location could be an important parameter within the modeling of the PV system. To develop the solar radiation models, information should be collected from the meteorological stations and is applied to estimate solar radiation where there is no observatory (Vishnupriyan and Manoharan 2018).

Quej et al. (2017) have conceived the prediction of the DGSR, and a curve fitting analysis and regression coefficient of solar radiation have been evaluated for different models. Kalogirou et al. (2017) have analyzed the hourly global solar radiation and in their work; a clearness index is used as input variables to analyze the frequency distribution of daily global irradiation and hourly irradiation. Vakili et al. (2017) have proposed the estimation of DGSR using an Artificial Neural Network based on meteorological data. In their work, the best model for developing a neural network is analyzed for more accuracy and reliable prediction of solar radiation.

Jeong et al. (2017) have proposed the relation between geostatistical and stochastic interpolation simulation and subsequently inferred that the geostatistical interpolation has been suggested once the gap between the topographic point and nearest neighbor's station is shorter. On the contrary, the stochastic interpolation is recommended when the relative distance is longer.

Baser and Demirhan (2017) analyzed the estimation of yearly mean daily horizontal global solar radiation through a fuzzy based mostly regression. In this work, the different modeling-based artificial intelligence approaches such as ANFIS,

V. Jegadeesan · A. Jayakumar (✉) · K. S. Srinivasan
Chennai Institute of Technology, Chennai 600069, India
e-mail: arunkumarj@citchennai.net

SVM, and ANN are analyzed. The exploratory variables are temperature, longitude, latitude, relative humidity, and altitude.

Sharma and Kakkar (2017) have forecasted solar irradiance estimation using time series analysis. For a medium and long run, the set of most similar days has been taken for forecasting solar radiation. A pro-energy algorithm is found to be compatible with long-run prognostication horizons. Jamil and Akhtar (2017) have proposed the estimation of monthly mean diffused solar radiation and analyzed that single input predictor clearness indexes are often used for the estimation of solar radiation based on the training and testing dataset model.

Jiang and Dong (2017) have forecasted the global horizontal radiation using forward regression on a quadratic kernel support vector machine. In this work, they focused on reducing the number of input parameters by selecting significant variables.

Chandel and Yadav (2017) have proposed the hybrid photovoltaic—wind system as the backup system for hydropower using ANN. The different input variables have been taken for both solar and wind systems. In addition, they also extended the methodology for the optimization of the system based on the need of demand. Jamil and Siddiqui (2017) have proposed the estimation of diffused solar radiation and furthermore developed an empirical model. Large data are used to estimate global solar radiation for different latitude variation. There are several meteorological and geographical variables, which impact solar radiation models.

Most of the literature focuses on the estimation of the monthly average DGSR. However, those models are not focused on south Indian regions, particularly at totally different latitudes, wherever an excellent potential of solar power exists.

2.2 Research Objective

To overcome the above drawbacks, a replacement approach was proposed to frame a solar radiation model using the pyrometer. Irradiance values more than 120 W/m^2 are considered as approximate bright sunshine for that day. The estimation of global solar radiation model is developed using air temperature instead of bright sunshine hours. The prime objectives of the investigation are

- To estimate the daily DGSR, where there is no observatory station exit.
- To evaluate the DGSR models for the warm–humid region.
- To reduce the dimensionality of the data.
- To select the most appropriate input parameters.
- To validate the GSR with experimental data.

In this present work, the cities that are chosen are Madurai, Chennai, Trichy, and Coimbatore which are identified based on different latitudes. Resource data are collected from Tamil Nadu Agricultural University, Ministry of New and

Renewable Energy (MNRE), and from National Renewable Energy Laboratory (NREL).

The collection of resource data is maximum temperature, minimum temperature, day length, latitude, longitude, month, relative humidity, and solar radiation. The most influencing input variables are selected by using the WEKA software. These models are validated using the testing dataset and finally, the best models are selected by using a statistical indicator such as MAPE, MAE, RMSE, and regression coefficient R . Figure 2.1 illustrates the study location of ten smart cities in Tamil Nadu.

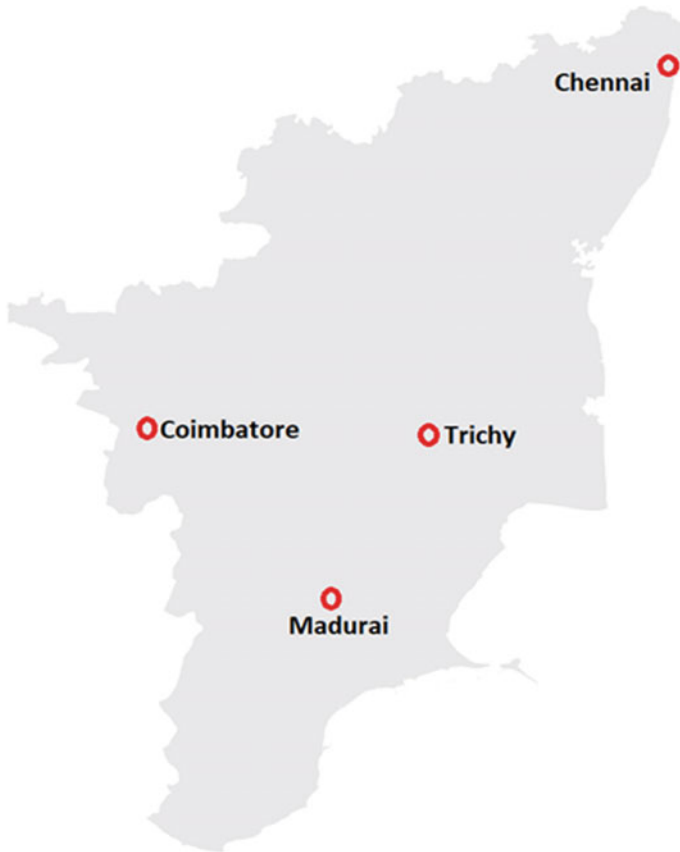


Fig. 2.1 South-Indian region under investigation (not to scale)

2.3 Models Development

2.3.1 Model Description

In the present study, to improve the accurate estimation, the performances of all developed models are analyzed by using statistical tools in regression analysis, Artificial Neural Network (ANN) and the CurveExpert simulation software. Initially, the input data is collected from Tamil Nadu Agriculture University and the different empirical models have been developed with different software. The best model was selected based on the accuracy which is evaluated with statistical indicator, namely mean square error, mean absolute percentage error, mean absolute error, root mean square error, and adjusted R^2 . The accuracy of the model can be enhanced by adjusting the weight and modifying the rules. The selected model is validated for the present location.

2.3.2 Evaluation Criteria

Model performance is evaluated with metrics that include the mean absolute percentage error (MAPE), root mean square error (RMSE), mean square error (MSE), mean absolute error (MAE), and coefficient of determination (R^2).

2.3.3 Sunshine-Based Models

Table 2.1 shows the empirical models using single input variables. Eight of the models that estimate GSR from bright sunshine hours and sunshine ratio are used as the key input parameter.

2.3.4 Temperature-Based Models

The four temperature-based empirical models are shown in Table 2.2.

2.3.5 Hybrid Model

The models presented in this category make use of more than one meteorological parameter for estimating the solar radiation. Table 2.3 shows the three hybrid models developed by using the temperature ratio.

Table 2.1 Different models for estimating the DGSR

Type	Equation
S1 model	$\frac{\bar{H}}{H_0} = a + b \left(\frac{\bar{s}}{s_0}\right)$
S2 model	$\frac{\bar{H}}{H_0} = a + b \left(\frac{\bar{s}}{s_0}\right) + c \left(\frac{\bar{s}}{s_0}\right)^2$
S3 model	$\frac{\bar{H}}{H_0} = a + b \left(\frac{\bar{s}}{s_0}\right) + c \left(\frac{\bar{s}}{s_0}\right)^2 + d \left(\frac{\bar{s}}{s_0}\right)^3$
S4 model	$\frac{\bar{H}}{H_0} = a \left(\frac{\bar{s}}{s_0}\right)^b$
S5 model	$\frac{\bar{H}}{H_0} = a + b \log \left(\frac{\bar{s}}{s_0}\right)$
S6 model	$\frac{\bar{H}}{H_0} = a + b \exp \left(\frac{\bar{s}}{s_0}\right)$
S7 model	$\frac{\bar{H}}{H_0} = a \exp \left(\frac{\bar{s}}{s_0}\right)^b$
S8 model	$\frac{\bar{H}}{H_0} = a \cos \varphi + b \left(\frac{\bar{s}}{s_0}\right)$

Table 2.2 Four temperature-based empirical models

Type	Equation
T1 model	$\frac{\bar{H}}{H_0} = a(T_{\max} - T_{\min})^{0.5} + b$
T2 model	$\frac{\bar{H}}{H_0} = a(T_{\max} - T_{\min})^{0.5} + b$
T3 model	$\frac{\bar{H}}{H_0} = a \ln(T_{\max} - T_{\min}) + b$
T4 model	$\frac{\bar{H}}{H_0} = \left(a + b \left(\frac{T_{\min}}{T_{\max}}\right)\right) \left(\frac{T_{\min}}{T_{\max}}\right)^c$

Table 2.3 Hybrid model for estimating the DGSR

Type	Equation
H1 model	$\frac{\bar{H}}{H_0} = a + b \left(\frac{\bar{s}}{s_0}\right) + c \left(\frac{T_{\min}}{T_{\max}}\right) + d(RH)$
H2 model	$\frac{\bar{H}}{H_0} = a + b \left(\frac{\bar{s}}{s_0}\right) + c \left(\frac{T_{\min}}{T_{\max}}\right)$
H3 model	$\frac{\bar{H}}{H_0} = a + b \left(\frac{\bar{s}}{s_0}\right) + c(RH)$

2.4 Model Description ANN

ANN is an intelligent system that imitates the behavior of the functional elements of the human brain, namely the neurons. Although the behavior of a single artificial neuron is quite simple, the network as a whole can be used to predict the behavior of even complex systems. Backpropagating network implements a propagating errors at the output nodes down to hidden nodes; these computed errors on hidden nodes drive the update of weights in $W_{(1,0)}$ (by delta rule).

Figure 2.2 represents a schematic of ANN, where n is the number of input parameters and x_i is the input parameter of i of the network. It is the feedforward

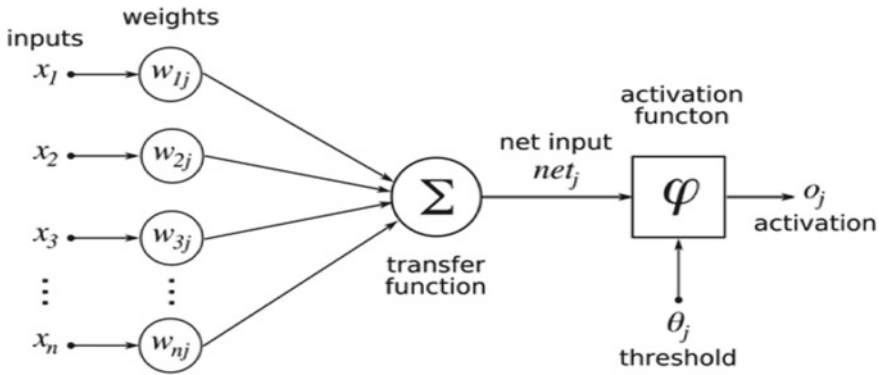


Fig. 2.2 Schematic of neural network

network where the first layer which is the input layer and the second layer which is the hidden layer are interconnected to the output layer.

$$U_{ij} = \sum_{i=1}^{\eta} (W_{ij}x_i) \tag{2.1}$$

where W_{ij} is the neuron weight and O_j is the trained output of the network.

$\Phi(v)$ is the activation function and in this, and the log-sigmoidal function is used as an activation function.

$$\Phi(v) = \frac{1}{1 + e^{(-av)}} \tag{2.2}$$

“ x ” is considered as the input of the activation function and “ a ” as the slope parameter.

Artificial Neural Networks and statistical modeling are two different approaches to predictive modeling. Table 2.4 shows the four ANN models to estimate the DGSR. The model was developed by using a single input parameter such as sunshine hours and temperature. Also, models have been developed by using the combination of sunshine hours, temperature, and relative humidity as the combination of input variables.

Table 2.4 Models developed by using ANN

Models	Variables
ANN-S	S, S_0
ANN-T	T_{max} , T_{min}
ANN-ST, TH, SH, STH	S, S_0 , T_{max} , T_{min} , RH

2.5 Discussion

The performances of Sunshine, Temperature, and Hybrid models are analyzed with the empirical model and are further developed with ANN for comparative analysis. Initially, a relevant input parameter for a prediction of DGSR is performed.

2.6 Sensitivity Analysis

Sensitivity analysis is that the technique of learning the behavior of a model to assess the output information square measure influenced by the amendment within the computer file. To assess the foremost influencing input parameter, a correlation analysis is performed, and regression plots are developed using a neural network as shown in Fig. 2.3. The maximum temperature is the first input parameter that gives the best correlation of 0.780 to predict the daily global solar radiation.

Sunshine hour is the second input parameter which gives a correlation of 0.666 to predict the DGSR. Relative humidity gives the least correlation of 0.336 to

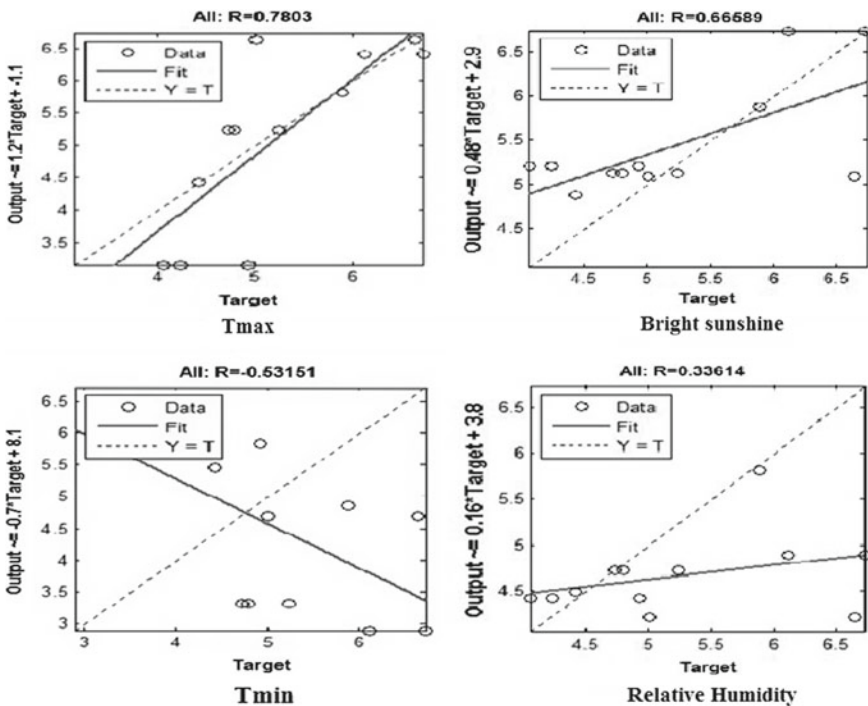


Fig. 2.3 Regression plots using ANN to show the correlation between GSR and various meteorological variables

Table 2.5 Correlation of meteorological variables with measured GSR developed incorporating ANN

Input variable	Correlation R	Rank
Bright sunshine	0.666	2
T _{max}	0.780	1
T _{min}	0.531	3
Relative humidity	0.336	4

predict the GSR. The results of correlation analysis and ranking of meteorological variables are presented in Table 2.5. A higher R value represents a better prediction results. The estimated R value ranges between 0.336 and 0.666 and is illustrated in Table 2.5.

2.7 Training Performance

The ANN temperature-based model (ANN-T) is less accurate compared to the sunshine input model (ANN-S). The error statistics of ANN models for estimation of DGSR is shown in Table 2.6. The combination of temperature and relative humidity gives less accuracy for prediction of global solar radiation. It is observed that the sunshine hour is the most important variable to predict the DGSR. It is also inferred that the ANN-ST model gives higher accuracy and also the absence of relative humidity does not affect the prediction.

Similarly, the ANN-STH model shows less accuracy with R value of 0.819 for Madurai and 0.829 for Trichy. For ANN-S, ANN-T, and ANN-ST models, the statistical error is higher than other developed models. Hence the ANN-ST model is well-suited for Coimbatore and Chennai. ANN-TH model gives less accuracy compared to other ANN models. In the present study, a single layer with 10 hidden neurons and with two to three input neurons are incorporated for an ANN model development. Training error statistics of best model (ANN-ST) for Trichy and Madurai are presented in Fig. 2.4. It is noted that the regression coefficient of the ANN-ST model gives the best R value for both Madurai and Trichy of about 0.993 and 0.996.

2.7.1 Testing Performance

The selected best ANN-ST model is tested for four sites in Tamil Nadu. The best model is selected based on the training error, which has less errors and high correlation. Figure 2.5 gives the Simulink model for testing analysis. Initially, the network has three layers such as an input layer, a hidden layer, and output layer. In the input layer, two parameters are taken as input such as sunshine radiation and temperature (minimum and maximum). The log-sigmoidal and purlin are the

Table 2.6 Error statistics of ANN models for the daily GSR estimation of four sites

Model	MSE (MJ ² m ⁻⁴ day ⁻¹)	Correlation R
<i>Madurai</i>		
S	0.004	0.992
T	0.294	0.990
ST	0.024	0.993
TH	0.883	0.813
SH	0.372	0.819
STH	0.001	0.906
<i>Trichy</i>		
S	0.002	0.982
T	0.139	0.967
ST	0.008	0.996
TH	0.002	0.819
SH	0.044	0.829
STH	0.122	0.905
<i>Chennai</i>		
S	0.029	0.829
T	0.899	0.931
ST	0.003	0.996
TH	1.015	0.710
SH	0.152	0.984
STH	0.001	0.957
<i>Coimbatore</i>		
S	0.059	0.919
T	0.530	0.925
ST	0.177	0.998
TH	0.330	0.799
SH	0.458	0.835
STH	0.289	0.961

functions of the network. Since the solar irradiance data vary for every month, it is also seasonal data which leads to nonlinear data.

In the hidden layer, five neurons are used and weights are obtained. Hidden to the output layer is the second layer where a single output is obtained. The solar irradiance data is obtained in the output layer. The Simulink model is tested for four sites and daily solar irradiance is predicted. The weight adjustment in the network is shown in Fig. 2.6. The five neurons carry the weight in the hidden layer and is a product with the input parameters. The single output solar irradiance is predicted accurately based on the collected data.

The regression curve is drawn between the measured and the predicted data and the weights in the hidden neurons are a dot product of the input parameters.

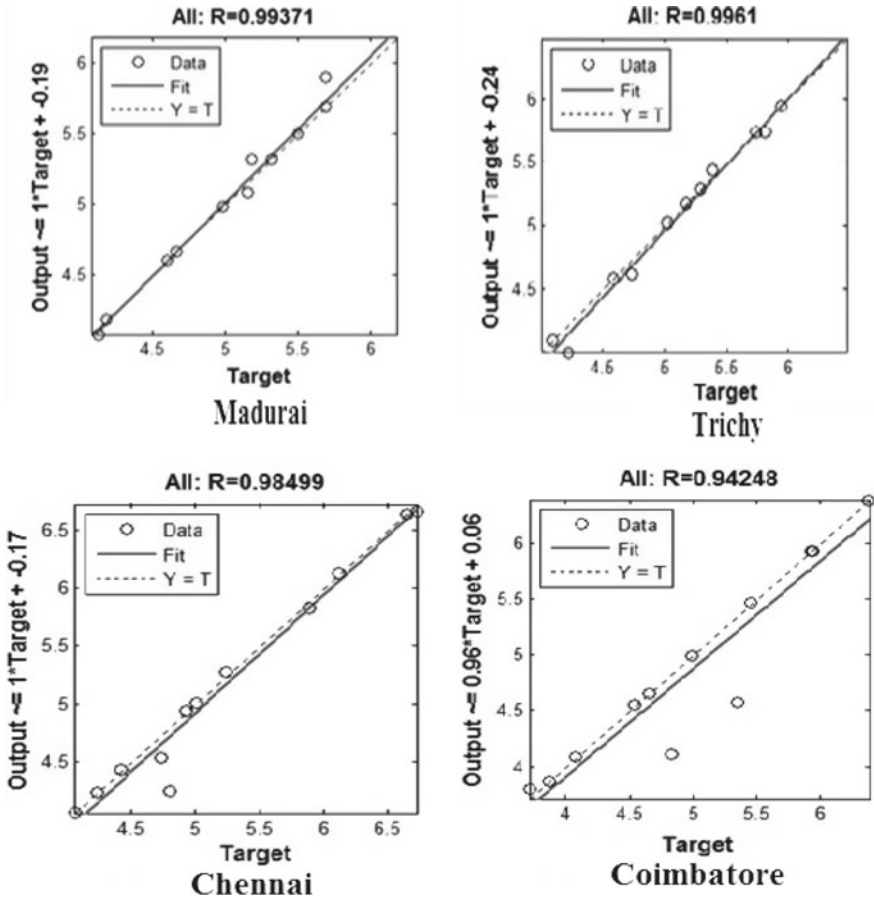


Fig. 2.4 Training error statistics of the best model (ANN-ST) for the selected location

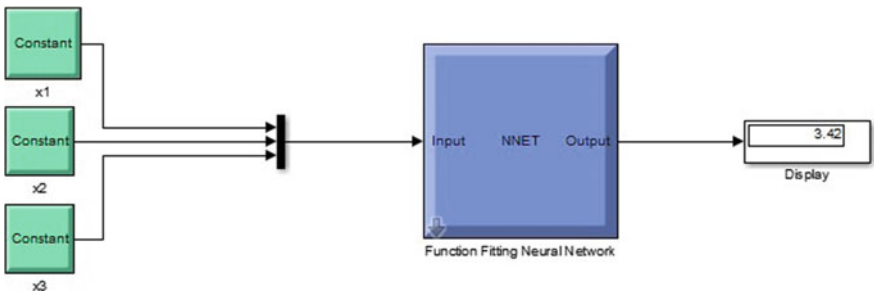


Fig. 2.5 Simulink of the selected best ANN-ST model

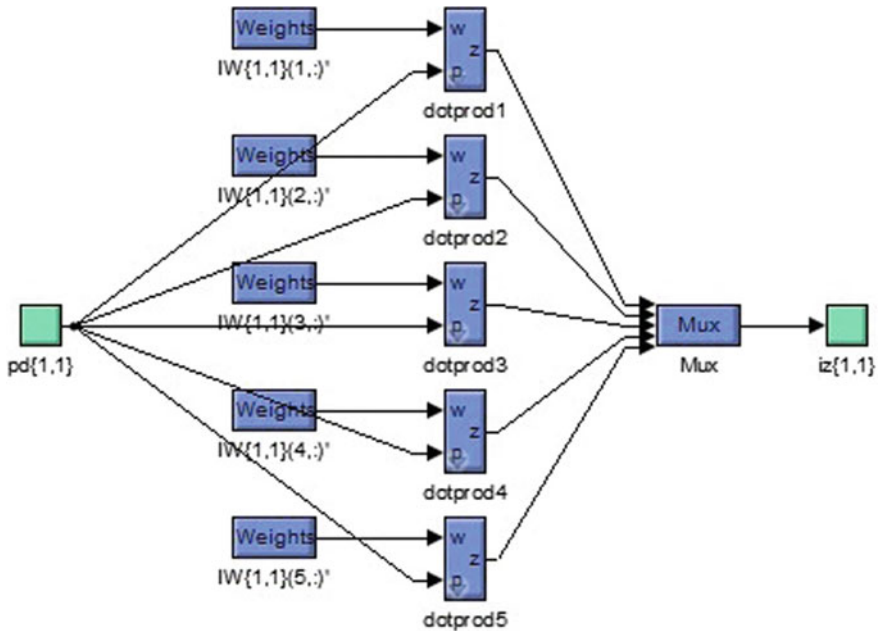


Fig. 2.6 Weight adjustment of the model network

$$\begin{pmatrix} w_{11} & w_{12} & w_{13} \\ w_{21} & w_{22} & w_{23} \\ w_{31} & w_{32} & w_{33} \\ w_{41} & w_{42} & w_{43} \\ w_{51} & w_{52} & w_{53} \end{pmatrix} = \begin{pmatrix} -0.058 & 1.967 & 2.426 \\ -1.672 & -1.475 & 0.916 \\ -1.005 & -0.026 & 2.060 \\ -1.316 & 1.370 & 1.144 \\ 0.103 & -1.441 & 1.683 \end{pmatrix}$$

$$\begin{pmatrix} b_1 \\ b_2 \\ b_3 \\ b_4 \\ b_5 \end{pmatrix} = \begin{pmatrix} 2.532 \\ 0.876 \\ -0.418 \\ -1.961 \\ -2.689 \end{pmatrix}$$

where

- w_{11} is the weight between the first input parameter and the first hidden neuron.
- w_{12} is the weight between the first input parameter and the second hidden neuron.
- w_{22} is the weight between the second input parameter and the second hidden neuron.
- w_{33} is the weight between the third input parameter and the third hidden neuron.
- b_1 is the bias of the first neuron.

b_2 is the bias of the second neuron.

The weight and bias between the hidden neuron and output layer is given as follows and it is the second layer of the network.

$$\begin{pmatrix} w_{31} \\ w_{32} \\ w_{33} \\ w_{34} \\ w_{35} \end{pmatrix} = \begin{pmatrix} -0.755 \\ -0.309 \\ 1.296 \\ 0.384 \\ -0.518 \end{pmatrix}$$

$$[b] = [0.408]$$

where

W_{ij} is the weight between the second hidden layer output and the output layer.

B is the bias of the hidden neuron.

The correlation between the measured and estimated GSR is shown in Fig. 2.7. The regression coefficient (R^2) value for Madurai is 0.9987 and 0.9926 for Trichy, which illustrates higher accuracy for the selected smart cities. Similarly, the regression coefficients for Coimbatore and Chennai are 0.999 and 0.988. The ANN model provides higher accuracy than an empirical model. By the comparative studies, it is analyzed that the ST model is the best one for the prediction of DGSR.

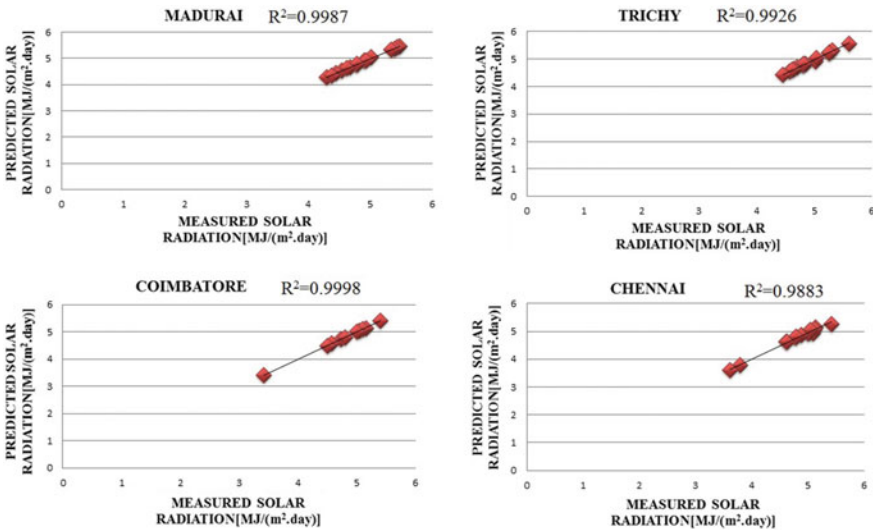


Fig. 2.7 Scatter plots showing the correlation between measured and estimated GSR from the selected model ANN (H4 or ST)

2.8 Performance Characteristics

In this section, the performance of the best evaluated parametric model is compared with the ANN-ST model. Thirteen models have been developed using the CurveExpert software for a different location. The ST-based parametric model (H4) gives the best result during training the data. Similarly, the ANN-ST model gives the best result with minimized error and improved performance. A comparison of measured and predicted data of ANN and the empirical model is shown in Fig. 2.8 for both the ANN and empirical-based model.

It illustrates that the ANN predicted data has high accuracy compared to the empirical-ST model. However, the mathematical model derived is not well-suited for the daily solar radiation prediction. For some of the days, the predicted data is far different from the measured data and the predicted data of ANN is closer to the measured data. The mean square error of ANN and the empirical model is shown in Fig. 2.9 and it is evaluated that the error between the measured and predicted data is minimized in the ANN.

When compared to ANN, the error calculated from the empirical study is higher and the accuracy is subsequently minimized. Hence the ANN-ST model can be used to solve a predictive-based approach. The performance indicator for both selected ANN-ST and the empirical-ST model is given in Table 2.7. The statistical indicator such as mean square error, mean absolute error, mean absolute percentage error, root mean square error, and regression coefficient for the four cities are computed. From Table 2.7, it is analyzed that the highest accuracy is achieved for

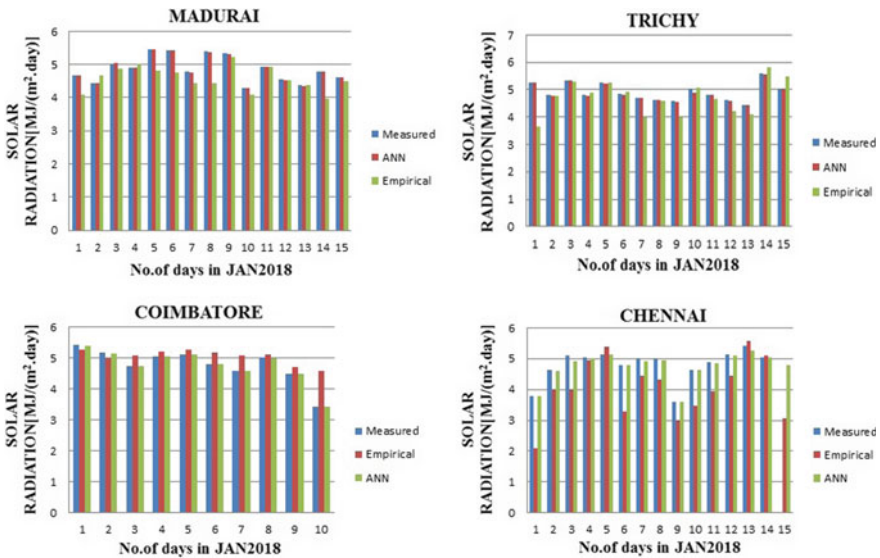


Fig. 2.8 Comparison of measured and predicted data of ANN and empirical model

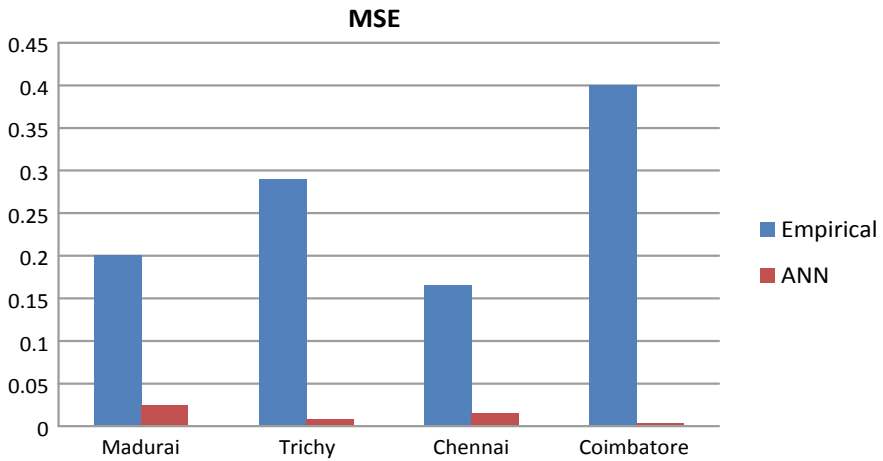


Fig. 2.9 Mean square error comparison between the ANN and empirical model

Table 2.7 Performance indicators of the ANN-ST and empirical-ST models for four sites

Model/ Location	MAE (MJ m ⁻² day ⁻¹)	MAPE (%)	MSE (MJ ² m ⁻⁴ day ⁻¹)	RMSE (MJ m ⁻² day ⁻¹)	R
<i>Empirical</i>					
Madurai	0.224	5.1	0.200	0.440	0.303
Trichy	0.16	3.2	0.29	0.538	0.388
Chennai	0.08	1.1	0.165	0.404	0.724
Coimbatore	-0.04	2.1	0.40	0.632	0.707
<i>ANN</i>					
Madurai	0.128	4.3	0.016	0.207	0.998
Trichy	0.149	3.0	0.022	0.173	0.992
Chennai	0.086	1.8	0.007	0.134	0.988
Coimbatore	0.055	1.0	0.003	0.110	0.999

the ANN-ST model. Initially, Coimbatore had the highest accuracy of 0.999 since it has a mild climate and solar radiation does not vary rapidly. This is followed by Madurai which achieved an accuracy of 0.998. For Trichy, the regression coefficient is about 0.992. Finally, Chennai had the lowest accuracy of 0.988.

The error statistics have been calculated between the measured and predicted data and the lowest accuracy was obtained for all the sites. Since the daily solar radiation and temperature changes rapidly, the cities, namely Madurai and Trichy have the lowest accuracy of 0.303 and 0.388. This is followed by Chennai and Coimbatore having an accuracy of 0.724 and 0.707. Since both are in the central and western part of Tamil Nadu, its results are not closer to 1, which denotes the highest accuracy. And compared to ANN-ST, the empirical-ST model gives the

worst performance for the four cities. Hence the ANN-ST model can be used for prediction of DGSR. This combination of temperature and sunshine-based ANN model is optimal for prediction of DGSR as extended in the southern states of India.

2.9 Conclusion

In the proposed work, empirical-and ANN-based solar radiation models are assessed for the prediction of DGSR. Three types of models specifically temperature, sunshine, and hybrid model are accessed. It is found that sunshine and temperature are the most influencing parameters for the estimation of DGSR and the relative humidity is the least influencing parameter. Further, this selected model has been tested for four cities in Tamil Nadu and subsequently, the error statistics are calculated. A higher value of the correlation coefficient for the empirical model is 0.707 and for ANN is 0.999. Comparing the RMSE, MAE, MAPE, RMSE, and regression coefficient values, it can be inferred that the ANN-ST model with both sunshine and temperature as input parameters exhibits better results.

Appendix

$$ME = \frac{1}{p} \sum_{i=0}^p (H_{i,e} - H_{i,m}) \quad (2.3)$$

$$MPE = \frac{1}{p} \sum_{i=0}^p \frac{(H_{i,e} - H_{i,m})}{H_{i,m}} \times 100 \quad (2.4)$$

$$MAPE = \frac{1}{p} \sum_{i=0}^p \left| \frac{(H_{i,e} - H_{i,m})}{H_{i,m}} \right| \times 100 \quad (2.5)$$

$$RRMSE = \frac{\sqrt{\left(\frac{1}{p} \sum_{i=1}^p (H_{i,e} - H_{i,m})^2 \right)}}{\frac{1}{p} \sum_{i=1}^n (H_{i,m})} \times 100 \quad (2.6)$$

References

- Arunkumar J, Chalmers A, Lie TT (2017) A review of prospects for adoption of fuel cell electric vehicles in New Zealand. *IET Electr Syst Trans* 7(4):259–266
- Baser F, Demirhan H (2017) A fuzzy regression with support vector machine approach to the estimation of horizontal global solar radiation. *Energy* 23:229–240
- Chandel SS, Yadav AK (2017) Solar energy potential assessment of western Himalayan Indian state of Himachal Pradesh using J48 algorithm of WEKA in ANN based prediction model. *Renew Energy* 75:675–693
- Jamil B, Akhtar N (2017) Estimation of diffuse solar radiation in humid-subtropical climatic region of India: comparison of diffuse fraction and diffusion coefficient models. *Energy* 131:149–164
- Jamil B, Siddiqui AT (2017) Generalized models for estimation of diffuse solar radiation based on clearness index and sunshine duration in India: applicability under different climatic zones. *J Atmos Solar Terrestrial Phys* 157–158:16–34
- Jeong DI, St-Hilaire A, Gratton Y, Belanger C, Saad C (2017) A guideline to select an estimation model of daily global solar radiation between geostatic interpolation and stochastic simulation approaches. *Renew Energy* 103:70–80
- Jiang H, Dong Y (2017) Global horizontal radiation forecast using forward regression on a quadratic kernel support vector machine: case study of the tibet autonomous region in China. *Energy* 133:270–283
- Kalogirou SA, Pashiardis S, Pashiardi A (2017) Statistical analysis and inter-comparison of the global solar radiation at two sites in Cyprus. *Renew Energy* 101:1102–1123
- Quej VH, Almorox J, Ibrakhimov M, Saito L (2017) Estimating daily global solar radiation by day of the year in six cities located in the Yucatán Peninsula, Mexico. *J Clean Prod* 141:75–82
- Sharma A, Kakkar A (2017) Development of modified pro-energy algorithm for future solar irradiance estimation using level and trend factors in time series analysis. *J Renew Sustain Energy* 9:1–16
- Vakili M, Sabbagh-Yazdi SR, Khosrojerdi S, Kalhor K (2017) Evaluating the effect of particulate matter pollution on estimation of daily global solar radiation using artificial neural network modeling based on meteorological data. *J Clean Prod* 141:1275–1285
- Vishnupriyan J, Manoharan PS (2018) Prospects of hybrid photovoltaic–diesel standalone system for six different climate locations in Indian state of Tamil Nadu. *J Clean Prod* 185:309–321

Chapter 3

Solar-Fed Hybrid Modular Multilevel Converter for Motor Drives



Lakshmi Krishnakumar and Elizabeth Rita Samuel

3.1 Introduction

Multilevel inverters are widely used in industrial applications, for example, in compressors, pumps, fans and conveyors. These variable-speed motor drives with high-power medium-voltage applications that use multilevel inverters for energy savings. There are four types of commercialized multilevel inverter topologies: neutral point clamped, flying capacitor, cascaded H bridge and modular multilevel converters. The main advantage of multilevel inverters is that with the reduced filter size, the harmonics can be mitigated and high output power can be generated by using a small DC input. Apart from the abovementioned advantage, these have disadvantages that the number of switching devices may increase with increase in the number of DC sources, the size of the filter increases and the design becomes complex. To overcome these disadvantages of the multilevel inverters, modular multilevel converters (MMC) will introduce an upper arm and lower arm with each arm containing N number of sub-modules (Hagiwara et al. 2013). The sub-modules (SM) consist of IGBTs, capacitors and diodes. The advantage of MMC is that it acts as a controllable voltage source converter and is able to control the sub-module individually. The output power gets increased and the total harmonic distortion (THD) is lowered by the introduction of the sub-modules. The MMC has the disadvantage that the capacitor voltage ripple increases as the current flows through the arm in low-speed motor drive since capacitor voltage is proportional to output current amplitude and inversely proportional to output frequency. The other drawbacks of traditional MMC are

L. Krishnakumar (✉) · E. R. Samuel
Rajagiri School of Engineering and Technology, Ernakulam, Kerala, India
e-mail: lakshmikrishnakumar018@gmail.com

E. R. Samuel
e-mail: elizabethrs@rajagiritech.edu.in

1. The common mode voltage with high magnitude is superposed on the motor which results in insulation and bearing current problems which may shorten the lifetime or may even damage the motor (Wang et al. 2013).
2. The circulating current gets injected into the arms of MMC that increases current stress and power loss due to which it requires oversized converters and high cooling components.
3. The control of the circulating current and common mode voltage is difficult which may cause instability during the transient process (Li et al. 2015).

To overcome the limitation of the traditional MMC, a new hybrid MMC topology is introduced which combines traditional MMC with DC-link series switch. The main advantage of this topology is that this lowers the capacitor voltage ripple at low speeds. Moreover, since no common mode voltage is imposed there is no bearing current and insulation problem. Thus the proposed hybrid modular multilevel converter (HMMC) is suitable for motor drives.

In Sect. 3.2, the study of the hybrid MMC topology is illustrated. The following section gives an explanation of the control scheme, followed by simulation and experiment results. Section 3.5 deals with the conclusion.

3.2 Operation Principle of Hybrid MMC

3.2.1 Topology of Hybrid MMC

Figure 3.1 shows the circuit configuration of the proposed hybrid MMC. Between the DC source and the MMC converter, a series switch S_s is placed. A hybrid MMC converter can be associated with or separated from the DC source with the series switch. Either thyristor or IGBT can be utilized as the series switch. To filter switching voltage harmonics, an RC snubber circuit (Rodriguez et al. 2010) is paralleled with the hybrid MMC. To ground the converter to earth, two grounding resistors R_g are utilized.

Each phase consists of two arms, the upper and lower arm which are connected through the arm inductance L . A total of N sub-modules are in each arm, and each sub-module is a half bridge. The term u_o is the output phase voltage, i_o is the output phase current and the DC terminal voltage of MMC is u_d . The voltage and current of the upper and the lower arm are represented by u_u, i_u, u_l and i_l . U_{dc} and i_{dc} are the DC source voltage and DC source current. The sub-module capacitor voltages are with an average voltage of $U_C = U_{dc}/N$.

According to Kirchhoff's voltage law,

$$U_o = \frac{1}{2} \left(u_l - u_u - L \frac{di_o}{dt} \right) \quad (3.1)$$

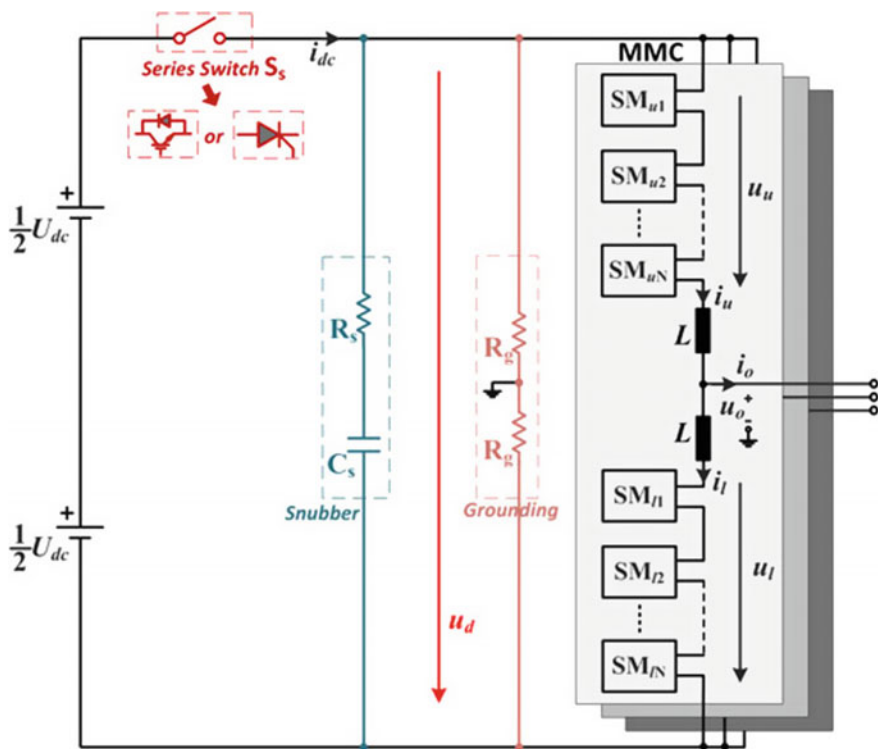


Fig. 3.1 Hybrid modular multilevel converter (Li et al. 2017)

$$U_d = u_l + u_u + 2L \frac{di_c}{dt} \quad (3.2)$$

Currents through the upper and lower arms are

$$i_u = i_c + \frac{1}{2} i_o \quad (3.3)$$

$$i_l = i_c - \frac{1}{2} i_o \quad (3.4)$$

The output ac voltage and current are

$$u_o = U_{OM} \cos(\omega t) \quad (3.5)$$

$$i_o = I_{OM} \cos(\omega t - \varphi) \quad (3.6)$$

where U_{OM} and I_{OM} are the amplitudes, ω is the output angular frequency and φ , the phase lag angle.

The output voltage amplitude U_{OM} can also be expressed by

$$U_{OM} = \frac{1}{2}mU_{dc} \quad (3.7)$$

where m denotes the modulation index varying from 0 to 1.

3.2.2 Operation of Sub-modules in MMC

Operation of the sub-module in traditional MMC is the same as that of the hybrid MMC. Sub-modules consist of IGBTs, diode and capacitor as shown in Fig. 3.2.

The working of the sub-module is explained with the help of Table 3.1.

3.3 Control Scheme

This section briefs on the suitable control scheme for hybrid MMC. Figure 3.3 demonstrates the complete control scheme of the system, comprising five principle controls. Overall energy balancing control, phase energy balancing control, arm energy balancing control, circulating current control and pulse width modulation (PWM) associated with SM capacitor voltage balancing are the five principle controls.

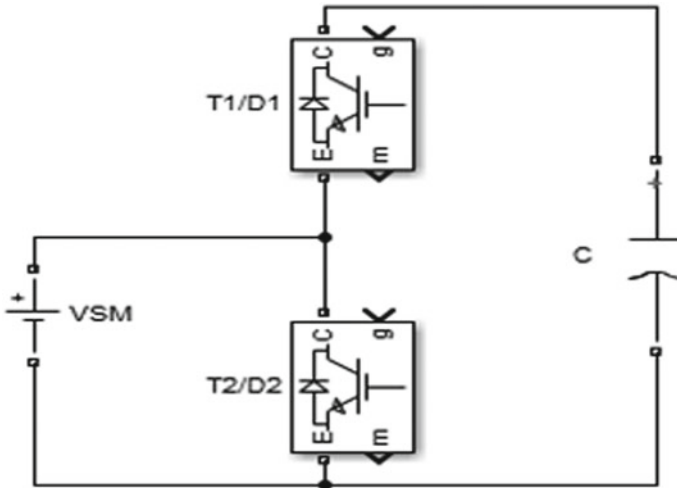
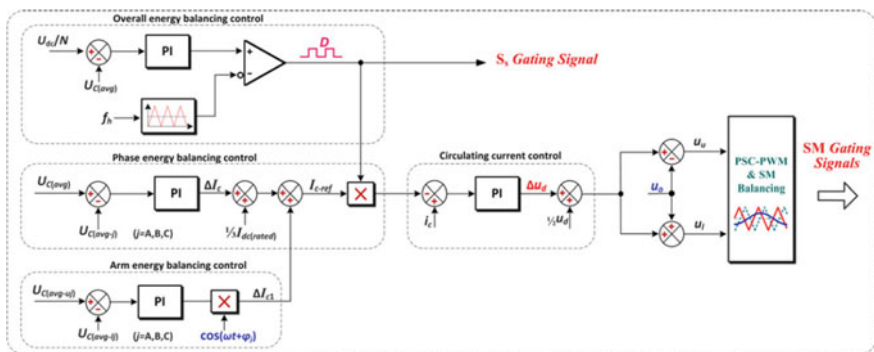


Fig. 3.2 Sub-module of MMC

Table 3.1 Operation of sub-modules

SM state	T1 state	T2 state	I_{SM}	V_C	I_{SM} flows	V_{SM}
ON	ON	OFF	>0	+	D1	V_{SM}
ON	ON	OFF	<0	-	T1	V_{SM}
OFF	OFF	ON	>0	0	T2	0
OFF	OFF	ON	<0	0	D2	0

**Fig. 3.3** Control block of MMC (Li et al. 2017)

3.3.1 Overall Energy Balancing

Overall energy balancing is done by

1. Regulation of series switch and
2. Generation of gating pulses for sub-modules of MMC.

Regulation of series switch

The main aim of the series switch regulation is to maintain the overall energy balance in the SM capacitor. The power balance between the DC input and AC output must be maintained. The difference between the input and output power will influence the energy stored in the capacitor, so to maintain the balance between the input and output power, the measured average value of all the SM capacitors should be kept equal to the reference value. For this purpose, the average value of the voltage across the SM capacitors measured is compared with the reference value and this error is fed into the error comparator for getting the duty cycle to regulate the series switch.

$$\frac{U_{dc}}{N} - U_{C(av)} = e(t) \quad (3.8)$$

where

U_{dc} is the input DC

$U_{C(avg)}$ is the measured average value of all the SM capacitors.

Generation of gating pulse

This stage includes four stages.

Phase energy balancing control, arm energy balancing control, circulating current control and pulse width modulation for SM capacitor voltage balancing.

Phase energy balancing control

This method is adopted to ensure that the total energy is equally distributed among the phases. $U_{C(avg)}$ is compared with $U_{c(avg)}$ of each phase (a, b, c) and the error is fed into the PI controller and the output value of the PI controller is the DC current adjusting component ΔI_c .

$$i_c = \frac{1}{3} i_{dc(rated)} \quad (3.9)$$

where

$i_{dc(rated)}$ is the rated DC current.

Arm energy balancing control

This is done to maintain the energy in each phase equally distributed in the upper and lower arms.

Here, the difference of average value of the capacitor voltage in upper and lower arm of each phase is taken and the error is fed into the PID controller to calculate the fundamental frequency current compensation component. The frequency current component ΔI_c is the product of the amplitude component of frequency current compensation component and the cosine of $\omega t + \theta$.

$$\Delta I'_c * \cos(\omega t + \theta) = \Delta I_c \quad (3.10)$$

where

$\Delta I'_c$ is the frequency current compensation component.

ΔI_c is the frequency current component.

Circulating current control

Aim of this method is to force the actual circulating current to follow the reference circulating current. Here, $I_{c(actual)}$ is compared with $I_{c(ref)}$ and fed into the PID controller and the output is ΔU_d . ΔU_d is the value required for adjusting to achieve the smaller SM capacitor ripple. The output of the circulating current control loop is $\Delta U_d + \frac{1}{2} U_d$, which is the reference value of the output voltage regulation. Finally,

the reference for PWM is obtained when, $u_u = u_{o(\text{ref})}$ for the upper arm and $u_l = u_{o(\text{ref})} + u_o$ for the lower arm, u_u and u_l are compared with the phase-shifted carriers for generating gate pulse for MMC.

where

$I_{c(\text{actual})}$ is the actual circulating current and
 $I_{c(\text{ref})}$ is the reference circulating current.

3.4 Phase Disposition PWM

3.4.1 Multicarrier PWM Technique

To generate a gate driving signal, pulse width modulation (PWM) utilizes one reference waveform and one carrier waveform. A reference waveform and a carrier waveform are used in pulse width modulation (PWM) to produce a gate driving signal. On the comparison between the reference signal and the carrier signal, the PWM is high if the reference signal is higher and low PWM if reference signal is lower than the carrier signal. The top switches are controlled by the PWM signal and the bottom switches by the inverse of the signal. In the case of HMMC, which consists of several half-bridge circuits in the converter, for which each requires an individual control, the use of multicarrier PWM controller technique is recommended. Different types of carrier-based PWM strategies are shown in Fig. 3.4.

3.4.2 Phase Disposition PWM (PD-PWM) Technique

In Phase Disposition, all the carrier signals are in the same phase. N number of identical and equally displaced triangular carriers from the zero axis are required. The switched output phase voltage level is obtained by comparing the carrier signals with the reference. The Phase Disposition technique is illustrated in Fig. 3.5. Similar to the previous technique, in this technique also if the reference

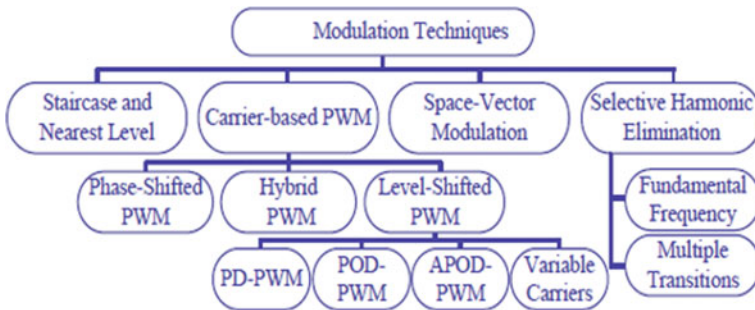


Fig. 3.4 Pulse width modulation classification (Rodriguez et al. 2010)

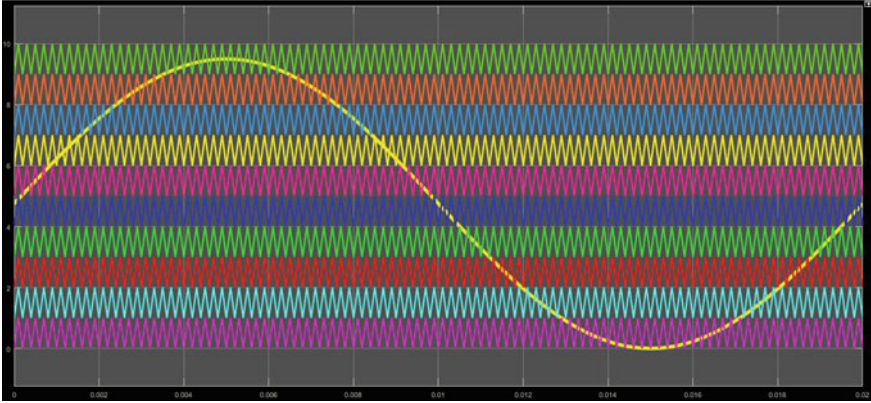


Fig. 3.5 Phase disposition PWM

signal is greater than the carrier, then a high output is produced by PWM and a low PWM in the case when the reference is lower than the carrier. The voltage variations corresponding to a triangular carrier are associated with the insertion or bypass of a particular SM. Based on the phase shift among the carrier waveforms, these techniques are further classified into PD (phase disposition), POD (phase opposition disposition) and APOD (alternate phase opposition disposition).

3.5 Modelling of PV

3.5.1 Photovoltaic Cell Circuit Model

Ideal Photovoltaic Model

An ideal photovoltaic cell consists of a single diode connected in parallel with a light-generated current source, I_{ph} where its output current, I , can be written as

$$I = I_{ph} \left[\exp\left(\frac{V}{nV_T}\right) - 1 \right] \quad (3.11)$$

where

- I_s is the cell saturation of dark current,
- V_T is the thermal voltage = KT_c/q ,
- K is the Boltzmann's constant = 1.38×10^{-23} J/K,
- T_c is the cell's working temperature,
- Q is the electron charge (1.6×10^{-19} C) and
- N is the ideality factor equal to 1.1.

Nonideal Photovoltaic Models

Photovoltaic Model with Series Resistance (Debnath et al. 2015)

The photovoltaic model with series resistance (R_s model) depicted in Fig. 3.6b is achieved with inclusion of series resistance R_s , hence, the output current can be derived as

$$I = I_{ph} - I_s \left[\exp \left(\frac{V + I R_s}{n V_T} \right) - 1 \right] \quad (3.12)$$

Photovoltaic Model with Series and Parallel Resistances (Debnath et al. 2015)

When the cell subjected to environmental conditions, Eq. (3.12) does not adequately represent the variations, especially at low voltages. A more practical model can be seen where series R_s and parallel resistances R_{sh} are introduced. Series resistance is very small, which arises from the ohmic contact between metal and semiconductor internal resistance. But shunt resistance is very large and represents the surface quality along the periphery, noting that in ideal case R_s is 0 and R_{sh} is ∞ .

$$I = I_{ph} - I_d - I_{sh} \quad (3.13)$$

$$I = I_{ph} - I_s \left[\exp \left(\frac{V + I R_s}{n V_T} \right) - 1 \right] - \left(\frac{V + I R_s}{R_{sh}} \right) \quad (3.14)$$

where

I_d diode current.

I_{sh} shunt current.

G solar insolation.

The photocurrent mainly depends on the solar insolation and cell's working temperature, which is described as

$$I_{ph} = [I_{sc} + K_1(T_c - T_{ref})] \frac{G}{G_{ref}} \quad (3.15)$$

where

I_{sc} solar cell short-circuit current,

G_{ref} reference solar insolation in W/m^2 .

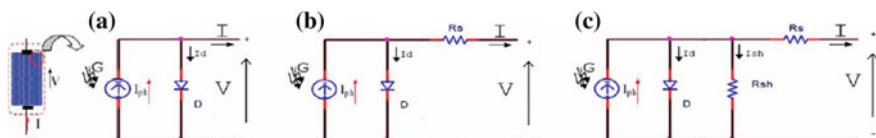


Fig. 3.6 Circuits model for PV cell **a** Ideal, **b** with series resistance, R_s , **c** with series and parallel resistance, R_s and R_{sh} (Rodriguez et al. 2010)

T_{ref} cell's reference temperature,
 K_I cell's short-circuit current temperature coefficient and
 G solar insolation in W/m^2 .

On the other hand, the cell's saturation current varies with the cell temperature, which is described as

$$I_S = I_{RS} \left(\frac{T_C}{T_{\text{ref}}} \right)^2 \exp \left[\frac{qE_g}{nK} \left(\frac{1}{T_{\text{ref}}} - \frac{1}{T_C} \right) \right] \quad (3.16)$$

where

I_{RS} is the cell's reverse saturation current at a reference temperature and a solar radiation,

E_g is the bandgap energy of the Si solar cell = 1.10 eV and

N is dependent on the PV technology.

The reverse saturation current at reference temperature can be approximately obtained as

$$I_{RS} = \frac{I_{SC}}{\exp \left(\frac{qV_{oc}}{nKT_C} \right) - 1} \quad (3.17)$$

3.6 Simulation and Results

Simulation is done for a 21-level hybrid modular multilevel converter and its performance is evaluated. It consists of 20 SMs, i.e. ten SMs in the upper leg and ten SMs in the lower leg. The gate signal is provided by the phase shift, level shift and staircase PWM technique. The output voltage is measured across the RL load and motor load. Table 3.2 shows the design parameters of the 21-level hybrid modular multilevel converter

The Simulink model of a 10-level hybrid modular multilevel converter is given in Fig. 3.7.

Table 3.2 Simulation parameters

Hybrid MMC parameter	
Number of sub-modules	$N = 20$
DC-source voltage	$U_{dc} = 8000 \text{ V}$
Nominal SM capacitor voltage	$U_C = 8000 \text{ V}$
SM capacitance	$C_{SM} = 4000 \mu\text{F}$
Arm inductance	$L = 1 \text{ mH}$
Rated output frequency	50 Hz
Rated phase current magnitude	250 A
Rated DC current	180 A

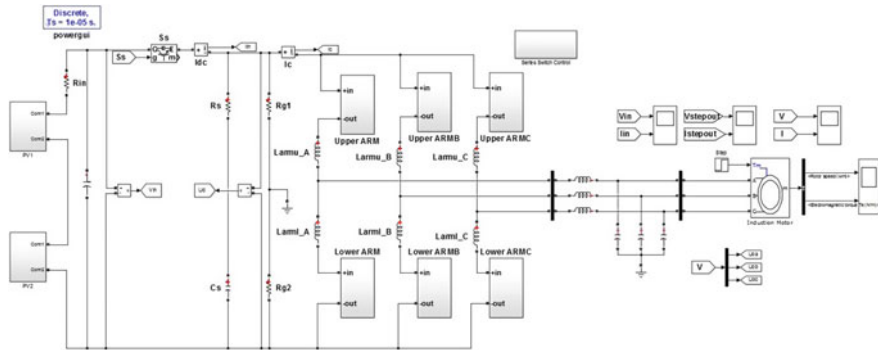


Fig. 3.7 Simulink model of hybrid MMC with PV

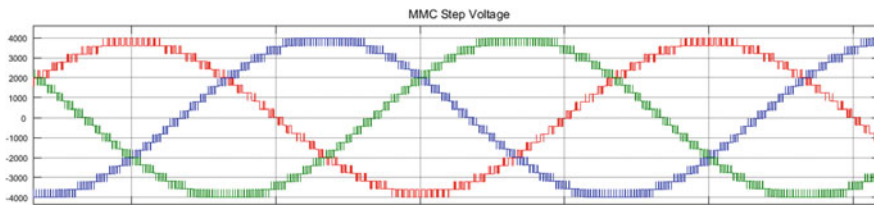


Fig. 3.8 Output (voltage) waveform of the 21-level hybrid modular multilevel converter fed PV

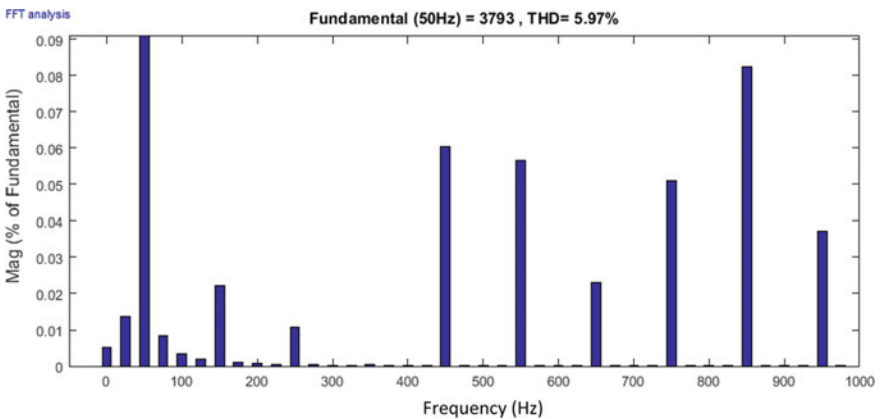


Fig. 3.9 FFT analysis for the 21-level hybrid modular multilevel converter

The output voltage waveform for 10-level hybrid modular multilevel converter based PV system is shown in Fig. 3.8. The peak magnitude of the output voltage is found to be 4000 V. The total harmonic distortion for the 21-level hybrid modular multilevel converter is found to be 5.97% which is found by FFT analysis and the spectrum is shown in Fig. 3.9.

3.7 Conclusion

In this paper, a three-phase 21-level hybrid modular multilevel converter based PV system employing PD PWM strategies with RL load is simulated using MATLAB software. As the capacitor voltage ripple of the traditional MMC is directly proportional to the output torque and inversely proportional to the motor speed, for high torque, low-speed application ripples will be high. Due to this drawback, widespread application in medium-speed motor drives has not been achieved. To overcome this, hybrid MMC has been proposed where a series switch is also introduced in traditional MMC to control the circulating current. The paper implements level shift pulse width modulation control (LSPWM) for the hybrid MMC to reduce the voltage ripple of the capacitor. LSPWM has been chosen in this paper mainly due to the simplicity of calculation involved with this control scheme and comparison to the other existing techniques. This control scheme also helps in the reduction of the total harmonic distortion (THD) by employing the PD PWM strategy in a 21-level hybrid modular multilevel converter where the THD is observed to be 5.97%.

References

- Debnath S, Qin J, Bahrani B, Saedifard M, Barbosa P (2015) Operation, control, and applications of the modular multilevel converter: a review. *IEEE Trans Power Electron* 30(1):37–53
- Hagiwara M, Hasegawa I, Akagi H (2013) Start-up and low-speed operation of an electric motor driven by modular multilevel cascade inverter. *IEEE Trans Ind Appl* 49(4):1556–1565
- Li B, Yang R, Xu D, Wang G, Wang W, Xu D (2015) Analysis of the phase-shifted carrier modulation for modular multilevel converters. *IEEE Trans Power Electron* 30(1):297–310
- Li B, Finney SJ, Williams BW (2017) A hybrid modular multilevel converter for medium-voltage variable-speed motor drives. *IEEE Trans Power Electron* 32(6):4619–4630
- Nagarajan B, Joseph S, Immanuel S, Boobalan G (2016) Phase disposition PWM multicarrier based 5 level modular multilevel inverter for PV application. *Middle-East J Sci Res* 24(S1): 26–32
- Rodriguez J, Bernet S, Steimer PK, Lizama IE (2010) A survey on neutral-point-clamped inverters. *IEEE Trans Ind Electron* 57(7):2219–2230
- Wang K, Li Y, Zheng Z, Xu L (2013) Voltage balancing and fluctuation suppression method of floating capacitors in new modular multilevel converter. *IEEE Trans Ind Electron* 60(5):1943–1954

Chapter 4

Pine Needles Biomass Gasification Based Electricity Generation for Indian Himalayan Region: Drivers and Barriers



Arvind Singh Bisht  and N. S. Thakur

4.1 Introduction

The Himalayas are the highest mountain range in the world. Because of their water resources in the form of glaciers and rivers as well as the forest environment, this region is essential for the ecological stability of the entire continent. The Himalayan region is home to a unique mountain ecosystem that serves as an important climate regulator. Over hundreds of years, this region has endured extreme clashes between financial modernization and the preservation of the environment. Seasonal forest fires of considerable magnitude are the norm in the region, occurring annually and destroying thousands of hectares of forest, thus causing a dramatic habitat loss for indigenous species, soil erosion, greenhouse gas emissions, loss of forest resources, wildlife, as well as respiratory diseases through pollutants and even sometimes the loss of human lives (Schaller 2016).

In 2016, 21,000 Himalayan wildfires were reported in India (Roberts Scribbler 2018). They began as early as February because of a dry winter and continued well into the summer. At the height of their fury, they threatened close to a hundred villages and caused seven people to lose their lives. Eventually, the government mobilized 9000 firefighters and Mi-17 helicopter fire suppression craft to fight the flames that affected over 21 districts in two Indian states (Indian Express 2018; Roberts Scribbler 2018).

In the short term, this may be seen as a local disaster, however, it must be noted that a warming of about 0.6 degrees Celsius per decade since 1977 in the Himalayas has caused a decline in the glaciers, and this is a global issue (Roberts Scribbler 2018).

A. S. Bisht (✉) · N. S. Thakur
Centre for Energy and Environmental Engineering, National Institute of Technology,
Hamirpur 177005, Himachal Pradesh, India
e-mail: abbi.b7@gmail.com

The dominant flora in this region is the Chir pine (*Pinus roxburghii*), mainly growing between elevations of the range 450–2300 m. Every year when pine needles fall to the ground during the summer season, they create a thick acidic carpet on the forest floor (FRI 2019). As a result, the soil below the carpet can no longer absorb water which creates an unsuitable environment for other species to grow. The needles are likewise not edible and in this manner, useless for faunae. Besides, the needles are highly flammable and forest fires in this way exceptionally visit (Bisht et al. 2014). This offers to ascend to soil erosion.

Pine needles are biomass and contain tremendous energy which can be converted into heat through direct combustion or into producer gas through gasification. The energy content of pine needles indicates that pine needles are a decent source to meet the energy requirements of the hilly regions in the Himalayas (Bisht and Thakur 2016). Constructive use of this resource would markedly improve the climate conditions and the economic and local development of this sensitive region.

Pine forests (*Pinus roxburghii*) cover large portions of the Himalayan regions and occur between 450 and 2300 m altitudes. The total area covered in the Indian Himalaya by pine forests is estimated to be 0.89 million hectares and is mostly found in Jammu and Kashmir, Himachal Pradesh, Uttarakhand, parts of Sikkim, West Bengal and Arunachal Pradesh under (FRI 2019). As per the Uttarakhand Renewable Energy Development Agency (UREDA), estimates indicate that the total area of pine forest in reserve forest in Uttarakhand is about 0.343 million hectares, which produces 2.058 million tons dry biomass (Uttarakhand Renewable Energy Development Agency 2018)—a huge amount of biomass that lies unused and causes harm.

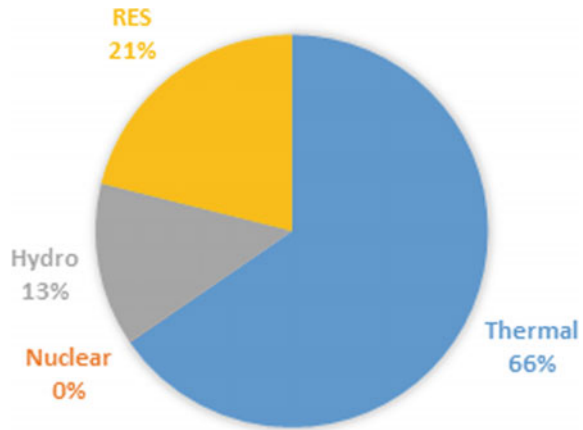
Biomass has a broad range of uses and users—gasification is one utilization pathway. Gasification of biomass provides an excellent solution to the problem of energy recovery and waste disposal. Since pine needles represent a genuine risk to forests from fires, their collection and use for energy recovery is an extremely appealing recommendation (Safi et al. 2004).

In this paper, a variety of research methods and different informants were used in order to obtain suitable material. Extensive reviews of literature, case studies, academic research, magazines, and journals, news articles, websites and Google scholar search results were conducted in order to accumulate relevant data. The important drivers which consider climate change mitigation, availability and socio-economic benefits were studied. The barriers to the implementation of this technology which include financial issues, policy barriers and logistical barriers were recognized through literature surveys.

4.1.1 Indian Energy Scenario

As per the statistics given by the Central Electricity Authority (Central Electricity Authority, Government of India October 2018), as shown in Fig. 4.1, the total installed generation capacity in India was 346.047 GW, out of which 221.767 GW

Fig. 4.1 Share of various energy resources in India



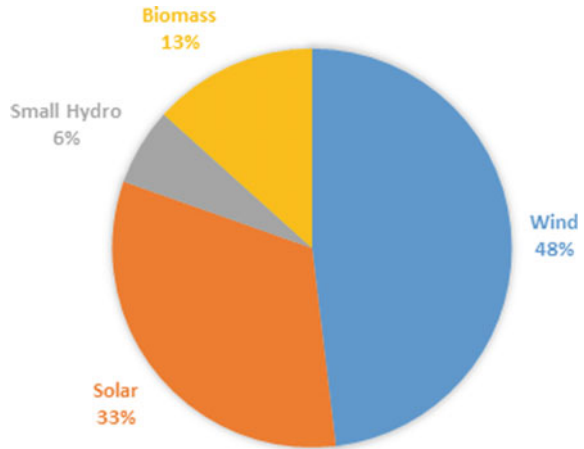
was through coal thermal route, 72.012 GW was through renewable energy sources, 45.487 GW was through large hydro and 6.780 GW was through nuclear (Central Electricity Authority Govt. of India Installed Capacity 2019).

India has an expected renewable energy potential of around 900 GW from commercially exploitable sources, viz., 750 GW solar power, Wind—102 GW (at 80 m mast height), Small Hydro—20 GW and Bioenergy—25 GW (MNRE 2015–2016). The Ministry of New and Renewable Energy (MNRE) Government of India has set a target of achieving 10,000 MW bioenergy by the year 2022 (2019).

India's 2022 renewable energy target of 175 GW capacities represents a rapid increase in renewable energy generation, but would still not suffice to satisfy the nation's electricity requirements. Between 2014 and 2030 under current policies, we estimate the average annual growth rate for solar and wind power generation at around 3%—about half the growth rate of overall electricity production. During the same period, under our current policy pathway, we project capacity additions of 154–267 GW for solar and wind power and 186–217 GW for coal power. As of July 2017, nearly 43 GW of coal-fired capacity is under construction, with another 100 GW announced or planned (at the pre-permit and permitted stages) (EndCoal 2017). Were all these plants to be built, this would result in considerable overcapacity. Ultimately, this would lead to a greater lock-in of carbon-intensive power infrastructure in India than what appears necessary (Climate Action Tracker 2018). It would seem desirable then, that wherever possible, renewable energy projects are implemented to supplement power, especially in rural scenarios, and where there is also a considerable ecological advantage, as in the case of pine needle gasification.

At present, the Indian renewable energy sector shown in Fig. 4.2 produces 72.012 GW in which contribution of different technologies are as follow Wind—34.615 GW, Small Hydro—4.506 GW, Bioenergy—8.730 GW and 24.021 GW solar power (MNRE 2015–2016). In addition to the obvious benefits of power generation, the removal of pine needles from the forest floors would also prevent the fires, which are now seen to have contributed to the warming in the region as

Fig. 4.2 Share of various renewable energy resources in electricity generation in India



well as globally. The fires also result in a loss of forest land, which is another crisis for the region.

As indicated in India's Nationally Determined Contribution (NDC), the nation intends to lower the emission's intensity of GDP by about 33–35% below 2005 levels, increase the share of power generation from renewable sources to 40% (equivalent to 26–30% of generation) and create an additional (cumulative) carbon sink of 2.5–3 GtCO₂e by an increase in forest and tree cover by 2030. Pine needles gasification and the constructive use of this biomass on a national scale seems an ideal project to help attain these environmental goals (Climate Action Tracker 2018).

At the COP 21, in December 2015, 195 countries committed to combating climate change and bringing down emissions so as to limit warming to 2 °C above pre-industrial times, preferably below 1.5 °C. For effective mitigation and adaptation, the necessity of clean energy access in developing countries was recognized as being indispensable (UNFCCC 2018).

India is responsible for 6% of the global CO₂ emissions after China, which accounts for 28%; the United States accounts for 16% and the European Union is responsible for 10%. In terms of per capita CO₂ emissions, 10 other countries are ahead of India.

As stated before, part of the initial commitment of the Paris Agreement involves a reduction by India of its carbon emission intensity—emission per unit of GDP—by 33–35% from 2005 levels over 15 years. Once again biomass gasification is a way to allow this to happen. This would mean India should move altogether from coal-based power generation to renewable energy sources. It should deliver 100 GW from solar, 60 GW from wind, 10 GW from biomass and 5 GW from small hydropower by 2022 (MNRE 2018). Another commitment under the treaty requires India to increase its forest cover by five million hectares along with an improvement in the quality of the green cover of an equal measure by 2030. The protection of Himalayan forests and the prevention of forest fires would be essential steps in attaining this objective.

4.2 Key Drivers

The key drivers for pine needle gasification based energy generation for the Himalayan region can be divided into the following categories:

- Technical feasibility
- Climate change mitigation
- Availability
- Socio-economic benefits

4.2.1 Technical Feasibility

4.2.1.1 Fuel Analysis of Pine Needles

The most significant properties of any biomass that are known to impact the gasification process are characterized by proximate and ultimate analysis (Dogru et al. 2002; Kirubakaran et al. 2009). Pine needles have cellulose—38.7%, hemicelluloses—17.7% and lignin—20.1%.

Proximate analysis characterizes the biomass feedstock for moisture content, fixed carbon, volatile material and ash content. During the combustion process, volatile material and inherently bound water are released in the form of vapour consisting of water, tar, oils and gases (Sricharoenchaikul and Atong 2009). The high value of fixed carbon is generally better suited for gasification. Ash represents the transformed minerals after the combustion of biomass. The moisture content in biomass consists of inherent moisture and surface moisture. For thermochemical conversion technologies, the biomass moisture content is an undesirable burden, which can make its ignition difficult. The proximate analysis of pine needle shows in Table 4.1 that the calorific value of the pine needles was 4947 kcal/Kg.

Ultimate analysis: ultimate analysis is basically an elemental analysis of biomass, involving measurement of carbon, hydrogen, oxygen, nitrogen and sulphur content (Seoa et al. 2010). It is necessary for calculating stoichiometric air requirements. The ultimate analysis of pine needles is shown in Table 4.2.

Table 4.1 Proximate analysis of pine needles

Parameter	%
Moisture content	9.8
Fixed carbon	16.8
Volatile material	71.1
Ash content	2.3

Table 4.2 Ultimate analysis of pine needles

Parameter	%
Carbon	53.01
Hydrogen	06.00
Nitrogen	40.40
Oxygen	00.59

4.2.1.2 Thermogravimetric Analysis (TGA)

Thermogravimetric analysis (TGA) is used to predict thermal stability or the pyrolysis process of biomass for a given temperature range (Simone et al. 2012). Pyrolysis is a thermochemical process and depends on temperature, heating rate, pressure, residence time, moisture, composition of biomass material and size of particles. The pyrolysis process converts biomass into charcoal, tar and volatile gases in the presence of an adequate temperature heating rate and an inert atmosphere. The pyrolysis gases may be used to fuel internal combustion engines and gas turbines (Quan et al. 2016). For the optimization of biomass power plants and to understand the behaviour of engines working on pyrolysis products, it is necessary to forecast pyrolysis (Kongkaewa et al. 2015).

Pine needles biomass samples for thermogravimetric analysis were taken from a local forest. Pyrolysis of pine needles was performed using thermogravimetric equipment. EXSTAR TG/DTA 6300 and Alumina pan were used. In order to achieve pyrolysis conditions, a nitrogen atmosphere was used.

The samples were heated from 10 °C/min heating rates in a nitrogen atmosphere. The thermal decomposition process consisted of three different main stages—dehydration, active pyrolysis and passive pyrolysis. The TGA curves show that there is an initial loss of moisture from the samples starting from room temperature and continuing up to about 185 °C. The nature of a TGA curve gives a clear sign about the number of phases of the thermal degradation as seen in Fig. 4.3. In the very beginning, the mass loss occurs in stage-I from room temperature to 185 °C, then in stage-II from 186 to 500 °C and the final state-III is extended up to 800 °C in stage-III.

Differential Thermogravimetric Analysis curves (DTGA) is shown in Fig. 4.4, which shows a major mass-loss peak, followed by a second peak. The second peak is small as compared to the first peak. The pyrolysis characteristics and DTGA (in $\mu\text{g}/^\circ\text{C}$) curves of pine needles are shown in Fig. 4.4. The pyrolysis of pine needles starts at 186 °C; its mass loss rate (in $\mu\text{g}/^\circ\text{C}$) increases sharply with increase in temperature and reaches a maximum value at 327 °C. The decomposition of pine needles in stage-II is linear up to the maximum value of the DTGA peaks. This is due to decomposition of cellulose and hemicellulose in the temperature range of 220–400 °C. The second DTGA peaks are quite visible; these are due to the decomposition of lignin at temperatures above 449 °C. Yang et al. (Yang et al. 2004) for the palm oil waste suggested that at temperatures above 350 °C,

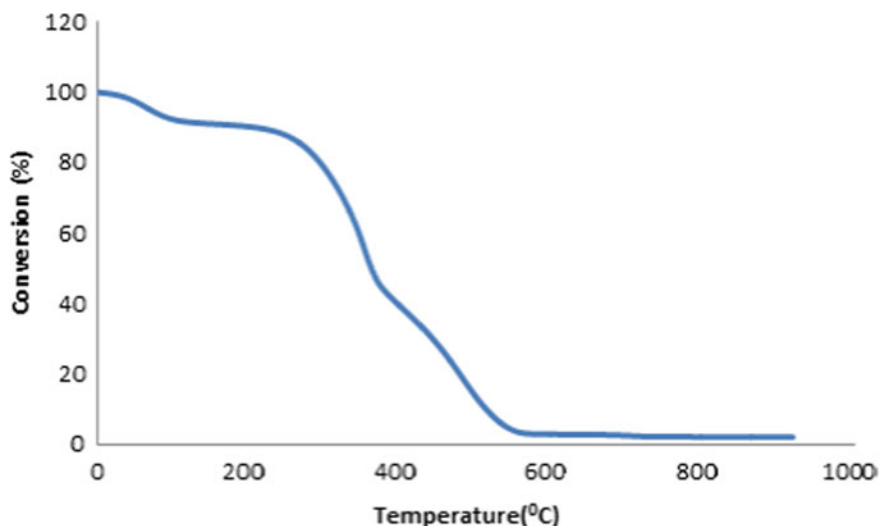


Fig. 4.3 TGA curve of pine needles biomass

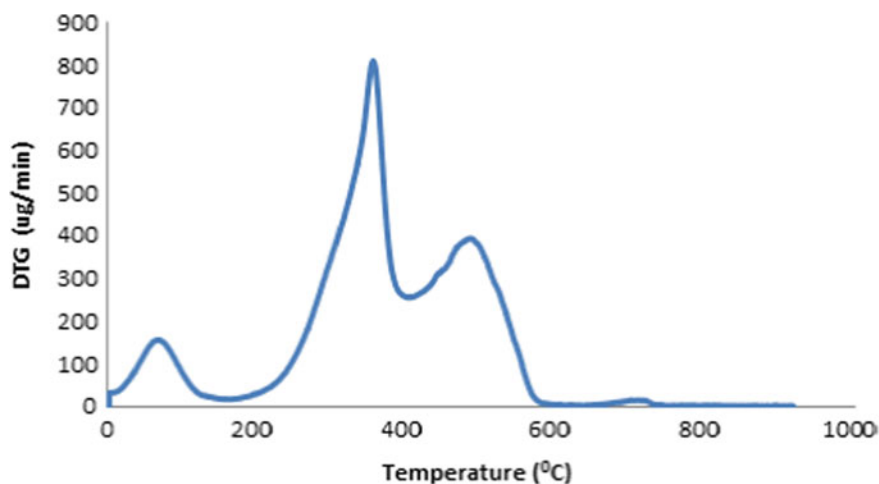
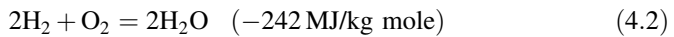
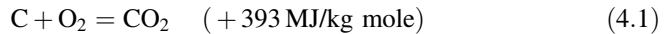


Fig. 4.4 DTGA curve of pine needles biomass

the second peak appears due to lignin decomposition. A similar trend of mass loss was observed by Gottipati and Mishra (Gottipati and Mishra 2011). In their study, in which the primary mass loss occurred roughly between 230 and 350 °C, and the second mass loss was reported between 350 and 580 °C for all samples.

4.2.1.3 Biomass Gasification Technology

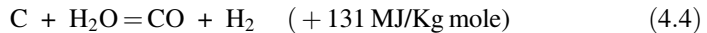
Biomass gasification is a promising bioenergy technique to turn raw low-value lignocellulose biomass into a high-value fuel gas, particularly for power generation (Bridgwater 2003; Caballero et al. 2000). Biomass gasification technology is a process of conversion of any solid biomass into gaseous fuel such as CO, H₂ and CH₄, called producer gas or syngas through its partial oxidation with gasification agent like air, water vapour, oxygen or their mixture (Kim 2009; Galindo et al. 2014). This process is defined as a thermochemical process limited to partial combustion and pyrolysis, which unlike the full combustion uses air/fuel ratios noticeably below the stoichiometric value (Warnecke 2000; Martínez et al. 2012). The chemical reactions for this process are shown below (Dutta et al. 2014; Higman and Van der Burgt 2003).



Boudouard reaction



Water Gas reaction



Methanation reaction



Biomass gasifier technology is a mature technology (Pereira et al. 2009). For the thermal application of biomass feedstocks, less than 50% moisture content is required; this biomass is then sun-dried and a moisture content between 10 and 15% is ensured before using it for gasification (Basu 2010). Gasifiers are widely and easily available in several designs and capacities to suit different requirements. Electricity can be generated by the system as and when required at the location required. Whereas other renewable energy sources like solar and wind-based units are more location and time specific, and have issues with reliability and consistency. Biomass gasifier based systems can provide steady reliable power over a long time period (Buragohain et al. 2010).

For smooth and trouble-free operation, the gasifier needs uniform-sized dry biomass. Most gasifier systems are designed either for woody biomass or dense briquettes made from loose biomass for loose pulverized biomass. The end product of biomass gasification is producer gas which can be used for generating motive power through internal combustion engines, which are then connected to electric generators to produce electricity (Prasad et al. 2014). The fuel-to-electricity

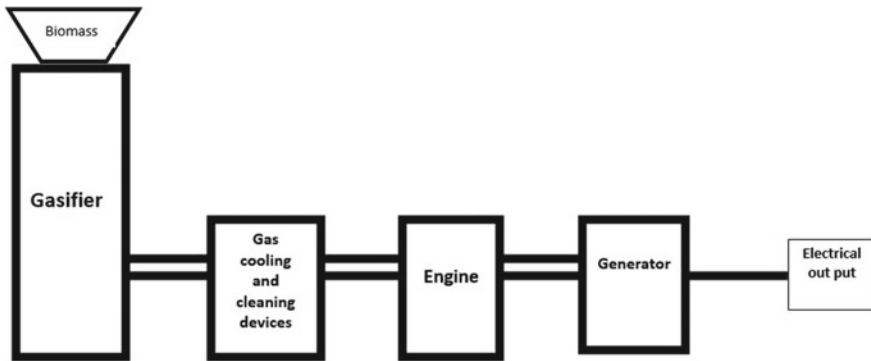


Fig. 4.5 Gasification plant setup

efficiency of gasification is much higher than that of direct combustion. Figure 4.5 shows the gasification plant setup. Since the gasification process is dependent upon several complex reactions, the quality of the resulting producer gas also depends on several factors like feedstock, operating conditions, reactor design, gas cooling and cleaning devices, and the gasification agent (Sansaniwal et al. 2017).

4.2.2 Climate Change Mitigation

Pine needles are the primary reasons for forest fires during the summer session in the Himalayan region. These fires damage the fertile top layer of soil and destroy the local ecology and grazing grounds for cattle. By utilizing pine needles in energy generation, local people will be encouraged to collect them, thus removing them from the forest floor. Pine needles as biomass is a CO₂ neutral fuel and, therefore, unlike fossil fuels, diesel does not contribute to net CO₂ emissions, which makes pine needles based power generation systems an attractive option in mitigating the adverse effects of climate change. In this way, we will not only generate energy from this biomass but also help to preserve and save the environment by

- Mitigation of climate change by replacing fossil fuels with pine needles gasification (renewable energy) due to its carbon-neutral behaviour.
- Preventing greenhouse gas emissions of forest fires.
- Prevention of deforestation through fires.
- Regeneration of biodiversity and protection of wildlife.

4.2.3 Availability

Indian pine forests spread over 8.9 Lakh Hectares and occur between 450 and 2300 m altitudes from Jammu and Kashmir, Himachal Pradesh, Uttarakhand, parts of Sikkim and Arunachal Pradesh (FRI 2019). The total available 0.89 million Hectares pine forest will produce approximately 10.591 million tons of pine needles biomass annually (MNRE 2019). For electricity generation, 4.5 tons of pine needles are sufficient to run a 100 kW gasifier for 24 h (MNRE 2012). One of the primary requirements for biomass-based gasification plants is locally available biomass to ensure smooth operation.

4.2.4 Socio-economically Beneficial

Biomass gasifier based systems are likely to create employment opportunities in rural areas for local people. These gasification plants provide job opportunities from the collection of biomass, system maintenance to distribution. A large portion of the Himalayan hilly states experience acute negative population growth because of the absence of job availability in these regions; individuals are moving to various urban areas in order to get jobs.

4.3 Barriers

The key barriers for pine needles gasification based energy generation for the Himalayan region can be divided into two categories:

- Economically viable
- Feasibility of collection, transport and storage.

4.3.1 Economically Viable

The primary segments of the capital expense of the biomass gasifier system are biomass gasifier unit included cooling and cleaning unit and an engine generator. Different parts of capital expense of gasifier system incorporate civil construction (room shed and concrete support various components of gasifier systems), biomass storage room, biomass preparation unit, electrical wiring, tar removal system, ash removal facility, initial investment cost for biomass gasification system is too high as compared to fossil fuel systems. The operating costs of the gasifier system include biomass collection charges, transportation charges, labour charges,

maintenance charges and replacement of spare parts on occasional basis (Buragohain et al. 2010). It is thus generally difficult for an average individual and a local community to invest in pine needles based gasification systems.

4.3.2 Feasibility of Collection, Transport and Storage

Due to geographical location, the only manual collection is feasible, which affected by the availability of manpower and their willingness to collect. Although biomass has advantages over other renewable energy technologies, it can be stored in advance and used when needed. Storage of biomass is needed to match supply and demand at all times because the availability of biomass is a seasonal process. Like other biomasses, pine needles can also be collected and stored. Collection, transportation and storage of biomass are cost intensive, which affect the running cost of the plant.

4.4 Conclusion

In the Himalayan region, there is a huge scope for the development of small-scale biomass gasification plants because of the availability of pine needles for energy generation in the region, which still remains unharnessed. Gasification projects have the potential to become the backbone of the local power sector in this mountainous region if they are supported in a competent manner by the government, at least in the initial stages.

Despite technical feasibility, there exist environmental and ecological benefits of using pine needles for energy generation. There are barriers related to economic viability, collection, storage and transportation. In order to achieve our energy and environmental goal, these barriers need to be explored in more detail so that policies and programmes targeting biomass gasification based energy generation in the future will have a more bespoke role to play in closing the gap between energy demand and environmental protection. In order to extensively develop pine needles based energy generation in the Himalayan region, good and enforceable policies with strong political will are necessary for the following areas:

- Establishment of suitable policies and rules and implementation of these in a proper time-bound manner.
- Encouragement of community participation/ownership.
- Manpower training with skill knowledge.
- Financial support for research and subsidy incentives to individual, private companies and communities.

References

- Basu P (2010) Gasification theory and modelling of gasifiers. In: Biomass gasification design handbook. Academic Press, Boston
- Bisht AS, Thakur NS (2016) Pine needle biomass a potential energy source for himalayan region. In: 7th ICEEE conference. IEEE Xplore, pp 1–4
- Bisht AS, Singh S, Kumar SR (2014) Pine needles a source of energy for Himalayan region. *Int J Sci Technol Res* 3:161–164
- Bridgwater AV (2003) Renewable fuels and chemicals by thermal processing of biomass. *Chem Eng J* 91:87–102
- Buragohain B, Mahanta P, Moholkar VS (2010) Biomass gasification for decentralized power generation: the Indian perspective. *Renew Sustain Energy Rev* 14:73–92
- Caballero MA, Corella J, Aznar MP, Gil J (2000) Biomass gasification with air in fluidized bed. Hot gas cleanup with selected commercial and full-size nickel based catalysts. *Ind Eng Chem Res* 39:1143–1154
- Central Electricity Authority Govt of India Installed Capacity (2019). <http://www.cea.nic.in/monthlyinstalledcapacity.html>. Accessed 09 Jan 2019
- Climate Action Tracker (2018). <http://climateactiontracker.org/countries/india.html>. Last accessed 07 Feb 2018
- Digman B, Joo HS, Kim, D-S (2009) Recent progress in gasification/pyrolysis technologies for biomass conversion to energy. *Am Inst Chem Eng Environ Prog Sustain Energy* 28(1):47–51
- Dogru M, Howarth CR, Akay G, Keskinler B, Malik AA (2002) Gasification of hazelnut shells in a downdraft gasifier. *Energy* 27:415–427
- Dutta PP, Pandeya V, Dasa AR, Baruah SD (2014) Down draft gasification modelling and experimentation of some indigenous biomass for thermal applications. *Energy Procedia* 54: 21–34
- FRI (2019), Indian Council of Forestry Research and Education, Dehradun. Chir pine (*Pinus roxburghii*). Dehradun, Forest Research Institute. http://www.frienvi.nic.in/WriteReadData/UserFiles/file/pdfs/Chir_Pine.pdf. Last accessed on 02 Nov 2019
- Galindo AL, Lora SL, Andrade RV, Giraldo SY, Jaén RL, Cobas VM (2014) Biomass gasification in a downdraft gasifier with a two-stage air supply: effect of operating conditions on gas quality. *Biomass Bioenergy* 61:236–244
- Gottipati R, Mishra S (2011) A kinetic study on pyrolysis and combustion characteristics of oil cakes: effect of cellulose and lignin content. *Fuel Chem Technol* 39(4):265–270
- Higman C, Van der Burgt M (2003) Gasification 1st ed. Gulf Professional Publishing
- Indian Express (2018). <http://indianexpress.com/article/india/india-news-india/uttarakhand-forest-fires-mi-17-choppers-to-spray-water-over-burning-forests-2778328/>. Accessed 20 Feb 2018
- Kirubakaran V, Sivaramakrishnan V, Nalini R, Sekar T, Premalatha M, Subramanian P (2009) A review on gasification of biomass. *Renew Sustain Energy Rev* 13:179–186
- Kongkaewa N, Pruksakitb W, Patumsawada S (2015) Thermogravimetric kinetic analysis of the pyrolysis of rice straw. *Energy Procedia* 79:663–670
- Martínez JD, Mahkamov K, Andrade RV, Lora EES (2012) Syngas production in downdraft biomass gasifiers and its application using internal combustion engines. *Renew Energy* 38:1–9
- MNRE (2012) Ministry of new and renewable energy. Government of India, Empowering rural India the RE way: inspiring success stories
- MNRE (2015–2016) Ministry of new and renewable energy. Government of India, Annual report 2015–2016
- MNRE (2018) Ministry of new and renewable energy. Government of India, Phiscal progress. <http://mnre.gov.in/mission-and-vision-2/achievements>. Last accessed 30 Dec 2018
- MNRE (2019) Ministry of New and Renewable energy Government of India, Tentative State-wise break-up of Renewable Power target to be achieved by the year 2022. <https://mnre.gov.in/file-manager/UserFiles/Tentative-State-wise-break-up-of-Renewable-Power-by-2022.pdf>. Last accessed 09 Jan 2019

- Pereira EG, Da Silva JN, De Oliveira JL, MacHado CS (2009) Sustainable energy: a review of gasification technologies. *Renew Sustain Energy Rev* 16:4753–4762
- Prasad L, Subbarao PMV, Subrahmanyam JP (2014) Pyrolysis and gasification characteristics of Pongamia residue (de-oiled cake) using thermogravimetry and downdraft gasifier. *Appl Therm Eng* 63:379–386
- Quan C, Gao N, Song Q (2016) Pyrolysis of biomass components in a TGA and a fixed-bed reactor: thermochemical behaviors, kinetics, and product characterization. *J Anal Appl Pyrol* 121:84–92
- Roberts Cribbler (2018). <https://robertscribblers.com/2016/05/03/the-fires-of-climate-change-are-burning-the-himalayas>. Accessed 10 Feb 2018
- Safi MJ, Mishra IM, Prasad B (2004) Global degradation kinetics of pine needles in air. *Thermochim Acta* 412:155–162
- Sansaniwal SK, Rosen MA, Tyagi SK (2017) Global challenges in the sustainable development of biomass gasification: an overview. *Renew Sustain Energy Rev* 80:23–43
- Schaller S (2016) The power of the pines—small-scale bioenergy deployment in the himalayas. Master Thesis, Graduate Institute of International and Development Studies, Switzerland
- Seoa DS, Parka SS, Hwanga J, Tae-U Yu (2010) Study of the pyrolysis of biomass using thermo-gravimetric analysis (TGA) and concentration measurements of the evolved species. *J Anal Appl Pyrol* 89:66–73
- Simone M, Barontini F, Nicoletta C, Tognotti L (2012) Gasification of pelletized biomass in a pilot scale downdraft gasifier. *Bioresour Technol* 116:403–412
- Sricharoenchaikul V, Atong D (2009) Thermal decomposition study on *Jatropha curcas* L. waste using TGA and fixed bed reactor. *J Anal Appl Pyrol* 85:155–162
- UNFCCC (2018). Adoption of the paris agreement. FCCC/CP/2015/L.9. United Nations. <https://unfccc.int/resource/docs/2015/cop21/eng/109r01.pdf>. Last accessed on 07 Jan 2018
- Uttarakhand Renewable Energy Development Agency (2018). <http://ureda.uk.gov.in/pages/display/142-pine-needle-based-project>. Accessed 20 Feb 2018
- Warnecke R (2000) Gasification of biomass: comparison of fixed bed and fluidized bed gasifier. *Biomass Bioenergy* 18:489–497
- Yang H, Yan R, Chin T, Liang DT, Chen H, Zheng C (2004) Thermogravimetric analysis-Fourier transform infrared analysis of palm oil waste pyrolysis. *Energy Fuels* 18:1814–1821

Chapter 5

Enhancement of Biofuel Quality Through Sustainable In-bed Additives



Joel George, P. Arun and C. Muraleedharan

5.1 Introduction

Energy generation from renewable and eco-friendly energy resources like biomass is significant in the context of sustainable development. A considerable amount of biomass in the form of crop residues is generated in the Indian agricultural sector (Hiloidhari et al. 2014). There is ample scope for utilizing these biomass resources to generate energy. Energy can be extracted from these biomasses through gasification, a thermochemical process (Basu 2010). Gasification technology is expected to play an important role in intensifying the use of biomass as a major sustainable and renewable energy source. However, a recognized setback of biomass gasification is related to the high tar content of the producer gas. Tar is a thick black highly viscous liquid which is a complex mixture of condensable hydrocarbons with a molecular weight larger than benzene (Devi et al. 2003). Gaseous feedstock generated from biomass through gasification is tar laden. The entrained tar in the producer gas is undesirable because of various hitches related with condensation, polymerization and formation of tar aerosols. Formation of excessive tar which interrupts the smooth functioning of downstream components is a technological barrier to implement commercial-scale biomass gasification technology. Further, the generation of tar lowers the overall conversion efficiency. The successful working of a gasifier using biomass as feedstock thus demands appropriate tar reduction and removal during gasification.

Enhancement of the quality and quantity of producer gas yield focused on biomass valorisation is thus a major concern in the gasification investigations. Calcium oxide can be used as an in-bed additive in fluidised bed gasification process. It is capable of performing the dual role as a catalyst and as a sorbent to enhance hydrogen yield and

J. George (✉) · P. Arun · C. Muraleedharan
Mechanical Engineering Department, National Institute of Technology Calicut,
Kozhikode, India
e-mail: joelpull@gmail.com

concentration, in the producer gas obtained in biomass gasification (Udomsirichakorn et al. 2013). Calcium oxide can be obtained by thermal decomposition of calcium carbonate which is generally found in rocks across the world. Further calcium carbonate is a major component of marine organism shells, snail shells, pearls and eggshells (Olivares-Marín et al. 2013). Residual shells in large quantities are produced from egg and egg derivative consumption. These shells pose a threat to the environment as a result of microbial action. Calcium carbonate is the primary ingredient of egg shell (90–95%) along with magnesium and protein (Olivares-Marín et al. 2013; Laca et al. 2017). The utilisation of residual raw eggshells can substitute the natural sources of calcium, conserve natural resources from rock and soil, reduce waste problem in households, reduce global warming, and promote green ceramic materials and products (Tangboriboon et al. 2012).

Calcination of eggshells at 900 °C for an hour transforms the chemical composition from calcium carbonate (CaCO_3) to calcium oxide (CaO) almost entirely (97–99%). The rhombohedral form is transformed completely into a face-centered cubic lime (CaO). The phase transformation from calcium carbonate (CaCO_3) to calcium oxide (CaO) depends on the calcination temperature and time. Higher the calcination temperature and longer the calcination time, the more complete the phase transformation. Calcium oxide is the most abundant component (97.4%) in the calcined egg shell (Witoon 2013). The feasibility of using calcined eggshells as sustainable in-bed additives in fluidised bed gasification process was investigated based on characterization studies and experimental investigations.

5.2 Materials and Methods

Selected agricultural crop residues—coffee husk and sawdust of particle size 300–500 microns were used as the feedstock in experimental investigation. The samples collected were air dried for 2–3 days to make it suitable for fluidized bed gasification. Calcined eggshells prepared from raw chicken eggshells were used as in-bed additives during the gasification process. Physico-chemical behavior of the biomass samples was analysed through characterization tests. Characterization of calcined eggshells was carried out to examine the physical and chemical properties of calcined eggshells. Enhancement of hydrogen yield from each biomass sample was assessed in experimental investigation.

5.2.1 Characterization of Biomass and Eggshell

Ultimate analysis was carried out to determine the elemental composition (C, H, O, N, and S) of biomass in percentage weight. The analysis was carried out using an ultimate analyzer (make: Elementar Vario EL III) at Sophisticated Analytical Instruments Facility (SAIF), STIC, Kochi. The proximate analysis determines the

Table 5.1 Results of ultimate analysis and proximate analysis

Biomass	Ultimate analysis (%)					Proximate analysis (%)			
	C	H	O	N	S	FC	MC	VM	AC
Coffee husk	41.82	6.07	50.3	1.66	0.14	17.3	10.4	64.4	7
Sawdust	44.58	6.2	48.8	0.42	0	14.6	11.2	72.1	2.1

FC Fixed carbon, *MC* Moisture content, *VM* Volatile matter, *AC* Ash content

percentage by weight of moisture content, volatile matter, fixed carbon and ash content in the biomass. Proximate analysis was carried out using laboratory facilities at National Institute of Technology Calicut (Table 5.1).

The morphologies of the dried raw egg shell and calcined egg shell were studied by scanning electron microscope (SEM; Philips XL30) to understand the structural changes during calcination. A carbonation test was carried out to measure the carbon dioxide sorption capacity of the calcined egg shells. The tests were carried out in a thermogravimetric analyser (TA Q50) in a carbonating atmosphere by replacing the N_2 purge gas flow with an equal amount of CO_2 . A comparison of carbonation was carried out between calcined eggshells and commercial CaO. Test samples were heated from ambient temperature to 700 °C and maintained for about 80 min. An FTIR analysis was carried out before and after carbonation to confirm the carbonation of calcined eggshells.

5.2.2 Experimental Investigation

The experimental investigations were carried out in a bubbling fluidised bed gasifier (Fig. 5.1). The detailed description of the experimental setup has been reported elsewhere (George et al. 2018). The heating chamber of the gasifier setup was pre-loaded with 1.8 kg bed material. The chamber was brought to pre-set temperature (700 °C) using heating coils, which takes about 4–5 h. The biomass was fed continuously and air supply rate was suitably controlled to ensure bed fluidisation and producer gas generation. The low pressure, low temperature steam (2 bar, 300 °C) was then injected (50 cm above the bed in the beginning of the freeboard zone) to enable gas reformation. The investigation was carried out in two phases. In the first phase steam injected air gasification of selected biomass was carried out with river sand as the bed material. In the second phase of the investigation, the bed of river sand was replaced by a bed consisting of a mixture of river sand and calcined eggshell in the ratio 2:1 by weight and the investigation procedure was repeated. Additionally 5% of calcined eggshell was added to biomass feed to take care of erosion. The conditioned gas in each case was analysed using a producer gas analyzer to determine the product gas composition. Different operating conditions were achieved by varying the biomass feed rate and bed temperature. Details of the operating conditions for different crop residues in experimental investigation are presented in Table 5.2.

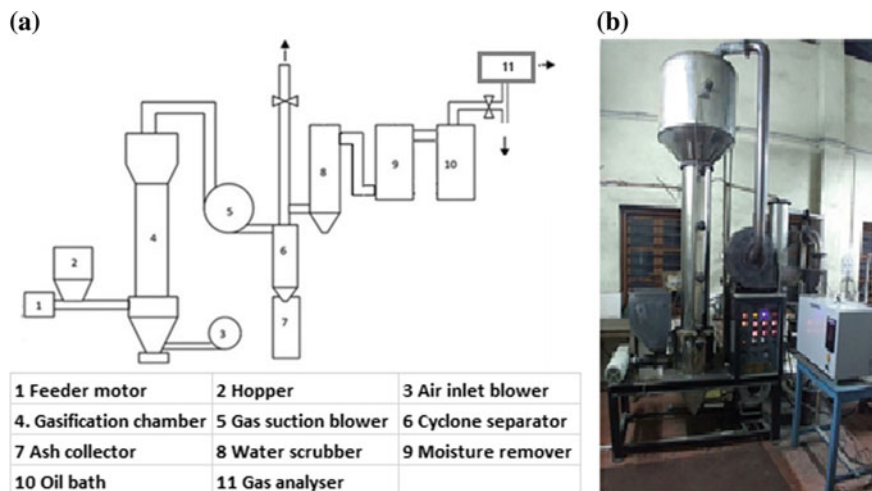


Fig. 5.1 Bubbling fluidised bed gasifier. **a** Experimental setup. **b** Photograph

Table 5.2 Details of operating conditions for different biomasses

Biomass	Operating condition	Feed rate (kg/h)
Coffee husk	T = 700–760 °C, ER = 0.38, SBR = 0.52	Air supply rate = 15.4 Biomass feed rate = 27.6
Coffee husk + calcined eggshell	T = 700–760 °C, ER = 0.38, SBR = 0.52	Air supply rate = 15.4 Biomass feed rate = 27.6
Sawdust	T = 680–740 °C, ER = 0.30, SBR = 0.56	Air supply rate = 17.8 Biomass feed rate = 27.6
Sawdust + calcined eggshell	T = 680–740 °C, ER = 0.30 SBR = 0.56	Air supply rate = 17.8 Biomass feed rate = 27.6

5.3 Results and Discussion

5.3.1 Feasibility of Calcined Eggshell Based on Characterization

Morphologies of egg shell and calcined egg shell in SEM analysis shown in Fig. 5.2 reveal the structural changes that occurred during calcination. Morphology of raw eggshell presents a rough and undulated crystal structure while calcined eggshell, an interconnected skeleton structure in which nano crystallites of CaO are

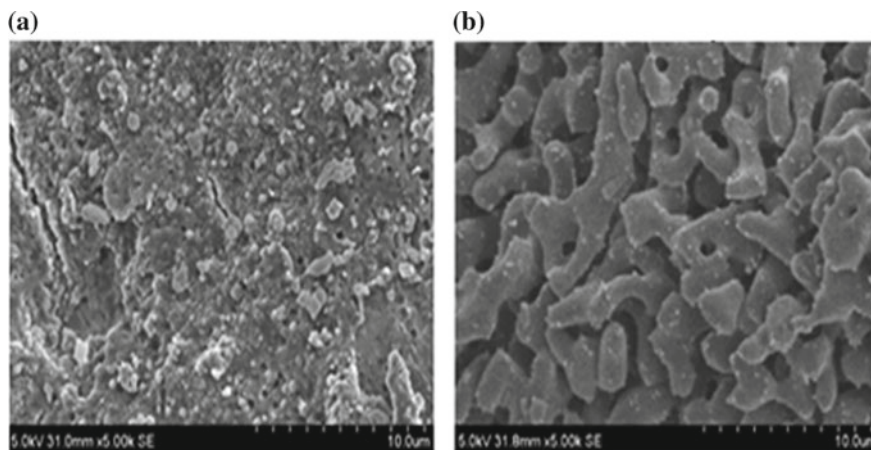


Fig. 5.2 Morphology of **a** egg shell and **b** calcined egg shell obtained in SEM

dispersed. Morphology of CaO obtained in SEM analysis confirms the porous nature of calcined eggshells which makes it a suitable sorbent.

Comparison of the carbonation capacities of commercial calcium oxide (CCO) and calcined eggshells (CES) was carried out in thermogravimetric analyser. An increase in weight during carbonation for CCO and CES due to the sorption of CO_2 was observed when the samples were maintained at $700\text{ }^\circ\text{C}$. The increase in weight of the sample with time during carbonation is presented in Fig. 5.3. Around 50% increase in weight is gained by both samples. It can be observed from Fig. 5.3 that sorption rate is more for CCO than CES in the initial period of the experiment. However towards the end the sorption rate of calcined eggshell is slightly higher.

The FTIR spectrums displayed in Fig. 5.4 confirm the sorption of CO_2 during the carbonation process. The peak at the extreme right (Fig. 5.4a) in the region for inorganic compounds (wavenumber range between 400 and 600 cm^{-1}), indicates the broad band vibration of CaO metal oxide. The peaks in the region around 724 – 924 cm^{-1} (875 and 712 cm^{-1} to be specific) in Fig. 5.4b indicate the presence of CaCO_3 as the basic component in the carbonized sample. However these peaks are absent in the spectrum of calcined egg shells (Fig. 5.4a).

5.3.2 Feasibility Based on Assessment of Gasification

The results of the experimentation carried out at specified operating conditions in the case of coffee husk and sawdust with additives (WA) and without additives (WOA) are displayed in Fig. 5.5. It is observed that within the operating temperature hydrogen, carbon monoxide, carbon dioxide and methane yields are increasing with increase in temperature with the addition of in-bed additives (WA).

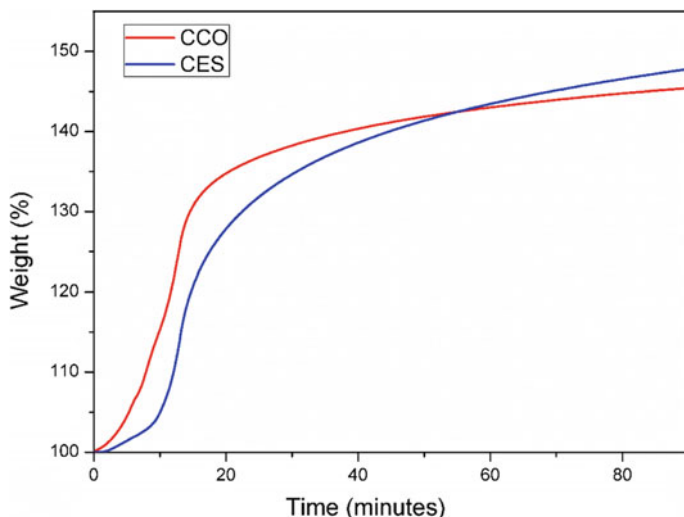


Fig. 5.3 Comparison of the carbonation capacities of CCO and CES

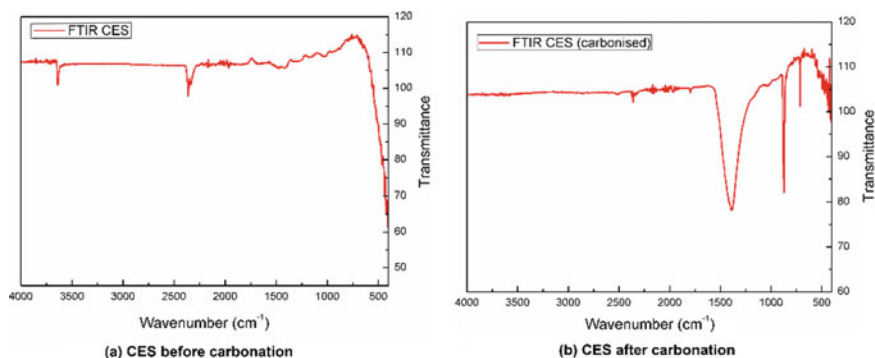


Fig. 5.4 FTIR spectrum of calcined eggshells

The corresponding yields obtained are higher than that without in-bed additives (WOA) in the case of hydrogen and carbon dioxide. However, in the case of carbon monoxide and methane the corresponding yields obtained with in-bed additives are lower than that without in-bed additives at each operating condition.

Generally hydrogen yield increases with increase in temperature. The endothermic reactions are enhanced with the increase in temperature increasing the hydrogen yield. The increase in hydrogen yield with the addition of in-bed additives is mainly attributed to CO shift and tar reforming/cracking reactions promoted by the presence of calcium oxide in calcined eggshells. In the experimental investigations carried out, an increase in hydrogen yield in the range 15–25% is generally

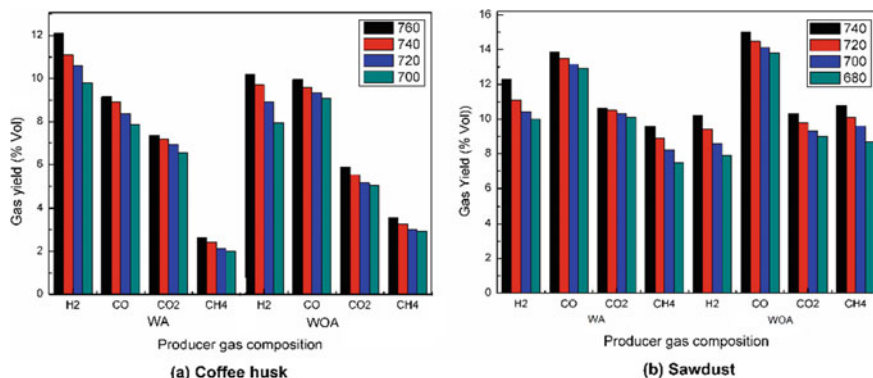


Fig. 5.5 Comparison of gas compositions and corresponding yield **a** coffee husk temperature range $T = 700\text{--}760$ °C, ER = 0.38 and SBR = 0.52, **b** sawdust temperature range ($T = 680\text{--}740$ °C, ER = 0.3 and SBR = 0.56)

observed within the operating temperature range. Comparing the hydrogen yields with additives (WA) and without additives (WOA) in the case of coffee husk and sawdust, it is observed that the increase in hydrogen yield (20%) in the case of sawdust is more than the increase in hydrogen yield (18%) in the case of coffee husk. This is mainly attributed to improved operating conditions like higher SBR and lower ER.

Carbon dioxide and carbon monoxide concentrations increase with increase in temperature. However, it is to be noted that CO concentration is lower and CO₂ concentration is higher in the case with in-bed additives (WA) than that without in-bed additives (WOA) (Fig. 5.6). This is attributed to enhancement of CO shift reactions promoted by the sorption of CO₂ in the presence of CaO in CES additives. However, sorbent activity of CaO is reduced at operating temperatures above 700 °C in the case of gasifiers operating at atmospheric pressure (Xu et al. 2005). As a result the carbon dioxide concentration in the reaction system tends to increase.

Apart from the higher operating temperatures at atmospheric pressure, the comparatively high value of equivalence ratio and low steam to biomass ratio might have affected the sorbent action. It is felt that even though the calcined eggshell additives were functioning as a sorbent, the sorbent quantity and sorbent action were inappropriate to meet carbon dioxide generated within the reaction system. The sorbent action of calcined eggshells is examined based on the analysis of the bed additive after the gasification process. Samples of bed additives remaining in the bed are analysed using FTIR techniques. The FTIR analysis revealed the existence of sharp peaks in the region around $724\text{--}924$ cm⁻¹ which indicates the presence of CaCO₃. The transformation of CaO in calcined eggshells to CaCO₃ is attributed to the absorption of CO₂ by calcined eggshells.

It is evident that by using calcined eggshell as in-bed additive, both H₂ concentration and yields as well as total gas yield increase. The decrease in CO concentration can be explained by the influence of CaO which absorbed CO₂ and

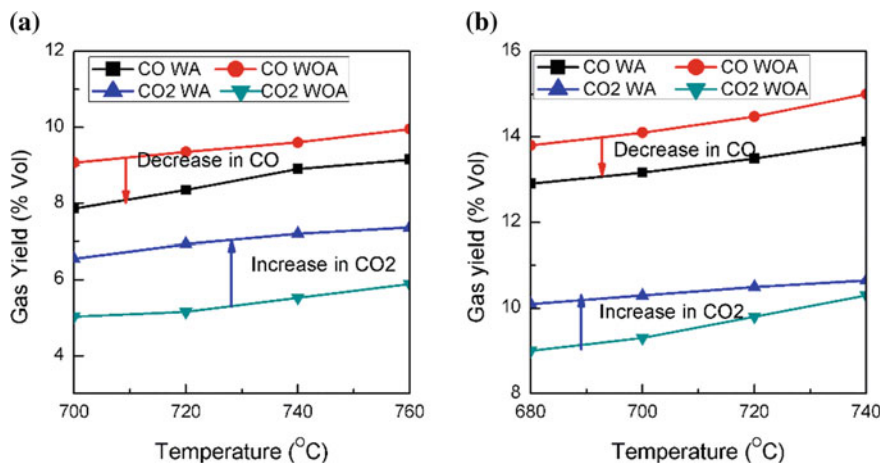


Fig. 5.6 Effect of in-bed additives on CO and CO₂ yields during the gasification **a** coffee husk **b** sawdust

lowered its partial pressure, thereby moving water—gas shift reaction in forward direction to enhance H₂ output or higher H₂ formation in the hydrocarbon reforming reactions. This is supported by the fact that the concentration of CH₄ obtained in the presence of CaO is less than that obtained from sand bed gasification.

5.3.3 Tar Yield

A bubbling fluidised bed gasifier generally operates within the temperature range 650–850 °C. In this temperature range generally secondary and tertiary tars are formed. Secondary tar products are characterized by phenolics and olefins. Among the tertiary products, toluene, naphthalene and benzene contribute a major share. Though tar is a mixture of various hydrocarbons, only the tar yield of the main components which occupies a major share in tar yield is considered.

The reduction in tar obtained by using calcined eggshell as the in-bed additives for sawdust in steam injected air gasification can be observed from the Fig. 5.7. Out of the different tar components, the yield of major tar components like, benzene, phenol, toluene and naphthalene was identified by GC-MS analysis. Presence of secondary tar components in the form of phenol occupied a major share (42.8%). The amount of tertiary tars identified as benzene, toluene and naphthalene occupied a share of 12.5%. Gravimetric tar which is not detected by GC-MS analysis contributed nearly 44.7% of the identified tar components. Catalytic action of CaO in calcined eggshell resulted in overall reduction (% Reduction) in tar yield by around 54%. Details of tar yield and their reduction in the presence of CaO are shown in Table 5.3.

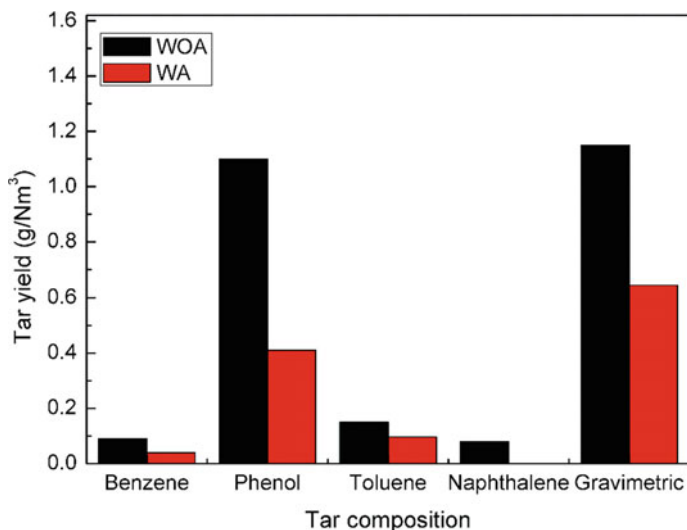


Fig. 5.7 Comparison of tar composition with additives (WA) and without additives (WOA)

Table 5.3 Tar yield and reduction with calcined eggshell

Tar type	Tar component	WOA (g/Nm ³)	WA (g/Nm ³)	% reduction
Secondary	Phenol	1.1	0.41	62
Tertiary	Benzene	0.09	0.04	57.5
	Toluene	0.15	0.096	
	Naphthalene	0.08	0	
Gravimetric	GC-MS undetectable	1.15	0.645	44
Total tar yield		2.57	1.191	54.3

5.4 Conclusion

The characterization of raw and calcined eggshells was carried out to assess the feasibility of using calcined eggshell as a substitute of CaO in biomass gasification. Based on the results of characterization tests calcined eggshell (CES) is considered as sustainable in-bed additive (as a catalyst) for tar reformation and sorbent for carbon dioxide absorption. Experimental investigations with and without the addition of CES revealed a pronounced catalytic action compared to sorbent action in the operating temperature range. An increase in hydrogen yield of 15–25% is obtained within the operating range. Catalytic action of CaO in calcined eggshell resulted in overall reduction in tar yield by around 54%. The sorbent action is inferred from the FTIR analysis of the left out bed additives which confirmed the

transformation of calcium oxide in CES to calcium carbonate. Based on the investigations carried out, it is concluded that calcined eggshells can be adopted as a sustainable in-bed additive in the fluidised bed biomass gasification process.

Acknowledgements Authors gratefully acknowledge the financial support provided by Ministry of New and Renewable Energy through R&D project on 'Investigation on bio-hydrogen production by thermo-chemical method in fluidised bed gasifier under catalytic support and its utilization' (No. 103/181/2010-NT).

References

- Basu P (2010) Biomass gasification and pyrolysis: practical design and theory. Elsevier Inc, Burlington, USA
- Devi L, Ptasiński KJ, Janssen FJJG (2003) A review of the primary measures for tar elimination in biomass gasification processes. *Biomass Bioenergy* 24:125–140
- George J, Arun P, Muraleedharan C (2018) Assessment of producer gas composition in air gasification of biomass using artificial neural network model. *Int J Hydrog Energy* 43 (20):9558–9568
- Hiloidhari M, Das D, Baruah DC (2014) Bioenergy potential from crop residue biomass in India. *Renew Sustain Energy Rev* 32:504–512
- Laca A, Laca A, Díaz M (2017) Eggshell waste as catalyst: a review. *J Environ Manag* 197:351–359
- Olivares-Marín M, Cuerda-Correa EM, Nieto-Sánchez A, García S, Pevida C, Román S (2013) Influence of morphology, porosity and crystal structure of CaCO_3 precursors on the CO_2 capture performance of CaO-derived sorbents. *Chem Eng J* 217:71–81
- Tangboriboon N, Kunanuruksapong R, Sirivat A (2012) Preparation and properties of calcium oxide from eggshells via calcination. *Mater Sci* 30(4):313–322
- Udomsirichakorn J, Basu P, Salam PA (2013) Effect of CaO on tar reforming to hydrogen-enriched gas with in-process CO_2 capture in a bubbling fluidized bed biomass steam gasifier. *Int J Hydrog Energy* 38(34):14495–14504
- Witton T (2013) Characterization of calcium oxide derived from waste eggshell and its application as CO_2 sorbent. *Ceram Int* 37(2):3291–32988
- Xu G, Murakami T, Suda T, Kusama S (2005) Distinctive effects of CaO additive on atmospheric gasification of biomass at different temperatures. *Ind Eng Chem Res* 5864–5868

Chapter 6

Development of a Systematic Design Procedure for Circulating Fluidized Bed Gasifier



P. Suraj, P. Arun and C. Muraleedharan

6.1 Introduction

Consequent to population growth and industrialization the energy demand has increased rapidly for electricity generation, heating, cooling and transportation. Energy has become an indispensable part of human life. According to review report on world energy by British petroleum (BP) global primary energy demand has increased by 1% (25 million tons of oil equivalent) in terms of coal. This rapid demand has resulted in the over exploitation which leads to air pollution and global warming, loss of biodiversity as well as depletion of the fossil fuel resources. The carbon emission is found to be increased by 1.6% in the year of 2017, while there was no much increase for the years from 2014 to 2016 (Dudley 2018). Taking into consideration the energy security as well as the climate change, the time has reached for a complete shift from fossil fuel to renewable resources like solar, wind, biomass etc. (Dasappa et al. 2003). Biomass is considered as the best among others as it is easy to store, carbon neutral, and abundantly available irrespective of location and climate (Kataki et al. 2015). Biomass can be processed into fuels either through biochemical or thermochemical routes. Bio chemical conversion needs some pretreatment to valorize the biomass and the process is time consuming also. Gasification is one among the thermochemical routes which converts carbonaceous materials into a synthesis gas in which major components are Carbon monoxide and Hydrogen along with less amount of other gases like Carbon dioxide and Methane.

P. Suraj (✉) · P. Arun · C. Muraleedharan

Department of Mechanical Engineering, National Institute of Technology Calicut,
Kozhikode, India

e-mail: surajvv121@gmail.com

P. Arun

e-mail: arun.p@nitc.ac.in

C. Muraleedharan

e-mail: murali@nitc.ac.in

© Springer Nature Singapore Pte Ltd. 2020

H. Drück et al. (eds.), *Green Buildings and Sustainable Engineering*,

Springer Transactions in Civil and Environmental Engineering,

https://doi.org/10.1007/978-981-15-1063-2_6

On conversion it reduces the carbon to hydrogen ratio and increases the heating value by rejecting the noncombustible components (Basu et al. 2010). The process of gasification takes place in a chemical reactor called gasifier and the performance of production of syngas in gasification depends on certain parameters like the type and size of feed stock, moisture content, gasification medium, temperature, bed material, and the type of gasifier used (George et al. 2016).

Gasifiers are classified on the basis of gas–solid contact mode and the direction of flow of both the fuel and gasifying medium. Major classification are fixed bed/moving bed, fluidized bed, and entrained flow type (McKendry 2002). In agriculturally dominant countries fluidized bed gasifier technology is suitable for gasification as it can handle a wide variety of solid fuels such as crop residues, forest residues, animal wastes, etc., and the problems related to updraft moving bed are eliminated in fluidized bed gasifiers (Natarajan and Nordin 1998; Alimuddin et al. 2010). Fluidized bed gasifier has a bed made of sand particles which are kept under semi-suspended condition by the passage of air, air-steam, or oxygen (gasifying mediums) at the appropriate velocity. Such type of gasifiers can provide a uniform temperature and excellent mixing. With the increased thermal inertia of the bed and uniform temperature distribution, it has fuel flexibility as well as less chance of ash sintering and agglomeration (Basu et al. 2010). The bed agglomeration is one of the major problems associated with gasification, especially in bubbling fluidized bed (George et al. 2018). As the gasifying medium is passed through the bed of fine particles of sand or inert materials in bubbling fluidized bed (BFB) gasifier, a channel like flow develops through the sand and the bed appears to be like boiling with bubbles forming at the bottom and as it rises, it gets coalesce and burst at the top (Atikah et al. 2016). The solid mixing rate in BFB is very high which aids the gasification but it reduces the carbon conversion efficiency as there is a chance for some unconverted solid to get with the waste stream of solids. On increasing the gas flow through the fluidized bed the void fraction will increase. Further increment in gas flow will cause difficulty in discerning the interface between the freeboard and fluidized bed. Such a fluidized bed in which particle is carried away and returned to bed is called circulating fluidized bed (Bain and Broer 2011; Marano and Ciferno 2002).

The circulating fluidized bed consists of a cyclone, riser and solid recycle device and it operates at a velocity greater than the terminal velocity of the particle. The bed material will get entrained with the gas stream to the top of the riser due to the high operating velocity (3–7 m/s), gets separated in the cyclone and solid returns to the bed. CFB is having high carbon conversion efficiency by providing more solid residence time within the loop. CFB provides good mixing, excellent heat and mass transfer characteristics and high efficiency (Basu 2006). It is noted that the cold gas efficiency of gasification process is in the range of 30–60% approximately. A cold gas efficiency of maximum 56.9% was reported by Yan et al. (Cao et al. 2006). The efficiency of gasification process depends on not only gasifier geometric parameters but operating conditions and biomass composition also. In the present work a systematic procedure is developed for the design of CFB by taking sand as bed material and air as gasifying medium. The paper illustrates the systematic design

procedure taking the case of a typical circulating fluidized bed gasifier of capacity 150 kW_{th} with a nominal gasification efficiency of 50% and saw dust considered as the biomass feedstock.

6.2 Materials and Methods

6.2.1 Materials

Among the different available bed materials, sand is found to be the most suitable one as it is easily available and has low cost. Sand particle with an average diameter of 0.0006 m is selected here. The sphericity of the sand particle is assumed to be close to 1. The physical properties of sand particles are listed in Table 6.1.

Saw dust is chosen as the feed stock as it is easily and locally available in large quantities. The properties and chemical composition of saw dust are given in Tables 6.2 and 6.3, respectively.

Table 6.1 Properties of bed material

Property	Sand
Sand density (kg/m ³)	2000
Bed particle size (m)	0.0006
Bed volume fraction	0.63
Initial bed height (m)	0.2
Sphericity	> 0.85
Gasifying medium	Air
Air density (kg/m ³)	1.2

Table 6.2 Properties of biomass

Property	Sawdust
Mean size (mm)	240
Solid density (kg/m ³)	960
Bulk density (kg/m ³)	240
Calorific value (MJ/kg)	15.25

Table 6.3 Results of Ultimate and Proximate analysis

Proximate analysis result of saw dust (% weight)		Ultimate analysis result of saw dust (% weight)	
Moisture (%)	12	Carbon	44.58
Volatile matter (%)	69	Hydrogen	6.2
Ash (%)	4	Nitrogen	0.41
Fixed carbon (%)	14	Oxygen	48.81

6.2.2 Factors Affecting the Design

The gasification process is highly influenced by the operating conditions like temperature, pressure, Equivalence Ratio (ER), etc. Hence, they are vital to be considered while designing a gasifier. The operating temperature is taken as 750 °C and the equivalence ratio (ER) as 0.2. This ER is used throughout the calculation. It is assumed that if sand particles are under fast fluidization condition, then the biomass particle with same or less size than sand will also be in fast fluidized state. So, all the hydrodynamic calculations are done by considering sand alone. The design procedure followed is given in Fig. 6.1.

6.2.3 Methods

See Fig. 6.1.

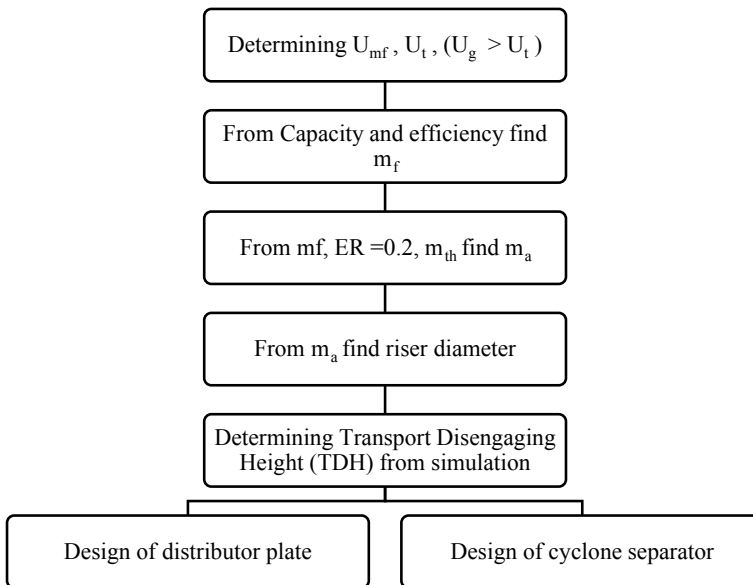


Fig. 6.1 Design procedure flow chart

6.3 Detailed Design Development

6.3.1 Minimum Fluidization Velocity Calculation

The circulating fluidized bed gasifiers usually operate in a fast fluidized regime where the gasification velocity will be within the range of 3–7 m/s. To determine the fast fluidization velocity for the given bed properties it is necessary to determine the minimum fluidization velocity (U_{mf}). Minimum fluidization velocity is the velocity at which the drag and buoyant force get balanced with gravity, which is given by Eqs. (6.1–6.3) (Brenner et al. 1994).

$$Re_{mf} = \frac{d_p U_{mf} \rho_g}{\mu_g} = [C_1^2 + C_2 Ar]^{0.5} - C_1 \quad (6.1)$$

$$Ar = \frac{\rho_g (\rho_p - \rho_g) g d_p^3}{\mu_g^2} \quad (6.2)$$

From (6.1) and (6.2) U_{mf} is calculated where $C_1 = 25.3$, $C_2 = 0.0651$ (Brenner et al. 1994).

6.3.2 Terminal Velocity Calculation

Now consider a medium which is stationary through which a particle falls freely under gravity with drag and buoyancy acting in the opposite direction. The particle accelerates until it reaches an equilibrium velocity called terminal velocity. When the superficial gas velocity is between the minimum fluidization velocity and terminal velocity it is said to be in bubbling fluidization regime and if the velocity is greater than terminal velocity it is said to be in fast fluidization. Terminal velocity (U_t) can be determined by,

$$U_t = \left[\frac{g d_p^{1.6} (\rho_p - \rho_g)}{13.9 \rho_g^{0.4} \mu_g^{0.6}} \right]^{0.71} \quad \text{for } 2 < Re \leq 500 \quad (6.3)$$

where

$$Re = \frac{d_p \rho_g U_t}{\mu_g} \quad (6.4)$$

U_t is calculated from Eq. (6.3) and (6.4).

6.3.3 Reactor Geometry Design

The main parts to be designed are riser, distribution plate and cyclone separator. The diameter of the riser can be determined from the flow rate of the gasifying medium and gasification velocity. The fuel feed rate (m_f) and stoichiometric air (m_{th}) required are determined to find out the required air flow rate. The rate at which the fuel is fed can be calculated for a capacity of 150 kW_{th} with conversion efficiency of 50% and biomass calorific value 15.25 MJ/kg.

$$m_f CV \eta = \text{Capacity} \quad (6.5)$$

Stoichiometric air (m_{th}) is determined from,

$$m_{th} = [0.1153C + 0.3434(H - O/8) + 0.0434S] \quad (6.6)$$

where C, H, O and S are the percentages of Carbon, Hydrogen, Oxygen and Sulfur, respectively.

Actual air flow rate (m_a) required through the riser with an equivalence ratio of 0.2 can be determined by substituting (6.5), (6.6) with $ER = 0.2$ in (6.7).

$$ER = \frac{m_a}{m_f \times m_{th}} \quad (6.7)$$

m_a is calculated from (6.7).

6.3.4 Calculation of Riser Diameter

Knowing the actual mass flow rate of air required, air flow velocity (U_g), and density of air (ρ_g), area of cross section of the riser (A_b) and the riser diameter (D) are calculated from (6.8) and (6.9).

$$m_a = \rho_g A_b U_g \quad (6.8)$$

$$A_b = \frac{\pi}{4} D^2 \quad (6.9)$$

6.3.5 Calculation of Riser Height

The height of the riser or the particle outlet height of riser can be found by determining the Transport disengaging height (TDH) and setting it as the limiting criteria. TDH is the height beyond which the particles disengage from the gas and

return to the bed. There is no or less carryover of particles beyond this height. The transport disengaging height is determined by numerical simulation of a 10 m long vertical pipe with all other conditions and diameter remaining the same.

Computational domain. The simulation was performed in a 2D domain with the aid of CFD software ANSYS Fluent 14. The riser domain is initially packed with 0.63 volume fraction of sand at an initial static height of 0.2 m. A finite volume approach is followed in which the convection terms in the equations are solved using first order discretization schemes and a convergence criteria of 10^{-3} is considered for each residual. Velocity inlet is given as the inlet boundary condition and pressure outlet as the outlet boundary condition, and a stationary wall with no slip condition. The Phase Coupled SIMPLE algorithm is used for pressure velocity coupling. The solution setup of the problem is tabulated in Table 6.4 and computational domain is shown in Fig. 6.2.

The 2D computational domain is split into 75000 numbers of quad dominant elements, which has been selected based on the grid independent test conducted by varying the number of elements from 27000 to 99000. Time averaged particle distribution is plotted along the riser height as shown in Fig. 6.3a. From the obtained particle distribution curve it is observed that the volume fraction distribution curve of sand particles at 75000 and 99000 number of elements is almost same and overlapping when compared to the result obtained with 40000 elements. When the calculation time is taken into consideration, simulation with 75000 number of element is more acceptable and shown in Fig. 6.3b. From the simulation of the 10 m column it is observed that the maximum fraction of particles is found to be distributed at a height less than 2 m as shown in Fig. 6.3b and there is no or less particle distribution above riser height of 3 m.

Table 6.4 Solution setup

Sl. No	Description	Values
1	Wall condition	No slip
2	Static bed height (H_0)	0.2 m
3	Time step size (s)	0.001
4	Number of iterations	20
5	No. of elements in grid	75000
6	Multiphase model	Eulerian
7	Number of phases	2
8	Phase 1	Sand
9	Phase 2	Air
10	Viscous model	K- ϵ
11	Solution scheme	Phase coupled SIMPLE
12	Drag model	Gidaspow

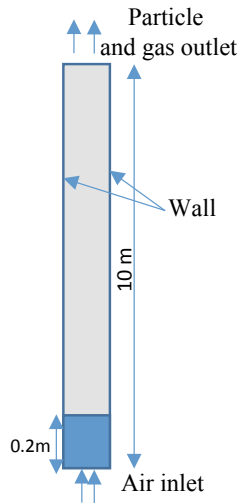


Fig. 6.2 Computational domain

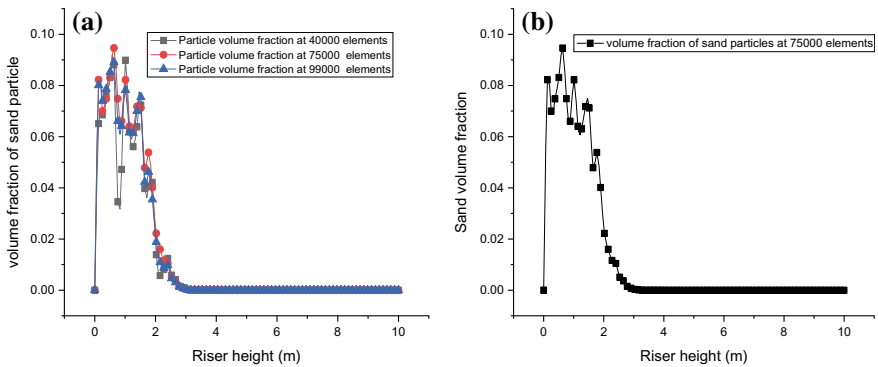


Fig. 6.3 **a** Average distribution of particles along the riser height at different number of elements. **b** Average particle distribution along the riser at 75000 number of elements

6.3.6 Design of Distributor Plate

The distributor plate ensures the homogenous distribution of the fluidizing medium (air). It supports the bed materials and there is no physical influence to the air flow beyond the distributor plate. A good rational design of distribution plate helps in reducing the auxiliary power consumption. Among the different types of distributor plates (perforated plate type, nozzle type, and sparge type), the perforated plate types are well suited for laboratory setups. In the design of a distributor plate, the

pressure drop across the plate is significant. As the pressure drop across the plate increases more homogenous will be the air supply. On increase in the pressure drop the auxiliary power required will also increase. The distributor pressure drop can be determined from (6.12). Pressure drop across the bed (ΔP_b) is calculated by finding the weight acting per unit area.

$$\Delta P_b = \frac{W}{A_b} \quad (6.10)$$

where weight of the bed calculated by knowing the particle volume fraction (ε_{mf})

$$W = A_b \times H_0 \times \varepsilon_{mf} \times \rho \times g \quad (6.11)$$

From (6.17)

$$\Delta P_d = \Delta P_b \left[0.01 + 0.2 \times \left(1 - e \left(-\frac{D}{2H_{mf}} \right) \right) \right] \quad (6.12)$$

The diameter of orifice (d_{or}) is taken as approximately three times the diameter of particle (d_p).

$$d_{or} = 3 \times d_p$$

Knowing the orifice diameter and the thickness of plate (t) the orifice discharge coefficient (C_d) and the gas velocity through the orifice (U_{or}) can be found.

$$C_d = 0.82 \left[\frac{t}{d_{or}} \right]^{0.13} \quad (6.13)$$

$$U_{or} = C_d \times \left[\frac{2 \times \Delta P_b}{\rho_b} \right]^{0.5} \quad (6.14)$$

From (6.13) and (6.14) U_{or} is calculated.

The number of orifices per square meter of distribution plate (N_{or}) can be determined by equating the flow rate of air entering the riser with total flow rate leaving the riser.

$$U_{op} \times A_b = N_{or} \times A_{or} \times U_{op}$$

i.e.

$$\frac{N_{or}}{A_b} = \frac{U_{op}}{U_{or}} \times \frac{4}{\pi \times (d_{or})^2} \quad (6.15)$$

From which the number of holes on perforated plate (N_{ord}) can be calculated.

$$N_{ord} = N_{or} \times A_b \tag{6.16}$$

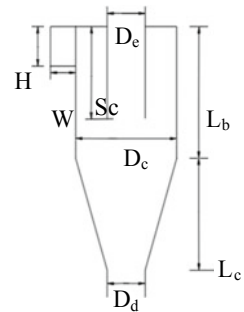
6.3.7 Design of Cyclone Separator

Cyclone separator is used for the separation of particle from the gas. Different available designs of cyclone separators are high efficiency cyclone, high through put cyclone and general purpose cyclones. A single optimum design is not suitable for all particle separation as it varies from process to process. The general purpose cyclones form a compromise between high efficiency and high throughput cyclones. The present study adapted a general purpose cyclone design proposed in (Design and fabrication of cyclone seperatos 2015). The dimensions of different parts are defined in terms of ratios of the cyclone body diameter as given in Table 6.5, which is schematically shown in Fig. 6.4. The body diameter of the cyclone can be determined from (6.17).

Table 6.5 Cyclone design

Part	Notation	Ratio
Outer diameter of cyclone	D_c	D_c
Length of body	L_b	$2 D_c$
Length of cone	L_c	$2 D_c$
Height of inlet	H	$D_c/2$
Width of inlet	W	$D_c/4$
Diameter of gas exit	D_e	$D_c/2$
Diameter of particle outlet	D_d	$D_c/4$
Length of vortex finder	S_c	$D_c/8$

Fig. 6.4 Schematic of cyclone separator



$$m_a = V_c \times \frac{D_c}{2} \times \frac{D_c}{4} \quad (6.17)$$

where $V_c = 3 \times U_g$.

Substituting (6.17) in (6.16) will give the value of D_c . Other values can be calculated as given in Table 6.5.

6.4 Results and Discussion

The minimum fluidization velocity $U_{mf} = 0.345$ m/s and terminal velocity from Eqs. (6.3) and (6.4) is found to be 3.7 m/s. The fast fluidization velocity is taken to be greater than the terminal velocity and it is approximately 3.8 m/s where the terminal velocity is calculated as mentioned in the design procedure. The fuel feed rate is 0.0199 kg/s for an equivalence ratio of 0.2 and gasification efficiency of 50%. From the theoretical and actual air flow rates the riser diameter is found to be 0.0762 m. Usually in gasifiers, the operating range of equivalence ratio falls between 0.2 and 0.7.

The design equivalence ratio is selected to be very low because during the fabrication or operation there are chances where the operating velocities may go beyond the design velocities. The low equivalence ratio selected during design helps to maintain the operating velocity and the fuel feed rate to fall in the desired range. In the design saw dust is selected as the biomass feed stock based on assumption that, once the system is designed for a fuel with lower calorific value and characteristic the system will work well with higher grades of fuels than saw

Fig. 6.5 Comparison of calorific value

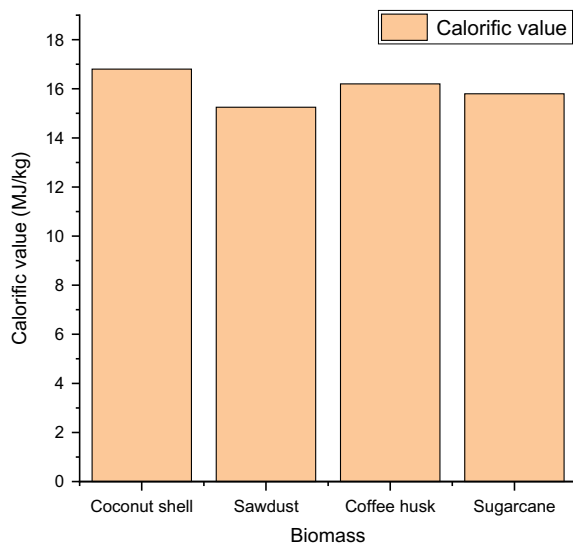
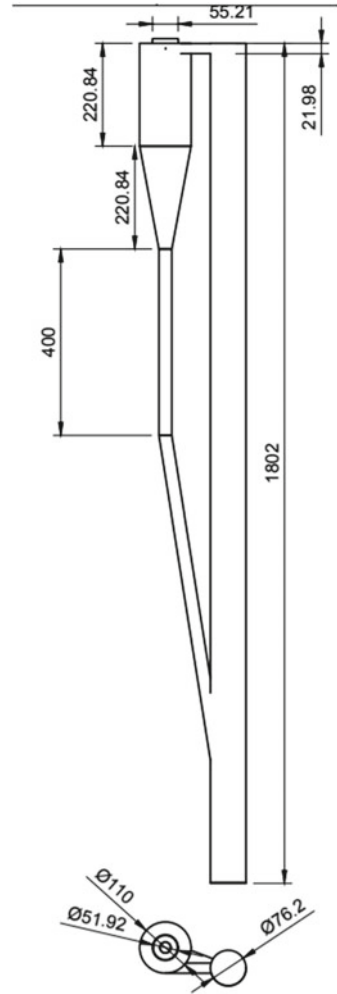


Fig. 6.6 Schematic of designed circulating fluidized bed gasifier (dimensions in mm)



dust such as coffee husk, sugarcane bagasse, etc. The Calorific value comparison of different available biomass is shown in Fig. 6.5.

In the simulation of the 10 m column with all other conditions remaining same, the distribution of sand particle above a riser height of 3 m is almost near to zero. Most of the particles are distributed at a height less than 2 m, hence a height of 1.8 m is selected as the maximum riser height where the outlet can be fixed.

The distributor plate is designed and pressure drop is found to be 110.48 kPa across the plate. Calculated orifice diameter is 1.8×10^{-5} m with an air velocity of 58.89 m/s. the number of orifice/hole on a 5 mm thick plate is 116. From (6.17) the diameter of the cyclone separator is found to be 0.11 m and the rest of the dimensions are calculated from the relations given Table 6.5. A diagram of CFB showing the design details is shown in (Fig. 6.6).

6.5 Conclusion

A systematic design procedure of a circulating fluidized bed gasifier of 150 kW_{th} capacity has been developed with sand as bed material and sawdust as biomass feedstock. Biomass selection was done by comparing the calorific value of different available feedstocks. The diameter of the riser was found out and transport disengaging height was identified as the limiting condition for fixing the outlet of the riser. The perforated plate type distributor plate and a general purpose type cyclone separator were designed which ensure good efficiency and throughput. A systematic design procedure should be always followed during the design of a CFB gasifier as each and every design as well as operating parameter affects the gasification process. The present work thus provides a systematic methodology for the design of circulating fluidized bed gasification reactor for a specified capacity and feedstock.

References

- Alimuddin Z, Zainal B, Lahijani P, Mohammadi M, Rahman A (2010) Gasification of lignocellulosic biomass in fluidized beds for renewable energy development: a review. *Renew Sustain Energy Rev* 14:2852–2862
- Atikah A, Abdullah N, Ha F, Inayat A (2016) Assessing the gasification performance of biomass: a review on biomass gasification process conditions, optimization and economic evaluation. *Renew Sustain Energy Rev* 53:1333–1347
- Bain RL, Broer K (2011) Chapter 3 Thermochemical processing of biomass: conversion into fuels, chemicals and power. National Renewable Energy Lab. United States
- Basu P (2006) Combustion and gasification of fluidized beds. Taylor & Francis Group
- Basu P (2010) Biomass gasification and pyrolysis, 1st edn. Elsevier
- Brenner H, Acrivos A, Bailey JE, Fan L (1994) Butterworth-Heinemann series in chemical engineering. Adsorpt Calc Model
- Cao Y, Wang Y, Riley JT, Pan W (2006) A novel biomass air gasification process for producing tar-free higher heating value fuel gas. *Fuel Process Technol* 87:343–353
- Dasappa S, Sridhar HV, Sridhar G, Paul PJ, Mukunda HS (2003) Biomass gasification—a substitute to fossil fuel for heat application. 25:637–649
- Design and fabrication of cyclone separator (2015). https://www.researchgate.net/publication/312160127_Design_and_fabrication_of_cyclone_separator
- Dudley B (2018) BP statistical review of world energy, 67th edn
- George J, Arun P, Muraleedharan C (2016) Stoichiometric equilibrium model based assessment of hydrogen generation through biomass gasification. *Procedia Technol* 25:982–989
- George J, Arun P, Muraleedharan C (2018) Experimental investigation on co-gasification of coffee husk and sawdust in a bubbling fluidised bed gasifier. *J Energy Inst*
- Kataki R, Chutia RS, Mishra M, Bordoloi N, Saikia R, Bhaskar T (2015) Recent advances in thermochemical conversion of biomass, 1st edn. Elsevier
- Marano JJ, Ciferno JP (2002) Benchmarking biomass gasification technologies for fuels, chemicals and hydrogen production. Prepared for U.S. Department of Energy

- McKendry, P. (2002). Energy production from biomass (Part 3): Gasification technologies. *Bioresour Technol* 83(1):55–63
- Natarajan E, Nordin AN (1998) Overview of combustion and gasification of rice husk in fluidized bed reactors. *Biomass Bioenergy* 14(5/6):533–546

Chapter 7

Analysis of Dynamic Behavior of Fluidized Bed Gasifier Using CFD



Nadeem Abdul Hameed, P. Arun and C. Muraleedharan

Nomenclature

α_g	Gas-phase volume fraction
α_s	Solid-phase volume fraction
\vec{v}_g	Gas-phase velocity vector, m/s
\vec{v}_s	Solid-phase velocity vector, m/s
ρ_g	Gas-phase density, kg/m ³
ρ_s	Solid-phase density, kg/m ³
p	Pressure, Pa
τ_g	Gas-phase shear stress tensor
τ_s	Solid-phase shear stress tensor
K_{gs}	Momentum exchange coefficient
p_s	Solid-phase pressure, Pa
Θ_s	Granular temperature, m ² /s ²
e_{ss}	Coefficient of restitution of the particle
$g_{0,ss}$	Radial distribution function
μ_g	Gas phase viscosity, kg/ms
I	Unit tensor
μ_s	Solid-phase shear viscosity, kg/ms
λ_s	Solid-phase bulk viscosity, kg/ms
d_s	Particle diameter, m
Gi	Gidaspow model
Sy	Syamlal-Obrien model

N. A. Hameed (✉) · P. Arun · C. Muraleedharan
Department of Mechanical Engineering, National Institute of Technology Calicut,
Kozhikode, India

e-mail: nadeemabdulhameed@gmail.com

P. Arun

e-mail: arun.p@nitc.ac.in

C. Muraleedharan

e-mail: murali@nitc.ac.in

Sc Schaeffer model
Jo Johnson model

7.1 Introduction

Increasing global energy demand, climate change and environmental pollution have forced the world community to emphasize on clean, green and renewable energy for sustainable development. Biomass is a prominent clean and sustainable energy source. Different conversion routes of biomass into energy are being studied extensively. Biomass gasification is a thermo-chemical energy conversion process whereby the solid biomass is converted to the useful gaseous product, syngas, which can be used to obtain the end products like electricity, heat, transportation fuels etc. (Sansaniwal et al. 2017). Fluidized bed technology is widely used in gasification due to its various advantages like better mass and heat transfer rate, good mixing properties, and temperature control. Modeling based on computational fluid dynamics has become popular in describing the dynamic behavior of gas–solid flow and chemical reactions in fluidized bed gasifiers and is used to optimize the gasifier designs (Baruah and Baruah 2014; Singh et al. 2013).

Studying the hydrodynamics of fluidized bed is important in developing an accurate model of a gasifier. Further development in hydrodynamic modeling is crucial for better understanding the phase interactions and thereby better control of the process (Philippsen et al. 2015). Two main approaches namely Euler–Euler and Euler–Lagrange are used for numerical modeling of multiphase flow in fluidized bed. Euler–Euler approach is computationally lesser intensive and is appropriate for applications like bubbling fluidized beds where volume fraction of the second phase cannot be neglected. The effect of different modeling parameters like gas–solid drag models (Loha et al. 2012; Sahoo and Sahoo 2015; Estejab and Battaglia 2015), turbulence (Anil et al. 2015), coefficient of restitution (Taghipour et al. 2005; Loha et al. 2014), specular coefficient (Loha et al. 2013), etc., have been studied by many researchers. Different models are used by researchers for the solid-phase viscosity terms, but studies focused on the effect of different viscosity models on bed hydrodynamics are very few. The present work deals with developing an Euler–Euler 2D multiphase model of fluidized bed with sand particles using ANSYS Fluent 14.0 and studying the effect of different viscosity models on the hydrodynamic behavior of the bed.

7.2 Numerical Modeling

7.2.1 Governing Equations

In the Euler–Euler two-fluid model used here, both the gas and solid phases are treated mathematically as interacting and interpenetrating continua. The governing equations for the model are as follows:

Continuity equations for gas phase and solid phase

$$\frac{\partial}{\partial t}(\alpha_g \rho_g) + \nabla \cdot (\alpha_g \rho_g \vec{v}_g) = 0 \quad (7.1)$$

$$\frac{\partial}{\partial t}(\alpha_s \rho_s) + \nabla \cdot (\alpha_s \rho_s \vec{v}_s) = 0 \quad (7.2)$$

Momentum equations for gas phase and solid phase

$$\frac{\partial}{\partial t}(\alpha_g \rho_g \vec{v}_g) + \nabla \cdot (\alpha_g \rho_g \vec{v}_g \vec{v}_g) = -\alpha_g \nabla p + \nabla \cdot \tau_g + \alpha_g \rho_g g + K_{gs}(\vec{v}_s - \vec{v}_g) \quad (7.3)$$

$$\frac{\partial}{\partial t}(\alpha_s \rho_s \vec{v}_s) + \nabla \cdot (\alpha_s \rho_s \vec{v}_s \vec{v}_s) = -\alpha_s \nabla p + \nabla \cdot \tau_s + \alpha_s \rho_s g + K_{gs}(\vec{v}_g - \vec{v}_s) \quad (7.4)$$

The momentum exchange coefficient is accounted using Gidaspow drag model (Gidaspow et al. 1992) and turbulence is accounted using standard per phase k - ϵ model. The solid properties are determined as a function of radial distribution function and granular temperature. The solid pressure is given by,

$$p_s = \alpha_s \rho_s \Theta_s + 2\rho_s(1 + e_{ss})\alpha_s^2 g_{0,ss} \Theta_s \quad (7.5)$$

The gas phase and solid-phase shear tensors are given by,

$$\tau_g = \alpha_g \mu_g \left(\nabla \vec{v}_g + \nabla \vec{v}_g^T \right) - \frac{2}{3} \alpha_g \mu_g \cdot (\nabla \cdot \vec{v}_g) I \quad (7.6)$$

$$\tau_s = \alpha_s \mu_s \left(\nabla \vec{v}_s + \nabla \vec{v}_s^T \right) - \alpha_s \left(\lambda_s - \frac{2}{3} \mu_s \right) (\nabla \cdot \vec{v}_s) I \quad (7.7)$$

The solid shear viscosity term (μ_s) in the equation for solid-phase tensor consists of three parts namely kinetic, collisional, and frictional part.

$$\mu_s = \mu_{s,kin} + \mu_{s,col} + \mu_{s,fr} \quad (7.8)$$

Two models popularly used by researchers for the kinetic part are Gidaspow model (Gidaspow et al. 1992) and Syamlal-Obrien model (Syamlal and Rogers 1993). The correlations are given below:

Gidaspow model

$$\mu_{s,\text{kin}} = \frac{10\rho_s d_s \sqrt{\Theta_s \pi}}{96\alpha_s (1 + e_{ss}) g_{0,ss}} \left[1 + \frac{4}{5} g_{0,ss} \alpha_s (1 + e_{ss}) \right]^2 \quad (7.9)$$

Syamlal-Obrien model

$$\mu_{s,\text{kin}} = \frac{\alpha_s d_s \rho_s \sqrt{\Theta_s \pi}}{6(3 - e_{ss})} \left[1 + \frac{2}{5} (1 + e_{ss})(3e_{ss} - 1) \alpha_s g_{0,ss} \right] \quad (7.10)$$

For the collisional part of solid shear viscosity, both of these models provide the same correlation.

$$\mu_{s,\text{col}} = \frac{4}{5} \alpha_s \rho_s d_s g_{0,ss} (1 + e_{ss}) \sqrt{\frac{\Theta_s}{\pi}} \quad (7.11)$$

For the frictional part of shear viscosity, mainly two models are available which are given by Schaeffer (1987) and Johnson and Jackson (1987).

Schaeffer's model

$$\mu_{s,\text{fr}} = \frac{p_s \sin(\phi)}{2\sqrt{I_{2D}}} \quad (7.12)$$

Model by Johnson and Jackson

$$\mu_{s,\text{fr}} = p_{\text{fr}} \sin \phi \quad (7.13)$$

$$p_{\text{fr}} = F_r \frac{(\alpha_s - \alpha_{s,\text{min}})^n}{(\alpha_{s,\text{max}} - \alpha_s)^p} \quad (7.14)$$

For solid bulk viscosity model prescribed by Lun et al. (1984) is commonly used.

$$\lambda_s = \frac{4}{3} \alpha_s \rho_s d_s g_{0,ss} (1 + e_{ss}) \left(\frac{\Theta_s}{\pi} \right)^{\frac{1}{2}} \quad (7.15)$$

7.2.2 Computational Domain and Solution Procedure

The computational domain used for the analysis is shown in Fig. 7.1. The parameters, properties, and the initial and boundary conditions used are listed in Table 7.1. The equations are solved and the simulations are carried out using the CFD package ANSYS Fluent 14.0. Finite volume method is used for domain discretization. A time step size of 0.001 s and convergence criteria of 10^{-3} for the maximum residuals are chosen for the simulation. The simulations are carried out for 15 s with time-averaging of parameters done from 5 to 15 s. Phase Coupled SIMPLE algorithm is used for pressure-velocity coupling. Second order implicit scheme and first order upwind scheme are used for the discretization of unsteady and convective terms, respectively. A grid independence study is conducted to select the appropriate grid size.

7.3 Experimental Setup

Figure 7.2 shows the schematic diagram of the experimental setup used for cold flow analysis of fluidized bed and determination of bed pressure drop. A riser made of acrylic glass with dimensions of 0.15 m inner diameter and 1.2 m height is used for the experiments. Sand particle is used as the bed material. Air is supplied using a centrifugal blower. Flow is regulated using a gate valve and the flow rate is measured by an orifice meter. They are connected using pipes of 50.8 mm inner diameter. Pressure tapings are provided along the riser which are connected to a U-tube manometer to determine the pressure drop. Superficial velocity is calculated using the manometer readings corresponding to the orifice meter.

Fig. 7.1 Computational domain

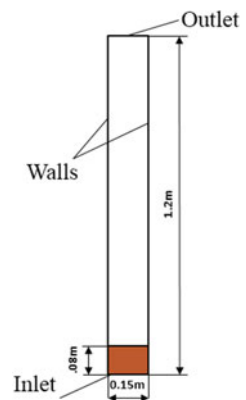
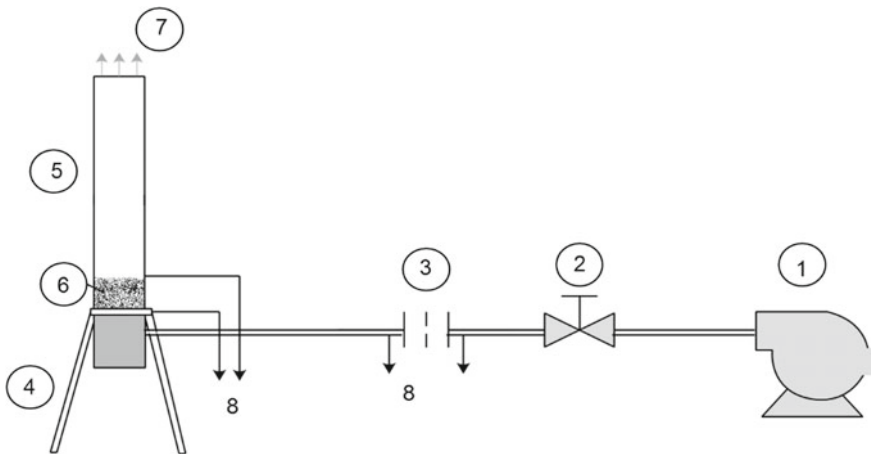


Table 7.1 Hydrodynamic parameters and other properties

Bed material	Sand particle
Particle density	2550 kg/m ³
Particle diameter	600 μm
Initial bed height	80 mm
Initial volume fraction	0.6
Gasifying agent	Air
Air density	1.177 kg/m ³
Air viscosity	1.846 × 10 ⁻⁵ kg/ms
Pressure outlet	1 atm
Inlet air velocity	0.4 m/s
Walls	No slip condition
Restitution coefficient	0.9



- 1 – Centrifugal air blower (Power: 0.5 hp, Flow rate: 500 m³/hr)
- 2 – Gate valve (Inner diameter: 50.8 mm)
- 3 – Orifice meter (Plate material: Brass, Orifice diameter: 28 mm)
- 4 – Stand (Mild steel)
- 5 – Riser (Acrylic tube, Length: 1200 mm, Inner diameter: 150 mm)
- 6 – Sand bed
- 7 – Outlet
- 8 – To U-tube manometer

Fig. 7.2 Schematic diagram of the experimental set up for cold flow analysis

7.4 Results and Discussion

The grid size for the model is chosen after conducting a grid independence study. The developed 2D numerical model of fluidized bed is validated by comparing the simulation results with the experimental results. The model is used to analyze the effect of using different viscosity models on different hydrodynamic parameters such as pressure drop across the bed, particle volume fraction and axial velocity.

7.4.1 Grid Independence Study

The grid is generated using uniform quad method available in the ANSYS Fluent's grid generation package. Simulations are carried out by varying the grid size (2448, 5000, 11400, 14749 and 20000 cells) and are checked for grid independence. Figure 7.3 shows the variation in time-averaged axial particle volume fraction and Table 7.2 shows the variation in time-average pressure drop value across the bed, on changing the grid size. It is observed that there is no significant change in volume fraction or pressure drop when the grid is made finer beyond a grid size of 14749 cells. Hence the grid of 14749 cells (element size = 0.0035 m) is chosen for the analysis.

7.4.2 Experimental Validation

The bed pressure drop obtained from simulation for different bed heights and velocities is compared with that from experiment (Fig. 7.4). The average percentage error in pressure drop prediction is 11.10%.

Fig. 7.3 Time averaged particle volume fraction along the central axis for different grid sizes

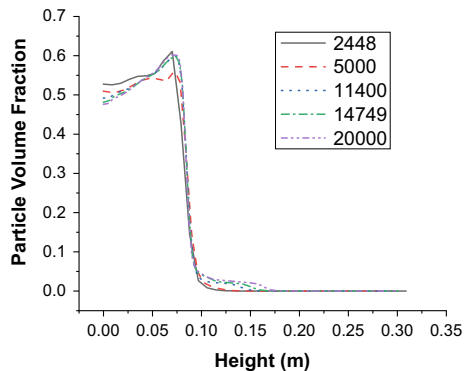
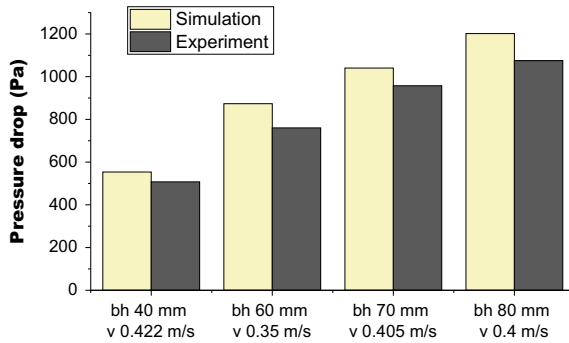


Table 7.2 Time-averaged pressure drop for different grid sizes

No. of cells	Time-averaged pressure drop (Pa)
2448	797.30
5000	794.91
11400	812.38
14749	813.53
20000	813.35

Fig. 7.4 Comparison of pressure drop obtained from simulation and experiment (bh = bed height, v = velocity)



7.4.3 Effect of Solid Viscosity Models

For kinetic and collisional parts of solid shear viscosity (together termed as granular viscosity in Fluent), two different models namely Gidaspow model and Syamlal-Obrien model are used. Simulations are carried out for cases with and without considering frictional part of shear viscosity and solid bulk viscosity terms. Two models namely Schaeffer and Johnson models are used for the frictional part. Lun model is used for the bulk viscosity. All other parameters are kept the same.

Figure 7.5 shows the percentage error in predicting bed pressure drop numerically using different viscosity model combinations with the experimentally found pressure drop of 1075.18 Pa for bed height of 80 mm and superficial gas velocity of 0.4 m/s. A minimum deviation of 10.85% is obtained for a combination of Syamlal-Obrien and Lun model without considering frictional viscosity (Sy-No-L). There is almost negligible change in pressure drop prediction when granular viscosity and bulk viscosity models are changed. Comparatively more change is observed when frictional viscosity models are changed. Johnson model predicts a larger pressure drop than Schaeffer. The predicted pressure drop is lowest when frictional viscosity is not accounted. The frictional viscosity is the contribution of friction between the particles to solid shear viscosity and accounts for the viscous-plastic transition which occurs when solid-phase particles reach the maximum solid volume fraction (Lun et al. 1984). It does not contribute in the dilute or viscous regimes, but only in dense regimes. The change in predicted pressure drop

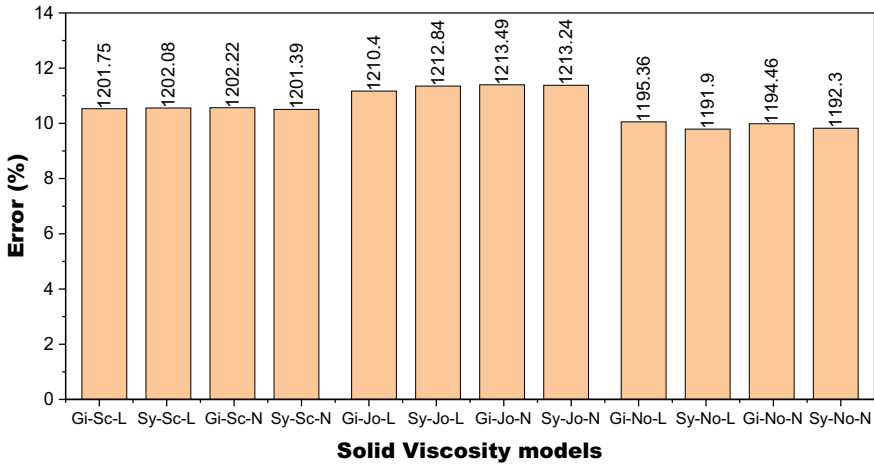


Fig. 7.5 Comparison of different combination of viscosity models with respect to time-averaged pressure drop and percentage error/deviation with experimental value

when frictional viscosity is added indicates the presence of dense region in the bed and hence frictional viscosity cannot be neglected.

It is observed from Fig. 7.6a that there is considerable variation in the axial velocity profile for simulations carried out with Johnson model for frictional viscosity from that of other simulations. All other simulations show similar profiles indicating that the sensitivity to different granular viscosity models are rather low. Figure 7.6b indicates that adding solid bulk viscosity model (Lun model) also has very less effect on predicting axial velocity of the particle. Figure 7.7a, b show that the predicted volume fraction has negligible change when the viscosity models are changed.

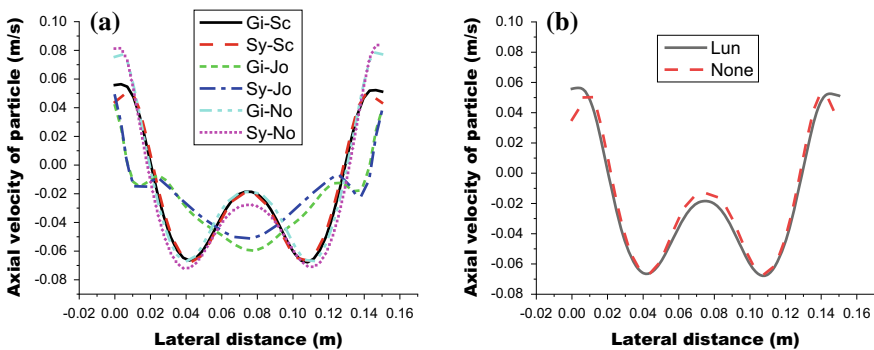


Fig. 7.6 Time-averaged axial particle velocity profile along lateral direction, a different granular and frictional viscosity models, b with and without Lun model for solid bulk viscosity

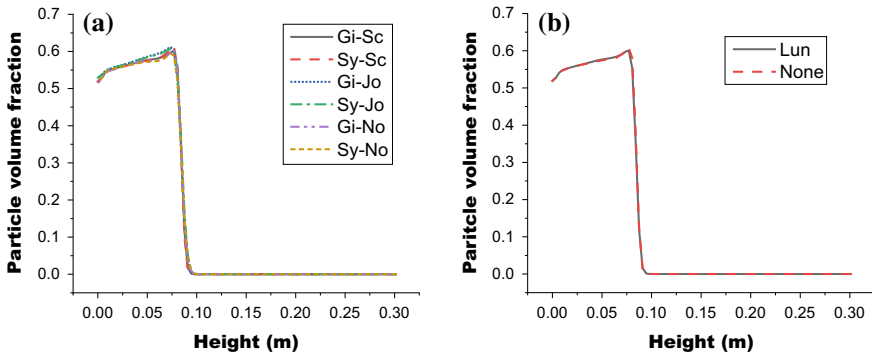


Fig. 7.7 Time-averaged particle volume fraction along the central axis, **a** different granular and frictional viscosity models, **b** with and without Lun model for solid bulk viscosity

The granular viscosity (kinetic and collisional part of shear viscosity) accounts for the particle momentum exchange due to translation and collision (FLUENT, ANSYS 2011). Syamlal-Obrien model neglects the kinetic viscosity in the dilute region. But it did not have much effect on predicting the hydrodynamic parameters as the bed is in the dense and viscous regimes. The solid bulk viscosity accounts for the resistance of granular particles to expansion and compression. But adding the bulk viscosity model of Lun did not show much effect on the prediction of hydrodynamic parameters.

7.5 Conclusion

A 2D Euler–Euler model of a bubbling fluidized bed with sand particles is developed. The pressure drop predicted by the model is compared with experimental results for different bed heights and velocities and an average deviation of 11.10% is found. Comparing the different combinations of solid viscosity models, the combination of Syamlal-Obrien and Lun without considering frictional viscosity has the least deviation (10.85%) from experimentally obtained pressure drop. Changing the granular viscosity and bulk viscosity models shows negligible effect on prediction of hydrodynamic parameters of the fluidized bed while changing the frictional viscosity models exhibits more effect on the prediction of hydrodynamic parameters of the fluidized bed. Hence, incorporating the accurate viscosity model will improve the prediction accuracy of the overall gasifier model. Further, experimental determination of other hydrodynamic parameters and their comparison with numerically predicted values will help in better understanding and selection of viscosity models.

References

- Anil M, Rupesh S, Muraleedharan C, Arun P (2015) Performance evaluation of fluidised bed biomass gasifier using CFD. *Energy Procedia* 90:154–162
- Baruah D, Baruah DC (2014) Modeling of biomass gasification: a review. *Renew Sustain Energy Rev* 39:806–815
- Estejab B, Battaglia F (2015) Assessment of drag models for Geldart A particles in bubbling fluidized beds. *J Fluids Eng* 138:031105
- FLUENT, ANSYS (2011) *Fluent 14.0 Theory Guide*. ANSYS Inc
- Gidaspow D, Bezburuah R, Ding J (1992) Hydrodynamics of circulating fluidized beds: kinetic theory approach. In: *Proceedings of the 7th engineering foundation conference on fluidization*, pp 1–5
- Johnson PC, Jackson R (1987) Frictional-collisional constitutive relations for granular materials, with application to plane shearing. *J Fluid Mech* 176:67–93
- Loha C, Chattopadhyay H, Chatterjee PK (2012) Assessment of drag models in simulating bubbling fluidized bed hydrodynamics. *Chem Eng Sci* 75:400–407
- Loha C, Chattopadhyay H, Chatterjee PK (2013) Euler-Euler CFD modeling of fluidized bed: influence of specularly coefficient on hydrodynamic behavior. *Particuology* 11:673–680
- Loha C, Chattopadhyay H, Chatterjee PK (2014) Effect of coefficient of restitution in Euler-Euler CFD simulation of fluidized-bed hydrodynamics. *Particuology* 15:170–177
- Lun CKK, Savage SB, Jeffrey DJ, Chepurniy N (1984) Kinetic theories for granular flow: inelastic particles in Couette flow and slightly inelastic particles in a general flowfield. *J Fluid Mech* 140:223–256
- Philippsen CG, Vilela ACF, Zen LD (2015) Fluidized bed modeling applied to the analysis of processes: review and state of the art. *J Mater Res Technol* 4:208–216
- Sahoo P, Sahoo A (2015) A comparative study on effect of different parameters of CFD modeling for gas-solid fluidized bed. *Part Sci Technol* 33:273–289
- Sansaniwal SK, Pal K, Rosen MA, Tyagi SK (2017) Recent advances in the development of biomass gasification technology: a comprehensive review. *Renew Sustain Energy Rev* 72:363–384
- Schaeffer DG (1987) Instability in the evolution equations describing incompressible granular flow. *J Differ Equ* 66:19–50
- Singh RI, Brink A, Hupa M (2013) CFD modeling to study fluidized bed combustion and gasification. *Appl Therm Eng* 52:585–614
- Syamlal M, Rogers W, O'Brien TJ (1993) *MFIX documentation: volume1, theory guide*. Natl Tech Inf Serv 1004
- Taghipour F, Ellis N, Wong C (2005) Experimental and computational study of gas-solid fluidized bed hydrodynamics. *Chem Eng Sci* 60:6857–6867

Chapter 8

Efficiency Improvement of Canal Top Solar Photovoltaic Power Plant with Reflectors



Rani Chacko and Asha Sajimon

8.1 Introduction

Power is the major requirement for economic development of a country. Increase in population results in reduced per capita land area and increased power demand. Depletion of fossil fuels and an increase in pollution calls for the need of sustainable energy for meeting power demand. Wide availability and emission free power conversion favor solar energy. Solar energy is converted into electric power by means of solar photovoltaic (SPV) cells. These solar cells are interconnected and sealed to form PV modules which are arranged in an array on the ground for power production. Large land area requirement is one of the primary constraints in the field of growth of conventional solar power plant. This situation leads to the new innovations like the roof top solar plant, floating solar plant and canal top power project (Kougias et al. 2016; Byrne et al. 2015; Rathore 2016; Sahu et al. 2016).

Solar cells produce a lower output voltage when they are subjected to the higher temperature because of increase in carrier recombination. Current increases due to the decrease in band gap (Solanki 2015). This leads to a marginal increase in current but a major reduction in voltage resulting in lesser efficiency due to increase in temperature (Dubey et al. 2013; Tobnaghi and Naderi 2015). Solar PV modules placed over canal operates at a lower temperature than conventional ground-mounted system. This lower operating temperature makes the canal top power plants to operate at an improved efficiency (Rathore 2016; Colmenar-Santos et al. 2016). A study conducted by Gujarat Energy Research and Management Institute (GERMI) on Canal top power plant states that the canal top system establishes stable generation even after three and a half years of sunlight exposure and continuous operation whereas, for ground-mounted PV panels, reduction in power output of 1% on a flat basis occurs. Due to this, the canal mounted solar panels

R. Chacko (✉) · A. Sajimon

Amal Jyothi College of Engineering, Kanjirapally, Kottayam, Kerala, India
e-mail: chacko.rani@gmail.com

are expected to have a life expectancy beyond 25 years (Shukla and Jani 2016). Another factor which affects the power output from a solar cell is the amount of irradiation reaching the panel. With the increase in irradiation there occurs an increase in both short circuit current and open circuit voltage (Solanki 2015). Incorporation of simple mirrors to solar panels at an appropriate angle can boost the output from a solar panel (Helmy et al. 2014; Arshad et al. 2014; Rizk et al. 2011; Sangani and Solanki 2007). The reduced operating temperature of canal top system makes it more efficient than a conventional ground-mounted system. Augustin et al. suggested modification of canal top system by placing reflectors in the inter-array space. It proposes a reflector design and tested it for a small model. Canal top systems with reflectors were found to be more efficient than ground-mounted systems with reflectors and a normal canal top system. It has been found that the overall efficiency of the system after incorporating reflector is around 11.68% which is more than 10.22% and 9.40% for a normal canal top SPV and ground-mounted SPV respectively (Augustin et al. 2016a, b). The objective of the project is to study and experimentally analyze Canal top solar power projects with the help of a miniature prototype. This paper proposes an economical design and experimentally analyses the effect of incorporating booster reflectors in the inter-array space of Canal top solar power plants in detail.

8.2 Reflector Design

Plane mirrors are used as reflectors in model setup because of its high reflective property than aluminum reflectors (Anand et al. 2014). Reflector design is based on the fact that, the incident ray falling on the top edge of the reflector gets reflected for maximum length. All other incident rays below this edge get reflected within the distance covered by the reflected ray from this edge as shown in Fig. 8.1.

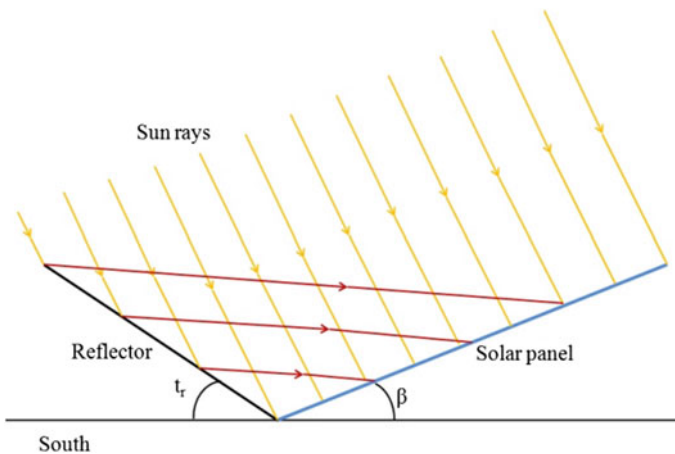


Fig. 8.1 Reflection profile from a reflector to solar panel for a particular altitude angle

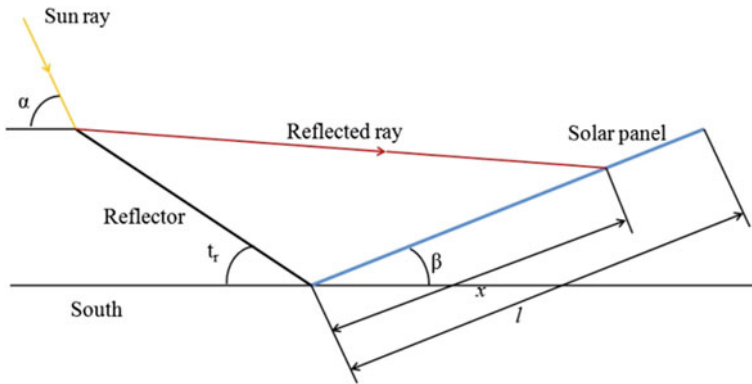


Fig. 8.2 Reflector panel arrangement

Reflector tilt angle t_r is optimized with the help of Fig. 8.2 (Augustin et al. 2016). Reflection to panel area depends on altitude angle. Maximum reflection occurs at higher α . When reflectors are designed for maximum α , there is maximum possibility for the incident ray to reflect on the panel at lower α .

An expression for x is obtained derived from triangle ABC

$$x = \frac{h \sin(\alpha - t_r)}{\sin t_r \sin(2t_r + \beta - \alpha)} \tag{8.1}$$

where x is the distance to which reflected ray can reach the panel and t_r is the reflector tilt angle. Reflector angle is optimized with the assumption that at greater α , x must be equal to l which is equal to panel length. Maximum α for a day corresponding to highest irradiation will be computed.

8.3 Prototype Design

A miniature model was designed for placing three solar panels with reflector arrangement. The experiment was conducted using this model to analyze the performance of the system with and without a reflector. The experiment was carried out on the roof top of Research Square block of Amal Jyothi College of Engineering, Kanjirappally. The details of solar panel used for experimental study are given in Table 8.1.

The distance for placing panels in order to avoid shading from adjacent panels can be found out using Eqs. 8.1 and 8.2 which are obtained from side view model for inter-array spacing as shown in Fig. 8.3 (Appelbaum and Bany 1979; Gardner 2009).

Table 8.1 Technical details of 40 W polycrystalline solar panel used in model setup

Name (unit)	Specification
Open circuit voltage V_{oc} (V)	20.94
Short circuit current I_{sc} (A)	2.76
Voltage at maximum power V_{mp} (V)	17.33
Current at maximum power I_{mp} (A)	2.5
Number of cells	36
Dimensions (mm)	490 × 680 × 25

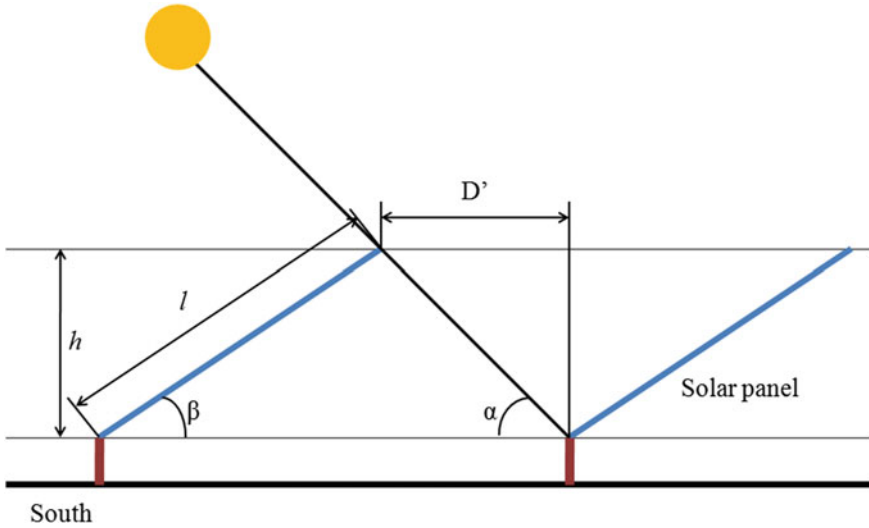


Fig. 8.3 Inter-array spacing calculation (side view)

$$h = l \times \sin \beta \tag{8.2}$$

where, h = height difference between top and bottom to the north of panel, l = length of solar panel = 0.49 m, β = tilt angle = 10, D' = maximum shadow length, α = solar altitude angle. α can be computed using Eq. 8.3 (Sukhatme 2010)

$$\alpha = \sin^{-1}[\sin \delta \sin \phi + \cos \delta \cos \phi \cos \omega] \tag{8.3}$$

$$D' = h / \tan \alpha \tag{8.4}$$

where ϕ is the latitude of the location which is 9.5° for the experiment location and ω is the hour angle. The maximum possibility of shading occurs in morning during the month of December. To avoid shading, solar altitude angle at 9:00 am on December 22 is taken (Szokolay 2007). The value of α during this time is obtained as 35° . Substituting all values h is obtained as 0.085 m and D' as 0.121 m.

In the above case, azimuth angle correction was not incorporated. The actual spacing between adjacent panels to avoid shading with azimuth angle correction is lesser than D' using Eq. 8.2 as shown in Fig. 8.4. The inter-array spacing is modified with azimuth angle correction. Therefore minimum distance to avoid shading can be obtained from Eq. 8.5 (Castellano et al. 2015).

$$D = D' \cos \psi \tag{8.5}$$

where ψ is the azimuth angle. At December 22nd 9:00 am ψ is 128.7° . Substituting values D is obtained as 0.07 m. Thus a minimum spacing of 0.07 m is required to avoid shading.

For designing reflectors, maximum α for a day corresponding to highest irradiation, i.e., value corresponding to 12:00 pm for every month is calculated using Eq. 8.4.

That is α of 88.45° (corresponding to the month of August) is considered for the design. When $\alpha = 88.45^\circ$, x is 0.49 m. At this condition corresponding to $\alpha = 88.45^\circ$, $x = 0.49$, $h = 0.085$ and $\beta = 10$, t_r is obtained as 44.2° which can be approximated to 44° . Reflector length is calculated using Eq. 8.6 as

$$L = h / \sin t_r \tag{8.6}$$

Substituting the values of h and t_r , L is obtained as 0.125 m. Incorporation of the reflector having length 0.125 m and an angle 44° in inter-array space modifies the

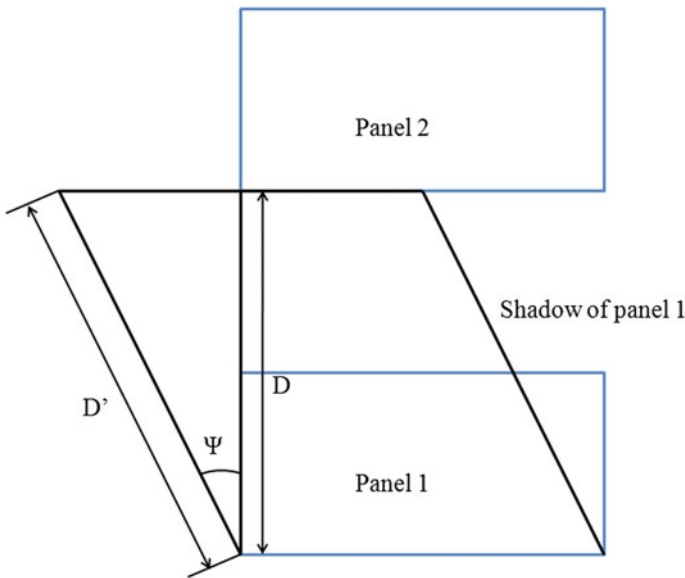


Fig. 8.4 Inter-array spacing calculation with azimuth angle (top view)

inter-array spacing to 0.089 m. This design is done without considering the azimuth angle. Inter-array space for canal top solar pv with reflectors is more than that of the inter-array space without reflectors.

8.4 Experimental Setup and Measurements

A miniature model was developed for experimental work using the design described in Sects. 8.2 and 8.3. The comparison work was done with the help of two solar panels placed on the mounting structure. By placing the mounting structure above ground, ground-mounted system is studied. For comparing the system with and without reflector, one panel is provided with a reflector and other is kept without a reflector. A rheostat of 50Ω , $5 A$ is connected to each PV panel as the load. The rheostat connected for each panel is adjusted from minimum to maximum position equally at the same time. Corresponding to each resistance, the values of voltage and current are noted. Power is calculated with the obtained voltage and current. From the calculated power values, the maximum value is taken as maximum power for the corresponding irradiation. The readings are taken at an interval of one hour from 9:30 am to 4:30 pm. The experimental setup is as shown in Fig. 8.5 and the measurement setup is as shown in Fig. 8.6. Four sets of comparison works are done.



Fig. 8.5 Experimental setup for a ground-mounted system and a canal top system

1. Comparison of ground-mounted system with and without reflector
2. Comparison of canal top system with and without reflector
3. Comparison of ground-mounted and canal top system without reflector
4. Comparison of ground-mounted and canal top system with reflector.

The performance of canal top system is studied by placing the structure above the trapezoidal canal tank as shown in Fig. 8.5. The comparison of ground-mounted system and canal top system is done by adjusting the position of mounting structure partially above the ground and rest above the tank. The comparison of both the system under normal condition and concentrated conditions was studied.

8.5 Results and Discussions

8.5.1 *Ground-mounted System with and Without Reflector*

The experimental work for comparing ground-mounted system with and without reflectors was carried out on April 8, 2017. The same set of experiment was repeated on April 10, 2017. Figures 8.7 and 8.8 provide efficiency comparison and panel front surface temperature comparison with and without reflector.

Result shows that the temperature of the system with reflector is more when compared to the system without a reflector. The average temperature rise for panel front surface is 1.5 °C when compared to the system without a reflector. The increase in panel temperature badly affects panel efficiency (Tobnaghi and Naderi 2015; Singh and Ravindra 2012; Kumar and Kaur 2014). Even though panel temperature is more for the system with a reflector when compared to the system without reflector, the efficiency of the panel with reflector is more. This is due to the

Fig. 8.6 Measurement setup



Fig. 8.7 Efficiency comparison of Ground-mounted system with and without reflectors

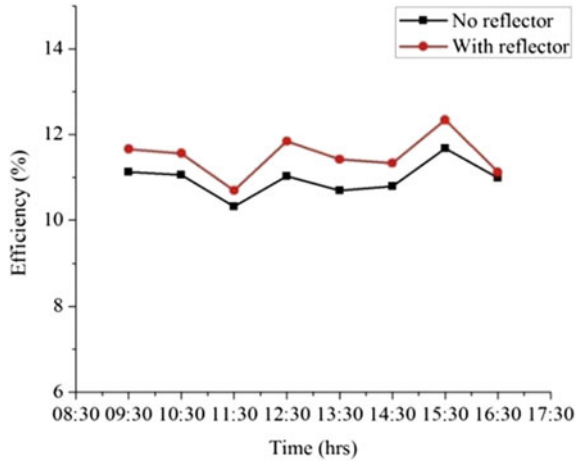
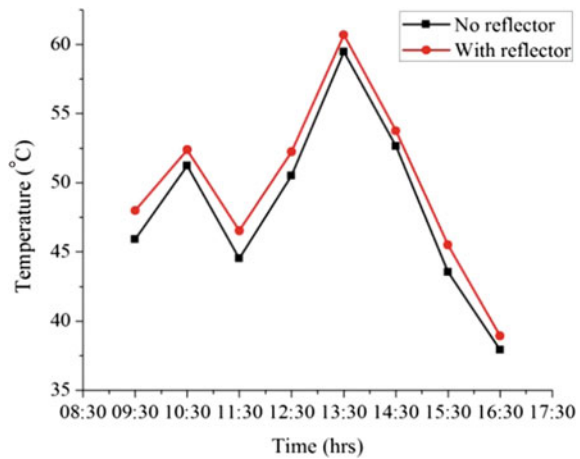


Fig. 8.8 Front surface temperature comparison of ground-mounted system with and without reflectors



fact that, the effect of the increase in irradiation predominates over the effect of temperature rise on panel efficiency due to reflectors. An average efficiency improvement of 4.9% is obtained for the system with a reflector compared to the system without a reflector.

8.5.2 Canal Top System with and Without Reflector

The analysis employed in the ground-mounted system was replicated for a canal top system on April 3, 2017 and April 4, 2017. Figures 8.9 and 8.10 shows efficiency

Fig. 8.9 Efficiency comparison of canal top system with and without reflectors

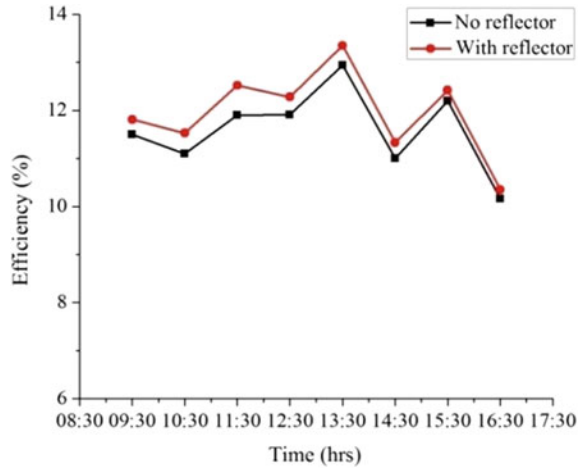
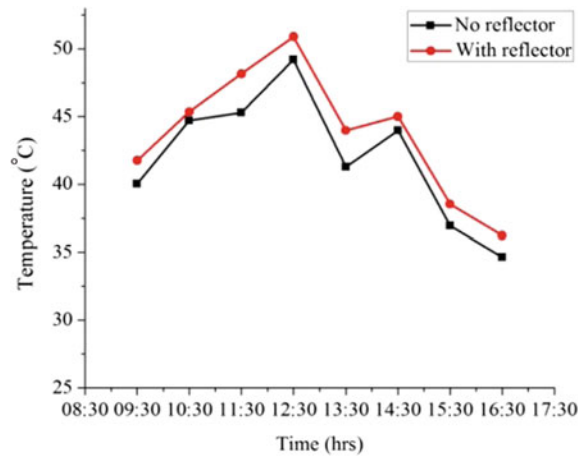


Fig. 8.10 Front surface temperature comparison of canal top system with and without reflectors



and panel front surface temperature comparison of the system with and without reflector obtained on April 4, 2017.

Power output from the panel with reflector is more when compared to the panel without reflector. Both the panel front surface and rear surface temperature increases for the system with reflectors. On average, Panel front and rear surface temperature increases by 1.7 °C and 0.9 °C respectively. The effect of irradiation overcomes the effect of temperature on panel efficiency and because of this, efficiency of the system with reflectors improves on an average by 3.09%.

8.5.3 Ground-mounted and Canal Top System Without Reflectors

Experiments were carried out in order to compare canal top and ground-mounted system under normal condition (system without reflectors) on April 19, 2017 and April 21, 2017. Figures 8.11 and 8.12 shows efficiency and panel front surface temperature comparison of ground-mounted and canal top system without reflectors obtained on April 19, 2017. The comparison work of ground-mounted and canal top system shows that the temperature of the panel at canal top is less compared to panel placed over the ground. Panel front surface and rear surface temperature of ground-mounted system is around 2.9 and 4.5 °C more than that of canal top

Fig. 8.11 Efficiency comparison of ground-mounted system and canal top system without reflectors

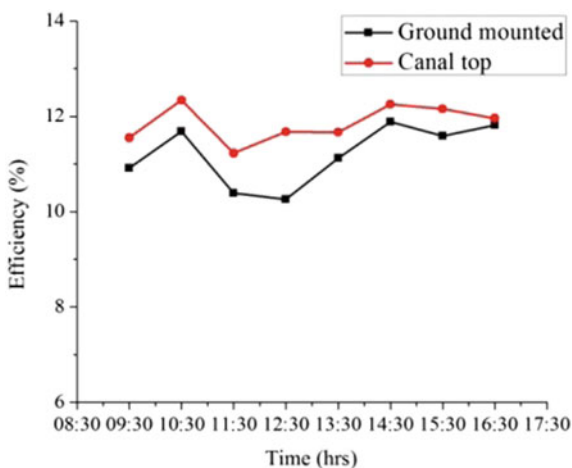
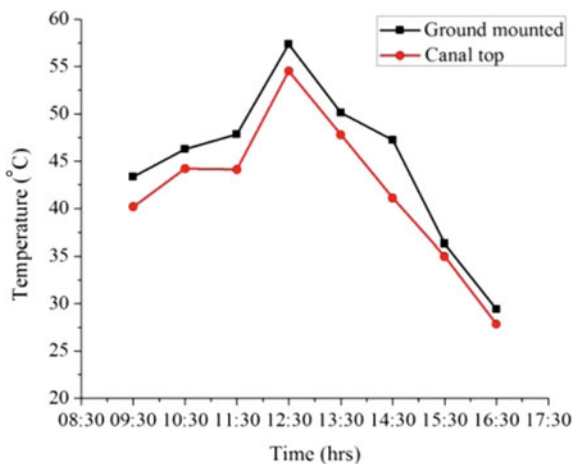


Fig. 8.12 Front surface temperature comparison of ground-mounted system and canal top system without reflectors



system. This reduction in panel temperature contributed an efficiency improvement of 5.9% for canal top system when compared to ground-mounted system.

8.5.4 Ground-mounted and Canal Top System with Reflectors

Comparison of ground-mounted and canal top system with reflector was carried out on April 18, 2017 and April 20, 2017. Figures 8.13 and 8.14 shows power efficiency and panel front surface temperature comparison of the system with reflector obtained on April 20, 2017. Figure 8.14 shows that panel at canal top operates at a

Fig. 8.13 Efficiency comparison of ground-mounted system and canal top system with reflectors

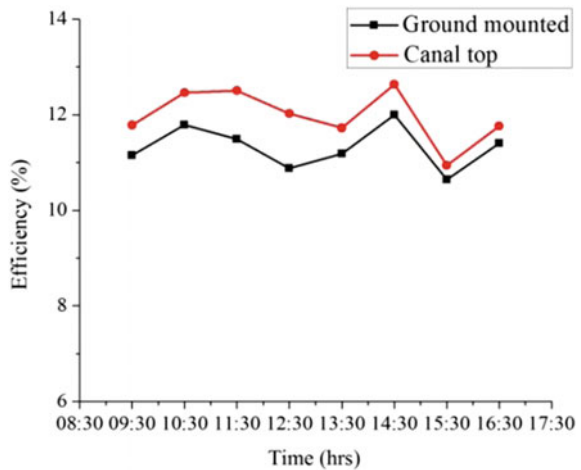
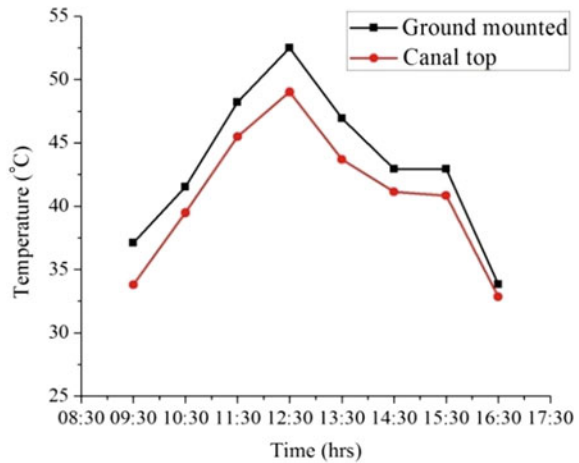


Fig. 8.14 Front surface temperature comparison of ground-mounted system and canal top system with reflectors



lower temperature when compared to panel placed above ground. There is an average decrease of 2.5 °C at the front surface for the panel at canal top, when compared to ground-mounted system. Figure 8.13 shows that an average efficiency improvement of 5.8% is obtained for a canal top system when compared to ground-mounted system due to reduced operating temperature of canal top system. Even though improvement in efficiency is slightly more for canal top system without reflector, average efficiency is more for canal top system with reflectors.

8.5.5 Reflector Redesign

Experiment results shows that the concentration of irradiation increases the temperature of the panel. Although efficiency is more for the panel with reflectors than the panel without reflectors, the increased operating temperature of the panel with reflectors can reduce the panel life (Shukla and Jani 2016). In order to reduce operating temperature of PV panel, a small modification is done to the reflector design. Reflector design is based on greater α , that is α corresponding to high irradiation time. Instead of optimizing reflector design on high irradiation time, a new design for optimizing reflection for low irradiation time is done. This is designed such that, the maximum concentration of irradiation at higher irradiation times (that is during noon time) is prevented. With this design, at high irradiation time (whenever the incident angle is greater than α value considered for design), the major portion of the incident ray will be reflected back and thus prevents extra temperature rise due to reflectors during these times. The new design is based on α corresponding to 11:00 am. In this way concentration and thereby power can be increased at low irradiation time and can reduce the temperature rise at noon time. For the new design, α values corresponding to 11:00 am throughout the year was analyzed. The reflector is redesigned for $\alpha = 69.58^\circ$ (α corresponding to the month of the August because the maximum value of α for 11:00 am series occurs during this month) and reflector angle is obtained as 34.8° which can be approximated to 35° . Figure 8.15 shows the effect of new reflector angle. For an incident angle at greater altitude angle α_1 , the reflected ray from reflector at old reflector angle ($t_{r1} = 44^\circ$) reaches the solar panel, whereas ray from the reflector at the new reflector angle ($t_{r2} = 35^\circ$) is reflected back. Therefore at high irradiation times (noon time), incident ray to reflectors are reflected back with the new design. For the Sun ray incident at an angle α_2 , which is smaller than α_1 , the reflected rays from both the reflectors reach the panel. For lower α times, the reflected ray from new reflector reaches at a greater distance when compared to the old reflector. Thus for low irradiation times, the concentration of irradiation is improved by new reflector than the old reflector. Experiments were done for comparing the performance of panel under old and new reflector angle for ground-mounted and canal top system.

Ground-mounted system at different reflector angle. The experimental setup for comparing the performance of the panel at old reflector angle (44°) and new reflector angle (35°) for ground-mounted system were done on April 7, 2017 and

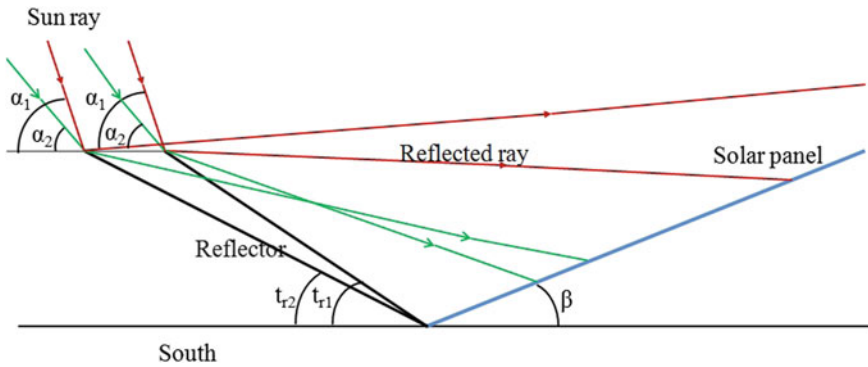


Fig. 8.15 Impact of reflectors at different reflector angles on solar panel

April 11, 2017. Figures 8.16 and 8.17 provide the efficiency and panel front surface temperature comparison of the ground-mounted system at different reflector angles obtained on April 7, 2017. Figure 8.17 shows that the front surface temperature of the panel at new reflector angle decreases on an average by 1.4 °C when compared to the panel at old reflector angle. The reason for temperature reduction with new reflector design in the morning is the uniform concentration of irradiation to the panel during these times. After 11:00 am an additional concentration of irradiation is prevented and this causes a decrease in temperature after this time. In this way, the overall temperature of the panel with new reflector design ($t_r = 44^\circ$) is lower than the panel with old reflector design ($t_r = 35^\circ$). Improved reflection during low irradiation time and temperature reduction with the system at new reflector design contributes to an increase in power output and efficiency of 1.6% when compared to the old reflector design as shown in Fig. 8.16.

Fig. 8.16 Efficiency comparison of ground-mounted system at different reflector angle

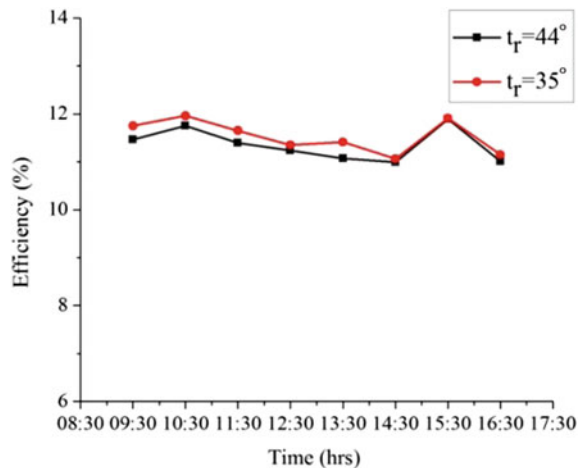
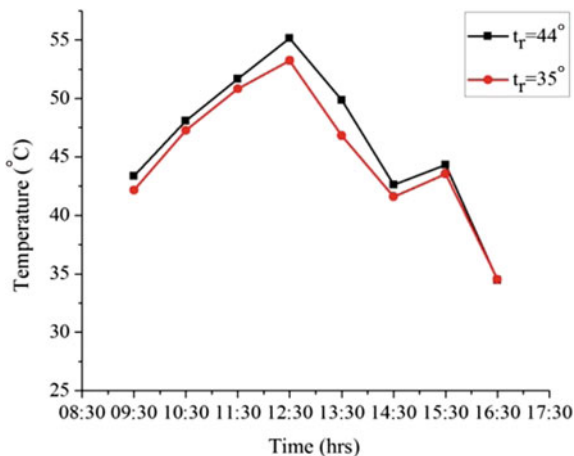


Fig. 8.17 Front surface temperature comparison of ground-mounted system at different reflector angle



Canal top system at different reflector angle. The experimental setup work for comparing the performance of panel with two reflector angles for canal top system are done on April 5, 2017 and April 22, 2017. Figures 8.18 and 8.19 indicate efficiency and panel front surface temperature comparison of the Canal top system at different reflector angles obtained on 5 April 2017. The front surface temperature for the panel at new reflector angle decrease on an average by 1.2 °C. An efficiency improvement of 1.42% is obtained for the panel at new reflector design compared to previous reflector angle. This is due to the improved reflection at morning time and reduced operating temperature throughout the day.

Fig. 8.18 Efficiency comparison of canal top system at different reflector angles

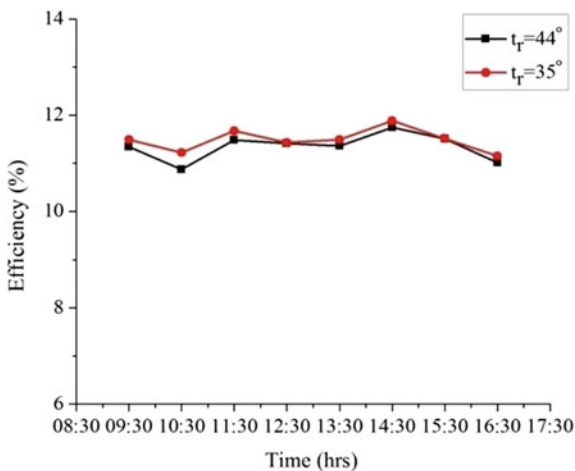
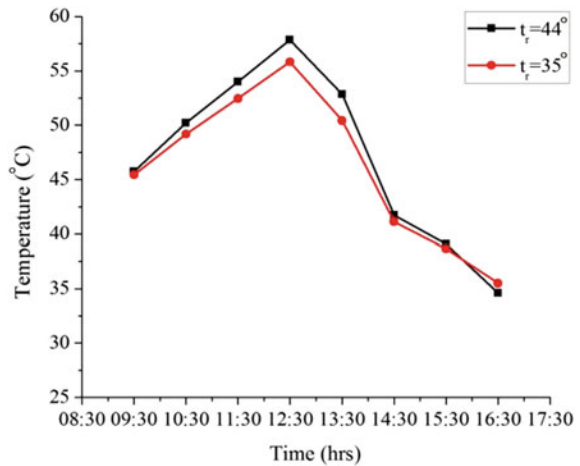


Fig. 8.19 Front surface temperature comparison of canal top system at different reflector angles



8.5.6 Water Loss Studies

In order to compare the water loss percentage for a canal top SPV and canal top SPV with reflectors, water loss studies are conducted. Water loss for a normal canal is calculated by keeping the tank open throughout the day. For calculating water loss for canal top SPV, panels are kept on the mounting structure above the tank. By placing reflectors on the inter-array spacing water loss for canal top SPV system with reflectors were also studied. All the three days has got almost same average irradiation and clear sky. Water loss for various systems is shown in Fig. 8.20. When comparing a normal canal top and canal top system with reflectors water loss

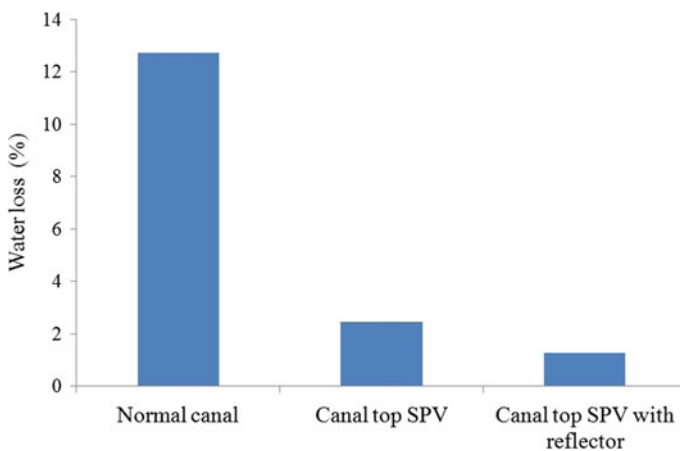


Fig. 8.20 Water loss comparison for various systems

for the system with reflectors is almost half the water loss for the system without reflectors.

The inferences obtained from different sets of experiment prove that canal top system is more efficient than a normal ground-mounted system. For a canal top system, the V_{OC} is more and I_{SC} is slightly less due to reduced operating temperature of the canal top system when compared to ground-mounted system. While analyzing the effect of irradiation and temperature on the efficiency of the system with reflectors, the effect of increase in irradiation is more than the effect of increase in temperature. This results in efficiency improvement of the system with reflectors for both the cases (ground-mounted and Canal top). Due to this fact, the V_{OC} and I_{SC} are greater for a system with reflectors when compared to the system without reflectors. Although the efficiency is improved along with the temperature rise for the system with reflectors, this temperature rise is a problem as it can reduce panel life and can create hot spots after a long period of operation. An economic solution is developed by simply modifying the design. With the redesigned reflector tilt angle temperature rise in the panel is low when compared to the previous design and also power produced by the panel with new reflector angle is more when compared to panel operating with old reflector angle. For analyzing the financial implication of the booster reflector addition to a canal top system, a rough estimation is done. The canal is assumed to be in the same location where the experimental work is done. Net present value (NPV) is calculated for both a canal top system with and without reflectors. Same length of canal is considered. Since inter-array spacing is more for a canal top system with reflectors, number of panels required to cover same length of canal is lesser hence the cost of panels and infrastructure too. Additional cost of reflectors and its structure were also considered approximately. For calculating NPV, lifetime of canal top system with reflectors is taken 1 year lesser than that of the canal top system without reflectors due to the increase in temperature due to reflection of radiation. This problem can be mitigated to a certain extent if the reflector is designed for lower radiation time reflection as explained in sections above.

8.6 Conclusion

The effective utilization of canal space for solar installation eliminates the land requirement for solar projects and natural cooling of panels solves the efficiency problem related to temperature rise. From the experimental studies, it was found that the booster reflectors arranged in the inter-array space of canal top system can increase the efficiency of the system. Booster reflectors are arranged in such a manner to provide the maximum concentration of irradiation to solar panels and this arrangement leads to a greater inter-array spacing than normal one without reflectors. This increase in inter-array spacing can reduce a considerable number of panels for a large project and can add economic benefit to the system. Besides, the water evaporation from the canal can further be reduced on account of complete

covering on top of the canal. The major problem with the reflector is the temperature rise of the panel. Although the canal top system operates at low temperature than ground-mounted system, the increased operating temperature with reflectors must be prevented to increase panel life. The redesigning of reflectors optimized for maximum reflection during low irradiation time can reduce the panel temperature rise during high irradiation time and can increase the panel efficiency.

Acknowledgements The authors would like to thank Dr. P. C. Thomas and Dr. Sheik Mohammed for the valuable comments and advice throughout this work. The authors wish to thank Dr. Z. V. Lakaparampil, Principal, Amal Jyothi College of Engineering and the Management of the college for support and lab setup provided. They would also like to thank Energy Management Centre, Trivandrum for the financial assistance rendered (EMC/ET&R/17/SPS/01).

References

- Anand VP, Khan MM, Ameen E, Amuthan V, Pesala B (2014) Performance improvement of solar module system using flat plate reflectors. In: 2014 international conference on advanced electrical engineering. ICAEE 2014
- Appelbaum J, Bany J (1979) Shadow effect of adjacent solar collectors in large scale systems 23:497–507
- Arshad R, Tariq S, Niaz MU, Jamil M (2014) Improvement in solar panel efficiency using solar concentration by simple mirrors and by cooling. In: 2014 international conference on robotics and emerging allied technologies in engineering. iCREATE 2014—proceedings, pp 292–295
- Augustin D, Chacko R, Jacob J (2016a) Canal top solar energy harvesting using reflector. *Glob Res Dev J Eng* 1:26–31
- Augustin D, Chacko R, Jacob J (2016b) Canal top solar PV with reflectors. In: 2016 IEEE international conference on power electronics, drives and energy systems (PEDES), Trivandrum, pp 7–11
- Byrne J, Taminiu J, Kurdgelashvili L, Kim KN (2015) A review of the solar city concept and methods to assess rooftop solar electric potential, with an illustrative application to the city of Seoul. *Renew Sustain Energy Rev* 41:830–844
- Castellano NN, Parra JA, Valls-Guirado J, Manzano-Agugliaro F (2015) Optimal displacement of photovoltaic array's rows using a novel shading model. *Appl Energy* 1:1–9
- Colmenar-Santos A, Buendia-Esparcia A, de Palacio-Rodríguez C, Borge-Diez D (2016) Water canal use for the implementation and efficiency optimization of photovoltaic facilities: Tajo-Segura transfer scenario. *Sol Energy* 126:168–194 (2016)
- Dubey S, Sarvaiya JN, Seshadri B (2013) Temperature dependent photovoltaic (PV) efficiency and its effect on PV production in the world—a review. *Energy Procedia* 33:311–321
- Gardner K (2009) Calculating inter-row spacing
- Helmy MA, Khalifa EM, Oksha AM, Elhaddad AW (2014) Effect of reflector application on performance under Egyptian conditions. *Sci Pap Ser Manag Econ Eng Agric Rural Dev* 14:103–106 (2014)
- Kougias I, Bodis K, Jager-Waldau A, Moner-Girona M, Monforti-Ferrario F, Ossenbrink H, Szabo S (2016) The potential of water infrastructure to accommodate solar PV systems in Mediterranean islands. *Sol Energy* 136:174–182
- Kumar S, Kaur T (2014) Solar PV performance-issues and challenges. *Int J Innov Res Electr Electron Instrum Control Eng* 2:2168–2172
- Rathore SS (2016) Canal top solar power plant an innovative initiative

- Rizk J, Nagrial MHM, Hellany A, Nagrial MHM (2011) Reflectors and concentrators for solar panels. In: Recent researches in environment, energy planning and pollution: proceedings of the 5th WSEAS international conference on renewable energy sources (RES'11), Rom. 1–3 July 2011. 2, pp 194–199
- Sahu A, Yadav N, Sudhakar K (2016) Floating photovoltaic power plant: a review 66:815–824
- Sangani CS, Solanki CS (2007) Experimental evaluation of V-trough (2 suns) PV concentrator system using commercial PV modules. *Sol Energy Mater Sol Cells* 91:453–459
- Shukla O, Jani BB (2016) Canal top solar PV plant in Gujarat 20–23
- Singh P, Ravindra NM (2012) Temperature dependence of solar cell performance—an analysis. *Sol Energy Mater Sol Cells* 101:36–45
- Solanki CS (2015) *Solar photovoltaics fundamentals, technologies and applications*. PHI Learning Private Limited, Delhi
- Sukhatme S (2010) *Solar energy principles of thermal collection and storage*. Tata McGraw Hill Education Private Limited, New Delhi
- Szokolay S (2007) Solar geometry. *J Chem Inf Model* 53:1689–1699
- Tobnaghi DM, Naderi D (2015) The effect of solar radiation and temperature on solar cells performance 39–43 (2015)

Chapter 9

Load Frequency Control of Microgrid: A Technical Review



K. S. Rajesh, S. S. Dash and Ragam Rajagopal

9.1 Introduction

Microgrid introduced by USA's CERTS (Consortium for Electric Reliability Technology Solutions), improves power quality, consumer credence and standards. (Chae et al. 2014). Microgrids are miniature power systems which encompass a cluster of interconnected loads and distributed energy resources which present itself as a single controllable entity with regard to the main grid. This uniqueness leads to integration of renewables, grid modernization, and meeting customer end power quality and standards (Pascual et al. 2015). It is also defined by interlinked loads and distribution resource management system which is capable of operating independently without depending on other grids. Various distributed resources in microgrid perform the integration from the electrical network (Katiraei et al. 2008). The propensity of the microgrid to reconnect and disconnect from main grid empower it to function in grid-connected and islanded modes. Dynamics of distribution networks play a very crucial role in determining power system stability (Jayawardena et al. 2015).

K. S. Rajesh (✉)

Department of Electrical Engineering, SRM IST, Chennai, India

e-mail: rajeshks.srm@gmail.com

S. S. Dash

Department of Electrical Engineering, GCE, Keonjhar, Odisha, India

e-mail: munu_dash_2k@yahoo.com

R. Rajagopal

Department of Electrical and Electronics Engineering, RSET, Ernakulam, Cochin, India

e-mail: ragamrajagopal@gmail.com

© Springer Nature Singapore Pte Ltd. 2020

H. Drück et al. (eds.), *Green Buildings and Sustainable Engineering*,

Springer Transactions in Civil and Environmental Engineering,

https://doi.org/10.1007/978-981-15-1063-2_9

9.2 Why Microgrid?

Microgrids are low-voltage electrical distribution networks, which are composed of DERs, ESS, loads, and they can be managed autonomously from the larger transmission network (Dorfler et al. 2014). Microgrid was introduced as a solution to the problems caused by depletion of fossil fuels, increased pollution rates and also for the efficient operation of utility grid (Sabzehgar 2015). The advantages and disadvantages offered by microgrid is summarized as follows (Hirsch et al. 2018).

9.2.1 Advantages

1. In case of a power outage or power quality issues at the utility, microgrid will isolate and separate itself from the utility without affecting the loads connected to it.
2. A microgrid can manage peak loads by load shedding if necessary or generation capacity can be enhanced by increasing the number of DG installations.
3. Microgrids can contribute to environment benefits by lowering the CO₂ emissions using distributed generators which are based on pollution-free generation.
4. Microgrid can reduce electricity costs of users by meeting the consumer electricity requirements either partly or fully.
5. CHP systems can be utilized to increase the overall system efficiency.
6. Microgrids are a ready solution to the consumer power requirement in places, which are commonly affected by natural disasters as it can be planned and put up easily in a short term.
7. The overall installation cost is less compared to conventional power system.

9.2.2 Disadvantages

1. In microgrid, voltage, frequency and power quality parameters should be controlled to acceptable standards while maintaining a balance between power and energy.
2. For storage of electrical energy battery banks are required which in turn will increase the space and maintenance requirements.
3. Resynchronization of microgrid with the utility grid is complex process.
4. Protection of microgrid is one of the biggest challenges faced during the implementation of Microgrids.
5. Microgrid need to address some issues posed by net metering and stand by charges.

9.3 Types of Microgrid

Microgrids can be classified into three types depending on its operational frequency namely AC microgrid, DC microgrid, and hybrid AC/DC microgrid. Each of them is described with figures in the following sub sections.

9.3.1 AC Microgrid

Over many decades, AC microgrids are conventionally used because of their advantages like efficient long-distance transmission capacity and also transformability to various levels of voltage. Based on the frequency ratings, distributed energy resources, energy storage devices and various loads are connected to this AC network with or without the use of a converter. Conventional sources of AC such as diesel generators, micro turbines, wind turbines, etc., can be directly connected, without any converters, to the AC network. For DC sources like PV systems, fuel cells, etc. DC to AC converters are used. Direct connection of AC loads to the grid is possible whereas rectifiers are required in the case of DC loads. Though AC microgrids offer many advantages, issues like complexity of controlling and synchronizing with the main network prevails (Sao and Lehn 2008). Layout of AC microgrid is shown in Fig. 9.1.

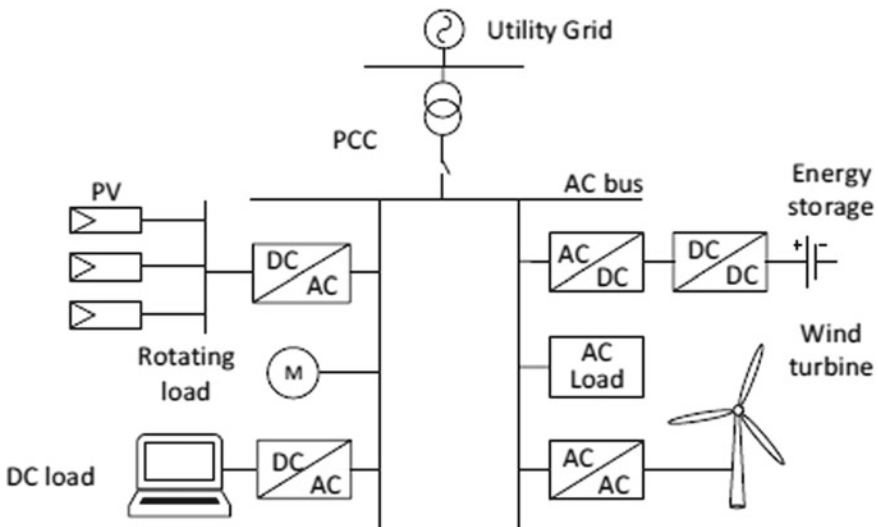


Fig. 9.1 Layout of AC microgrid (Zhou and Ho 2016)

9.3.2 DC Microgrid

DC Microgrid is a gaining attention these days because it can be rightly used for small-scale industries as well as for residential applications (Sannino et al. 2003). The aforesaid disadvantages of AC microgrids such as control complexity and synchronization with utility grid is no longer prominent in DC microgrid. The advantages offered by DC microgrids are ease of installation, elimination of inverter and fuel costs. Power Quality issues are also not prevalent in DC Microgrids. As many equipment's DC powered nowadays DC microgrids are gaining importance. Figure 9.2 shows the layout of Dc microgrid.

9.3.3 Hybrid AC/DC Microgrid

Hybrid AC/DC microgrids are composed of AC and DC sub grids interconnected through bidirectional converters (Liu et al. 2011). In unique AC/DC microgrids, many AC-DC conversions are there and this can be avoided through the

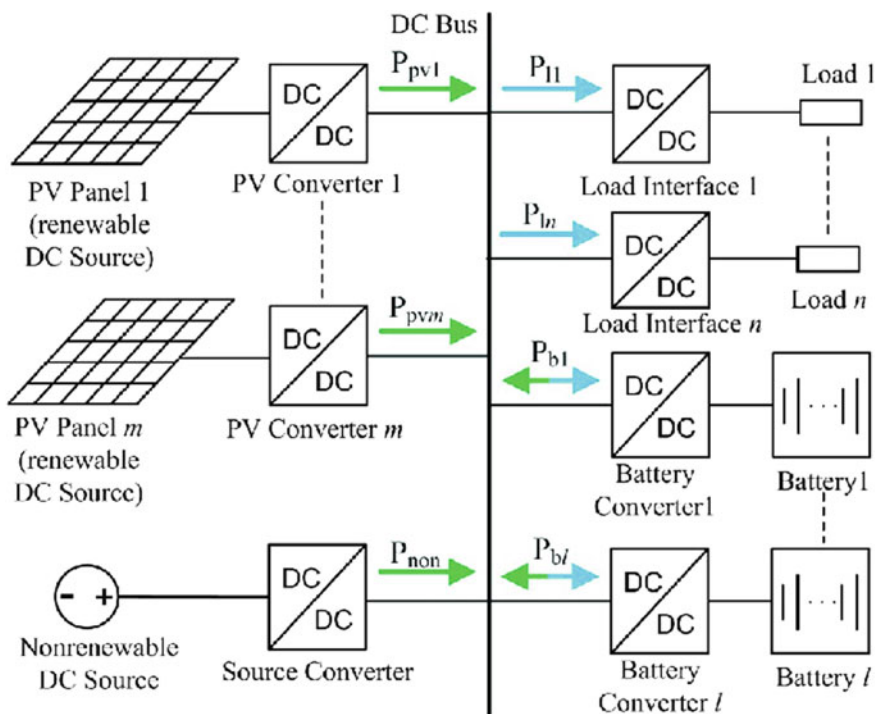


Fig. 9.2 Layout of DC microgrid (Zhou and Ho 2016)

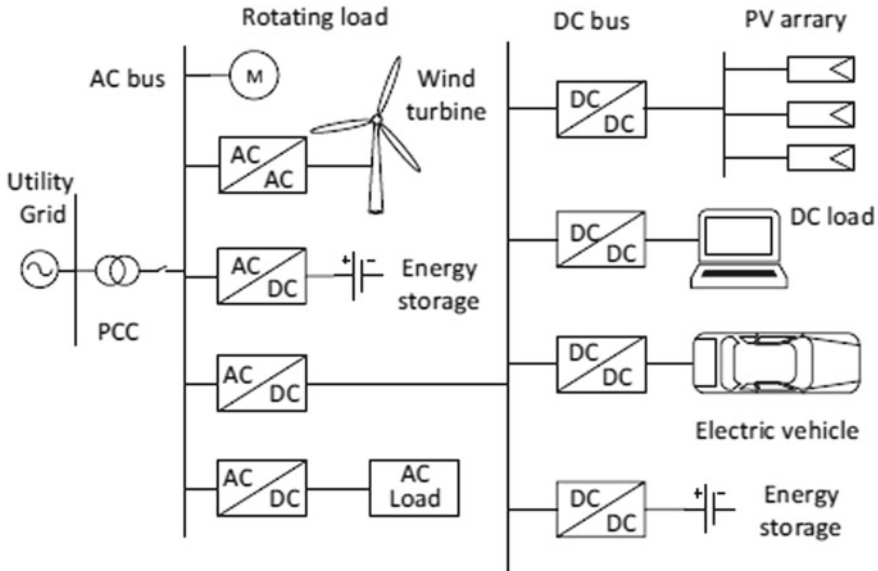


Fig. 9.3 Layout of hybrid microgrid (Zhou and Ho 2016)

implementation of a hybrid system. Here, DC sources and loads are connected to DC subsystem while AC sources and loads are connected to the AC subsystems and power can be exchanged between them using bidirectional converters. ESS are preferably connected to DC subsystem. An outline of hybrid microgrid is depicted in Fig. 9.3. This system consists of AC as well as DC sources and loads and the converters which connect them. Figure 9.3 shows the layout of hybrid microgrid.

9.4 Operating Modes of Microgrid

The various renewable energy resources like small Hydro, Ocean, wind, PV, energy storages, etc., are comprised into the MG for rural area electrification where utility access is not possible (O’Neill-Carrillo et al. 2018). The inclusion of multiple distributed generations to the MG, dramatically reduce the call for high voltage transmission-distribution systems. Microgrids with a single source of DER suffer from the problem of instability. Microgrids with multiple DERs are a solution to this issue whereby, these sources will contribute in achieving improved stability, efficiency and also it enhances quality and reliability of supply (Sharma and Singh 2015). MG provide higher flexibility and support as it can be operated in both grid-connected and islanded modes and also DERs can be located physically close to each other or distributed geographically (Kulkarni et al. 2017). Two working modes are described as follows.

9.4.1 Grid-Connected Mode

In this mode, microgrid is connected to the main grid through PCC under the condition that main grid is not affected with any power quality disturbances. Critical loads may be operated in this mode which requires a reliable energy source confining to the standard power quality standards (Ragam et al. 2018). Advantages of Grid-connected mode of operation are: It provides reliability of power and also renders stable operating condition for the grid by acting as a backup source. Also the need for ESS is considerably reduced, thereby reducing the investment cost. This mode helps in increasing the revenue since surplus power generated can be fed into the main grid. Fuel operating costs can be reduced by utilizing power from the grid when the cost is low, i.e., during off-peak hours.

9.4.2 Islanded Mode

As the name suggests, in this mode microgrid will get isolated and can operate autonomously without any co-ordination with main grid. When grid power is not available, the breaker connected at PCC disconnects microgrid from the grid and keep the loads live by the power supplied by local DGs connected to it (Dube and Sindhu 2015). Islanded mode of the microgrid helps to provide backup power to sensitive loads connected to it which are prone to voltage disturbances. Islanding can be of two types, intentional and unintentional. When microgrid is isolated from main grid because of maintenance or repair works in main grid, it is intentional islanding. Islanding resulting from faults in the utility grid is called unintentional islanding.

9.5 Microgrid Architecture

To maintain voltage and frequency within specified limits in islanded operating mode, all micro-sources should share load equally which has resulted in different types of microgrid architectures.

9.5.1 Centrally Controlled Architecture

Microgrid central controller (MGCC) reduces the cost of operation since MG network has its own DERs to supply the load in times of network congestion (Kaur et al. 2016). MGCC is installed at the interfacing point with PCC. The amount of power which the microgrid can take from the distribution system can be optimized

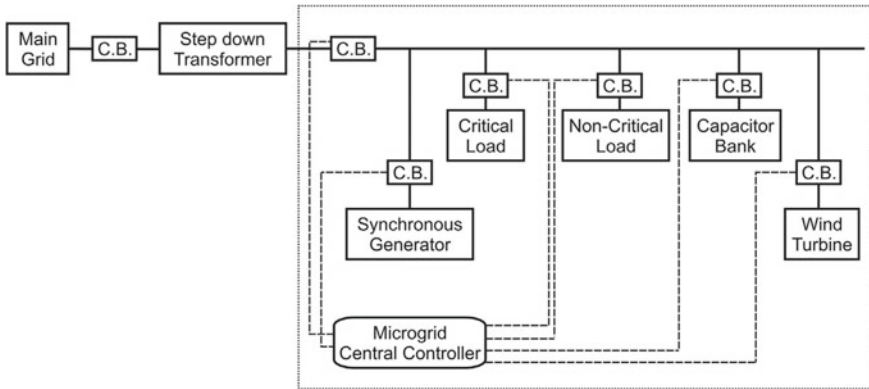


Fig. 9.4 Architecture of centrally controlled microgrid (Kaur et al. 2016)

based on various factors like electricity price, gas price, etc. MGCC sends the predefined control signals to the micro-source controller and load controller thereby controlling the active and reactive power generated by micro sources. Figure 9.4 shows the architecture of this scheme.

Another method of decentralised control without using any communication links is based on droop control strategy (De Brabandere et al. 2004). All DGs can share the load in a network by controlling the voltage and frequency by means of droop characteristics. The concept of plug and play is implemented by using this concept.

Yet another method is based on MAS control. Multiagent systems control is used to solve complex problems which are difficult for a single agent or a system to solve by negotiating with other agents thereby improving the overall system stability. To receive sensor data or to issue commands, agents can be employed which can either be a software or a hardware tool. Also an agent can collaborate with other agents in various other systems. This agent should be able to react promptly with changing environments, makes apt decisions and should be able to interact rightly with other agents (Meng et al. 2016). Figure 9.5 shows the typical decentralised microgrid. MAS architecture is shown in Fig. 9.6.

The above cluster consists of distribution management system (DMS) which control all the MGs. Each MG consists of a MG central controller (MCC) which in turn controls micro source controllers (MSC) and load controllers (LC). MCC is the interface between DMS and MG.

9.5.2 Autonomous Control Architecture

In this mode of control, every MS have its own autonomous control. Here MGCC is not required and no need for any communication links between micro sources. This makes possible plug and play capability for MGs (Nikkhajoee and Lasseter 2009).

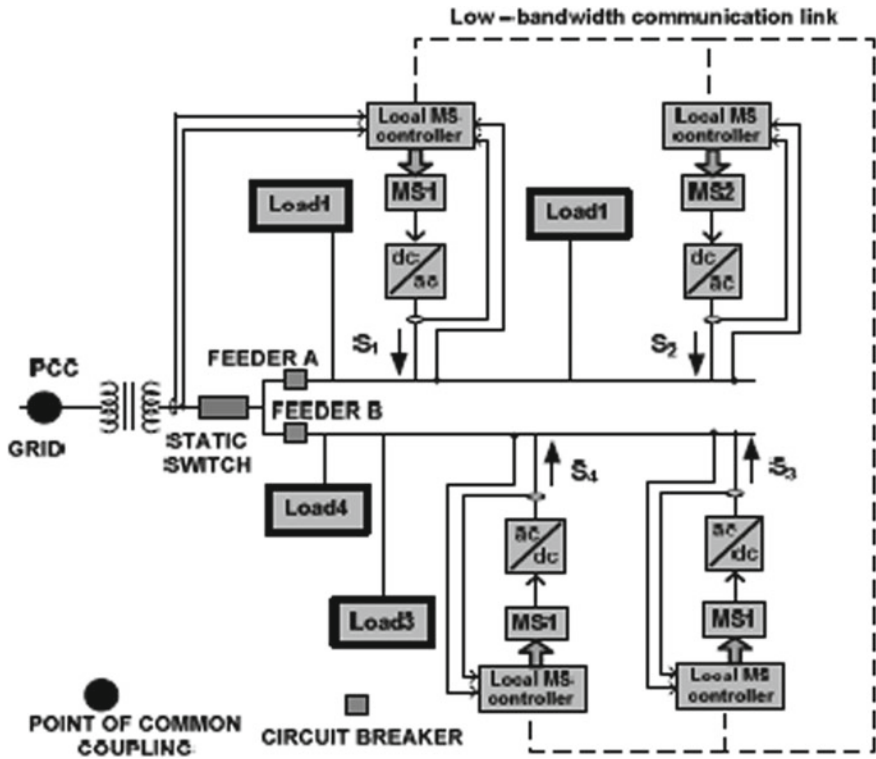


Fig. 9.5 Architecture of decentralized microgrid (Guerrero et al. 2007)

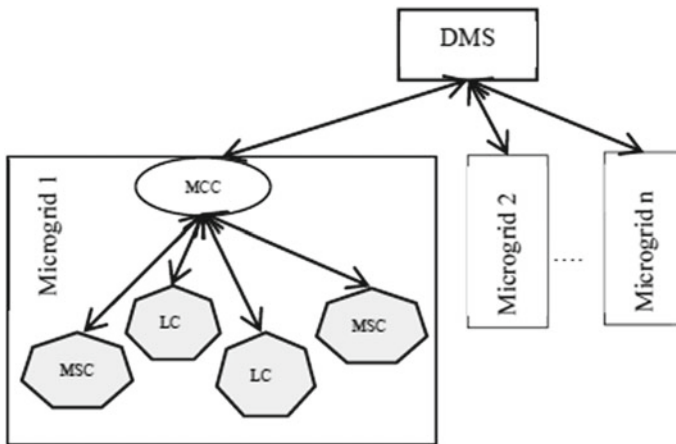


Fig. 9.6 MAS architecture (Meng et al. 2016)

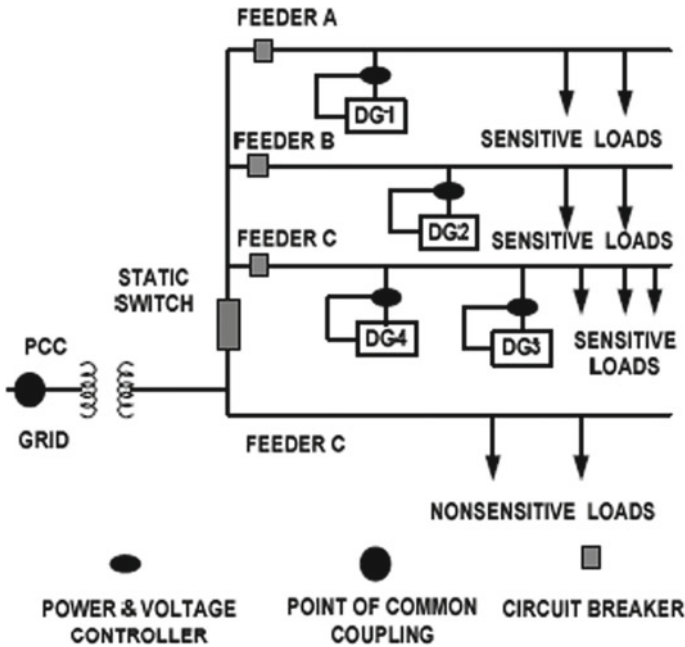


Fig. 9.7 Autonomous control architecture (Nikkhajoei and Lasseter 2009)

To ensure reliable operation in the event of a micro-source failure, another MS can be included in the network as a reserve for meeting MG load requirements. Figure 9.7 shows the schematic diagram.

9.5.3 Unit Power Control Configuration

In this configuration each DER regulates the voltage at the point of connection with grid and also the power injected by each source to the grid. In grid-connected mode, whenever a change in load occurs, extra power is to be supplied by the grid to the MG since every MS regulates to constant output power. This configuration is ideal for CHP applications because power production depends on heat demand which contributes to higher efficiency (Piagi and Lasseter 2006). When islanding occurs, P/f droop function ensures that power balancing has occurred in the island which means local load requirements are met. Figure 9.8 shows the schematic of this configuration.

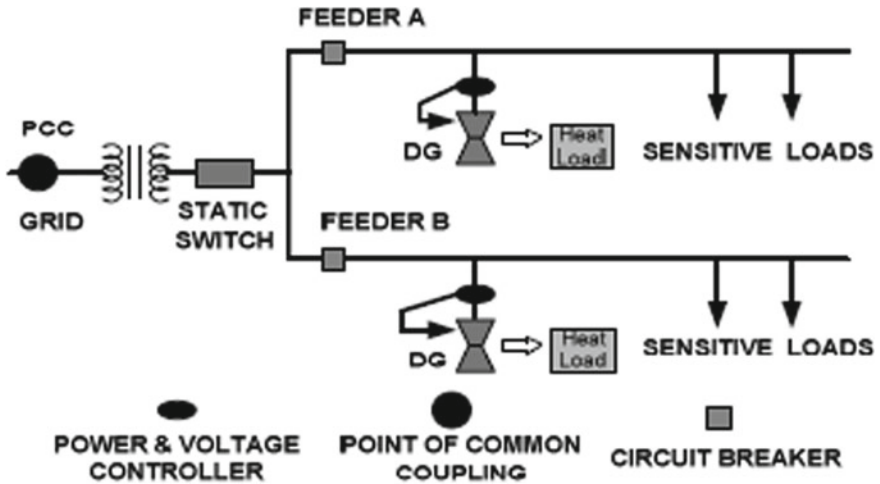


Fig. 9.8 Unit power control configuration (Piagi and Lasseter 2006)

9.5.4 Feeder Flow Configuration

As the name implies, in this architecture only radial feeders are considered. Here, the voltage at connection point and the power flowing into the feeder are regulated by the DG at points A, B, C, and D as shown in Fig. 9.9. Also each DG will regulate its power output to balance the demand in each feeder, thereby making utility grid feel that MG is a constant load. Here also when MG is islanded, droop functions ensure power balance (Piagi and Lasseter 2006). Figure 9.9 shows the feeder flow configuration.

9.5.5 Mixed Control Configuration

This configuration is a mix of feeder flow and unit power configurations where the advantages of both are combined. Here some of the DGs will regulate their output while others control the feeder power flow thereby some units operating at their maximum efficiencies by utilization of waste heat while other taking power from grid in times of demand.

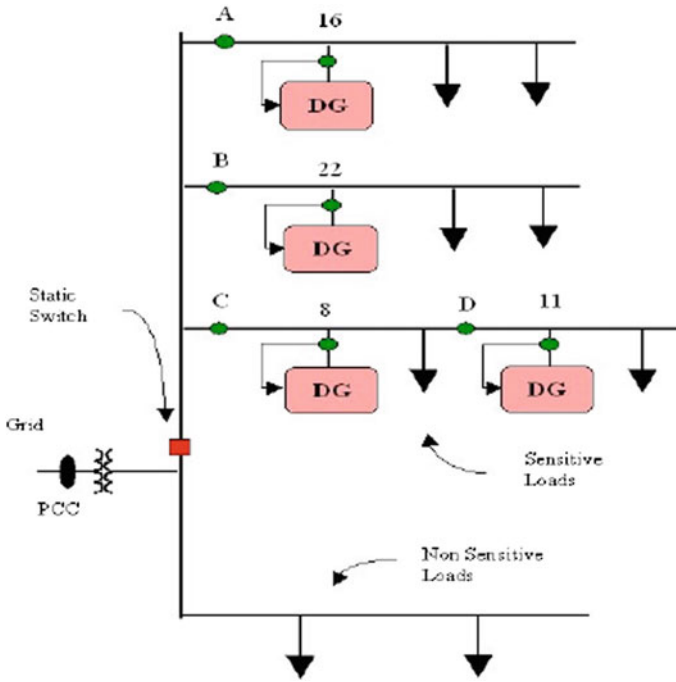


Fig. 9.9 Feeder flow configuration (Piagi and Lasseter 2006)

9.6 Control Strategies of Microgrid

Microgrid control strategies are mainly of two types, Master slave control and peer-to-peer control (Prasenjit Basak et al. 2011). Constant voltage and frequency in microgrid is maintained by the main control unit of master slave control. The distributed generators connected to the microgrid follow PQ control strategy while the main control unit operate based on V/f control strategy and provide required active and reactive power to the system. Master-slave control provides two layers of control in which the upper master controller sends control commands to sub slave controllers. One of the most important features of microgrid is its plug and play facility and it is implemented through peer-to-peer control. Under this, control equipment's can be connected or removed anytime without affecting other DGs in the network. PQ control, Droop control and V/f control are the three strategies used to control DGs. Droop control is a common control strategy in peer-to-peer control. The ideal operating frequency is calculated using real power output from a generator in droop control method which increases the system stability and offset the effect of fast changing loads (Yubing et al. 2008).

9.6.1 PQ Control

This mode of control is used for grid-connected systems which contain both AC and DC sources (Lopes et al. 2006). Depending on the resource type, control scheme varies and this type of control is applicable for AC sources which have an inverter interfaced with it. For PQ control of inverter, DERs are controlled to get a constant real and reactive power output. Active power will be supplied by the inverter and the reactive power injected into the system depends on the set point of the microgrid central controller. Also in this mode DER along with the inverter behaves as a current-controlled voltage source converter.

9.6.2 V/f Control

This control mode is suitable for DERs in islanded mode of operation because the voltage and frequency references of these sources in PQ mode will be lost in this condition. So the control strategy changes from PQ to V/f control (Rasoolzadeh and Salmasi 2018). To provide the same imbalance as with the main grid, all storage devices should have adequate reserve capacity. The set points of other DERs will not be much affected as they should be set depending on supply and demand.

Droop Control. When multiple micro-sources engage in providing power balance, they will follow either the voltage droop or the frequency droop method (Rasoolzadeh and Salmasi 2018). Based on these methods, operating point of the DGs will be changed so as to maintain the same power imbalance caused by isolation of main grid.

$$\omega = \omega^* - m(P - P^*) \quad (9.1)$$

$$V = V^* - n(Q - Q^*) \quad (9.2)$$

where P^* and Q^* are the reference real and reactive power, ω^* and V^* are the grid rated angular frequency and voltage amplitude, ω and V are the references, and m and n are the slopes of the droop characteristics. The strategy of droop control is that each DG shares the power demand according to its own droop characteristic functions. The droop characteristic is shown in Fig. 9.10.

The disadvantages possessed by this method when resynchronized with the main grid are high level of voltage distortion, poor voltage regulation and loss of synchronism with the main grid (Chamana and Bayne 2011).

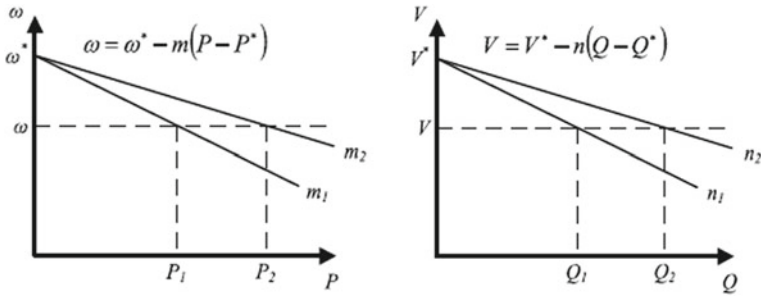


Fig. 9.10 Droop characteristics

9.7 Control Aspects of Microgrid

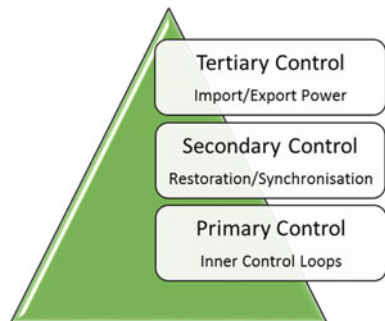
For standardization of grid control architectures, ANSI/ISA 95 has proposed international standards for developing interface between utility and control systems. Based on these standards, a hierarchical control level is proposed for the MG as shown in Fig. 9.11.

Tertiary Control: Regulates the flow of power between MG and utility at PCC.
 Secondary Control: Ensures that the frequency and amplitude deviations are within the limits inside MG. Also synchronization loops are included for connection/disconnection from the utility grid. Figure 9.11 shows the schematic of this control architecture.

Primary Control: This is used for the control of inner DG units which are basically droop control methods.

Inner Control Loops: These loops will regulate the output voltage and current while maintaining system stability (Martin-Martínez et al. 2016).

Fig. 9.11 Hierarchical control architecture of MG



9.7.1 Inner Control Loop

Inner control loops are referred to as zero control level as it contains the basic hardware controls. Power Electronic interfaces are required as an interface between MG and MS. The final stage of these interfaces will contain converters which are usually CSIs or VSIs. They contain current and voltage control loops so that synchronism with the grid can be maintained under islanded/grid-connected modes. CSIs usually require algorithms like MPPT for their optimal operation. In general these loops can contain a combination of VSI and CSIs, or VSIs connected in parallel to from MG. The main function of this level control is to provide an operating point for the voltage and current loops of DERs. The control technique used here is PQ/voltage control (Lopes et al. 2006).

9.7.2 Primary Control

The connection of more than one, voltage source inverter in parallel, results in the production of circulating active and reactive power. The primary level will adjust the amplitude and frequency set points of the voltage reference to offset this effect. The theory used here is to decrease the frequency when active power increases which is incorporated in the inverters using P/Q droop control method (Josep 2013).

In conventional droop control methodology, the line impedance is considered to be inductive when connected to a large power system. But in LV networks like MG, the output impedance is almost resistive in nature as it depends on control strategy offered by the power electronic device in the inner control loop. So modified droop control methods need to be implemented for this purpose. Virtual impedance implementation is one of the methods where a virtual impedance loop is formed in addition to inner control loops. This virtual impedance will be a predominating factor, so line impedance can be almost treated as an inductive value like in conventional droop methods with the advantage of no power losses, thereby increasing efficiency (Guerrero et al. 2009).

The functions offered by this level can be summarized as

- a. Stabilization of voltage and frequency is one of the major functions because in the event of islanding, due to mismatch of active and reactive power, stability issues arise in MG.
- b. For sharing of active and reactive power, plug and play facility without any communication links should be offered for DERs.
- c. Circulating currents mitigation is another feature.
- d. Energy balance between DGs and ESS.

9.7.3 Secondary Control

The function of secondary control is to restore the frequency and amplitude deviations produced by the load changes/changes in power generation inside MG. The present frequency and amplitude levels in MG are sensed (ω_{MG} and E_{MG}) and it is compared with the reference value (ω^*_{MG} and E^*_{MG}). The errors which are processed in compensators are sent to all units to restore the original frequency and magnitude of the output voltage. These controls will ensure that voltage and frequency deviations are regulated to zero value. Another function is to restrain the grid frequency variations within a tolerable limit. Secondary control does the restoration process in a droop-controlled MG (Mehrzi-Sanir and Irvani 2009). Figure 9.12 shows this control scheme.

9.7.4 Tertiary Control

This mode ensures the optimal operation of microgrid by managing the power flow between MG and utility grid. This is done by adjusting the amplitude and frequency of DER voltages. Tertiary control can be used to improve the power quality at PCC. To overcome the issue of voltage instability islanding detection has to be implemented to isolate the MG and also the tertiary control loops from the main grid. Tertiary control is also responsible for coordinating the operation of multiple

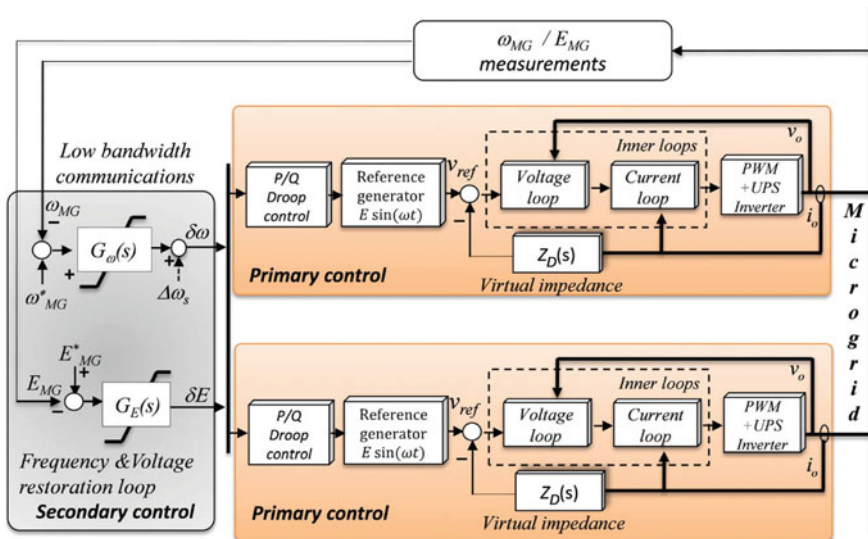


Fig. 9.12 Primary and secondary control of AC MG (Guerrero et al. 2011)

microgrids interacting with one another in the system, and communicating needs or requirements from the main grid.

When a non-planned islanding scenario occurs, the tertiary control tries to absorb active power from the grid which in turn causes frequency to decline. When it deviates from the expected values, for safety purpose, the microgrid is disconnected from the grid, and all tertiary control loops are disabled (Rajesh et al. 2017). Figure 9.13 shows the summary of functions of hierarchical control.

9.8 Load Frequency Control of Microgrid

Microgrid operates in Grid-connected/Islanded mode. When a mode transfer need to be effected, due to deficiency of active power, frequency deviation due to momentary mismatch in supply and demand, usually occurs in islanded MG (Pogaku et al. 2007; Diaz et al. 2009). As a result of the frequency fluctuation of the microgrid, system frequency may change rapidly and this can eventually lead to a blackout unless there is an adequate spinning reserve available for balancing the microgrid (Pecas Lopes et al. 2006; Katiraei et al. 2005). The concept of LFC is proposed to overcome the above said shortcomings.

LFC refers to the control of active power and frequency in a power system. The general control algorithm for LFC was developed by Cohn in 1971 and he defined the term “area control error” (ACE), which refers to the sum of the net tie-line power error and the product of the frequency error with a frequency bias constant. When ACE is regulated to zero, the control algorithm has returned the frequency and tie-line power errors to zero implying a balance is achieved between generation and load. Achieving frequency balance is crucial for stable operation of small and isolated microgrid systems as generations are limited/intermittent.

ESS which is an integral part of MG network can be used for fast active power compensation thereby improving the performance of LFC. Various control techniques can be applied to primary/secondary control loop of MG to ensure that the set points of the MG are adapted to the optimality requirement of the MG and the frequency and average voltage deviations are regulated toward zero after any change in load or supply (Ma and Shr 2015).

In (Mehrizi-Sani and Iravani 2010; Mohsen Azizi and Ali Khajehoddin 2018), several aspects of implementing secondary frequency control in MG are discussed. Secondary control of MG based on potential function method for every controllable unit is described in (Mehrizi-Sani and Iravani 2010), where the set points are determined by a MG central controller (MGCC) to optimize the performance of MG. To overcome the shortcomings of a central controller, a distributed secondary control is proposed in (Shafiee et al. 2014). DSC includes tertiary control which is used to optimize MG operation with the main grid. DSC also includes the advantage of reactive power sharing (Fig. 9.14).

Serban and Marinescu (2011) proposes an electronic load controller (ELC) consisting of smart load and battery energy storage system, which maintains

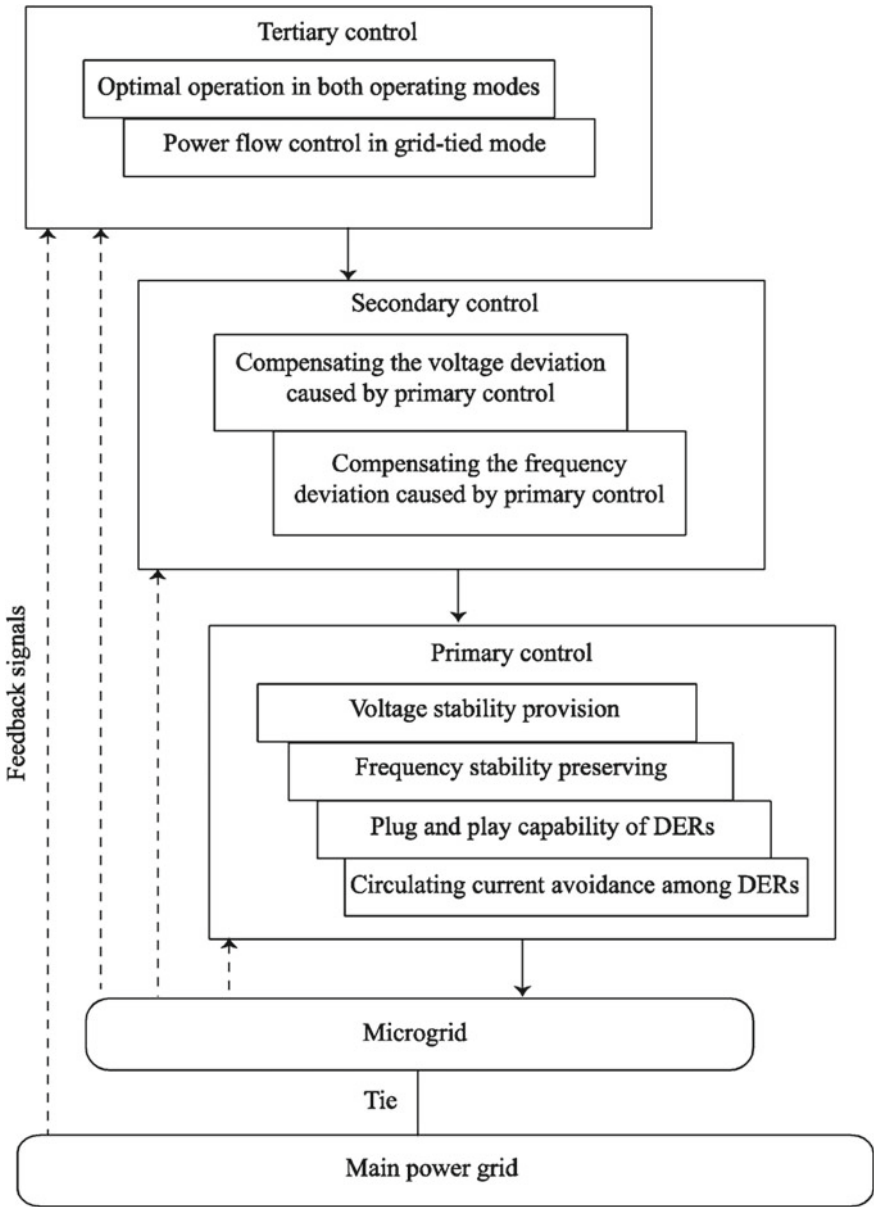


Fig. 9.13 Summary of functions of hierarchical control (Pogaku et al. 2007)

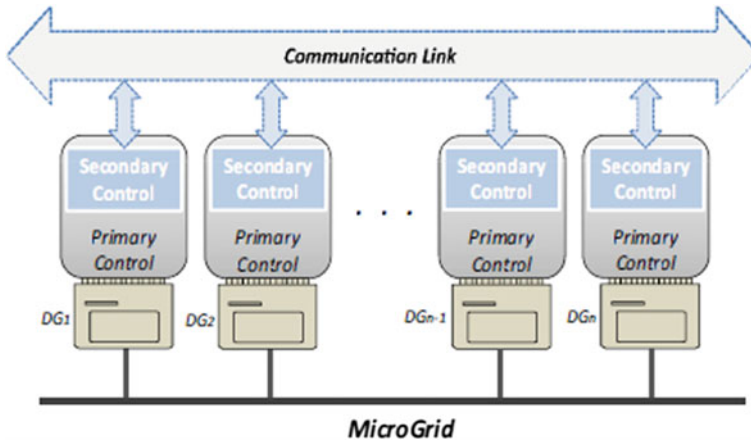


Fig. 9.14 Block diagram of distributed secondary control in MG (Shafiee et al. 2014)

active power balance in case of both energy excess production and shortage. SL heat power can be utilized for the improvement of overall system efficiency. In (Gu et al. 2013), a co-operative frequency control method consisting of MGCC and MGLC is proposed.

For implementation of frequency control, a Hopfield fuzzy neural network control is adopted and for extension of battery life SOC control is utilized. For the reliable operation of the hybrid MG interconnected with DERs, an optimization of control parameters is necessary. Various methods like Ziegler-Nichols method (Mallesham et al. 2011) and various optimization techniques such as Simulated Annealing (SA) (Bensenouci and Ghany 2007), Genetic Algorithm (GA) (Mahdavian et al. 2012), etc., are exploited to find a most appropriate solution to this problem. Metaheuristic optimization algorithms such as particle swarm optimization (PSO) combined with fuzzy logic is applied to maintain frequency deviation within limits in (Bevrani et al. 2012) (Fig. 9.15).

Kayalvizhi and Vinod Kumar (2017) proposes an intelligent adaptive neuro-fuzzy based model inference droop controller for regulated frequency and voltage control in MG. An adaptive fuzzy based PID optimized by sine-cosine algorithm is proposed in (Rajesh and Dash 2018) for controller design so as to minimize the frequency deviation and power fluctuation resulting from sudden load swings in MG.

In Etemadi et al. (2012), corresponding to generation units of multiple DERs a separate robust controller is designed. The authors put forward a decentralised control strategy for islanded MG operation. In Han et al. (2015), for frequency regulation in an autonomous MG, a μ -based robust controller is proposed which is designed via the D-K iteration method. A robust μ -synthesis controller is proposed in Kahrobaeian and Mohamed (2013) where robust stability as well as robust performance of the microgrid in presence of parameter uncertainties and uncertain

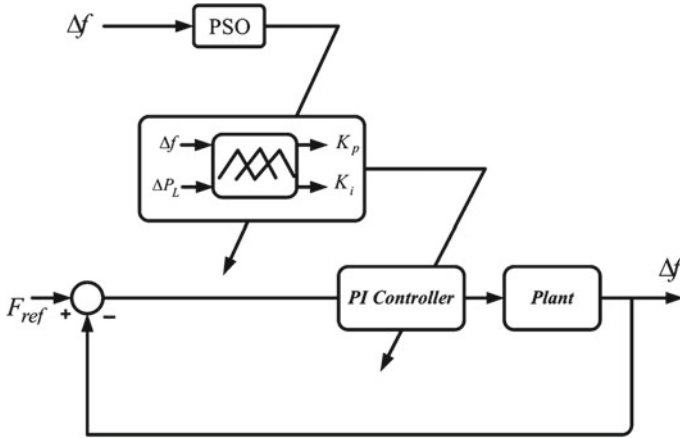


Fig. 9.15 Block diagram of fuzzy based PSO controller (Bevrani et al. 2012)

resonant peaks caused by connection of PFC capacitors is ensured. (Li et al. 2014) Also presents μ -synthesis based controller methodology. Hossain et al. proposes a H_∞ robust controller for power sharing in both Grid-connected and islanded modes of MG operation. Hossain et al. (2014), Babazadeh and Karimi (2013) put forward H_∞ based robust control strategies for an islanded operation of microgrid. The complexity introduced by robust state feedback controllers is one of the main problems in adopting robust controller design. However, since MG size is small as compared with conventional power plants, this method proves powerful for applying to controller design problems (Packard and Doyle 1993; Morari and Zafirion 1989).

In (Harikumar and Ushakumari 2014), authors propose a Biogeography-based Optimization technique for tuning PID controller for LFC in a hybrid microgrid. This method of PID tuning proves to be superior in achieving both transient and steady-state stability in case of sudden disturbances. In (Doost Mohammadi et al. 2014), the authors presented an approach to divide the MG into virtual areas and control the frequency of the microgrid by using the tie-line error which is called Virtual Area Control Error (VACE) instead of just using the frequency deviation error (Fig. 9.16).

Tae et al. (2012) proposes a PSO-based multiagent LFC algorithm developed in JAVA for communication with resource agents for frequency stabilization once MG enters islanded mode. Modeling of power system is done using RTDS.

For MG islanded mode operation, μ -synthesis-based robust decentralized controller is developed for AVR and LFC systems of a generator. The proposed controller ensures proper coupling between various islanded zones without any communication links between the local controllers (Mohsen Azizi and Ali Khajehoddin 2016).

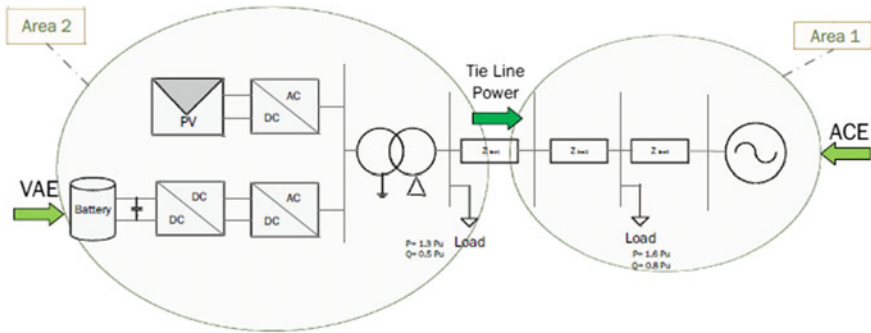


Fig. 9.16 Block diagram of MG division into two areas (Doost Mohammadi et al. 2014)

9.9 Future Trends

The clustered microgrids are the future trends in the area. The coordination and control of microgrid clusters are the most challenging one which deserve detailed study. Here each single microgrid can transact with the utility and among themselves for exchange of power. Intricate control algorithms and dependable communication systems are paramount for ensuring feasibility of microgrid clusters (Bidram and Davoudi 2012).

The plug and play capability of the microgrid is mostly based on droop control, which needs to be improved to handle voltage and frequency variations and better reactive power sharing. As hybrid microgrid facilitate the bidirectional power flow between AC and DC lines, the converter control strategy to be improved to meet the continues power requirement originate from plug and play capability of devices such as DG, ESS or loads (Fang 2016; Unamuno 2015).

LFC based on H_{∞} and μ -synthesis controllers provides many benefits and (Bevrani et al. 2016) concludes by establishing superiority of structured/parametric-based control theory such as μ -synthesize over H_{∞} for islanded MG control. Future work in this area includes application of robust controllers to grid-connected MG for their frequency stabilization.

The future of hierarchical control is mainly related to energy management systems in which reference values are taken from and given to tertiary control loops to optimize the MG efficiency. Also multi agent based metaheuristic control techniques can be adopted for power management of MG where optimization of performance index like fuel cost, maintenance cost, etc., can be implemented by intelligent agents (Hettiarachchi et al. 2019).

9.10 Conclusion

To meet all the energy needs of future, microgrids are an attractive solution as they integrate both renewable and non-renewable sources. As the number of DGs in the microgrid network increases, communication, and control techniques required becomes complex. In this paper, a broad perspective on various types of microgrid, modes of operation and an overview of hierarchical control methodologies are also discussed which can be concluded by stating that primary level droop control is suitable for small-sizes MGs. Centralized secondary control applies to small-sizes MGs and decentralized control applies to large size MGs. Tertiary control is most suited for grid-connected MG operation. LFC of microgrid is a promising field and lot of researches are being done in this area which includes various intelligent control methods to application of robust controllers in islanded mode of MG operation. This paper provides a comprehensive review on various load frequency control methodologies in microgrid.

References

- Babazadeh M, Karimi H (2013) A robust two-degree-of-freedom control strategy for an islanded microgrid. *IEEE Trans Power Del* 28(3):1339–1347
- Bensenouci A, Ghany AMA (2007) Step-wise optimum adaptive variable-structure load-frequency control design using simulated annealing. In: *Proceedings of the IEEE international symposium on industrial electronics*, pp 318–323
- Bevrani H et al (2012) Intelligent frequency control in an AC microgrid: online PSO-based fuzzy tuning approach. *IEEE Trans Smart Grid* 3(4):1935–1944
- Bevrani H, Feizi MR, Ataei S (2016) Robust frequency control in an islanded microgrid: H_∞ and μ -synthesis approaches. *IEEE Trans Smart Grid* 7(2)
- Bidram A, Davoudi A (2012) Hierarchical structure of microgrids control system. *IEEE Trans Smart Grid* 3(4)
- Chae W-K, Lee H-J, Hwang S-W, Song I-K, Kim J-E (2014) Isolated microgrid's voltage and frequency characteristic with induction generator based wind turbine, smart grid and renewable. *Energy* 5:180–192
- Chamana M, Bayne SB (2011) Modeling and control of directly connected and inverter interfaced sources in a microgrid. In: *2011 North American power symposium*
- De Brabandere et al (2004) A voltage and frequency droop control method for parallel inverters. In: *IEEE 35th annual power electronics specialists conference*, vol 4, pp 2501–2507
- Diaz G, Gonzalez-Moran C, Gomez-Aleixandre J, Diez A (2009) Complex-valued state matrices for simple representation of large autonomous microgrids supplied by PQ and VF generation. *IEEE Trans Power Syst* 24(4):1720–1730
- Doost Mohammadi et al (2014) Novel load frequency control approach based on virtual area error in a microgrid including PV and battery. In: *IEEE PES general meeting*
- Dorfler F, Simpson-Porco JW, Bullo F (2014) Breaking the hierarchy: distributed control and economic optimality in microgrids. *IEEE Trans Control Netw Syst* 3(3):155–166
- Dube A, Sindhu A (2015) Comparative analysis of passive islanding detection methods for grid connected distributed generators. In: *Annual IEEE India conference (INDICON)*
- Etemadi AH, Davison EJ, Irvani R (2012) A decentralized robust control strategy for multi-DER microgrids—Part I: Fundamental concepts. *IEEE Trans Power Del* 27(4):1843–1853

- Fang X, Yang Q, Wang J, Yan W (2016) Coordinated dispatch in multiple cooperative autonomous islanded microgrids. *Appl Energy* 162:40–48
- Gu W et al (2013) Cooperative control to enhance the frequency stability of islanded microgrids with DFIG-SMES. *Energies* 6(8):3951–3971
- Guerrero JM et al (2009) Control strategy for flexible microgrids based on parallel line-interactive UPS systems. *IEEE Trans Ind Electron* 56(3):726–735
- Guerrero JM et al (2007) Decentralized control for parallel operation of distributed generation inverters using resistive output impedance. *IEEE Trans Ind Electron* 54(2):994–1004
- Guerrero JM, Vasquez JC, Matas J, de Vicuna LG, Castilla M (2011) Hierarchical control of droop-controlled AC and DC microgrids—a general approach toward standardization. *IEEE Trans Ind Electron* 58(1):158–172
- Guerrero JM, Chandorkar M, Lee T-L, Loh PC (2013) Advanced control architectures for intelligent microgrids—Part I: Decentralized and hierarchical control. *IEEE Trans Ind Electron* 60(4):183–195
- Han Y et al (2015) Robust control for microgrid frequency deviation reduction with attached storage system. *IEEE Trans Smart Grid* 6(2):557–565
- Harikumar R, Ushakumari S (2014) Biogeography based tuning of PID controllers for load frequency control in microgrid. In: International conference on circuit, power and computing technologies [ICCPCT]
- Hettiarachchi HWD et al (2019) Review of applications of fuzzy logic in multi-agent-based control system of AC-DC hybrid microgrid. *IEEE Access* 7:1284–1299
- Hirsch A et al (2018) Microgrids: a review of technologies, key drivers and outstanding issues. *Renew Sustain Energy Rev* 90:602–611
- Hossain MJ et al (2014) Robust control for power sharing in microgrids with low-inertia wind and PV generators. *IEEE Trans Sustain Energy* 6(3):1067–1077
- Jayawardena AV, Meegahapola LG, Robinson DA, Perera S (2015) Representation of a grid-tied microgrid as a reduced order entity for distribution system dynamics and stability studies. *Electr Power Energy Syst* 73:591–600
- Kahrobaei A, Mohamed YAI (2013) Direct single-loop μ -synthesis voltage control for suppression of multiple resonances in microgrids with power-factor correction capacitors. *IEEE Trans Smart Grid* 4(2):1151–1161
- Katiraei F, Iravani MR, Lehn PW (2005) Micro-grid autonomous operation during and subsequent to islanding process. *IEEE Trans Power Del* 20(1):248–257
- Katiraei F, Iravani R, Hatziagyriou M, Dimeas A (2008) Controls and operation aspects of microgrids. *IEEE Power Energy Mag* 6(3):54–65
- Kaur A, Kaushal J, Basak P (2016) A review on microgrid central controller. *Renew Sustain Energy Rev* 55:338–345
- Kayalvizhi S, Vinod Kumar DM (2017) Load frequency control of an isolated micro grid using fuzzy adaptive model predictive control. *IEEE Access* 5:16241–16251
- Kulkarni OV, Doolla S, Fernandes BG (2017) Mode transition control strategy for multiple inverter-based distributed generators operating in grid-connected and standalone mode. *IEEE Appl Power Electron Conf Expos (APEC)* 53(6): 5927–5939
- Li P et al (2014) The realization of flexible photovoltaic power grid-connection μ -synthesis robust control in microgrid. In Proceedings of IEEE PES general meeting conference and exposition, National Harbor, MD, USA, pp 1–5
- Liu X, Wang P, Loh PC (2011) A hybrid AC/DC microgrid and its coordination control. *IEEE Trans Smart Grid* 2(2):278–286
- Lopes JAP et al (2006a) Defining control strategies for microgrids islanded operation. *IEEE Trans Power Syst* 21(2):916–924
- Lopes JAP et al (2006b) Defining control strategies for microgrids islanded operation. *IEEE Trans Power Syst* 21:916–924
- Ma C-T, Shr T-H (2015) Power flow control of renewable energy based distributed generators using advanced power converter technologies. *J Clean Energy Technol* 3(1):121–129

- Mahdavian M et al (2012) Load frequency control for a two-area HVAC/HVDC power system using hybrid genetic algorithm controller. In: Proceedings of the 9th international conference on electrical engineering/electronics, computer, telecommunications and information technology (ECTI-CON), pp 1–4
- Mallesham G et al (2011) Ziegler-Nichols based controller parameters tuning for load frequency control in a microgrid. In Proceedings of the IEEE international conference on energy, automation, and signal
- Martin-Martínez F, Sánchez-Mirallas A, Rivier M (2016) A literature review of microgrids: a functional layer based classification. *Renew Sustain Energy Rev* 1133–1153
- Mehrzi-Sani A, Iravani R (2010) Potential-function based control of a microgrid in islanded and grid-connected modes. *IEEE Trans Power Syst* 25(4):1883–1891
- Mehrzi-Sanir A, Iravani R (2009) Secondary control for microgrids using potential functions: modeling issues. In Proceedings of CIGRE conference on power systems
- Meng L, Sanseverino ER, Luna A, Dragicevic T, Vasquez JC, Guerrero JM (2016) Microgrid supervisory controllers and energy management systems: a literature review. *Renew Sustain Energy Rev* 60(C):1263–1273
- Mohsen Azizi S, Ali Khajehoddin S (2018) Robust decentralized voltage and frequency control of generators in islanded microgrids using μ -synthesis. In: 2016 IEEE energy conversion congress and exposition (ECCE), pp 1–8
- Morari M, Zafirion E (1989) Robust process control. Prentice-Hall, Englewood Cliffs, NJ, USA
- Nikkhajoei H, Lasseter RH (2009) Distributed generation interface to the CERTS microgrid. *IEEE Trans Power Del* 24(3):1598–1608
- O’Neill-Carrillo E, Jordan I, Irizarry-Rivera A, Cintron R (2018) The long road to community microgrids: adapting to the necessary changes for renewable energy implementation. *IEEE Electr Mag* 6(4):6–17
- Packard A, Doyle J (1993) The complex structured singular value. *Automatica* 29(1):71–109
- Pascual J, Barricarte J, Sanchis P, Marroyo L (2015) Energy management strategy for a renewable-based residential microgrid with generation and demand forecasting. *Appl Energy* 158:12–25
- Piagi P, Lasseter RH (2006) Autonomous control of microgrids. IEEE PES Meeting, Montreal
- Pogaku N et al (2007) Modeling, analysis and testing of autonomous operation of an inverter-based microgrid. *IEEE Trans Power Electron* 22(2):613–625
- Prasenjit Basak et al (2011) Simulation of microgrid in the perspective of integration of distributed energy resources. In: 2011 international conference on energy, automation and signal
- Ragam R, Palanisamy K, Paramasivam S (2018) A technical review on control strategies of active power filters. In: IEEE international conference on emerging trends and innovations in engineering and technological research (ICETIETR), pp 1–6
- Rajesh KS, Dash SS (2018) Load frequency control of autonomous power system using adaptive fuzzy based PID controller optimized on improved sine cosine algorithm. *J Ambient Intell Humaniz Comput* 1–13
- Rajesh KS et al (2017) A review on control of AC microgrid. *Renew Sustain Energy Rev* 7:814–819
- Rasoolzadeh A, Salmasi FR (2018) Reduced-order dynamic model for droop-controlled inverter/converter-based low-voltage hybrid AC/DC microgrids—Part 2: DC sub-microgrid and power exchange. *IET Smart Grid* 1(4):134–142
- Sabzehgar R (2015) A review of AC/DC microgrid—developments, technologies, and challenges. In: 2015 IEEE green energy and systems conference (IGESC)
- Sannino A, Postiglione G, Bollen MH (2003) Feasibility of a DC network for commercial facilities. *IEEE Trans Ind Appl* 39(5):1409–1507
- Sao CK, Lehn PW (2008) Control and power management of converter fed microgrids. *IEEE Trans Power Syst* 23(3):1088–1098
- Serban I, Marinescu C (2011) Aggregate load-frequency control of a wind-hydro autonomous microgrid. *Renew Energy* 36(12):3345–3354

- Seung CT, Saleem A, Wu Q, Østergaard J (2012) Agent based particle swarm optimization for load frequency control of distribution grid. In: 2012 47th international universities power engineering conference (UPEC), pp 1–6
- Shafiee Q, Guerrero JM, Vasquez JC (2014) Distributed secondary control for islanded microgrid—a novel approach. *IEEE Trans Power Electron* 29(2):1018–1031
- Sharma V, Singh I (2015) Microgrids: a review. *Int J Sci Res (IJSR)* 4(7)
- Unamuno E, Barrena JA (2015) Hybrid AC/DC microgrids—Part II: Review and classification of control strategies. *Renew Sustain Energy Rev* 52:1123–1134
- Yubing D, Yulei G, Qingmin L, Hui W (2008) Modelling and simulation of the micro sources within a microgrid. In: 2008 international conference on electrical machines and systems
- Zhou Y, Ho CNM (2016) A review on microgrid architectures and control methods. In: IEEE 8th international power electronics and motion control conference

Part II
Energy Efficient Buildings and Intelligent
Technologies for Smart Cities

Chapter 10

ICT as a Tool for the Structured Management of Urban Sprawl



K. S. Krishnaveni and P. P. Anilkumar

10.1 Introduction

The 2018 Revision of World Urbanization Prospects produced by the United Nations Department of Economic and Social Affairs (UNDESA) highlights that in between years 2018 and 2050, the size of the global urban population shall be highly focused in just a few Asian and African countries like India, China, Nigeria, etc., and collectively they will account for an expected increase of 35% of world's urban population (United Nations Department of Economic and Social Affairs 2018). The metropolitan inhabitants of India have grown-up expeditiously from 18% (1950) to 34% (2018) and predicted to be 54% in 2050. This uncontrolled urbanization together with unprecedented population growth and unplanned developmental activities will lead to chaotic urbanization which lacks basic infrastructure provisions, efficiency in functioning and totally disregards urban aesthetics. This type of urban development which is out of control can be regarded as urban sprawl (Zhang 2000).

Urban sprawl refers to the outgrowth of urban areas triggered by unplanned, uncontrolled, uncoordinated and irregular form of urban development focused by a host of factors. It can be perceived along the fringe of cities, along main roads, and roads linking a city, which deficiencies basic comforts like hygiene, preserved water, prime fitness center, etc. as the designers were incompetent to foresee such development during scheduling, plan and decision-making. Some of the identifiable characteristics of urban sprawl are vast spatial dispersion of urban activities and forms away from the city center, auto dependent development, unique linear expansions across road substructure and the advent of huge open zones with spreaded urban forms, forming a high separation between inhabited and marketable uses with destructive impacts on the publics living in these areas and the ecosys-

K. S. Krishnaveni (✉) · P. P. Anilkumar
Department of Architecture and Planning, NIT Calicut, Kozhikode, India
e-mail: krishnaveni_p170062ar@nitc.ac.in

tems. As a result of urban sprawl the urban growth forms making space more consistent and at the same time even more unbalanced which shall be highly objectionable. In the present days urban sprawl is often classified as a key challenge to urban sustainability and its consequences, whether good or bad, are necessary to be evaluated towards achieving a sustainable urban growth (Davis and Schaub 2005).

Urban sprawl can be often cited as a driver of several challenges to urban sustainability and viewed more negatively in planning literatures because it aggravates socioeconomic segregation due to exclusive housing markets and generates innumerable environmental impacts including greenhouse gas emissions, air pollution, congestion due to increased commuting, etc., (Carruthers and Ulfarsson 2002). Urban sprawl has many undesirable penalties for inhabitants and the surroundings, such as higher rate of pollution (air, sound and water), augmented traffic mortalities and holdups, loss of farming capacity, augmented car addiction, higher taxes, enlarged surfeit into rivers and lakes, destructive effects on human wellbeing, increased chances for flood, diminution in communal capital and loss of natural habitats, wildlife and public space. To conclude, urban sprawl put away incalculable acres of woods, grazing, forests and swamps which may result in urban decay, social dysfunction and ecological degradation.

Information and Communication Technologies (ICT) offer immense potential to regenerate the chaotic urban areas in an efficient way. The increased use of ICT will lead to an acceleration of people relocating from urban centers to urban peripheries eventually. In most cities, life at the city center is made miserable primarily due to traffic congestion, environmental pollution and lack of land space/area. With ICT supported technologies, people need not travel to city center anymore because they are able to do things sitting at home. The ICT component enables, planning better metropolises that offer better quality of life expectancy for its occupant's while being more sustainable and price effective. Legislative Planning and administrative strategies should include provisions for the impact of the growth of the info society and ICT on planning. This is an explanatory study suggesting use of ICT-enabled tools in taming the negative effects of urban sprawl for urban regeneration.

10.2 What Is ICT?

There is no particular, general definition for ICT. ICT includes all devices, applications, networking constituents, and schemes that jointly allow individuals and organizations (i.e., business, non-commercial agencies, governments) to interact in the digital domain. It represents a wider, more complete list of all constituents related to computer and digital know-hows.

Margaret Rouse (2018) showed the components of ICT sector, Fig. 10.1, which shows the moderate development of ICT thespians by far. The list of ICT constituents is comprehensive and continues to grow depending on the ICT implemented in different zones.

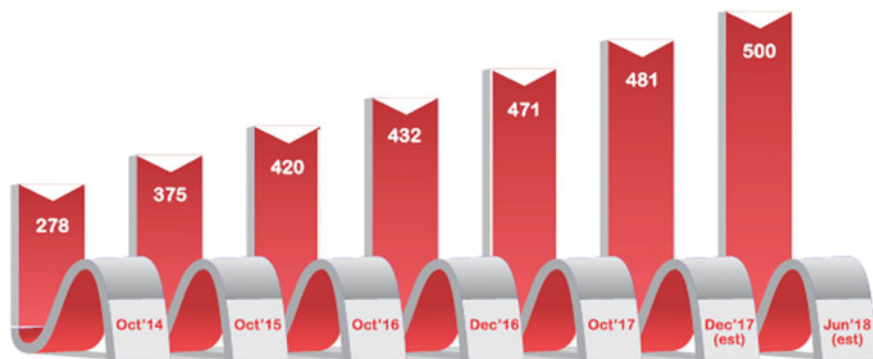


Fig. 10.1 Components of ICT (*Source* Margaret Rouse 2018)

ICT plays a vital role in viable urbanization development to confirm the best class of living milieu for its citizens. The EU definition unambiguously refers to ICT as a core constituent of smart solutions. In this vision, ICT is an instrument to develop solutions for further executing smart enterprises. ICT is evaluated both for itself and as a technology supporting smart facets such as agility, e-governance and so on (Carruthers and Ulfarsson 2002). Hence, ICT investments in the city will empower the scheming of smarter cities which offer better class of life for the inhabitants in a more sustainable and cost-effective means.

10.3 ICT Statistics of India

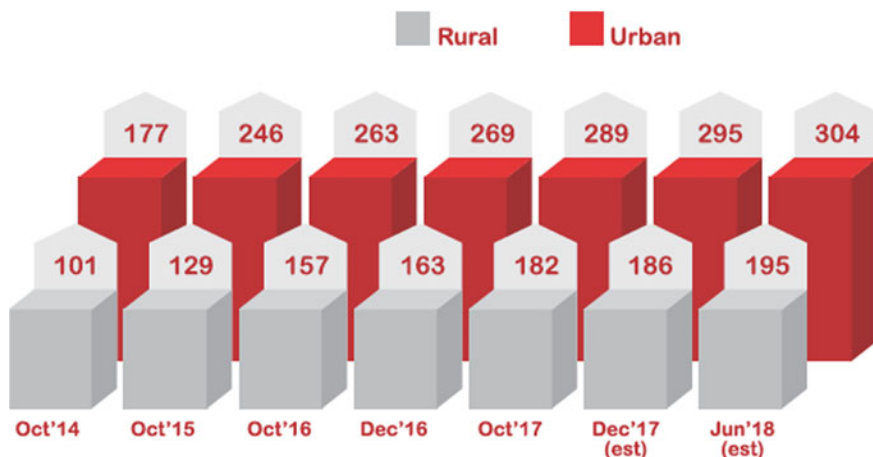
The annual survey exercise I-cube, undertaken by The Internet and Mobile Association of India (IAMAI) and KANTAR IMRB on December 2017, estimated 481 million internet users in India, which emphasizes a growth of 11.34% over December 2016 projected figures (IAMAI 2018). It is assessed that India will be having about 500 Million internet users by June 2018 (Fig. 10.2). Some of the interesting findings from the survey are shown in the figures below.



Source: Kantar-IMRB I-Cube 2017, All India Users Estimates, October 2017

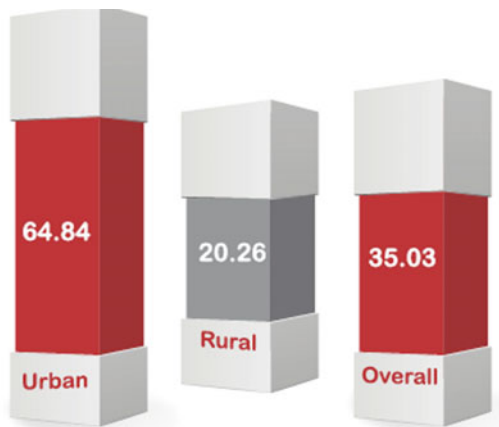
Fig. 10.2 Internet users in India (in millions)

There is a rapid pace of growth of internet users in Urban India. It is estimated to have 304 Mn urban internet users by June, 2018 whereas the rural internet users will be around 195 Mn by June 2018 (Fig 10.3). The internet usages in Urban India is 64.84% in December 2017, whereas in non-urban India, it is merely 20.26% (Fig. 10.4). Top nine Indian cities account for 35% of urban internet users in India. Delhi, Mumbai and Kolkata are the three major cities in Urban India with highest internet penetration (Fig. 10.5). In terms of frequency of usage almost 62% of urban population uses internet on a daily basis (Fig. 10.6). Urban India internet users access internet mainly for online communication. Second popular activity among them is for entertainment purposes/tele-leisure purposes (Fig. 10.7).



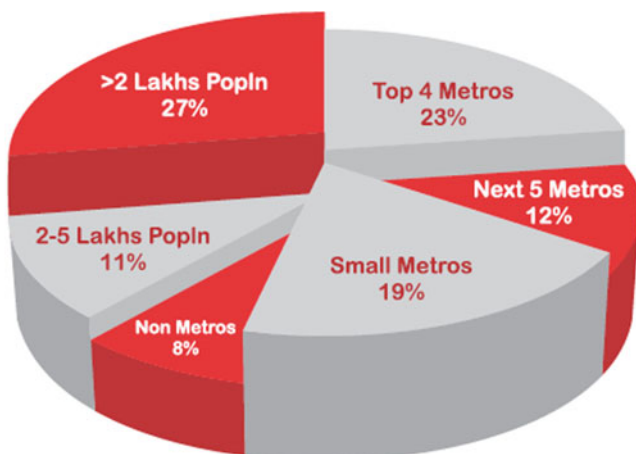
Source: Kantar-IMRB I-Cube 2017, All India Users Estimates, October 2017

Fig. 10.3 Internet users: rural-urban analysis (in millions)



Source: Kantar-IMRB I-Cube 2017, All India Users Estimates, October 2017

Fig. 10.4 Internet penetration (as % of population)



Source: Kantar-IMRB I-Cube 2017, All India Urban Internet Users Estimates, October 2017

Fig. 10.5 Urban internet users by town class (in %)

10.4 How ICT Can Tame the Negative Effects of Urban Sprawl?

The process of urban sprawl typically befalls around the outskirts of city, thereby untying the places where people work, shop, leisure, study, etc., from the place where they reside. It causes limited access to community substructure, such as public conveyance, which is indispensable for the everyday travel of the inhabitants to their places of work—which are often located in significant areas. The impacts of

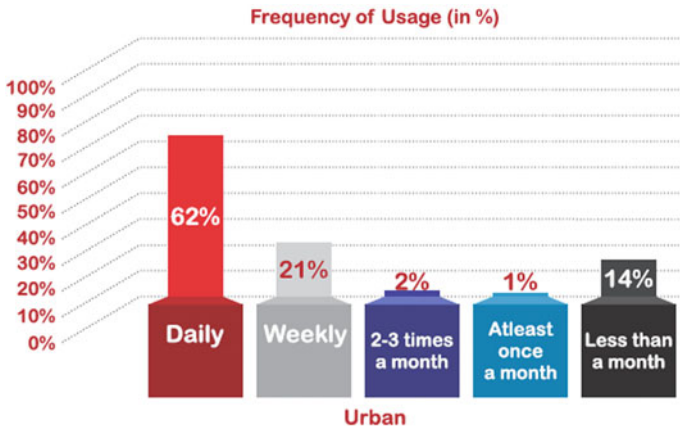


Fig. 10.6 Frequency of usage (in %) (Source KANTAR-IMRBI I-Cube 2017, all India users estimates, October 2017)

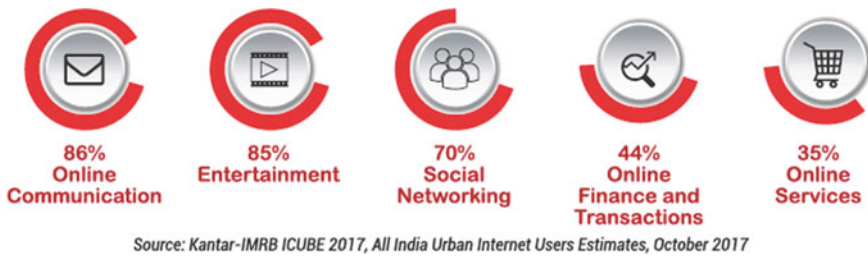


Fig. 10.7 Purpose of access (in Urban India)

sprawling urban growth affect not only the rich but the poor as well. The less earning group lives far unconcerned from the combined city center where super-market run, amenities and job openings are focused. The higher earning groups own their own cars for conveyance between city center and suburbs will face highway congestions arising from frequent trips to the city center. It may contribute to the emission of high levels of CO₂ into the atmosphere which directly impairs the environmental quality of the cities. Our ultimate aim is to contain the impacts of urban sprawl within a smaller circle with less extent of congestion, pollution, etc., by adopting the latest ICT-enabled technologies.

There arises a question of concern regarding the development pattern resulting from ICT penetration: Does the city develops in a centralized or sprawled fashion as a result of ICT penetration? In fact, ICT can help and unhelp in the process of reducing the impacts of urban sprawl. In principle both the trends of centralization and dispersion are conceivable because ICT provides immense liberty for sites of various doings and its success being subject to on how this independence of site is executed in an effective way. ICTs if used in a wise and comprehensive way, helps

metropolises and their inhabitants become more justifiable by reducing the impacts of uncontrolled urban sprawl to a considerable extent. However, it is not certain that ICT resolutions alone spontaneously lead to more sustainable consequences. In this paper, we elaborate the ICT applications in residential land-use, transportation sector and other service sectors like education, commercial, health, etc., to tame uncontrolled urban sprawl.

10.4.1 ICT Applications in Residential Land-Uses to Tame Urban Sprawl

The most commonly cited feature of urban sprawl is low-density single family dwellings with larger lots which consume huge amounts of previously unoccupied or productive land. This sprawling pattern of development gives rise to larger distances between housing units and segregate different land-uses, thereby residents are forced to depend on automobiles for commuting. Shrinking household sizes with increasing house sizes is a characteristic feature of residential areas in a sprawled city. In order to limit urban sprawl, we need to build higher density housing or concentrated living in which ICT has a major role to play.

As the residential development becomes highly dense, there will be reduction in energy consumption and cost of urban services. Of most significance is the diminishing of transport cost as density increases. In a low-density sprawled residential development people are more dependent on private cars for commuting, whereas in higher density residential development reliable and frequent public transportation systems will be fully functional with considerable reduction in energy costs. The key factor seen in higher density urban areas is the ease of access which has critical implications for a sustainable quality of urban life. In addition, this will create new employment opportunities and greater choice of employment.

The growing violence and the feeling of insecurity are the two major challenges to high-density concentrated living around the world. ICT has immense potential to address these two challenges in an effective and efficient manner (Sokido and Bhaduri n.d). ICT regional systems can be utilized for monitoring wrongdoings and enhancing security in city neighborhoods (Dameri 2017). In overall terms, ICT-enabled higher density residential development creates more diversity and vitality to tame the negative effects of low-density sprawled residential growth.

When it comes to security in high density patterns of development like apartments, condos, duplexes, etc., ICT-enabled tools that contains the newest know-hows, offers instinctive yet complete solutions, and provides 24/7 harmony. It also offers video shadowing, building mechanization, access switch, community amenities, safety, wireless locking, and round the clock alarm monitoring all from a single platform by improving functioning efficiency while offering an intelligent, smart living, state-of-art facility, to the inhabitants. With a single swipe on your smartphone, you can check the status, locks, lighting, heating—even cameras-at anytime, anywhere. An ICT-enabled access control system is considered to be a

repository of data regarding the building and the residents-who is onsite, where they are, and even when they're likely to be going. In the event of a theft or trespass, an ICT-enabled alarm will get activated and the security guards are alerted so that response can be initiated or emergency services summoned and hence it helps in achieving added piece of mind. Also, ICT-enabled high density residential units harness wide range of community amenities like club rooms, gyms and swimming pools, etc., in which one central system is capable of controlling the access and management of these facilities (Multifamily dwelling solutions 2018).

The idea of compact mixed-use development can be considered as a solution to tame uncontrolled urban sprawl of undesired type. This type of mixed-use development highlights that urban happenings should be located nearer, organized to ensure better admittance to service areas and conveniences required for daily living that is well integrated with public conveyance, pedaling and walking, with highly effective utility and infrastructure experience together with mix of land-uses. It can also help in maximizing safety and surveillance of people. Mixed land-use per se did not require much ICT for its functioning. But mixed land-use becomes easier to adapt if an element of ICT or network comes into picture. For example, the technique of geofencing can be used for safety and security purposes in a large mixed-use building where people live, work and play. It is a kind of barrier for motive devices or, radio frequency identification (RFID) tags when they pass in or out the limits created practically by the geofencing technology. It can be formed for both inside and out-of-doors, as per the obligation. The expertise used for geofencing includes GPS, radio frequency identification (RFID), Wi-Fi or cellular data. The geofences themselves can be highly tailored, such as a specific range around a household or any site; or established via a predefined set of boundaries, like schools, or the grocery shop, etc. It can also help immensely in the fields of home and office automation too.

10.4.2 ICT Applications in Transportation Sector to Tame Urban Sprawl

The OECD report highlights that urban sprawl adversely impact urban mobility because of greater commuting time and distance. Long commuting time results in shorter period of leisure and takes a toll on the urban residents well being. In sprawling cities, large distances discourage sustainable modes of transport like public transport, bicycle, walking, etc., as the urban population is spread over a wide area. The more sprawling a city becomes the more private vehicles/cars become necessary. Compared to the core city, the public transport frequency is very less in the suburbs. Even a small trip to the nearest grocery shop or medical store requires the use of car. To live in a sprawled city means driving to work, driving to education, driving to leisure, etc., and may end up in congestion, pollution etc. A sprawling city generates vastly larger amounts of CO₂ and pollution compared to

a more compact city. ICT's possess immense potential for travel and transport substitution by providing telework/e-work options for inhabitants of sprawled cities. This will help in the reduction of environmental footprint and reduction in demand of office facilities and transport infrastructures. This section analyses the effects of ICT penetration in mobility sector, employment and leisure to reduce the impacts of urban sprawl by trip reduction.

ICT Penetration in Mobility Sector. City life is becoming so difficult, polluted and congested mainly because of the huge volume of vehicular traffic. For example, if we take a parcel of land in the city core, a major part will be occupied by roads and vehicles. This type of growth is against the compact city concept. If there is a reduction in the number of roads, automatically the city size will shrink. But it is not possible because of the rising number of vehicles day by day which directly portrays the increase in number of trips which are triggered by the various functioning sectors of the city like employment, education, recreation, health care, etc., Reichman (1976) has divided the purpose of trip and action types into three: subsistence or mandatory (work and work related) which can be otherwise called "*compelled*", maintenance (shopping, medical, banking, other personal business) which can be otherwise called "*personal*", and discretionary or leisure which can be stated as "*free*" activities (Mokhtarian and Salomon 2006).

More trips contribute more traffic issues which in turn cause more emissions, which is bad for the sustainability of environment. The various negative effects of increasing transport are pollution, casualties, space consumption, and reduction in urban quality of life, etc. Mobility is considered to be the medium to accomplish the proper functioning of these different sectors. Integration with latest ICT technologies will help to contain people within the city so that large discount can be seen the approximate number of trips made for various functions of different sectors. As a result, city will stop its tendency to sprawl together with reduction in road space and parking space. Because of ICT can reduce mobility requirements, it will indirectly contribute to the reduction of transport related land-use too.

A sprawled city is very much dependent on automobile transport as it is located in the suburban area. In such cases, daily shuttle of this populace to the city center will cause traffic and street congestion together with CO₂ emissions, which directly harms the ecological quality of cities and negatively impacts the work and life balance. The need to commute will diminish when one can get things done with the help of ICT-enabled tools. Telecommuting, e-services, e-commerce, tele-leisure, tele-banking, teleshipping, telemedicine, etc., have impact on the traffic and transport characteristics of a particular region (Talvitie 2003). Instead of automobile dependent sprawled pattern of urban growth, we require more public transport facilities like bus and auto rickshaw, metro services, rapid transport and more walkability options like pedestrian pathways. And all these various means of sustainable transport could be linked to through the ICT technologies to get better outcomes. These kinds of ICT-enabled technologies will obviate the need of physical travel and thus reduces the traffic congestion of undesired type in an effective way. As a sample, an Intelligent Transport System encompassing

ICT-enabled tools helps in gathering and distribution of information which in turn can lessen traffic; it definitely impacts on surroundings or work-life steadiness. In short, ICT penetration in the mobility sector will help to reduce air and noise pollution, reduce traffic congestion, increase the safety of people, improves transfer speed and reduces the cost of transport.

In addition, ICT can be used to make different modes of travel more attractive. One example is the facility of Wi-Fi internet networks on buses, trains, etc. It will enable the travelers to stay linked and turn traveling time into useful work time. ICT can also help in making the traveling more suitable. The internet facility is progressively being used to reserve tickets in prior of travel. Services to reduce the inconvenience due of congestion, cancellations and/or delays are now available in a user friendly manner. Google Maps “Traffic” feature aids users to visualize “live” traffic conditions as well as the forecast conditions at any given situation/interval of the day/week. Accidents are one major issue faced by sprawled cities. ICT plays a major role in reducing accidents by collision, blind spot radar, symbol readings, lane keeping, driver attentiveness, night visualization, speed limit, etc. ICT can also be used to improve safety by providing prior warning such as obstacles or presence of other vehicles, presence of emergency vehicles, or limited surface control, etc. (Shrivastava 2012).

ICT Applications in Employment Sector. One of the first ever application of ICT on working practices is the adoption of teleworking/e-working/telecommuting with ICT-enabled tools. “The Electronic Cottage” concept introduced by (Toffler 1980) encouraged the formation of more favorable relationships between work, family and public by enabling better operational conditions, less stress, less duration traffic jams, more leisureliness, etc., by using the limitless possibilities of computer networks. Depending on the inclusions, class of work and the preference of workforces, telecommuting can be applied in different ways. As the role of home change to office, it will bring flexibility to work and will increase 24/7 phenomenon. It also helps the employers to preserve wealth by having compact work space in the city core. Cheap foreign labor can be sort out in some work phases with the help of ICT infrastructure which can be termed as “electronic immigrants” (Pelton 1992). The global broadcastings infrastructure has made it conceivable to commute from any locality where the employee can associate up with the system.

Home centered or remote working can be enabled through videoconferencing, net meetings, VoIP such as Skype, Google duos and Hotmail messenger etc. (Shrivastava 2012). In order to transform home space into an office space, one requires quick performing broadband connectivity, a landline or Wi-Fi connection and a system. The likely net reductions in travel will results in carbon reduction, decrease in accidents, air pollution and noise, etc. (Smith Institute Homepage 2008).

The internet, social network sites like Skype, Facebook, YouTube, and mobile phones are ICT that bring convenience and expediency to people’s activities today. Some of the jobs of the scientists can be done even if they are just sitting in front of their computers with internet connections. Office workers either in the managerial

or rank and file positions made their paper works trouble-free and effortless through the use of computers. Owners and employees in the business firms make their dealing and transactions with their customers and clients lightly without traveling and spending thousands of pesos. Farmers are guided on what are the latest trend in growing and increasing their farm productions. Government officials make their communications and transactions a lot easier through the use of ICTs (Bocar and Biong 2015).

ICT Applications in Recreation/Leisure. ICT have potential impacts on recreation/leisure activities and associated travel. ICT helps in the in house replacement for the outside home form of leisure activity. Mokhtarian and Salomon (2006) highlighted four methods by which ICT can have emotional impact on leisure happenings and tourism. The sparing of a customary activity with an ICT complement, the creation of new ICT activities, generation of ICT-enabled rearrangement of time to other activities, and ICT as an implementer of leisureliness doings. With the advent of ICT technologies, people residing in the suburbs does not need to travel much to the city center for watching a movie or having dinner from a star hotel of their choice. Smartphone technology has made it easier to access entertainment from anywhere anytime. By sitting at home itself we can now enjoy access to a huge collection of movies and TV shows, with the help of high speed broadband connectivity. Similarly, food of your choice from top restaurants in the city will be delivered in your doorstep with ICT capabilities. Books, magazines, newspapers, etc. are getting replaced by latest ICT-enabled online news reports and live news streaming, eBooks and online magazines. The improvement of these skills has made individuals halt inside, read online, play online games/movies/music, chat with friends, etc. This means that an increase in technologies provides us with more ways of entertaining ourselves. With ICT penetration, wide range of entertainment opportunities are accessible both in the comfort of your own home and while on the move. People's social connectedness becomes much easier with the advent of ICT-enabled technologies like internet, social network sites like Skype, Facebook, YouTube and mobile phones, etc., are examples of ICT that connects people with the member of their family, and friends, who are away from them. Through these ICTs people are able to make relationships with other people who are at far distance and even those whom they have not meet (Bocar and Biong 2015). Another ICT intervention in the field of leisure/entertainment is simulated travel, which is the capability to experience events, etc. through technology. Involvement in the event thru the net by video and can communicate with other members, live, through a communicating social platform. As this cannot not be a straight experience, but it certainly makes them sense as a part of the event and they might feel, enjoy and rejoice though their partaking. All these ICT interventions in entertainment and leisure sector will reduce the number of trips made from the sprawling city to the city center in a considerable amount thereby reducing the impacts of urban sprawl.

10.4.3 *ICT Applications in Service Sector*

ICT-enabled tools are penetrating into the services sector in a fast and diversified manner. Internet purchase with household supply is ever more popular. Electronic banking which is concerned with doing all these transactions from home or office without visiting the branch; anytime by using ATM's, telephones, internet and mobiles, etc., for doing banking services is a good example. In the vision statement of Reserve Bank, the objective is to actively promote e-transactions with a concept towards less hard money society. Electronic commerce in which buying and selling of goods and services primarily employing internet is an alternative to traditional businesses. ICT provides unlimited possibilities in the fields of public services and delivery systems for citizens. Online libraries, telemedicine, virtual education, etc., are some other fastest developing ICT-enabled services for the benefit of citizens. As the location of services will become a matter of least priority in ICT-enabled cities, we can cut short the traveling cost and save time to a considerable extent. Other examples include transactions such as vehicle excise duty payment online and music via high speed broadband and the post office's website allowing payment and home printing of stamps for parcels, direct streaming of films. The vast possibilities of ICT will lead to dematerialization in which a large number of products and services are delivered online. Online shopping and E-commerce will help us to save much time dedicated for searching of products, its pricing and associated trips made. It also helps in reducing the traffic congestion and energy savings. Replacement of letters with e-mail communication will help in instantaneous communication by reducing the environmental footprint.

ICT Applications in Health-care Sector. Health-care systems in sprawled cities where cities extend to rural areas face many issues like absenteeism of efficient doctors and most importantly lack of proper facilities and referral systems to urban hospitals and specialist centers. ICTs have immense possibility to face these tasks by sprawled cities giving accessibility, high-quality fitness care service area which is cost-effective. Recent developments in and growing obtainability and use of, ICTs by the common man have been the major initiators of e-health techniques over the past years. Health-care facilities are developed and operated in an incoherent way in many of the sprawled cities. Some of the interesting initiatives in the application of ICT in health care in India are listed as follows.

Telemedicine. Telemedicine, which is an e-health solution makes use of ICTs to overcome terrestrial barricades and thereby growth in access to better fitness care services at a remote or distant location. Telemedicine literally means "healing at a distance" can be anything from the discussion of health professionals for seeking advice over patient problems, to complex transmission of medical records, clinical information, and diagnostic tests results through technical devices (Sood 2007). Telemedicine uses high bandwidth for information transmissions for video conferences, broadcasting, and virtual reality. The sparing of equivalent forms of communiqué with digital means, combined with a rapid drip in the rate of ICTs, have flashed extensive attention in the use of telemedicine amongst health-care

benefactors and have permitted health-care establishments to envisage and devise new and more effective ways of giving attention. By the promotion of Internet the pace of ICT advancements has further speeded up, thereby escalating the scope of telemedicine to comprehend Web-based applications (e.g., Tele-consultations and conferences through the Internet) and hypermedia tactics (e.g., digital pictures and audio-visuals).

By the usage of telemedicine we can support societies which are conventionally underserved as it overwhelms distance and time obstructions between health-care suppliers and patients. Furthermore it can provide social-wellness and economic-wellness as well to patients, their relations, health specialists and the health systems including enhanced patient-provider communiqué and scholastic openings. Beyond cost and convenience, the benefits of telemedicine are increased access to health care to remote patients and hospitals, improves health outcomes by immediate transmission of health records and data, reduces health-care costs for patients by employing home monitoring programmes, overcome health-care shortages because of the irregular distribution of health-care providers, access to specialist located in urban centers so that instead of driving to a hospital located in the city core patients can get immediate access to the specialist through the concept of telemedicine.

Mobile Health or m-Health. Mobile health which is a subset of e-health can be defined as the usage of transportable devices to deliver medicinal and community health services. This includes mobile application improvement like voice calling, short messaging service (SMS) and wire-free data broadcast to allocate or collect health info or to directly supply health-care facilities (Abbas et al. 2016). Figure 10.8 shows the use case diagram of a health-care app. The mobile and web app will let a person search for a specialist or a laboratory throughout a city. A user may search for all specialists available in a clinic, all specialists available nearby as well all specialists available at a particular time of day. All clinics are at some location that has appropriate coordinates in terms latitude and longitude. Moreover, the app has a list of laboratories along with location and test directory. The user may find price of any test and compare price of a test among different laboratories.

ICT Applications in Education Sector. Residents of sprawled cities have similar needs to those of people living near the city center, but are disadvantaged in a number of ways. ICT in Education could play a major role for the human resource development in sprawled cities and remote areas for education, health, agriculture, commerce and other areas. ICT based distance learning facility, off campus course delivery, outreach facilities, online video lectures, etc., will help a lot in developing human capital by providing higher education to students living in sprawled communities. Open and Distance E-Learning programmes will alleviate the geographical constraints and higher rate of savings in cost compared to traditional mode of studying. One teacher can be used to teach many students over wide geographical area and remote areas through the use of teleconferencing. “Anyone anytime anywhere” feature of ICT is considered to be a revolutionary change in education system which helps to provide better education opportunities for all,

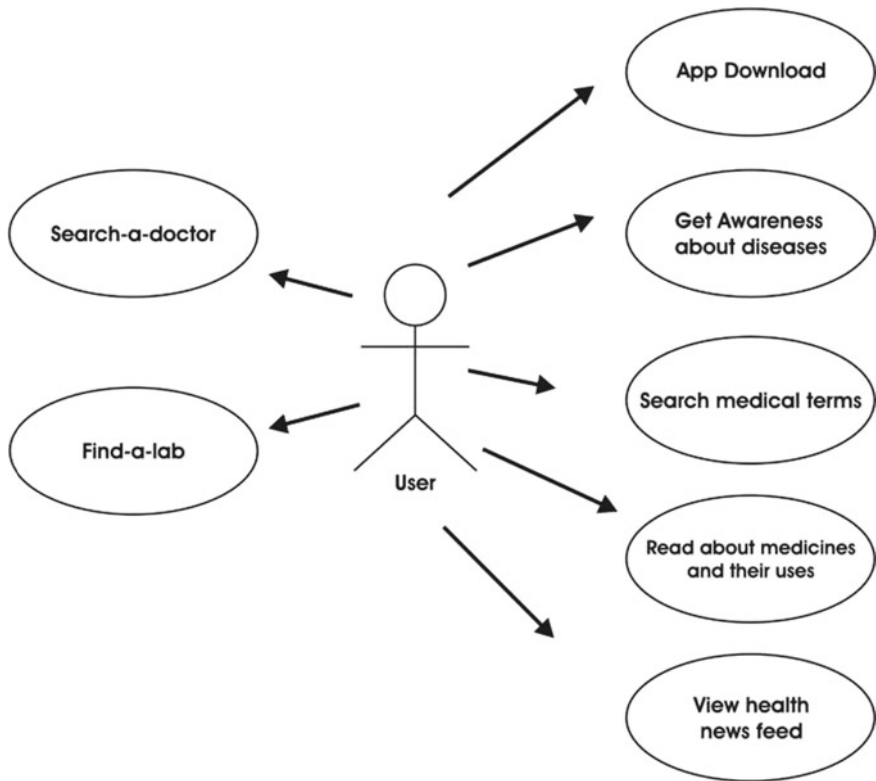


Fig. 10.8 Use case diagram of healthcare app (Source Abbas et al. 2016)

especially to those living in sprawled city or remote areas. ICT-enabled education will improve the access to a lot of e-resources, collaboration and activity of group of learners, equity and the life quality in sprawled communities. Teaching will be more effective and learning will be more experimental with the use of ICT. With ICT-enabled technologies, the students will get online lectures, notes, study materials from top universities across the world with a split of second. Nowadays, e-mail communication is mainly employed for the immediate delivery of reports to parents about their child's performance. In addition, teachers can offer individual support to their students with ICT help. Administrators, teachers, students and parents will get benefits from this kind of ICT supported the online communication systems. Besides teaching and learning, ICT-enabled tools can be used effectively for socialization, classroom management, evaluation, assessment, etc. (Bocar and Biong 2015). Thus, ICT can be considered as an effective medium for teaching, learning and making educational process more interesting and meaningful.

10.5 Discussions

Urban sprawl is an omnipotent issue and world over people are thinking ways to control it. Amongst the multiple control strategies, intelligent use of ICT range of applications is one of the viable methods to control urban sprawl, especially in developing countries where background ICT infrastructure is good. Although ICT has the potential to tame the negative effects of urban sprawl of a region to a great extent, there are multiple issues and challenges confronting the effective implementation of ICT for sprawl control. Some of the challenges of ICT to tame urban sprawl and recommendations to overcome these are dealt here.

10.5.1 ICT-enabled Urban Sprawl Control by Developed Countries and Developing Countries

The phenomenon of urban sprawl is considered to be a global issue as it is evident in developed countries as well as developing countries. The context, dynamics, indicators, causes and impacts of urban sprawl in developed countries have points of departures from developing countries like India. Population growth together with socio-economic factors in the urban areas determines the dynamics of urban sprawl in both developed countries and developing countries. In developing countries, people move to the urban fringes because there is not enough space for them to live at the city core whereas in developed countries sprawl occurs because of the luxurious need for more space. Larger homes with larger lots, preference for low-density developments, and increase in space coupled with drop in household sizes fuels urban sprawl in developed countries like U.S. In developing countries, there is increased share of vacant lands and lowering densities at the urban fringes as lands are being held from developmental activities.

In a developing country like India with sound ICT infrastructure, the problems arising out of urban sprawl can be solved in an efficient way using ICT-enabled technologies. In developed countries, urban sprawl cannot be effectively tamed by ICT as ICT penetration in fringe areas are very less compared to a developing country like India where ICT-enabled technologies are available even in the rural fringes. Developed countries invest for ICT-enabled technologies in fringe areas only after conducting so many studies on its commercial viability, feasibility, etc., whereas in a country like India, rather than giving priority to commercial viability, the purpose and immense potential of ICT is taken into consideration while delivering ICT to rural and fringe areas.

The global digital divide can be defined as the technological gap between developed and developing countries because of a large number of socio-economic factors like lack of knowledge, confidence, skills, high prices of data, low-income, insufficient infrastructure or broadband coverage. In order to overcome the issues related to unequal access to ICT, the government should take action in three key

policy areas: (i) targeting affordability by lowering of prices (ii) closing of infrastructural gaps by public investments and (iii) developing skill sets and digital literacy (OECD 2017).

Most developed countries across the world are at advanced stages of latest ICT revolutions characterized by ‘highly modern’ technology whereas most developing countries are standing at the levels of ‘standard-modern’ technology. The process of ‘technological leapfrogging’ can be adopted by developing countries to hurdle several stages to rapidly change from ‘standard-modern’ to ‘highly modern’ technologies (Bhagavan n.d.). Technological leapfrogging generally occurs in three stages, 1. A hop-step in which the developing countries import and absorb highly modern technology, 2. A jump effort in which the developing countries produce, replicate and improve the imported technology, and 3. State-of-the-art situation in which the developing countries move on to innovations on its own. Over time, developing countries reinforces this process and helps in spreading the network wider and quicken the transition.

10.5.2 Need for ICT Literacy of Citizenry

One of the important indicators of ICT penetration in developing as well as developed countries is the education levels of its citizens. To get maximum benefits from the unlimited opportunities of the information society, citizens need both digital and analogue skills (OECD 2017). Lack of knowledge, confidence and skills are considered to be some of the important barriers, pointing to the necessity of raising levels of education to allow citizens to benefit from numerous online opportunities. ICT policies should be linked to savings in education in order to generate necessary human skills and raise education standards to transform citizens as more effective online users. In order to turn internet into an efficient tool for development, policy makers must tackle both the supply-side challenges which includes high prices and infrastructure deficiencies together with the demand-side challenges which exist outside the ICT ecosystem (ITU 2017). Figure 10.9 highlights the demand and supply side to increase the internet usage. Broader socio-economic factors which are not related to ICT need to be considered and taken care of for bringing more people online. People need analogue skills which include basic literacy, numeracy, etc., together with digital literacy to get full advantage of the immense capabilities of ICT and information society.

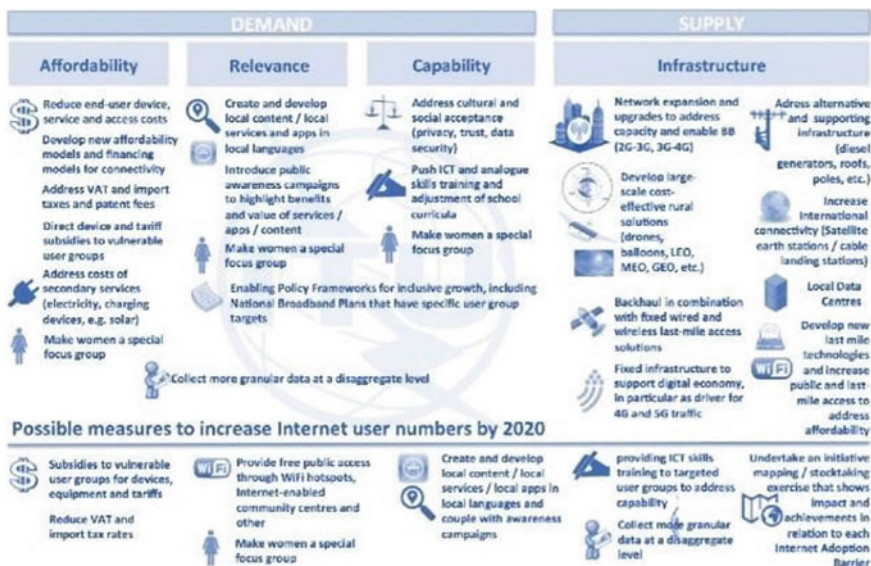


Fig. 10.9 Demand- and supply-Side measures to increase internet use (Source ITU 2017)

10.5.3 Requirements for Making the ICT System State-of-the-Art

As ICT-enabled technologies are growing at an alarming rate day by day, it is very much inevitable to standardize and allow for interoperability of these systems for better performance. Integration of various applications and interfaces which enable service use and information extraction form the basis of interoperability. In simpler terms, it is the collaboration of peoples, systems and services. With ICT interventions like cloud computing, open data, plug and play, etc., the importance of interoperability is on increase all the time. As a result of interoperability, it is possible to integrate various types of software with different functions, thereby minimizing the need for intervention in terms of implementation on each software element. Additionally, the maintenance and the extension of the system can be assured at limited cost and least effort. In short, improved interoperability can result in cost savings, scalability, modularity, robustness, effectiveness, flexibility, and transparency.

Another important requirement is the scalability of the ICT system for sprawl control. It is simply an attribute which refers to the ability of a network, process, software, etc., to grow and manage the need of increased demand. A scalable system is more adaptable to the varying needs or influx of demands of its users. It is considered as a symbol of competitiveness and stability. Once the ICT system becomes popular, there will be a sudden increase in the number of users. So we must keep in mind the fact that ICT systems should be scalable. For example, if we

design a system for 10,000 people in the beginning, and if we want to extend the service to 50,000 people in the near future, we can gradually add on the feature for serving 50,000 people using the property of scalability.

10.5.4 Need for a Comprehensive and Updated GIS Database for Efficient Sprawl Control

GIS can help in the easy and efficient determination of the spatial and temporal distribution of urban sprawl in a region. Together with latest remote sensing techniques, GIS can tackle issues related to sprawl, encroachment, traffic, air and noise pollution, etc. Fine grained policy decisions can be taken by the planner with the help of GIS enabled spatial information. Urban planners can extrapolate the future growth patterns of the city using GIS-enabled tools and remote sensing techniques. The best way to improve access to the GIS data for taming urban sprawl is the implementation of a web-based GIS database. Lack of GIS experts, insufficient user support, nonavailability of proper software and hardware, unreliable power supply, and slow internet access are the major setbacks to the GIS usage in developing countries context. High-quality spatial data can be made use of for sprawl control with better training and networking among GIS experts. Widespread effort can be made to incorporate GIS and remote sensing techniques in the educational curriculum. Comprehensive and updated GIS database will give us a clear picture of various parts of city where development is restricted, where you want to conserve, where you want a particular pattern of development, etc. All these activities need some sort of explorations taking stake of the existing situation which all necessitates the presence of a comprehensive GIS database for the city.

10.6 Conclusion

The problem of urban sprawl is a matter of concern in many Indian cities. Compared to city dwellers, people in a sprawled city lives in larger houses with larger lots and depends solely on automobiles for commuting to work, education, leisure, etc. This will ultimately result in increased commuting time and traffic congestion, increase of abandoned and polluted land, destruction of farmland and open space, increased air pollution and levies additional costs on neighboring cities. If left unchecked, uncontrolled urban sprawl may cause detrimental effects to overall sustainability.

ICT have immense potential to regenerate the chaotic urban areas in an efficient way. Whether ICT can positively promote sprawl or control sprawl is a debatable topic, this paper attempts to discuss the ways and means by which the detrimental effects of urban sprawl can be controlled by analyzing the sector-wise or land-use

wise impacts of ICT penetration. A large variety of network applications like online shopping, online social networking, bill payment, ticket booking, etc., are the outcomes of ICT penetration. In a sprawled city, ICT offers potential for transport and travel substitution. With ICT-enabled options like telecommuting or telework there will be substantial reduction of commuting time which results in increased productivity for individual, employers and the community. The fourth infrastructure 'ICT' helps the cities to get connected, wisely managed with efficient environment comprising of smart buildings, health care and transportation systems.

ICT's can be used effectively to mitigate the environmental impacts generated by urban sprawl. For example, dematerialization (online shopping, online delivery, e-commerce, etc.), travel and transport substitution (telework, telecommuting, etc.), home automation and ICT-enabled high-density mixed land-uses development, etc., will help in the reduction of environmental footprint, pollution potential, etc., and helps in the more efficient use of resources so as to increase the energy efficiency. The key to tame the impacts of uncontrolled urban sprawl is not the ICT's, but how it is implemented and used. However, to fully comprehend the prospective of ICTs for justifiable urban growth, an ICT empowering surroundings has to be shaped. This includes providing infrastructure, methodological platforms, building liable governance models and focusing profoundly on education and aptitude building to ensure the potential.

References

- Abbas Z, Aquil Burney SM, Bari A (2016) Few ICT applications for improved healthcare service delivery in developing countries. *Int J Multidiscip Sci Eng* 7(6)
- Bhagavan MR (n.d.) Globalization of technology—technological leapfrogging by developing countries
- Bocar AC, Biong CT (2015) Role of information and communication technology: its impact on students' learning and the extent of effects to social, recreational and sports activities. *Am J Inf Sci Comput Eng* 1(2):59–67
- Carruthers J, Ulfarsson GF (2002) Fragmentation and sprawl: evidence from interregional analysis. *Growth Change* 33:312–340
- Dameri RP (2017) Smart city implementation-creating economic and public value in innovative urban systems. Springer
- Davis C, Schaub T (2005) Trans-boundary study of urban sprawl in the Pacific Coast region of North America: the benefits of multiple measurement methods. *Int J Appl Earth Observ Geoinform* 7(4):268–283
- IAMAI Homepage, <https://www.iamai.in>. Accessed 15 November 2018
- ITU (2017) Connecting the unconnected-working together to achieve connect 2020 agenda targets
- Margaret Rouse: ICT definition, <https://searchcio.techtarget.com/definition/ICT-information-and-communications-technology-or-tecnolo>. Accessed 20 November 2018
- Mokhtarian PL, Salomon UCD (2006) The impacts of ICT on leisure activities and travel: a conceptual exploration. UC Davis Publication
- Multifamily dwelling solutions, <https://www.ict.co/Apartments>. Accessed 25 November 2018
- OECD (2017) Aid for trade at a glance 2017: promoting trade, inclusiveness and connectivity for sustainable development

- Pelton JN (1992) Future view. Communications, technology and society in the 21st century. Johnson Printing
- Reichman S (1976) Travel adjustments and life styles – a behavioral approach. In: PR Stopher, AH Meyburg (eds) Behavioral travel-demand models. D.C. Heath and Company, Lexington, MA, pp 143–152
- Shrivastava M (2012) Reducing the need of travel through ICT. Int J Comput Sci Inf Technol Secur (IJCSITS) 2(6). ISSN 2249-9555
- Smith Institute Homepage (2008) Can homeworking save the planet, http://www.smithinstitute.org.uk/publications/can_homeworking_save_the_planet.htm
- Sokido DL, Bhaduri S (n.d.) Safety and security in high density-high rise dwelling forms—The Case of Addis Ababa, Ethiopia
- Sood SP et al (2007) Differences in public and private sector adoption of telemedicine: Indian case study for sectoral adoption. Stud Health Technol Inform 257–268
- Talvitie J (2003) The impact of information and communication technology on urban and regional planning. Helsinki University of Technology Institute of Real Estate Studies
- Toffler A (1980) The third wave. Collins, USA
- United Nations Department of Economic and Social Affairs: World urbanization prospects: The 2018 revision, UNDESA (2018)
- Zhang T (2000) Land market forces and government's role in sprawl: the case of China. Cities (2):123–135

Chapter 11

Modelling and Simulating the Thermal Comfort Aspects of Natural Ventilated Classrooms in Hot-Humid Climates



P. V. Sasidhar, Kratika Shrivastava and M. Ramgopal

11.1 Introduction

Increasing requirement of thermal comfort and improvements in living standards in developing countries has led to an increase in the amount of energy consumption of buildings. In India, the building sector represents about 33% of total electricity consumption, with the commercial and residential sector accounting for 8% and 25% respectively (Taulo 2012). In the next few decades, India is expected to have the world's largest set of young people. The compound annual growth rate of the higher education sector in India is mounting from 10.16% to 17.5% by 2025. The number of higher education institutions in India has seen more than 50 fold growth in the last six and half decades (Yeravdekar and Tiwari 2012). Also there is a growing urge to increase the quality of higher education in India. Studies show that, among other things, the quality of indoor environment affects the teaching and learning aspects of classrooms significantly (Mishra and Ramgopal 2015). Providing a thermally comfortable environment is shown to reduce absenteeism among the students. Passive cooling techniques have proven to be of great utility in such scenarios to reduce thermal discomfort (Pellegrino et al. 2016). These are techniques for achieving comfort by natural means, i.e., without consuming minimum or no additional energy so that a sustainable solution could be achieved. Hence they are preferred over active cooling systems which are highly energy intensive. Studies show that in case of naturally ventilated classrooms, the outdoor climate variations influence the behaviour of the occupants and their perception of comfort. This has resulted in development of several adaptive comfort equations for different climates (Mishra and Ramgopal 2015; Yao et al. 2010; de Carvalho et al. 2013; Nematchoua et al. 2014; Indraganti et al. 2014).

P. V. Sasidhar (✉) · K. Shrivastava · M. Ramgopal
Department of Mechanical Engineering, Indian Institute of Technology Kharagpur,
Kharagpur, West Bengal, India
e-mail: sasidhar.perakam@gmail.com

Adaptive thermal comfort models suggest a wider range of acceptable temperatures by considering the adaptations of the subjects to the local outdoor climate. This opens up the scope for natural ventilation of buildings and use of various low energy passive systems (Givoni 1991; Omrany et al. 2016; Panchabikesan et al. 2017). There are various passive techniques used in buildings to control the natural flow of air and heat into the buildings (Omrany et al. 2016). But the performance of a passively cooled or naturally ventilated building depends strongly on the climatic conditions, so it is essential to evaluate the buildings for each of the climatic zones (Panchabikesan et al. 2017).

Toe and Kubota (2015) investigated vernacular passive cooling techniques and their potential application for improving indoor thermal comfort of naturally ventilated, modern brick terraced houses in Malaysia. Assessment of passive cooling techniques for high and low thermal mass building was done. Samani et al. (2016) compared different passive cooling techniques of shading, natural ventilation, reflective coatings (cool paints) and increased thickness of interior gypsum plaster for these buildings to tackle overheating in hot climates. The findings of this comparison bring insights into the effectiveness of passive cooling techniques that can be highly beneficial at the design level. The authors were able to achieve acceptability of 80% of ASHRAE 55 by the combined implementation of all techniques.

Though studies are already carried out on use of passive cooling methods, their application on thermal comfort of classrooms has not been reported. Hence in this paper, the improvement in thermal comfort levels of a naturally ventilated classroom located in a hot and humid climate is studied in a systematic manner. A reference classroom building conforming to National Building Code (NBC) of India (NBC 2005) is considered for the study. The performance of this building is simulated using EnergyPlus.

11.2 Development of Classroom Model and Validation

11.2.1 Reference Classroom Model

The classroom is modelled using EnergyPlus software (EnergyPlus 2015) with a legacy open studio plug-in as an auxiliary interface. The plug-in is installed in Google Sketchup and used to create the geometrical model of the reference classroom as shown in Fig. 11.1a. The geometry of the classroom was based on an actual, naturally ventilated classroom with 216 m² floor area and a height of 3.42 m as shown in Fig. 11.1b. The material properties are given in Table 11.1. The windows have solar transmittance of 0.837 and visible transmittance of 0.898.

The surfaces, floor, and roof of the geometrical model are converted to objects in a single thermal zone and the boundary conditions are given by specifying them as exposed to outdoor or unexposed as the internal surface. The roof and all the walls

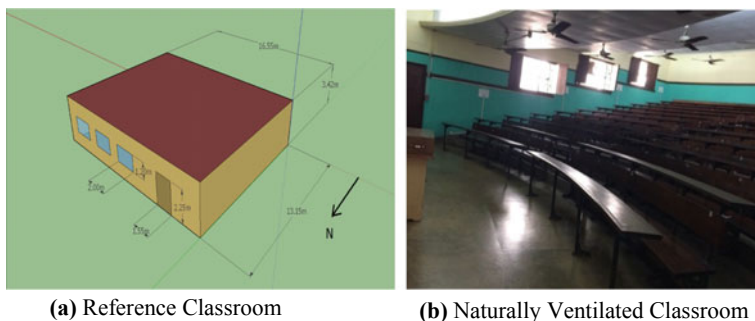


Fig. 11.1 a Reference classroom. b Naturally ventilated classroom

Table 11.1 Materials and their properties

Component	Area (m ²)	Material	Conductivity (W/mK)	Density (kg/m ³)	Specific heat (J/kgK)
Walls	183.3	200 mm brick with masonry plaster	0.89	1920	790
Roof	216	200 mm thick concrete with masonry plaster	1.11	800	920
Floor	216	200 mm thick concrete with masonry plaster	1.11	800	920
Windows	14.4	3 mm clear glass in mild steel frame	0.9	–	–
Doors	6.9	25 mm wood	0.15	608	1630

except the west wall are exposed to outdoor conditions. The outdoor conditions are provided by weather files to EnergyPlus which contains typical hourly data of solar radiation, temperature, wind speed, humidity, and atmospheric pressure. Simulations are carried out for the Indian city of Kolkata (22. 6° N, 88.4° E).

11.2.2 Validation of the EnergyPlus Model

To verify the modelling procedure and boundary conditions specified, several measurements of temperatures and relative humidity are taken inside the classroom shown in Fig. 11.1b and are compared with the simulated hourly average indoor air temperatures for three days. Measurements are taken using temperature and humidity sensors to sense the inside room temperature and relative humidity, globe thermometer is used to estimate mean radiant temperature and Hobo data logger is used to record the data. Measurements were taken for a span of 84 h. The simulation was performed by taking the reference classroom model with 500 mm thick

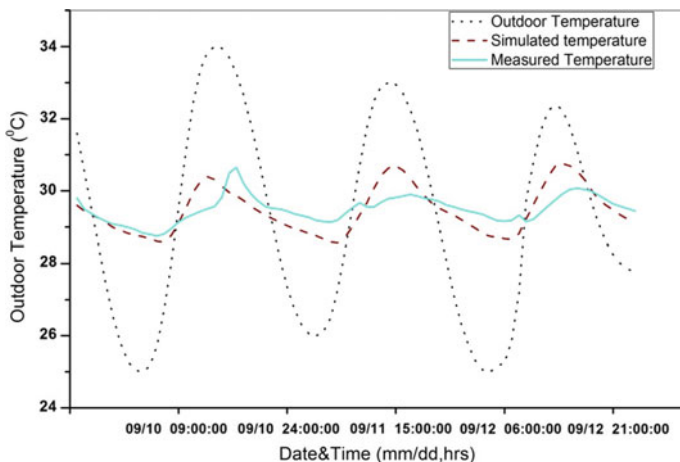


Fig. 11.2 Comparison between measured and simulated operative temperatures

walls and 200 mm concrete slabs for roof and floor. For convenience, the classroom was considered without any occupants with windows being closed for 84 h. Measurements were also taken at various positions inside the classroom and a variation of ± 1.5 °C was found. Since the variation is not very large, it is neglected and a uniform temperature is considered across the classroom. The simulated results in terms of operative temperature are compared with the calculated operative temperatures of the actual classroom using the measured temperatures. Figure 11.2 shows the comparison between simulated values and values obtained from measurements. In spite of some uncertainty in the input values provided for simulation a reasonably good agreement can be seen between the simulated and measured values indicating the correctness of the approach.

11.2.3 Thermal Performance of the Model

After verifying the correctness of the approach with actual data on an existing classroom, next the reference classroom as per NBC standards is constructed in EnergyPlus (Fig. 11.1a). Based on NBC recommendations (NBC 2005), the classroom is considered to have an occupancy of 54 i.e. 0.25 person/m² with classes being held from 8 a.m. to 6 p.m. with one hour recess from 1 p.m. to 2 pm. An activity level of 1 met (58.2 W/m²) is considered for the students, who are assumed seated. An average heat transfer area (DuBois area) of 1.8 m² per person is considered based on ASHRAE recommendations. Simulations are run from March 15 to June 15, which is the typical summer duration in sub tropical climate of India for a typical metrological year. TARP (Thermal Analysis Research Program) algorithm is used for calculating inside and outside surface convection heat transfer

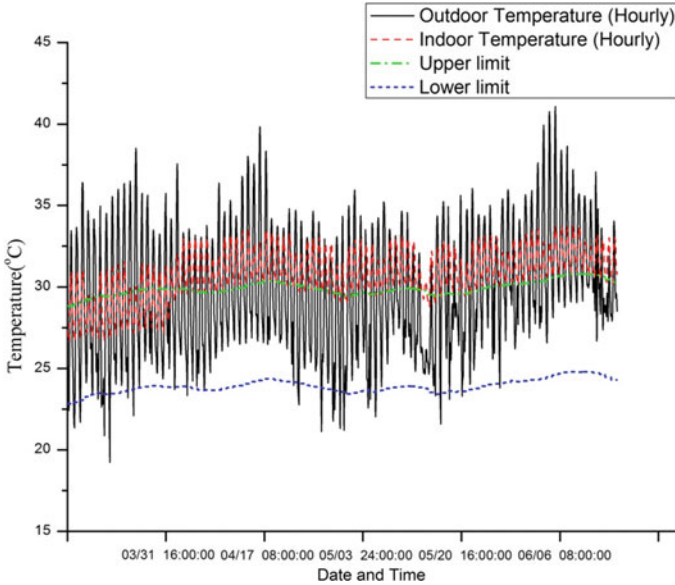
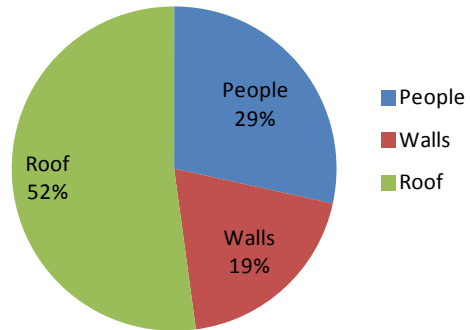


Fig. 11.3 Variation of simulated operative temperatures inside the reference classroom

coefficients. The adaptive thermal comfort limits for the effective temperature inside the classroom are based on 80% acceptability limits of EN 15251 standards (EN 15251). It is seen that for the reference classroom the simulated temperatures inside the classroom are mostly outside the comfort limits as shown in Fig. 11.3, indicating the need for improving the thermal comfort. To understand the reasons for high indoor temperatures, contributions of heat transfer for a typical summer day from major heat sources are calculated and are shown in Fig. 11.4.

As shown in Fig. 11.4, the heat gain through the roof contributes maximum heat due to direct solar radiation of the exposed roof. This is followed by contribution due to occupants, walls (9% due to exposed east wall) and windows. Hence to improve the thermal comfort aspects, during summer months, passive cooling

Fig. 11.4 Contribution of different heat sources to room heat gains on 21st June



techniques which can reduce these heat gains are to be identified and evaluated. Several passive techniques like increased thermal insulation, increased thermal mass, cool roofs, shading, overhangs, night ventilation, etc., can be considered. In this study, based on the heat gain distribution and ease of implementation, the following measures are considered and evaluated: occupant density, class scheduling, window overhangs and wall shading, nocturnal ventilation, and reflective coatings (cool paints).

11.3 Results and Discussion

Results are obtained by introducing the methods identified for mitigating the discomfort. These are: overhangs to block heat gain from windows, tree shadings to block the east wall heat gain, cool paints to block roof heat gain, night ventilation to offset heat gain by walls, and scheduling to regulate heat gain by occupants according to peak outdoor conditions. The individual effect of each of these and their cumulative effect on comfort are obtained from simulations. The details used in the simulation for each technique are discussed in following subsections. The simulations performed for the reference classroom (baseline model) defined earlier. Results for the baseline model for summer months indicate 21.32% of total summer comfort hours and only 9.1% of occupied comfort hours. The results obtained from simulation for each of the techniques listed above for summer months (March 15 to June 15) are discussed in the following subsections.

11.3.1 Scheduling

Generally, classes are held for the whole duration of working hours in an educational institution. For the reference classroom, it is from 8 a.m. to 6 p.m. with a recess for one hour, i.e., from 1 to 2 p.m. In this study, two other schedules are taken into consideration, one with classes held for alternate hours in the specified classroom and the other being no classes in the duration when peak outside temperature occurs, i.e., from 1 to 3 p.m. The impact of these three schedules on indoor temperature and thermal comfort of occupants has been assessed. Figure 11.5 shows the variation of indoor temperature with number of hours for May 20th and 21st. Both alternate and peak scheduling, results in decreasing the peak temperature inside the classroom. The study suggests that if peak scheduling is applied, there is a noticeable increase in occupied comfort hours as compared to baseline scheduling, even though this alone is not sufficient. Alternate scheduling may not be acceptable due to practical reasons for classrooms.

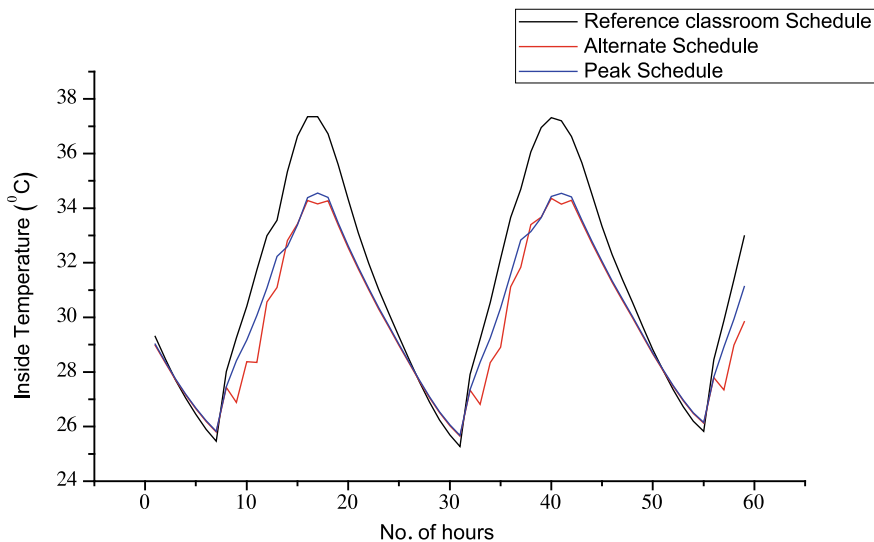


Fig. 11.5 Inside temperatures on 20th and 21st May for different type of schedulings

11.3.2 Occupant Density

It can be seen from Fig. 11.4, that contribution of occupancy load is about 29% which is a very significant amount, therefore simulation is performed where the occupancy rate is varied from 0.5 to 0.25 person/m² in steps which is the occupancy range for educational institutions according to National Building Code (NBC 2005) and its effect on total comfort hours is analyzed. Study considered three occupancy variations of 108, 70, and 54. It could also be noted that there is a increment of 3% in occupied comfort hours as the occupancy is changed from 108 to 54.

11.3.3 Wall Shading and Window Overhang

The depth of the window overhang is taken based on the projection factor (=depth of overhang/height of the window) of 0.83 which is in accordance with (Sadafi et al. 2011). The width of the overhang is same as the width of the window. Shading with trees along the east wall of the room is also simulated. Trees are kept 4 m away from the east wall and 5 m in height. They are distributed in such a way that they cover the whole width of the east wall, i.e., 13 m. Results show that with these measures, the total comfort hours increases to 24.23% (from 21.23 % of baseline) of total hours and occupied comfort hours increases to 11.79% (from 9.1%) of total comfort hours for summer months. Since these measures are easy to implement, they are recommended.

11.3.4 Nocturnal Natural Ventilation

To study the effect of nocturnal ventilation, the schedule of opening windows is given at night time when the outdoor temperature is lower than inside temperature. For simulation, it is assumed that all the windows are kept open from 9 p.m. to 6 a.m. From Fig. 11.6, it can be observed that the outdoor dry bulb temperature is lower than the inside temperature during the night hours. To utilize this environmental condition for the benefit of building cooling, windows were kept open at night time, which resulted in decreasing the peak temperature occurring inside the classroom with respect to reference classroom. Figure 11.6 shows that the peak temperature occurring inside the classroom for four days of May 20th–23rd have reduced by about 2 to 3 °C, leading to an increase in the percentage of comfort hours.

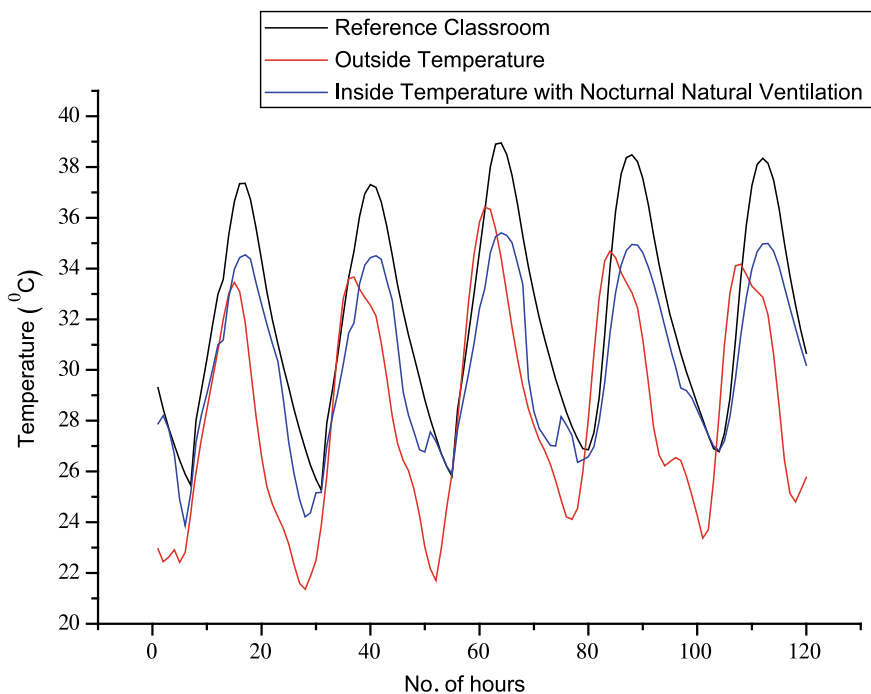


Fig. 11.6 Comparison of inside and outside temperature on 20th May to 23rd May for Nocturnal Natural Ventilation

11.3.5 Use of Reflective Coatings (Cool Paints)

According to ASHRAE standards, paint materials having a solar reflectance value of 0.7 or more are characterized as cool paints. Hence for simulation purposes, paint materials having solar reflectance values of 0.7 or more (solar absorptance values of 0.3 or less) are considered for reflective coatings of roof and walls. Since the roof is the main contributor with 52% of total heat input to the classroom, it is the most crucial component. However, in the simulation, cool paints are applied on the roofs as well as walls. Results are obtained for solar absorptance values varying from 0.1 to 0.3. As expected use of cool paints have proven to be of greatest impact as it directly reduces the heat transfer from the roof which contributes to 52% of heat gain to the room.

11.3.6 Effect of Individual and Combined Techniques for Complete Year

Based on the results obtained for summer months, study is extended to cover the complete year. Results obtained for summer months as well as complete year are summarized in Table 11.2. Comfort hours are defined based on the adaptive

Table 11.2 Combination of various passive cooling techniques and their effect on thermal comfort for summer months and all year around

Passive cooling technique		Summer months		All year around	
		Percentage of occupied comfort hours (%)	Percentage of comfort hours (%)	Percentage of occupied comfort hours (%)	Percentage of comfort hours (%)
Reference classroom		9.1	21.32	23.73	37.60
Scheduling	Alternate	10.69	21.86	23.33	38.17
	Peak	11.38	21.37	28.13	37.86
Occupancy	108	6.12	20.34	20.38	36.35
	70	8.51	21.06	22.69	37.19
	54	9.10	21.32	23.73	37.60
Nocturnal natural ventilation		10.29	32.05	24.31	41.92
Shading and window overhang		11.79	24.23	26.88	40.86
Cool paints	0.3	16.71	38.22	42.46	53.74
	0.2	21.49	45.52	48.69	58.91
	0.1	31.05	57.84	60.42	65.31
Nocturnal natural ventilation + shading and overhang + cool paints (absorptance = 0.1)		34.03	62.63	66.5	69.12

thermal comfort limits model as reported for naturally ventilated classrooms by Mishra and Ramgopal (2015). From the Table 11.2 it can be seen that qualitatively the impact of the various measures is same for summer as well as whole year, though quantitatively there is a huge difference. From the table it can be seen that the cumulative effects of all the methods suggested increase the occupied comfort hours for summer months from 9.1 to 34.03%, whereas the total comfort hours for the same months the increase is from 21.32 to 62.63%. These values for whole year are 23.73–66.5% (occupied comfort hours) and 37.6–69.12% (total comfort hours).

11.4 Conclusions

Effects of several simple and easily implementable measures on thermal comfort aspects of naturally ventilated classrooms are obtained through building simulation using Energy Plus. Results show that cumulatively these measures increase the occupied comfort hours for summer months from 9.1% of the baseline to 34.03%. The greatest impact is provided by the use of highly reflective cool paints as the classroom has an exposed roof. Since the total comfort hours increase from 21.32 to 62.63%, shifting the classes entirely into cooler hours of the day may be most beneficial. Some of the other measures that can be considered are use of mechanical night ventilation, use of phase change materials and evaporative cooling of roof.

References

- de Carvalho PM, da Silva MG, Ramos JE (2013) Influence of weather and indoor climate on clothing of occupants in naturally ventilated school buildings. *Build Environ* 59:38–46
- EN 15251 Standard, “DS/EN 15251:2007: Indoor environmental input parameters for design and assessment of energy performance of buildings addressing indoor air quality, thermal environment, lighting and acoustics,” p. 54, 2007
- EnergyPlus Version 8.5, EnergyPlus Engineering Reference, US Department of Energy, Berkeley, 2015
- Givoni B (1991) Performance and applicability of passive and low-energy cooling systems. *Energy Build* 17:177–199
- Indraganti M, Ooka R, Rijal HB, Brager GS (2014) Adaptive model of thermal comfort for offices in hot and humid climates of India. *Build Environ* 74:39–53
- Mishra AK, Ramgopal M (2015) A thermal comfort field study of naturally ventilated classrooms in Kharagpur, India. *Build Environ* 92:396–406
- NBC, Bureau of Indian Standards 2005. In: Kisan M, Sangathan S, Nehru J, Pitroda SG (ed) *National Building Code of India 2005*. Bureau of Indian Standards, New Delhi
- Nematchoua MK, Tchinda R, Orosa JA (2014) Adaptation and comparative study of thermal comfort in naturally ventilated classrooms and buildings in the wet tropical zones. *Energy Build* 85:321–328
- Omrany H, Ghaffarianhoseini A, Ghaffarianhoseini A, Raahemifar K, Tookey J (2016) Application of passive wall systems for improving the energy efficiency in buildings: A comprehensive review. *Renew Sustain Energy Rev* 62:1252–1269

- Panchabikesan K, Vellaisamy K, Ramalingam V (2017) Passive cooling potential in buildings under various climatic conditions in India. *Renew Sustain Energy Rev* 78(May):1236–1252
- Pellegrino M, Simonetti M, Chiesa G (2016) Reducing thermal discomfort and energy consumption of Indian residential buildings: Model validation by in-field measurements and simulation of low-cost interventions. *Energy Build* 113:145–158
- Sadafi N, Salleh E, Haw LC, Jaafar Z (2011) Evaluating thermal effects of internal courtyard in a tropical terrace house by computational simulation. *Energy Build* 43(4):887–893
- Samani P, Leal V, Mendes A, Correia N (2016) Comparison of passive cooling techniques in improving thermal comfort of occupants of a pre-fabricated building. *Energy Build* 120:30–44
- Taulo J (2012) Energy conservation Building Code user guide. *Energy Policy* 6(8):56–78
- Toe DHC, Kubota T (2015) Comparative assessment of vernacular passive cooling techniques for improving indoor thermal comfort of modern terraced houses in hot-humid climate of Malaysia. *Sol Energy* 114:229–258
- Yao R, Liu J, Li B (2010) Occupants adaptive responses and perception of thermal environment in naturally conditioned university classrooms. *Appl Energy* 87(3):1015–1022
- Yeravdekar DVR, Tiwari G (2012) The higher education system in india and its impact on the economy. *SSRN Electron. J* pp 1–21

Chapter 12

Green Building Rating Systems and Energy Efficiency of a Building from the Building Lifecycle Perspective



Nina Lazar  and K. Chithra 

12.1 Introduction

The three basic needs of man include shelter along with food and clothing. Shelter refers to the structure or building which protects us from extreme climate, wild animals and also a place for rest. Initial versions of buildings/shelter were merely the natural environment like trees and caves. Down the timeline, the man started using natural materials to build shelters. Later materials like bricks, glass, and concrete are being used in building construction. Buildings were always an integral part of human history. However, the impacts of buildings on the economy, society, environment have significantly changed. The eighteenth and nineteenth century witnessed a significant transition due to the so-called industrial revolution. After this turning point, the impact of developmental activities increased tremendously and witnessed a growing concern towards the environment (Hossaini et al. 2015). In this context, the concept of sustainable buildings gained global importance. The World Green Building Council (WGBC) got instituted to promote sustainable construction practices. More than 70 Green Building Council (GBC) exist under the broad umbrella of WGBC (Home World Green Building Council 2017). For assessing the sustainability level of buildings different GBC's has developed different Green Building Rating Systems (GBRS). GBRS covers different domains of sustainability, like Energy Efficiency, Water Efficiency, Sustainable Materials, Indoor Environmental Quality, and Sustainable Sites.

Statistics show that buildings consume 30–40% of the total global energy use and 30% of global carbon dioxide emissions. In this context, it is very much relevant to find out the scope for reducing the energy consumption in buildings, and

N. Lazar (✉) · K. Chithra
Department of Architecture & Planning, NIT Calicut, Kozhikode, Kerala, India
e-mail: nina_p170032ar@nitc.ac.in

K. Chithra
e-mail: chithrak@nitc.ac.in

it is achieved by carefully analysing the whole lifecycle of a building. The GBRS is an essential tool to assess and to reduce energy consumption in buildings. The current study aims to investigate the weight given for various phases of the building lifecycle by analysing different GBRS. The general framework of the existing GBRS is investigated. The study outcome would be extremely beneficial while refining and developing the GBRS towards achieving sustainability. The effectiveness of GBRS has a vital role to play towards achieving the goals of sustainability (Lazar and Chithra 2019).

12.2 Research Methodology

The current study starts with the review of existing GBRS followed by the selection of GBRS for the study. The criteria and mandatory requirements of the GBRS selected were thoroughly reviewed. The weight for each stage of building lifecycle was found out by analysing the benefits of each criterion and mandatory requirement towards each stage of the building lifecycle. The study outcome would be useful for developing GBRS and also for enhancing and modifying the existing GBRS towards attaining sustainability. The research methodology followed in the current study is illustrated (Fig. 12.1).

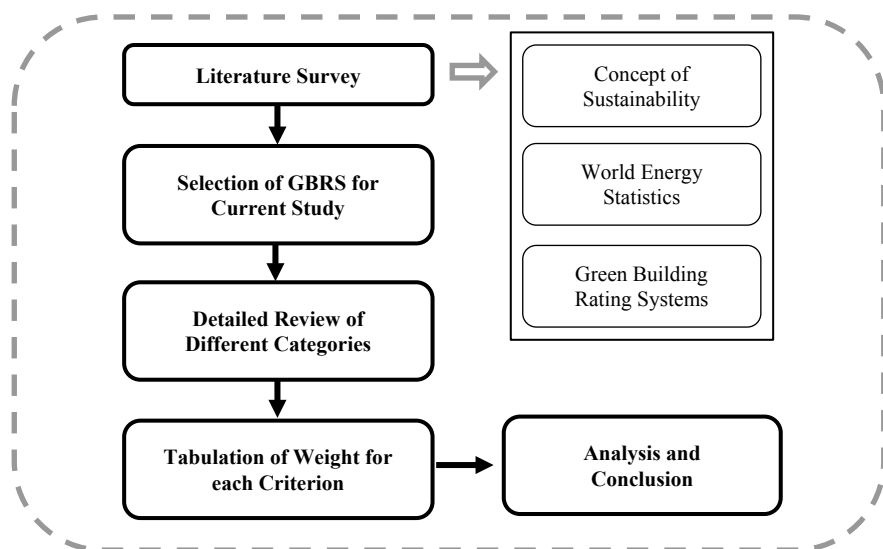


Fig. 12.1 Research methodology

12.3 Literature Survey

12.3.1 Energy Statistics

Buildings consume 30–40% of the total global energy use (WBCSD 2018). As per the report of the Intergovernmental Panel on Climate Change, 40% of global energy is consumed by the building sector. Sector-wise electricity consumption of various countries (Fig. 12.2) also indicates high electricity consumption by the building sector (residential and commercial). By adapting, integrating, and expanding sustainable and energy efficient concepts to buildings, the potential to reduce energy use is tremendous.

As per the data in 2014, India is the fourth largest electricity consumer in the world following China, the United States, and the European Union (CEA 1947). Almost 33–34% of India’s electricity is consumed by the building sector (Fig. 12.3). The growth of electricity consumption in India is shown (Fig. 12.4).

59% of Kerala’s electricity is consumed by the building sector (residential and commercial (Fig. 12.5)) (KSEB 2017). Electricity consumption in Kerala follows an increasing trend. The projections for the next 10 years show that there will be a 54% increase in electricity consumption of Kerala (Fig. 12.6) (KSEB 2017; Kerala ENVIS Centre 2019).

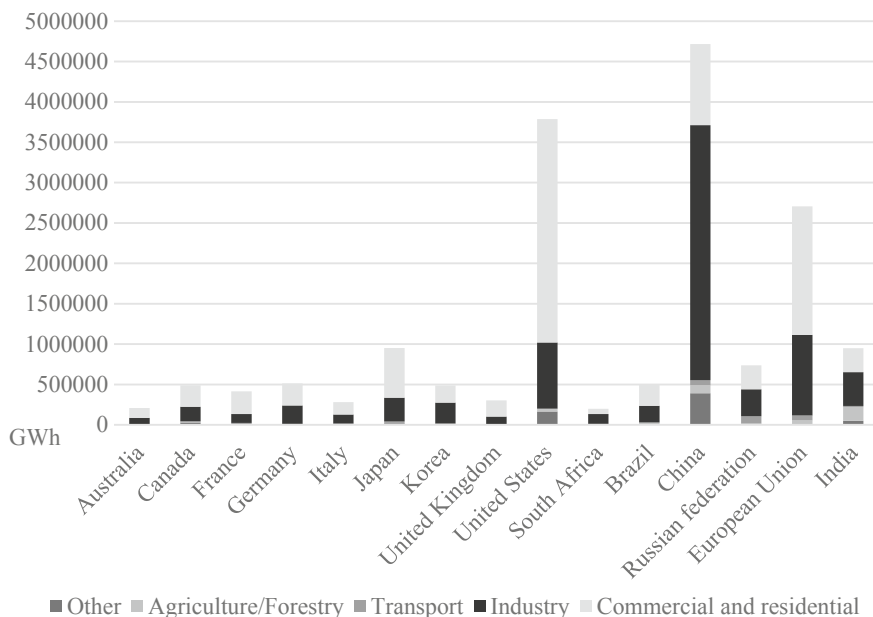


Fig. 12.2 Sector-wise electricity consumption in various countries (Data Source International Energy Agency)

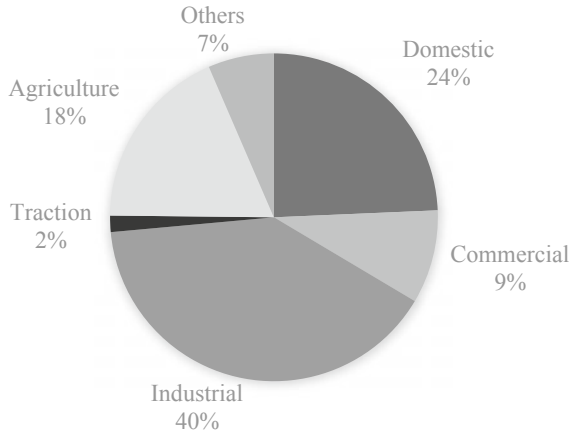


Fig. 12.3 Sector-wise consumption of electricity in India 2017 (Data Source Growth of electricity sector in India 1947–2017, CEA, Govt. of India, 2017)

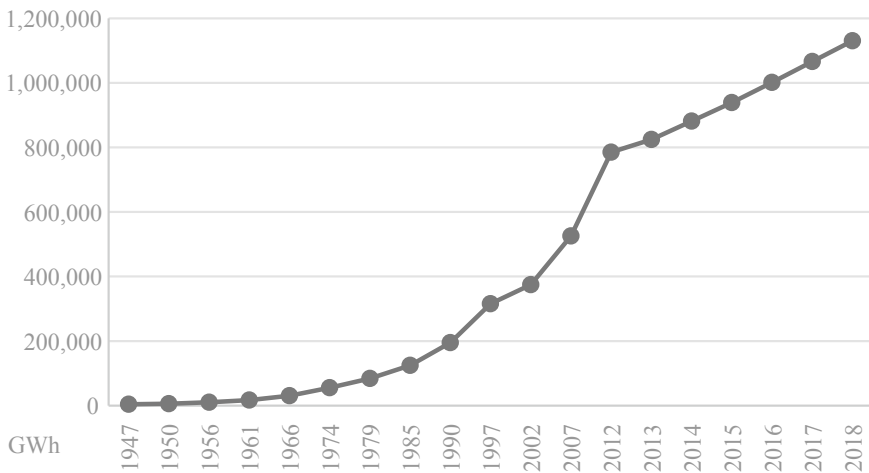


Fig. 12.4 Year wise electricity consumption in India (Data Source Growth of electricity consumption in India 1947–2017, CEA, Govt. of India, 2017)

As per Mckinsey Report published in 2010, 70–80% of India in 2030 is yet to build, i.e., between 700 and 900 million square metres of residential and commercial space will be built each year until 2030 (Sankhe 2010). According to Census of India 2011, 31.5% of the total Indian population, lives in urban areas and will rise to 50% by 2030. The projections indicate that we are rapidly moving towards the worst scenario unless otherwise sufficient measures are taken. A revolution in the architectural field is very

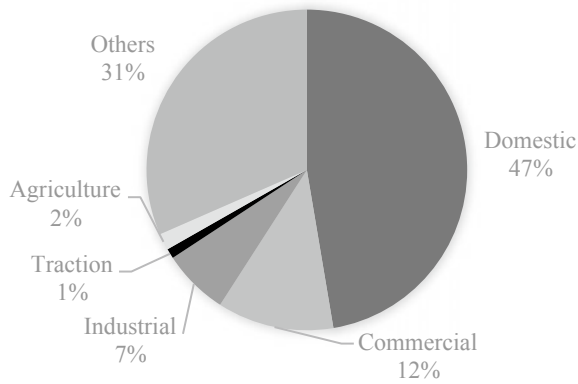


Fig. 12.5 Sector-wise consumption of electricity in Kerala 2017 (Data Source Power System Statistics, 2016–17, KSEB)

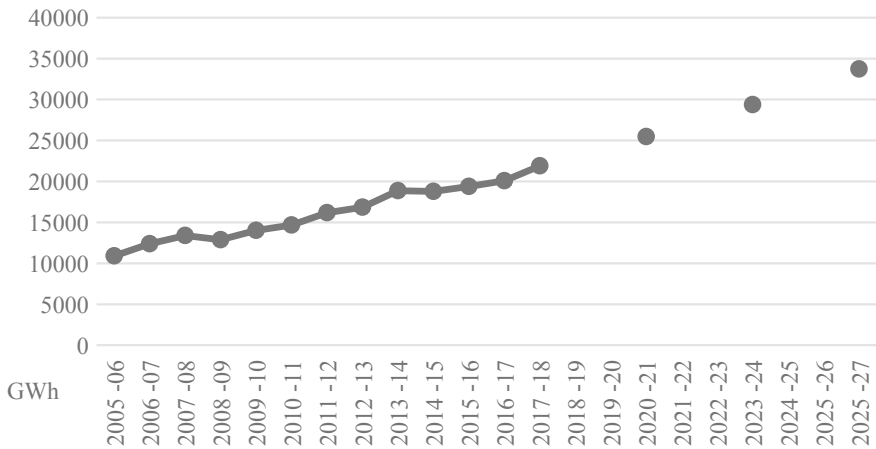


Fig. 12.6 Year wise electricity consumption in Kerala (Data Source Power System Statistics, 2016–17, KSEB; ENVIS Centre: Kerala)

much necessary. Sustainable development and quantification of the energy impact of buildings attain greater importance all over the world and much more in case of developing countries.

12.3.2 Sustainability and Building Sustainability

After the industrial revolution, sustainability has attained much popularity. During recent years, the term sustainability has been given a new purpose and meaning.

The most common definition for sustainable development is provided by the Brundtland Report (WCED 1987). The definition given by the Brundtland Report is also in accordance with the concept put forward by the reports of the International Union for Conservation of Nature (IUCN) (IUCN et al. 1980, 1991). The definition of sustainable development is still in the evolution stage. The efforts made in building sector towards sustainable development led to the concept of sustainable buildings (Kang 2015). According to WGBC, minimising environmental impacts and maximising social and economic value over a building's whole lifecycle, i.e., from design, construction, operation, and maintenance, through to renovation and eventual demolition makes a building sustainable and energy efficient.

12.3.3 Existing Rating Systems for Buildings

To recognise buildings that meet sustainable requirements, GBRS have been put forward by various GBCs under WGBC. The first and foremost GBRS was the Environmental Assessment Method developed by Building Research Establishments (BRE), widely known as BREEAM. BREEAM was established in the year 1990 in the United Kingdom and has been implemented in 78 countries around the world (BREEAM 2017). BREEAM Technical Manual, SD233 2.0, 2016, was considered for the current study (BRE Global 2017). The GBRS, which is second in line, is the Leadership in Energy and Environmental Design (LEED). LEED is the most recognised rating system at the global level and got implemented in 170 countries approximately (LEED 2017). LEED was developed in the year 1998 in the United States. LEED Version 4 was considered for the study (USGBC 2016).

The Green Rating for Integrated Habitat Assessment (GRIHA) and the Indian Green Building Council (IGBC) Rating System are the two GBRS that exist in India. IGBC got established in the year 2001, as a part of the Confederation of Indian Industry (CII) (Indian Green Building Council and Accessed 22 October 2017). New Buildings Version 3.0 of IGBC was also considered for the current study. GRIHA was developed by The Energy and Resources Institute (TERI). GRIHA was adopted by the Government of India in 2007 as the national rating system for green buildings (GRIHA 2017). GRIHA Version 2015 was also considered for the study (GRIHA Council 2016). For the current study, the IGBC rating system and GRIHA were considered along with LEED and BREEAM, the most widely studied GBRS (Li et al. 2017).

Each of the rating systems consists of mandatory requirements and criteria under different categories. A building needs to satisfy all the mandatory requirements to get qualified to go to the certification. If all of the mandatory requirements are not satisfied the building is not eligible for certification. Satisfying each of the criteria the building is assigned to get scores or credits, the total score achieved by the building determines the certification level of the building.

12.3.4 Energy Efficiency and Green Building Rating Systems

All four rating systems developed has given due importance to energy efficiency. The weight given for Energy Efficiency category by the four selected rating systems is shown (See Figs. 12.7, 12.8, 12.9 and 12.10). Energy Efficiency category is the dominant category in all the four rating systems with 26% weight in LEED (Fig. 12.7), 22% weight in BREEAM (Fig. 12.8), 28% in IGBC (Fig. 12.9) and 20% in GRIHA (Fig. 12.10). However, all the domains address or try to reduce energy consumption directly or indirectly.

Material category tries to reduce energy consumption by reducing the embodied energy of materials and transportation energy. Sustainable Sites category tries to reduce energy by selecting a site near basic amenities, thereby reducing the amount of fuel used. Indoor Environmental Quality category tries to provide as much as daylight and comfort to the occupants, thereby reducing the electricity consumption

Fig. 12.7 Category-wise weight in LEED

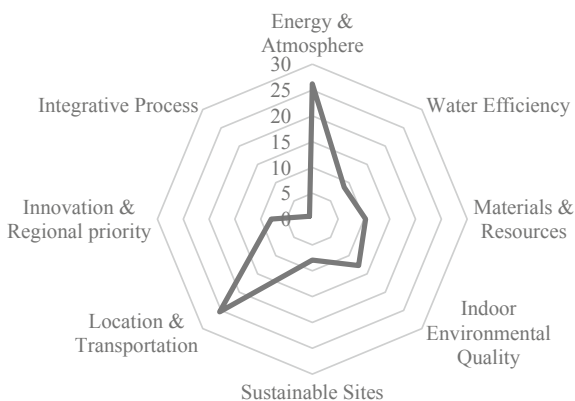
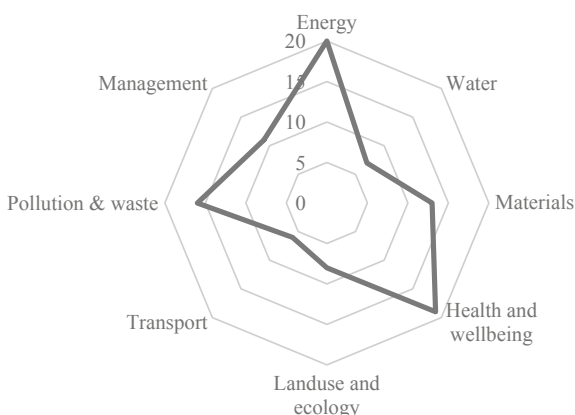


Fig. 12.8 Category-wise weight in BREEAM



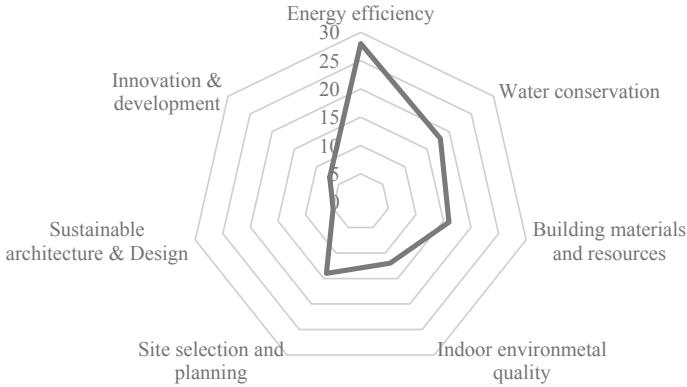


Fig. 12.9 Category-wise weight in IGBC

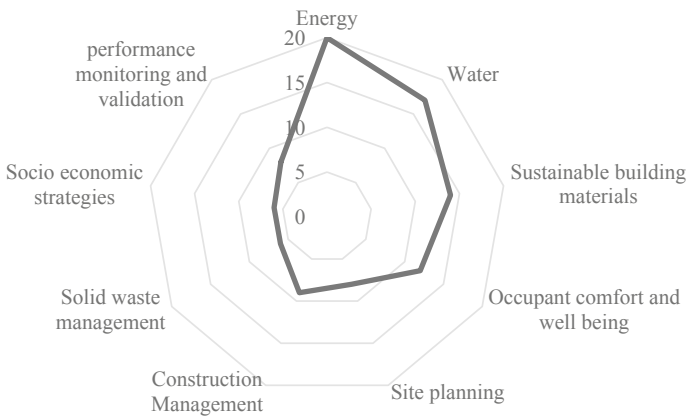


Fig. 12.10 Category-wise weight in GRIHA

on artificial lights and other mechanical systems for comfort. Water Efficiency category aims to reduce water consumption, thereby indirectly saving on electricity consumption.

12.4 Tabulation of Weight for Building Lifecycle Stages

Each mandatory requirement and criterion were analysed in detail to arrive at the weight for each stage of the building lifecycle. The following assumptions were considered in the process. In case a single lifecycle stage is benefited by implementing a mandatory requirement and criterion, 100% weight is allotted for that

specific stage. If two stages are benefited, 50% weight is allocated for the two stages. If three stages are benefited, 33.33% weight is assigned for those three stages, and so on. The results were tabulated, and further analysis was done by preparing 100% stacked bar charts.

12.4.1 Mandatory Requirements

The weight for all the stages was tabulated against each mandatory requirement and calculated the total weight for each lifecycle stage against each category for all the selected GBRS. For easy comparison, the weight was then converted to percentage. Further, 100% stacked bar chart was prepared to compare different categories of each rating system (Figs. 12.11, 12.12, 12.13 and 12.14).

The total weight given for each lifecycle stage by the mandatory requirements of the selected GBRS was plotted and compared (Fig. 12.15). Mandatory requirements have given more weight to building operation stage. Construction stage has also given importance. However, production, transportation, and demolition stages are the least considered.

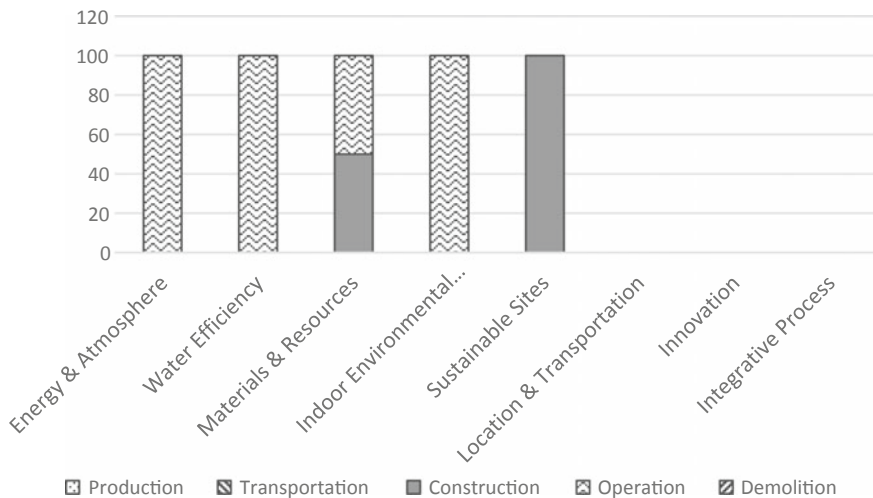


Fig. 12.11 Bar chart showing category wise weight for building lifecycle stages for LEED mandatory requirements

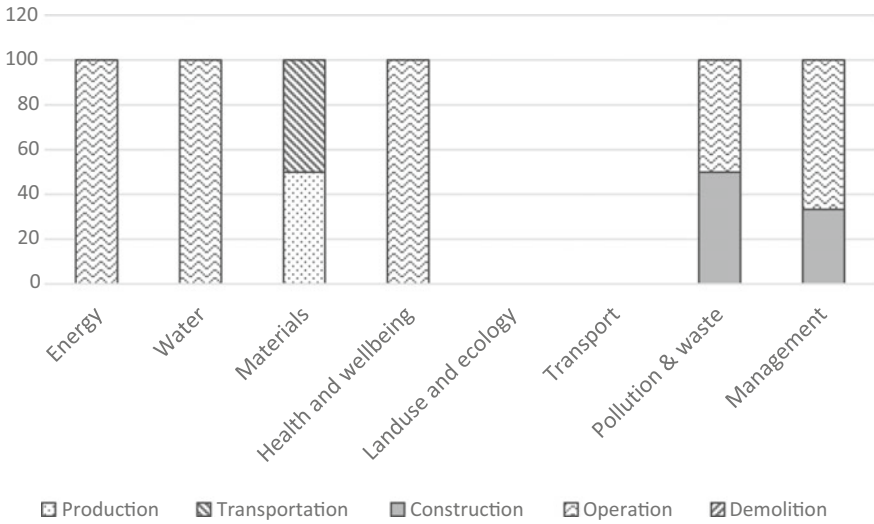


Fig. 12.12 Bar chart showing category wise weight for building lifecycle stages for BREEAM mandatory requirements

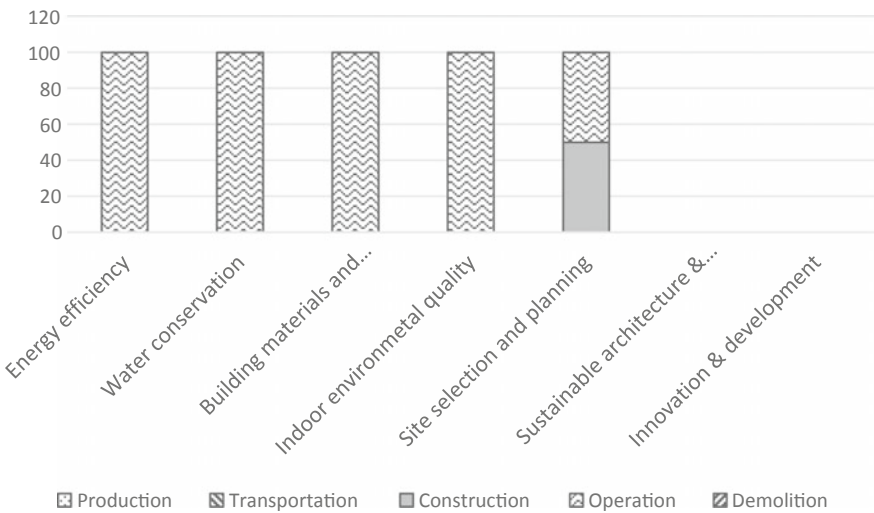


Fig. 12.13 Bar chart showing category wise weight for building lifecycle stages for IGBC mandatory requirements

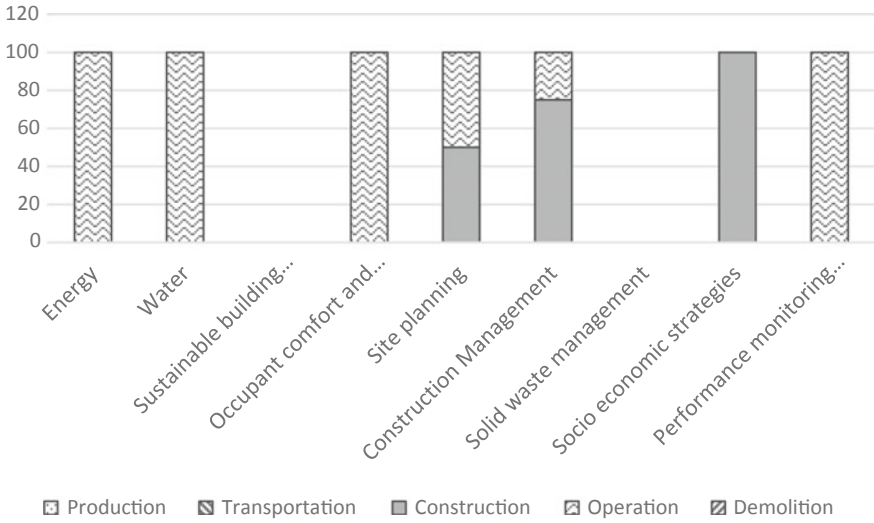


Fig. 12.14 Bar chart showing category wise weight for building lifecycle stages for GRIHA mandatory requirements

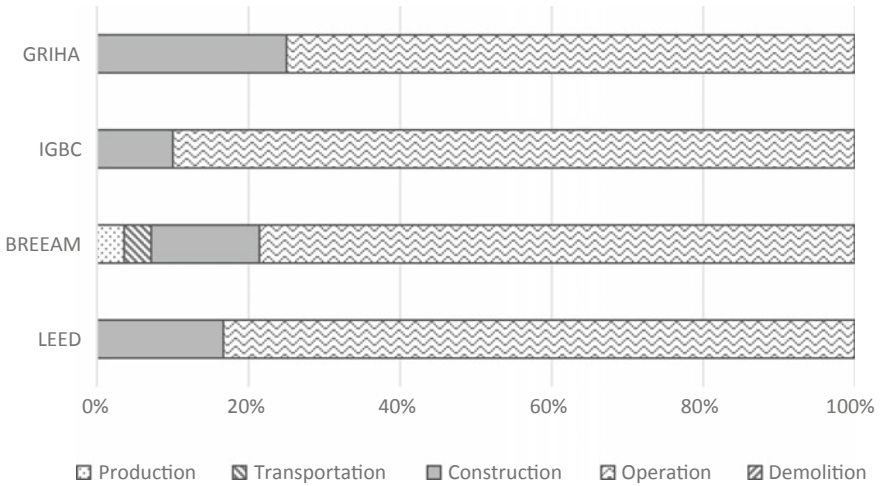


Fig. 12.15 Bar chart showing weight for building lifecycle stages for mandatory requirements of selected rating systems

12.4.2 Criteria

The weight allotted for all the stages were tabulated against each criterion. The weight is multiplied by the corresponding credit points of each criterion and the total scores for each lifecycle stages against each category is calculated for all the selected GBRS. For easy comparison, the total scores were converted to a percentage. Further, 100% stacked bar chart was prepared to compare different categories of each rating system (Figs. 12.16, 12.17, 12.18 and 12.19).

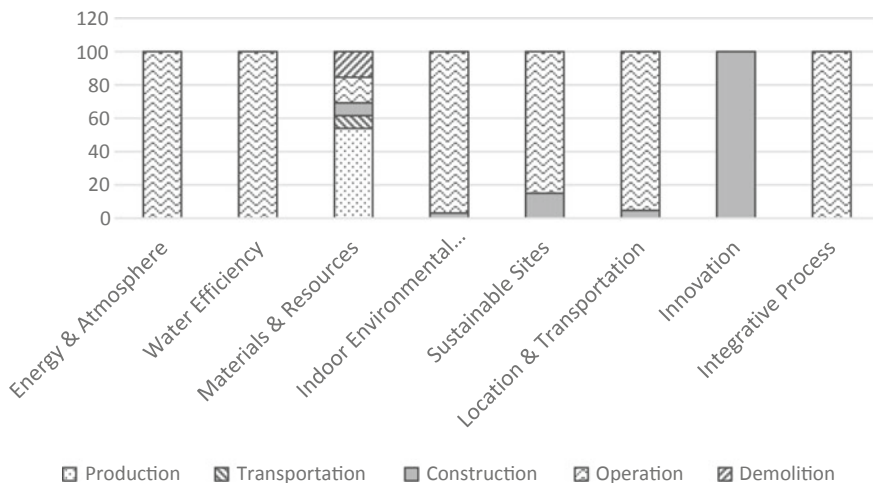


Fig. 12.16 Bar chart showing category wise weight for building lifecycle stages for LEED criteria

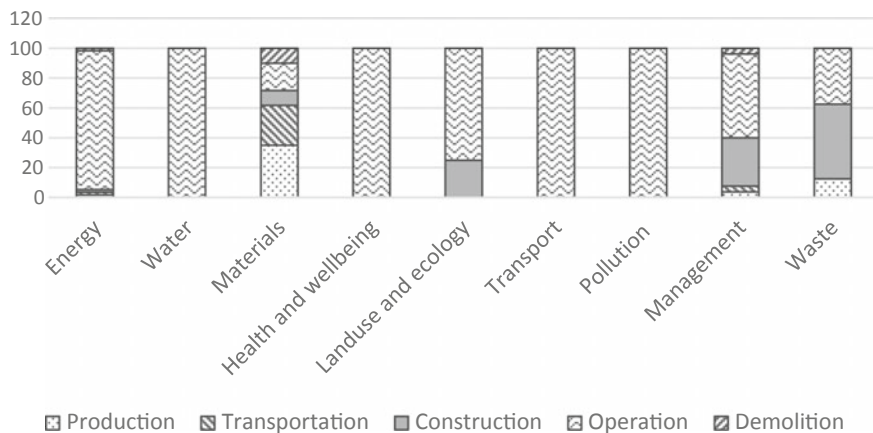


Fig. 12.17 Bar chart showing category wise weight for building lifecycle stages for BREEAM criteria

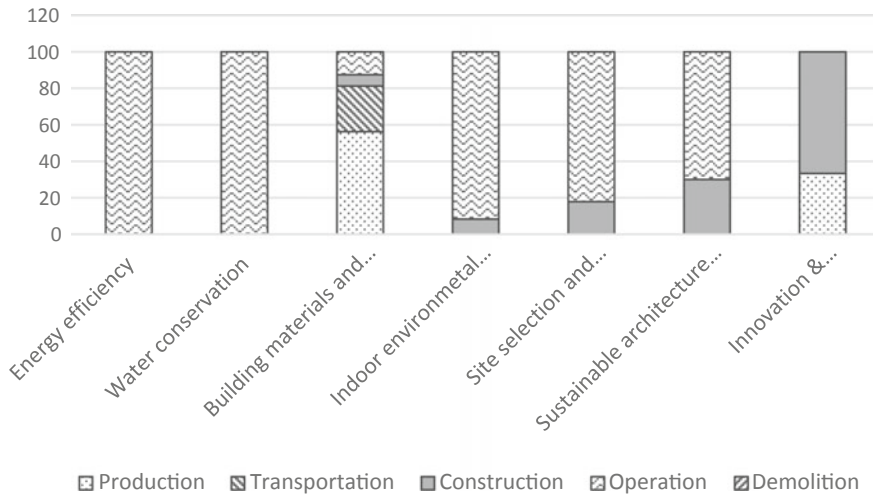


Fig. 12.18 Bar chart showing category wise weight for building lifecycle stages for IGBC criteria

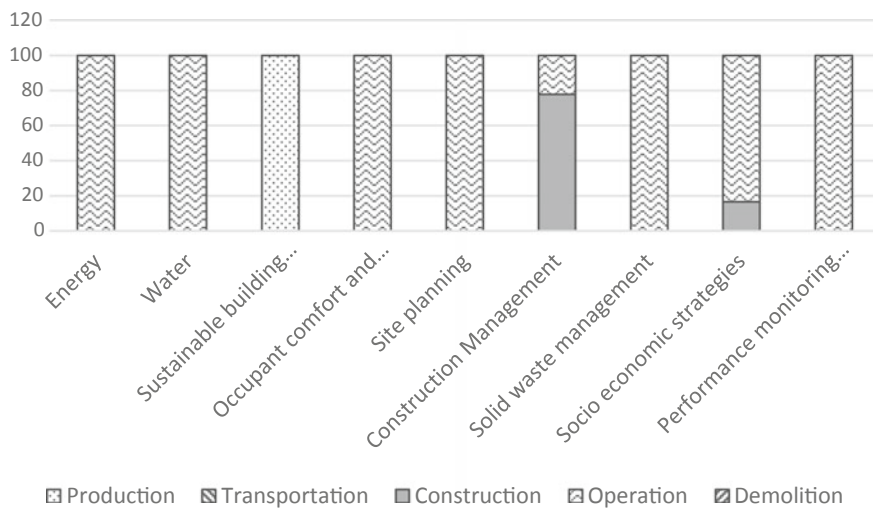


Fig. 12.19 Bar chart showing category wise weight for building lifecycle stages for GRIHA criteria

The total weight given for each lifecycle stage by the criteria of the selected GBRS was plotted and compared (Fig. 12.20). Criteria of the selected GBRS have given more importance to building operation stage. Construction stage and production stage has also given importance. However, transportation and demolition stages are the least considered.

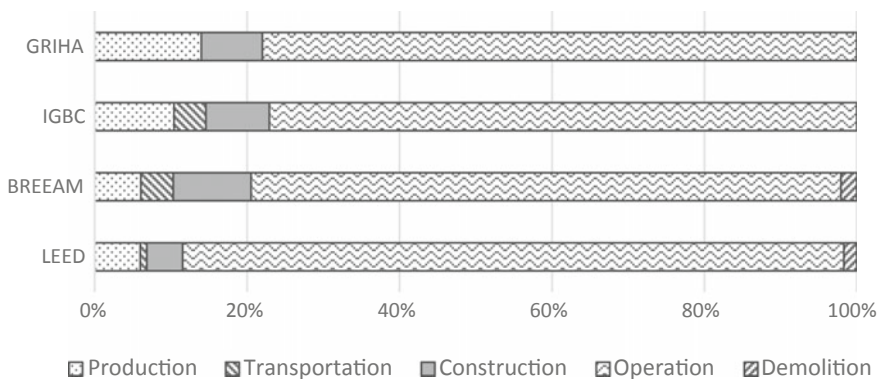


Fig. 12.20 Bar chart showing weight for building lifecycle stages for the criteria of selected rating systems

12.5 Analysis and Discussion

12.5.1 Mandatory Requirements—Weight for Building Lifecycle Stages

The LEED categories, ‘Location and Transportation,’ and ‘Innovation and Integrative Process’ does not have any mandatory requirement. A building is eligible for LEED Certification even if the building satisfies none of the criteria in the Location and Transportation category. Energy and Atmosphere category, Water Efficiency category, and the Indoor Environmental Quality category have given 100% weight to the operation stage. Sustainable Sites category has given 100% weight to the construction stage. Materials and Resources category have given 50% weight to both construction and operation stage. Mandatory requirements of LEED have given more weight to the operation stage followed by construction stage. Production, Transportation, and Demolition stages are least considered by the mandatory requirements of the LEED rating system.

The BREEAM categories, ‘Transport,’ and ‘Land use and Ecology’ does not have any mandatory requirement. It means that a building is still eligible for BREEAM Certification even if the building satisfies none of the criteria in Land use and Ecology category and Transport category. Energy category, Water category and Health and Wellbeing category have given 100% weight to the operation stage. Pollution and Waste category have given 50% weight to both construction and operation stage. Management category has given 33% weight to the construction stage and 67% weight to the operation stage. Materials category has given 50% weight to the production stage and 50% weight to the transportation stage. Mandatory requirements of BREEAM rating system have provided more weight to

the operation stage followed by construction stage, production stage, and transportation stage. Demolition stage is considered by the mandatory requirements of the BREEAM rating system.

The IGBC categories, ‘Innovation and Development,’ and ‘Sustainable Architecture and Design’ does not have any mandatory requirement. A building is eligible for IGBC Certification even if the building satisfies none of the criteria in the Sustainable Architecture and Design category. Energy Efficiency category, Water Conservation category, Indoor Environmental Quality category, and Building Material and Resources category has given 100% weight to operation stage. Site Selection and Planning category has given 50% weight to both construction and operations stage. Mandatory requirements of IGBC rating system have given more weight to the operation stage followed by construction stage. Production, transportation, and demolition stages are least considered by the mandatory requirements of the IGBC rating system.

The GRIHA categories ‘Solid Waste Management’ and ‘Sustainable Building Materials’ does not have any mandatory requirement. A building is eligible for GRIHA Certification even if the building satisfies none of the criteria in the Solid Waste Management category and Sustainable Building Materials category. Energy category, Water category, Occupant Comfort and Wellbeing category and Performance Monitoring and Validation category have given 100% weight to operation stage. Socio-economic Strategies have given 100% weight to the construction stage. Site Planning category has given 50% weight to the construction stage and 50% weight to the operation stage. Construction management category has given 75% weight to the construction stage and 25% weight to the operation stage. Mandatory requirements of GRIHA have given more weight to the operation stage followed by construction stage. Production, transportation, and demolition stages are least considered by the mandatory requirements of the GRIHA rating system.

12.5.2 Criteria—Weight for Building Lifecycle Stages

In LEED rating system Energy and Atmosphere category, Water Efficiency category, and Integrative Process category has given 100% weight to operation stage. Sustainable Sites category has given 100% weight to the construction stage. Indoor Environmental Quality category, Sustainable Sites category and Location and Transportation category has given weight to both construction and operation stage with marginal weight to the construction stage. Materials and Resources category has given weight to all the building lifecycle stages with marginal weight to transportation, construction, operation, and demolition stages. Criteria of LEED rating system have given more weight to the operation stage followed by production and construction stage. Transportation and demolition stages are least considered by the criteria of the LEED rating system.

In the BREEAM rating system Transport category, Water category and Pollution category has given 100% weight to the operation stage. Energy category has given weight to all the building lifecycle stages with more weight to the operation stage and very marginal weight to other stages. Materials category and Management category has given weight to all the building lifecycle stages. Land use and Ecology category has given weight to both construction and operation stages. The Waste category has given weight to production, construction, and operation stages. Criteria of the BREEAM rating system have given more weight to the operation stage followed by construction stage, production stage transportation stage, and demolition stage.

In the IGBC rating system, Energy Efficiency category and Water Conservation category has given 100% weight to the operation stage. Materials category has given weight to all the building lifecycle stages. Indoor Environmental Quality category, Site Selection and Planning category, and Sustainable Architecture and Design category have given weight to both construction and operation stages. Mandatory requirements of IGBC rating system have provided more weight to the operation stage followed by production, construction, and transportation stages. Demolition stage is least considered by the criteria of the IGBC rating system.

In the GRIHA rating system Energy category, Water category, Occupant Comfort and Wellbeing category, Site Planning category, Solid waste management category, and Performance Monitoring and Validation category have given 100% weight to operation stage. Sustainable Building Materials have given 100% weight to the production stage. Socio-economic Strategies and Construction Management categories have given weight to both operation and construction stages. Mandatory requirements of GRIHA have given more weight to the operation stage followed by production and construction stage. Transportation and demolition stages are least considered by the criteria of the GRIHA rating system.

12.6 Conclusion

In all the rating system except the GRIHA rating system, Materials category has given weight to all the lifecycle stages. Energy, Water, and Indoor Environmental Quality category in all the rating system has given more weight to the operation stage. In all the rating system except GRIHA, Site Planning category has given weight to both operation and construction stage. Considering the overall framework, LEED, BREEAM, and IGBC follow a similar structure than GRIHA. This may be because LEED and BREEAM is an international rating system, and IGBC is also an Indian version of LEED. Therefore, three of them follow a similar structure. The GRIHA rating system is the national rating system of India and follows a different structure.

The study investigates the weight considered for building lifecycle stages by comparatively analysing various GBRS. The outcome of this research shows that GBRS have given more weight to the operation stage. All other stages are least

considered from the viewpoint of the building lifecycle. The reason could be the extended operating period and higher operation and maintenance costs (Kang 2015). Even though all other stages are short term in duration, their impact is considerable in comparison with operation stage. The building stakeholders shall be exposed to the realities of building lifecycle energy and corresponding costs and its implications towards sustainable development. Minimisation of the use of low embodied energy resources to be ensured, so that the buildings are low impact (Home World Green Building Council 2017). The study was limited to four GBRS. However, the outcome of the study is substantial to conclude that more importance shall be given to production, transportation, construction and demolition stages while moving towards sustainability. The outcome of research indicates the need for considering all the lifecycle stages for achieving sustainability.

References

- Administrative profile: Health—status of environment related issues—Kerala ENVIS Centre, Ministry of Environment and Forests (2019)
- BREEAM, <http://www.breeam.com/>. Accessed 22 October 2017
- BRE Global Limited (2017) BREEAM international new construction 2016. Technical Manual SD233 2.0. United Kingdom
- CEA, Ministry of Power, Govt of India: growth of electricity sector in India from 1947–2017. New Delhi (2017)
- Green Buildings Rating System India: GRIHA Home, <http://grihaindia.org/>. Accessed 22 October 2017
- GRIHA Council (2016) The energy and resources institute: GRIHA V-2015
- Home World Green Building Council, <http://www.worldgbc.org/>. Accessed 26 July 2017
- Hossaini N, Hewage K, Sadiq R (2015) Spatial life cycle sustainability assessment: a conceptual framework for net-zero buildings. *Clean Technol Environ Policy* 17(8):2243–2253
- Indian Green Building Council, <https://igbc.in/igbc/>. Accessed 22 October 2017
- IUCN, UNEP, WWF (1980) World conservation strategy. Living resource conservation for sustainable development. Gland, Switzerland
- IUCN, UNEP, WWF (1991) Caring for the earth. A strategy for sustainable living. Gland, Switzerland
- Kang HJ (2015) Development of a systematic model for an assessment tool for sustainable buildings based on a structural framework. *Energy Build* 104:287–301
- KSEB: Power System Statistics (2017)
- Lazar N, Chithra K (2019) Green building rating systems from the perspective of the three pillars of sustainability using point allocation method. In: Drück H, Pillai R, Tharian M, Majeed A (eds) *Green buildings and sustainable engineering*. Springer Transactions in Civil and Environmental Engineering. Springer, Singapore. https://doi.org/10.1007/978-981-13-1202-1_14
- LEED, <https://new.usgbc.org/leed>. Accessed 22 October 2017
- Li Y, Chen X, Wang X, Xu Y, Chen P-H (2017) A review of studies on green building assessment methods by comparative analysis. *Energy Build* 146:152–159
- Sanke S et al (2010) India's urban awakening : building inclusive cities, sustaining economic growth. McKinsey Q
- USGBC (2016) LEED v 4 for building design and construction

- WBCSD (World business Council for Sustainable Development): Driving city-scale action for energy efficiency in buildings: outcome report of the Energy Efficiency in Buildings (EEB 2.0) project, Geneva, Switzerland (2018)
- WCED (1987) Our common future: report of the World Commission on Environment and Development

Chapter 13

Recent Trends in Use of Phase Change Materials for Sustainable Thermal Management of Buildings: A Review



Rohini Sibi, Rajesh Baby and Bennet Kuriakose

13.1 Introduction

Owing to the necessity for conservation of energy, developing energy-efficient systems has gained crucial importance. Nowadays, construction industry is reckoned to be contributing to worlds 40% of energy consumption (Fig. 13.1). Development of energy-efficient buildings and thereby reducing the carbon footprint is thus of crucial importance. The HVAC systems are proven to be contributing a great extend to the energy consumption of buildings. Thus, the saving in energy consumption in buildings had become a major solution for global energy problems (Lukić et al. 2012).

Incorporation of thermal energy storage into buildings is not only an effective method of minimising energy consumption but also a method to reduce the mismatch between energy supplied and energy demand. The biggest share of the energy consumption of a building is utilised to maintain a comfortable internal temperature. The internal temperature varies with solar radiation, which heats the building at day time and terrestrial radiation cools it at night. In hot climate, the best way for energy efficiency is to store solar radiation in the building shell and discharges it overnight. One of the possible methods to achieve this is the use of Phase Change Material (PCMs), which accumulates the latent heat in phase change. The usage of PCMs in buildings helps to maintain the temperature into a constant

R. Sibi (✉)

Student, St. Joseph's College of Engineering and Technology, Palai, Kerala, India
e-mail: rohini.sibi.2013@gmail.com

R. Baby

Associate Professor, Department of Mechanical Engineering, St. Joseph's College of Engineering and Technology, Palai, Kerala, India

B. Kuriakose

Associate Professor, Department of Civil Engineering, St. Joseph's College of Engineering and Technology, Palai, Kerala, India

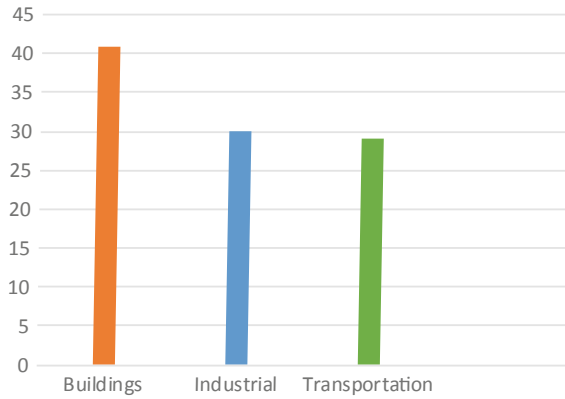


Fig. 13.1 Apportioning of energy consumption by various sectors (Lukić et al. 2012)

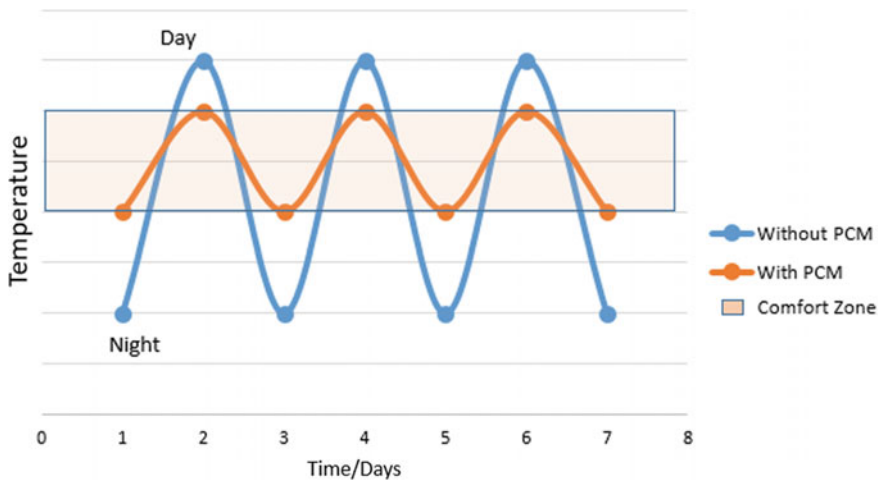


Fig. 13.2 Use of PCMs in buildings: temperature is fixed to a range by passive cooling method (Lukić et al. 2012)

comfort zone of humans (Fig. 13.2). PCMs can be incorporated in buildings in many ways, viz., direct mixing, immersion, impregnation, and microencapsulation. PCMs can be applied on walls, ceilings, floors and roofs according to the requirements.

This paper presents the trends in the usage of PCMs for efficient thermal management of buildings especially situated in regions of the tropical climate. The experimental, as well as numerical studies on PCMs incorporated in buildings, are presented. From the previous studies it is concluded that usage of PCMs is a cost-effective method for improving thermal efficiency of buildings.

13.2 Experimental Studies on Buildings with PCMs

Various researchers carried out experimental studies on buildings incorporated with PCMs (Pasupathy and Velraj 2008; Nazi et al. 2017; Mettawee and Ead 2013; Biswas and Abhari 2014; Zhong et al. 2015). These researches performed detailed studies on the temperature variations in buildings using PCMs. Different types of PCMs were used at different locations of experimental buildings, the summary of which is presented in Table 13.1.

Pasupathy and Velraj (2008) conducted an experimental study on two identical experimental rooms of size 1.22 m × 1.22 m × 2.44 m, one with PCM and another without. PCM was embedded on the roof of one room between the rooftop slab and bottom concrete slab. Plywood panels of thickness 6 mm were used for insulating the walls. Inorganic salt hydrate (48% CaCl₂ + 4.3% NaCl + 0.4% KCl + 47.3% H₂O) was used as the PCM which was made as a panel of thickness 2.54 cm. The mixture was stored in a closed stainless steel metallic containers of capacity 0.1 m³. The PCM mixture was prepared by mixing the salts in the required proportion in water. Resistance Temperature Detectors (Type PT100) were used at different depths in the panel. The temperature variation was measured at every 1 h interval. The experiment was conducted during the months of January and February. The results from this study showed that environment has very little effects on the inner surface of the concrete slab as the heat energy is absorbed by the PCM panel in the roof.

Nazi et al. (2017) performed a detailed study on the passive cooling of PCM in a high rise building situated in Putrajaya, Malasia, with a tropical climate. Two air-conditioned (AC) rooms were considered, the former is an office room in which the AC system is maintained during office hours, whereas, the latter is a server room air-conditioned for 24 h of the day. In this study, Bio PCM blanket M182/Q29 was used with a melting temperature of 29 °C. The results showed that the office room incorporated with PCM yielded better thermal efficiency than the server room. It was noted that, night-time ventilation was required for the effectiveness of PCM.

Table 13.1 Studies on the tropical region

Author(s)	PCM location	PCM name	PCM type	Location
Pasupathy and Velraj (2008)	Roof	Salt hydrate	Inorganic	Chennai, India
Nazi et al. (2017)	Walls and roof	Bio PCM blanket	Organic	Putrajaya, Malasia
Mettawee and Ead (2013)	Ceiling	Coconut fatty acid	Organic	Cairo, Egypt
Biswas and Abhari (2014)	Walls	Paraffin	Organic	South Carolina, US
Zhong et al. (2015)	Glass window	Paraffin	Organic	China

The study by Metawee and Ead (2013) explained the usage of cost-effective PCM using organic coconut fatty acid, which can be employed in tropical climate. An experimental chamber was constructed and the PCMs were encapsulated in cans and was placed on the ceiling of the chamber. The study was conducted to determine the characteristics of PCM in three ways, viz., time of phase change, characteristics of heat transfer when contact with ambient air and characteristics of heat transfer with forced convection. Thermocouples used for measuring the temperature were placed on top and bottom surfaces of PCM location. The results from the study showed that the utilisation of PCM with high thermal conductivity needs to consider the thickness of the container. The time of phase change took a long time for natural convection and for the forced convection the PCM container surface was able to decrease the temperature by 1.29 °C.

Biswas and Abhari (2014) conducted experimental and numerical investigations of buildings incorporated paraffin wax was used as PCM and was applied on the walls of a building. Some parts of the building envelope containing PCM was exposed to the environment for the air circulation from outside and allowed for the natural weathering. The temperature sensors and some other instruments placed in the building measured the conditions of temperature, weather conditions, humidity, wind velocity and solar irradiance. The exterior wall with PCM layer inside had better performance at a lower cost than the wall with PCM in cavities.

Zhong et al. (2015) performed a simulation study on the dynamic heat transfer of the PCM filled glass window. The different thermophysical properties of Paraffin MG29 PCM were investigated and was applied on different windows on sunny and rainy days. It was found that the thermal performance can be improved by the temperature difference between the liquid and solid phases.

13.3 Numerical Studies on Buildings

In this section, the numerical studies performed by various researchers on buildings incorporated with PCMs are reviewed. The summary of the reviewed works is presented in Table 13.2.

Table 13.2 Numerical studies of PCM in the tropical region

Author(s)	PCM location	PCM name	PCM type	Method used
Alwadhi (2012)	Window shutter	n-Octadecane, n-Eicosane, Paraffin	Organic	Finite difference method
Yahay and Ahmad (2011)	Ceiling	Lauric-stearic acid	Eutectic	Finite difference method
Alawadhi and Alqallaf (2011)	Roof	n-Eicosane	Organic	Finite element method
Ciulla et al. (2013)	Multiwall structure			Fourier differential equation

Alwadhi (2012) conducted a numerical study on the usage of n-Octadecane, n-Eicosane, and paraffin as PCMs in buildings using Finite Difference Method (FDM). The results showed that PCM on window shutters had a capacity to reduce the heat gain through the window by about 23%. The melting point of the PCM used should be close to the upper temperature limit of the window.

The FDM study by Yahay and Ahmad (2011) were on the PCM impregnated in gypsum boards which were used as ceiling. The PCM selected for the analysis was eutectic mixture of lauric-stearic acid and was immersed in the gypsum boards. The ceiling components were able to reduce the peak indoor temperature by 2 °C. The study concluded that PCMs can improve thermal performance and energy savings, especially in single storey buildings.

Alawadhi and Alqallaf (2011) studied the reduction in cooling load in building with a roof incorporated with PCM using Finite Element Method (FEM). The objective was to utilise the latent heat of fusion to reduce the heat gained during the peak hours. The PCM used in this study was n-Eicosane. The results showed that the heat change at the indoor surface of the roof was reduced up to 39% for the selected PCM.

Ciulla et al. (2013) developed a numerical solution for finding the temperature inside PCMs in buildings. The numerical algorithm was based on Fourier Differential Equations (FDE). This method was based on the spatial and temporal derivatives of the heat diffusion equation in relation to space and time. This helped to solve heat transfer problems in different multiwall structures like sandwich panels incorporated with PCMs.

13.4 Concluding Remarks

A review on experimental and numerical studies regarding the usage of PCMs in buildings situated in tropical climatic region is carried out in this paper. The previous studies showed that the usage of PCM one of the best alternative methods for reducing the carbon footprint from the construction industry. As PCMs have the ability to store latent heat, it is found to be very useful for keeping the indoor temperature to a steady comfortable state. From the studies it is observed that more efficiency is achieved when PCMs are incorporated in walls. However, the demands furthermore studies on the usage of PCMs in tropical regions like India. One such study by the authors is underway.

References

- Alawadhi EM (2012) Using phase change materials in window shutter to reduce the solar heat gain. *Energy Build* 47:421–429
- Alawadhi EM, Alqallaf HJ (2011) Building roof with conical holes containing PCM to reduce the cooling load: numerical study. *Energy Convers Manag* 52:2958–2964

- Biswas K, Abhari R (2014) Low-cost phase change material as an energy storage medium in building envelopes: Experimental and numerical analyses. *Energy Convers Manag* 88:1020–1031
- Ciulla G, Lo Brano V, Messineo A, Peri G (2013) A numerical solution that determines the temperature field inside phase change materials: application in buildings. *J Civ Eng Manag* 19(4): 518–528
- Lukić P, Tamburić J, Stojić D (2012) Energy efficiency of buildings with phase-change materials. *Arch Civ Eng* 10(3):343–352
- Mettawee ES, Ead I (2013) Energy saving in building with latent heat storage. *Int J Therm Environ Eng* 5(1):21–30
- Nazi W, Wang Y, Chen H, Zhang X, Paul A (2017) Passive cooling using phase change material and insulation for high rise office building in tropical climate. In: 9th international conference on applied energy, ICAE 2017, Cardiff, UK
- Pasupathy A, Velraj R (2008) Effect of double layer phase change material in building roof for year round thermal management. *Energy Build* 40(3):193–203
- Yahay NA, Ahmad H (2011) Numerical investigation of indoor air temperature with the application of PCM gypsum board as ceiling panels in buildings. *Procedia Eng* 20:238–248
- Zhong K, Li S, Sun G, Zhang X (2015) Simulation study on dynamic heat transfer performance of PCM-filled glass window with different thermophysical parameters of phase change material. *Energy Build* 106:87–95

Chapter 14

Energy Analysis, Simulation, and Comparison of a Commercial Building Using Standard Approach and AECOSim



Geon Clinton, Akshayakumar V. Hanagodimath
and Shrihari K. Naik

14.1 Introduction

Energy crisis has evolved into its dynamic form from the mid 1970s, around the globe, due to the extensive use and negligent use of the resources. Infrastructures, industries, and transportation are the major factors that hold responsible for the energy consumption happening across the world (Meir and Owlfsen 2015). With the increasing population, the needs of energy is only going to increase at a rapid rate. Electricity that is consumed in the daily routine is produced by fossil fuels which are on the verge of going extinct in the near future (Meir and Owlfsen 2015).

The practices which hold responsible for the energy crisis are as follows:

1. Negligence of the available resources,
2. Extensive usage of the resources.

An individual spends an average of 70% of his life span inside a building. A comfortable indoor environment can not only improve the occupants' working efficiency but also preserves their health. To achieve a comfortable indoor environment in an energy-efficient building is a goal that draws the attention of professionals from architecture, civil, mechanical, and electrical engineering.

Geon Clinton · A. V. Hanagodimath (✉) · S. K. Naik
Department of Civil Engineering, M. S. Ramaiah University of Applied Sciences,
Bangalore, India
e-mail: akshay.g9807@gmail.com

Geon Clinton
e-mail: geonclinton@rediffmail.com

S. K. Naik
e-mail: naikshrihari@gmail.com

Energy modeling and simulation is a technique used to perform energy analysis on a building to measure the energy efficiency of a building. The results obtained maybe in the form of electrical consumption, cost, infiltration loss, embodied energy, and many more areas.

14.2 History of Energy Simulation

Energy simulation and analysis are bound to some conditions and it requires some preliminary data that is important to perform the simulation process. Simulation was discussed in the year early to the 1960s, wherein they built a simple energy criteria model as they wanted to simulate the energy performance of the building, by maintaining a comfortable indoor environment. In the early 1990s, Bouchlaghem and Lethermen tried in implementing the thermal insulation analysis (Niu 2015).

Al-Homound had reported that there are various areas in which the energy analysis has to be improved and thus, submitted a study including the lighting criteria in it and it consisted of about 14 different variables in it (Cong 2015).

14.2.1 Direct Search Technique

Optimal point of the energy consumption is already known, and variable point of energy consumption is found using this technique (Cong 2015).

14.2.2 Genetic Algorithm

Arguably the most efficient technique of all, as about 605 of the researches were conducted through genetic algorithm and the improvements are continuously progressing even now. The genetic algorithm is the most preferred technique to carry out energy optimization of a building (Niu 2015).

14.3 Simulation Software—AECOSim Energy Simulator

EnergyPlus, a powerful industry standard simulation engine, was used to calculate building performance reporting and documentation. Simulations were run to generate documentation and reports that are ASHRAE Standard 90.1 compliant and LEED certified. Building layouts can be easily imported directly from multiple file formats to easily reuse existing data, without the need for third-party applications to

interpret the data, design, simulate, and analyze building mechanical systems, environmental conditions, and energy performances. It is also used to create 2D/3D energy models and to document and generate reports of peak loads, annual energy calculations, energy consumptions, carbon emissions, and fuel costs.

Work seamlessly between industry CAD, BIM, and AEC applications such as Micro Station, AutoCAD, Revit, and others with support of multiple software platforms.

14.4 Methodology

14.4.1 Various Approaches to Attain Energy Efficiency

Negotiated: Negotiation between the client and contractor is done without standards. No proper standards are set and everything depends on the contractor or the construction industry to decide.

Standard: Negotiation between the client and the contractor is done setting up standards. A set of standard values are set and it is seen to that by the end of the project the set standards are met.

Life Cycle Cost: The complete life cycle is considered and the maximum life cycle with minimal cost is considered.

Analyzing the approaches available, the standard approach was selected as the suitable approach to obtain the required energy efficiency.

14.4.2 Identification and Selection of an Existing Commercial Building

The commercial building selected had a plinth area of about 4150 sq.ft per floor and it was a G+2 storey building (see Figs. 14.1 and 14.2). It was constructed with all

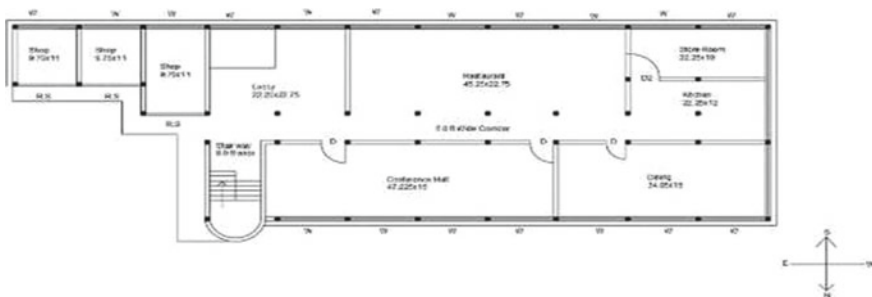


Fig. 14.1 Plan of the existing building (ground floor)

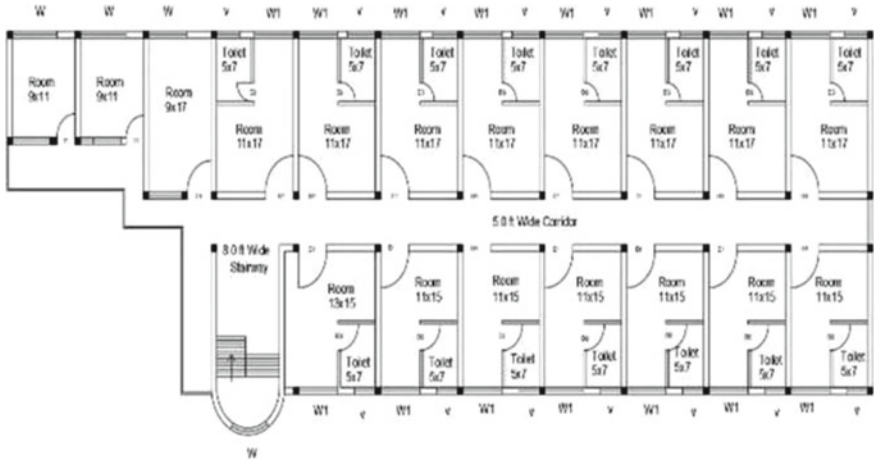


Fig. 14.2 Plan of the existing building (first and second floor)

conventional materials such as wire cut bricks, granite flooring, and reinforced concrete slabs. It was equipped with compact fluorescent bulbs and electric room heaters for the space heating and cooling purpose.

Details of the building selected:

Hotel Coorg

Near Convent Junction

Madikeri - 571201.

The Plinth Area = 4150 Sq.ft (Per Floor)

14.4.3 Estimation of Material Quantity and Electricity Consumption

Materials were estimated and the cost of the selected commercial building was thus calculated to be about INR 1,93,76,122. The rates were referred from the Public Works Department (PWD) scheduled rates of Bangalore (PW and IWTD 2016).

Electricity consumption of the building:

$$E(\text{kWh/day}) = P(W) \times t(\text{h/day}) / 1000(W/\text{kW}) \tag{1}$$

E Total electricity (kWh)

T Operational hours per day

P Capacity of the equipment

Electrical appliances and calculation of electricity consumption for conference hall in the month of January is as follows:

- i. Air Conditioners were being used on an average of 1 h in a day
- ii. 10 ceiling fans were being used for 3 h Exhaust fans were being used for 1 h
- iii. 15 tube lights and 5 CFL were used on an average of 6 h per day.

Therefore, the electrical consumption for the conference hall was 300 kWh in the month of January. The electricity consumption for the whole building was 10,298 kWh. Similarly, the electrical consumption was calculated for every room and every month individually.

14.4.4 Embodied Energy

Embodied energy is the total energy involved in the manufacturing of a material (Davis and Maini 2013). It is calculated from the start of the extraction of the raw materials, till the product is dismantled. The types of embodied energy calculations are: Cradle to grave; Cradle to gate; Cradle to site (Table 14.1).

Cradle to site calculations were done as the dismantling process was not considered and the calculations were done with respect to the standards given (Davis and Maini 2013). Embodied energy calculations provided a value of 98,26,725 MJ for the existing building and 84,90,839 MJ for the proposed building.

14.4.5 Selection of the Suitable Approach and Alternate Materials

Standard Approach:

Comparing the three approaches available, standard approach was found to be more relevant and thus the standards were set to 40–50% reduction of energy consumption.

Alternative materials proposed to increase the energy efficiency of the building are as follows:

Walls—Poro-thermal blocks:

Poro-thermal blocks are dry, strong and simple to use and these are the factors that make the poro-thermal blocks different and efficient when compared to other waling

Table 14.1 Embodied energy coefficients of materials

Brick	5170 MJ/m ³
Plain cement concrete	2367 MJ/m ³
Steel	34.8 MJ/kg
Transportation	11.93 MJ/km

systems. Porothermal blocks gives the factor of low carbon emission and the materials can be reused to a life span of about 150 years. The unit density of the blocks are 850 kg/m^3 , dry conductivity is 0.29, and has a compressive strength of 10 N/mm^2 . Thermal insulation is a major advantage that makes these blocks more energy efficient than any other walling materials (Wienerberger 2014).

Extensive Gardening:

Soil layers of 3–15 cm depth are done and herbs are planted for environmental beneficiary purposes. This is effective just to maintain the interior heat intensity and to maintain the room temperature at a stable rate. Extensive gardening helps in maintaining the indoor temperature, thereby reducing the usage of space cooling appliances. The extensive gardening is done on the terrace of the building for an area of 330 sq.m.

Vertical Gardening:

Vertical Gardening is preferred to be the best option for the indoor column criteria. It is a technique of growing plants inside a small space which can in turn maintain the temperature inside the building. The area of columns provided with vertical gardening is 52 sq.m, considering all rooms provided. All the columns in the restaurant, lobby, and reception area of the building are provided with vertical gardening to maintain the indoor air quality.

Sit and Heat Technology (HVAC System):

Sit and Heat is an energy-efficient heater, built into cushions. With Sit and Heat, one can experience more comfort, more warmth, and save up to 95% on energy costs. Sit and Heat is available with an adaptor or with a battery pack. Sit and Heat cushions are placed in every chair and every resting area, which will act as a heating appliance and in turn save 40% of electricity used for space heating.

LED lights:

LED lights are used in place of the CFL bulbs, thereby saving electricity used for the lighting purpose. 60% of the electricity is saved in the lighting criteria of the building. Minimum lighting criteria of different rooms per sq.m are Halls-500 lx, Restaurant-500 lx, bedroom-150 lx, and stairs-75 lx. Considering the minimum luminance, the lighting in conference hall consists of 18 LED lights of 9 W capacity.

Slabs—Filler Slabs:

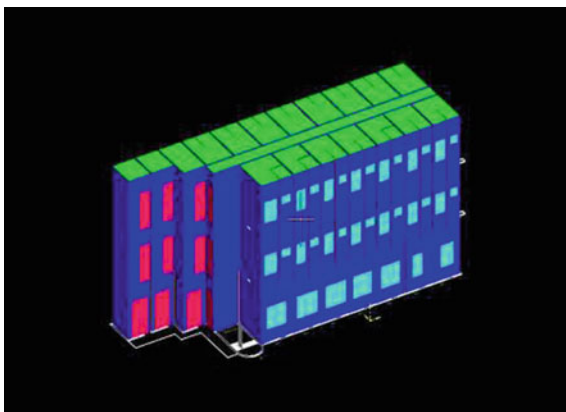
Filler slabs are concrete slabs wherein the filler materials are placed in the tension zone so that we can reduce the unwanted concrete without compromising the strength criteria of the slab (Ayush 2015). An internal cavity is provided in the filler slabs so that it can provide good thermal insulation and energy savings can be done in the building. The reduction of concrete in the filler slab was 52 cum. Four filler material blocks were placed for a span of 1 m slab. The total number of filler blocks needed for the filler slab of the building was found to be 5886 numbers and a total

concrete quantity of 130 cum. Concrete in tension zone cannot be easily replaced completely and thus the concrete in the tension zone is replaced partially, and the filler materials used are Mangalore tiles considering the cost criteria (Ayush 2015).

14.4.6 Energy Modeling and Simulation

AECOSim energy simulator is the simulation tool used to obtain results of energy consumption. AutoCAD files of the drawings are imported to the AECOSim software window in order to start the simulation process. Results obtained were in the forms of electricity consumption, CO₂ emission, and infiltration losses. Simulation and modeling (see Fig. 14.3) were done for both existing building and the proposed building in order to compare the results, measuring the energy efficiencies. Weather profile used for the simulation was the Bangalore weather profile. Materials, HVAC systems, lighting, space heating, and cooling appliances used for the respective buildings were entered with the help of the respective managerial tools available in the system and the software recognized the materials and were assigned according to the users requirements. Modeling was done using the tracing and modeling tools available and the materials were assigned by the manager tools of the software. Modeling was completed and the simulation process was carried out as per ASHRAE 2010 standards which is available in the software by default. Electricity consumption of the existing building was found to be 1,65,807 kWh and electricity consumption of the proposed building was found to be 83,341 kWh. CO₂ emission was 1,57,822 kg for the existing building and 79,327 kg for the proposed building. Infiltration losses of the existing building were found to be 25,371 W and that of the proposed building was 19,626 W. Simulation was mainly done to validate the results obtained from the software with the manually calculated results.

Fig. 14.3 Energy modeling using AECOSim



1,63,888 kWh was the electricity consumption calculated by energy consumption calculator and 1,65,807 kWh was the electricity consumption by the existing building obtained from the simulation tool.

14.5 Results and Discussion

Energy simulation was carried out for the existing building and the proposed building, on a yearly basis, and the results obtained showed that, the total energy efficiency increased by 50%.

Figure 14.4 shows the cost of both existing and proposed buildings. It is observed that, in order to achieve an energy efficiency of 50%, an additional cost of 24% will be incurred. The cost of the building built with conventional materials was found to be INR 1,55,01,677 and the cost of the proposed building, implementing the energy-efficient techniques, was calculated to be INR 1,93,76,122.

Figure 14.5 shows the comparison between the embodied energy consumption of the existing building and the proposed energy-efficient building, and the results showed that there was a 14% energy reduction. The embodied energy consumption for the existing building was around 98, 26,725 MJ and the proposed embodied energy consumption was calculated to be around 84,90,839 MJ. Figure 14.6 shows the comparison of the electricity consumption and CO₂ emission of the existing building and the energy-efficient building and the results showed that there was a reduction of around 50% in the energy consumption. Electricity consumption of the existing building was 1,65,807.68 kWh and the electricity consumption of the proposed energy-efficient building was calculated to be 83,341.72 kWh. CO₂ emission of the existing building was around 1,57,822.38 kg and the CO₂ emission of the proposed energy-efficient building was around 79,327.98 kg (Table 14.2).



Fig. 14.4 Cost comparison

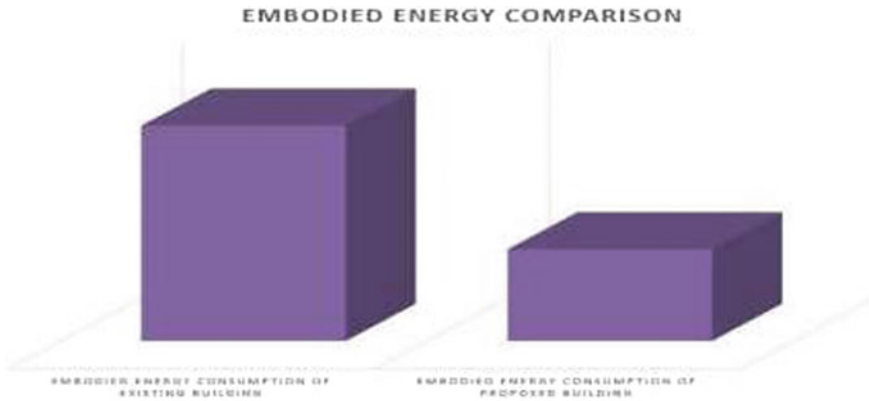


Fig. 14.5 Embodied energy



Fig. 14.6 Electricity consumption and CO₂ emission

Table 14.2 Summary of results

	Existing building	Proposed building	Savings	Difference (%)
Electricity (kW)	1,65,807.68	83,341.72	82,465.96	49.7 (Saving)
CO ₂ (kgCO ₂)	1,57,822.38	79,327.98	78,494.4	49 (Saving)
Embodied energy (MJ)	98,26,725.882	84,90,839.164	13,35,886.71	13.59 (Saving)
Cost (Rs)	1,55,01,677.97	1,93,76,122.96	-38,74,444.99	24 (Increase)
Infiltration loss (W)	25,371.4	19,626.03	5,745.4	22.6 (Saving)

14.6 Conclusion

The energy simulation process was proved to be an efficient technique to analyze the energy consumption of a structure. It was concluded that, by implementing the standard approach, planning and execution of energy-efficient techniques, the energy consumption can be reduced to about 50% and this in turn will help in reducing the CO₂ emissions. The cost factor increased to about 25% of its initial cost but considering the energy savings, it proved to be an efficient option.

Energy simulation is the need of the hour and implementing this technique at every stage of construction would be very effective in planning an energy-efficient building.

References

- Ayush (2015) Filler slab as a continuous T-beam slab
Cong Z (2015) Analysis of energy simulation models
Davis L, Maini S (2013) Embodied energy data compilation. Earthen Architecture, Auroville Earth Institute
Horeca, Sit and heat technology
Meir, Owlson T (2015) Energy efficiency in buildings
Niu (2015) Optimal building envelope design based on simulated performance: history, current status and new potentials
PW and IWTD (2016) Schedule of rates. In: Schedule of rates
Wienerberger (2014) Wienerberger building materials

Chapter 15

Effect of Column Configuration on the Behaviour of Stone Column Supported Ground



M. P. Vibhoosha, Anjana Bhasi and Sitaram Nayak

15.1 Introduction

Rapid growth of industrialisation demands construction challenges to the geotechnical practitioners because of the scarcity of suitable lands. Due to the advancement in ground improvement techniques, weak soils characterised by low bearing capacity, stability problems and differential settlement which were discarded earlier can be made suitable for construction.

Among various methods of ground improvement, soil reinforcement technique is considered as one of the most versatile and cost-effective methods. For flexible and lightly loaded structures like embankments and storage tanks, columnar structures are the best suited reinforcement. Compared to pile foundations the stone columns are more compressible and it does not require a hard stratum underneath. Stone columns are suitable for a wide variety of soils like soft clay, loose sand, peat, etc. The liquefaction tendency of loose sand during earthquake can be effectively reduced by this method (Mitchell and Huber 1985).

On application of vertical load, the upper portion of stone column bulges and obtains lateral resistance from the neighbouring weak soil. Thus, minimal stress was transferred to the deeper layers. The high permeability and granular nature of stones accelerate the consolidation in soft clay and decrease the construction time of embankment over such soils.

The stone column technique was applied on wide variety of soils from 1950s (Barksdale and Bachus 1983). The stone column supported ground was analysed most commonly by unit cell approach since it reduces the simulation time and represents the actual geometry and loading condition.

M. P. Vibhoosha (✉) · S. Nayak
NITK Surathkal, Mangalore, India
e-mail: vibhoosha@gmail.com

A. Bhasi
NIT Calicut, Kozhikode, Kerala, India

Ambily and Gandhi (2007) found out the stress distribution in stone columns by using finite element package PLAXIS. The load carrying capacity of stone columns can be improved effectively by encasing them with suitable geosynthetic material (Murugesan and Rajagopal 2007). The percentage increment in load carrying capacity was dependent upon the stiffness of the encasement used. Nayak et al. (2014) installed stone columns in dispersive soil and carried out load tests. They found out that granular columns improve the stiffness and load carrying capacity of the ground. The effect of various parameters such as area ratio, diameter of stone columns and end conditions were also studied.

The effect of column configuration on the load carrying capacity of stone column supported ground was analysed in this paper. Finite element package ABAQUS was used for developing 3D numerical models.

15.2 Finite Element Analyses

Unit cell approach was considered for developing the models. The diameter of the unit cell was 283 mm and the diameter of stone column was 90 mm which corresponds to an area ratio 10% (Nayak et al. 2014). Floating stone columns were considered for the analyses with L/D ratio 6, where L and D are the depth and diameter of stone columns, respectively. Drainage blanket was provided over the stone columns with 30 mm thickness.

15.2.1 Finite Element Scheme of the Present Study

To account real soil behaviour, it is necessary to carry out coupled analysis which essentially couples pore fluid flow and stress–strain behaviour together. This result in both displacement and pore fluid pressure degrees of freedom at the nodal points.

A commercial finite element program ABAQUS (SIMULIA 2016) was used for the entire analyses. This program has the capability to carry out coupled analysis based on the generalised consolidation theory of Biot (1941). The global equilibrium equations are modified to

$$\begin{bmatrix} k & L \\ L^T & -\Phi\Delta t \end{bmatrix} \begin{Bmatrix} u_{t+\Delta t} \\ \pi_{t+\Delta t} \end{Bmatrix} = \begin{Bmatrix} f_{t+\Delta t} \\ v_{n_{t+\Delta t}} \end{Bmatrix} \quad (15.1)$$

Here, $[k]$ is the stiffness matrix of the soil, $[L]$ is the interaction term between the soil and the pore fluid, $[\Phi]$ is the matrix governing the dissipation of pore fluid, $u_{t+\Delta t}$ is the nodal displacement vector, $\pi_{t+\Delta t}$ is the nodal pore pressure vector, $f_{t+\Delta t}$ consists of the incremental applied load terms and $v_{n_{t+\Delta t}}$ consists of load term corresponding to seepage forces on the boundary.

15.2.2 Properties of Materials Used for Modelling

The various materials used for the analyses were soft clay, stones and sand. The properties were selected from the literature (Murugesan and Rajagopal 2012). The soft clay was modelled using the Modified Cam-Clay material model. A linear-elastic, perfectly plastic model with the Mohr–Coulomb failure criterion was used to model the stone column and the sand (Table 15.1).

15.2.3 Models Developed for the Analyses

Influence of column configuration, i.e. for same area ratio increasing the number of columns of smaller diameters for same depth was analysed with the help of the developed numerical model. Area replacement ratio of 10% was selected and it is attained by a 90 mm diameter single column as well as with a group of 52 mm diameter columns as shown in Fig. 15.1. Schematic representation of the developed full 3D model is shown in Fig. 15.2.

Table 15.1 Properties of various materials (Murugesan and Rajagopal 2012)

Parameter	Notation	Clay	Stone column	Sand	Unit
Material model	–	Modified cam clay	Mohr–Coulomb	Mohr–Coulomb	–
Unit weight	γ	17	18	18	kN/m ³
Permeability	K	2.3×10^{-9}	1.2×10^{-4}	1.2×10^{-5}	m/s
Young's Modulus	E	–	48,000	20,000	kN/m ²
Poisson's ratio	ν	0.3	0.3	0.3	–
Cohesion	C	12	4	3	kN/m ²
Friction angle	ϕ	–	42	28	degree
Dilation angle	Ψ	0	10	4	degree

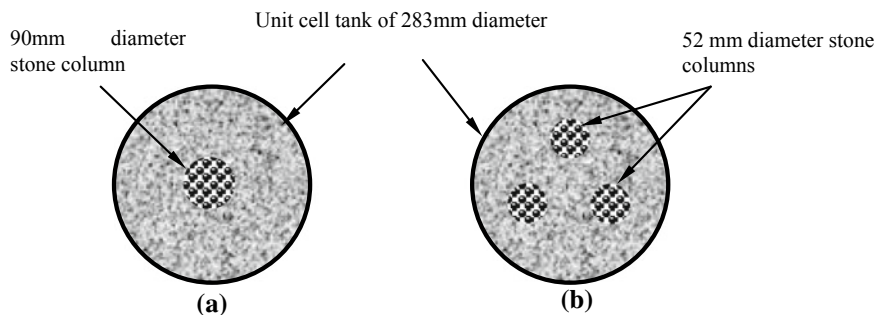
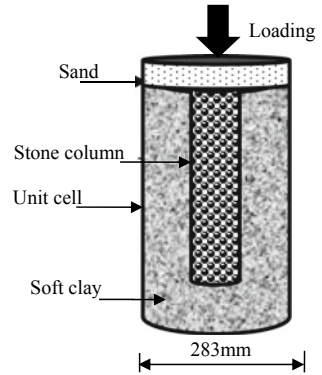


Fig. 15.1 Column configurations for same area ratio **a** single column, **b** three columns

Fig. 15.2 Schematic diagram of the finite element model developed



15.2.4 Boundary Conditions

Vertical sides were horizontally fixed and the base was fully fixed to prevent rigid body motion. The groundwater table was set at the clay layer top and free drainage was simulated by giving zero pore pressure boundary condition.

15.2.5 Elements Used for Meshing

In both the models, the meshes were arranged, in order to have the same element size vertically to eliminate any possible errors arising from the mesh arrangement. 20-node stress–pore pressure elements with reduced integration (C3D20RP) were used to represent the clay layer and the stone column, and 20-node stress only elements (C3D20R) were used for the sand layer.

15.2.6 Methodology

The initial soil conditions were simulated in the geostatic step. After that the stone columns were installed by activating the corresponding element in the model with suitable boundary conditions. The loading was continued till a settlement value of 10 mm was obtained (IS: 15284-2003).

15.3 Results and Discussion

15.3.1 Load-Carrying Capacity—Settlement Behaviour

The load-carrying capacity corresponding to 10 mm settlement was taken from the numerical results. Figure 15.3 shows the load intensity settlement behaviour of unreinforced soil, soil reinforced with single stone column and group of stone columns. It was clear that the stone column improves the load-carrying capacity of soft soil by 45%. The percentage improvement obtained with group of stone columns with smaller diameter was even more and the summary is given in Table 15.2. The load-carrying capacity of the soil reinforced with group of columns was improved by 12% than the soil with single column. Since construction of smaller diameter columns were easy and economical, smaller diameter columns can be preferred than a single large diameter column of same area replacement ratio.

The load-carrying capacity improvement due to the installation of stone column was a result of the resistance offered by the surrounding soil against its lateral bulging under vertical loading. The closer spacing of smaller diameter columns increases the confinement effect to the stone column from the neighbouring soil. It also reduces the bulging tendency of the stone columns which leads to the improvement in load-carrying capacity.

The improvement in stiffness of the stone column treated ground was quantified by a term stiffness ratio, which is the ratio of stress value of treated ground to that of untreated ground for the same settlement. The stiffness ratio against normalised settlement (ratio of settlement (Δ) to diameter of granular column (D)) for different cases is plotted in Fig. 15.4.

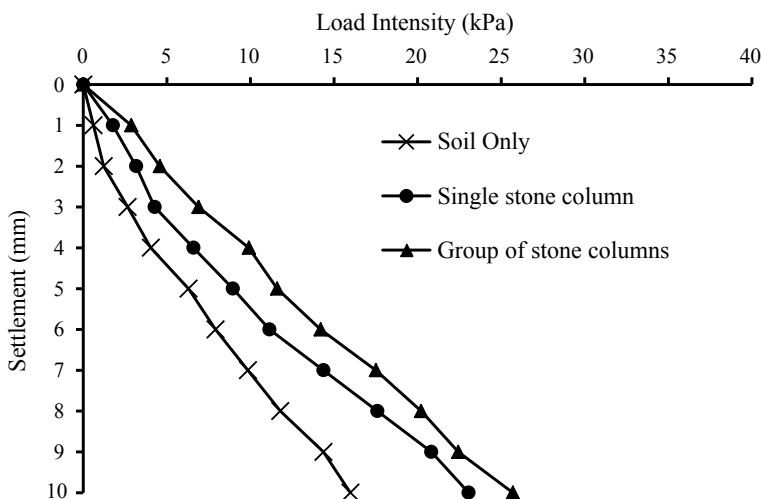
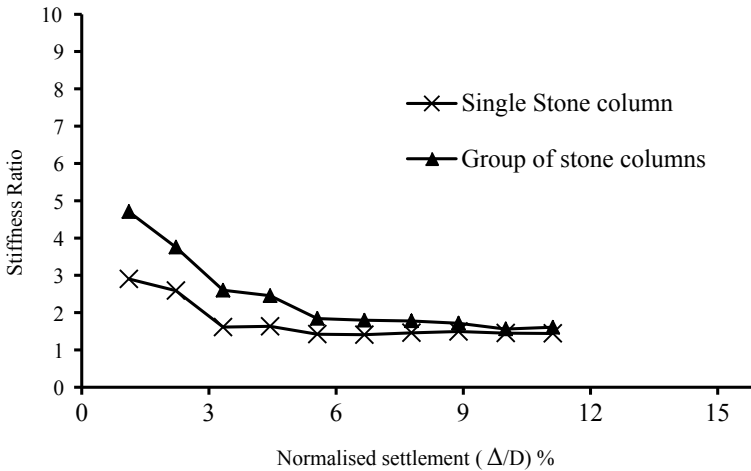


Fig. 15.3 Load-carrying capacity settlement response under various cases

Table 15.2 Summary of load-carrying capacity under various conditions

Different cases	Load-carrying capacity (kPa)	% increase in load-carrying capacity
Untreated soil	15.98	–
OSC	23.05	45
OSC group	25.70	61

**Fig. 15.4** Variation of stiffness ratio with normalised settlement for different cases

From the graph, it is clear that the stiffness ratio was high in the beginning, and started decreasing and attained a constant value in both the cases. Also, the stiffness ratio was more for group of columns in all settlement values.

15.4 Conclusions

The performance of soft clay reinforced with stone columns was analysed by using finite element approach. The effect of column configuration on the load intensity—settlement behaviour was studied by unit cell idealisation. Following conclusions were made based on the numerical results.

1. The load-carrying capacity of soft soil can be improved by stone column method and the percentage increment in the load-carrying capacity was 45%. The mechanism was the passive resistance from the surrounding soil against the lateral bulging of stone columns.
2. For the same area replacement ratio, smaller diameter columns have better performance than a large diameter single column. Since construction of smaller

diameter columns were easy and economical, smaller diameter columns can be preferred than a single large diameter column of same area replacement ratio.

3. The stiffness ratio was also more for smaller diameter column installed ground than a single large diameter column of the same area ratio. Thus compared to a single column, smaller diameter columns yield better stiffness.

References

- Ambily AP, Gandhi SR (2007) Behavior of stone columns based on experimental and FEM analysis. *J Geotech Geoenviron Eng* 133(April):405–415
- Barksdale RD, Bachus RC (1983) Design and construction of stone columns. Federal Highway Administration, RD-83/026
- Biot MA (1941) General theory of three-dimensional consolidation. *J Appl Phys* 12(2):155–164
- IS: 15284-2003 Indian standard code of practice for design and construction for ground improvement-guidelines. Part 1: stone columns, India
- Mitchell JK, Huber TR (1985) Performance of a Stone Column Foundation. *J Geotech Eng* 111 (2):205–223
- Murugesan S, Rajagopal K (2007) Model tests on geosynthetic-encased stone columns. *Geosynth Int* 14(6):346–354
- Murugesan S, Rajagopal K (2012) Geosynthetic-encased stone columns: numerical evaluation. *Geotext Geomembr* 24:349–358
- Nayak S, Dheerendra Babu MR, Shivashankar R, James N (2014) Performance of granular columns in dispersive soils. *Proc Inst Civil Eng Geotech Eng* 167(1):72–82

Chapter 16

A Novel Machine Learning System to Improve Heart Failure Patients Support



J. Dheebea and J. Jeba Sonia

16.1 Medical Background

Heart failure affects 26 billion of people all over the world (Health Catalyst article entitled 2018). Heart Failure (HF) is an alteration of structure named vascular stiffening and functioning of heart that leads to an inadequate pumping function (Strait and Lakatta 2012). Inadequate pumping of heart leads to an insufficient amount of oxygen flow to the internal organs, tissues, and blood. Oxygen is essential for organs and tissues for performing metabolic activities. Because of slow function of heart, possibility of buildup of sodium and unwanted water in lungs and in other tissues called edema. The main indications of heart failure are shortness of breath, fatigue, edema, increased heart rate, etc. (American Heart Association 2017). Heart failure is a life-threatening stage (Elfadil and Ibrahim 2011) and it leads to death if it left unattended. The clinical course of heart failure is chronic and the patient is in steady condition and hospitalized with continuous observation. With the help of some therapies, the criticality will be reduced. The global occurrence of Heart Failure is accelerating because of the age of the population and extending survival of patients affected with coronary diseases. In this case to reduce the human risk, we need a medical support system that helps to assist the HF patients.

J. Dheebea (✉) · J. J. Sonia
School of Computer Science and Engineering, Vellore Institute of Technology,
Vellore, India
e-mail: dummy@gmail.com

© Springer Nature Singapore Pte Ltd. 2020
H. Drück et al. (eds.), *Green Buildings and Sustainable Engineering*,
Springer Transactions in Civil and Environmental Engineering,
https://doi.org/10.1007/978-981-15-1063-2_16

16.2 Introduction

Medical decision support systems speedily growing as the important tools for medical practitioners since the quantity of available data increases along with the responsibility to provide effective care. Here we present a Medical Decision Support System (MDSS) that comes with a movable kit for getting hold of medical parameters which permits the support to telemonitoring functions. The MDSS system provides smart functions with the help of different machine learning methods which we matched to find the best method that performs better with the present data in our database and distinct for the HF field. The above system yields many outputs that can be viewed with the help of an interface tool called HF Administrator. This can have two choices like to bring about the demographics of the patient, the continuous check-ups and to train the artificial intelligent methods with the help of patient data. The device can be used to show the output of the system after the AI was trained adequately. The description and all the smart functions of this tool along with the comparison of different machine learning methods with the best method are explained in this paper.

16.2.1 Project Goals (Final Output)

The aim of this device is to provide the end-users like the physicians to give the necessary outputs like Criticality Assessment, Type Prediction, Short-range prediction, Sequential follow-up comparison, and Overall Prediction.

Criticality Assessment: It is a three-level assessment (mild, moderate, critical) of actual HF criticality.

Type Prediction: It predicts the type of HF of the patient and also the acute episodes that possibly

Short-Range Prediction: It shows the indication of the chances of occurrence of a serious problem. Since these cases are sensitive, it needs the data for training on daily basis.

Sequential follow-up comparison: It is a clear view of various parameters of the patient in treatment in different dates of follow-ups. Histograms and line charts are used for showing the follow-ups.

Guidelines of therapy: It is the outcome that shows the doctor, that all the targets are achieved based upon the guidelines. Some classes of drugs need some regular follow-ups to check whether to increase or decrease or whether the dose is tolerated by the patient.

From the above goals, some of them are achieved using machine learning algorithms using proper training which was explained in Chap. 4. The end users of this device may change based on the application needed and it may be heart

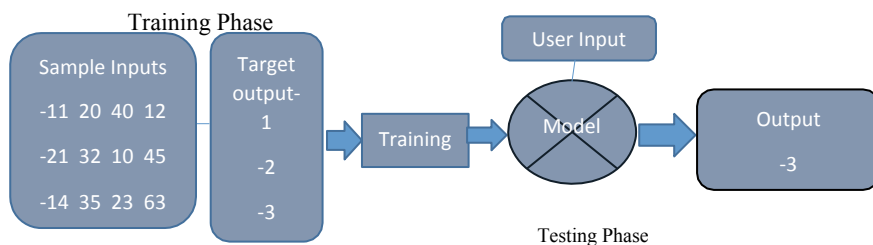


Fig. 16.1 Supervised learning representation

specialists or other non-technical. For the non-technical staff, criticality assessment output is much useful. For example, in a home-based monitoring setup, a nurse often goes to the home of the patient for taking some measurements and feed the results using a tablet device. The smart core device will answer with the criticality assessment which will be sent to the patient's doctor or to the heart specialist and he will sort his patient based on the severity. The more details based on this procedure are explained in the following literature (Guidi et al. in press, 2012a, b).

16.2.2 Supervised Training

One of the machine learning algorithms used is the supervised learning training method. Here the input will be given based on the observation and the desired output is also given. The training pair consists of one input value with the target value, which is explained in Fig. 16.1. The training is having training and testing phases. After the training phase, a reusable model is taken as the output and during testing phase, new inputs that the system never knows before are given to test how the system behaves for both the sets of inputs. It is not necessary to know the learning procedure because the system from the proof of the information given and it individually finds the required output.

16.3 The HF_ADMIN Device

16.3.1 Scope of Device

The device main goal is to get back the parametric data of actual patients at the time of outpatient visits appropriate for training a machine learning procedure. As given in Fig. 16.1, every follow-up should be assisted by a "Target output", i.e., the assessment of the HF by the heart specialist. The next aim is that the device acts as a

special-purpose control panel for the treatment of HF patients, together with the main management and several other useful functions interconnected to the disease.

16.3.2 Device Design

This device has been constructed in deep cooperation with doctors for satisfying real time essentials in terms of both subjects and usability which are taken during outpatient visits. The necessity of usability which targets to diminish the device's impact on the casualty visits workflow. To confirm that the doctor can take actual and instant benefit from the use of the device in cardiology casualty visits, the device comprises of some practical structures such as the Alteration of Diet in Renal Disease calculation (ADRD), smart therapy unit which discovers the drug molecules to suggest based on dose and an instructor that confirms that the guideline of procedures are strictly followed. In this section, we will label in detail the device and its parts like parameter attainment, follow-up displays, criticality assessment based on AI methods, Smart Therapy unit, asynchronous compilation unit, short-range prediction, module for asynchronous compiling, etc. For patient demographics, all of these units work together by an HF_ADMIN_device.

16.3.3 Patient Management

Selection of a particular patient is possible in this section whether he is already included in the database or needs to be added as a new name. The complete information about the patient is present in the database and also we can visualize the updated data related to the patient's consultant. Figure 16.2 shows the personal

The screenshot displays a web-based interface for patient management, divided into several sections:

- Patient Section:** Includes a search bar with "Find Patient" and "Name" labels, and an "Add New" button. Below is a table with columns "Name" and "ID".
- Patient Registry Section:** Contains input fields for "Name:", "Date of Birth:", "Address:", "Age:", and "Sex:", along with a "Calculate Enrollment Score" button.
- Consultant Section:** Includes input fields for "Name:" and "Phone:", and an "E mail:" label.
- Action Buttons:** Three large buttons at the bottom: "Add New Follow-up" (with a plus sign), "Follow-up Evaluation" (with a magnifying glass icon), and "Prognosis Calculator" (with a heart and pulse icon).

Name	ID
Smith	
Luca	
John	
Andru	

Fig. 16.2 Patient monitoring interface

information of the patient, consultant information, and prognosis details of the patient.

16.3.4 Enrollment Mark

This attribute is for the calculation of the risk of extending hospitalization based on the practical score. This device needs the contribution of some functional parameters such as the BNP (Brain Natriuretic Peptide) and Ejection Fraction of heart altogether with some other structural parameters such as the total number of hospitalization records of patient for HF complication or for other factors. This model delivers a possibility of risk score. If the HF patient seems to be at great risk of re-hospitalization then it is appropriate to be enrolled in the scheme and it may be helpful for the training of the Machine.

16.3.5 Parameters Attainment

This section is used by the heart specialist during his daily visits. In Fig. 16.3. It is shown that having five sections. The first section is noted with the personal details and enrollment details of the patient. The calculation of the prognosis score can be calculated in the second section. Frequent updates and daily measurements are

The screenshot shows a web-based input mask for a medical application, organized into five main sections:

- Parameters (Frequent Update):** Includes input fields for Follow-up date, Heart Rate (Bpm), Actual Weight (Kg), Systolic Bp, and Diastolic Bp.
- ECG Parameter:** A list of checkboxes for Rhythm, L.B Branch Block, Pacemaker, and Ventricular Tachycardia, along with radio buttons for ICD and ICD/CRT.
- Etiology:** A list of checkboxes for Chronic Heart Disease, Hypertension, and Valvular Heart Disease.
- Patient Registry:** Includes input fields for Name, Date of Birth, Address, Age, Sex, Phone, and E mail.
- Consultant:** A section with a "Calculate Enrollment Score" button.
- Criticality:** Radio buttons for Mild, Medium, and Critical.
- Disease Evolution:** Radio buttons for Stable, Improvement, and Worsening.
- Therapy:** A text area for "Description..." and a "Save and Analyze" button.

Fig. 16.3 Input mask

calculated in the third section. Therapy details and the follow-ups are given in the fourth section. Section 16.5??? is committed to exposing the progress and position of HF patients based on three classes by the doctor. This detail will be taken as the target output in the process of supervised learning techniques. Various input parameters given by this attainment mask will then bring together with all these target outputs that are mild-medium-critical and improvement-no change-worsening which will be useful for outputs as explained in the introduction section. Some buttons are given to save the details, view back and analyze. After pressing analyze button the user of the device When the “analyze” button is clicked, the user is supposed to select prompted to choose any one from artificial intelligence trained with the system’s database or with a default database fixed in the system.

16.3.6 Follow-Ups Display

In this pane, the user can select a follow-up of the particular patient and see its number values and an overall summary report of various existing problems of the patients and details about the treatment. It is also having a graphical outlook of several patient’s follow-up records and the option to select it needs to display or not some of the parameters and to choose one from the three different types of charts. This output is called the Chronological follow-up evaluation. A follow-up can be also examined by using AI techniques (Guidi et al. 2012) if it was not treated during the concerned outpatient visit.

16.3.7 Smart Therapy Unit

Smart particle discovering: In the parameter attainment mask, there is another one part that was given to therapy management, i.e., the doctor can enter the therapy suggested to the patient. For some specific drugs types like ACE inhibitors, angiotensin receptor blockers, beta-blockers by taking the amount in milligrams, the smart system which is on the basis of fixed thresholds, will automatically identify the active component and highlights if the dosage for that particular drug is considered as high, medium or short.

Therapy Guidelines Unit: The usage of this guidelines unit is explained in the introduction part. This unit helps the heart specialist to be sure that the recommended level of maximum tolerable dosage as mentioned in the guidelines is provided to the patient. In specific, with the help of details given as current in the method of Smart particle discovery unit, for the sets of drugs beta-blockers, angiotensin receptor blockers, ACE inhibitors, treatment is categorized as low-middle-high for that particular patient. Then it will be presented as a target for

various follow-up dosages of these drugs. If treatment remains without change through numerous follow-ups without any increase in dose then an alarm will sound and the specialist is requested to evaluate whether this condition is desired or not.

16.4 Core of Intelligence

With the help of the supervised training technique explained in the above sessions and our database, the system is trained to give outputs like criticality assessment and HF Type prediction. The outputs of short-term prediction and long-term prediction are not given because they need training. Short-term prediction needs the monitoring of the patient on a regular basis. The long-term prediction is also not carried because it needs a continuous follow-up and for getting details it takes more time. The intelligent core system is having the output for the criticality assessment and HF prediction.

16.4.1 Database

The two functions are trained with an unknown database of HF patients, with different criticality degrees which are treated by the Cardiology Departments. The database totally consists of a full of 130 records from 90 patients, including starting and regular follow-up data. In the data collection phase, the cardiologist provided the given HF criticality assessment in the following three levels: Mild, Medium and critical, which was kept in the database. After a great collection of data, the condition of every patient in terms of HF type was calculated and combined with the concern record. This will help to train the system using a supervised method. Some of the ML input parameters are taken from previous literature related to HF. For an accurate analysis of the patient, the instrumental parameters should go together with various past medical parameters. Different variables in database which are utilized as input for the Machine Learning methods are the following:

Anamnestic data like patient_age, patient_gender,

Instrumental data like patient_weight, Ejection Fraction (EF), Heart Rate of the patient, ECG Parameters (atrial fibrillation true/false left bundle branch block true/false), ventricular tachycardia true/false), Brain Natriuretic Peptide (BNP), Systolic Blood Pressure, Diastolic Blood Pressure.

The following table shows the Criticality assessment and prediction type in the database (Table 16.1).

Table 16.1 Criticality assessment parameters

Criticality assessment	Mild	Medium	Critical
No. of patients	50	35	46
Prediction type	Constant	Rare	Frequent
No. of patients	109	12	10

Table 16.2 Varied parameters for better result

Method	Parameter investigated
Neural network	No. of hidden layers
SVM	Combination of two SVM
Neuro-Fuzzy Genetic method	No. of fuzzy rules and generations
CART	Pruning level
Random forest	No. of features for each tree

16.4.2 Details of Machine Learning Techniques

Neural Network (NN): NN is trained at regular intervals by changing the number of hidden neurons from 2 to 8. For HF criticality assessment 5 hidden layers are used and for prediction of HF type 8 hidden layers are specified.

SVM: SVM is a binary classifier and in trial and error method, all the we tried all the possibilities of permutations and good results were achieved with SVM tree and we obtained the best results with the grouping of critical Vs non- critical and then analysed the mild and medium criteria.

Neuro-Fuzzy Genetic Method: Using this method, the suitable and best results are reached with a population of 28 individuals, each composed by 45 fuzzy rules and the algorithm rounds for more than 550 generations.

CART: The CART was tested by the system itself with different levels of pruning. Best results in finding criticality are gained with a prune level of 2.

Random Forest: Various tests are performed to obtain a suitable performance with various features for each tree. Suitable parameters are set to stabilize the error rate. Various tests are made for generating better accuracy and it was done in the MatLab environment and finally integrated with the HF_Admin unit (Table 16.2).

16.5 Performance Evaluation

For comparing and evaluating the performance of the machine learning techniques. To make use of the available data, each record of the database is considered as the information of follow-ups. In the same manner, a database consists of 130 different

heart patients each one is having a single follow-up. The follow-up details are collected over slightly longer period of time like 6–8 months and the parametric attainment and health condition of the surveyed patient was changed which helps to validate the approximation defined. Multiclass accuracy formula was used to calculate the performances of the three classifiers (Sokolova and Lapalme 2009).

$$\text{Accuracy} = \sum_{i=1}^{\text{No.ofclass}} \frac{\text{TP}_i + \text{TN}_i}{\text{TP}_i + \text{TN}_i + \text{FP}_i + \text{FN}_i} \quad (16.1)$$

TP: True Positive; TN: True Negative; FP: False Positive; FN: False Negative.

16.6 Discussion of Results

The validation results of several machine learning methods are given in Tables 16.3 and 16.4. Random Forest algorithms perform better in case of automatic criticality assessment. CART attained somewhat lesser performance than Random Forest and it had the benefit to deliver a clear and understandable model. CART (Pecchia et al. 2011) is using the If—Then rules. Different values of BNP and EF are measured and the theme was considered as CHF. In the case of criticality assessment, Random Forest and CART (Pecchia et al. 2011) formed better results when compared with various literatures that measure HF severity other studies that assess HF severity such as (Yang et al. 2010) which classifies HF related patients in three groups based on the levels of accuracy. In the above justification tables, the STD will be considered as very high in criticality assessment. The performance of the system is said to be fold-dependent since the developed system is not noticing the medium status. The various test that is done and the various accuracy levels are explained in the above tables. Random Forest algorithm is the best algorithm which is better combining accuracy levels and some errors are also committed (additional information about Random Forest algorithms are given in (Karpievitch et al. 2009)). Accuracy is not only considered as the most significant factor for measuring the performance of the system. The procedure of making decision in this kind of support systems should be understandable by the human. In this regard, CART

Table 16.3 Criticality assessment performance

ML method	Accuracy in %	STD	Errors
Neural network	76.8	7.2	0
SVM	79.3	9.2	3
Neuro-Fuzzy Genetic method	68.9	9.7	1
CART	80.8	8.7	2
Random forest	82.3	7.3	1

Table 16.4 RF type prediction performance

ML method	Accuracy in %	Accuracy in %	Errors
Neural network	83.62	10.7	0
SVM	84.1	11.5	7
Neuro-Fuzzy genetic method	84.4	11.3	5
CART	86.5	11.1	8
Random forest	84.5	11	4

method is considered to be best one and the accuracy of CART is somehow lower than Random Forest. CART is not using prior knowledge (Melillo et al. 2013) but the rule set of CART is considered to be consistent. CART algorithm selected the most applicable features for making the decisions which are easily understandable by technical and non-technical. Table 16.1 values for HF type prediction are said to be biased because of irregularity between various patients with stable HF values and also the dataset comprised of clustered data. Because of this condition, the most efficient methods to handle that data. An accurate HF prediction set must need a well-balanced database with greater number of independent events like patients.

16.7 Conclusion

A Decision Support System to enhance the support for patients affected by Heart Failure (HF) is proposed in this paper. The necessity for this medical system is mainly because of the continuously growing number of patients who are suffering from acute diseases because of numerous factors which include the aging of society. Specifically, HF is considered as a chronic and life-threatening disease with great prevalence and it can be managed by the usage of various remote monitoring systems. For a heart failure patient, for monitoring the progress of parameters and complete an apt intrusion in therapy might be conclusive for the outcome of the patient. The proposed MDSS systems objective is to enable monitoring situations by automatically yielding results understandable even by non-specialist of cardiology physicians and non-technical staff, about the criticality and type of HF prediction. For providing these outcomes we compared various types of Machine Learning algorithms and concluded that the CART method outperforms well for reaching the goal. For making a physically understandable decision-making procedure, CART produces an accuracy level of 80.8% in criticality assessment calculation and 86.5% accuracy in HF type prediction. Overall CART is considered as the best algorithm among the compared machine learning algorithms.

References

- Health Catalyst article entitled (2018) Artificial intelligence improves accuracy of heart failure readmission risk predictions
- Strait JB, Lakatta EG (2012) Aging-associated cardiovascular changes and their relationship to heart failure. *Heart Fail Clin* 8(1):143–164
- American Heart Association (2017) Article on heart failure
- Guidi G, Melillo P, Pettenati MC, Milli M, Iadanza E A system to improve continuity of care in heart failure patients. In: *IFMBE Proceedings* (in press)
- Guidi G, Iadanza E, Pettenati MC, Milli M, Pavone F, Biffi Gentili G (2012) Heart failure artificial intelligence-based computer aided diagnosis telecare system. *ICOST 2012, Lect Notes Comput Sci* 7251:278–281
- Guidi G, Pettenati MC, Miniati R, Iadanza E (2012) Heart failure analysis dashboard for patient's remote monitoring combining multiple artificial intelligence technologies. In: *2012 Annual international conference of the IEEE engineering in medicine and biology society*, pp 2210–2213
- Sokolova M, Lapalme G (2009) A systematic analysis of performance measures for classification tasks. *Inf Process Manag* 45(4):427–437
- Karpievitch YV, Hill EG, Leclerc AP, Dabney AR, Almeida JS (2009) An introspective comparison of random forest based classifiers for the analysis of cluster-correlated data by way of RF++. *PLoS One* p e7087
- Breiman L (2001) Random forests. *Mach Learn* 45(1):5–32
- Yang G, Ren Y, Pan Q, Ning G (2010) A heart failure diagnosis model based on support vector machine. In: *IEEE International conference on biomedical engineering and informatics*, no. Bmei, pp 1105–1108
- Levey AS, Coresh J, Balk E, Kausz AT, Levin A, Steffes MW, Hogg RJ, Perrone RD, Lau J, Eknoyan G (2003) National kidney foundation practice guidelines for chronic kidney disease: evaluation, classification, and stratification. *Ann Intern Med* 139(2):137–147
- Smith SF (1980) A learning system based on genetic adaptive algorithms. PhD dissertation, Department of Computer Science, University of Pittsburgh
- Elfadil N, Ibrahim I (2011) Self organizing neural network approach for identification of patients with congestive heart failure. In: *International conference on multimedia computing and systems (ICMCS)*, pp 1–6
- Pecchia L, Melillo P, Bracale M (2011) Remote health monitoring of heart failure with data mining via CART method on HRV features 2011. *IEEE Trans Bio-Med Eng* 58:800–804
- Levy WC, Mozaffarian D, Linker DT, Sutradhar SC, Anker SD, Cropp AB, Anand I, Maggioni A, Burton P, Sullivan MD, Pitt B, Poole-Wilson PA, Mann DL, Packer M (2006) The seattle heart failure model: prediction of survival in heart failure. *Circulation* 113:1424–1433
- Lee DS, Austin PC, Rouleau JL, Liu PP, Naimark D (2003) Predicting mortality among patients hospitalized for heart failure derivation and validation of a clinical model (EFFECT). *Hospitals* 290:2581–2587
- Fonarow GC, Adams KF, Abraham WT, Yancy CW, Boscardin WJ (2005) Risk stratification for in-hospital mortality in acutely decompensated heart failure: classification and regression tree analysis. *JAMA* 293:572–580
- Melillo P, De Luca N, Bracale M, Pecchia L (2013) Classification tree for risk assessment in patients suffering from congestive heart failure via long-term heart rate variability. *IEEE J Biomed Health Inf* 17:727–733

Chapter 17

Study of Air Distribution in Operating Room



M. A. Rinjesh, C. Muraleedharan and V. K. Vikas

17.1 Introduction

Hospitals are the important destiny of health care services, in which surgical operation theater plays a vital role. It is very significant to maintain the comfort of patient and surgical staff for the successful completion of any surgery. It is a challenging task, as the comfort level of immuno-suppressed patient and the working staff will be different. According to the ASHRAE handbook (ASHRAE 2003), temperature within the room should be in between 18 and 22 °C and relative humidity should be in the range of 50–60%. Surgical site infections (SSIs) are the infections occurring after the completion of surgery up to 30 days. The main reason for post-surgical death case is SSI. Due to the presence of contaminants such as dust particles and bacteria at the surgical site lead to the SSI. So the air conditioning system of an operating theater should satisfy both comfort and contaminant removal purposes. The effectiveness of the contaminant removal depends upon the flow pattern adopted. There are different types of flow distribution, such as laminar air flow (LAF), turbulent mixed air flow, temperature controlled air flow etc. Out of which the most commonly used type is laminar air flow by Whitcomb and Clapper (1966). The idea of LAF is to swipe away any micro-biological contaminants such as dust particles and bacteria from the surgical site. The main problem associated with the LAF is the presence of obstacles such as surgical lamp and equipment. The present work is the analysis of the laminar air flow and the effect of position of surgical lamp and supply velocity on flow distribution numerically.

M. A. Rinjesh (✉) · C. Muraleedharan · V. K. Vikas
Department of Mechanical Engineering, National Institute of Technology Calicut,
Kozhikode, Kerala, India
e-mail: rinjesham@gmail.com

© Springer Nature Singapore Pte Ltd. 2020
H. Drück et al. (eds.), *Green Buildings and Sustainable Engineering*,
Springer Transactions in Civil and Environmental Engineering,
https://doi.org/10.1007/978-981-15-1063-2_17

17.2 Methodology

17.2.1 Description of Baseline Model

Using Ansys 19.2 software a full-scale model of an operating room is designed. The room is of 7 m length and equal breadth with 3 m floor to ceiling height. The inlet temperature is taken as 20 °C. The designed model is shown in Fig. 17.1 along with various occupants and equipment. The human body and all other equipment are represented in the shape of a rectangular block for simplicity and suitable materials are assumed.

The operating room consists of six members of surgical staff, patient, surgical equipment, tables, bed and surgical lights. The details are presented in Table 17.1.

Air enters the room through a supply grill of dimensions 2.8×2.8 m positioned exactly at the center of the roof and leaving through four exhaust grilles each of dimensions 1.2×0.55 m positioned 0.34 m from floor level at center of each side wall.

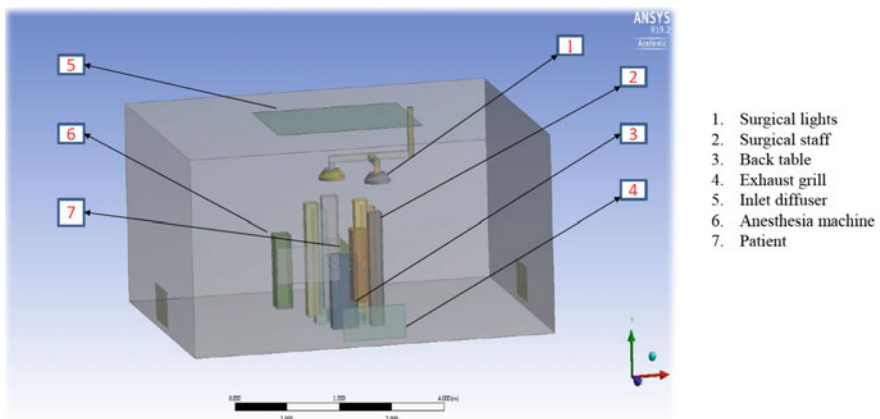


Fig. 17.1 Full-scale operating room chamber

Table 17.1 Dimensions of various equipment and occupants and their heat dissipation

Items	Dimensions	Heat dissipation
Operating table	1.9×0.6×0.85 m	None
Surgical lights (2)	0.5 m in diameter	150 W each
Surgical staff (6)	0.3×0.25×1.7 m high	100 W each
Anesthesia machine	0.5×0.3×1.2 m high	200 W
Machine 1	0.5×0.3×1.6 m in high	None
Patient	0.3×0.25×1.7 m high	46 W
Back table	0.5×0.3×1.1 m high	None

Grid independency test was performed to ensure that the result would not vary on increasing the number of cells. The final grid size is fixed to be 500000 elements with 90000 nodes.

The effect of surgical lights on flow patterns was analyzed with two different configurations of the lights at two different velocities at inlet. The simulation cases were shown in Fig. 17.2. In the first orientation, one light was above the head of patient and other light, above the surgeons at the side, which is a standard configuration followed by hospitals. In the second configuration both lights were above the patient, one above the face and other above the abdomen. Two different velocities were chosen arbitrarily. One is 0.18 m/s and other one is 0.38 m/s. So a total of four simulations were carried out to find the best flow pattern, and to prove that the first configuration is the best configuration of the surgical lights in an operating room. The two different configurations are shown in Figs. 17.3 and 17.4, respectively.

Boundary conditions

The system is assumed to be in steady state with uniform inlet velocity and temperature. The inlet velocity is taken as 0.18 and 0.38 m/s for two different cases and the inlet air temperature as 20 °C. Heat loads of various occupants and equipment used are as given as in Table 17.1.

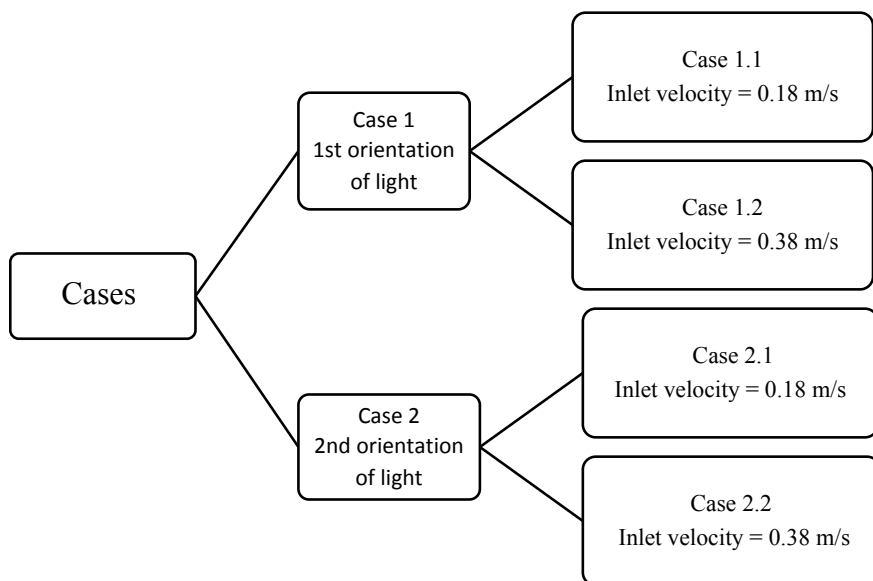


Fig. 17.2 Details of simulations carried out

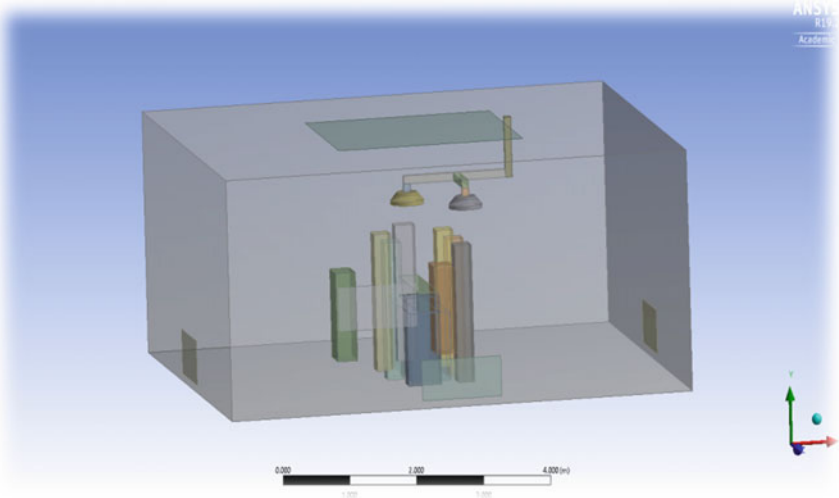


Fig. 17.3 First configuration of lights

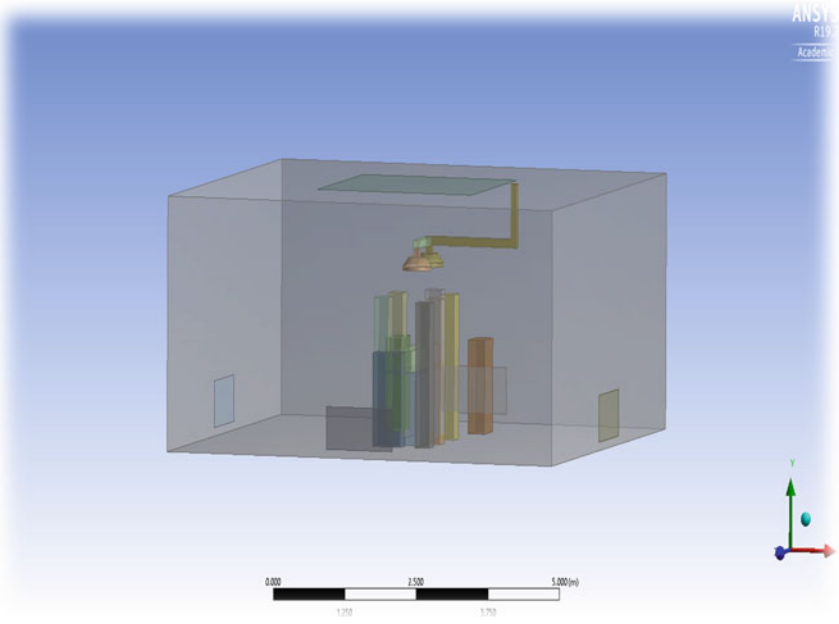


Fig. 17.4 Second configuration of lights

17.3 Results and Discussion

Airflow patterns

Figures 17.5, 17.6, 17.7 and 17.8 show the velocity vector and contour plots at two different planes, at positions exactly crossing the surgical lights. From the figures, it can be observed that the medical lamp configuration influences the flow pattern considerably. The velocity of flow just underneath the lamp reduced to very low value in the configuration, in which both lamps are above the bed. Due to the reduction of velocity the contaminants will be entrapped in these regions and the chance for infection is high. The exact values of velocity at different location are plotted as bar diagrams in Figs. 17.9, 17.10, 17.11 and 17.12. The locations are marked in Fig. 17.13.

From the bar diagrams it is evident that along the lines passing through the corners of the inlet diffusers, the variation in velocity is insignificant. Whereas the variation in velocity along lines passing through the surgical lights is significant. Just underneath of the surgical lamps the velocity drops and air flow diminishes. At this region if any contaminant enters, it stays there and will not wash out by the LAF. This reduction is severe in the second configuration of surgical lamp. The flow patterns are almost similar for both the inlet velocities, but for proper washing action of LAF somewhat higher velocity, i.e., 0.38 m/s is needed. For proper washing away of contaminants, more than 0.2 m/s velocity is essential. The proper washing is happened in the first configuration of the lamp which is shown in Fig. 17.14.

From Fig. 17.14, it is evident that the washing velocity is reduced to less than 0.2 m/s in the second configuration of the medical lamps.

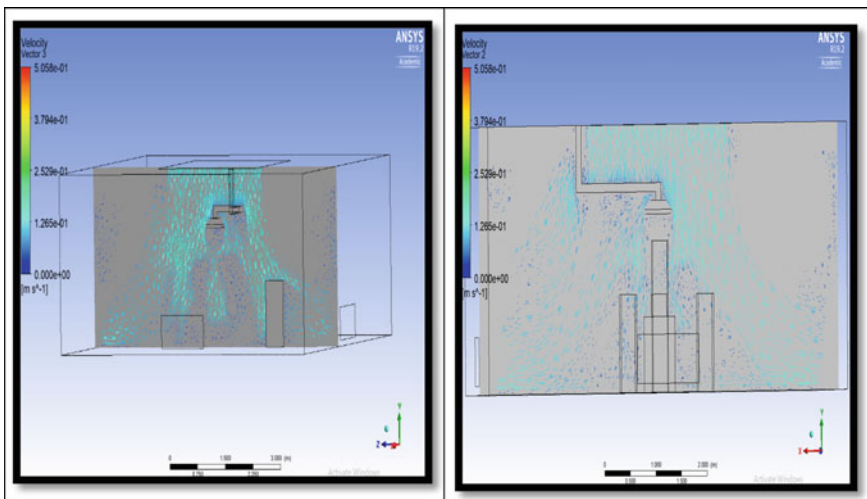


Fig. 17.5 Vector plot: Case 1.1

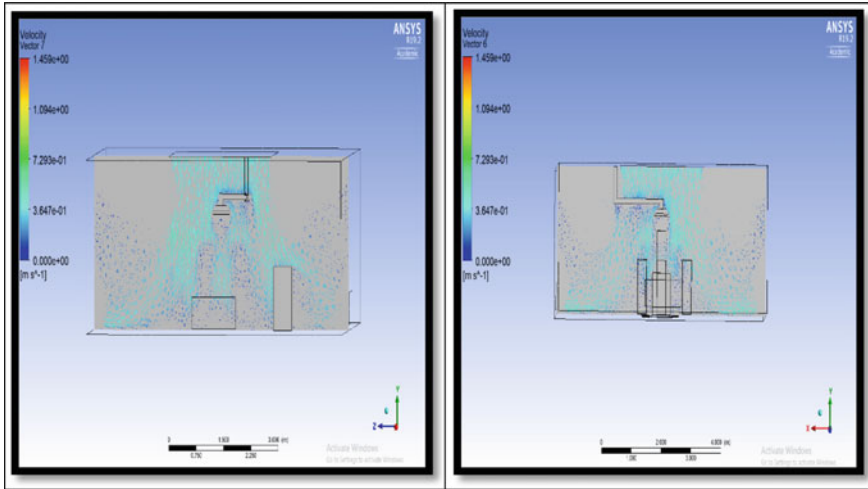


Fig. 17.6 Vector plot: Case 1.2

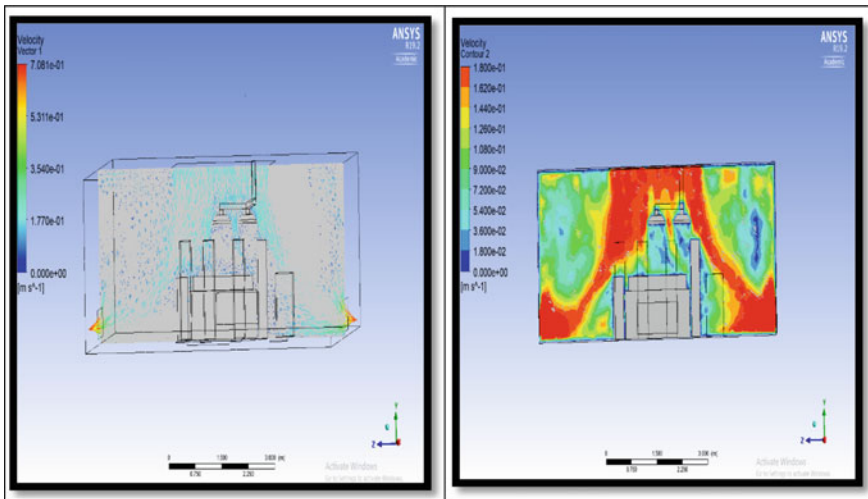


Fig. 17.7 Vector plot and velocity contour: Case 2.1

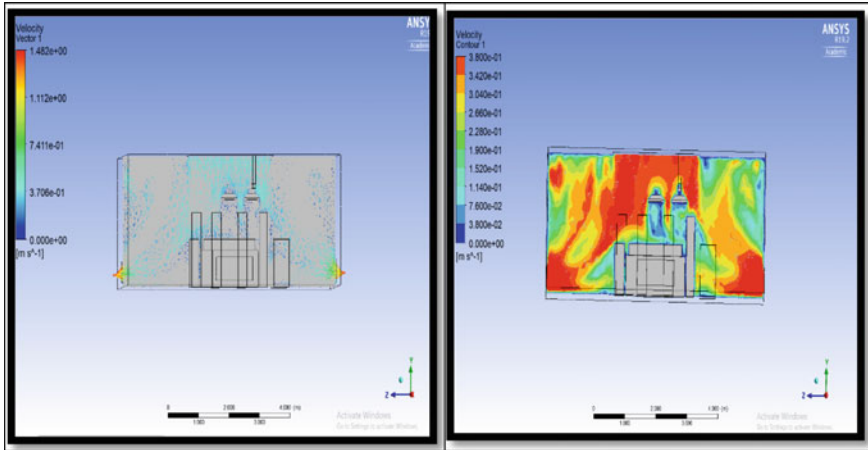
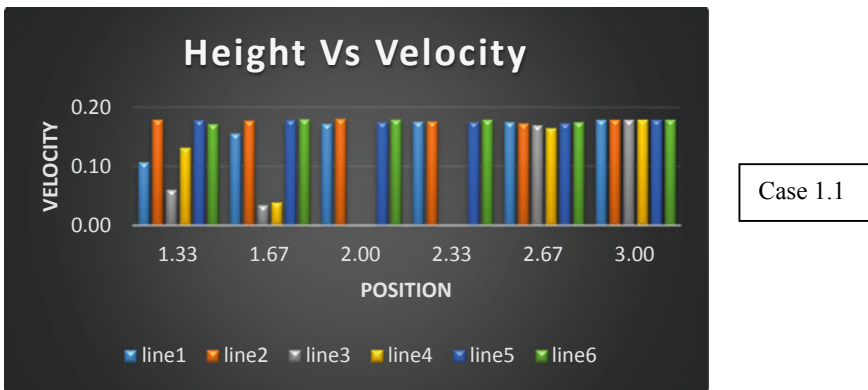
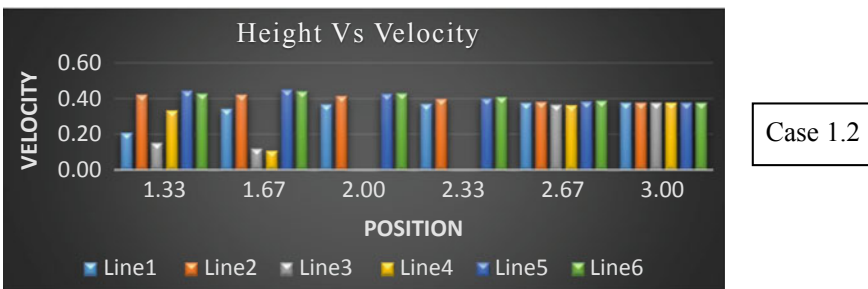


Fig. 17.8 Vector plot and velocity contour: Case 2.2



Case 1.1

Fig. 17.9 Variation of velocity with height for case 1.1



Case 1.2

Fig. 17.10 Variation of velocity with height for case 1.2

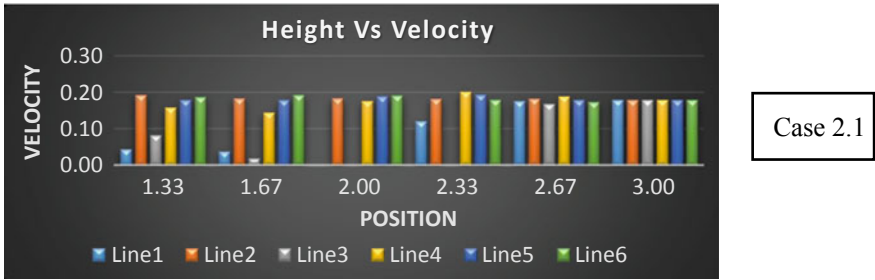


Fig. 17.11 Variation of velocity with height for case 2.1

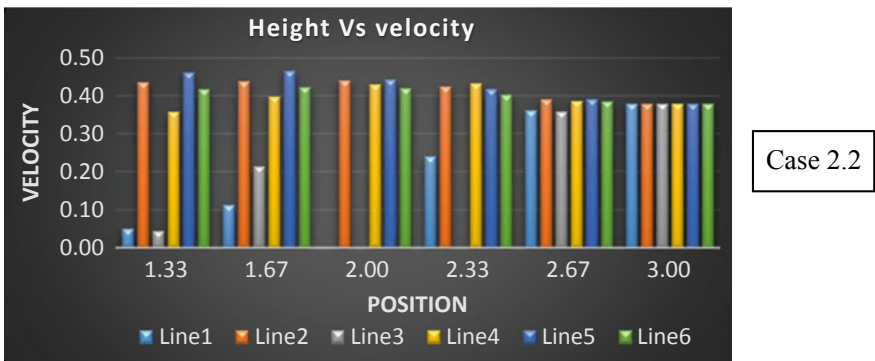


Fig. 17.12 Variation of velocity with height for case 2.2

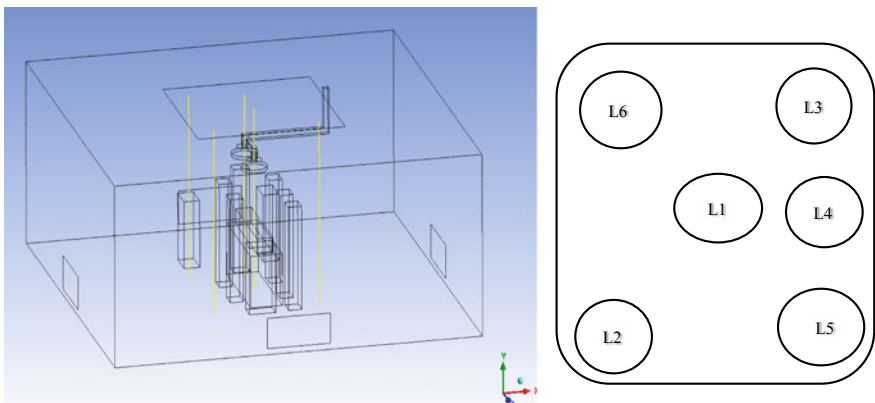


Fig. 17.13 Different locations of line along which the bar diagram showing the variation of velocity with respect to height is plotted

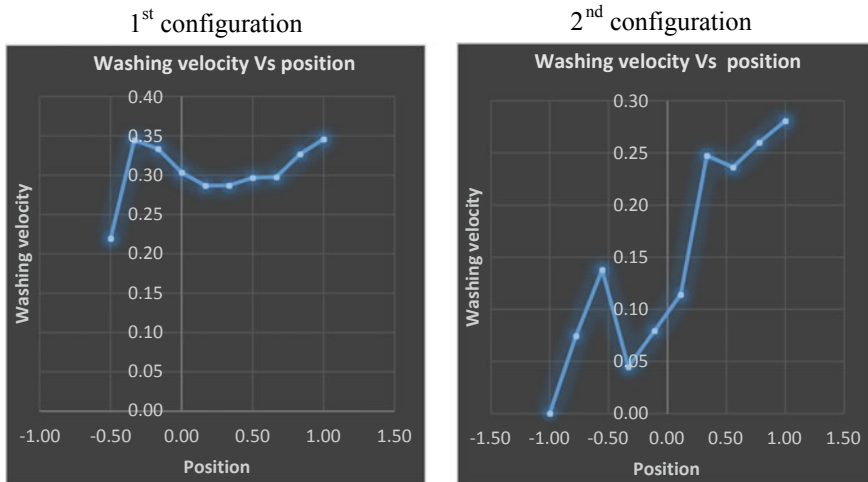


Fig. 17.14 Comparison of washing velocity at inlet velocity 0.38 m/s

17.4 Conclusions

After CFD analysis of the air distribution in surgical operating rooms considering the influence of geometry of room on turbulence of flow within the room, and the effect of position of surgical light and supply velocity on air distribution pattern the following conclusions are made.

- The best flow patterns are obtained in the first orientation of light, i.e., when one light is above the patient and one at the side. This is a standard configuration of lights obtained from DIN 4799.
- The flow velocity just underneath the medical lamp reduced to very small value in the configuration in which both the lamps are above the bed.
- If some contaminant reaches this region, they will stay longer and travels randomly.
- Washing velocity should be greater than 0.2 m/s for proper washing effect. This is achieved only in Case 1.2.
- So the best configuration is configuration 1 and the inlet velocity should be somewhat high and not much high, because it will affect the comfort of surgeons and patient.

References

- ASHRAE (2003) ASHRAE handbook: applications, American society of heating, Refrigerating and Air-Conditioning Engineers, Atlanta, GA
- ASHRAE TC 9.6 (2008) ANSI/ASHRAE Standard 170-2008. Ventilation of healthcare facilities. American Society of Heating, Refrigerating, and Air-Conditioning Engineers, Atlanta

- Brohus H, Balling KD, Jeppesen D (2006) Influence of movements on contaminant transport in an operating room. *Indoor Air* 16(5):356–372. <https://doi.org/10.1111/j.1600-0668.2006.00454.x>
- Chow T-T, Yang X-Y (2003) Performance of ventilation system in a non-standard operating room. *Build Environ* 38(12):1401–1411. [https://doi.org/10.1016/S0360-1323\(03\)00155-0](https://doi.org/10.1016/S0360-1323(03)00155-0)
- Chow TT, Yang XY (2005) Ventilation performance in the operating theatre against airborne infection: numerical study on an ultra-clean system. *J Hosp Infect* 59(2):138–147. <https://doi.org/10.1016/j.jhin.2004.09.006>
- Chow TT, Lin Z, Bai W (2006) The integrated effect of medical lamp position and diffuser discharge velocity on ultraclean ventilation performance in an operating theatre. *Indoor Built Environ* 15(4):315–331. <https://doi.org/10.1177/1420326X06067802>
- Memarzadeh F, Jiang, J (2004) Effect of operation room geometry and ventilation system parameter variations on the protection of the surgical site. In: *Proceeding of IAQ 2004*. Tampa, 15–17 March 2004
- Memarzadeh F, Manning AP (2002) Comparison of operating room ventilation systems in the protection of the surgical site/discussion. *ASHRAE Trans* 108(2):3
- Whitcomb JG, Clapper WE (1966) Ultraclean operating room. *Am J Surg* 112(5):681–685. [https://doi.org/10.1016/0002-9610\(66\)90104-8](https://doi.org/10.1016/0002-9610(66)90104-8)
- Woloszyn M, Virgone J, Mélen S (2004) Diagonal air-distribution system for operating rooms: experiment and modeling. *Build Environ* 39(10):1171–1178. <https://doi.org/10.1016/j.buildenv.2004.03.013>
- Woods JE, Brayman DT, Rasmussen RW, Reynolds GL, Montag GM (1986) Ventilation requirements in hospital operating rooms—part I: control of airborne particles. *ASHRAE Transactions* 92:396–426

Chapter 18

Building-Integrated Photovoltaics (BIPV) in India: A Framework for TRIZ-Based Parametric Design



Avantika Srivastava, Tarun Kumar , Kriti Bhalla and Vishal Mishra

18.1 Introduction

We humans are not facing a shortage of energy. We are facing a technical challenge in capturing it and delivering it to consumers—Jostein Eikeland

In today's world, energy is the primary driver of all economic activity and is essential for developmental activities. Thus, it is essential to evaluate and conserve available resources, to consolidate the economic and environmental feasibility of untapped renewable sources of energy (Traversa and Idriss 2012). All of these technologies should be novel, efficient, renewable, safe, user friendly and environmentally sustainable (Traversa and Idriss 2012). Fulfilling power generation has become a significant concern since the rate of power production does not match the growing power demand thus, leading to a severe energy crisis. This increasing demand gives much stress over the existing power generating sources. Non-renewable resources of energy fail to cope with the ever-increasing needs; further, these resources result in harmful emissions making them unclean energy resource, thus leaving an adverse impact on the environment (Leonzio 2017). To cope with the rising power demand there is a need to switch from conventional

A. Srivastava
The Green Side Production, Bangalore, India

T. Kumar (✉)
Indian Institute of Science, Bangalore, India
e-mail: tarunkumar@iisc.ac.in

K. Bhalla
Ramaiah Institute of Technology, Bangalore, India

V. Mishra
Vijaya Vittala Institute of Technology, Bangalore, India

sources of energy to a renewable and sustainable source of energy. To meet the target, a large amount of energy is required than what is currently generated. Thus, it is essential to switch to renewable energy resources.

Renewable energy is in demand as it has the potential to mitigate environmental emissions and improve public health. Renewable Energy Sources can reuse and produce energy such as solar, wind, geothermal energy and biomass (Squalli 2017). To make the future energy-sufficient, new emerging ideas must be incorporated that will create a primarily new world, depicted by the greater use of renewable energy resources like Solar power (Sindhu et al. 2017). Today's technology-driven urban lifestyle stress on more electricity consumption. Due to the use of more electricity-consuming appliances and machines, the electricity demand will double by 2060 (World Energy Council 2016). Therefore, requirements for a low carbon future incentivise us to make significant changes in the building models or face downfall.

Photovoltaic systems are characterised by Active solar technologies. This technology converts energy from sunlight directly into electricity, using large arrays of solar panels, which can be integrated into a building to produce power (Wald and Rodeck 2012).

The amount of sunlight that gets absorbed by the earth in one minute can power an entire planet for a year. The technology needed to harness this power has been around for over sixty years but has not always been aesthetically applied. Now, with recent advances in solar technology, solar tiles can be seamlessly installed into the buildings. This integration of photovoltaic cells on the building as primary components of the building is called Building-Integrated Photovoltaics (BIPV). In this system, the PV panels are integrated into building components such as walls, roofs or windows to capture the maximum amount of sunlight and heat (Baljit et al. 2016).

18.2 Literature Review

BIPV is a kind of building system and the workpiece of an architect. BIPV modules may differ depending upon their applications. Different types of modules are (1) Classic (framed), (2) Thin Film (3) Roof-tiles with solar cells, (4) Transparent Monocrystalline, (5) Coloured solar cells, (6) Semi-transparent Micro-Perforated, (7) Amorphous cells. These modules can be further customised based on module shapes, colour, Transparency, cell type, lamination size, lamination construction, module voltage, heat/noise isolation (Roberts 2009) (Table 18.1).

Solar energy is considered one of the cleanest sources of energy; however, there are a few drawbacks that should be carefully discerned. The manufacturing cost is high; also the high requirement of maintenance make it challenging to be used widely. Furthermore, this system can be influenced by weather. Cloud cover, rain, snow and hail storm may damage the system (QC Solar 2013). While the module size is limited, a very accurate shading analysis needs to be made before the system

Table 18.1 Comparison of different types of photovoltaic panels

Types of Cells →	Monocrystalline	Polycrystalline	Thin Film
↓ Factors			
Cost	Rs. 45-50 /W	Rs. 37-48/W	Rs. 12-15/W
Output (250w)	1.5 m ²	2.2m ²	6m ²
Efficiency	14-19%	12-16.5%	4.7%
Availability	less	high	high
Performance Temp. Range	0-20°C	≥45°C	≥60°C

installation. Additionally, the analysis of light and shadow effects are very significant while designing a building, which is decided by the facade to a great extent. The BIPV junction boxes are often too big and glued on the backside of the panel, which spoils the magnificence of the whole building. This comes as a challenge to an architect, as there is a need to hide it (Prasad 2005).

18.2.1 Indian Scenario

India contributes is one of the highest consumers of primary energy demand and its economy would become five times its current size in 2040. India is on the path of becoming the most populous country by 2027 leaving behind China (World Energy Council 2016). Due to a high GDP growth rate, India emerges as a major driving force in global trends, with all modern fuels and technologies playing a part. India has stepped up the installation and use of solar energy by:- a) providing subsidies, b) focussing on expanding its markets with increased operational efficiency, and c) deploying various government schemes and programs (World Energy Council 2016).

18.3 Methodology

A comparative analysis was done to understand the currently available technology of ‘building-Integrated Photovoltaics in India through a comprehensive literature review. Three buildings retrofitted with photovoltaics were studied namely—a residential building in Trivandrum, Kerala; Central Public Works Department in Dehradun; and National Institute of Advanced Studies, Bangalore. Subsequently, various building-design parameters were identified using TRIZ methodology to

develop a framework for BIPV based parametric design. Using this framework, a preliminary 3D-building model was designed on Sketchup software which was later analysed for total power production. (TRIZ Method is a systematic approach to solve the challenging problems by an inventive method called ‘*Teoriya Resheniya Izobretatelskikh Zadach*’ developed by ‘Genrich Altshuller.) Later, a reference model was proposed illustrating the importance of BIPV based solar buildings as the primary power generating units of the solar city.

18.4 Results

Table 18.2 illustrates the various features of BIPV case studies (literature-based), which was carried out to understand the design and integration of photovoltaics in buildings. While Table 18.3 summarises, the results obtained from three primary case studies of buildings retrofitted with PV in different places.

Table 18.2 Examples of the usage of BIPV from literature

Project	Location	Capacity (MW)	Size	Year	Remarks
Longyangxia dam Solar park	Qinghai, China	850	27 km ²	2015	The total installed capacity shall be increased up to 77 GW in future
Harvard University	Cambridge, Massachusetts, U.S.A.	2.14		2003–2017	Various buildings in Harvard University has BIPV integration
Ludesch Town Hall	Ludesch, Bludenz, Austria	0.0198	204.2 m ²	2006	<ul style="list-style-type: none"> •Pitched roof •Solar-glass laminated-PV •17.5% transparency •Monocrystalline •Used as sun shade
Solar roof Speicher	Speicher, Switzerland	0.173	1100 m ²	2014	<ul style="list-style-type: none"> •Pitched roof •Sports center •Monocrystalline •East-west orientation •Opaque
The New York Stillwell Avenue Subway Station	Brooklyn, New York	250 annually	7,100 m ²	2004	<ul style="list-style-type: none"> •Glazed roof with PV panels •2,730 thin-film modules •Cover 15% of power

Table 18.3 A case study of photovoltaic powered building systems at different locations

Case study city	Location	Area (m ²)	Technology used	Energy produced	Energy savings
Dehradun	30.318°N 78.029°E State: Uttarakhand	900	Polycrystalline cells	12 KW	50% energy consumption rate
Trivandrum	8°28'N, 76°57'E State: Kerala	30	Polycrystalline cells	1 KW	90% energy consumption rate
Bangalore	13°01'N, 77°33'E State: Karnataka	778	Polycrystalline cells	100 KW	50% energy consumption rate

Table 18.4 TRIZ based morphological analysis of different design ideas

Type	Monocrystalline ●	Polycrystalline ●	Thin Film	Transparent ●
Paint	Reflecting ●	Absorbing ●	Solar Dye ●	
Position	Roof	Wall ●	Facade ●	Windows ●
Cost	High ●	Affordable ●	Low ●	
Energy Efficiency	High ● ●	Average ●	Low	
Novel Technology	Sun tracking	Temperature tracking ●	Self Cooling ●	Still ●
	● D1	● D2	● D3	

Various design parameters were put together to come up with three innovative design ideas by group brainstorming. These design ideas were later formulated to the conceptual stage by TRIZ methodology (as shown in Table 18.4). Three building designs D1, D2 and D3 were created using the framework and compared against each other using the weighted mean method.

A 14-floor high-rise model was created based on the combination of best features of these three design ideas. The building was well integrated with photovoltaic panels on the dome, the exterior wall, and windows. The total amount of energy

Table 18.5 Energy calculation of the proposed building design model

Dome power yield *Design basis: dome radius = 12.5 m = $\left(\frac{1}{2}\right) \times$ $(4 \times \pi \times R^2 \times 250 \div 2.2) \times (1/3) = 38 \text{ kW}$	Panel power yield *Design basis: $250 \text{ W}/2.2 \text{ m}^2 = (250 \div 2.2) \times$ $W \times L \times N = 68.2 \text{ kW}$
Transparent panel power yield *Based on available PV cell output @ $125 \text{ W}/\text{m}^2 = 52.5 \text{ kW}$	Cumulative power yield = 158.5 kW Energy units saved = 792 units (Considering 5 horns of effective sunlight) Greenhouse gas emissions saved = 5 tonnes/day

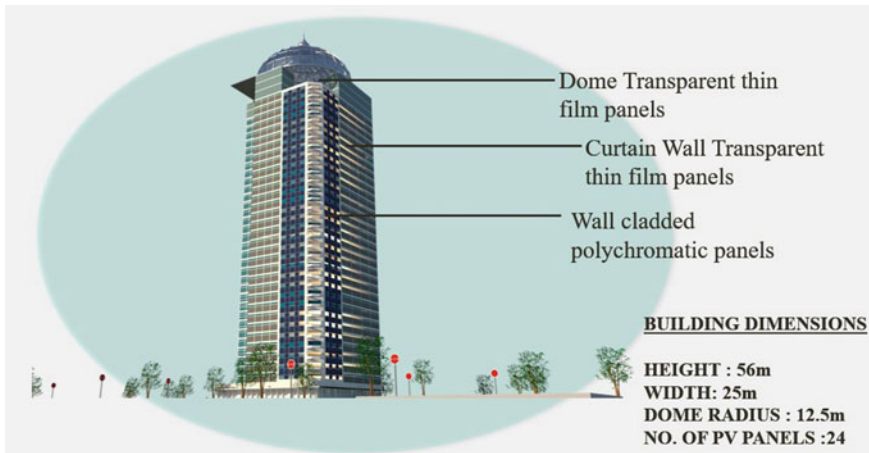


Fig. 18.1 Proposed design model for BIPV high-rise building

created from the photovoltaic panels was calculated (see Table 18.5). The total energy generated was 158.5 KW, which is enough to meet the power requirement of the building. Also, the building saved 5 Tonnes of greenhouse gases (GHG) emission per day (Fig. 18.1).

The proposed building model could work as a power production unit by giving back unused power to the grid, thus reducing the carbon emission level. The combination of these technologies with innovative design ideas would play a significant role in the development of solar-powered home; acting as the primary unit of solar cities. Finally, a reference model for solar city was proposed which would generate sufficient energy from the sun (Fig. 18.2).

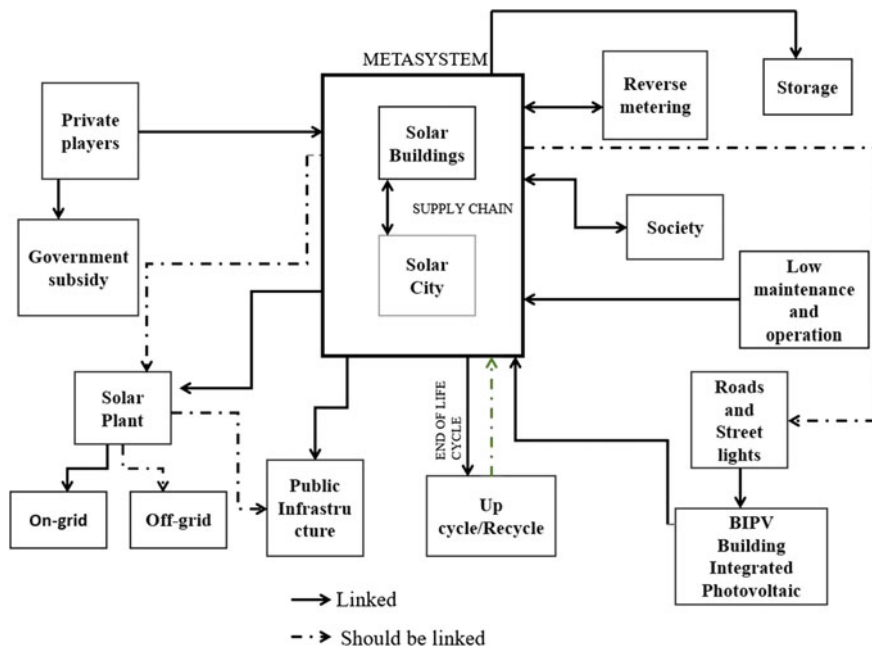


Fig. 18.2 Proposed reference model for the solar city based solar home

18.5 Discussion

It can be inferred from Table 18.2 that solar parks need a large area which makes them practically infeasible in congested urban areas such as those found in Indian cities. While as seen in the Harvard university example, BIPV integration in an educational campus would be far more rewarding in terms of energy generation if done in a coordinated and planned way. Moreover, Ludesch Townhall uses its roof and sun-shades to integrate monocrystalline laminated PV with 17% transparency, thus making a case for public buildings to adopt BIPV in a big way. The New York Stillwell Avenue subway station uses thin-film modules in an innovative manner while reducing the efficiency of the cells as a trade-off.

In Table 18.3, It can be seen that most Indian buildings are retrofits (and use polycrystalline cells), highlighting the fact that the photovoltaic integration was not part of the original building plan, but an afterthought. Hence, we need to integrate consideration of BIPV integration at the early design stages of building design.

In Table 18.4, the various parameters identified by the TRIZ method was listed as (a) type of solar cells; (b) Type of paint (c) Position of Photovoltaic Integration; (d) cost of the technology; (e) Energy efficiency and (f) novel technologies used (e.g. Movement/tracking type and self-cooling, etc.). A combination of the three

designs D1, D2, and D3 combined with creative planning helps authors come up with a model building which performs quite well in terms of energy efficiency as seen in Table 18.5. While this preliminary building model is only the starting point as a huge number of designs can be created using this TRIZ based framework which can be populated along the rows and columns over time. The quality of design data assessed would directly impact the quality of designs generated.

Finally, a meta-system of solar buildings acting as a basic unit of solar cities was defined and proposed. It can be inferred by Fig. 18.2 that storage and disposal (End-of-Life) would be major challenges in the coming future to solar cities. While low maintenance and operation costs are factors that are still far from achieved in the Indian context. Unused power can be transferred to the grid and consumers can earn monetary benefits in terms of power-units. A capacity-building program addressing the technical repair capability of service providers in Tier 2 and Tier 3 cities would be needed. This proposed city, would not only generate power for itself but will also provide energy for energy-starved rural areas. A synergy between government and private players needs to be attained to manufacture, install, operate, maintain and recycle photovoltaics on an urban scale.

18.6 Conclusion

The results of integrating solar panels in the building would be the generation of clean solar energy which would reduce the stress on non-renewable and polluting sources of energy. Commercial Buildings, institutional buildings, and modern-day residences can become Independent power-producers. Various designs can be created using the proposed TRIZ-based parametric design framework that suits both building aesthetics and energy efficiency. It was found that buildings designed utilising the proposed framework could significantly reduce the overall energy load on the power grid and become energy neutral or energy positive in the true sense. Solar power generation can significantly advance buildings' sustainability through improved energy performance and renewable energy generation. Moreover, the upscaled solar building model can serve as a nucleus for providing impetus to smart cities program of the government of India. This methodological analysis shows that solar power generation can significantly advance buildings' sustainability through improved energy performance and renewable energy generation. The proposed reference model for a solar city based on solar buildings as the primary power generating unit needs to be studied further for its impact on the environmental sustainability of the building sector.

References

- Baljit SSS, Chan H-Y, Sopian K (2016) Review of building integrated applications of photovoltaic and solar thermal systems. *J Clean Prod* 137:677–689. <https://doi.org/10.1016/j.jclepro.2016.07.150>
- Leonzio G (2017) Solar systems integrated with absorption heat pumps and thermal energy storages: state of art. *Renew Sustain Energy Rev* 70:492–505. <https://doi.org/10.1016/j.rser.2016.11.117>
- Prasad D, Snow M (2005) *Designing with solar power: a source book for building integrated photovoltaics (BIPV)*. London
- QC Solar (2013) Advantages and disadvantages of BIPV. Available from <http://www.qc-solar.com/news/32370.html>
- Roberts SG (2009) *Building integrated photovoltaics: a handbook*. Birkhäuser Architecture
- Sindhu S, Nehra V, Luthra S (2017) Solar energy deployment for sustainable future of India: hybrid SWOC-AHP analysis. *Renew Sustain Energy Rev* 72:1138–1151. <https://doi.org/10.1016/j.rser.2016.10.033>
- Squalli J (2017) Renewable energy, coal as a baseload power source, and greenhouse gas emissions: evidence from U.S. state-level data. *Energy* 127:479–488. <https://doi.org/10.1016/j.energy.2017.03.156>
- Traversa E, Idriss H (2012) Materials for renewable and sustainable energy provides the connection between materials, energy, and sustainability. *Mater Renew Sustain Energy*. <https://doi.org/10.1007/s40243-012-0002-x>
- Wald N, Rodeck C (2012) Executive summary. *New Dir Youth Dev* 2012:7–11. <https://doi.org/10.1002/yd.20038>
- World Energy Council (2016) *World energy scenario 2016*. Available from https://www.worldenergy.org/wp-content/uploads/2016/10/World-Energy-Scenarios-2016_Full-Report.pdf

Part III
Green Materials and Green Manufacturing

Chapter 19

Production of Semi-lightweight Concrete Using Calcite Powder Pellets as Coarse Aggregates



P. Parthiban  and J. Karthikeyan

19.1 Introduction

In recent period, industrial waste usage becoming more popular in sustainability development. It protects the environment from the depletion of natural resources. Concrete is the highest consumable material used by human resources. It is the only product which contains maximum amount of non-renewable natural resources (Sakai and Noguchi 2012). Waste management becomes most challenging process for disposing ash in open environment (Terzić et al. 2015). The main advantages of lightweight concrete such as reduction of dead weight which leads to minimizing reinforcement and footing size, reduction in the size of the beam, column, and slab give more space availability, very good thermal insulation, more fire resistance and easy to transport (Kayali 2005). From the point of environment view, raw materials used for the production of lightweight concrete were obtained from industrial by-products. This will lead to the reduction of mining materials from natural resources. This paper deals with the production of semi-lightweight concrete using artificially made lightweight aggregates. In recent days, most of the renewable energy is generated from biomass such as agricultural wastes and forestry wastes. Once the energy is obtained, the ash generated was disposed in the open environment. It will contaminate the soil, leaching toxic substances into the ground-water and polluting environment by spreading through air and causing severe health problems to human lives (Vol et al. 1997). To avoid such unsustainability, the biomass wastes should properly utilize in the field of construction. Despite many advantages, lightweight concrete having limitations for using in some parts of building structures. Enormous investigations were done to develop high performed

P. Parthiban (✉) · J. Karthikeyan
National Institute of Technology-Tiruchirappalli, Tiruchirappalli, India
e-mail: parthiban.structural@gmail.com

J. Karthikeyan
e-mail: jk@nitt.edu

lightweight aggregates concretes having bulk density lesser than 1900 kg/m^3 than conventional concrete, but equal strength in the range of 30–80 MPa (Kiliç et al. 2003). In this research, calcite powder obtained from wood ash is used to produce lightweight aggregates as well as semi-lightweight concrete also prepared using those lightweight coarse aggregates.

19.2 Materials Used

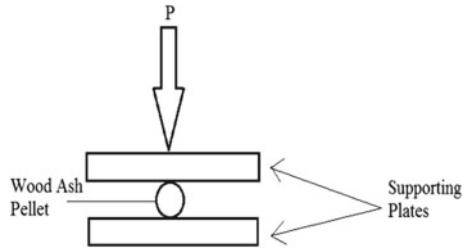
OPC 53 (Ordinary Portland Cement 53) was used for the entire mix in accordance with IS 269-2015 (kupdf.net_is-269-2015). The specific gravity and consistency were found to be 3.15 and 32% respectively. Coarse aggregate is artificially prepared Calcite powder pellets which have a specific gravity, water absorption and dry rodded density in 2.0, 24% and 1040 kg/m^3 respectively. Class F fly ash was used in the production of pellets which conforming to ASTM C618 (2010). Fine aggregate is river sand classified under grade III followed as per IS 383-2016 (2016) which has a specific gravity of 2.5 and water absorption as 0.6%. Super Plasticizer is used to maintain proper workability.

19.3 CPP Production

To achieve a good quality of sLWC, well-qualified pellets should be prepared and used for the production of sLWC. For that reason, five different types of CPP were prepared by altering the source materials without affecting the chemical composition. The source materials which are used in the preparation such as Waste cement, Fly ash (Class F) and Calcite powder. Pelletization technique is followed to prepare the pellets. Pelletization is done with the help of pelletizer shown in Fig. 19.1. A drum-type pelletizer with 650 mm Dia. and 220 mm depth which has two inclined blades at an angle of 45° is equipped. The drum is rotating at 36 rpm with the help of AC motor. The capacity of the drum is enough to produce 5 kg of pellets in a single round. This technique is the most economical, and most comfortable way of producing pellets compare to other techniques (i.e., sintering). The detailed specifications and properties of five types of CPP were given in Table 19.1. After the pelletization, the fresh pellets were set to dry for 24 h for hardening. After confirming the hardness of pellets by pressing with a finger, the CPP was kept in curing for 28 days to achieve adequate strength.

Fig. 19.1 A drum-type pelletizer**Table 19.1** Description and properties of CPP

ID	Description	Specific gravity	Bulk density (kg/m ³)	Water absorption (%)	(ICS) Crushing strength of individual pellets (MPa)
CPN	Calcite powder + NaOH (2 M)	1.89	968	28	2.36
CPF	Calcite powder (50%) + fly ash (50%)	1.92	1056	26.8	2.42
CPC	Calcite powder (70%) + cement (30%)	2.00	1157	29.4	2.75
CCP	Cement coated pellets	2.01	1300	22.5	3.48
CFC	Calcite powder (60%) + fly ash (20%) + cement (20%)	2.0	1140	23	4.44

Fig. 19.2 Load setup for ICS

19.4 Experiments Conducted on CPP

The experiments conducted on CPP are specific gravity, water absorption, bulk density and crushing strength of the individual pellet. The results were shown in Table 19.1. The crushing strength of pellets was determined using the formula given in Eq. (19.1) (Ugur and Ozturan 2010). CBR apparatus is used to determine the individual Crushing strength (ICS). Figure 19.2 illustrates the load set up. CPP is kept between two plates by loading diametrically. Crushing strength is determined by the sustainability of the pellet to maximum load. Minimum 20 Nos. of pellets is tested to determine adequate strength.

$$\sigma = \frac{2.8 \times P}{\pi \times X^2} \quad (19.1)$$

where

- σ = crushing strength (MPa),
- P = fracture load (N),
- X = distance between two plates.

19.5 Results and Discussion on the Properties of CPP

As it can be seen from Table 19.1, five different types of CPP (shown in Fig. 19.3a–f) were named as CPN, CPF, CPC, CCP, and CFC. The specific gravity of CPN is found to be 1.89 which comes under the lightweight category. CPN is made up of Calcite powder binding with a NaOH (2 M) solution. The preparation process involves calcite powder alone which leads to the reduction in bulk density as 968 kg/m³ compares to other CPP. The internal structure of CPN is found to be more porous due to the loose packing of calcite fines. CPN is prepared by coagulation of calcite powder using NaOH solution. When the CPN is kept for drying, the NaOH solution gets evaporated and makes the CPP more porous. This fact will lead to more water absorption as 28% and a reduction in ICS of CPP.

CPF is made up of 50% Calcite powder and 50% fly ash. By adding fly ash in CPP making, the internal structure has been improved. Water absorption also gets

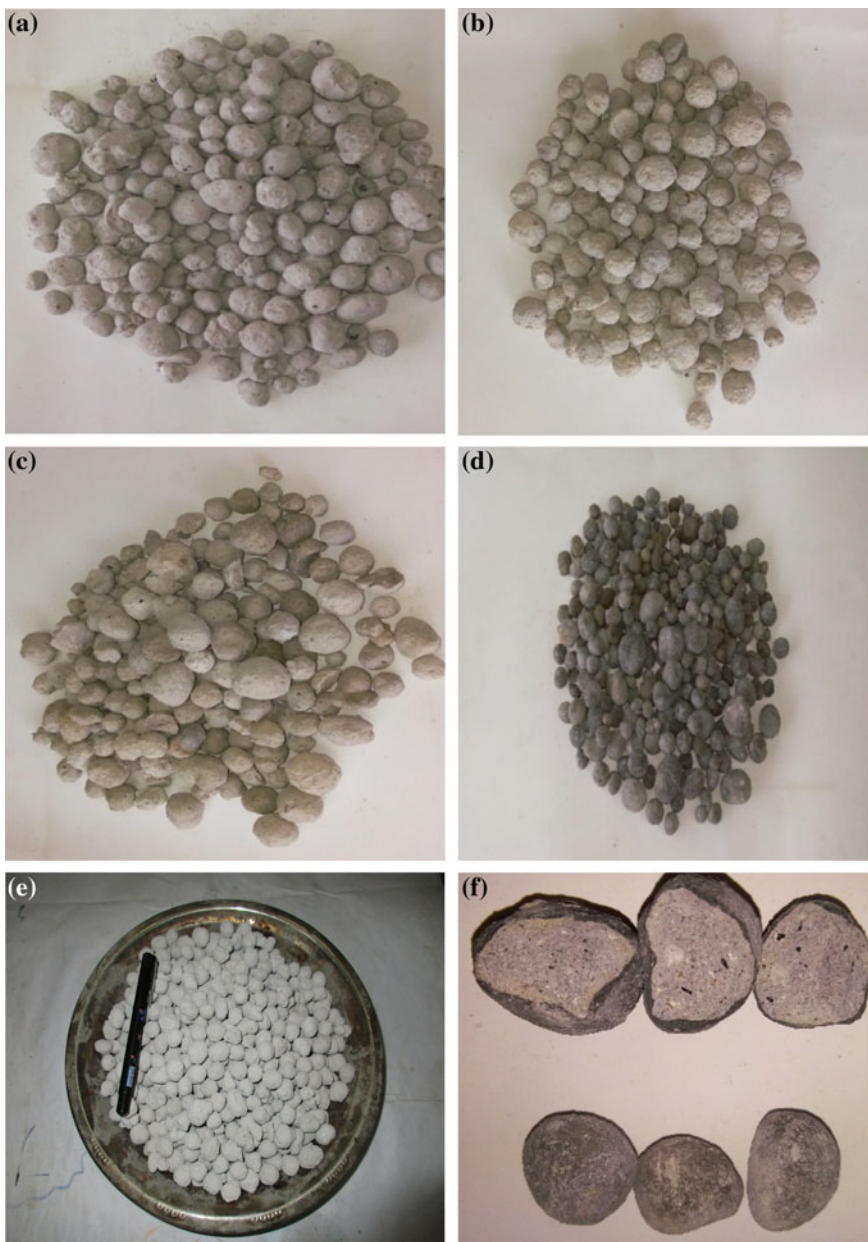


Fig. 19.3 a Calcite fines + NaOH(2 M), b calcite fines (70%) + cement (30%), c calcite fines (50%) + fly ash (50%), d cement coated pellets, e calcite fines (60%) + fly ash (20%) + cement (20%), f broken CCP with outer cement layer

reduced when compared to CPN. This will lead to the enhancement of ICS. In CPC, 70% of calcite powder is pelletized with 30% of cement which gives better ICS with water absorption as 29.4% which is found to be higher when compared with other CPP. This is attributed to the fact that the part of the calcite powder is higher than the cement content. Cement hydration involves in the strengthening of pellets rather than the micropores increases. Further, CPF pellets were coated with cement paste for strengthening purposes and referred as CCP. The properties of CPF were determined as 3.48 MPa of ICS, water absorption as 22.5% which is found to be lower than previous CPP. This is because of outer layer of cement diminishes the penetration of moisture into the CCP meanwhile, it increases the ICS. The outer cement layer acts as a shell membrane which protects the CCP from failure to some extent. From the test results of previously made CPP, CFC is prepared with better properties by the composition of calcite powder (60%), cement (20%), and fly ash (20%). The ICS is found to be 4.44 MPa with adequate water absorption as 24%, specific gravity as 2.0 and bulk density as 1140 which is most predominant values than other CPP. Finally, CFC is selected for the production of sLWC.

19.6 Results and Discussion on sLWC

ACI 211.1 method (Barton et al. 1998) was followed for mix design (shown in Table 19.2). sLWC is prepared by varying cement content as 300, 400 and 450 kg/m³ by using CFC as coarse aggregates. Cube specimens of size 100 mm × 100 mm × 100mm were prepared for compressive test and cylinder of size 100mm × 200mm were prepared for young's modulus test. Compressive strength was tested after 1-day, 7-days and 28-days curing. Modulus of elasticity was tested after 28-days curing. The graph between stress versus strain was shown in Fig. 19.4. The test results were given in Table 19.3. The maximum compressive strength of 28.4 MPa was achieved for 450 kg/m³ cement sLWC. The density of sLWC is found to be 2153 kg/m³. The highest elastic modulus as 21 GPa was achieved for 450 kg/m³ cement content.

Table 19.2 Mix details and slump

Cement (kg/m ³)	Fine aggregate (kg/m ³)	Coarse aggregate (kg/m ³)	Water (kg/m ³)	Plasticizer (kg/m ³)	Water/cement ratio	Slump (mm)
300	684	541	102	3.6	0.34	160
400	830	550	132	7.2	0.33	210
450	921	673	135	8.1	0.3	180

Fig. 19.4 Stress-strain graph

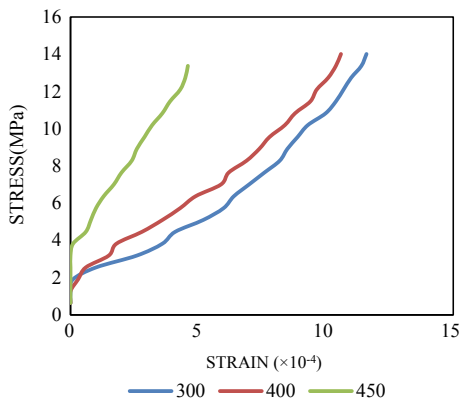


Table 19.3 Compressive strength, Young’s modulus and density of sLWC

Cement (kg/ m ³)	Compressive strength (MPa)			Young’s modulus (GPa)	Density (kg/ m ³)
	1-day	7-days	28-days		
300	6.6	18.4	23.8	11.11	2156
400	9.9	19.5	26.9	11.23	2183
450	13.3	20.1	28.4	20.93	2194

19.7 Conclusions

The following conclusion were drawn from the test results:

- A new lightweight aggregate was prepared from waste calcite powder in an economical and efficient way.
- From five different CPP, CFC with the composition of calcite powder, cement, and fly ash gives the better properties compared to other CPP.
- The maximum compressive strength of 28.4 MPa was achieved using 450 kg/m³ cement. Meanwhile, it has high modulus of elasticity as 21 GPa.
- Finally, M25 grade sLWC was achieved using calcite powder pellets.

References

ASTM C618-12a (2010) Standard specification for coal fly ash and raw or calcined natural pozzolan for use. ASTM, 3–6 <https://doi.org/10.1520/c0618>

Barton SG, Bell LW, Berg GRU et al (1998) Standard practice for selecting proportions for structural lightweight concrete (ACI 211. 2–98) reported by ACI Committee 211. Most 98:1–18

IS 383 (2016) Coarse and fine aggregate for concrete—specification

- Kayali O (2005) Flashag—new lightweight aggregate for high strength and durable concrete. [https://doi.org/10.1016/0091-3057\(87\)90012-8](https://doi.org/10.1016/0091-3057(87)90012-8)
- Kiliç A, Atiş CD, Yaşar E, Özcan F (2003) High-strength lightweight concrete made with scoria aggregate containing mineral admixtures. *Cem Concr Res* 33:1595–1599. [https://doi.org/10.1016/S0008-8846\(03\)00131-5](https://doi.org/10.1016/S0008-8846(03)00131-5)
kupdf.net_is-269-2015(1).pdf
- Sakai K, Noguchi T (2012) The sustainable use of concrete—preface. In: Sustainable use of concrete, pp i–xii. <https://doi.org/10.1016/j.biomaterials.2010.08.032>
- Terzić A, Pezo L, Mitić V, Radojević Z (2015) Artificial fly ash based aggregates properties influence on lightweight concrete performances. *Ceram Int* 41:2714–2726. <https://doi.org/10.1016/j.ceramint.2014.10.086>
- Ugur N, Ozturan T (2010) Effects of lightweight fly ash aggregate properties on the behavior of lightweight concretes. *J Hazard Mater* 179:954–965. <https://doi.org/10.1016/j.jhazmat.2010.03.098>
- Vol B, Obernberger I, Biedermann F et al (1997) Concentration of inorganic elements in biomass fuels and recovery in different ash fractions. *Biomass Bioenergy* 12:211–224

Chapter 20

Solar Desalination Using Modified Parabolic Trough Concentrator



D. Deebhesh, B. Sreejith and O. Arjun

20.1 Introduction

Fresh water is essential for all the living beings. Two-third of the earth is covered by water. But pure water available for human use is very less. Majority of the water is available in earth in the form of saline water in sea. By removing salt and minerals from water, we can obtain pure water.

Desalination is the process of removing salt and mineral components from the saline water. Reverse osmosis, Membrane Distillation, Forward osmosis, Electro dialysis (ED) and Electro Dialysis Reversal (EDR) are some of the methods used for desalination of water. The common method is to boil saline water and condense the steam. The old technology used heat from fossil fuel to convert water into steam. The fossil is an expensive and unsustainable energy source on which we cannot depend for a long time. So we need to use other source like renewable energy for the conversion. The main source of renewable energy is the sun.

In this article, feasibility of a simple system utilizing modified parabolic trough concentrator to extract pure water from saline water using solar energy is discussed. Objectives of the present study are fabrication of solar desalination system with modified parabolic trough concentrator, calculation of its performance characteristics, and study of various parameters effecting the performance of the system.

D. Deebhesh · B. Sreejith (✉) · O. Arjun
Department of Mechanical Engineering, Government Engineering College,
Kozhikode, Kerala, India
e-mail: sreejith@geckkd.ac.in

D. Deebhesh
e-mail: deebheshdevan@gmail.com

O. Arjun
e-mail: oarjun115@gmail.com

20.2 Literature Review

A common technique used for desalination is reverse osmosis. In this method, saline water is forced through the rolls of membrane and leaves the salt behind. The most expensive challenge is the fouling of membrane by microbial organism (Pugsley et al. 2016).

There are many desalination systems developed using solar energy. One of the common methods is solar still. The main disadvantage of solar still is that the production rate is very low compared to other technologies.

Utilizing solar collectors we can increase the production rate of solar still. Utilizing the solar concentrator can achieve the temperature above 100 °C. Ahmed Hamed et al. (2006) studied concentrating solar power for sea water thermal desalination. Extensive pilot plant tests for one year was performed and analysed the performance using Fresnel Concentrating solar power (CSP) collector in Saudi Arabian climatic conditions.

Al-Sulaiman et al. (2015) conducted a detailed analysis of a system using a parabolic trough concentrator (PTC) for humidification dehumidification (HDH) desalination. He performed a Thermodynamic analysis of the HDH desalination systems with two configurations integrated with parabolic trough concentrator.

Yadav et al. (2013) performed an experiment on PTC with various reflector material such as Stainless steel sheet, Aluminium foil and Aluminium sheet. Using stainless steel, a temperature of 42.1 °C was obtained which can be used for room heating. Air temperature of 48.2 and 52.3 °C was obtained at outlet using aluminium foil and aluminium sheet, respectively.

Kasaeian et al. (2015) developed a fabricated parabolic trough with steel mirror. Vacuum tube painted in black, black chrome coated copper bare tube, black chrome coated non evacuated copper glass enveloped tube, and vacuumed copper tube with black chrome coating were used in his experiment. They concluded that the highest absorptivity and thermal conductivity is for copper absorber tube having black chrome coating.

Montes et al. (2010) studied the use of a thermofluidynamic model of parabolic trough concentrator. Energy balancing is used here and evaluated the performance with oil, molten salt, or water/steam, as different working fluids.

Pradhana et al. (2016) developed a compound parabolic trough collector with heat pipe. Thermal efficiency of the system is slightly higher for 45° and slightly lower for 25° inclination of PTC. After one hour, water attained a temperature of 100 °C and the water started to boil, so this can be used to boil water.

Solar desalination is a method of desalinating saline water using solar energy. Solar desalination methods can be divided into two; direct and indirect methods. In direct method the solar collector is directly coupled with the desalination system. Solar still is most commonly used in desalination and distillation.

In indirect method there are two separate systems in which one is used for collecting the radiation like photovoltaic and other a separate conventional desalination plant. The production rate is usually directly proportional to the efficiency of the plant. Indirect solar desalination system solar having solar photovoltaic panels coupled with reverse osmosis is common nowadays.

Zurigat et al. (2004) done a modelling and performance analysis of a regenerative solar desalination unit. They identified various parameters effecting the performance and concluded that the regenerative solar still have 20% more efficiency than the conventional type. Qiblawey and Banat (2008) explained solar thermal desalination technologies.

Pugsley et al. (2016) described about global applicability of solar desalination. He reviewed different literature and analysed economic and environmental feasibility. Reverse osmosis driven desalination is the leading technology but the cost of water is more than that of fossil fuel powered desalination.

Shafii et al. (2016) manufactured and studied a modified solar desalination system using evacuated tube flat plate collector. He introduced a passive desalination system which effectively utilizing the advantages of twin glass evacuated tube collector. He developed the system with the solar collector functioning as basin. This configuration increases efficiency of the system due to decrease in thermal resistance and maximum production was determined as $0.83 \text{ kg}/(\text{m}^2 \text{ h})$.

Mosleh et al. (2015) developed a desalination system combining heat pipe, twin glass evacuated tube and linear parabolic trough concentrator. They tested the system and observed that efficiency and production rate of the modified system has been increased up 65.2% and $0.933 \text{ kg}/\text{m}^2 \text{ h}$ respectively.

20.3 Solar Thermal Collector

Solar thermal collectors are devices which gains heat by absorbing sunlight. Common solar collectors are solar hot water panels, solar parabolic trough, solar towers, solar air heater, etc.

20.3.1 *Parabolic Trough Concentrator (PTC)*

In the field of power generation parabolic trough concentrator (PTC) plays a major role since 1980. The main components of a parabolic trough collector are a concentrator and a receiver. The concentrator is in the shape of a parabola and the receiver is provided on the focal axis of the parabola.

20.3.2 Design Parameters of PTC

Concentration Ratio

It is the ratio of the effective area of the aperture to the surface area of the absorber. For parabolic dish the value changes from unity to few thousands. It is also known as geometric concentration ratio and area concentration ratio.

$$CR_g = \frac{A_a}{A_r} \quad (20.1)$$

A_a effective area of aperture

A_r surface area of absorber

Aperture (w)

It is the opening plane of the concentrator through which the solar radiation passes. For a cylindrical or linear concentrator, it can be characterized by its width, while for a surface of revolution; it was characterized by the diameter of the opening.

Acceptance Angle ($2\theta_a$)

It is defined as the angle at which beam radiation may deviate from normal to aperture plane and yet reach the absorber. Collectors with large acceptance angle need occasional tracking, whereas collectors with small acceptance angle need continuous tracking.

Intercept Factor (γ)

It is the fraction of radiation, which is reflected or refracted from the concentrator and is incident on the absorber. Its value will be close to unity.

20.3.3 Thermal Performance of PTC

The thermal performance of PTC is determined by solar efficiency factor η . It is defined as the ratio of net heat gain to the solar radiation energy based on diffuse reflection area of solar collector.

$$\eta = \frac{\dot{m}C_p(T_{out} - T_{in})}{I(A_a - A_s)\rho} \quad (20.2)$$

where

\dot{m} water flow rate

C_p specific heat

P reflectivity

A_s	shaded area
A_a	aperture area
T_{out}	outlet temperature
T_{in}	inlet temperature
I	solar intensity.

20.4 Desalination System with Modified PTC

The proposed system consists of a modified parabolic trough concentrator, receiver and a condenser. Receiver outlet is connected to the condenser. The steam produced from the receiver is passed to the condenser and condenses. Water coming through the outlet of the condenser is desalinated water.

20.4.1 Modification in PTC

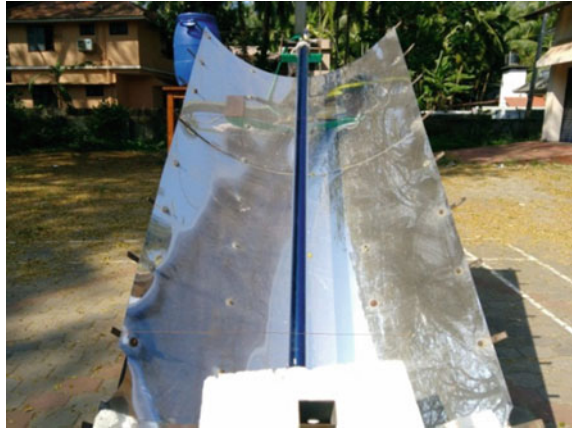
For efficient energy transfer conduction and convection losses must be minimum. For achieving this, vacuum can be provided and insulation can be used in the collector. A selective coating can be provided for maximum absorption of radiation and minimizing the re-radiation from the collector. For a PTC, energy loss occurs in the form of conduction as well as convection. Energy transferred to the working fluid is reduced due to these losses. More efficient systems like evacuate glass tube collectors can be used to overcome these issues. In this type of collector, the space between two concentric glass tubes is evacuated and a selective coating is provided to the inner glass tube.

A modified PTC is used in the proposed desalination system (Arjun and Sreejith 2018). The reflecting material used here is acrylic glass which is cheap. An evacuated absorber tube is introduced. A desalination unit is attached to the PTC. The desalination system is connected to the outlet of the collector. Arrangement was performed in such a manner that the steam produced from saline water condenses on the condenser walls of desalination system. The feed water rate is adjusted to produce steam from the receiver. The total setup is adjusted to required inclination and a condenser is attached to the outlet of the receiver tube.

The receiver used here is concentric glass tubes and space between them is evacuated. The inner tube is coated with a selective coating. The modified PTC is shown in the Fig. 20.1. The working fluid is circulated inside the collector for more effectiveness. Tracking has to be done for proper concentration of solar rays on the receiver tubes. The tracking was done by manually rotating the collector according to the position of the sun.

The evacuated tubes are made up of borosilicate, which is very strong with high transparency (>92%). The outer tube is designed in such a manner that the dispersion is minimum.

Fig. 20.1 Parabolic trough concentrator



The evacuated tube means the removal of air between the two concentric tubes. The vacuum between the tubes is an excellent insulation to the heat loss due to the convection and conduction loss. The heat from the radiation is absorbed in the inner tube with minimum heat loss.

The barium getter is placed on the base of the container. The inner surface may release absorbed gas after a long time. The getter continuously removes the gases. The getter is the clear indicator of the vacuum inside. The silver colour changes to white which means the vacuum is completely lost.

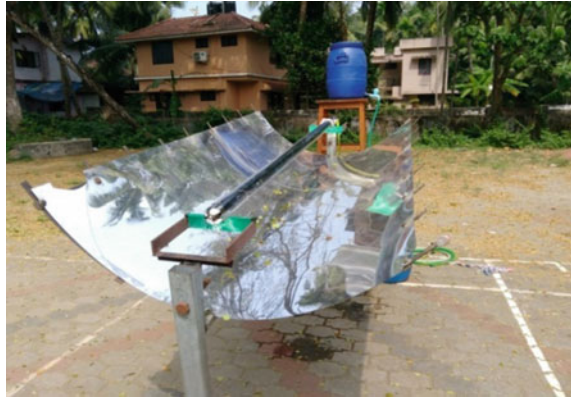
The absorber coating is a base layer of aluminium placed outside of the inner tube which is followed by a layer of AlN (aluminium nitride). This coating is an excellent absorber of solar radiation and minimum reflectivity. The selective coating used here is CuO thin film which is made by sputtering. Specification of receiver is shown in Table 20.1.

Table 20.1 Specifications of receiver

Material of glass	Borosilicate glass
Length	1800 mm
Outer diameter	57 mm
Inner diameter	47 mm
Thickness of glass tube	Outer tube thickness: 1.8 mm, inner tube thickness: 1.6 mm
Selective coating type	AlN/CU—Sputtering
Vacuum rate	$P \leq 5.0 \times 10^{-4}$ Pa
Coefficient of thermal expansion	$3.3 \times 10^{-6}/k$
Cost	810/Piece

Table 20.2 Specifications of PTC

Width of the concentrator, W	1 m
Length of the concentrator, L	1.8 m
Rim angle of the trough, ϕ	90°
Concentration ratio, C	5.2
Aperture area, Aa	1.8 m ²
Focal length	0.25 m
Half acceptance angle	1.50

Fig. 20.2 Experimental setup for performance analysis

In this experiment the material used for parabolic reflector is acrylic glass which has a reflectivity nearly same as that of miro sun. The specification of the parabolic trough concentrator is given in the Table 20.2. Figure 20.2 shows the experimental setup.

20.4.2 Desalination Unit

The desalination unit consists of a condenser made of aluminium attached to the outlet of the parabolic trough. It is a cylindrical shaped condenser where steam from the saline water condenses and produce pure water. It is of 12 cm diameter and 85 cm length. The inlet is provided on the base of the cylinder and outlet is provided on bottom side wall. Condenser is exposed to the atmosphere and heat from the wall is lost due to the convection. The condenser in the desalination system is shown in Fig. 20.3.

During the experiment, it was observed that saline water was entering the condenser resulting in mixing of row saline water with pure water. Two different methods were used between the receiver and the condenser to eliminate this mixing. First method shown in Fig. 20.4 uses a steam trap. Water entering to the condenser gets trapped in the steam trap provided. The second configuration is providing a bypass system between the PTC and condenser as shown in Fig. 20.5. Water entering the condenser has been removed through the bypass provided.



Fig. 20.3 Condenser

Fig. 20.4 Experiment setup using steam trap



Fig. 20.5 Experiment setup using bypass



20.5 Thermal Performance of a Solar Desalination Unit

The efficiency of solar desalination unit can be determined by following equation:

$$\eta = \frac{\dot{m}h_{fg}}{AI} \tag{20.3}$$

where

- \dot{m} production rate
- h_{fg} latent heat of water
- A projected area of tube.

20.6 Experiment

For the preliminary study the efficiency of the parabolic trough collector using saline water was estimated. For this, the performance test runs on 4 different flow rate and the inlet temperature, outlet temperature and solar intensity are measured. The efficiency was calculated using Eq. 20.2. The PTC is arranged in south- east direction and tracking is made manually. For measuring the temperature, K-type thermocouples are used at inlet of the receiver tube and outlet of the receiver tube.

The calibration curves of the thermocouples are shown below, in Figs. 20.6 and 20.7 respectively.

The whole setup was arranged in an inclined angle. The steam from the receiver moves upward and condenses in the condenser. The outlet flow rate is measured using a measuring jar. The experiment was conducted between 9 am to 5 pm., and

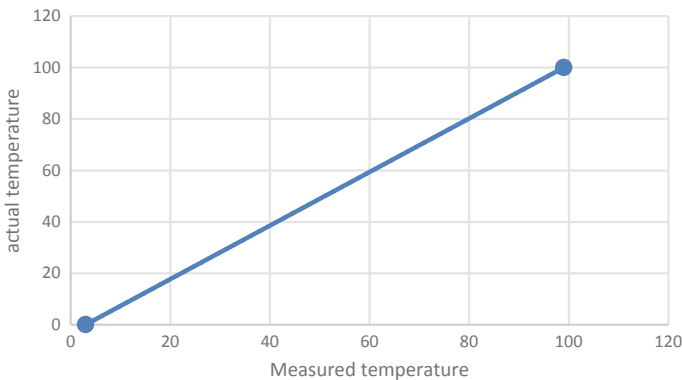


Fig. 20.6 Calibration curve of thermocouple 1

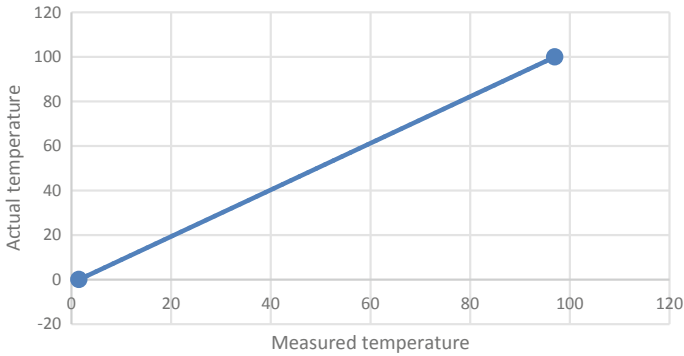


Fig. 20.7 Calibration curve of thermocouple 2

the readings were noted at 1 h interval. Feed water was provided at an interval of 15 min. Solar intensity was measured using a lux meter. The temperature at inlet, outlet, steam, condensed water and condenser wall were noted.

Readings were noted separately with steam trap and bypass for 35° inclination of PTC. Another set of experiments were performed by changing the angle of inclination of modified PTC and results are compared. The experiments were performed at 25°, 35° and 45° inclination of modified PTC to determine the optimal angle of inclination.

20.7 Results and Discussion

The experiment was carried out at Government College of Engineering, Westhill, Kozhikode (11.28627°N, 75.769965°E) during the period of March 2018. The maximum temperature and efficiency data for different flow rate is given in Table 20.3.

Table 20.3 Experiment result with varying flow rate

Sl.No.	Inlet temp (°C)	Outlet temp (°C)	Mass flow rate (Kg/s)	Intensity of radiation (W/m ²)	Heat absorbed (W)	Net radiation strike on trough (W)	Efficiency (%)
1	38.1	78.2	0.005	954	838.09	1473.58	56.87
2	40.2	86.5	0.004	972	774.136	1501.38	51.56
3	39.8	101.2	0.0025	966	641.63	1492.11	43
4	39	106.1	0.0017	950	476.8126	1467.40	32.49

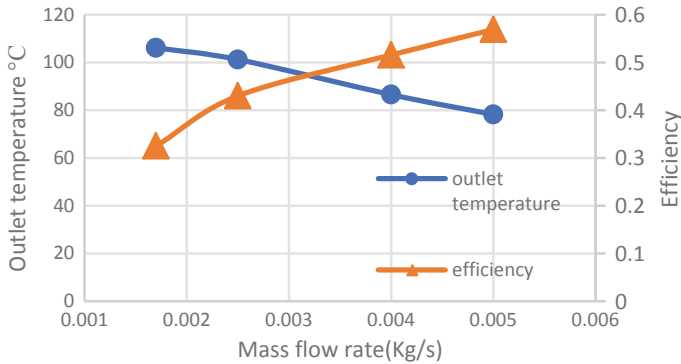


Fig. 20.8 Variation of efficiency and outlet temperature with mass flow rate

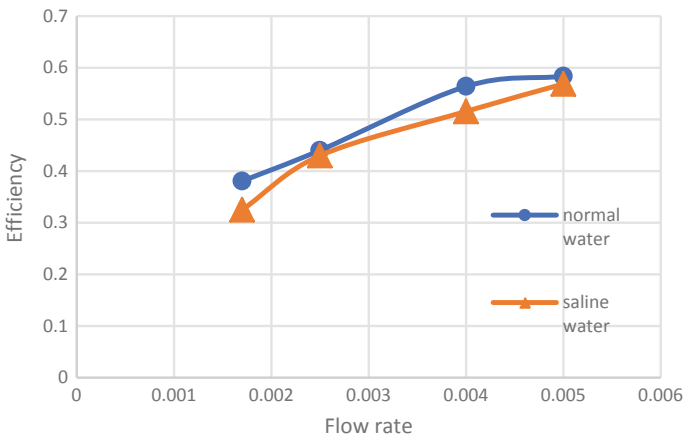


Fig. 20.9 Variation of efficiency of PTC using normal water and salt water

Variation of efficiency and outlet temperature with mass flow rate for saline water is shown in the Fig. 20.8. Comparison of efficiencies of normal and saline water is shown in the Fig. 20.9. The outlet flow temperature and efficiency are inversely proportional. Efficiency of PTC with saline water is less compared to that of normal water.

The yield for each experiment with steam trap and bypass were noted at 35° inclination of PTC. Figure 20.10 shows the variation of efficiency of system with trap and bypass. One can observe that the system with bypass has higher efficiency.

Three different experiments were conducted on the system with bypass to determine the effect of angle of inclination of PTC on performance. Experiments were done on three angles 25°, 35° and 45°.

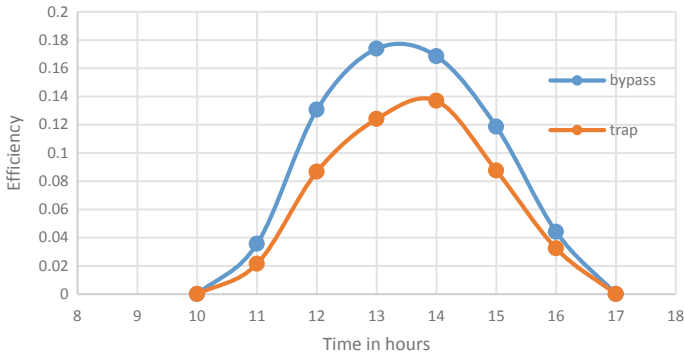
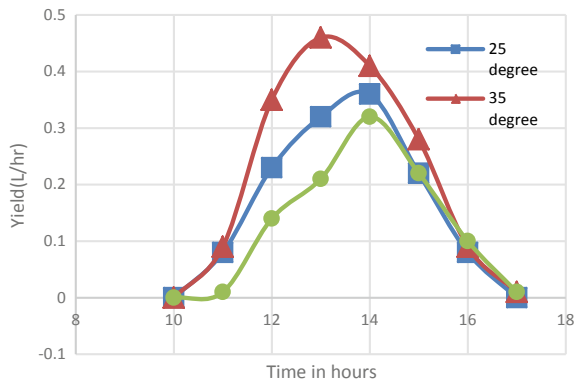


Fig. 20.10 Variation of efficiency curves of bypass and trap

Fig. 20.11 Comparison of yield for 3 inclination angles



Comparison of yield and efficiencies for the three angles are shown in the Figs. 20.11 and 20.12 respectively. For the system with 25° inclination, maximum yield and efficiency of 0.36 l/h and 13.34% respectively was obtained at 2 PM. By analysing the yield curve we can see that the maximum yield was obtained for the 35° inclined experiment. The lower yield obtained is for the 45° inclined experiment. Maximum yield of 0.32 l/h was obtained at 45° inclination at 2 PM. Same trend can be observed on the efficiency curve. The maximum efficiency has been obtained for the 35° and minimum for 45° inclination.

For 45° inclination the efficiencies lower due to less solar radiation received because of the angle. So the steam production is lower and there for the efficiencies are also decreased. For the 25° angle more radiation will concentrate on the tube but bubble problem will arise in this case. The steam bubble produced will not move smoothly to upper side because of the low inclination.

Both the radiation and the bubble smooth moving are optimal for the 35° inclination. So the maximum efficiencies and the maximum yield are obtained for 35° inclination.

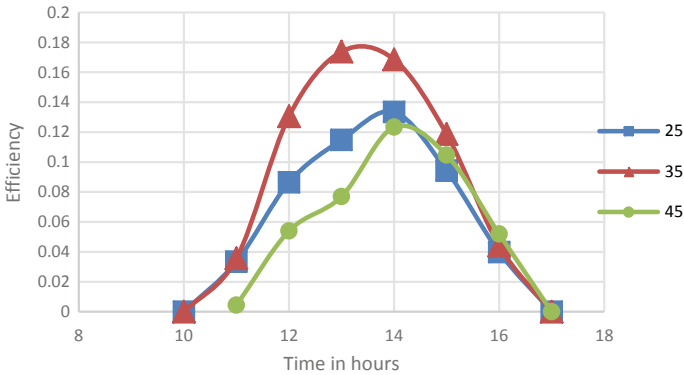


Fig. 20.12 Comparison of efficiency for 3 inclination angles

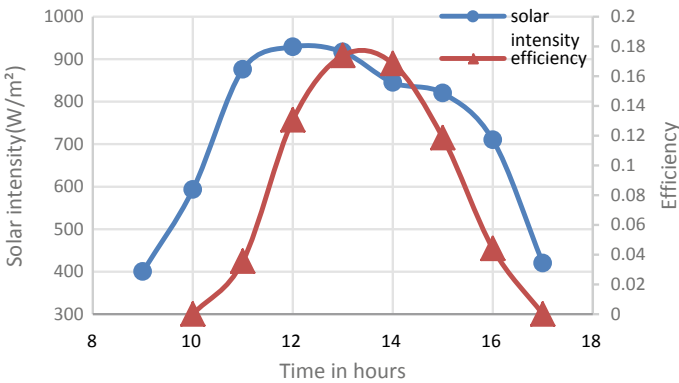


Fig. 20.13 Variation of solar intensity and efficiency with time in hours for 35° inclination

Figure 20.13 shows the variation of solar intensity and efficiency with time in hours for the system with bypass having 35° inclination of PTC. Figure 20.14 showing the comparison between solar intensity and yield for 35° inclination, and Fig. 20.15 shows the comparison between yield and efficiency for the system.

From Fig. 20.13 we understand relation between the solar intensity and the efficiency. The graph shows that the maximum efficiency of 17.38% was obtained after the maximum solar intensity available. Efficiency was low in the morning and increase to a peek at 1 PM, then it decreases. Efficiency increases with increase in solar intensity.

From Fig. 20.14 we can understand the relation between yield and solar intensity. Like efficiency yield increases with increase in solar intensity. Maximum yield of 0.46 l/h obtained after the peak of solar intensity.

The efficiency and the yield show a similar trend. Both have same shape and changes accordingly as shown in the Fig. 20.15.

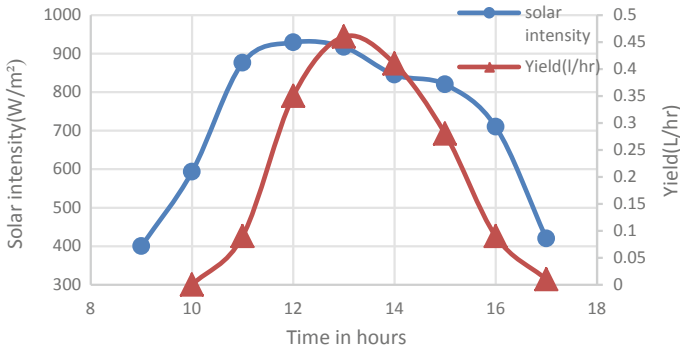


Fig. 20.14 Variation of solar intensity and yield for 35° inclination

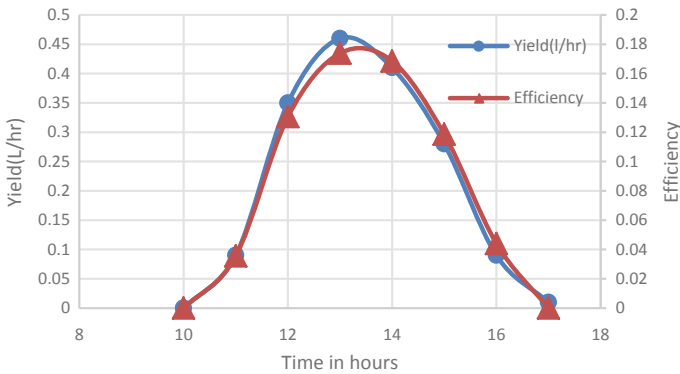


Fig. 20.15 variation of yield and efficiency for 35° inclination

20.8 Conclusions

From the study, it has been concluded that efficiency of modified PTC with salt water is slightly lower than normal water. Maximum efficiency was obtained for the desalination system with bypass compared to steam trap. This is due to lower condensation of steam in bypass compared to steam trap. Maximum efficiency and yield was obtained for 35° of inclination of PTC.

Comparing to an existing system containing evacuated tube with working fluid as ethanol (Kumaresan et al. 2017), this system is so simple and easy to manufacture. There are no complicated operations for this system. Design is simple and we can obtain an efficiency of 17.38%, compared to 22.1% in the earlier system.

This system can be used in residential area with low cost. Proper tracking can improve the performance. Automatic tracking system can be introduced for this purpose.

References

- Ahmed Hamed O, Kosaka H, Bamardouf KH, Al-Shail K, Al-Ghamdi AS (2006) Concentrating solar power for seawater thermal desalination. *Desalination* 396:70–78
- Al-Sulaiman FA, Zubair MI, Atif M, Gandhidasan P, Al-Dini SA, Antar MA (2015) Humidification dehumidification desalination system using parabolic trough solar air collector. *Appl Therm Eng* 75:809–816
- Arjun O, Sreejith B (2018) Modification of a parabolic trough collector and its energy analysis. In: *Proceedings of second international conference on progressive developments in mechanical engineering*, pp 435–442
- Kasaeian A, Daviran S, Danesh Azarian R, Rashidi A (2015) Performance evaluation and nanofluid using capability study of a solar parabolic trough collector. *Energy Convers Manag* 89:368–375
- Kumaresan G, Sudhakar P, Santosh R, Velraj R (2017) Experimental and numerical studies of thermal performance enhancement in the receiver part of solar parabolic trough collectors. *Renew Sustain Energy Rev* 77:1363–1374
- Montes MJ, Abánades A, Martínez-Val JM (2010) Thermofluidynamic model and comparative analysis of parabolic trough collectors using oil water/steam molten salt as heat transfer fluids. *J Solar Energy Eng* 132:140–146
- Mosleh HJ, Mamouri SJ, Shafii MB, Sima AH (2015) New desalination system using a combination of heat pipe, evacuated tube and parabolic through collector. *Energy Conversion Manage* 99:141–150
- Pradhan D, Mitra D, Neogi S (2016) Thermal performance of a heat pipe embedded evacuated tube collector in a compound parabolic concentrator. *Energy Proc* 90:217–226
- Pugsley A, Zacharopoulos A, Deb Mondol J, Smyth M (2016) Global applicability of solar desalination. *Renewable Energy* 88:200–219
- Qiblawey HM, Banat F (2008) Solar thermal desalination technologies. *Desalination* 220:633–644
- Shafii MB, Mamouri SJ, Lotfi MM, Mosleh HJ (2016) A modified solar desalination system using evacuated tube collector. *Desalination* 396:30–38
- Yadav A, Kumar M (2013) Experimental study and analysis of parabolic trough collector with various reflectors. *World Academy Sci Eng Technol* 7(12):1659–1663
- Zurigat YH, Abu-Arabi MK (2004) Modelling and performance analysis of a regenerative solar desalination unit. *Appl Therm Eng* 24:1061–1072

Chapter 21

Thermal Performance of Loop Heat Pipes Using Nanofluids



Jobin Jose and Rajesh Baby

21.1 Introduction

The loop heat pipes (LHPs) operate on a multi-phase fluid-flow cycle which is maintained by a capillary medium in the evaporator. It is a heat transfer device which can transmit a large amount of heat over a long distance with negligible temperature difference. In steady-state operation these heat pipes have high thermal conductance. Thus, LHPs are also known as super thermal conductors. Their advantages include electricity-free operation, no moving parts, and ability to work even with small temperature differences and transfer heat energy over long distances with negligible pressure drop (Adoni et al. 2010).

Pauken et al. (2000) experimentally studied the heat transfer characteristics of LHP with two working fluids, i.e. ammonia and propylene. The constant conductance performance of the LHP was found to be 170 W/K with ammonia and 44 W/K for propylene. The thermal performance of an LHP with acetone as working fluid was experimentally studied by Riehl et al. (2005). Results show that the system could present reliable performance in all situations with power level as low as 1 W. Also higher operating temperatures can be obtained when evaporator is above the condenser. Bai et al. (2000) developed a model for start-up process on the basis of node network method. These nodes were mainly classified into two, namely, fluid nodes and wall. Zhao et al. (2010) introduced a solar water heater based on LHP technology. It resulted in the reduction of fossil fuel consumption and carbon emissions associated with buildings hot water production and supply. Vlassov and Riehl (2005) developed a considerably precise condenser and transient nodes in the compensation chamber and evaporator and was found that model was able to predict

J. Jose (✉) · R. Baby
Department of Mechanical Engineering, St. Joseph's College of Engineering
and Technology, Palai, Kerala, India
e-mail: jobinjose93@gmail.com

transient behaviour of LHP within 3–4 °C of accuracy. Lin et al. (2010) conducted fundamental study of a dual compensation chamber. The experimental results show that a V-shaped curve operational curve is obtained for heat loads above 50 W. Thermal behaviour of a cryogenic LHP was experimentally studied by Gully et al. (2011) for space applications. Results indicate that a small heating load applied to the cold reservoir allowed to maintain a constant subcooling and the system behaves as a capillary loop. Vasiliev et al. (2009) developed a LHP for cooling of high power electronic components. The experimental results suggest that when high power dissipation levels are available low conductivity wick should be adopted for LHP applications.

Huang et al. (2009) categorised the start-up phenomenon of LHP into four modes, i.e. oscillation, failure, normal and overshoot. In the failure mode, evaporator temperature could not reach a steady-state instead it continues to rise. In oscillation mode, evaporator temperature increased due to the continued heat input and vapourisation of the fluid. Zhang et al. (2013) developed a solar photovoltaic heat pump system for generating hot water. After the experimental investigations the thermal, electrical and overall efficiency of the module were 40%, 10%, and 50%, respectively. The systems overall performance coefficient was 8.7. Jose et al. (2018) conducted a review on recent advances on loop heat pipes. It was concluded that investigations based on LHPs using nanofluids were scarce. The thermal performance of LHP using alumina nanoparticles was experimentally investigated by Akshay et al. (2018). It was found that the evaporator temperature can be reduced by 12% using nanofluids than deionised water.

The application of nanofluids in LHP is a challenging area of research, which is in its growing stages. The present study deals with the numerical investigations on the thermal performance of LHPs using nanofluids. The nanofluids considered are silica–water, copper–water and alumina–water nanofluid at 2% nanoparticle concentration. Heat input ranges from 40 to 320 W in steps of 40 W. The thermal performance of the LHPs using nanofluids are compared with that of deionized water (baseline case).

21.2 Numerical Modelling

A three dimensional model of LHP is designed as shown in Fig. 21.1. The detailed specifications of LHP are shown in Table 21.1.

The simulation is performed in the commercial software package ANSYS FLUENT. The 3D model of LHP is made in Catia V5 and is exported to ANSYS 14. The heat flux of 23,000 W/m² is applied on the evaporator base. The initial temperature is taken as 22 °C. After modelling the LHP, it is meshed with an element size of 2,40,514 as shown in Fig. 21.2.

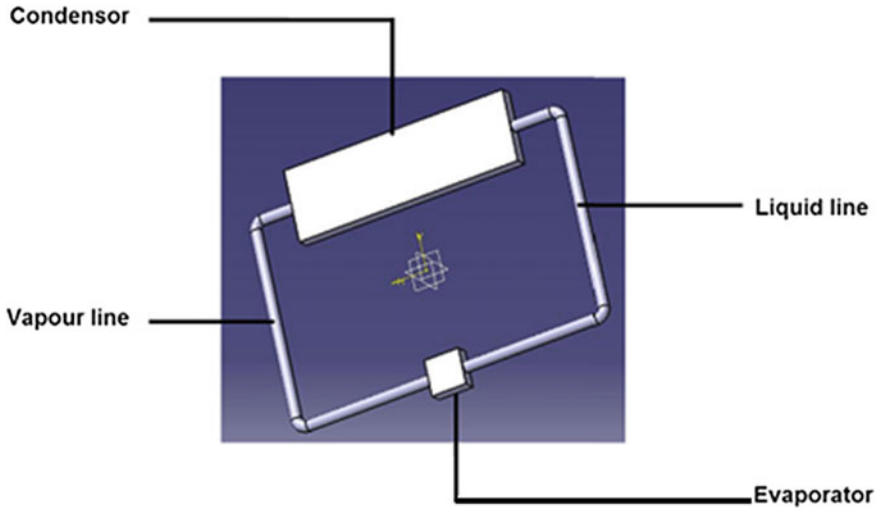
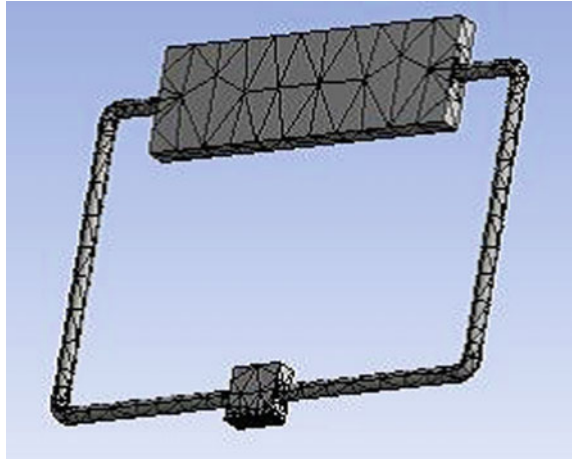


Fig. 21.1 Model of LHP used in the present study

Table 21.1 Specifications of LHP used for the numerical analysis

Specification	Dimension/material
<i>Evaporator</i>	
Dimension (mm)	L45 × W45 × H22
<i>Compensation chamber</i>	
Dimension (mm)	L45 × W38 × H22
Material	Copper
<i>Condenser</i>	
Dimension (mm)	L315 × W96 × H60
Material	Acrylic
<i>Vapour line</i>	
Outlet diameter (mm)	13
Inlet diameter (mm)	11
Length (mm)	490
<i>Liquid line</i>	
Outlet diameter (mm)	13
Inlet diameter (mm)	11
Length (mm)	490

Fig. 21.2 Meshed model of LHP



21.3 Governing Equations

During operation, the coated surface of the evaporator will absorb the heat input provided. Part of the absorbed energy will be dispersed back to the ambient while the remaining energy will be absorbed by the heat pipe fluid. This process is expressed as:

$$Q_e = Q_i - Q_{\text{loss},e} \quad (21.1)$$

where Q_e = heat absorbed by evaporator and Q_i = heat input. Assuming the evaporator surface temperature to be T_e , the heat loss $Q_{\text{loss},e}$ from the evaporator to the ambient is expressed as (US Department of Energy 1992):

$$Q_{\text{loss},e} = \frac{T_e - T_{\text{amb}}}{R_{\text{amb}}} \quad (21.2)$$

$$R_{\text{amb}} = \left(\frac{1}{h_{\text{amb}}} + \frac{1}{\sigma Q_e (T_e + T_{\text{amb}})(T_e^2 + T_{\text{amb}}^2)} \right) \frac{1}{A_e N_e} \quad (21.3)$$

where T_{amb} = ambient temperature, A_e = evaporator area, N_e = number/quantity, σ = Stefan Boltzmann constant, Q_e = emissivity of evaporator, h_{amb} = ambient convective heat transfer coefficient and R_{amb} = thermal resistance by ambient. The absorbed heat Q_e is instantaneously taken away by means of the heat pipes loop. This could be achieved by condensation of vapour on the condenser surface and evaporation of liquid in the evaporator section. This part of heat Q_{e-c} is written as (US Department of Energy 1992; Riffat et al. 2005):

$$Q_{e-c} = \frac{T_e - T_c}{R_e + R_w + R_v + R_f + R_c} \quad (21.4)$$

where R_e , R_w , R_v , R_f , and R_c represents thermal resistance of evaporator, wick, vapour line, and condenser, respectively. Since the condenser temperature is high, certain amount of the heat which is transferred to the condenser surface will be dissipated to the ambient. The heat output from the condenser Q_o is expressed as:

$$Q_o = Q_c - Q_{loss,c} \quad (21.5)$$

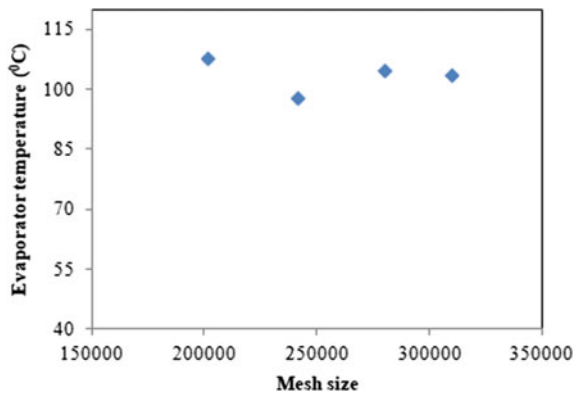
Assuming the condenser surface with the temperature of T_c , $Q_{loss,c}$ which is the heat dispersion from the condenser to the ambient could be similarly calculated by using Eq. (21.2).

21.4 Grid Independence Study and Validation

Grid independence study was performed to analyse the influence of mesh size on the numerical results. The maximum evaporator temperature is measured at different mesh sizes. Among them, four mesh sizes were selected considering the variation of obtained results from the experimental result available in the literature (Huang et al. 2009). The maximum evaporator temperature for different mesh sizes is shown in Fig. 21.3.

The maximum evaporator temperature obtained from the present study is 98.15 °C for a mesh size of 2,40,514 and that reported in the experimental work is 101.24 °C with a percentage deviation of only 3%. So, the grid size corresponding to 98.15 °C is used for further numerical investigations.

Fig. 21.3 Evaporator temperature at different mesh sizes



21.5 Results and Discussions

21.5.1 Effect of Nanofluids on Evaporator Temperature

The evaporator temperature of LHP for heat input ranging from 40 to 320 W using deionised water, alumina–water, copper–water and silica–water nanofluids are shown in Fig. 21.4. It is observed that evaporator temperature increases with the increase in heat input in all cases. But evaporator temperature of the LHP is lower when nanofluids are used. The reduction in evaporator temperature obtained by LHP using alumina–water, copper–water and silica–water nanofluids are 20%, 25% and 27%, respectively. Among the nanofluids, maximum reduction in evaporator temperature is obtained when silica–water nanofluid is used. Thus, LHP will be able to absorb more amount of heat which makes it suitable for thermal management of electronic devices.

21.5.2 Effect of Nanofluids on Transient Temperature Distribution of LHP

The transient temperature distribution of LHP using deionised water, copper–water, silica–water and alumina–water nanofluids are shown in Fig. 21.5. Heat input is varied from 40 to 320 W in steps of 40 W. It can be observed that with the addition of nanoparticles, the temperature of LHP at all points reduced significantly than using deionised water. It is found that LHP takes 800 s to attain steady-state when deionised water is used as working fluid. But when nanofluids are used it is reduced to almost 650 s. It is due to better thermal properties of nanofluids. Maximum reduction in evaporator temperature and time required to attain steady-state is

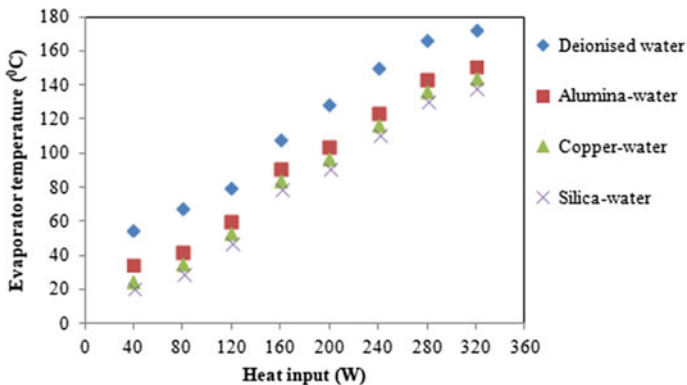


Fig. 21.4 Evaporator temperature versus heat input

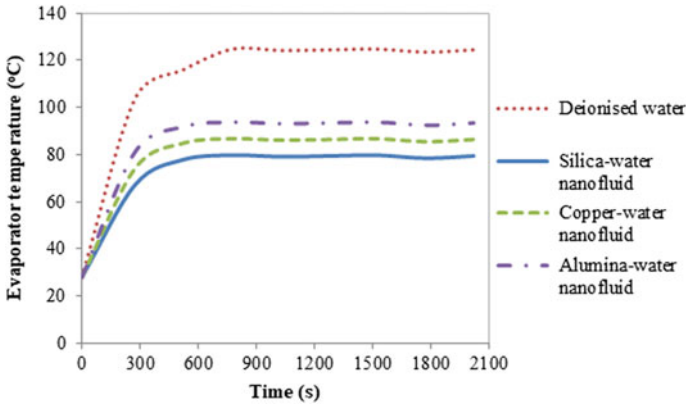


Fig. 21.5 Transient temperature distribution of LHP

possible with the use of nanofluids. From the present study, it is found that silica–water nanofluid is best suited as a working fluid for enhanced thermal performance of LHP.

21.5.3 Effect of Nanofluids on the Thermal Resistance of LHP

Thermal resistance of LHP is a measure of its ability to transfer a sufficient amount of heat per unit amount of heat supplied. When deionised water is used LHP suffers from greater thermal resistance. But when deionised water is replaced by nanofluids thermal resistance will be low. This is due to enhanced thermal properties of nanofluids.

Thermal resistance (R_t) of LHP can be expressed as

$$R_t = \frac{T_e - T_c}{Q} \tag{21.6}$$

where T_e = evaporator temperature, T_c = condenser temperature and Q = heat input. According to Eq. (21.6), thermal resistance of LHP using deionised water, alumina–water, copper–water and silica–water nanofluids are 0.33 °C/W, 0.21 °C/W, 0.16 °C/W and 0.12 °C/W, respectively. It is found that there is a remarkable reduction in the thermal resistance of LHP with the nanofluids. Among the nanofluids, silica–water nanofluid offers the lowest thermal resistance. Thus, LHP will be able to transfer heat energy over great distances which enables LHP for used in wide range of applications.

21.6 Conclusions

Loop heat pipes were numerically investigated to determine its thermal characteristics using nanofluids. The heat input was varied from 40 to 320 W in steps of 40 W and nanofluids were taken at 2% nanoparticle concentration. The following conclusions are drawn from this work:

1. Evaporator temperature of LHP increases with increase in heat input. But it is lower for LHP using nanofluids than baseline case.
2. Silica nanoparticles reduced the evaporator temperature of LHP significantly than other working fluids. Nearly, 27% reduction in evaporator temperature is obtained.
3. LHP using nanofluids attained steady-state faster than baseline case. The steady-state is attained by LHP about 150 s earlier in comparison with the baseline.
4. Thermal resistance of LHP is reduced when nanofluids were used. Silica–water nanofluid provides the least thermal resistance.

References

- Adoni AA, Ambirajan A, Jasvanath VS, Kumar D, Dutta P (2010) Theoretical studies of hard filling in loop heat pipes. *J Thermophys Heat Transf* 24:173–183
- Akshay J, Joseph AJ, Jose J, Baby R (2018) Enhancement of the thermal performance of a loop heat pipe using alumina-water nanofluid: an experimental investigation. In: IOP conference series material science and engineering, vol 396, India, p 012058
- Bai L, Lin G, Wen D (2000) Modelling and analysis of start-up of a loop heat pipe. *Appl Therm Eng* 30:2778–2787
- Gully P, Mo Q, Yan T, Seyfert P, Guillemet L, Thibault P, Liang J (2011) Thermal behaviour of a cryogenic loop heat pipe for space application. *Cryogenics* 51:420–428
- Huang BJ, Huang HH, Liang TL (2009) System dynamics model and start-up behaviour of loop heat pipe. *Appl Therm Eng* 29:2999–3005
- Jose J, Baby R (2018) Recent advances in loop heat pipes: a review. In: IOP conference series material science and engineering, vol 396, India, p 012060
- Lin G, Li N, Bai L, Wen D (2010) Experimental investigation of a dual compensation chamber loop heat pipe. *Int J of Heat Mass Transf* 53:3231–3240
- Pauken M, Rodriguez JI (2000) Performance characterisation and model verification of a loop heat pipe. Society of automotive engineers, paper no. 2000-01-0108
- Riehl RR, Dutra T (2005) Development of an experimental loop heat pipe for application in future space missions. *Appl Therm Eng* 25:101–112
- Riffat SB, Zhao X, Doherty PS (2005) Developing a theoretical model to investigate thermal performance of a thin membrane heat-pipe solar collector. *Appl Therm Eng* 25:899–915
- US Department of Energy (1992) DOE fundamentals handbook: thermodynamics, heat transfer and fluid flow. USA
- Vasiliev L, Lossouarn D, Romestant C, Alexandre A, Bertin Y, Piatsiushyk Y, Romanenkov V (2009) Loop heat pipe for cooling of high-power electronic components. *Int J Heat Mass Transf* 52:301–308

- Vlassov SV, Riehl RR (2005) Modelling of a loop heat pipe for ground and space conditions. SAE international paper, paper no. 2005-01-2935
- Zhang X, Zhao X, Xu J, Yu X (2013) Characterization of a solar photovoltaic/loop-heat-pipe heat pump water heating system. *Appl Energy* 102:1229–1245
- Zhao X, Wang Z, Tang Q (2010) Theoretical investigation of the performance of a novel loop heat pipe solar water heating system for use in Beijing. *Appl Therm Eng* 30:2526–2536

Chapter 22

Life Cycle Assessment of Traditional Handloom Silk as Against Power-loom Silks: A Comparison of Socio-economic and Environmental Impacts



Kriti Bhalla, Tarun Kumar , Jananee Rangaswamy, Ranjana Siva and Vishal Mishra

22.1 Introduction

Silk is a fine filament derived from silkworms, domesticated or otherwise, after series of processes and stages. India, the second-largest producer of silk, is well-known for the variety of silk fabrics produced viz., Mulberry silk, Tasar silk, Muga silk, Eri silk (Government of India 2014). The origin of the silk fabric can be traced back to the ancient Indus Valley civilization of India, though the majority of sources suggest China to be the originator, where it was believed to have initiated by *Lady Hsi-Ling-Shih*, wife of the mythical *Yellow Emperor* (Good et al. 2009; TexereSilk 2013). In China, the specially reared and woven silk from the *Bombyx mori* soon spread through Asia via the specially assigned silk routes (Boulnois 2005).

The process of silk farming—also called Sericulture under the agriculture-based occupation—is widely practised in the rural sectors of India (Gangopadhyay 2008). The production process of silk fabrics can be carried out by two different methods: Handlooms and Power-looms. It has been observed that labour intensive handloom silk industries are most commonly found in the rural areas whereas the power-loom

K. Bhalla
SOA, Ramaiah Institute of Technology, Bengaluru, India

T. Kumar (✉)
Indian Institute of Science, Bengaluru, India
e-mail: tarunkumar@iisc.ac.in

J. Rangaswamy
BMS School of Architecture, Bengaluru, India

R. Siva
Ramaiah Institute of Technology, Bengaluru, India

V. Mishra
Vijaya Vittala Institute of Technology, Bengaluru, India

silk machinery is used mostly in the suburban and urban silk industries (Nainar 2016; Bhavya 2014). The stages of sericulture and cocoon spinning usually take place in the rural areas.

In the state of Karnataka, the majority of silkworms bred, are in the southern part of the state, which has now become vulnerable to water scarcity, urbanisation, and a shortage of agricultural labour. Mysore—a city in the state of Karnataka which is famous for its Silk—where sericulture has been a traditional practise for more than 215 years, was initiated by the then Mysore ruler, Tipu Sultan. Mysore sericulture industry survived even when other sericulture industries across the nation suffered turbulence (Department of Sericulture 2017). Silk *saris* (traditional attire worn by woman in India) are very valuable textile products which are symbols of pride to the privileged classes and means of employment to the masses. The sericulture industry has provided non-agrarian employment to 10.67 lakh people, with preference to women (Department of Sericulture, Government of Karnataka 2016).

With the recent turn of events, performing a Life Cycle Assessment (LCA) has become a necessity to assess the efficiency of the process and product and to reduce the harmful emissions into the environment (Vollrath et al. 2013). This paper aims to quantitatively analyse the production process of Silk fabric and infer the most energy-consuming and emitting stages, and to propose solutions to make the whole production process environment and resource-friendly. An analysis of this nature comparing handloom and power loom production has not been done in the past. This is the essence of “Industrial Ecology” as explained by John Ehrenfeld (National Research Council 1996).

22.2 The Making of Silk Fabric

The production process of silk starts with the cultivation of mulberry plants. Karnataka, the state of Mysore Silk, has the largest cultivated area of mulberry farms extending up to 166,000 ha (Datta 2002). The specified amount of herbicides and pesticides are sprayed to ensure healthy growth of the plants. The mulberry leaves are collected and used as feed for the silkworm larvae which grow bigger in size into healthy white silkworms, upon consumption of the mulberry leaves. The feeding stage takes about twenty eight days for completion. The well-fed silkworms are grouped and placed in a special cocoon rearing cane-stand provided with partitions in the form of concentric circles. The silkworms slowly form a closely-knit cocoon around themselves, which is made of *sericin* emitted from their mouth (Vollrath et al. 2013). This process takes only two days and is followed by selling the finest cocoons in a regulated market. It is then ready for purchase by the industries for the process of degumming and reeling. Once purchased, the cocoons are boiled in a weakly alkaline solution to kill the pupae inside; and to weaken *sericin* thereby loosening the cocoon strands, and preparing it for reeling. Reeling produces raw silk threads directly from the cocoon with the help of a spinning

wheel. The raw threads are then evened out in density with a *charkha* or spinning wheel, enthusiastically promoted by Mahatma Gandhi for the spinning of *Khadi* handloom.

In recent times, the single spinning wheel has been replaced by a semi-automated spinning wheel that can handle up to eight spindles of yarn, increasing the produced output of yarn and in turn increasing the efficiency. The spun yarn is once again introduced in the market to be purchased by silk production facilities. These production facilities dye the yarns by matching with the required colour sample. The bales of yarn are then inserted into the handloom or power-loom, and the process of silk weaving takes place manually or automatically, respectively.

The breeding of silkworms requires specific climatic conditions as the worms cannot tolerate extreme weather. Luckily, there is no necessity of artificial conditioning for breeding in Karnataka, as in the rest of India (Fetcher 2013).

The stages of Silk production have been depicted in the form of a flowchart in Fig. 22.1 and represented with the help of images in Fig. 22.3a–g. The market price of a single handloom silk *sari* is close to €65 while that of a power-loom silk *sari* starts from €9 (Craftsvilla 2017). With increased awareness among the people, the energy efficiency of each life-cycle stage in the production of the silk fabric has become very crucial. Moreover, LCA also helps in determining the immediate effects on the surrounding environments and hidden feedback loops in the system (Bhalla et al. 2018).

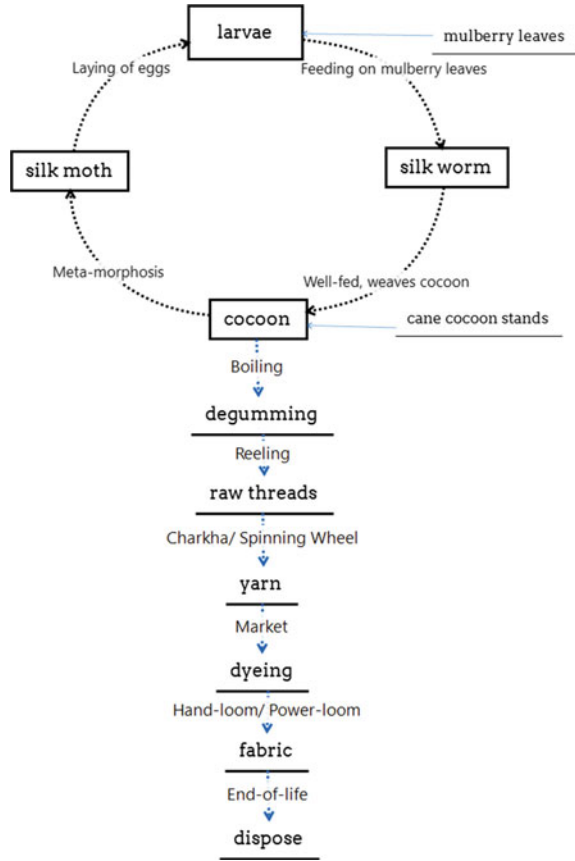
22.3 Methodology

The process of silk production is studied by visiting the silk producing village in *Sidlaghatta Taluk* (Bangalore Rural). A qualitative socio-economic LCA is conducted to assess relative impact factors based on verbal interviews of the master weaver, supervisor, workers, and data from Silk Board of India.

An in-depth analysis of the stages involved in the production of silk fabric is done for handloom and power-loom production processes; using case-based references and study of literature sources. It should be noted that the processes from cocoon formation to dyeing; and fabric production till disposal are the same for both handlooms and power-looms. The differences lie only in the warping and wefting stages, which have been accounted for in the Life Cycle Assessment.

The comparative Life Cycle Assessment is carried out with the help of GaBi Educational Software while employing CML 2001 impact assessment method. A life-cycle-based analysis makes it easier to quantify data and state with informed clarity, about the efficiency or inefficiency of a given process or product. The already available flows in ecoinvent database (an existing database in GaBi), and collected primary data are used to simulate the Indian conditions. Some data feeds are inserted manually with calculated approximations and references from other literature. The primary processes identified and calculated for is as mentioned

Fig. 22.1 Making of silk

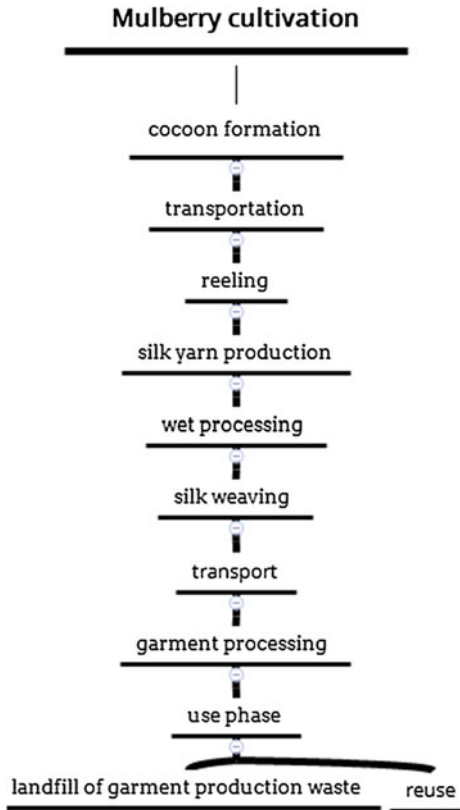


below in Fig. 22.2. Finally, a model framework for sustainable handloom-based rural settlement is proposed to improve the existing socio-economic health of handloom industry based on the results from the case study, and the LCA.

22.4 Case Study

Sidlaghatta Taluk, located 60 kms from Bangalore City, is the administrative centre for the surrounding group of villages—all of which are majorly involved in the handloom silk production. The several Mulberry farms spread across the open fields ensure the healthy growth of the silkworm, *Bombyx Mori*. There are close to seven cocoon breeding shelters in the village, where cocoons are bred until ready for the market. Villages in the *Sidlaghatta Taluk* are self-sufficient, in the sense, all activities from the breeding stage till the fabric and stitching stage are carried out independently by the supervisors, weavers, and retailers of the village itself.

Fig. 22.2 Primary processes of silk production



The cocoon breeding shelters are semi-open with natural ventilation and light, while the handloom industry requires a closed space to work in, with less interference from the natural ventilation.

The reeling process, common to both handloom and power-loom, involves degumming of the cocoon by boiling in weakly alkaline water. This process causes skin problems to the workers. The weavers and workers in the power-loom industry face hearing problems after spending long durations in the high levels of noise produced by the power-loom machines (Fig. 22.3).

22.4.1 Functional Unit and Scope of Analysis

The *functional unit* is taken as one kilogramme (kg) of woven Silk fabric (from Handloom or Power-loom). The scope of the analysis is defined from the sericulture process to the end-of-life of the Mysore silk fabric. *System Boundary* consists of all *primary processes* to produce Silk fabric, while *secondary processes* such as manufacturing of farm equipment, transport vehicles, and power loom machinery

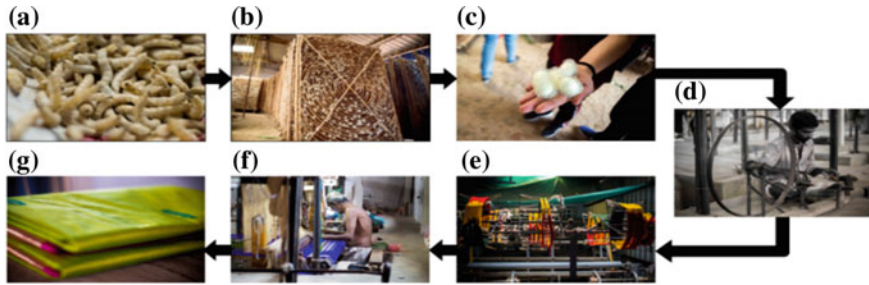


Fig. 22.3 a Silkworms; b suspended cane cocoon stands; c cocoons; d silk yarn production on charkha; e semi-automated spinning wheel; f silk weaving; g finished silk garment

have not been considered due to lack of time, increasing complexity, and data uncertainty (Fig. 22.4). Human labour is not considered in the present study.

22.5 Results

The qualitative analysis of relative impacts of various silk production processes in the rural handloom sector (as shown in Table 22.1) shows that child labour is comparatively low throughout the life-cycle, while female workforce participation rate is relatively higher in the weaving process. Heritage and skill preservation are high in rearing and weaving process. Moreover, social innovation is comparatively higher than technical innovation (in the form of co-operative business models). The ergonomics of the equipments is poor which led to occupational hazards except in cultivation and rearing stages. Labour safety measures and wages are low while the living conditions are better than their urban counterparts.

Results obtained from the GaBi simulation software are computed. On comparing the embodied energy in the specified processes, it is found that handloom silk fabric consumed significantly lesser energy (355 MJ/kg) in comparison to power-loom silk fabric (418 MJ/kg) as shown in Table 22.2. The energy-intensive power loom silk weaving process consumed 62 MJ/kg of energy which was 15% of total energy; while handloom silk weaving consumed negligible energy as most of the weaving is human labour intensive. The graphs for climate change (global warming potential, GWP 100 years), human toxicity potential, acidification potential, and eutrophication potential have been computed for Handloom silk fabric and power-loom silk fabric as depicted in Figs. 22.5a, b and 22.6a, b.

Silk weaving process turns out to have the highest acidification potential as compared to other processes in power-loom industries, while it has negligible impact in handloom industries. The use-phase of silk fabric, common to both handloom and power-loom, also emits high amounts of energy owing to the maintenance processes involving petrochemicals, ironing and drying over its lifetime (54.1 MJ/kg). Also,

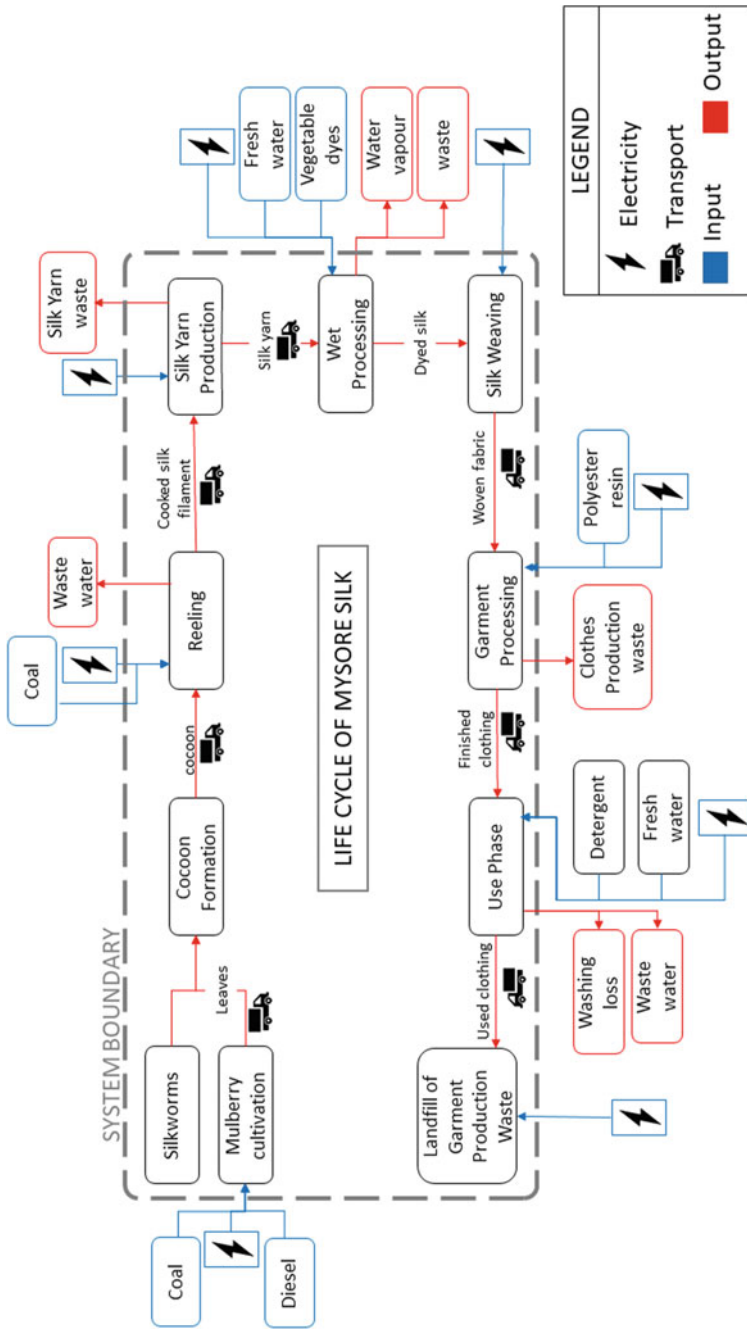


Fig. 22.4 Life cycle of Mysore silk (adapted from Bhalla et al. (2018))

Table 22.1 Socio-economic analysis of silk production LCA (adapted from Bhalla et al. (2018))

SOCIO-ECONOMIC FACTORS	STAGES OF SILK MANUFACTURING			
	MULBERRY CULTIVATION	COCOON REARING	REELING & YARN PRODUCTION	WEAVING
CHILD LABOUR	● ○ ○	● ○ ○	● ○ ○	● ○ ○
WORKING CONDITIONS	● ● ○	● ● ○	● ○ ○	● ● ○
GENDER EQUITY	● ◐ ○	● ○ ○	● ● ○	● ● ◐
HERITAGE CONSERVATION	● ● ○	● ● ●	● ● ○	● ● ○
WORKING HOURS	● ● ○	● ● ○	● ● ○	● ● ○
LABOUR SAFETY	● ● ○	● ● ○	● ○ ○	● ○ ○
SKILL PRESERVATION	● ● ○	● ● ●	● ● ○	● ● ●
LIVING CONDITIONS	● ● ○	● ● ○	● ● ○	● ● ○
WAGES	● ○ ○	● ○ ○	● ● ○	● ● ○
CAPITAL INVESTMENT	● ● ○	● ○ ○	● ● ◐	● ● ◐
SOCIAL INNOVATION	● ● ○	● ● ○	● ● ○	● ● ◐
TECHNICAL INNOVATION	● ○ ○	● ● ○	● ● ○	● ◐ ○
ERGONOMICS OF EQUIPMENTS	● ○ ○	● ● ○	● ○ ○	● ○ ○
OCCUPATIONAL HAZARD	● ○ ○	● ○ ○	● ● ●	● ● ○

Table 22.2 Energy consumed in handloom and power loom processes

Processing method	Stages of production		Total energy consumed (in MJ/kg)
	Weaving	All other processes	
Handloom	0	355	355
Power loom	62.8	355.2	418

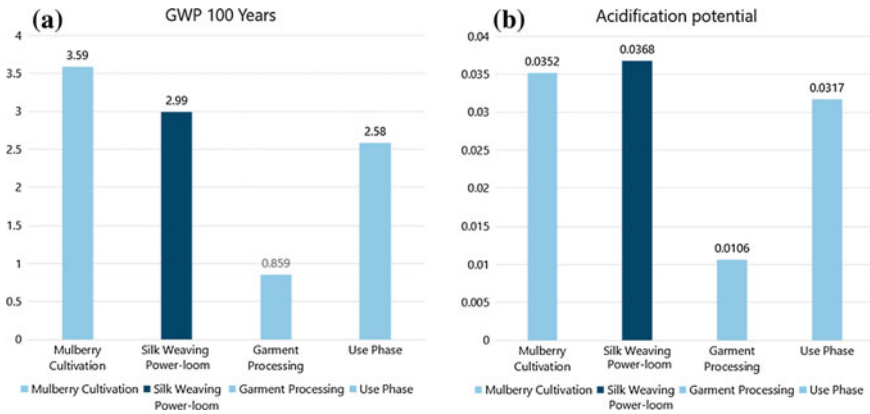


Fig. 22.5 **a** GWP 100 years emission into the air in kg CO₂ equivalent; **b** acidification potential in kg-SO₂ equivalent

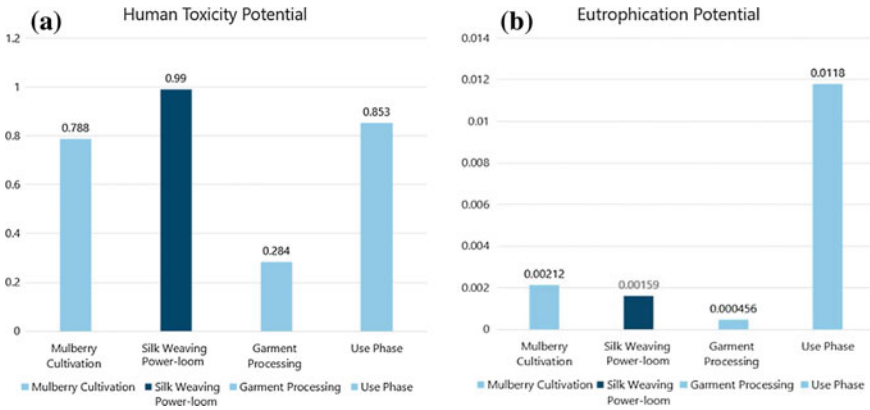


Fig. 22.6 **a** Human toxicity potential in kg-DCB equivalent; **b** eutrophication potential in kg-phosphate equivalent

the use phase of silk fibre extends to 10 years and above, not including the reuse phase. The end-of-life of silk fabric results in the reuse of the fabric or dumping as landfills.

However, the process of mulberry cultivation consumes the maximum amount of resources and fossil fuels, while Silk weaving (in power-loom) and use phase are the other major contributors as shown in Fig. 22.5 (which is computed using **EI99-Egalitarian method of calculation** to depict the relative contributions of different stages of Silk manufacturing process). The relative contribution of the different stages of silk production in the embodied energy—as obtained from the simulation model—has been represented graphically in Fig. 22.7.

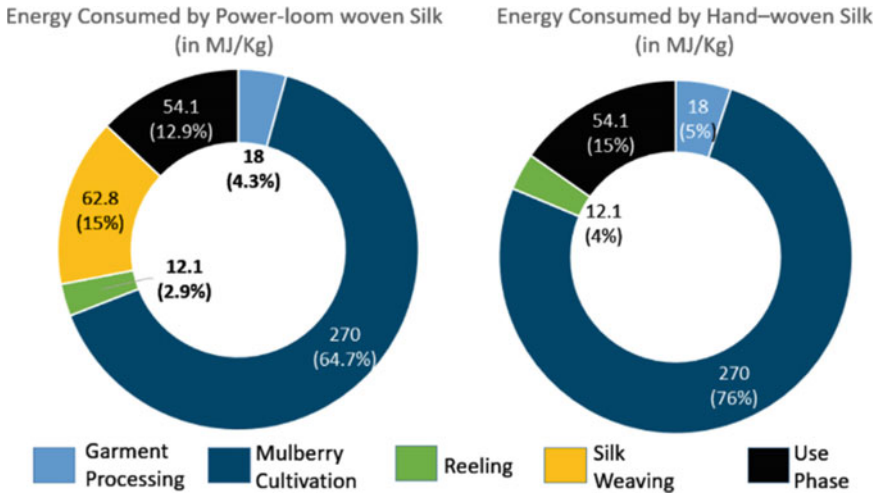


Fig. 22.7 Embodied energy per kg fabric: power loom woven silk versus handloom-woven silk

22.6 Conclusion

This study shows that handloom silk, as expected, is more energy-efficient and environment-friendly owing to the use of manual labour for the silk weaving process when compared to the power-loom. The handloom industries in the rural areas are more sustainable than their urban power-loom counterparts (Figs. 22.7 and 22.8).

Fig. 22.8 Normalization value for power loom (relative contribution)

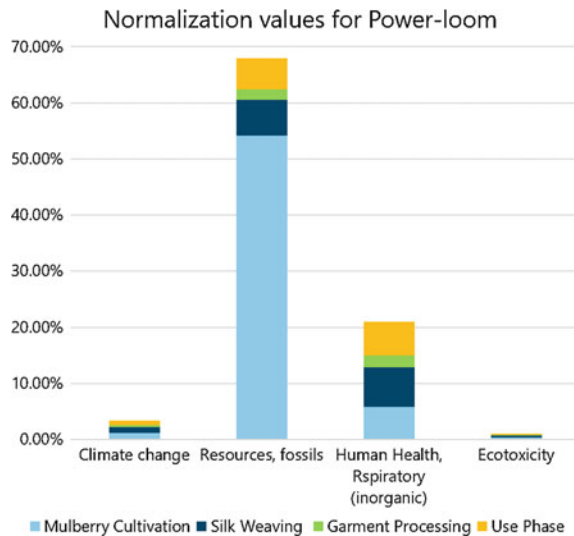
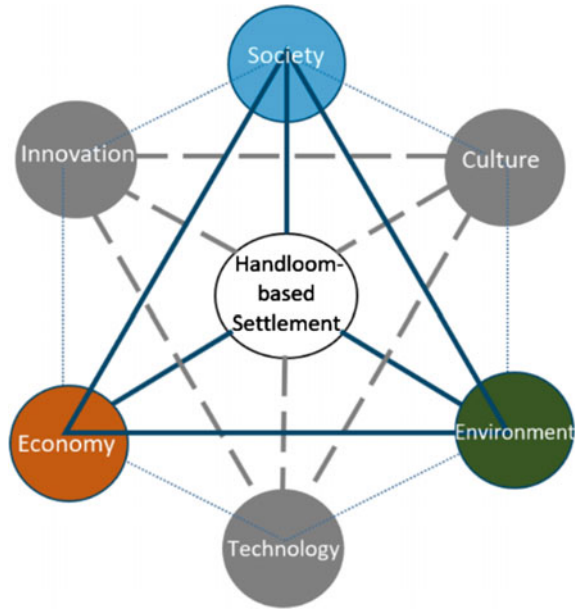


Fig. 22.9 Proposed model for a sustainable handloom-based rural settlement (*Mi*)



Harmful emission into the air is primarily from mulberry cultivation in both production methods. Fertilisers and herbicides used for mulberry cultivation could be the major reasons for negative environmental impacts during the cultivation phase of mulberry plants.

In the use phase, it was assumed that a cloth material would undergo 20–30 washes (Dry-cleaning) during its life-cycle, which resulted in high water usage, water pollution by ester-based detergents and microfibrils thereby justifying the high values obtained during the use phase of the fabric for eutrophication potential (0.0118 kg-Phosphate equiv.), human toxicity level (0.853 kg-DCB equiv.). Furthermore, though the manual weaving process is quite slow and inefficient, it not only generates many employment opportunities for the deprived millions in India, but also helps to preserve the traditional craft and culture. Keeping the socio-economic factors in mind, design-based interventions would make the handloom process more favourable and efficient by increasing labour safety and health, thereby reducing the occupational hazards that are involved in certain processes of Silk production.

A handloom-based rural settlement model (*Mi*) (as shown in Fig. 22.9) was proposed with society, economy, and environment as its three pillars. With socio-economic innovation, green technology-based economy, and a culture based on social ethos and environmental sustainability, would form the core of such rural and decentralised settlements. A cluster of such handloom-based rural settlements would form a sustainable local agglomeration.

The Silk-handloom industry can provide mass employment and self-reliance to the rural society, while adding to the environmental benefits. Such local handloom-based agglomerations, when preferred over centralised model of technology-intensive industries, could provide an alternative pathway for sustainable development.

References

- Bhalla K, Kumar T, Rangaswamy J (2018) An integrated rural development model based on comprehensive Life-Cycle Assessment (LCA) of Khadi-Handloom Industry in rural India. *Procedia CIRP* 69:493–498. <https://doi.org/10.1016/j.procir.2017.11.072>
- Bhavya AP (2014) Economic evaluation of silk weaving by handlooms and power looms in Tumkur district. <http://krishikosh.egranth.ac.in/bitstream/1/5810004144/1/Th10860.pdf>. Last accessed 27 Sept 2018
- Boulnois L (2005) *Silk road: monks, warriors & merchants* (Trans by Helen Loveday), vol 66. Geneva, Switzerland, Editions Olizane
- Craftsvilla (2017) Mysore silk sarees: a lesson in handloom, history and style. <https://www.craftsvilla.com/blog/mysore-silk-sarees-handloom-history-style/>. Last accessed 21 Nov 2018
- Datta RK (2002) Central Silk Board mulberry cultivation and utilization in India. <http://www.fao.org/livestock/agap/frg/mulberry/Papers/HTML/Datta.htm>
- Department of Sericulture (2017) History of sericulture. Government of Tamil Nadu. <http://tensericulture.gov.in/SericultureNov12/History.htm>
- Department of Sericulture, Government of Karnataka (2016) Sericulture in Karnataka. <https://www.karnataka.gov.in/Sericulture/english/Pages/Objectives.aspx>
- Fetcher K (2013) *Sustainable fashion and textiles*. Routledge
- Gangopadhyay D (2008) Sericulture industry in India—a review. *India Science and Technology*
- Good IL, Kenoyer JM, Meadow RH (2009) New evidence for early silk in the Indus Civilization. *Archaeometry* 51:457–466. <https://doi.org/10.1111/j.1475-4754.2008.00454.x>
- Government of India (2014) Silks of India. <http://www.csb.gov.in/silk-sericulture/silks-of-india/>
- Nainar N (2016) Making room for the loom. <https://www.thehindu.com/features/metroplus/society/Making-room-for-the-loom/article14630795.ece>
- National Research Council (1996) *Linking science and technology to society's environmental goals*. National Academies Press
- TexereSilk (2013) History of Silk. https://texeresilk.com/article/history_of_silk
- Vollrath F, Carter R, Rajesh GN, Thalwitz G, Astudillo MF (2013) Life cycle analysis of cumulative energy demand on sericulture in India. In: 6th BACSA international conference, pp 1–13

Chapter 23

Nano Lithium Grease (NLG): Tribological Property Evaluation of Coconut Oil-Based Lithium Grease Added with Ceria Nanoparticles



Jibin T. Philip, Chacko Preno Koshy, C. M. Shajahan
and Basil Kuriachen

23.1 Introduction

In this era of nanotechnology, systems and materials are being confined to and studied at nanometer scales. With reduction in size of equipment and machineries, the need for lubrication at extreme pressure conditions is becoming a substantial requirement needing lubricating solutions. Moreover, in conditions where machineries are in continuous operation, machineries that are not easily accessible to be lubricated, machineries working under extreme conditions of temperature, pressure, heavy load at slow speeds, etc. the employability of lubricating oils is far from possible which increases the demand for greases which can easily stick to the surface and form lubricating films (Mohamed et al. 2015; Ji et al. 2011; Sommer and Haas 2016).

The potential advantages of using nanoparticles as lubricant additives are its ability to use chemistries that are insoluble in nonpolar base oils, less surface interactions, capability to form tribo-films, non-volatility and high thermal stability (Spikes 2015). The synthesis of nanoparticles is achieved by two processes, viz., physical processes and chemical processes. The physical processes that are widely used include high energy ball milling, inert gas condensation, wire explosion, ion sputtering, arc discharge, laser ablation, etc. However, the need for large energy sources and ineffective control on particle size make the physical processes

J. T. Philip (✉) · B. Kuriachen

Department of Mechanical Engineering, National Institute of Technology Mizoram, Aizawl
796012, Mizoram, India

e-mail: philip.jibin07@gmail.com

C. P. Koshy

Department of Mechanical Engineering, Saintgits College of Engineering, Kottayam 686532,
Kerala, India

C. M. Shajahan

Department of Mechanical Engineering, MGM College of Engineering and Technology,
Muvattupuzha, Ernakulam 686667, Kerala, India

© Springer Nature Singapore Pte Ltd. 2020

H. Drück et al. (eds.), *Green Buildings and Sustainable Engineering*,

Springer Transactions in Civil and Environmental Engineering,

https://doi.org/10.1007/978-981-15-1063-2_23

noneconomical. In chemical methods, nanoparticles are developed starting from atoms. They include chemical reduction, sol–gel method, precipitation method, solvothermal synthesis, photochemical synthesis, electrochemical synthesis, etc. (Chen and Chang 2004; Verdon et al. 1995; Yadav and Srivastava 2012; Zhou et al. 2007; Wang 2007). A wide range of nanoparticles such as MoS₂, CuO, TiO₂, and ZnO₂ have been tested as lubricant additives by many researchers in the past. The major reasons for the utilization of nanoparticles as lubricant additives are due to its shape, less chemical reactivity, non-volatility, etc. Further, the size, shape, concentration, and dispersion stability of the nanoparticles are the major factors which determine the friction reduction and anti-wear properties of the nanolubricants (Spikes 2015). Coconut oil finds its place in the list of lubricants derived from vegetable oils such as palm oil, olive oil, and rapeseed oil.. The main constituent of coconut oil is a saturated acid namely lauric acid (Jayadas and Nair 2006; Jayadas et al. 2007; Koshy et al. 2014, 2015a, b; Thottackkad et al. 2012).

Based on the above reviews, the bottom-up approach of chemical processing namely precipitation method was used to synthesize the CeO₂ nanoparticles. The morphology and formation of the nanoparticles were confirmed using advanced characterization techniques such as High-Resolution Transmission Electron Microscopy (HR-TEM), and Energy Dispersive Spectroscopy (EDS). Moreover, the uniform mixing of coconut oil with the nanoparticles was achieved using an ultrasonicator and magnetic stirrer. The LiOH salt was treated with the fatty acids in the coconut oil to obtain the required nano-grease. The high temperature and uniform mixing conditions were maintained till the end. Further, the tribological properties such as COF and SWR of the formulated nano-grease were studied using a four-ball tester.

23.2 Experimental Methodology

23.2.1 Materials

The precursors used for the synthesis of CeO₂ nanoparticles are Ceric Nitrate Hexahydrate, Iso-propanol, Distilled water, and Ammonia solution. The starting materials used for the preparation of NLG are coconut oil (base-oil), LiOH (salt), and CeO₂ nanoparticles. The entire procedure was carried out by mixing the precursors and starting materials in proper proportions for the respective synthesis processes.

23.2.2 Synthesis of CeO₂ Nanoparticles

The 0.1 M aqueous solution of precursors, were mixed thoroughly in the desired ratio. The prepared solution was stirred for 30 min at 60 °C, using a magnetic stirrer with heating arrangement. The temperature and the pH of the solution were

checked repeatedly using a pH meter. Aqueous ammonia was added dropwise to vigorously stirring solution, and the pH was maintained above the value of 10 to keep the solution basic so that the particles formed will be of nanometre size. On the addition of aqueous ammonia, solution turned pale yellow and mixture was stirred for about 2 h. The precipitates were collected by filtration and washed repeatedly with distilled water to remove excess ammonia. The slurry was then dried for 4 h at 500 °C in a muffle furnace. A porous yellow powder was obtained which was crushed to get fine powder and calcinated at 500 °C for 1 h to obtain nanosized CeO₂ particles. The particles are then powdered by crushing to obtain the required nanoparticles. These particles formed should be kept secured from environmental moisture to prevent agglomeration to get converted into larger micro/millimeter particles. The various stages of CeO₂ nanoparticle synthesis are shown in Fig. 23.1.

23.2.3 Preparation of Nano-grease

The required amount of base-oil is mixed with the nanoparticle additives in proper proportion and mixed thoroughly using a magnetic stirrer/ultrasonicator for a period of 1 h. After the solution formed is properly mixed to form a uniform composition, different proportions of LiOH thickeners are added to find an optimum quantity of it

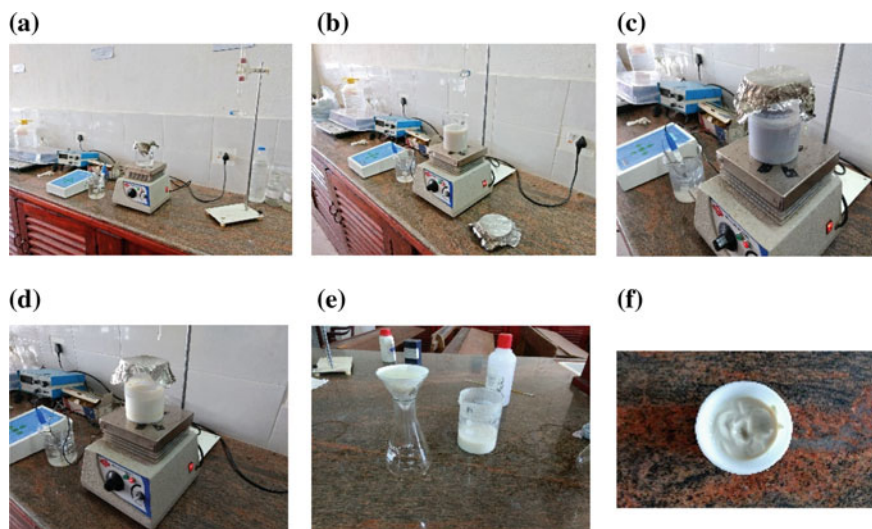


Fig. 23.1 Stages of CeO₂ nanoparticle synthesis **a** Precursors mixed in desired ratio heated at 60 °C **b** Solution turns light yellow on addition of NH₄OH **c** Solution turned pale red **d** Solution turned pale yellow after heating for 1 h **e** Filtering process **f** Wet CeO₂ nanoparticles **g** Calcination at 500 °C in muffle furnace **h** Grounded and powdered form **i** Prepared CeO₂ nanoparticles

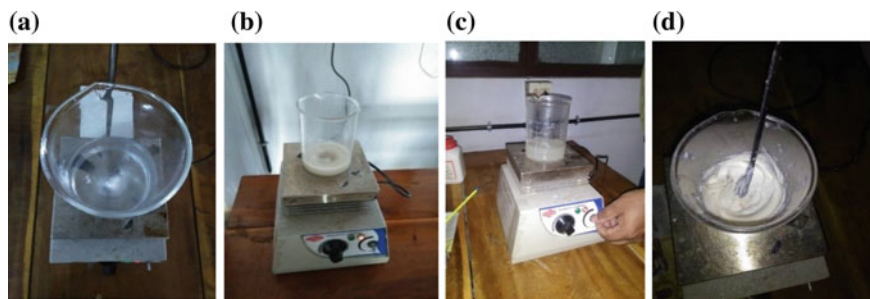


Fig. 23.2 Stages of NLG synthesis **a** Coconut oil in beaker mixed on a magnetic stirrer, **b** Nanoparticle is added and solution is heated to 120 °C, **c** LiOH and acetone are added, **d** Obtained nano-grease

required to form nano-grease. The mixture is stirred thoroughly using the same magnetic stirrer at a temperature of about 100–120 °C. The mixture starts to harden during the process and needs to be transferred to any system which imparts hard mixing or can be hand mixed in case of small quantities. Further, when the proper mixing has been done the required nano-grease is produced and can be tested for its tribological properties for its utilization in commercial applications which demand the use of greases. The various preparation stages of the NLG are as shown in Fig. 23.2.

23.3 Results and Discussion

23.3.1 Characterization of Nanoparticles

The high-end characterization techniques such as HR-TEM and EDS were carried out on the synthesized CeO_2 nanoparticles to get a detailed insight into its shape and composition.

High-Resolution Transmission Electron Microscopy (HR-TEM). The HR-TEM images of the synthesized CeO_2 nanoparticles are shown in Fig. 23.3. It is clear from the images that the size of the nanoparticles formed are very less than 100 nm and possess a nearly spherical morphology. Further, the size distribution is found to be almost uniform. There are other advanced characterization techniques such as X-ray Diffractogram (XRD), and Scanning Electron Microscopy (SEM) for further detailed studies.

Energy Dispersive Spectroscopy (EDS). Energy dispersive spectrum (EDS) is taken for finding the elemental composition in the sample. EDS analysis was done on the synthesized cerium oxide which was prepared by the means of chemical method. The EDS spectrum of the synthesized cerium oxide nanoparticle is shown in Fig. 23.4. The formation of CeO_2 confirmed from the spectra which shows the

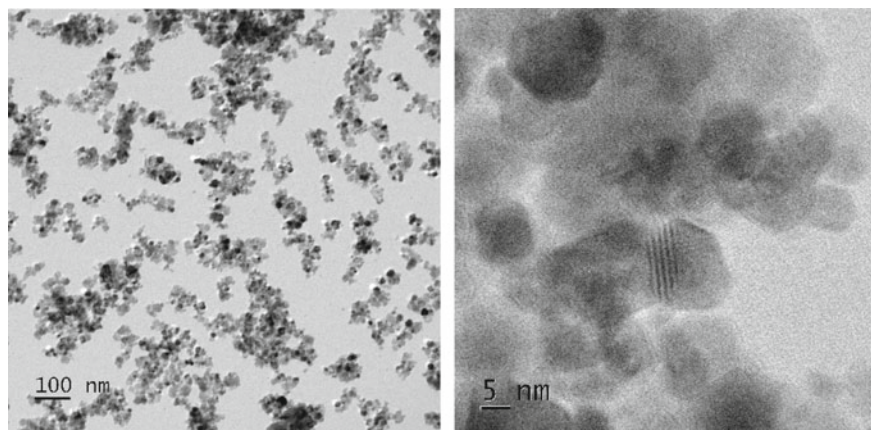


Fig. 23.3 HR-TEM images of CeO₂ hybrid nanoparticles

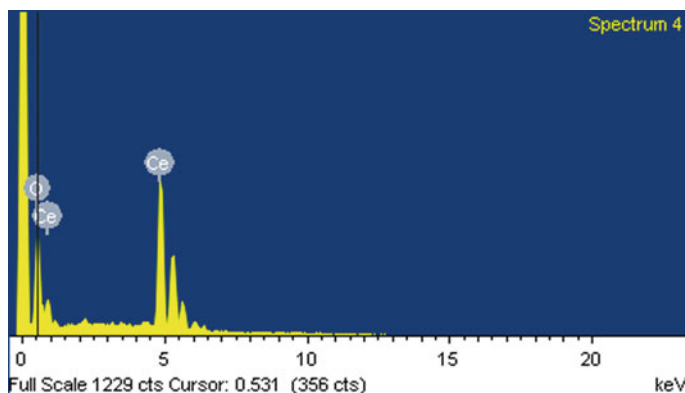


Fig. 23.4 EDS spectrum obtained from primary nanocrystalline CeO₂

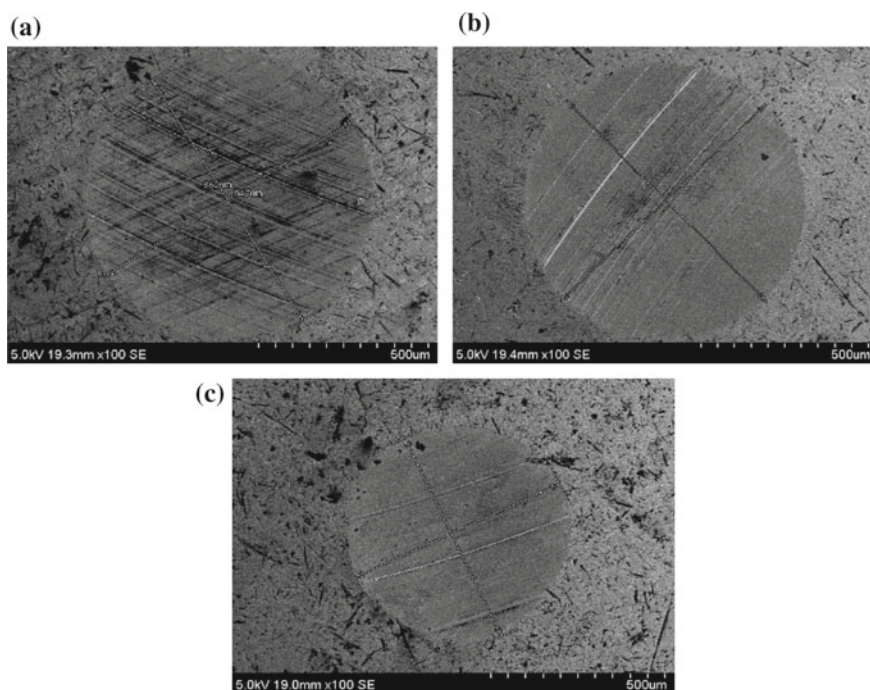
peaks for cerium and oxygen atoms. Moreover, the weight and atomic percentages of components present in the synthesized sample are as shown in Table 23.1.

23.3.2 *Tribo-Tests*

The tribological studies to determine the frictional and wear properties of the prepared nano-greases were performed using a four-ball tester. The obtained Scanning Electron Microscopy (SEM) wear scar images of the balls when used with different combinations of nano-greases on the tester are as shown in Fig. 23.5 and Table 23.2 shows the wear scar details. From the obtained wear scar images and the

Table 23.1 Weight and atomic percentage of elements present in synthesized CeO₂ nanoparticles from EDS data

Element	Weight (%)	Atomic (%)
O (K)	16.01	62.55
Ce (L)	83.99	37.45
Total	100	100

**Fig. 23.5** Wear scar images of the formulated nano-greases **a** with coconut oil + 7.5% LiOH (without nanoparticles), **b** with coconut oil + 10% LiOH + 0.5% CeO₂ nanoparticles, **c** with coconut oil + 10% LiOH + 1% CeO₂ nanoparticles**Table 23.2** Wear scar details

Grease composition (%)	Wear scar diameter (mm)
Coconut oil + 7.5% LiOH (without nanoparticles)	0.82
Coconut oil + 10% LiOH (without nanoparticles)	0.71
Coconut oil + 15% LiOH (without nanoparticles)	0.85
Coconut oil + 10% LiOH + 0.5% CeO ₂ nanoparticles	0.63
Coconut oil + 10% LiOH + 1% CeO ₂ nanoparticles	0.67

wear scar diameter values, it can be observed that the nano-greases possess a greater lead over the greases without nanoparticles. The friction and wear properties were found to be better due to the presence of CeO₂ nanoparticles.

23.4 Conclusions

The following conclusions were derived from the present experimental investigations.

- The CeO₂ nanoparticles with uniform size distribution can be prepared by the chemical process, namely, precipitation method.
- From the characterization of nanoparticles using HR-TEM and EDS, the results obtained are (a) The size of nanoparticle was very less than 100 nm. (b) The particles possess a nearly spherical morphology. (c) The presence of Ce and O in the composition was confirmed using EDS analysis.
- Highly advanced characterization techniques can be employed for better morphological and topographical studies of the nanoparticles.
- The tribo-tests using four-ball tester confirmed the efficiency of nano-greases over other conventional greases due to its better wear and frictional properties.
- Wear scar diameter formed with usage of nanoparticles was found to be 0.63 mm which is less compared to the 0.82 mm obtained by usage of greases without nanoparticles.
- Coefficient of friction in case of nano-greases was also comparatively less.
- Finally, the reduction in wear and friction can be due to the conversion of sliding to rolling motion due to the presence of spherical ceria nanoparticles.

Acknowledgements We would like to convey our sincere gratitude to Kerala State Council for Science Technology and Environment (KSCSTE), Trivandrum (Order No: C4/16/INNOVATE/2016/KSCSTE) for providing the financial assistance for this initiative.

References

- Chen HI, Chang HY (2004) Homogeneous precipitation of cerium dioxide nanoparticles in alcohol/water mixed solvents. *Colloids Surf A Physicochem Eng Asp* 242(1):61–69
- Jayadas NH, Nair KP (2006) Coconut oil as base oil for industrial lubricants -evaluation and modification of thermal, oxidative and low temperature properties. *Tribol Int* 39(9):873–878
- Jayadas NH, Nair KP, Ajithkumar G (2007) Tribological evaluation of coconut oil as an environment-friendly lubricant. *Tribol Int* 40(2):350354
- Ji X, Chen Y, Zhao G, Wang X, Liu W (2011) Tribological properties of CaCO₃ nanoparticles as an additive in lithium grease. *Tribol Lett* 41(1):113–119
- Koshy CP, Rajendrakumar PK, Thottackkad MV (2014) Experimental evaluation of the tribological properties of CuO nano lubricants at elevated temperatures. In: Proceedings of international conference on advances in tribology and engineering systems, Springer, India, pp 391–402

- Koshy CP, Rajendrakumar PK, Thottackkad MV (2015a) Analysis of tribological and thermo-physical properties of surfactant modified vegetable oil-based CuO nano-lubricants at elevated temperatures-an experimental study. *Tribol Online* 10(5):344–353
- Koshy CP, Rajendrakumar PK, Thottackkad MV (2015b) Evaluation of the tribological and thermo-physical properties of coconut oil added with MoS₂ nanoparticles at elevated temperatures. *Wear* 330:288–308
- Mohamed A, Osman TA, Khattab A, Zaki M (2015) Tribological behavior of carbon nanotubes as an additive on lithium grease. *J Tribol* 137(1):011801
- Sommer M, Haas W (2016) A new approach on grease tribology in sealing technology: influence of the thickener particles. *Tribol Int* 103:574–583
- Spikes H (2015) Friction modifier additives. *Tribol Lett* 60(1):1–26
- Thottackkad MV, Perikinalil RK, Kumarapillai PN (2012) Experimental evaluation on the tribological properties of coconut oil by the addition of CuO nanoparticles. *Int J Precis Eng Manuf* 13(1):111–116
- Verdon E, Devalette M, Demazeau G (1995) Solvothermal synthesis of cerium dioxide micro crystallites: effect of the solvent. *Mater Lett* 25(3):127–131
- Zhou W, Wang, ZL (2007) *Scanning microscopy for nanotechnology: techniques and applications*. Springer
- Yadav TP, Srivastava ON (2012) Synthesis of nanocrystalline cerium oxide by high energy ball milling. *Ceram Int* 38(7):5783–5789
- Zhou F, Zhao X, Xu H, Yuan C (2007) CeO₂ spherical crystallites: synthesis, formation mechanism, size control, and electrochemical property study. *J Phys Chem C* 111(4): 1651–1657

Chapter 24

Exploiting the Potentials of Graphene Nano-platelets for the Development of Energy-Efficient Lubricants for Refrigeration Systems



S. S. Sanukrishna and M. Jose Prakash

24.1 Introduction

The global power consumption pattern is drastically increasing from the past decades. Exponentially growing energy demands necessitate invention of heat transfer medium such as coolants and lubricants having better thermal transport properties, in diverse thermal systems. The performance of lubricants directly affects global energy consumption. Because of it, augmenting the thermophysical and tribological properties of lubricants is imperative. The addition of chemical compounds is a common way to improve the thermophysical and tribological capabilities of coolants and lubricants. The development of various nanoparticles has opened up new avenues in various fields including cooling, lubrication, medicine, composite, etc. Metallic and metal oxide nanoparticles, carbon and its derivatives (fullerenes, onions, nanotubes and graphene), have been used nowadays to develop nano-coolants and nanolubricants.

SUS Choi of Argon National Laboratory proposed the concept of nanofluids in 1995 (Eastman et al. 2001). Since 1995, researchers are actively involved in this new research frontier. Choi and Eastman and Das et al. reported an increase in thermal conductivity of engine oil by 40%, when Cu nanoparticles are suspended with it. Moreover an upsurge of 150% for the case of multiwalled carbon nanotube

S. S. Sanukrishna (✉) · M. Jose Prakash
Department of Mechanical Engineering, TKM College of Engineering,
Kollam 691005, Kerala, India
e-mail: sanukrishna@sctce.ac.in

M. Jose Prakash
e-mail: josetkm@tkmce.ac.in

S. S. Sanukrishna · M. Jose Prakash
University of Kerala, Thiruvananthapuram, Kerala, India

suspensions (Kumar et al. 2014; Sharif et al. 2016). In 2008, Baltez et al. exposed the anti-friction potentials of CuO, ZrO₂ and ZnO nanoparticles. The advent of graphene, a derivative of graphite, enriches the new research frontline. Few studies are available in literature regarding the potential of graphene as an additive to different base fluids by Rasheed et al. and Senatore et al. in 2013 and 2015 (Rasheed et al. 2016; Berman et al. 2014). Few experimental investigations in literature reported the potential of lubrication characteristics of nano-oxides as well (Alves et al. 2013; Borda et al. 2018). One of the state-of-the-art methods to enhance the thermal performance of nanofluids is the use of advanced nano materials having unique properties than that of metals and metal oxide nanoparticles. Carbon and its allotropes are gained attention as additives to conventional heat transfer fluids and lubricants due to their unique morphological and thermophysical properties. Graphene and carbon nanotubes are the most popular members of carbon family. The 2D material shows much uncommon mechanical and thermal behaviour. Because of this, it is expected to be a potential alternate material for different applications, in addition to heat transfer enhancement.

Comprehensive studies focusing on graphene nanolubricants are scarce. It is vital to investigate the thermal transport phenomenon, rheological and tribological characteristics of graphene-based nanofluids and nanolubricants owing to its different nature from other nanoparticles. This study mainly focuses on the thermal and rheological and tribological characterization of graphene–Polyalkylene glycol (PAG) nanolubricant. Specifically, to determine the thermophysical properties like thermal conductivity and viscosity of graphene-based nanolubricant at different composition and temperatures. Furthermore, studies are conducted to illuminate the wear preventive characteristics of the novel nanolubricant.

24.2 Methodology

24.2.1 Preparation of Nanolubricant

The vital step as far as nanofluids are concerned is the preparation and stabilization.

Extra precautions are needed to achieve a stable suspension without any flocculation. The two-step method is adopted for the preparation of the nanolubricant. Graphene–PAG nanolubricants are prepared at various volume fractions 0.07, 0.09, 0.2, 0.4 and 0.6 vol.%. The stabilization is assured with the use of magnetic stirrer and subsequent ultra-sonication with an ultrasonic agitator for 6 h. No evidence of sedimentation or coagulation is noticed after 5 days of preparation. Spectral absorbance study with UV–Vis spectroscope confirms the stability.

24.2.2 Determination of Thermal Conductivity

Transient hot wire method is the widely accepted method for the measurement of thermal conductivity of liquids. The KD2 Pro thermal property analyser (Decagon devices, Inc., USA) working based on the transient hot wire principle is used for the thermal conductivity studies. The accuracy for thermal conductivity is $\pm 5\%$. The apparatus meets ASTM D5334 standard. The temperature of the sample is kept constant using a constant temperature bath (F-25, Julabo, Germany). The accuracy of the refrigerated bath is $0.01\text{ }^{\circ}\text{C}$. The thermal conductivity of the nanolubricant is measured in the temperature range of $20\text{--}50\text{ }^{\circ}\text{C}$.

24.2.3 Measurement of Rheological Behaviour

The rheological characterization of graphene–PAG nanolubricant is accomplished with a Brookfield LVDV II + Pro Cone/Plate rheometer together with the constant temperature circulator. Before the commencement of experimental measurements, the viscometer is calibrated with calibration standard fluid. The rheological data are acquired with Rheocalc software after attaining the steady state condition with in the torque range of $10\text{--}100\%$ at different shear rates and temperature.

24.2.4 Measurement of Tribological Characteristics

The friction reduction and anti-wear characteristics of the base lubricant (PAG oil) and the nanolubricant are studied with a four-ball tribo-tester. The tests are conducted according to ASTM D 4172-94 standard. The wear scars appeared on the three lower balls are measured with an optical microscope with an accuracy of $\pm 0.001\text{ mm}$. The friction reduction and anti-wear characteristics of the lubricant modified with graphene nanoparticles with different volume fractions ($0.1, 0.4$ and $0.6\text{ vol.}\%$) are determined.

24.3 Results and Discussion

24.3.1 Thermal Conductivity

Figure 24.1 shows the variation of thermal conductivity of graphene–PAG nanolubricant at different volume fractions. The thermal conductivity upsurges with increase in particle concentrations. The maximum enhancement in thermal

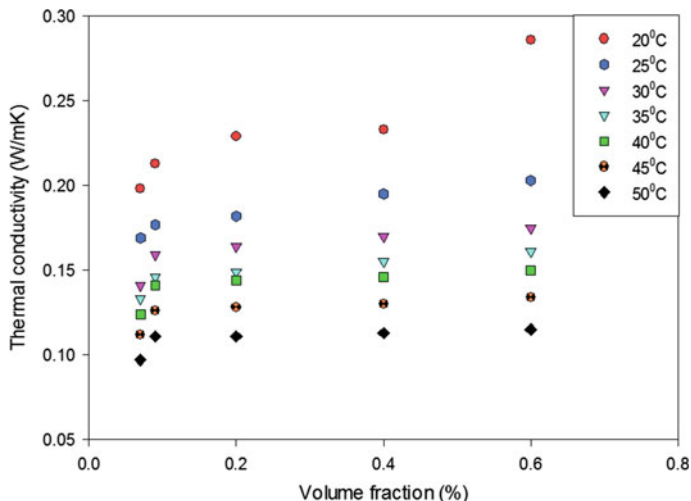


Fig. 24.1 Thermal conductivity versus volume fraction

conductivity is observed as 48% compared to the pure lubricant at a particles concentration of 0.6 vol.% and temperature of 20 °C.

The key factors responsible for the anomalous increase in thermal conductivity are

(i) The Brownian motion effect of nanoparticles in the base fluid (ii) molecular layering of the liquid and (iii) the higher values of thermal conductivity of dispersed solid nanoparticles compared to base fluid.

It is also evident from the figure that intensification of temperature results in the deterioration of thermal conductivity of the nanolubricant. The same behaviour is exhibited by the pure fluid as well. However, of all the particle concentration considered, the nanolubricant exhibits higher thermal conductivity than the pure lubricant. The phenomenon can be attributed to the following factors: (i) at elevated temperatures, the liquid molecules move away from each other, and hence the mean free path between them increases. This reduces the possibility of collision between the molecules which eventually decreases the thermal conductivity.

24.3.2 Rheological Studies

In order to explicate the effect of graphene nanoparticles on the rheological characteristics of PAG lubricant, extensive experimental studies with graphene are conducted. Experiments are conducted with different particle concentrations (0.07–0.6 vol.%). The temperature is varied from 20 to 90 °C and experiments are

conducted at different shear rates. Three sets of data are collected at specified test conditions and averaged to minimize the experimental uncertainty.

Effect of Particle Concentration on Viscosity of Nanolubricants

Figure 24.2 represents the variation of viscosity with respect to volume fraction and shear rates at lower and higher temperatures considered for the study.

The graphene–PAG nanolubricant at all concentrations and temperatures exhibits an increase in viscosity with volume fractions. The maximum viscosity displayed by graphene–PAG nanolubricant is 317cP. It is observed at lower shear rate and temperature. As the particle dosing level increases, the effect of Van der Waals force become more prominent, which eventually consequences formation of greater nano-clusters. This phenomenon constitutes increased shear stress between the layers of fluid and finally results the enhanced viscosity.

Effect of Temperature on Viscosity

Figure 24.3 portrays the variation of viscosity with respect to temperature. No wonder, here as well, the nanolubricant shows similar trends as in the case of the pure nanolubricant as shown. The viscosity at all particle concentrations diminishes with increase in temperature.

The hindrance offered by the nano-racemes against the movement of fluid layers may be the possible reason for the enlarged viscosity at lower values of temperatures. Intensification of temperature causes weakening of Van der Waals attractive force between the nano-additives and eventually segregates the flocculants. The weakening of intermolecular force causes decrease in viscosity.

Rheological Characteristics of Pure Lubricant

The shear-dependent viscosity variation is plotted to characterize the rheology of pure and nanolubricant. The shear rate is varied from 3.75 to 225 /s.

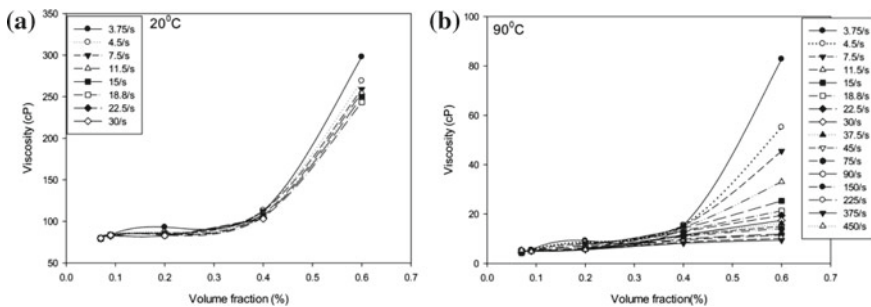


Fig. 24.2 Viscosity versus volume fractions at different shear rates at **a** temperature = 20 °C, **b** temperature = 90 °C

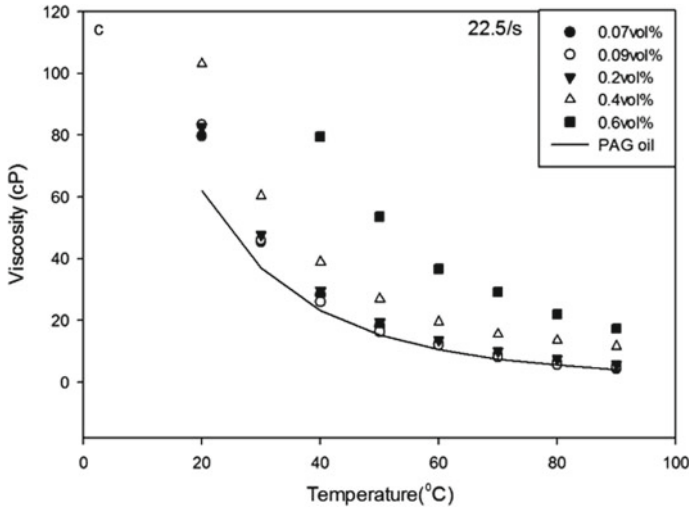


Fig. 24.3 Temperature-dependent viscosity variation of graphene-PAG at different particle concentrations

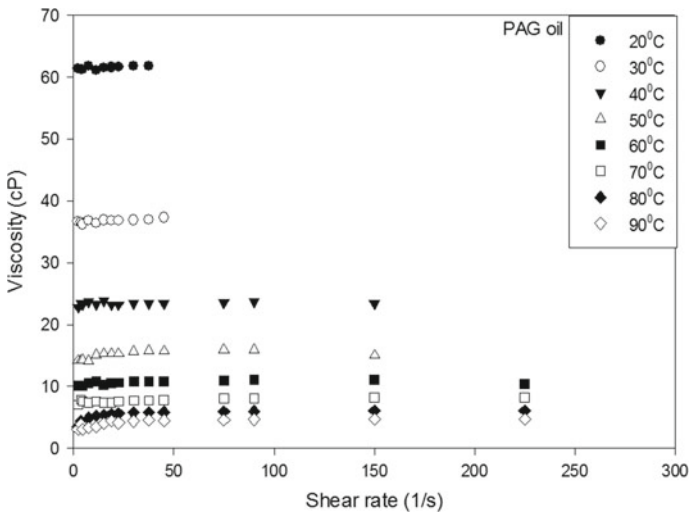


Fig. 24.4 Viscosity variations of pure-PAG oil with shear rates at different temperatures

Figure 24.4 depicts the variation of viscosity with shear rate for pure lubricant. It is evident from the figure that over a temperature range considered, the viscosity of the pure lubricant does not rely on the shear rate and shows the Newtonian behaviour.

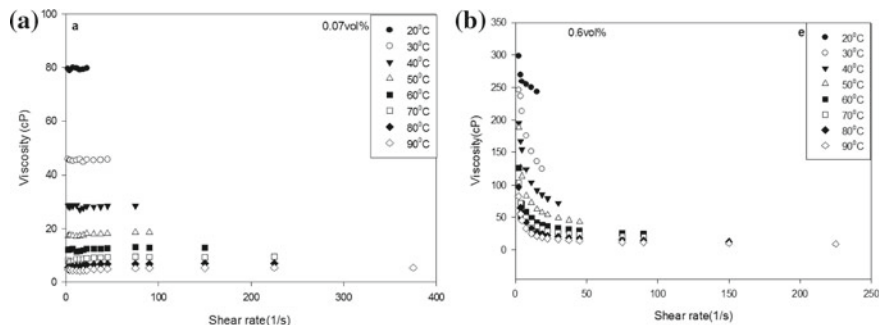


Fig. 24.5 Variations of viscosity with shear rates at different temperatures, at **a** volume fraction = 0.07%, **b** volume fraction = 0.6%

Rheological Behaviour of Graphene–PAG Nanolubricant

The viscosity of graphene nanolubricant at different shear rates is elucidated to observe whether it behaves as Newtonian or non-Newtonian fluid.

From Fig. 24.5, it is obvious that at lower particle concentrations (0.07 vol.%), graphene–PAG nanolubricant behaves almost in a Newtonian manner. However, as the particle dosing level increases, the behaviour has been transformed into non-Newtonian with significant shear thinning. It is also observed that at elevated shear rates the shear thinning is insignificant and the fluid tends to be Newtonian.

24.3.3 Anti-wear Characteristics of Nanolubricants

The friction reduction and anti-wear characteristics of the base lubricant and the lubricant modified with graphene nanoparticles with different volume fractions (0.1, 0.4 and 0.6 vol.%) are determined. The tribological studies of graphene–PAG nanolubricant reveal that the nanolubricant has good friction reduction characteristics especially at lower concentrations. Figure 24.6 shows the variation of coefficient of friction with respect to time.

Graphene nanolubricant at a volume fraction of 0.1% displays maximum decrease in friction coefficient compared to the other concentrations. It is measured as 42.86% less compared to pure lubricant. The graphene-based nanolubricant displays better anti-wear characteristics with reduced wear scar diameter under all particle concentrations. The maximum decrease in the diameter of scar is noticed at the lowest particle concentration. At 0.1% particle concentration the drop in wear scar diameter is 35.18% with respect to pure PAG lubricant, and the corresponding decrement in WSD at 0.4 and 0.6 vol.% particle concentrations are 25.2% and 9.58%, respectively. Figure 24.7 and Fig. 24.8 demonstrate the comparative wear scar diameter and wear scar images of graphene nanolubricant, respectively.

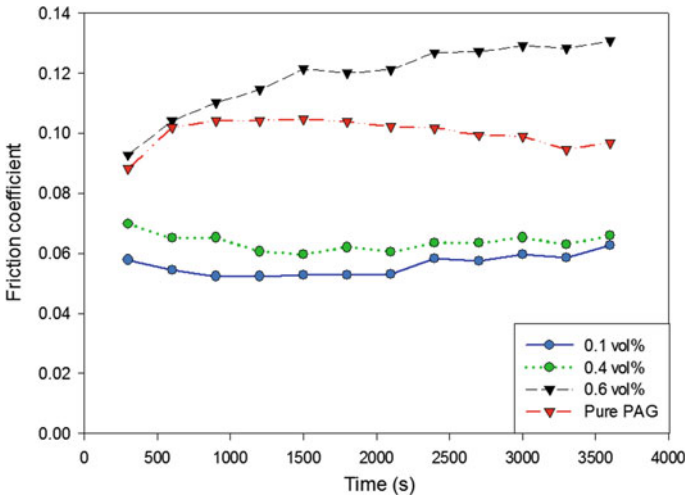


Fig. 24.6 Friction coefficient of graphene-PAG nanolubricant

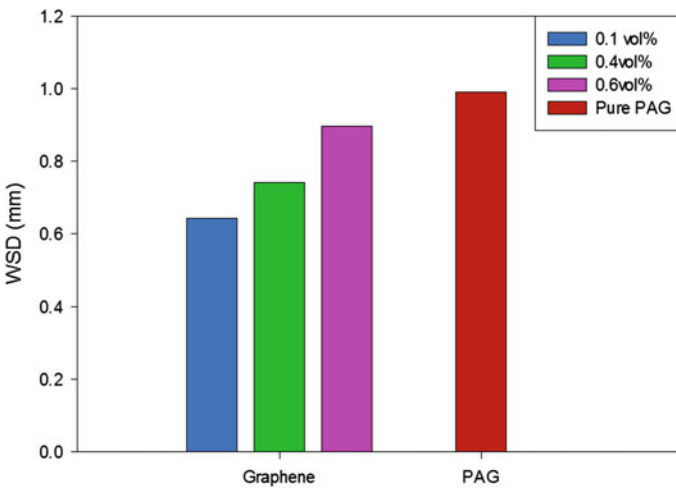


Fig. 24.7 Comparison of wear scar diameters with graphene-PAG nanolubricant and pure lubricant

The nanolubricant shows excellent tribological properties than the base lubricant. The mechanisms which are responsible for the tribological improvements of nanolubricants are categorized into direct and indirect effects. The direct effect includes the 'Ball bearing effect' and the formation of nano-film (tribo-film). The indirect effects are mainly due to the polishing and mending effects. The nanoparticles may act as tiny ball bearing rolling over the mating surfaces,

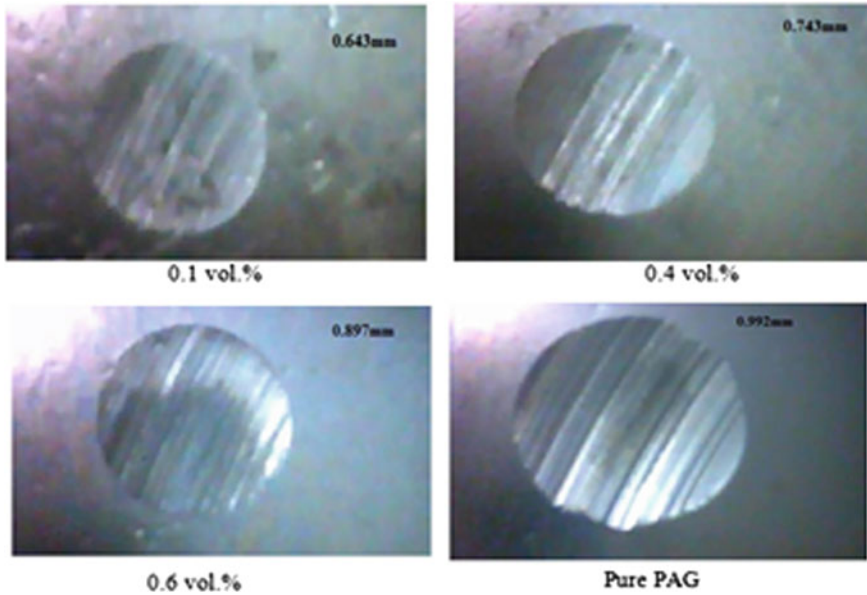


Fig. 24.8 Wear scar images

which prevents the surface asperity interlocking and breaking. Thus eliminates the three body abrasion. The nano-film serves as a surface protective layer. The mending effect of nanoparticles comes into play if there is any cuts that occur on the surface. In such circumstances the nano-material gets filled on the groves to reduce the acceleration of wear rate.

24.4 Conclusions

The effect of graphene nano-platelets on the thermal rheological and tribological characteristics of polyalkylene glycol compressor lubricant is studied. The major findings derived from the investigation are (i) the volume fraction and temperature have crucial impact on the thermal conductivity and viscosity of the lubricant (ii) the Newtonian to non-Newtonian transformation is evidenced for the case of nanolubricants (iii) the graphene nanoparticles display excellent anti-wear and friction reduction characteristics (iv) the optimum concentration is suggested as 0.1 vol.%. From the experimental studies, it is concluded that graphene nanolubricant can be considered as an alternative lubricant for refrigerant compressors. The application of the novel type of lubricant may lead to the development of energy-efficient HVAC systems.

References

- Alves SM, Barros BS, Trajano MF, Ribeiro KSB, Moura E (2013) Tribological behavior of vegetable oil-based lubricants with nanoparticles of oxides in boundary lubrication conditions. *Tribol Int* 65:28–36
- Berman D, Erdemir A, Sumant AV (2014) Graphene: a new emerging lubricant. *Mater Today* 17:31–42
- Borda FLG, de Oliveira SJR, Lazaro LMSM, Leiróz AJK (2018) Experimental investigation of the tribological behavior of lubricants with additive containing copper nanoparticles. *Tribol Int* 117:52–58
- Eastman JA, Choi SUS, Li S, Yu W, Thompson LJ (2001) Anomalously increased effective thermal conductivities of ethylene glycol-based nanofluids containing copper nanoparticles. *Appl Phys Lett* 78:718–720
- Kumar PCM, Kumar J, Tamilarasan R, Sendhil Nathan S, Suresh S (2014) Heat transfer enhancement and pressure drop analysis in a helically coiled tube using Al₂O₃/water nanofluid. *J Mech Sci Technol* 28:1841–1847
- Rasheed AK, Khalid M, Rashmi W, Gupta TCSM, Chan A (2016) Graphene based nanofluids and nanolubricants—review of recent developments. *Renew Sustain Energy Rev* 63:346–362
- Sharif MZ, Azmi WH, Redhwan AAM, Mamat R (2016) Investigation of thermal conductivity and viscosity of Al₂O₃/PAG nanolubricant for application in automotive air conditioning system. *Int J Refrig* 70:93–102

Chapter 25

Experimental Study on Mechanical Properties of Areca Nut Fibre-Reinforced Self-compacting Concrete



L. Divakar, Abhishek Pulgur Venkatesha Babu,
R. K. Chethan Gowda and S. Nithin Kumar

25.1 Introduction

Congestion of urban spaces is leading to construction of more high-raised buildings around the globe, as a result the reinforcement requirement has substantially increased. The height of the building and bulky reinforcements lead to difficulties in placing and compaction of concrete resulting in the decrease in the overall efficacy of the design. Thus, SCC has been extensively used in recent times.

The addition of fibres in SCC has shown significant improvement in the flexural strength and crack arresting properties of concrete (Khayat and De Schutter 2014; Neves and de Almeida 2005; Khaloo et al. 2014; Aslani and Nejadi 2013). The review of literature indicates that the majority of the experimental studies were conducted using artificial fibres and only few studies with the use of natural fibres in the SCC have been carried out. The impact of natural fibres in the normal cement concrete has been studied which shows improved performance in crack arresting, flexural and impact strength (Thomas and Ramaswamy 2007; Musmar 2013). These mechanical properties of the composite are influenced by various factors such as characteristics of fibres, nature of the cement-based matrix, mixing procedure, casting and curing conditions (Aziz and Paramasivam 1982). Tahar et al. (2017) studied the effect of date palm and polypropylene fibres on the fresh and hardened properties of the SCC and indicated that SCC with date palm fibres exhibited variation in the flowability, but no changes in the hardened properties as compared to SCC with polypropylene fibres. Kaushik et al. (2017) studied the flexural strength of jute fibre reinforced epoxy/polyester composites and reported an improvement of the flexural strength as a result of adding jute fibre. Padamaraj et al. (2016) conducted experimental studies on the areca fibre and coir fibre composites

L. Divakar (✉) · A. P. V. Babu · R. K. Chethan Gowda · S. Nithin Kumar
Department of Civil Engineering, Ramaiah University of Applied Sciences, Bengaluru,
Karnataka 560056, India
e-mail: divakar.l.ce.et@msruas.ac.in

and the results indicate improved performance of the areca fibres in terms of flexural, tensile, hardness and impact properties as compared to the coir fibres. Ashok et al. (in press) has reported the enhancement of the impact, flexural strength and hardness of the areca infused composites.

Areca fibres are extracted from the husk of beetle nuts; these can be used as fibres in the fibre reinforced cement composites. The tensile strength and elastic modulus of areca fibres are about 50 and 750 MPa (Nayak and Mohanty 2018). These properties have encouraged various researchers to study the influence of the addition of areca fibres on the strengths of the composites. The effect of the influence of the areca fibres on the properties of the SCC has not been studied. This paper discusses the influence of the variation of the % of areca fibres on the fresh and hardened properties of the SCC.

25.2 Experimental Details

25.2.1 Materials Used

In this study, 53 grade Ordinary Portland Cement (OPC) manufactured by Ultratech Cement Ltd and Class F fly ash are used as cementitious materials in the ratio of 70:30.

Fly ash was procured from M/S ACC plant, Bengaluru. Chemical composition of fly ash was determined by X-Ray fluorescence. The pertinent properties of cementitious materials and chemical composition of fly ash are provided in Tables 25.1 and 25.2, respectively.

Manufactured sand (M-sand) and 12.5 mm down size angular granite stones which are Saturated Surface Dry (SSD) are used as fine and coarse aggregates from the locally available source. Particle size distribution curve of M-sand is indicated in Fig. 25.1 from which it could be observed that it conforms to zone-II. Physical properties of coarse and fine aggregates are given in Table 25.3. Auromix 300 Plus manufactured by FOSROC Chemicals (India) is used as super plasticizer with concrete, which complies with IS: 9103-1999 (2007).

Areca husks were collected from an Areca plantation near the city Davanagere, Karnataka. The husks were chopped into three equal parts where the middle third is

Table 25.1 Physical properties of cementitious materials

Materials	Cement	Fly ash	Relevant standard
Specific gravity	3.1	2.2	IS 4031-part 11 1988
Specific surface area	305 m ² /kg	325 m ² /kg	IS 4031-part 2 1999
Normal consistency	31%	NA	IS 4031-part 5 1988
Initial setting time	120 min	NA	IS 4031-part 5 1988
Final setting time	250 min	NA	IS 4031-part 5 1988

Table 25.2 Chemical composition of fly ash

Oxides	SiO ₂	Al ₂ O ₃	Fe ₂ O ₃	CaO	Na ₂ O	K ₂ O	SO ₃
% of oxides in fly ash	56.21	28.50	8.56	1.50	0.28	1.14	0.25

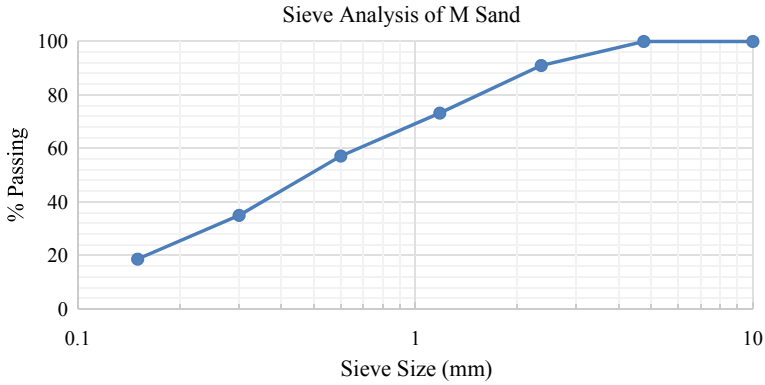


Fig. 25.1 Particle size distribution of fine aggregate (M-sand)

Table 25.3 Physical properties of coarse and fine aggregates

Materials	Coarse aggregate	Fine aggregate	Relevant standard
Specific gravity	2.70	2.70	IS2386-part 3-1963
Bulk density (Kg/m ³)	1318	1678	IS2386-part 3-1963
Water absorption (%)	0.4	1.8	IS2386-part 3-1963

Fig. 25.2 Areca nut fibre



soaked in water for about 5 days. The soaking process loosens the fibres which can then be easily extracted as shown in Fig. 25.2. The fibres were mixed with concrete in saturated surface dry condition. The parameters pertaining to areca fibres are tabulated in Table 25.4.

Table 25.4 Physical properties of areca fibres

Physical properties	
Diameter (mm)	0.38
Aspect ratio (L/d)	40–70
Density (g/cm ³)	1.1
Water absorption (%)	50
Tensile strength (N/mm ²)	114.2
Young's modulus (N/mm ²)	325

25.2.2 Methods

Concrete Mix Design. Trials of mix design are carried out on the general guidelines of IS 10262-2009. The basic tests for all the ingredients of concrete are carried out for determining the final mix-design parameters. The details of the final mix is tabulated in Table 25.5.

Mixing and Casting. The ingredients were mixed in a motor-driven rotary drum-type mixer. The coarse and fine aggregate were added without any water addition at this stage. After a couple of rotations, cement and fly ash are added together and one-third of the water with the super plasticizer diluted in it is added. The mixer drum is rotated while the fibres are being added in very small instalments so as to ensure proper dispersion of fibres into the medium. After all the fibres are added, one-third of the mixing water is added into the drum. After a few rotations of the drum, the remaining water is added and mixed until the mix is uniformly consistent about 4–5 rotations.

Five mixes were prepared with different percentage of areca fibres in it, i.e. 0, 1, 1.5, 2, 2.5 and 3%, and these mixes are named as M0, M1, M1.5, M2.0, M2.5 and M3.

Table 25.5 Details of mix design

Constituents		Content kg/m ³	Remarks
Total cementitious content	Cement	390	Water to binder ratio, W/B = 0.39
	Fly ash	210	
Fine Aggregates (FA)		540.8	
Coarse Aggregates (CA)		716.34	
Water		240	
Specific weight of concrete		2097.14	

25.3 Results and Discussion

25.3.1 Fresh Concrete Mixes

The capability of the concrete to flow, resistance to segregation and passing ability is measured using the slump flow test, V-funnel test and L-box test (as per EFNARC specifications). The slump values for different mixes is tabulated in Table 25.6. In general, it was observed that the workability of the concrete decreases with the increase in fibre content in concrete mixes. Hence in view of the requirement of self-compacting concrete and drastic reduction of workability with increase in fibre percentage, sufficiently higher binder content is selected. The maximum slump was observed for conventional self-compacting concrete and minimum slump was observed for 3% areca fibre. The passing ability of concrete mix decreases with increase in areca fibre content. The segregation resistance was observed more at 3% of areca fibre.

25.3.2 Hardened Concrete Mixes

Compression Test. The compression test is carried out in compression testing machine with the maximum load carrying capacity of 2000 kN, and the test is done as per IS: 516-1959 (IS: 4031 Part-11 1988) guidelines. The cubes of dimension $150 \times 150 \times 150$ mm were cast. The compressive test is carried after 7 days and 28 days of curing. The cubes with different percentages of areca fibre, i.e. 0, 1, 1.5, 2, 2.5 and 3% in it are tested. The results are tabulated in Table 25.3 and the variation of compressive strength is shown in Fig. 25.3. From the results presented in Table 25.7 and Fig. 25.3, it can be observed that the compressive strengths of all the mixes, in general, decrease with an increase in fibre contents. This can be attributed to, the increase in fibre content, and the number of paste–fibre interfaces will increase resulting in reduced compressive strengths.

Table 25.6 Details of fresh concrete tests of SCC with different percentage of fibres

Mix	Slump flow observed (mm)	V-funnel Time (s)	L-Box H2/H1	% of SP dosage
M0	690	7	0.98	0.5
M1	680	8	0.95	0.5
M1.5	674	9	0.89	0.6
M2.0	669	11	0.86	0.6
M2.5	655	11	0.82	0.8
M3.0	652	12	0.81	1.0

Fig. 25.3 Variation of compressive strength versus percentage of fibres

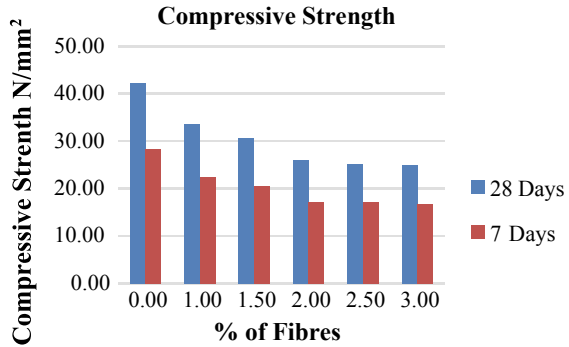


Table 25.7 Compressive strength of hardened concrete

Mix	Compressive strength (N/mm ²)	
	7 days	28 days
M0	27.95	42.36
M1.0	22.54	33.64
M1.5	20.53	30.65
M2.0	17.21	26.08
M2.5	17.21	25.09
M3.0	16.8	25.00

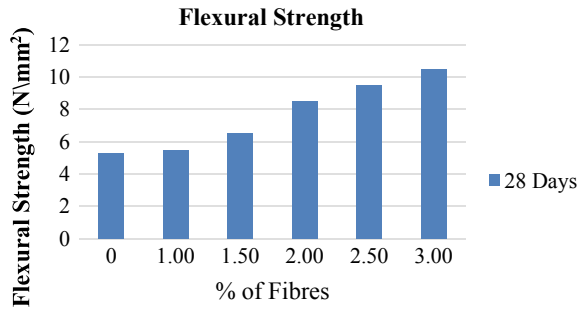
From Table 25.7, one can infer that the mixes, M1, M1.5, M2.0, M2.5 and M3, have achieved reasonable lower compressive strengths, i.e. 21%, 28%, 38%, 41% and 41%, respectively, with reference to the control mix (M0).

Flexural Strength of Concrete. The flexural strength test is carried out in universal testing machine with the maximum load carrying capacity of 400 kN and the test is done as per IS: 516-1959 guidelines. The beams of dimension 100 × 100 × 500 mm were cast. The flexural test is carried after 28 days of curing. The beams with different percentages of basalt fibre, i.e. 0, 1, 1.5, 2 and 2.5% in it are tested. The results of flexural test are tabulated in Table 25.8 and the variation of flexural strength is shown in Fig. 25.4.

Table 25.8 Flexural strength of hardened concrete

Mix	Flexural strength (N/mm ²) 28 days
M0	5.3
M1.0	5.50
M1.5	6.50
M2.0	8.50
M2.5	9.50
M3.0	10.50

Fig. 25.4 Variation of flexural strength versus percentage of fibres



From Table 25.8, and Fig. 25.4, it can be seen that flexural strengths of the mixes increases with an increase in the fibre content. Mixes M1, M1.5, M2, M2.5, and M3, recorded the high flexural strength with a strength increase of 4, 18, 38, 44, and 50%, as compared to the control mix (M0).

25.4 Fibre Distribution in Matrix

Specimens after testing were visually inspected for the rupture surface and fibre distribution. It was found that the fibre distribution was uniform for 1, 1.5 and 2% fibre dosages. Clumping and balling of fibres was observed for 2.5 and 3% fibre dosages. This can be seen from Fig. 25.5.

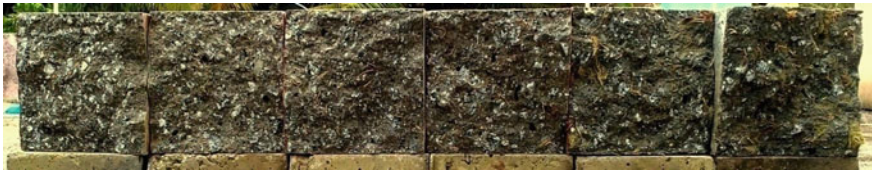


Fig. 25.5 Fibre distribution in flexure specimens post failure-from left to right [M0, M1, M1.5, M2, M2.5 and M3]

25.5 Conclusions

In the present study, areca nut fibre reinforced self-compacting concrete mixes are developed to investigate the mechanical strength properties, in which areca fibres are added in different proportions; such developed concrete mixes were tested for their fresh and hardened state.

Following conclusions are drawn based on the results of studies conducted in the present study.

- In general, it was observed that the workability of the concrete decreases with the increase in fibre content in concrete mixes.
- The compressive strength of concrete mixes M1, M1.5, M2, M2.5 and M3, decreases by 21%, 28%, 38%, 41% and 41%, respectively, with reference to the control mix (M0).
- The flexural strength of concrete mixes M1, M1.5, M2, M2.5 and M3, increases by 4%, 18%, 38%, 44%, and 50%, respectively, with reference to the control mix (M0).
- The factors affecting the compressive strength characteristics are percentage of fibre content and distribution of fibres in concrete mixes in the order of their influence.

25.6 Suggestions for Future Directions

In view of the experiments conducted and the results the following scope for future work has been suggested.

- The studies on impact and splitting tensile strengths can be performed.
- A comparison between surface modified and non-surface modified areca fibres as reinforcing agent can be studied.
- A detailed analysis of variations in workability can be done to assess the optimum fibre dosage in view of workability.
- Durability studies on areca fibre reinforced concrete can be done.

References

- Ashok RB, Srinivasa CV, Basavaraju B (in press) A review on the mechanical properties of areca fiber reinforced composites. *Sci Mater Technol*
- Aslani F, Nejadi Sh (2013) Self-compacting concrete incorporating steel and polypropylene fibers: compressive and tensile strengths, moduli of elasticity and rupture, compressive stress–strain curve, and energy dissipated under compression. *Compos B Eng* 53:121–133

- Aziz M, Paramasivam A (1982) Prospects for natural fiber reinforced concretes in construction. *Int J Cem Compos Light Concr* 4:75–82
- EFNARC (2005) Specification and guidelines for self-compacting concrete, Feb 2002
- IS: 516 (1959) Methods of tests for strength of concrete. Bureau of Indian Standards, New Delhi, India
- IS: 10262 (2009) Concrete mix proportioning-guidelines. Bureau of Indian Standards, New Delhi, India
- IS: 2386 Part-03 (1963) Methods of tests for aggregates for concrete. Bureau of Indian Standards, New Delhi, India
- IS: 4031 Part-02 (1999) Methods of physical tests for hydraulic cement. Bureau of Indian Standards, New Delhi, India
- IS: 4031 Part-05 (1988) Methods of physical tests for hydraulic cement. Bureau of Indian Standards, New Delhi, India
- IS: 4031 Part-11 (1988) Methods of physical tests for hydraulic cement. Bureau of Indian Standards, New Delhi, India
- IS: 9103 (1999) Concrete admixtures specifications. Bureau of Indian Standards, New Delhi, India
- Kaushik P, Jaivir J, Mittal K (2017) Analysis of mechanical properties of jute fiber strengthened epoxy/polyester composites. *Eng Solid Mech* 5(2):103–112
- Khaloo A, Raisi EM, Hosseini P, Tahsiri H (2014) Mechanical performance of selfcompacting concrete reinforced with steel fibers. *Constr Build Mater* 51:179–186
- Khayat KH, De Schutter G (eds) (2014) Mechanical properties of self-compacting concrete. State-of-the-art report of the rilem technical committee 228-MPS on mechanical properties of self-compacting concrete, vol 14. Springer
- Musmar M (2013) Tensile strength of steel fiber reinforced concrete. *Contemp Eng Sci* 6(5):225–237
- Nayak S, Mohanty JR (2018) Influence of chemical treatment on tensile strength, water absorption, surface morphology, and thermal analysis of areca sheath fibers. *J Nat Fibers* 1–11
- Neves RD, de Almeida JCOF (2005) Compressive behaviour of steel fibre reinforced concrete. *Struct Concrete* 6(1):1–8
- Padmaraj NH, Keni LG, Chetan KN, Mayur S (2018) Mechanical characterization of areca husk coir fiber reinforced hybrid composites. In: PMME 2016, materials today: proceedings, vol 5, pp 1292–1297
- Thomas J, Ramaswamy A (2007) Mechanical properties of steel fiber-reinforced concrete. *J Mater Civ Eng ASCE* 19:385–392
- Tioua T, Kriker A, Bali A, Barluenga G, Behim M (2017) Properties of self-compacting concrete with natural and synthetic fibers. *Spec Publ* 240:24.1–24.10

Chapter 26

Development of Eco-friendly Geopolymer Concrete Using M-Sand



Dhavamani Doss Sakthidoss 
and Thirugnanasambandam Senniappan 

26.1 Introduction

At the moment all of us are dwelling in the realm of technology and advanced creations almost in each and every field. These advancements brought us to the next level of amusing experience. In the same time, there are also many problems that have arrived as the effect of these advancements. One such problem in the field of construction is depletion of natural raw material for construction. The other burning issue around the world is global warming as a result of high emission of greenhouse gases into the atmosphere. The former issue is here because of the continued utilization of natural raw materials, particularly in the field of construction. At the current scenario, there is a vast development in the infrastructure in the world. High utilization of construction materials is required to fulfil the need of construction industries. Concrete is one of the predominant materials used in the construction. It consists of cement as a binder, sand, and blue metal as filler and water for mixing of concrete. All these materials are obtained from natural sources. Today due to continuous consumption of limestone (raw material for cement), river sand (fine aggregates) and water are becoming extinct. Continuous utilization will lead to complete extermination of these materials. So we are in the fix to find an alternative for these natural resource materials. On the other hand, the production of cement requires high energy efficiency to burn the natural limestone. During the burning of limestone at elevated temperature it will emit higher amount of carbon dioxide to the atmosphere, which is an important source of greenhouse gases into the atmosphere. Around four percent of total pollution throughout the world is contributed by the cement industries. One molecule of cement produces one molecule of carbon dioxide (McCaffrey 2002).

D. D. Sakthidoss (✉) · T. Senniappan
Annamalai University, Annamalainagar, Cuddalore 608002, India
e-mail: dhavamanidossphd@gmail.com

T. Senniappan
e-mail: agstsai@gmail.com

It is a major headache for scientists since the percentage increase of global warming is increasing day by day. These problems can be minimized by utilizing the waste materials which are in abundant quantity. In our country there is a lot of burned coal waste in the thermal power plants available in the form of fly ash. Fly ash is a hazardous waste if it is dumped unsafely. It is also a painful problem for the authorities in the thermal power plants across the country, to dispose these fly ashes in a safe way. So using these fly ashes as complete replacement for cement in the production of concrete will attain a fruitful solution for both the issues. The river sand is almost in the extinct state in our country. M-Sand may be used to overcome the shortage of natural river sand in the construction (Kumars and Kotian 2018). In this research we are focusing on the suitability of these materials as an alternative to conventional concrete by using geopolymer concrete with M-sand.

26.2 Geopolymer Concrete

Geopolymer concrete is manufactured by using inorganic polymers rich in silica and alumina. There is a huge list of silica–aluminium resource materials such as kaolinite, metakaolin, fly ash, and rice husk ash. Among them, fly ash was chosen for manufacturing geopolymer concrete with M-sand as aggregate. Fly ash is a material that has similar properties of cement except the binding property. So to initiate the binding property of fly ash, an alkaline solution is added during mixing of concrete. In this context, water is mainly reduced to a greater extent. The alkaline solution is a combination of sodium or potassium hydroxide and sodium or potassium silicate solution. The name geopolymer was devised by Dr. Joseph Davidovits, a French scientist in 1978 (Davidovits 1994; Hardjito and Rangan 2005). The chemical constituents of geopolymer source materials are comparable to natural zeolite compounds but with different microstructure. The geopolymer materials are amorphous in nature whereas zeolite materials are crystalline in nature (Palomo et al. 1999). The chemical reaction takes place in the alkaline medium is very fast and it is a polymerization process on silica and alumina resulting in the formation of three-dimensional polymeric chain structure consisting of Si-O-Al-O bonds (Davidovits 1999). During the process of curing or further drying period the water from the geopolymer concrete is expelled from the matrix of geopolymer concrete. This will aid the concrete with discontinuous nanopores and hence the performance of the geopolymer concrete is increased. Through this process it is noted that unlike the cement concrete the water in geopolymer concrete has no chemical reaction with the cementitious material. The little amount of water added in geopolymer concrete during mixing is only for workability enhancement (Hardjito and Rangan 2005; Davidovits 1999). In addition with fly ash Ground Granulated Blast Furnace Slag (GGBS) is also added to enhance the properties of geopolymer concrete. M-Sand (replacement for natural river sand) and crushed stones are used as filler materials in geopolymer concrete. Figure 26.1 shows the casting and curing of geopolymer concrete.

Fig. 26.1 Casting and curing of geopolymer concrete



26.3 Properties of Materials

26.3.1 Cement

Ordinary Portland cement is used for casting conventional concrete. The grade of cement selected for the research is 53 grade. The cement used is conforming the IS: 12269-1987 (IS 1988, 1989). The properties of cement are shown in Table 26.1.

26.3.2 Fly Ash

By its terminology it is understood, that fly ash is blown through the tall chimneys during the process of burning coal in the thermal power plants. Fly ash substances are smaller and finer than the OPC. Dust collection system is used to collect the fly ash before they reach the atmosphere mechanically or using electrostatic precipitators (Hardjito and Rangan 2005). Fly ash is rich in silica, aluminium, iron, calcium oxide with smaller amount of potassium, magnesium, titanium, sulphur, and

Table 26.1 Physical properties of 53 grade OPC

SI. No.	Physical properties	Test results	IS: 2269-1987 stipulations
1	Specific gravity	3.15	–
2	Particle size range	6.6–31 μm	–
3	Initial setting time	42 minutes	30 minutes
4	Final setting time	235 minutes	600 minutes
5	Specific surface area	0.337 m^2/g	225 m^2/g
6	Normal consistency	35 %	–
7	Soundness test	3 mm	10 mm
8	Compressive strength	53.25 N/mm^2	53 N/mm^2

Table 26.2 Physical properties of fly ash

SI. No.	Physical properties	Test results
1	Specific gravity	2.1
2	Particle size range	4–16 μm
3	Bulk density	995 kg/cm^3
4	Compressive strength	53.55 N/mm^2

sodium. The fly ash is classified into class C and class F types. Based on the content of Calcium Oxide decides the type of fly ash. Class C type consists of CaO more than 20% and class F type consists of CaO lesser than 10%. Class F type fly ash is also known as low calcium fly ash and it is more suitable for geopolymer concrete (Malhotra and Ramezaniapour 1994). The fly ash used in this research is obtained from Mettur thermal power plant which is classified as class F type. The properties of class F fly ash are shown Table 26.2.

26.3.3 *Ground Granulated Blast Furnace Slag (GGBS)*

GGBS is a fine powder obtained by quenching glassy and granular iron slag, a byproduct of steel or iron. GGBS has similar composition like cement with different proportions (Pithadiya and Nakum 2015). GGBS is added in geopolymer concrete to enrich the properties of geopolymer concrete such as binding and mechanical properties. The addition of GGBS also eliminates the usage of water curing, since the geopolymer concrete with GGBS will confirm ambient curing (Kiran et al. 2015). The properties of class F fly ash are shown in Table 26.3.

26.3.4 *Manufacturing Sand (M-Sand)*

M-S sand is manufactured by crushing of tough granite stones. M-Sand has many advantages compared to river sand. It is manufactured in industries, which will ensure proper particle shape and size of the material. The impurities present in the M-Sand can be removed. The cubical shape of the M-Sand will ensure the packing

Table 26.3 Physical properties of GGBS

SI. No.	Physical properties	Test results
1	Specific gravity	2.65
2	Particle size range	0.4–40 μm
3	Bulk density	1220 kg/m^3
4	Specific surface area	422 m^2/kg

Table 26.4 Physical properties of M-Sand

SI. No.	Physical properties	Test results
1	Specific gravity	2.70
2	Particle size range	150 μ –4.75 mm
3	Bulk density	1820 kg/m ³
4	Fineness modulus	2.85 m ² /kg
5	Grading of M-Sand	Zone II as per IS: 383–1970

of the matrix and will increase the mechanical properties of the geopolymer concrete. The properties of class F fly ash are shown Table 26.4.

26.3.5 Coarse Aggregate

The natural crushed stone is used. Clean hard and dense crushed granite stone of size passing 20 mm and retained 12.5 mm sieves are taken for the study. The properties of coarse aggregates are shown in Table 26.5. The coarse aggregate chosen for test confirms the IS: 2386-1963 part IV and V (IS 1963, IS 1963).

26.3.6 Alkaline Solution

Alkaline solution is a mixture of sodium/potassium silicate and sodium/potassium hydroxide (Davidovits 1999). For economical and better performances, sodium hydroxide, and sodium silicate solutions are used (Xu and van Deventer 2000). The alkaline solution will stimulate the binding capacity of fly ash. The alkaline solution concentration depends upon the amount of sodium hydroxide dissolved in the solution. The concentration of the alkaline solution is also known as molarity of solution. The properties of sodium hydroxide and sodium silicate solution are given in Tables 26.6 and 26.7.

Table 26.5 Physical properties of coarse aggregate

SI. No.	Physical properties	Test results
1	Specific gravity	2.70
2	Water Absorption	0.5 %
3	Bulk density	1535 kg/m ³
4	Fineness modulus	6.75 m ² /kg
5	Aggregate crushing value	29 %

Table 26.6 Specification of sodium silicate solution

Specification	
Chemical formula	$\text{Na}_2\text{O} \times \text{SiO}_2$ (colour less)
pH	Neutral
Assay of Na_2O	7.5–8.5%
Assay SiO_2	25–28%
Wt per ml 20 °C	1.35 g/ml
Appearance	Liquid (Gel)

Table 26.7 Specification of sodium hydroxide

Specification	
Purity	97% minimum
Sulphate (SO_4)	0.05% maximum
Potassium (K)	0.1% maximum
Zinc (Zn)	0.02% maximum
Leda (Pb)	0.001% maximum
Chloride (Cl)	0.1% maximum
Carbonate (Na_2CO_3)	2% maximum
Silicates (SiO_3)	0.05% maximum
10% Aqueous solution	Clear and colourless
Iron (Fe)	0.001% maximum

26.3.7 Super Plasticizer

To enhance the workability of concrete, suitable super plasticizer is used. In this work, naphthalene based super plasticizer is used. 0.40% by weight of cementitious material of SP is used. The specific gravity of the SP used is 1.2.

26.4 Experimental Findings

26.4.1 Mix Proportion

In this research, three types of mixes are proportioned to cast cube specimens of M30 grade with different types of materials. The first mix is designed for M30 conventional concrete. The second mix is designed for M30 grade geopolymer concrete and the third mix is designed for M30 grade geopolymer concrete with M-Sand. The ratio is kept constant for all the mix proportions as 1: 2.12: 3.37. The sodium silicate solution to sodium hydroxide ratio is fixed at 2.5. The molarity of the solution is 8 M. The alkaline solution to fly ash ratio is taken as 0.47. The alkaline solution should be prepared before 24 h prior to mixing of geopolymer concrete. The sodium pellets are dissolved in little amount of water and leave it for

some hour. After that the sodium silicate solution is mixed with the sodium hydroxide and this solution is kept at room temperature for 24 hours.

26.4.2 Casting and Mixing of Conventional Concrete

The conventional concrete specimens are cast by mixing cement and sand thoroughly until uniform appearance occurs, then the matrix is mixed with crushed stone and mixed for 4 minutes then water is added. Half of the water is mixed with concrete materials initially and in the remaining water SP is added. Then the water with SP is stirred well and it is added with concrete material and mixed thoroughly. The completely mixed concrete is poured into steel moulds of size $150 \times 150 \times 150$ mm. Slump test is conducted and a slump value of 60 mm is obtained.

26.4.3 Casting and Mixing of Geopolymer Concrete with and Without M-Sand

The material used for geopolymer concrete is different from cement concrete. In geopolymer concrete cement is completely replaced by 50% of fly ash and 50% of GGBS. In one mix river sand is used as fine aggregate and in another mix river sand is fully replaced by M-Sand. Crushed stones are used as coarse aggregate. First, the fly ash and GGBS are completely mixed and then it is mixed with fine aggregate for 2 minutes and then coarse aggregate is added and again mixed for 2 minutes. The 24 h prior prepared alkaline solution is partially mixed with all the materials. Then in remaining solution, SP is added to enhance the workability. Then the mixture is mixed well for two to 3 minutes and the concrete is poured into steel moulds of size 100 mm x 100 mm x 100 mm. Slump test is conducted and true slump is obtained for both the mixes with sand and M-Sand as fine aggregate in geopolymer concrete. Figure 26.1 shows the casting process of concrete cubes and the ambient curing of geopolymer concrete cubes.

26.4.4 Curing and Testing of Specimens

The cast cube specimens are cured and tested to determine compressive strength. The conventional cube specimens are cured underwater for 28 days. The geopolymer cubes are cured under ambient curing condition which completely eliminating water curing. The conventional cubes take 28 days for complete (90%)

Table 26.8 7 days compressive strength of conventional concrete

SI. no.	Cube specimen size (mm)	Weight of specimen (kg)	Ultimate load (kN)	Compressive strength (N/mm ²)	Average compressive strength (N/mm ²)
1	150 × 150	8.826	731	32.49	31.67
2	150 × 150	8.729	682	30.31	
3	150 × 150	8.774	725	32.22	

Table 26.9 14 days compressive strength of conventional concrete

SI. no.	Cube specimen size (mm)	Weight of specimen (kg)	Ultimate load (kN)	Compressive strength (N/mm ²)	Average compressive strength (N/mm ²)
1	150 × 150	8.830	772	34.31	35.70
2	150 × 150	8.725	860	38.22	
3	150 × 150	8.770	780	34.67	

Table 26.10 28 days compressive strength of conventional concrete

SI. no.	Cube specimen size (mm)	Weight of specimen (kg)	Ultimate load (kN)	Compressive strength (N/mm ²)	Average compressive strength (N/mm ²)
1	150 × 150	8.831	865	38.44	38.80
2	150 × 150	8.730	870	38.67	
3	150 × 150	8.729	885	39.35	

hardening while geopolymer concrete takes 24 h for hardening and can be tested after that. The compressive strength of conventional concrete specimens at 7, 14 and 28 days is given in Tables 26.8–26.10. Testing the conventional and geopolymer concrete cube testing is shown in Fig. 26.2. The compressive strength of geopolymer concrete with river sand and M-Sand are given in Tables 26.11 and 26.12.

The compressive strength is compared and the results are shown in Figs. 26.3, 26.4, 26.7 and 26.8. The compressive strength of geopolymer concrete is higher than conventional concrete and the compressive strength of geopolymer concrete with manufactured sand is higher than geopolymer concrete with river sand.



Fig. 26.2 Testing of concrete specimens

Table 26.11 3 days compressive strength of geopolymer concrete with river sand

SI. no.	Cube specimen size (mm)	Molarity (M)	Weight of specimen (kg)	Ultimate load (kN)	Compressive strength (N/mm ²)	Average compressive strength (N/mm ²)
1	100 × 100	7.5	2.436	396	39.60	39.50
2	100 × 100	7.5	2.458	387	38.70	
3	100 × 100	7.5	2.476	402	40.20	

Table 26.12 3 days compressive strength of geopolymer concrete with M-Sand

SI. no.	Cube specimen size (mm)	Molarity (M)	Weight of specimen (kg)	Ultimate load (kN)	Compressive strength (N/mm ²)	Average compressive strength (N/mm ²)
1	100 × 100	7.5	2.445	446	44.60	43.77
2	100 × 100	7.5	2.496	438	43.80	
3	100 × 100	7.5	2.396	429	42.90	

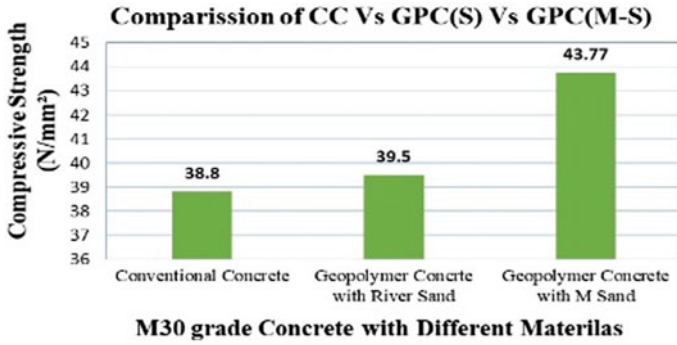


Fig. 26.3 Comparison of M30 concrete CC vs GPC(S) vs GPC(M-S)

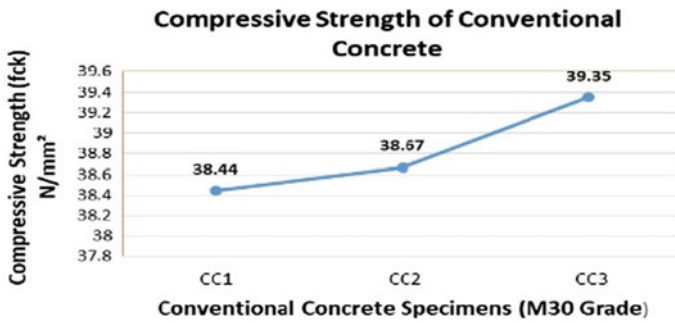


Fig. 26.4 Compressive strength of conventional concrete at 28 days

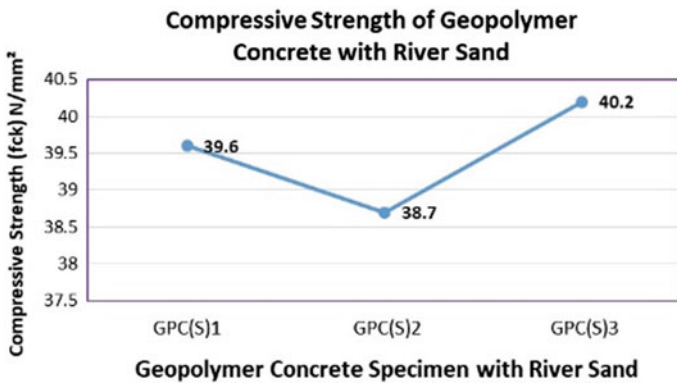


Fig. 26.5 Compressive strength of M30 grade geopolymer concrete with river sand (GPC(S))

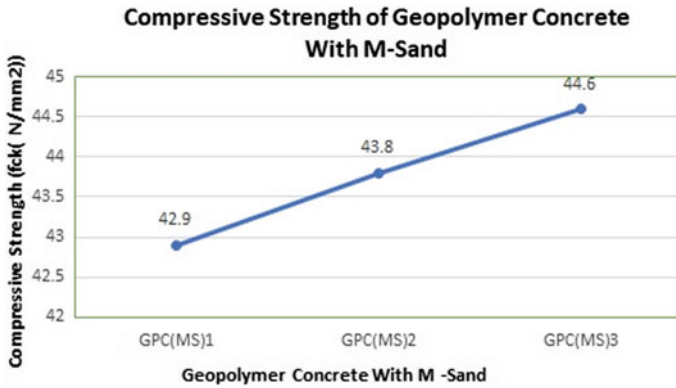


Fig. 26.6 Compressive strength of M30 grade geopolymer concrete with M- Sand (GPC(M-S))

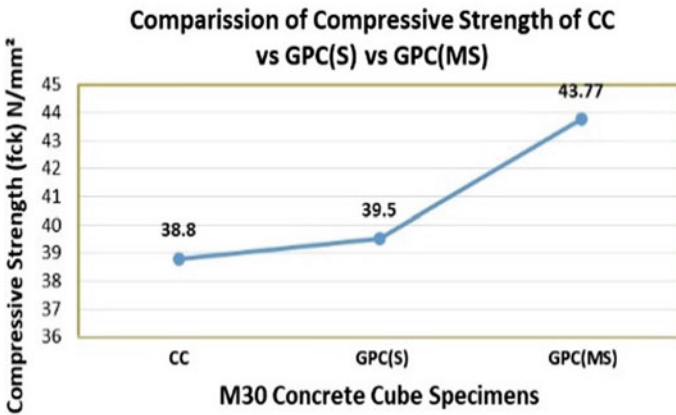


Fig. 26.7 Comparison of compressive strength of CC vs GPC(S) vs GPC(M-S)

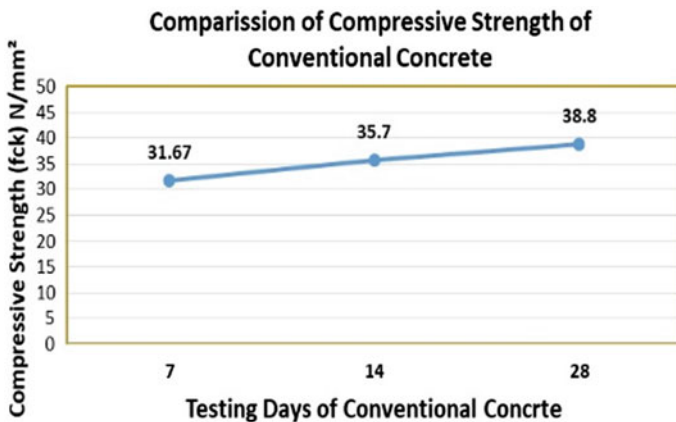


Fig. 26.8 Comparison of compressive strength of conventional concrete at 7, 14 and 28 days

26.5 Results and Discussions

The experimental results of the geopolymer concrete with M-Sand is encouraging well. The geopolymer concrete attains higher value than traditional concrete in 3 days, where traditional concrete attains in 28 days. Figures 26.3–26.8 show that the representation of results obtained by the compressive strength on concrete specimens of conventional concrete and geopolymer concrete with river sand and M-Sand. The average values are taken and standard error values have been considered from Figs. 26.4–26.6. The concrete with geopolymer exhibits higher strength than conventional concrete are shown in Figs. 26.3 and 26.7.

26.6 Conclusions

Conventional concrete, geopolymer concrete with river sand and geopolymer concrete with M-Sand are cast. Among them, geopolymer concrete with M-Sand shows better compressive strength than the other types of concrete. This is due to the presence of fly ash and GGBS, which are rich in silica and aluminium. The geopolymer concrete with river sand shows higher compressive strength than conventional concrete but lesser than the geopolymer concrete with M-Sand attributed to the superior gradation of M-Sand.

The experimental results convey that the geopolymer concrete shows better compressive strength and the following conclusions are made:

1. The compressive strength of conventional concrete is 31.67 N/mm², 35.70 N/mm², 38.80 N/mm² on 7, 14, 28 days, respectively.
2. The compressive strength of geopolymer concrete with river sand is 39.50 N/mm². It is 2.6% higher than conventional concrete.
3. The compressive strength of geopolymer concrete with M-Sand is 43.77 N/mm². It is 12.81% higher than conventional concrete and 10.81% higher than geopolymer concrete with river sand
4. Water is mandatory for curing up to a period of 28 days for conventional concrete but ambient curing is sufficient for geopolymer concrete for 24 hours. It will minimize the use of water and the time consumption during constructions.

References

- Davidovits J (1994) High-Alkali cements for 21st century concretes in concrete technology, past, present and future. In: Kumar Metha P (ed) Proceedings of V. Mohan Malhotra Symposium. ACI SP-144, pp 383–397
- Davidovits J (1999) Chemistry of geopolymeric systems, terminology. Geopolymer '99 International conference, France

- Hardjito D, Rangan BV (2005) Development and properties of low calcium fly ash—based geopolymer concrete. Research report GC 1, Faculty of Engineering, Curtin University of Technology, Perth, Australia
- IS 2386 (1963) Methods of test for aggregates for concrete. Part IV Mechanical Properties. Bureau of Indian standards, New Delhi, India
- IS 2386 (1963) Methods of test for aggregates for concrete, Part V Soundness. Bureau of Indian standards, New Delhi, India
- IS: 4031 (1988) Method of Physical test of Hydraulic Cement. Bureau of Indian standards, New Delhi, India
- IS 12269 (1989) Specification for 53 grade ordinary Portland cement. Bureau of Indian standards, New Delhi, India
- Kiran T et al (2015) Impact test on geopolymer concrete slabs. *Int J Res Eng Technol* 4:110–116
- Kumars S, Kotian RS (2018) M-SAND, an alternative to the river sand in construction technology. *9(4):98–102*
- Malhotra VM, Ramezani pour A (1994) Fly ash in concrete. Ontario, Canada, CANMET, Ottawa
- McCaffrey R (2002) Climate change and the cement industry. *global cement and lime magazine (Environmental Special Issue)*, 15–19
- Palomo A et al (1999) Alkali-activated fly ashes, a cement for the future. *Cem Concr Res* 29 (8):1323–1329
- Pithadiya PS, Nakum AV (2015) Experimental study on geopolymer concrete by using GGBS. *Int J Res Eng Technol* 04:185–187
- Xu H, van Deventer JSJ (2000) The geopolymerisation of alumino-silicate minerals. *Int J Miner Process* 59(3):247–266

Chapter 27

Mechanical and Durability Study of Steel Fiber-Reinforced Geopolymer Concrete



Abhishek Pulgur Venkatesha Babu, R. K. Chethan Gowda,
L. Divakar, C. Vachan, Rajath Raj, C. H. Sri Karan
and R. D. Sayabanna

27.1 Introduction

Cement Concrete (CC) is one of the abundantly used material in construction industry according to some estimates its usage is only next to water. The primary composition of the Cement Concrete is Ordinary Portland Cement (OPC) and other naturally available raw materials. The production of OPC is environmentally intrusive process because for every ton of cement production equivalent amount of carbon dioxide is released to atmosphere and also about 50% of raw materials procured are deemed not suitable for OPC production (Meyer 2009; Chen et al. 2010; Peng et al. 2013). These lead to various environmental problems such as global warming, leaching in landfills, natural resource exhaustions, excessive mining, etc. This necessitated the adaption of environmentally friendly materials, industrial byproducts, and waste materials, etc., for production of concrete which has same or better properties as compared to CC. Waste materials such as Flyash (FA), Rice-Husk Ash (RHA), sugarcane bagasse ash, silica fume, Ground Granulated Blast furnace Slag (GGBS), etc., have been either used as replacement to cement or as standalone material to produce Geopolymer Concrete (GPC) or alkali-activated slag concretes (Singh et al. 2015; Provis 2014).

The serviceable life of the concrete structure depends on the durability properties of the concrete. Concrete structures exposed to aggressive environments are not serving the intended life as concrete deteriorates faster under such conditions. The hydration products of OPC are factors which influence the durability properties of

A. Pulgur Venkatesha Babu (✉) · R. K. Chethan Gowda · L. Divakar ·
C. Vachan · R. Raj · C. H. Sri Karan · R. D. Sayabanna
Department of Civil Engineering, M.S. Ramaiah University of Applied Sciences,
Bengaluru 560056, Karnataka, India
e-mail: abhishek.pulgur@gmail.com

CC. Geopolymer concrete has good sulfate and acid resistance (Mehta and Siddique 2017; Ban et al. 2017; Wang et al. 2016). The geopolymer concrete incorporated with steel fibers exhibit better flexural strength and tensile strength as compared with GPC without fibers, fiber incorporation also increases the post cracking behavior of concrete increasing the structural integrity of GPC. Most of the GPC are flyash based, the durability studies of GPC with flyash and GGBS have little information in the literature survey, and with this research gap the mechanical and durability properties of the concrete with steel fibers have been investigated.

27.2 Experimental Procedure

27.2.1 Materials Used

In this study, geopolymer concrete is prepared by the 50:50 combination of the GGBS and class F flyash for binder. The GGBS was procured from ACC plant and whereas flyash was procured from Raichur thermal power plant. The chemical properties of the binder were determined using X-Ray fluorescence which is presented in Table 27.1. The physical properties such as specific gravity, specific surface area, soundness and loss of ignition are determined according to relevant IS standards are presented in Table 27.2. Manufactured sand (M-Sand) is used for the fine aggregate and 20 mm down angular granite is used for coarse aggregates, both these were procured from locally available sources. The physical properties such as specific gravity, fineness modulus, water absorption, bulk density were determined and are presented in Table 27.3.

Hooked end steel fibers having aspect ratio of 80 were procured from Chennai was used to prepare Steel fiber-reinforced geopolymer concrete. The impurities present in the steel were tested and are indicated in Table 27.4. The activator used was sodium based which was mixture of 14 M sodium hydroxide and sodium silicate solution. The water glass modulus of the sodium silicate used in the study was about 2.34. The sodium hydroxide solution was prepared from 97% pure NaOH flakes. The ratio of sodium silicate to sodium hydroxide solution was maintained at 2.5.

Table 27.1 Chemical composition of fly ash and GGBS

Sample %	SiO ₂	Al ₂ O ₃	Fe ₂ O ₃	CaO	Na ₂ O	K ₂ O	SO ₃
Fly ash (type F)	56.21	28.50	8.56	1.50	0.28	1.14	0.25
GGBS	30.35	15.75	1.85	36.52	0.36	0.45	0.14

Table 27.2 Physical properties of Binder materials

Materials	Fly ash	GGBS	Relevant standard
Specific gravity	2.0	2.85	IS 4031-part 11-2005
Specific surface area	325 m ³ /kg	350 m ³ /kg	IS 4031-part 2-1999
Loss on ignition	0.75%	2.1%	IS 1727-1967
Soundness (expansion)	1 mm	1 mm	IS 1727-1967 and IS 4031-1968

Table 27.3 Physical properties of aggregates

Materials	Coarse aggregate	Fine aggregate	Relevant standard
Specific gravity	2.8	2.45	IS 2386-part 3-1963
Bulk density	1685.2 kg/m ³	1623.91 kg/m ³	IS 2386-part 3-1963
Water absorption	0.3%	1.3%	IS 2386-part 3-1963
Fineness modulus	7.17	3.65	IS 2386-part 1-1963

Table 27.4 Mix proportions of GPC

Mixture	Coarse aggregate (kg/m ³)	Fine aggregate (kg/m ³)	Fly ash (kg/m ³)	GGBS (kg/m ³)	Activator solution (kg/m ³)	Fibre content ^a	Super plasticizer ^a
SF2	1200	600	240	160	200	2	2

^aFibre content in % of weight of total binder considered

27.2.2 Methods

The mix proportion of the geopolymer concrete was done according to Patankar et al. (2015) and the mix proportion considered for the study is indicated in Table 27.5, the mix proportion considered for the study had given excellent compressive strength, flexural and tensile characteristics was considered from previous research (Pulgur et al. 2019). The fresh properties of the concrete were determined using slump test which was done accordance to IS 1199-1959 (1959). Geopolymer

Table 27.5 Fresh and mechanical properties of GPC

Mixture	Slump value (mm)	Compressive strength (MPa)		Flexural strength (MPa)		Split tensile strength (MPa)		No. of hammer blows	
		07 days	28 days	07 days	28 days	07 days	28 days	Initial crack	Ultimate failure
SF0	100.5	30.84	38.45	3.81	5.473	2.36	2.7	4	13
SF2	78.75	38.54	47.24	4.84	7.41	3.03	3.47	6	23
CC	120	25.5	45.36	3.84	7.52	2.9	3.38	–	–

concrete specimens were prepared in accordance with IS 516 for compressive strength, flexural strength and split tensile strength. The specimens were cast, covered with plastic sheet and kept in ambient temperature for 24 h and demolded. The specimens were tested for compressive strength on 7 and 28 days according to IS 516-1959, flexural strength in accordance to both IS 516-1959 and split tensile strength on 28 days conforming to IS 516-1959 (1959). The chemical durability properties was conducted in accordance with the Francis et al. (2017), The cube specimens are cured in ambient temperature for 28 days after demolding the initial weight and surface characteristics are noted, then the specimens are immersed in H_2SO_4 and HCl solution whose pH is maintained 1 until the specimens are taken out for testing before which the physical aspects are noted.

27.3 Results and Discussion

27.3.1 *Fresh Concrete Mixes*

Fiber reinforced geopolymer concrete was prepared using Flyash and GGBS as the binder materials with steel fiber of weight equal to 2% of binder content. Ability of the flow of concrete and resistance to segregation was measured using slump test. The slump values for different trials are tabulated in Table 27.5.

27.3.2 *Tests on Hardened Concrete Mixes*

Compression test. The compression test was carried out using compression testing machine of capacity of 2000 kN as per IS: 516-1959 (Okoye et al. 2017) guidelines. Cubes of dimension $100 \times 100 \times 100$ mm were casted and cured in ambient condition.

The compressive test for the cubes was carried after 7 days and 28 days. The results are tabulated in Table 27.5. From the results presented in Table 27.5, it can be observed that there is 32% increase in the compressive strength from 7 days to 28 days. Presence of the GGBS as the binder material helps in gaining the appreciable compressive strength in first seven days. Addition of GGBS increases the demolding strength of the concrete.

Flexural Strength of Concrete. The flexural strength test was carried out flexural testing machine IS: 516-1959 guidelines. The beams of dimension $100 \times 100 \times 500$ mm were casted and kept in ambient condition. Test was performed after 7 days and 28 days. The results of flexural test are tabulated in Table 27.5. From Table 27.5, it can be observed that

Durability test on Concrete. Durability test was conducted on specimen of 10 cm cubes. The cubes were first air cured for 28 days and were then shifted to the

Table 27.6 Variation of density and compressive strength

Mix	Acid attack							
	HCl		H ₂ SO ₄		HCl		H ₂ SO ₄	
	% loss in weight				% loss in strength			
	56 days	84 days	56 days	84 days	56 days	84 days	56 days	84 days
SF2	1.52	2.88	0.78	3.35	16.03	20.55	23.82	29.92
CC	13.88	31.8	18	26.52	28	35	32	40

crates containing 1pH solution of HCL and H₂SO₄ (Bakharev 2005; Ganesan et al. 2015). The cubes are placed in the crates for another 28 days. After 56 days loss in density and compressive strength of the concrete blocks were measured and the results are tabulated in Table 27.6. The same procedure was followed after 84 days, i.e., exposure of 56 days. From Table 27.6 it can be observed that there is a decrease in compressive strength of the cube of about 15% when exposed to HCl and 23% when exposed to H₂SO₄. The results of the study are in comparison of the test conducted by Francis et al.

27.4 Conclusions

In the current study, the durability effects of SFRGPC exposed to acidic environment are studied experimentally. The following conclusions are drawn:

- The surface of the geopolymer concrete was intact and no loose material was evident as compared CC specimens
- The geopolymer concrete exhibited good resistance when exposed to various acidic environments both in terms of loss in strength and loss in weight
- The loss in weight was only around 2.88% and 3.35% for the GPC specimens exposed to HCl and H₂SO₄ solutions
- The loss in strength was also around 20 and 30% for the GPC specimens exposed to HCl and H₂SO₄ solutions.

References

Bakharev T (2005) Durability of geopolymer materials in sodium and magnesium sulfate solutions. *Cem Concr Res* 35(6):1233–1246
 Ban CC, Ken PW, Ramli M (2017) Mechanical and durability performance of novel self-activating geopolymer mortars. *Procedia Eng.* 171:564–571
 Chen C et al (2010) Environmental impact of cement production: detail of the different processes and cement plant variability evaluation. *J Clean Prod* 18(5):478–485

- Ganesan N, Abraham R, Raj SD (2015) Durability characteristics of steel fibre reinforced geopolymer concrete. *Constr Build Mater* 93:471–476
- IS 1199 (1959) Methods of sampling and analysis of concrete. Bureau of Indian Standards, New Delhi, India
- IS 516 (1959) Methods of tests for strength of Concrete. Bureau of Indian Standards, New Delhi, India
- Mehta A, Siddique R (2017) Sulfuric acid resistance of fly ash based geopolymer concrete. *Constr Build Mater* 146:136–143
- Meyer C (2009) The greening of the concrete industry. *Cem Concr Compos* 31(8):601–605
- Okoye FN, Prakash S, Singh NB (2017) Durability of fly ash based geopolymer concrete in the presence of silica fume. *J Clean Prod.* <https://doi.org/10.1016/j.jclepro.2017.02.176>
- Patankar SV, Ghugal YM, Jamkar SS (2015) Mix design of fly ash based geopolymer concrete. *Adv Struct Eng* (Elsevier, India)
- Peng J et al (2013) Modeling of carbon dioxide measurement on cement plants. *Adv Mater Res* 610–613(1):2120–2128
- Provis JL (2014) Geopolymers and other alkali activated materials: why, how, and what? *Mater Struct* 47(1–2):1–25
- Pulgur A, Divakar L, Chethan Gowda RK, Nagesh B (2019) Influence of steel fibres on mechanical properties of geopolymer concrete. In: Drück H, Pillai R, Tharian M, Majeed A (eds) *Green buildings and sustainable engineering*. Springer transactions in civil and environmental engineering. Springer, Singapore
- Singh B et al (2015) Geopolymer concrete: a review of some recent developments. *Constr Build Mater* 85:78–90
- Wang WC, Wang HY, Tsai HC (2016) Study on engineering properties of alkali activated ladle furnace slag geopolymer. *Constr Build Mater* 123:800–805

Chapter 28

Performance of Plantain Fibre in Nutmeg Shell Concrete



Elsa Paul, Eami Eldhose, Anju Anna Thomas, Chrismica M. Thomas
and Jeena T. Wilson

28.1 Introduction

28.1.1 Use of Agro-Waste in Concrete

The rapidly growing construction industry creates a demand for a large volume of building materials. It leads to fast depletion of conventional aggregate sources and results in the shortage of resources. This has degenerated the environment. Thus, these materials should be consumed carefully and also alternate materials need to be investigated to replace the naturally available aggregates, so as to promote sustainable development (Apeksha et al. 2017; Jnyanendra and Basarkar 2016).

Also, conventional concrete is brittle and weak in tension, this weakness could be controlled to some extent by the inclusion of a sufficient volume of certain fibres. The fibres bridge the cracks developed in concrete and increases the ductility by improving the post cracking behaviour of concrete. Also, addition of fibres in the plain concrete will improve the impact resistance, control the cracking due to shrinkage and also reduce the bleeding of water.

Further, with an increase in world population, waste generation has increased rapidly leading to a potential negative impact on the environment. As per estimates, India's agricultural industry generates more than 600 million tonnes of wastes every

E. Paul · E. Eldhose (✉) · A. A. Thomas · C. M. Thomas · J. T. Wilson
Department of Civil Engineering, Rajagiri School of Engineering and Technology,
Rajagiri Valley, Kakkanad, Kerala 682039, India
e-mail: eamielldho@gmail.com

E. Paul
e-mail: elsap@rajagiritech.edu.in

C. M. Thomas
e-mail: chrisi2296@gmail.com

J. T. Wilson
e-mail: jeenawilson08@gmail.com

year. This leads to serious disposal issues. Promoting the reuse of these wastes as sustainable construction materials can control the waste accumulation, air pollution caused due to crop residue burning as well as the expense on building materials.

This scenario has given rise to several studies on the usage of solid wastes produced by agricultural industries in the construction industry. Some of these studies investigated and reported are on coconut shell, oil palm shell, sugarcane bagasse ash, groundnut shell, oyster shell, sawdust, rice husk ash, cork, etc. (Jnyanendra and Basarkar 2016). The strength properties by replacing 25% fine aggregates with groundnut shell were studied and it produced lightweight aggregate concrete which could be used where low stresses are present (Sada et al. 2013). It was also found that groundnut shell panels are suitable for non-load-bearing partition walls and the acceptable range is between 30 and 70% replacement (Kimeng et al. 2015). Experimental investigations were conducted on crushed nutmeg shells as aggregate in concrete and found that the concrete mix containing 50% replacement of fine aggregate using nutmeg shells is an optimum replacement percentage for fine aggregate (Eami et al. 2018). Studies on the effect of using high reactivity metakaolin on the properties of banana fibre reinforced concrete found that the peak value of flexural strength was obtained at a fibre content of 0.5% (Prasannan and Nivin 2018).

From these studies, it is clear that innovations in the construction industry can concentrate on the use of suitable agricultural wastes or by-products for partial replacement of conventional materials used in the production of concrete. The present study carried out is on the use of waste nutmeg shell as partial replacement of fine aggregate in the production of concrete and to improve the tensile strength of the nutmeg shell concrete by adding plantain fibres in the concrete. The study was achieved by varying the percentages of plantain fibres.

Application of Crushed Nutmeg Shell as Fine Aggregate. World production of nutmeg is estimated to an average between 10,000 and 12,000 tonnes per year. India ranks second in the production after Indonesia, with Kerala accounting for more than 90% production. Nutmeg shells are agricultural farm waste obtained after picking out the seed inside. The hardened covering of nutmeg seed is called a nutmeg shell and for a long period, nutmeg shell, after picking out the fruit inside are treated as a solid waste.

Nutmegs are fruits under the category of drupe or stone fruit. A drupe has an outer fleshy part (exocarp), surrounds a shell of hardened endocarp with a seed (kernel) inside. The hardening of endocarp (nutmeg shell) is due to the deposition of lignin. Chemically, lignins are cross-linked phenolic polymers. It lends rigidity and slows down the decay of the shells (Fig. 28.1).

Use of Plantain Fibres in Concrete. The plantain fibres are the fibres obtained from the pseudostem of the banana plant. India ranks first in the production of plantain with an annual output of about 14.2 million tonnes. The plantain fibre is made of lignocellulose material in which lignin provides resistance against natural decay and cellulose is responsible for the mechanical properties of the fibre. Plantain waste, when leftover for decomposition, emits a large volume of methane gas and carbon dioxide, which has a negative impact on the environment and increases

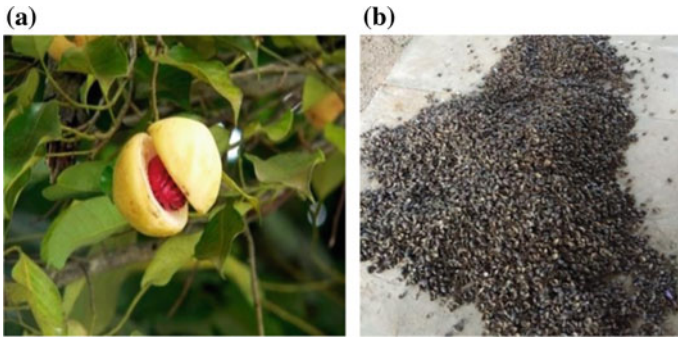


Fig. 28.1 a Nutmeg fruit b Nutmeg shells

global warming every year. These fibres can be easily extracted from the stem either by means of machine or by manual labour.

Tensile tests on banana fibre showed that the rate of strain has a significant role in the stress-strain behaviour of fibre. It was found that at lower strain rates some of the fibres showed proof for strain hardening (Samrat and Raul 2008). Unlike brittle fibres like glass and carbon fibres, cellulose fibres are flexible in nature.

Also, studies have shown that suitable treatments on the surface of fibre can improve the mechanical bonding, and thereby increases the interaction between the fibre and the matrix, by increasing the cellulose exposed fibre surface. Also, plantain being an acidic fruit material it has a pH value below seven and concrete being alkali in nature (pH value above 7), chemical pretreatment of plantain fibre has to be done to increase its pH value comparable with that of concrete. Pretreatment of cellulosic fibre using alkali is one of the common methods used to fabricate good quality fibres. This treatment removes the impurities present on the surface of the fibre (Marwan and Nasim 2015) (Fig. 28.2).

Fig. 28.2 Plantain fibre



28.2 Experimental Investigation

The present study was carried out for M25 grade concrete, as per IS standards. The target mean strength for the concrete design is given by the equation:

$$\text{Target mean strength} = f_{ck} + 1.65 \times S$$

where,

f_{ck} = Characteristic compressive strength of concrete (MPa)

S = Standard deviation = 4 (From IS: 456-2000)

Therefore,

$$\text{Target mean strength} = f_{ck} + 1.65 \times 4 = 31.6 \text{ MPa.}$$

28.3 Materials Used

Waste nutmeg shells were collected from various nutmeg plantations of Kerala. These shells were sun-dried and crushed to a size such that it passes through 4.75 mm IS sieve and retains on 150 μm IS sieve. Engineering properties of these nutmeg shell used are presented in Table 28.1 (Fig. 28.3). Grain size analysis of nutmeg shell was carried out and the results are presented in Table 28.2.

The average diameter of the fibre was 300 μm . These fibres were washed, dried, filtered and chemically treated by immersing in 5% NaOH solution for 3 h. This removes the impurities and roughens the fibre so as to improve its bonding and durability. The obtained fibres were then cut short to 40 mm size.

Portland Pozzolana Cement conforming to IS: 1489-1991 with specific gravity of 2.8 was used for the study. The fine aggregate used was M-sand conforming to Zone I. It had a specific gravity equal to 2.4 when tested according to the standards. Coarse aggregates with size less than 20 mm were used in the study. Tests were conducted on coarse aggregates as per the standards to find its properties. Properties of fine aggregates and coarse aggregates are given in Table 28.3.

Table 28.1 Test results of nutmeg shells

Sl. No	Particulars	Test results
1.	Specific gravity	1.25
2.	Bulk density	0.667 g/cc
3.	Water absorption	1.45%
4.	Fineness modulus	4.72
5.	Coefficient of curvature	2.98

Table 28.2 Sieve analysis for nutmeg shells

Sieve opening (µm)	Weight retained (g)	% weight retained	Cumulative % weight retained	% Finer
4750	127	12.7	12.7	87.3
2360	344	34.4	47.1	52.9
1180	176	17.6	64.7	35.3
600	163	16.3	81	19
300	64	6.4	87.4	12.6
150	22	2.2	89.6	10.1
Pan	4	0.4	90	10

Fig. 28.3 % Finer versus sieve opening—nutmeg shells

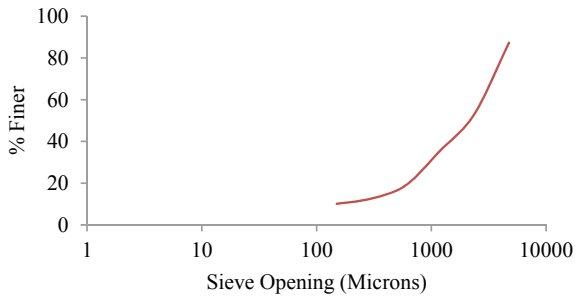


Table 28.3 Test results for aggregates

Sl. No	Particulars	Test results	
		Coarse aggregates	Fine aggregates
1.	Specific gravity	2.93	2.4
2.	Bulk density	1.58 g/cc	1.62 g/cc
3.	Fineness modulus	4.029	4.35
4.	Crushing strength	23.01	–

28.4 Preparation of Concrete Specimens

The plantain fibre reinforced nutmeg shell concrete was casted by adding fibres to the mix containing 50% replacement of fine aggregate using nutmeg shells. In order to ensure uniform mixing of fibres, it was added to concrete mixture before the addition of water. Slump test was conducted for each replacement mix to find the workability of the concrete as per the standards. The fresh concrete had an average slump value of 50 mm (medium slump). The concrete cubes, beams and cylinders casted were cured in the water pond for 28 days and the strength tests were conducted to find the compressive strength, split tensile strength and the flexural strength of concrete. Compressive strength of concrete was obtained by loading in

compression testing machine. Splitting tensile strength and flexural strength of the concrete was found by loading cylinders and beams.

28.5 Results and Conclusions

28.5.1 Compressive Strength

The compressive strength of the concrete cubes was found after 7 and 28 days of water curing while the concrete cylinders were tested after 28 days of curing. The obtained results are tabulated as shown in Fig. 28.4.

From Fig. 28.4 and Table 28.4, it is clear that the compressive strength of the concrete increased with the addition of fibre. The maximum strength was obtained for a concrete mix containing 0.25% addition of fibre. However, the compressive strength decreased with further addition of fibre.

28.5.2 Flexural Strength

The flexural strength of the concrete beams was found after 28 days of water curing. The obtained results are tabulated as shown in Table 28.5.

From Table 28.5 it is seen that when fibre content is increased there is an increase in flexural strength with a maximum at 0.25% addition of fibre. However, the flexural strength further decreases by increasing the percentage of fibre added (Fig. 28.5).

28.5.3 Split Tensile Strength

The split tensile strength of the concrete cylinders was found after 28 days of water curing. The obtained results are shown in Fig. 28.6.

Fig. 28.4 Compressive strength of fibre reinforced concrete cubes

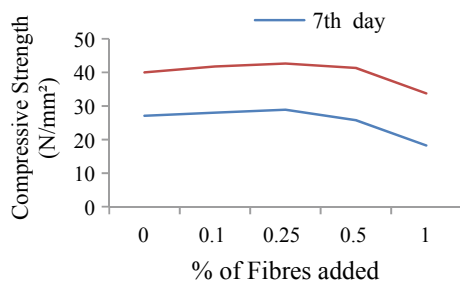


Table 28.4 Compressive strength of fibre reinforced concrete cylinders

Sl. No	% of fibres added (%)	Maximum load (kN)	Compressive strength (N/mm ²)
1.	0	500	28.29
2.	0.1	530	29.99
3.	0.25	560	31.68
4.	0.5	480	27.16
5.	1	390	22.06

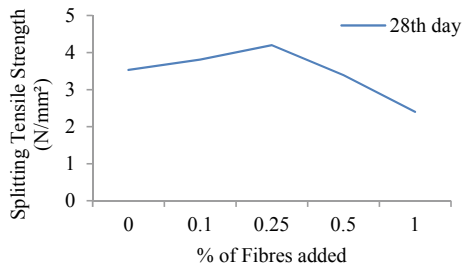
Table 28.5 Flexural strength of fibre reinforced concrete beams

Sl. No.	% of fibre added (%)	Maximum load applied (kN)	Modulus of rupture (MPa)
1.	0	14	5.6
2.	0.1	15	6.0
3.	0.25	17	6.8
4.	0.5	12	4.8
5.	1	7	2.8

Fig. 28.5 Fibre reinforced beam



Fig. 28.6 Split tensile strength of fibre reinforced concrete cylinders



From Fig. 28.6 it is seen that when fibre content is increased there is an increase in split tensile strength with a maximum at 0.25% of fibre. However, when the fibre content is increased beyond this value a downward slope in the graph was observed. This may be due to the fact when fibres are added, initially the finer sized fine

aggregates enter into the surface pores in the fibre creating a better bonding between the fibre and mix, however further addition of fibres causes formation of bulk fibre in the mix decreasing the bonding. Hence there is an optimum value of fibre to cement ratio, beyond which the compressive strength decreases and 0.25% was taken as the optimum fibre content.

28.6 Conclusions

The study was conducted considering the disposal problem of waste nutmeg shells, shortage of conventional fine aggregates, and poor tensile strength of concrete. Abundant availability of plantain fibre near the site makes it a feasible reinforcing material in concrete. Utilisation of banana fibre in concrete creates an effective method for the waste management of plantain leftover. This decreases the need for a waste disposal infrastructure, reduces the charge on landfills and also reduces crop residue burning. Also, the recent demand created by the concrete industry creates an additional livelihood for the banana producers.

This experimental investigation aimed to study the performance of plantain fibre in the compressive, split tensile and flexural strengths of nutmeg shell aggregate concrete. Based on the results of this experimental study, the following conclusions could be drawn:

- i. The hardened properties of the concrete improved with the addition of plantain fibres. The peak 28th day compressive strength was obtained for a mix containing 0.25%.
- ii. The maximum flexural strength was found to be 21.4% more than the control mix. The decrease in the strength of the concrete is due to improper distribution and orientation of fibres within the mix, which is difficult to achieve. This is because, at high dosage of fibres, the workability of the mix decreases and formation of the bulk fibre reduces the bonding within the mix.
- iii. Using nutmeg shells as partial replacement of fine aggregate can reduce the material cost in construction. This can be used in rural areas and places where nutmeg and plantain are abundant.

References

- Apeksha K, Sarvesh KJ, Rajkumar R, Giridharan S, Elavivekan M (2017) Performance of coconut shell as coarse aggregate in concrete. *Construct Build Mater (Science Direct)* 140:150–156
- Eami E, Anju AT, Elsa P (2018) Performance of nutmeg shell as fine aggregate in concrete. *NFiCE2018, IIT Bombay, Paper ID: DJCE40*, pp 22–23
- Jnyanendra KP, Basarkar SS (2016) Concrete using agro-waste as fine aggregate for sustainable built environment—review. *Int J Sustain Built Environ (Science Direct)* 5(2):312–333

- Kimeng HT, Mustapha S, Olurotimi OE, Kigha F (2015) Feasibility study of the use of groundnut shells as fine aggregate in light weight concrete construction. *Int J Adv Res Eng* 1(1):13–16
- Marwan M, Nasim U (2015) Effect of banana fibers on the compressive and flexural strength of compressed earth blocks. *Buildings*(ISSN 2075-5309) 5:282–296
- Prasannan D, Nivin S, et al (2018) Comparative study of banana and sisal fibre reinforced concrete with conventional concrete. *Int J Pure Appl Math* 118(20):1757–1765
- Sada BH, Amartey YD, Bako S (2013) An investigation into the use of groundnut shell as fine aggregate replacement. *Nigerian J Technol* 32(1):54–60
- Samrat M, Raul F (2008) Banana fibers—variability and fracture behaviour. *J Eng Fibers Fabrics* 3(2)

Chapter 29

Performance Evaluation of Composite Shear Wall



S. Sariganath and Milu Mary Jacob

29.1 Introduction

Shear walls have been widely used as lateral load resisting system in concrete buildings in the past, especially in high-rise buildings. It is seen that reinforced concrete shear walls with boundary elements used in buildings resist seismic effects, which has several disadvantages during large cyclic displacements, thus results in spalling and splitting failure of the wall and also leads to serious deterioration of stiffness, reduction in strength, development of tension cracks, and localized compressive crushing. In case of steel plate shear wall, buckling failure occurs. Composite shear wall overcomes these disadvantages of concrete and steel plate shear wall. The advantages of composite structure include low life cycle cost, lighter materials, steel section used will act as formwork, thermal efficiency is more, more corrosion resistance, etc.

In recent years, regarding construction efficiency and economy, steel plate shear wall has been used in numbers of buildings and achieved satisfactory results. However, overall buckling of the steel plate shear wall will result in reduction of shear strength, stiffness, and energy dissipation capacity of the whole system. It could be prevented by adding stiffeners to the steel plate, which, however, will result in additional fabricate on costs.

The connections of the boundary frame can undergo relatively large cyclic rotations as well as somehow larger inter-storey drifts, due to relatively large inelastic deformations of the panel, in structures with steel shear walls. On the other

S. Sariganath (✉) · M. M. Jacob
Department of Civil Engineering, Saintgits College of Engineering,
Kottayam, Kerala, India
e-mail: sariganaths31@gmail.com

M. M. Jacob
e-mail: milu.mary@saintgits.org

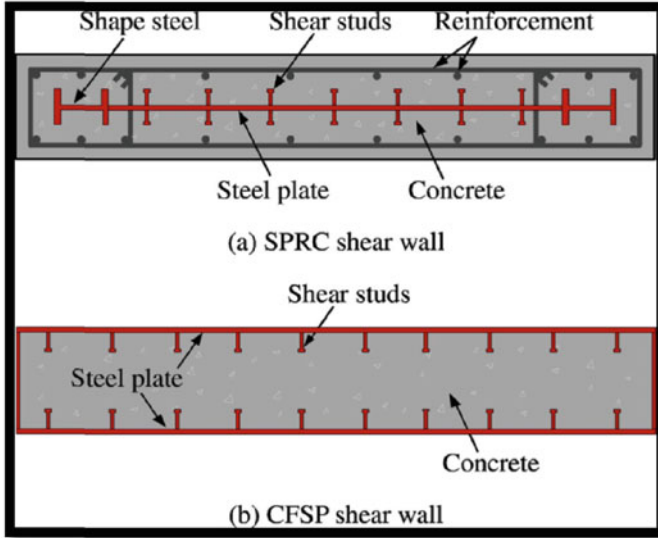


Fig. 29.1 Elements of composite shear wall (Wang et al. 2017)

hand, in steel buildings, composite shear walls can combine the advantages of the reinforced concrete shear wall and steel shear wall together to increase and stimulate the usage of shear wall systems.

The main components of a composite shear wall include steel wall, concrete wall, boundary columns, boundary beams (Fig. 29.2), shear connectors, connection of steel wall to boundary beams and columns, and beam-to-column connections are the main components of composite shear walls as shown in Fig. 29.1.

29.2 Background

Bin Wang et al. (2017) conducted a study on the behavior and application of SPRC shear walls in China Mainland. Then the modeling techniques with the aid of software OpenSees to simulate the hysteretic behavior of SPRC shear walls are presented and validated by typical experimental results. The verified numerical model is further used in the parametric study focusing on a number of important parameters, including the steel plate ratio, the axial compressive load ratio, the concrete strength, and the web reinforcement ratio. The results of this parametric study were used for the practical implementation of SPRC shear wall in China Mainland.

Farhad Ahmadi et al. (2014) conducted an experimental study of the seismic performance of cantilever-reinforced concrete masonry shear walls. About 30

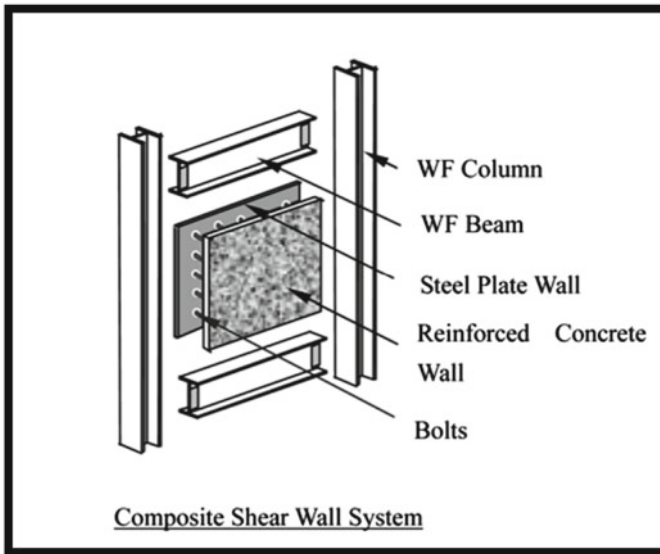


Fig. 29.2 Elevation of composite shear wall

cantilever shear wall specimens, made of fully grouted reinforced concrete masonry, were tested under reversed cyclic loading. In the result, flexural capacity and initial stiffness increased with increasing axial load and vertical reinforcement ratio, displacement ductility decreased with increasing axial load, walls with lower aspect ratios experienced more rapid strength degradation than did walls with higher aspect ratios, and the displacement at failure (80% of maximum loads) increased as the aspect ratio increased.

Ranjani R et al. (2017) conducted a finite element analysis of steel plate shear wall provided with slots of different shapes such as circular, triangular, and hexagonal forms. These slots are placed inclined to the plate. Here a composite steel plate shear wall is adopted which has a steel plate sandwiched between two concrete panels. These concrete panels provide lateral restraint to the steel plate. The shear wall was modeled and analyzed in ANSYS 16.2 workbench and the results show that the composite shear wall can withstand under cyclic loads. Introducing slots in the inner steel plate act as a passive energy dissipater and providing slots also results in reduction of the total weight of the structure and also reduces wastage of material.

Qihong Zhao (2004) conducted experimental studies of three-storey composite shear wall specimens with and without gap between the shear wall and the perimeter frame. The specimen with gap in between was able to tolerate 33 cycles of shear displacements and reach maximum inter-storey drift of more than 0.05 whereas the specimen without gap in between was able to tolerate 17 cycles of shear displacements. The bolts connecting the reinforced concrete walls to steel

plate shear walls were able to ensure the composite action by bracing the steel plate shear wall to the reinforced concrete shear wall and preventing the overall buckling of steel plates. During late cycles and after shear yielding of the steel plate, inelastic local buckling of the steel plate shear wall occurred in the areas between the bolts. From the test, it was concluded that by introducing the gap in the innovative system, damage to concrete walls under relatively large cycles was much less than the damage to concrete walls in the traditional system.

From the background, experiment studies show that as the axial load on shear wall increases, shear displacement decreases and provision of slots in steel plate in shear wall helps to increase energy dissipation capacity and also reduces self weight of structure. The concrete panels over the steel sheet act as lateral restraint to the steel plate in between and hence reduce buckling of plate.

29.3 Numerical Analysis

A parametric study was performed by varying the spacing of stiffeners and shear studs, respectively. In these models, stiffened steel plate is sandwiched between concrete panels. The stiffened steel plate and shear studs used are mild steel materials, having a yield strength of 250 N/mm^2 , $E = 206,980 \text{ MPa}$ and the concrete panels used are of M30 grade, having poisson's ratio 0.15, $E = 27,386 \text{ MPa}$ and compressive strength of 30 N/mm^2 . After carrying out mesh convergence, the size of the mesh was optimized to 20 mm and based on that models were meshed. In the analysis, "solid 65" concrete and the reinforcing bars were treated as bar element "link 180". The concrete uses multi-linear isotropic property and the steel bars uses bilinear isotropic property. The contact between the steel and concrete interface is defined by COMBIN39.

29.3.1 Variation of Stiffener Spacing

The composite shear wall taken for analysis is of $1.2 \text{ m} \times 3 \text{ m}$ dimension. The composite shear wall consists of corrugated sheet which is sandwiched between concrete panels and shear connectors were provided over steel plate to improve the shear resistance. The shear wall was provided with reinforcement bars for the uniform distribution of stresses over the wall and was designed according to American Code 2010.

The stiffeners spacing and shear studs spacing were fixed after carrying out different trials of numerical analysis. The results from the analysis were compared to evaluate the effect of spacing in the behavior of shear wall. Hat stiffener was used for stiffening purpose and initially the spacing between the stiffeners was fixed by varying the numbers of stiffeners within the wall, that is stiffeners were placed at spacing from span/6 to span/4, respectively, (as shown in Table 29.1) and the

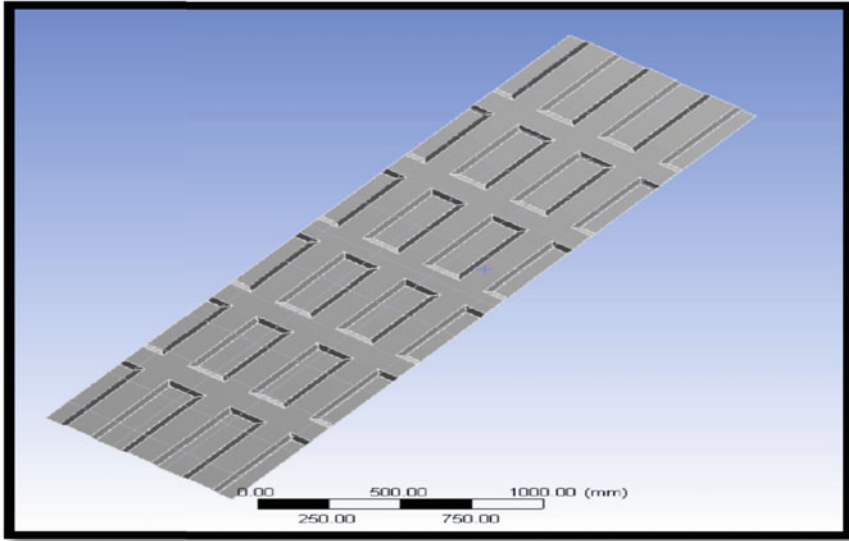


Fig. 29.3 Corrugated steel sheet with 5 stiffeners

Table 29.1 Stiffener spacing

No of stiffeners	Stiffener Spacing (mm)
2	1000
3	750
4	600
5	500

model was analyzed. From the analysis, it was concluded that the model with 5 numbers of stiffeners (stiffener spaced at span/6) had lateral displacement within the limit (as shown in Fig. 29.3). The permissible limit of deflection was 0.2% of the height of the storey.

The models shown in Fig. 29.3 was then sandwiched between concrete panels of 100 mm thickness and then analyzed for lateral deflection. Figure 29.4 shows model of corrugated sheet analysed.

According to AISC 2010, the permissible limit for lateral displacement is 6 mm for this model and the deformation of models with different numbers of stiffeners is shown in Table 29.2. Hence model with stiffeners spaced at span/6 spacing is adoptable (Fig. 29.5).

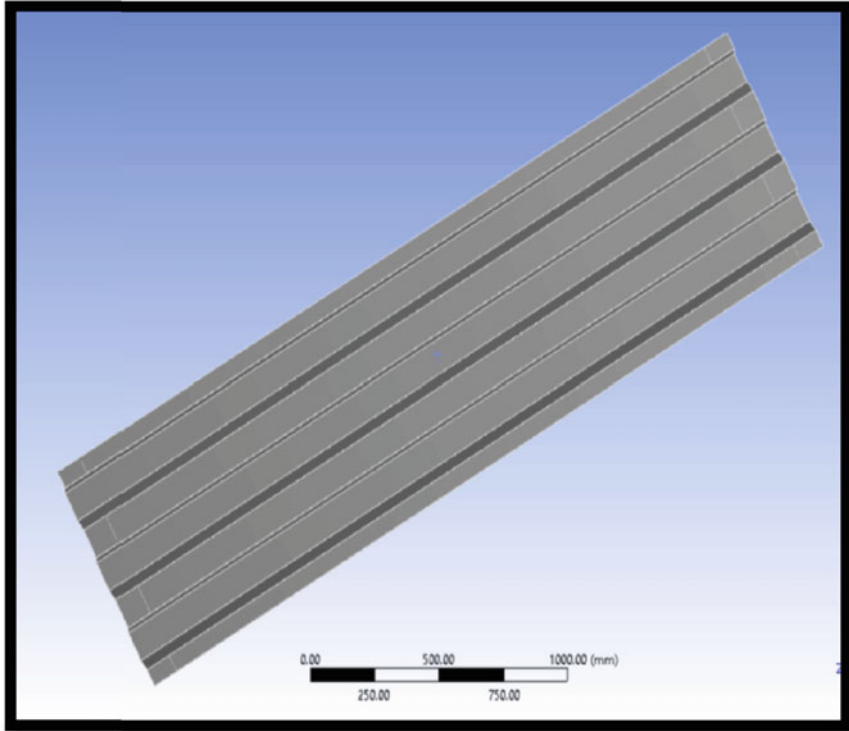


Fig. 29.4 Corrugated steel sheet without stiffeners

Table 29.2 Deformation corresponding to stiffener number

No. of stiffeners	Deformation (mm)
5	5.6720
4	6.4498
3	6.7311
2	7.2245
No stiffener	7.7839

29.3.2 Variation of Shear Stud Spacing

The spacing of shear studs has to be optimized by considering various spacing. From the above analysis, it was concluded that the model with a stiffener spacing of span/6 performed better and hence the studs were placed over this model at span/2.5, span/4 as shown in Fig. 29.6, span/8, respectively, and the deflection of the specimen was analyzed to evaluate its behavior. The figures shown below represent the arrangement of shear studs over a 3 m long model.

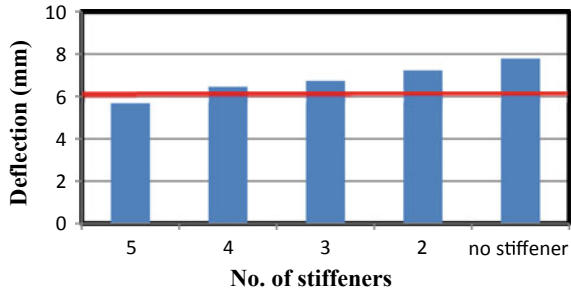


Fig. 29.5 Graph showing variation of deflection

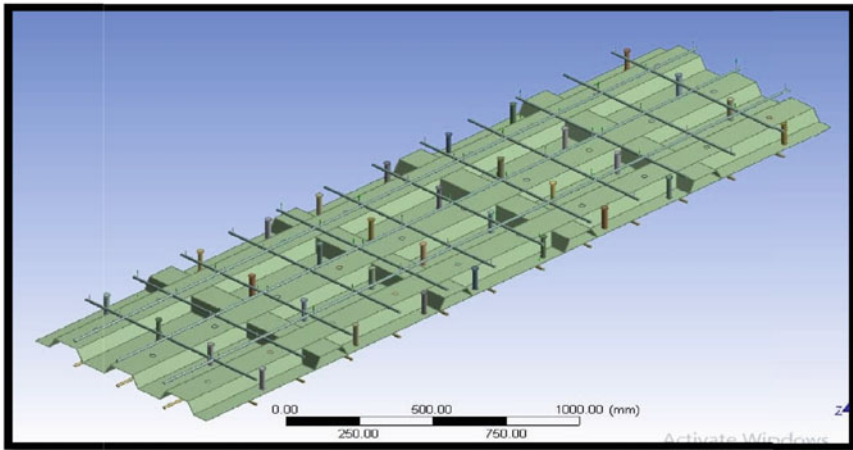


Fig. 29.6 Arrangement of shear studs at 300 mm distance

From the analysis, it was found that the model with stiffener spacing (Fig. 29.7) and shear studs spaced at span/8 (Table 29.3) had a deflection, which was within the limit the permissible limit (Fig. 29.8).

29.3.3 Analysis of Composite Shear Wall Models with Different Aspect Ratio

For composite shear walls, the size of the model is limited based on the aspect ratio limit provided by AISC 2010. According to AISC, the aspect ratio of composite shear wall should be $0.8 \leq H/L \leq 2.5$. Based on this limitation, the height (H) and length (L) of the composite shear wall was varied so that the difference in behavior of the shear wall can be evaluated.

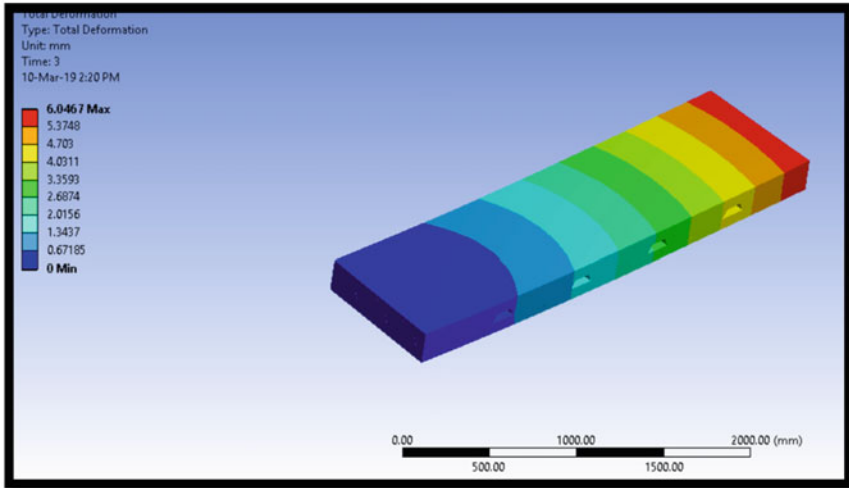
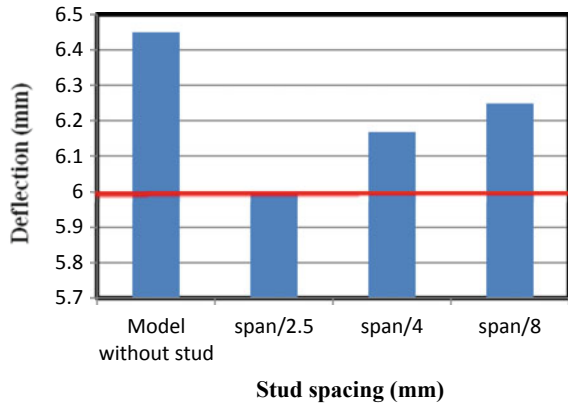


Fig. 29.7 Deformation of model with shear studs at 150 mm spacing

Table 29.3 Deformation corresponding to stud spacing

Spacing of studs (mm)	Deformation (mm)
Without stud	6.4498
Span/8 (150 mm)	6.0467
Span/4 (300 mm)	6.1676
Span/2.5 (450 mm)	6.2482

Fig. 29.8 Graph showing variation of deflection



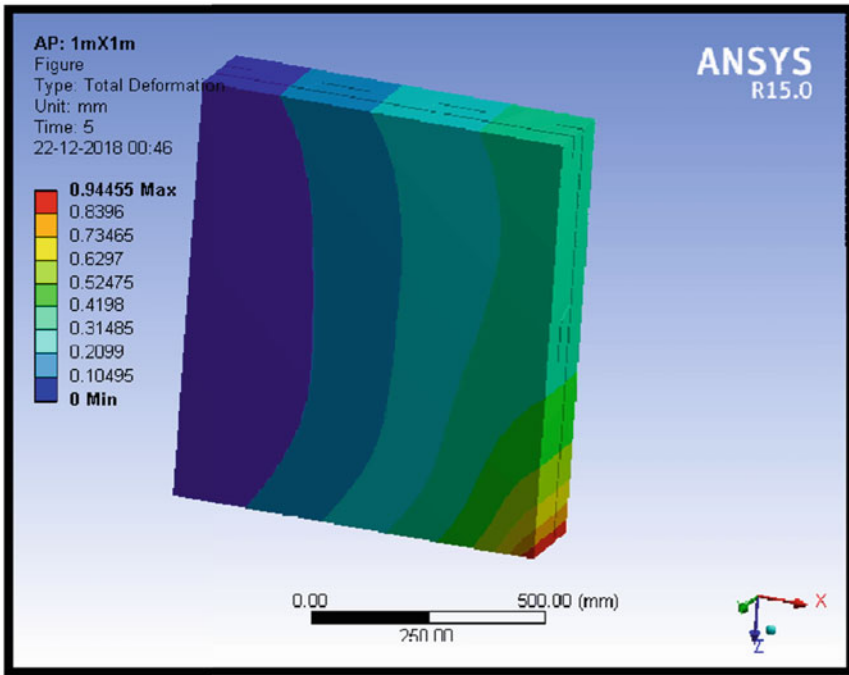


Fig. 29.9 Total deformation of 1 m × 1 m model

For that models of size 1 m × 1 m, 1.2 m × 2 m, 1.25 m × 2.5 m, 1.2 m × 3 m having aspect ratios 1, 1.5, 2, 2.5, respectively, and shear studs were provided in all models at 150 mm distance. The models were provided with fixed support at the bottom end, and the load was applied at the top-right edge, and the results were evaluated for analyzing the deflection of the specimen.

In case of model with aspect ratio 1 m × 1 m, the analysis result is shown in Fig. 29.9.

In case of model with aspect ratio 1 m × 2 m, the analysis result is shown in Fig. 29.10.

From Table 29.4, we can infer that as height increases, displacement of the model also increases and its variation is shown in Fig. 29.11.

29.3.4 Analysis of Scaled Model

The scaled model was selected whose aspect ratio (L/h) is within the limit of 0.8 and 2.5. Hence, the dimension of the specimen was fixed as 1 m × 1 m whose aspect ratio is 1.

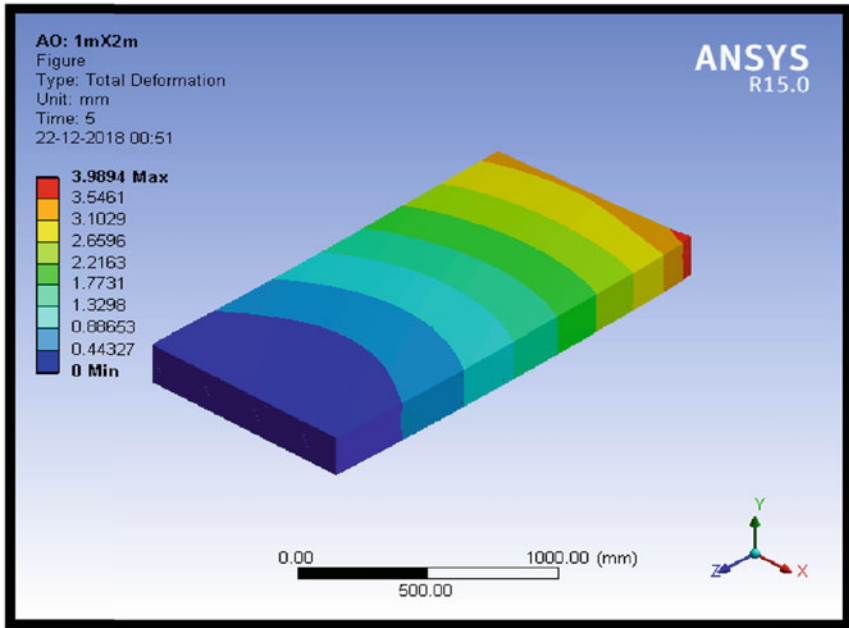


Fig. 29.10 Total deformation 1 m × 2 m model

Table 29.4 Results of models with different aspect ratios

S.no	Model size	Deflection (mm)
1	1 m × 1 m	1.4078
2	1 m × 1.5 m	2.5025
3	1 m × 2 m	3.9894
4	1 m × 2.5 m	5.8913

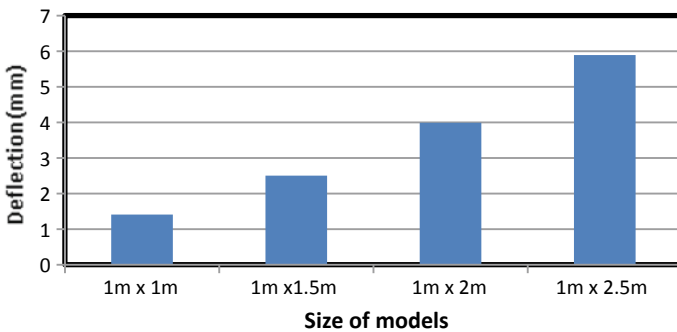


Fig. 29.11 Graph showing variation of deformation

29.3.4.1 Analysis of RC Shear Wall Model

In order to find out the difference in behavior of the ordinary reinforced concrete (RC) shear wall and composite shear wall, the analysis was carried out. The RC model and composite shear wall models were designed by providing minimum amount of steel content. Based on the design, the RC shear wall was provided with 16 mm diameter bars in the horizontal as well as vertical directions at a distance of 150 mm center to center. The model has a dimension of 1 m × 1 m and the support condition, loading pattern is same as that of composite shear wall. The analysis was carried out to find the deflection difference between RC (Fig. 29.12) and composite shear wall. To evaluate the exact behavior of the above-mentioned models, hysteresis curve is needed to conclude its ductility behavior, energy dissipation capacity, etc. From the nonlinear analysis, we can infer the nonlinear behavior of the model.

29.3.4.2 Analysis of Model with Corrugated Sheet

The corrugated sheet is an important component in composite shear wall for improving the shear resistance. In order to reduce the out of plane displacement and

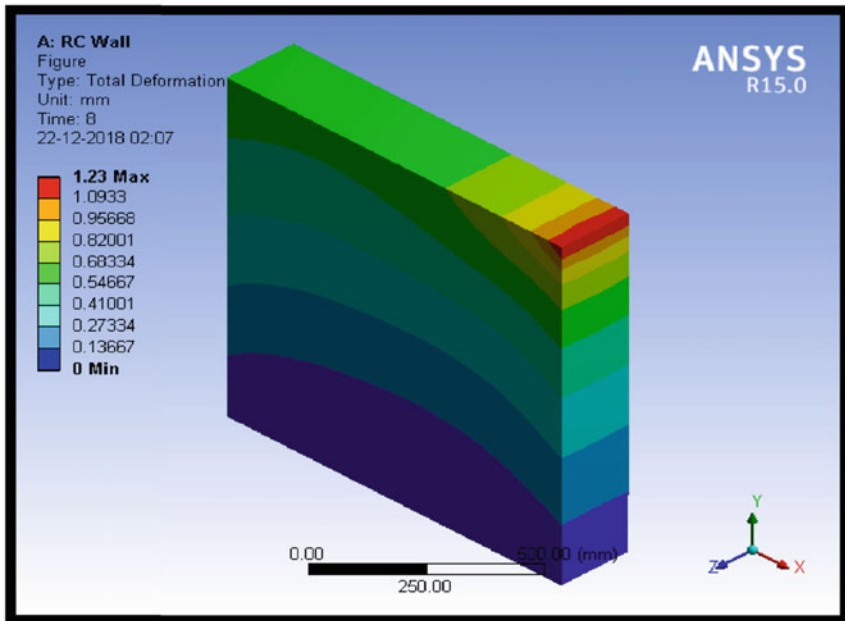


Fig. 29.12 Total deformation of RC shear wall model

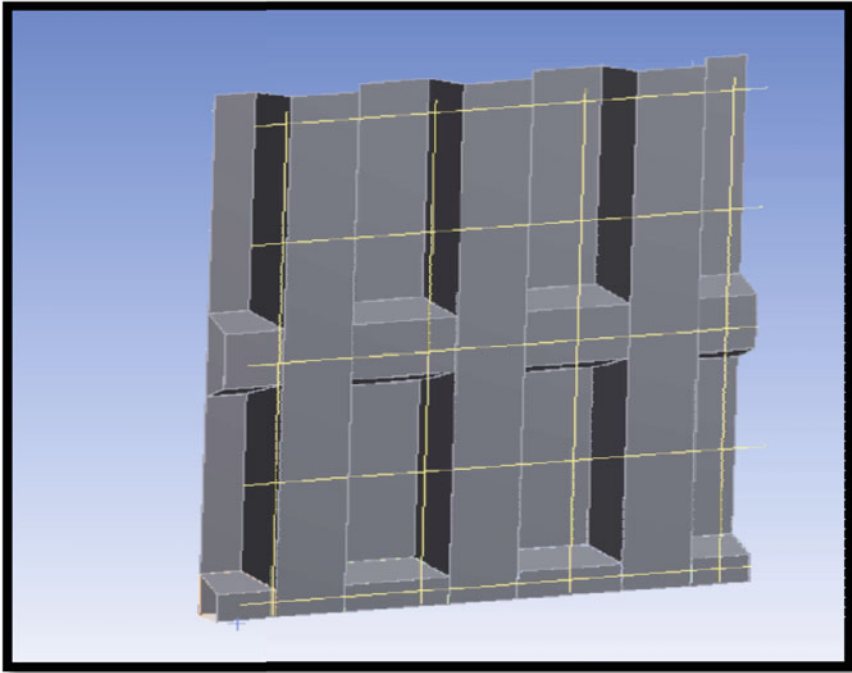


Fig. 29.13 Corrugated steel sheet with reinforcements for scaled model

to improve the torsional resistance of the composite shear wall, hat stiffeners were provided in the specimen and were optimized at the middle portion of the sheet (as shown in Fig. 29.13), so that it prevents the buckling of the steel plate. This stiffened steel plate was then sandwiched between concrete panels (Fig. 29.14) and was then loaded laterally. The load was given in 5 cycles at an interval of 100 kN till 500 kN. Since the aim of the analysis was to compare the performance of composite shear wall with reinforced concrete shear wall, analysis was also done in case of RC shear wall.

From the analysis (Fig. 29.16), it was found that the displacement of the model was 1.497 mm under the action of 500 kN at its top-right edge and the failure load of the specimen was found to be 370 kN. The nonlinear deflection of the specimen (Fig. 29.15) is 11.312 mm. Hence, the stiffness of the model is 3.3×10^7 N/m.

29.3.4.3 Analysis of Model with Corrugated Sheet and Shear Studs

For the effective transfer of shear between concrete and corrugated sheet, shear connectors were placed over the corrugated sheet for better interaction with the interface concrete (Fig. 29.17) and analysis was done in a similar manner as mentioned above. The analysis result is shown in Figs. 29.18 and 29.19.

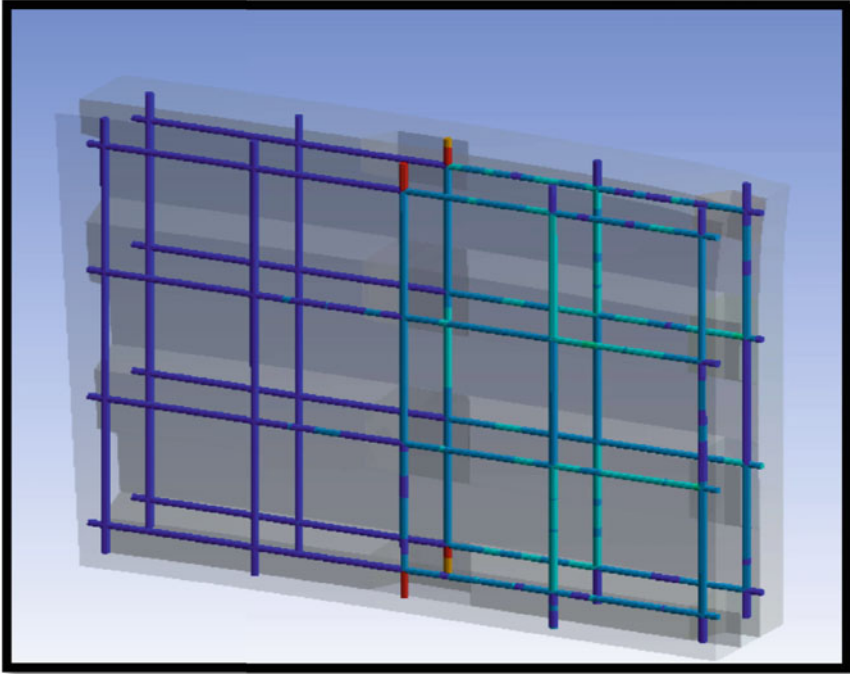
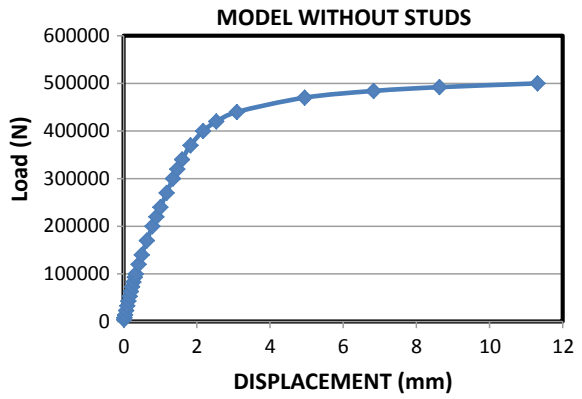


Fig. 29.14 Reinforcing bars in composite shear wall

Fig. 29.15 Non linear deformation of model without shear studs



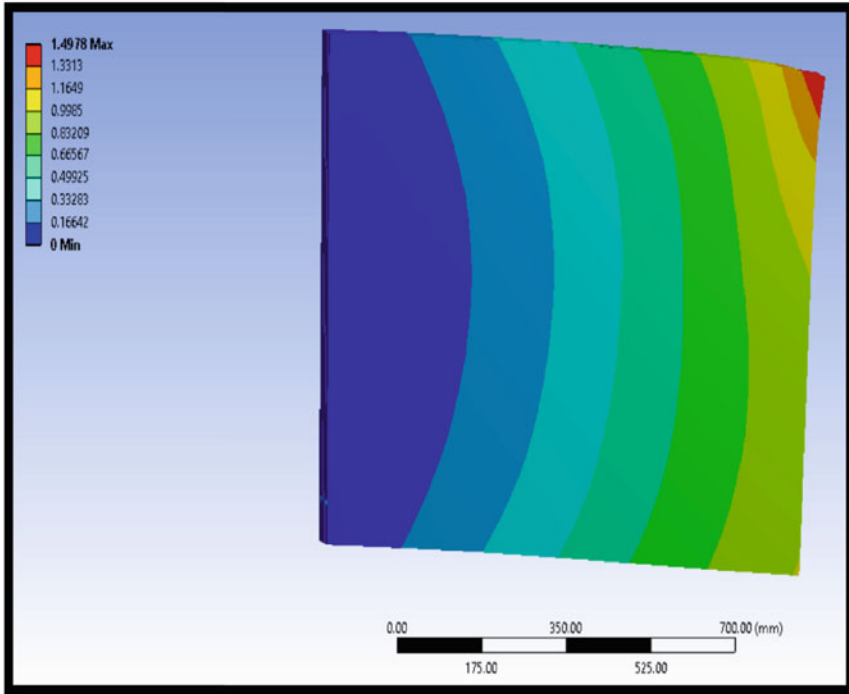


Fig. 29.16 Total deformation of model without shear studs

According to AISC 2010, the deflection is limited to 0.2% of height of the storey = $0.002 \times 1000 = 2 \text{ mm}$

Hence, the deflection is within the elastic limit and the failure load of the specimen was found to be 340 kN. The nonlinear deflection of the specimen (Fig. 29.19) is 8.55 mm. Hence, the stiffness of the model is $3.09 \times 10^7 \text{ N/m}$.

Table 29.5 and Fig. 29.20 shown below shows a comparison of results.

29.4 Conclusion

From the numerical analysis, it was inferred that the composite shear walls with stiffeners performed better than ordinary reinforced shear walls. According to American Institute of Steel Construction (AISC) 2010, aspect ratio limits were specified. Based on which, dimensions of the composite shear wall specimen have been fixed. Following are the results inferred from the analysis;

- Optimum number of stiffeners was determined in order to avoid out of plane displacement, which is equal to span of specimen/6.

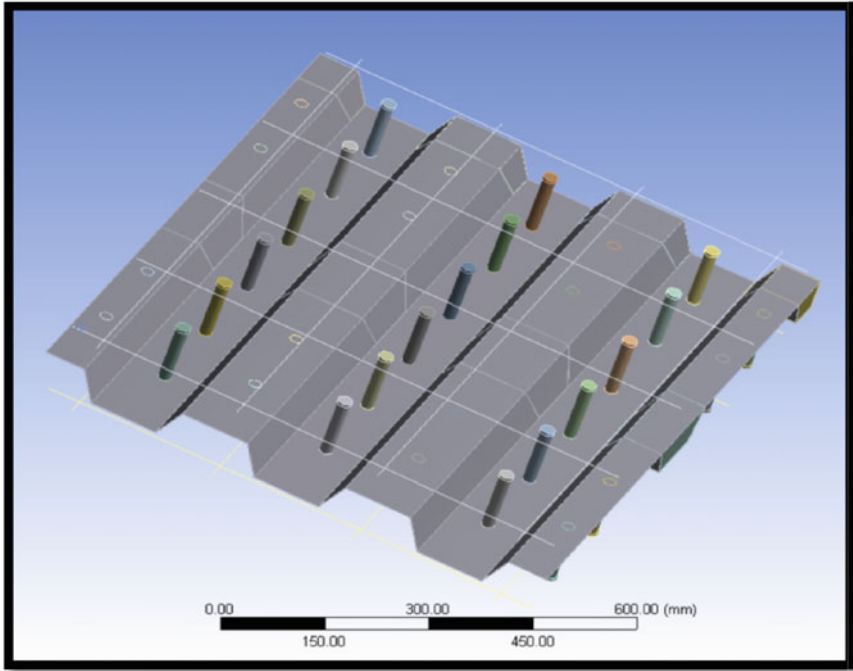


Fig. 29.17 Shows corrugated sheet along with studs

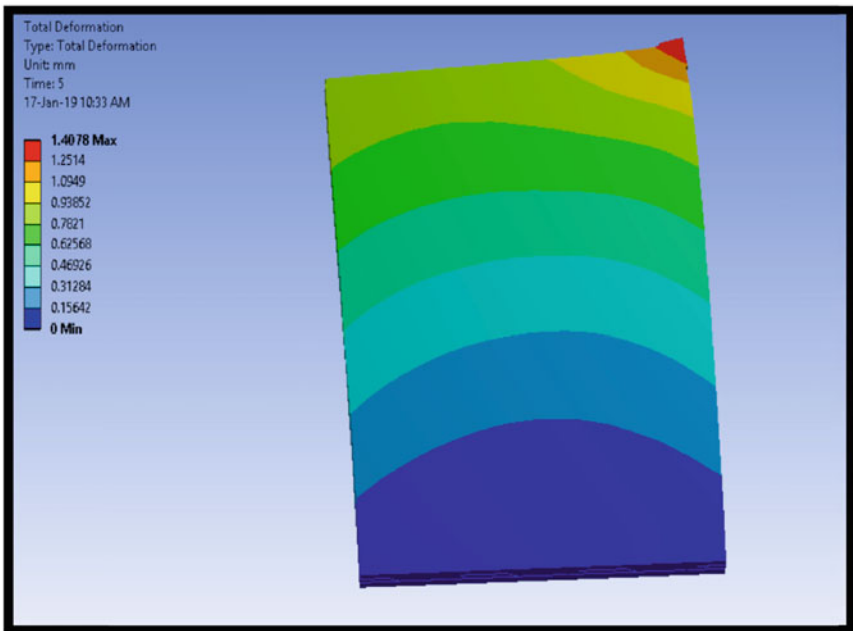


Fig. 29.18 Deflection of the model with studs

Fig. 29.19 Non linear deformation graph of model with studs

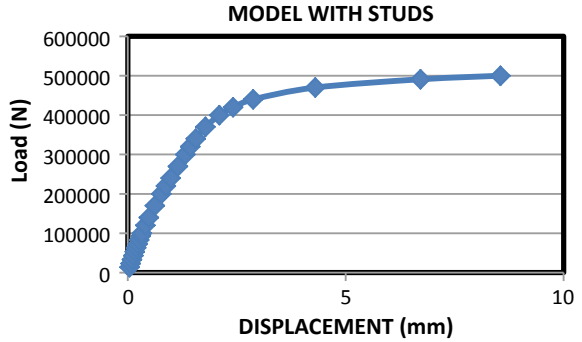


Table 29.5 Shows the results obtained from analysis

S.no	Model type	Deflection (mm)
1	RC shear wall	1.23
2	Composite shear wall with corrugated sheet and studs	1.4078
3	Composite shear wall with corrugated sheet and without stud	1.4970

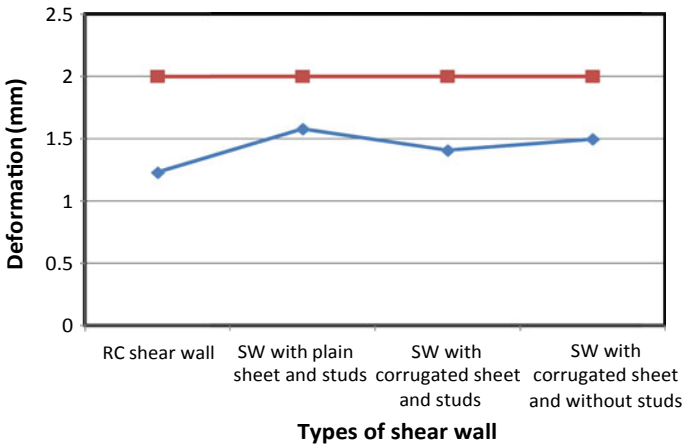


Fig. 29.20 Graph showing variation of deformation

- By the provision of shear studs at span/6 spacing over stiffened corrugated steel plate, the deformation of the model got improved when compared to RC shear wall.

- By evaluating results obtained from analyzing models with different aspect ratios, it was observed that the deflection increases with an increase in height of the model by 2.88%.
- Lateral stiffness of composite steel-concrete shear wall is increased due to stiffened structural steel by 9.9%.

References

- Ahmadi F, Hernandez J, Sherman J, Kapoi C, Klingner RE, McLean DI (2014) Seismic performance of cantilever-reinforced concrete masonry shear walls. *J Struct Eng* 140 (9):04014051
- Ranjani R, Sindhu PK (2017) Post buckling analysis of composite shear wall. *Imperial J Interdisc Res*, 3
- Wang B, Jiang H, Lu X (2017) Seismic performance of steel plate reinforced concrete shear wall and its application in China Mainland. *J Constr Steel Res*, 131:132–143
- Zhao Q, Abolhassan Astaneh-Asl M, ASCE (2004) Cyclic behavior of traditional and innovative composite shear walls. *J Struct Eng*

Chapter 30

Condensation and Associated Microbial Growth in Air-Conditioned Healthcare Facilities in Tropical Climate—A Case Study



V. K. Vikas, C. Muraleedharan and B. Hariprasad

30.1 Introduction

Nowadays, the norms related to health care facilities are becoming more stringent and to cope up with the same, more and more healthcare facilities which were not air-conditioned previously adapt air-conditioning or mechanical ventilation. Due to the relatively high energy demand for round the clock operation of an HVAC system for the whole building envelops the usual practice is to selectively condition the areas of more importance while keeping the other areas unconditioned. Another strategy to reduce the energy demand is to reduce the duration of operation according to the requirement. It is to be noted that the rate of outside air required for maintaining internal air quality (IAQ) as per the standards is relatively high in health care facilities (Ninomura et al. 2001).

The tropical climate provides relatively high enthalpy for the outside air both sensible and latent heat wise. In order to reduce the high installation cost and to make the system less complicated, most of the old installations and even new ones do not rely on treated fresh air units to provide pretreated fresh air to the different zones in the building envelop. This creates a unique problem in such buildings as condensation of moisture at selective places and associated microbial growth. This can happen inside the conditioned zone or even outside walls of the conditioned zone, which may be inside the hospital itself. The presence of fungus and mold is visible in most of the health care facilities at several places, even inside the supply and return air diffusers of sterile areas. It is to be noted that, there are several areas

V. K. Vikas (✉) · C. Muraleedharan
Department of Mechanical Engineering, National Institute of Technology Calicut,
Kozhikode, Kerala, India
e-mail: vikasvk@gmail.com

B. Hariprasad
ASHRAE Associate, ASHE Member, Stat Consultancy Pvt Ltd, Trivandrum, India
e-mail: hariprasad@statconsultants.com

such as, above the false ceiling plenum, inside the air distribution ductwork, air handling units (AHU), drain pans, etc. where the microbes may get an opportunity to germinate and proliferate even without being noticed. Since the mechanical air distribution network associated with the HVAC system can distribute the spores of these microbes throughout the building, it can cause a potentially dangerous situation.

30.2 The Case Study

The healthcare facility under this study is situated in Kerala, a state in the south part of India where the outside atmospheric conditions are hot and humid most of the seasons resembling a typical monsoon tropical climate. Thick vegetation, the presence of water bodies and two rainy seasons make the climate humid most of the time with an average relative humidity above 60%. Since the ambient temperature seldom lowers below 20 °C, heating facility is not normally provided with the HVAC except a few areas where relative humidity has to be maintained within limits at low inside dry bulb temperature. One typical example is the operating rooms. The hospital is centrally air-conditioned with a plant capacity of approximately 750 TR in a central water chilling plant. Insulated chilled water pipelines are used to distribute the refrigeration to the individual air handling units at different zones in the hospital. The fresh air requirements are met with untreated outside air in different zones with quantities specified as per ASHRAE guidelines (Koenigshofer 2013). Similarly, the air is exhausted directly outside locally adjacent to the zone itself and no heat recovery is being done. AHUs are provided with 20 µm synthetic filter before the chilled water coil. The temperature control at different zones is carried out by modulating the chilled water flow rate through the coil of the AHUs using two port valves controlled locally by a temperature control unit. The patient rooms are conditioned using chilled water fan coil units with on-off control valves. A dedicated fresh air AHU is provided for the patient rooms in common. It is to be noted that patient rooms on a specific floor of the hospital are not air-conditioned. Two courtyards are provided with skylight roof within the building.

The present problem is noticed as the discoloration on several places mainly on walls and ceiling including the walls of the courtyard. The housekeeping section repainted the section, but the same thing happened again in 6 months. The color shade difference was annoyingly noticeable at the courtyard, on the walls of the air-conditioned floors in contrast to the non-air-conditioned floors. A detailed analysis of condensation problem on the exterior surface of the building is readily available (Aelenei and Henriques 2008) but it is interesting to note that no visible fungal growth noticed on the exterior wall of the building.

As part of the study, a thorough inspection of the building was done from the service areas to the sterile areas like operating rooms. The above false ceiling areas, plumbing, electrical shafts, service floors, AHU and janitor rooms, etc. are also

included. During the inspection, the presence of microbial growth was found at several places with varying intensity. Samples were collected and sent to the laboratory for culture and the microbial was identified as *Aspergillus Niger* (*A. Niger*), a mold family generally called a black mold. The estimated germination time for the species under the conditions found is less than a day in which the relative humidity (more specifically the water activity) acts as the controlling variable (Bonner 2019; Van Dijk 2002).

The areas where the microbial growth was noticed can be classified into four categories as below.

30.2.1 On the Walls Separating Conditioned and Unconditioned Zones

The wall separating the conditioned and unconditioned areas like the walls adjacent to the courtyard, toilets, shafts that are open to the outside, etc. are prone to the condensation of moisture. It is to be noted that the outside envelope of the building also falls in this category and not at all affected by any visible dew formation or microbial growth. The radiant heat received by direct or indirect solar radiation and the moving air reduces the chance for dew formation (Aelenei and Henriques 2008) and hence avoiding one favorable condition for the microbial growth.

The courtyard receives the exhaust of toilets adjacent to it which is having relatively high relative humidity (RH). This creates a higher dew point temperature for the air at the courtyard. The air is almost stagnant due to the partial covering over the top and only diffused solar radiation through the semi-transparent roofing sheet is received inside the courtyard. The acquired data of temperature and RH of the air of the courtyard and skin temperature of the walls adjacent to the air-conditioned room reveals that the condensation happens only during wee hours.

The toilets of rooms beneath the air-conditioned zones show severe problems. The high dry bulb and wet bulb temperatures due to the use of hot water for bathing purpose ease the chance for condensation under the ceiling. It is to be noted that the patient room toilet exhaust is not continuously working and it is switched off manually by the user. The lesser air change rate accelerates the evaporation of water from the floor and condensation at the relatively cool ceiling. Some of the ceilings of toilets started dripping from the ceiling after a bath using hot water (Fig. 30.1).

30.2.2 Inside the Air-Conditioned Zone Adjacent to Another Zone with a Different Set Temperature

Even though the RH and dry bulb temperature (dbt) are maintained relatively low inside the air-conditioned areas (Ninomura et al. 2001), dew formation and

Fig. 30.1 Ceiling of an unconditioned room beneath an air-conditioned zone



Fig. 30.2 Wall of an air-conditioned room showing microbial growth due to dew formation due to the direct impact of primary air from adjacent room unit



associated microbial growth (Fig. 30.2) are visible. One of the main areas is the lower floor of the operating rooms. The operating rooms are maintained normally at 18 °C dbt and the floor slab is not provided with any sort of thermal insulation. This condition favors the dew formation especially in areas where equipment producing high latent heat—such as sterilizers, vaporizers, and gas burners, are used.

Even though the room is designed for a dbt of 25 °C and RH of 50%, the supply condition of air is at a lower temperature and higher RH. Insufficient diffusion of this primary air with the room air is also causing condensation problems in conditioned zones. Use of supply air registers instead of diffusers increases the severity of this problem. The diffusers placed close the walls even caused condensation on the other side of the wall in the same zones at few points. The modulating valves for the control of the chilled water flow rate through the cooling coil of the AHU alter the supply air condition. A sudden closure will increase the possibility of condensation on a wall, which is cooled sufficiently due to the primary air. Even though this is not a continuous phenomenon, the dew formed in such situation can be pulled into the wall due to the capillary action of the micropores and increase the moisture. It is found from similar case studies that even weekly cycles of condensation in sub-artic region promoted the microbial growth in ventilation ducts (Pasanen et al. 1993).

30.2.3 In an Air-Conditioned Zone Which Is not Conditioned Round the Clock

In order to save energy, some areas such as outpatient, and reception are not air-conditioned round the clock. After the peak hours, the air-conditioning system is switched off and the doors to the outside environment are kept open. The masonry structure which is cooled when the air-conditioning system is functioning maintains a lower temperature due to the thermal energy storage capacity. Depending on the dew point temperature of the zone air, there is a chance for the condensation on these cold structures. Close to the doors that open to the outside, even visible condensation and microbial growth were found at few points.

30.2.4 Return Grills of the Operating Rooms

This is one case which has to be dealt with much seriousness. The return grilles kept at the lower levels of the operating rooms show severe microbial growth in their louvers and also inside the return ductwork. It is assumed that the air traveling from outside through the exhaust blower causes this condensation while the blower is in switched off condition. It has to be noted that there is no foolproof mechanism provided to arrest the inward diffusion/flow of outside air through this path. There is no filter provided in this line and hence even pressure fluctuations resulting from door openings can create a flow through this path. Since any dispersion of the microbial spores can create aseptic conditions in the operating rooms, this has to be seen with utmost importance.

30.3 Thermo-hygro-metric Explanation of the Problem

The primary aim of this study is to find out the reason and to take remedial actions to avoid condensation related problems. Moreover, much modification in a full-fledged hospital is difficult and invites a lot of related issues. So the analysis is done on an engineering level rather than on a research perspective. The four types of condensation problems discussed above are classified into two as the first two are created by condensation due to the heat transfer through a composite material like a plastered brick wall or concrete. In the third and fourth types, the condensation is happening on the surface which is exposed to the conditioned air itself which makes the problem much interesting. The Thermal diffusivity of the material and the changes in the psychrometric properties of the conditioned air create this type of condensation. The problem is formulated with an electrical analogy of thermal conduction neglecting minor factors.

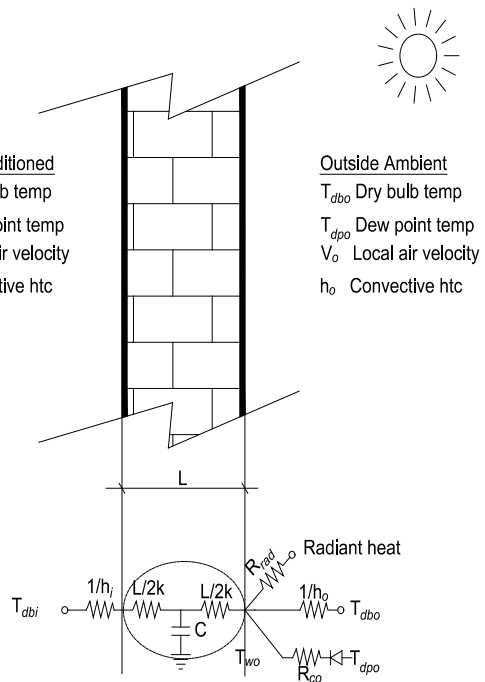
30.3.1 Case 1 and 2

Case 1 and Case 2 are represented as in Fig. 30.3. In Case 2, the absence of solar radiation and a lower enthalpy of air are expected. The thermal conductivity of the composite partition, its thermal capacity, and the convective heat transfer coefficients (inside h_i and outside h_o) determine the probability of condensation on the surface with air inside and outside the partition with different psychrometric properties. The thermal diffusivity of the material creates a finite time lag for the heat transfer which makes the analysis much complicated since the outside ambient air psychrometric properties cycle drastically during the time of the day.

For simplicity, assuming the inside and outside properties to be constant for a prolonged period thus assuming almost steady-state conditions and also neglecting the effect of radiation to be negligibly small, the inside and outside heat transfer coefficients play a critical role in deciding the outside wall temperature. In a steady-state condition, the effect of thermal storage C is neglected. A higher inside heat transfer coefficient (h_i) per unit area and higher heat transfer coefficient per unit area outside (h_o) make the outside surface temperature of the wall to the lowest when $T_{dbi} < T_{dbo}$.

The dew point depression of the outside air decides the chance for the condensation. A lower dew point depression arising out of close to the saturation with high relative humidity increases the chance of condensation. When the dew point

Fig. 30.3 Conditions representing Case 1 and 2 and corresponding electrical analogy



temperature of the outside air T_{dpo} falls below the wall temperature T_{wo} , the condensation starts and another heat transfer mechanism is started with a thermal resistance of R_{co} . The wall is assumed to be dry in the initial condition and no vaporization is expected. The condensate thus formed can be either absorbed by the wall if it is porous due to capillary action or can form dew over the surface if the surface is coated with a water-impermeable coating. The first case reduces the visible dew formation but as the moisture penetrates into the interior portion of the wall, can supplement the moisture for the growth of microbial over the surface even when the thermal conditions are not favorable for condensation.

It is interesting to see that the thermal radiant heating at the surface decreases the chance of condensation. The walls exposed to sunlight was found to be free from any visible condensation on the building envelop.

30.3.2 Case 3 and 4

These cases are different from the former two that the driving potential for the condensation is created by the air on the same side of the wall due to the transient changes in the psychrometric properties of air with respect to the time. Also, the thermal diffusivity of the partition and the convective heat transfer coefficient for the wall air interface decide the chance for condensation. Before going into the details few things are considered that cause the thermal swing.

Thermal and hygrometric swing. These are the transient changes in the thermo-hygrometric properties of the air in a particular area in an air-conditioned zone and can be because of any or several of the below-mentioned factors.

1. Intermittent infiltration of outside air through the door opening.
2. Intermittent operation of the air-conditioning unit in a zone.
3. Rapid change in the average cooling coil temperature due to thermostat operation.
4. Rapid change in heater surface temperature in a reheat coil.
5. Due to the functioning of Variable air volume (VAV) mixing box
6. Automatic direction control of louvers in air supply registers.

Due to the swing, if the dry bulb temperature of the air gets changed, it causes a heat transfer from the wall or to the wall as shown in Fig. 30.4. This phenomenon is for a short period so that the temperature variation deeper inside the material is of lesser magnitude compared to the surface. The thermal diffusivity causes this nonlinearity. The thermal charging and discharging cycle causes a temperature difference with the wall T_{wi} with the dew point temperature of the air in contact. Assuming the initial surface to be dry, the temperature differential $T_{dpi}-T_{wi}$ creates the driving potential for condensation. A lower convective heat transfer coefficient h_i , the rapid rate of change in dry bulb temperature swing and high relative humidity augment the condensation.

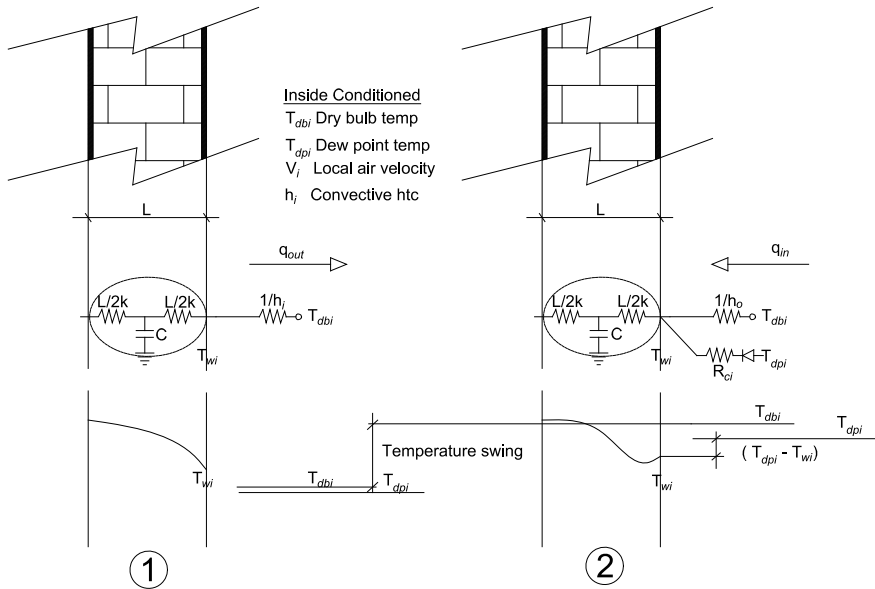


Fig. 30.4 Heat transfer from the wall or to the wall

The direct impact of the primary supply air to a medium having a high thermal diffusivity will cause a higher chance for condensation during a rapid temperature swing at higher humidity.

30.4 Remedial Measures

A little consideration will show that considering the abovementioned factors during the design of the building not only prevents the chances for condensation but also can save energy.

- (i) The peripheral walls should be constructed with bricks with a thermal break. Thermal insulation with insulated panels provided at inside of the walls using materials with a good fire rating and OSHAS rating is recommended. If the material used in such insulation is permeable to moisture, an impermeable layer should be provided to prevent condensation inside the material.
- (ii) The diffusers used in the conditioned zones should have a high entrainment ratio and should be placed at sufficient distance from the solid obstructions. Grilles, jet diffusers, and slot diffusers should be selected carefully after assuring enough distance available for the diffusion of primary air.
- (iii) During the selection of air handling units, overrating the capacity can cause higher temperature swing due to the on-off cycle. If a continuous modulation

is provided for the chilled water or the refrigerant, the constants for the control loop should be selected to avoid large overshoot in temperature of the supply air.

- (iv) It is always good to keep the building at slightly positive pressured with respect to the ambient by carefully balancing the fresh air and ventilation. The condensation possibilities close to the fenestrations can be avoided by blocking the possibilities of infiltration.
- (v) During the rainy seasons, the grand sensible heat factor will become worse and the ability of the air handling units to handle latent heat also will decrease. Additional dehumidifiers should be provided to limit the relative humidity within limits.
- (vi) The toilets should be provided with sufficient ventilation round the clock and the exhaust from the toilet should be discharged to open area outside the building. If the transfer air from the room is not used for the air change in the toilets, dehumidified fresh air should be used.

30.5 Conclusions

The present study points out to the importance of some of the factors to prevent the condensation of water vapor at the building structure. Since the building is situated in a place with a typical tropical climate and two rainy seasons, designing the air-conditioning system with the average values of outside relative humidity will not be a wise decision for health care facilities. Although the microbial growth found in the present case study is not of serious health concern for a healthy adult, it cannot be tolerated in a healthcare environment. The spores of these microbes can be transferred through the air distribution network and can get transferred across different zones.

Disclaimer Appropriate permission from the hospital authorities was obtained for collecting samples for conducting this study. The instrumentation setup used for the collection of data is tested and confirmed that they will not affect the sterile nature of the area and will not create harmful radio frequency interference to the system and equipments. The entry into the various zones is done with all safety precautions as per the guidelines of the hospitals.

References

- Aelenei D, Henriques FMA (2008) Analysis of the condensation risk on exterior surface of building envelopes 40:1866–1871
- Bonner JT (2019) A study of the temperature and humidity requirements of *Aspergillus Niger*. *Mycologia* 40(6):728–738. <https://www.jstor.org/stable/3755321>
- HVAC design manual for hospitals and clinics. ASHRAE

- Ninomura P, Bartley J, Ashrae M (2001) New ventilation guidelines for health—care facilities. ASHRAE J 4
- Pasanen P, Pasanen A, Jantunen M (1993) Water condensation promotes fungal growth in ventilation ducts 3:106–112
- Van Dijck PWM (2002) On the safety of *Aspergillus Niger*—a review 426–435

Chapter 31

Numerical Evaluation of Composite Slabs



Ajma Mohan and Milu Mary Jacob

31.1 Introduction

The composite slabs are formed using corrugated metal sheets over which reinforced concrete is placed. The metal sheet acts as permanent formwork as well as tensile reinforcement. Concrete floor slabs reinforced with composite steel decking is shown in Fig. 31.1. The popularity of composite construction is increasing because of the number of advantages it has over conventional slabs. In composite slabs additional steel reinforcement may be provided only for preventing shrinkage and for proper distribution of load. In the case of continuous slabs, reinforcing steel is required to resist the negative bending moment at the supports. The type of slabs when used for flooring helps in saving construction time and building materials. Some of the other advantages are that they help in reducing the cost of foundation, this type of construction has better fire resistance and seismic resistance. Finally, the steel sheeting is extremely light, and transportation and construction are easier compared to conventional construction methods.

In the composite type of floor slabs bonding between the metal deck and the reinforced concrete above it is provided by the mechanical interlock by the virtue of embossments on the metal deck slab. A mechanical interlock is needed between the steel profile as well as the overlaying concrete.

A. Mohan (✉) · M. M. Jacob
Department of Civil Engineering, Saintgits College of Engineering and Technology,
Kottayam, India
e-mail: ajma.g.mohan@gmail.com

© Springer Nature Singapore Pte Ltd. 2020
H. Drück et al. (eds.), *Green Buildings and Sustainable Engineering*,
Springer Transactions in Civil and Environmental Engineering,
https://doi.org/10.1007/978-981-15-1063-2_31

Fig. 31.1 Elements of composite slab with profiled steel decking

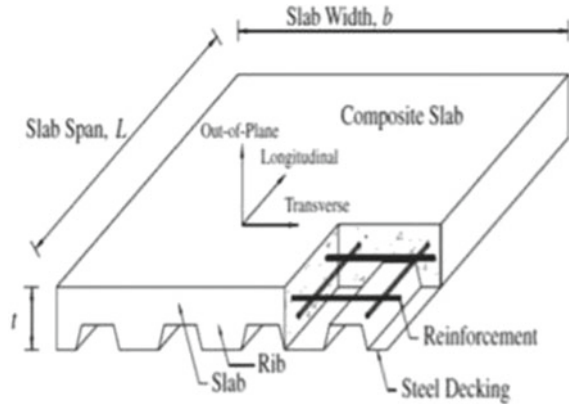
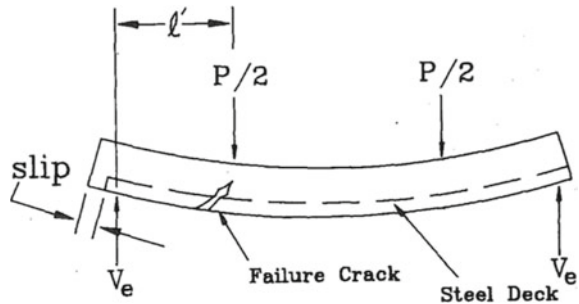


Fig. 31.2 Shear bond failure at interface



31.1.1 Behaviour of Composite Slab

The composite slab generally consists of corrugated metal sheet and overlying concrete. The concrete can be of plain cement concrete or reinforced cement concrete. Different types of shear connectors can be used to prevent the relative slip between the metal sheet and concrete. Type of connectors includes stud connectors, bar connectors, tee connectors, channel connectors, horseshoe connectors, etc. Common failure modes in composite slabs can be defined as shear failure at supports, shear bond failure which may occur at the steel–concrete interface (Fig. 31.2) as well as the flexural failure.

31.2 Background

Composite slab constructed using metal deck and concrete is being widely accepted and used because it has a large number of advantages over conventional construction methods. Factors which affect the structural performance of composite slabs are mainly the horizontal bond characteristics at the steel–concrete interface as well as the shape of embossments on the steel profile. These investigations and experimental studies helped to know about the relationships already investigated.

Siddh et al. (2016) The variation in behaviour of composite slab with the profiled steel deck is studied. The steel deck thickness and effect of notch is tested. By introduction of notches (v shaped) the load-carrying capacity of composite slabs is considerably increased. Sheet thickness is an important factor which affects the load-carrying capacity of composite slab.

Suthitha and Lokeshwaran (2016) Three composite slab specimens were cast in two different ways, normal type, and skewed type. The slabs with skew angle have increased stiffness and therefore load-carrying capacity of skew type slab is found to be higher than that of conventional floor slab. Also the mid-span deflection of skew type slab is lesser.

Swaminathan et al (2016) Comparison between diff types of shear connectors was carried out in this study. Slabs were casted using bolded stud shear connectors as well as headed stud shear connectors. Push out tests was carried out on 6 test specimens. Initial crack load and maximum slip were compared. The composite slab modelled with headed shear connectors exhibits lesser slip compared to those with bolted stud shear connectors.

Manjunath and Sureshchandra (2014) The paper describes experimental studies on concrete slab with decking. The behaviour of deck slab with and without embossments is studied using flexural tests. Effect of bond strength is analysed using slip test. Comparison is done between slabs with mechanical bond as well as slabs with chemical bond.

Merool et al. (2014) Composite deck slabs modelled with varying aspect ratio were tested. Experiments were performed to estimate the load at first crack, deflection, and load-carrying capacity. It was found in the study that the slabs with higher aspect ratios have higher stiffness compared to ones with smaller aspect ratios. The increased stiffness results in improved strength of the slabs.

Hedao et al. (2012) Structural behaviour of composite slabs was studied by numerical studied as well as by conducting experimental studies. The shear span is identified as an important parameter which determines the type of failure on the composite slab.

Chen and Shi (2008) A new approach in the finite element study of composite type of construction is presented here. The study aims at solving the major problems which arise while assigning the contact between the profiled steel sheet and the concrete. The new approach of finite element analysis is verified by comparing the test results to values obtained by conducting an experimental study.

Marimuthu et al. (2007) Factors affecting behaviour of the composite steel deck slab were studied; mainly the shear span, depth, width, and position of embossments. The type of failure in composite slabs with shorter shear span and longer shear span are characterised by shear bond failure and flexural failure, respectively.

Crisinel and Marimon (2004) The study presents a new design approach for predicting the composite slab behaviour. In the study, a new approach is carried out to combine results obtained from conventional material tests as well as small-scale tests conducted on a simple model.

Chen (2003) The study aims at understanding the shear bond action in the composite slabs. Simply supported and continuous composite slabs were studied with varying end constraints. The shear bond strength of composite slab increases with the end anchorage. However, it is the shear bond between metal deck and concrete rather than the strength of anchored studs which governs the load-carrying capacity.

Burnet and Oehlers (2001) An innovative type of push tests to stimulate the bond characteristics precisely are proposed in the study. The study is conducted on both dovetail as well as trapezoidal cross sections and using mechanical and chemical bond. After conducting this study, new guidelines for the development of new type metal profiled sheets are presented.

Tenhovuori and Leskela (1998) The bond failure of composite slabs in the longitudinal shear connection was studied. Parametric studies are carried out by conducting non-linear calculations based on the method of finite elements and results are compared to find out the critical factors. Comparison between the present methods of analysis as per Eurocode 4 part 1-1 and a new system for improvement, simplification and the unification of the methods are proposed.

Calixto et al. (1998) Experimental investigations were carried out on full-scale one-way composite slabs with ribbed decking. Effect of different aspects was investigated, namely, the thickness of profiled steel sheet, total slab height, and shear span. The effect of stud bolt-type connectors on the end anchorage of the composite slab was also studied. Throughout the tests, deflection at the mid-span, slip at the ends and strains developed in metal decking were measured. All the results clearly indicate that the composite slabs with stud bolt connectors exhibit better performance.

Wright et al. (1987) In this study 200 composite slab elements were tested experimentally and the results obtained were compared with available methods of design. The study paid careful attention to the different phases of a composite slab, i.e., construction, composite slab action, and composite beam action phase. The study proves that the variation in concrete strength is insignificant for composite slabs. Also the crucial parameter which determines the strength of composite slab is identified as the height of embossments. The paper also concludes that the present design procedures for composite slab construction are safe and maybe a bit conservative in certain cases.

These literature have clearly demonstrated the importance and advantages of using composite slabs. Based on all the literature studied, it can be concluded that the factors affecting the load-carrying capacity and failure of composite slabs are

height, shape, and orientation of embossments in the profiled metal decking of composite slab. Performance tests can only give accurate judgment as each metal deck profile as it has its own unique mechanism of shear transfer.

31.3 Validation

The study selected for validation is G. Ranzi et al. “Full-scale tests on composite steel–concrete beams with steel trapezoidal decking,” *Journal of Constructional Steel Research*; ELSEVIER. A part of the experimental study using 2 shear studs per trough is analysed using the software and the results are compared.

31.3.1 Modelling

The composite slab was modelled with steel profiled sheet decking and reinforced cement concrete above it. The concrete used is of grade M 25 grade designed as per the relevant Indian Standard code was chosen for concreting. Mild steel reinforcement mesh of 7 mm diameter bars was laid in the composite slab. The modelled slab and the test setup from the ANSYS software are shown in Fig. 31.2 (Fig. 31.3).

31.3.2 Result

Max deflection of the composite slab is found out to be 5.37 mm and the max deflection corresponding to the same load was 5.52 mm in the journal. Similarly, all the deflections from model and journal are given in Table 31.1 (Fig. 31.4).

Fig. 31.3 Modelled composite slab

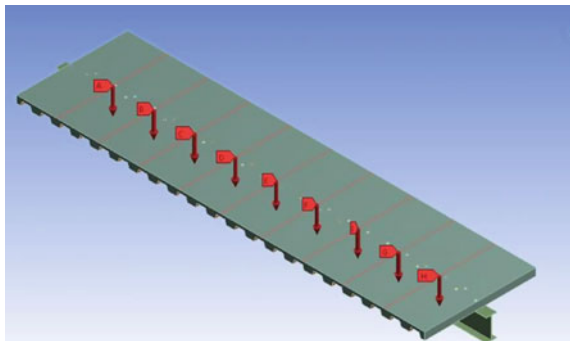
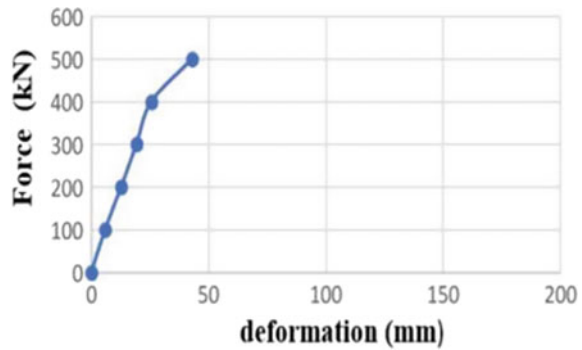


Table 31.1 Deflection of model

Force (kN)	Deformation from model (mm)	Deformation from journal (mm)
0	0	0
100	5.82	6
200	12.70	13
300	19.23	20
400	25.63	27
500	42.98	45

Fig. 31.4 Graph plotted from software analysis

31.4 Numerical Study

The present study aims at determining the deflection of simply supported slab with varying parameters. 3-D model of composite slab consisting of concrete and profiled steel deck is analysed in ANSYS WORKBENCH to identify the behaviour of composite slab with varying parameters. The concrete slab was modelled using Solid 65 (8 node element) whereas the steel deck slab was modelled using Shell 181 (4 node element). The steel reinforcement was modelled using Link 8 (2 node element). Contact was considered as bonded that is, vertical separation between metal sheet and concrete slab was restricted.

31.4.1 Description of Model

Concrete is considered as material with multilinear isotropic hardening. The stress-strain graph of concrete used is shown in Fig. 31.5. Whereas the profiled steel sheet was considered as material with bilinear isotropic hardening. The material properties of steel and concrete are given in Tables 31.2 and 31.3, respectively.

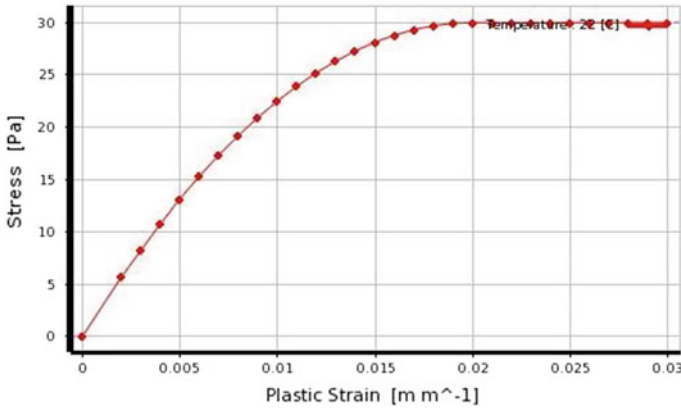


Fig. 31.5 Stress strain graph of concrete used

Table 31.2 Material properties of concrete

Properties	Values
Density	2500 kg/m ³
Poisson’s ratio	0.18
Elastic modulus	27386 N/mm ²
Yield strength	30 N/mm ²

Table 31.3 Material properties of steel

Properties	Values
Density	7850 kg/m ³
Poisson’s ratio	0.3
Elastic modulus	2 × 10 ⁵ N/mm ²
Yield strength	250 N/mm ²

Sketch showing the details of embossments and sectional details are given in Fig. 31.6. Total depth of slab is taken as 110 mm. These dimensions remain same for all models. Roller support is provided at the right end and hinges at the left. Mild steel reinforcing meshes with bar diameter 6 mm at 250 mm c/c were used in the model. These meshes were placed 25 mm from the top surface of the profiled sheet. The load was applied as two-line loads distributed across the width of the slab by transferring the actuator load to two beam sections (ISMB 150, I beam of depth 150 mm) placed across the width of the slab. The load is applied is selected as 500 kN. Figure 31.7 shows the slab modelled with loads applied.

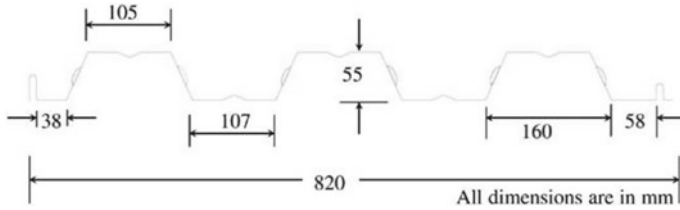


Fig. 31.6 Diagram showing cross-sectional details of slabs

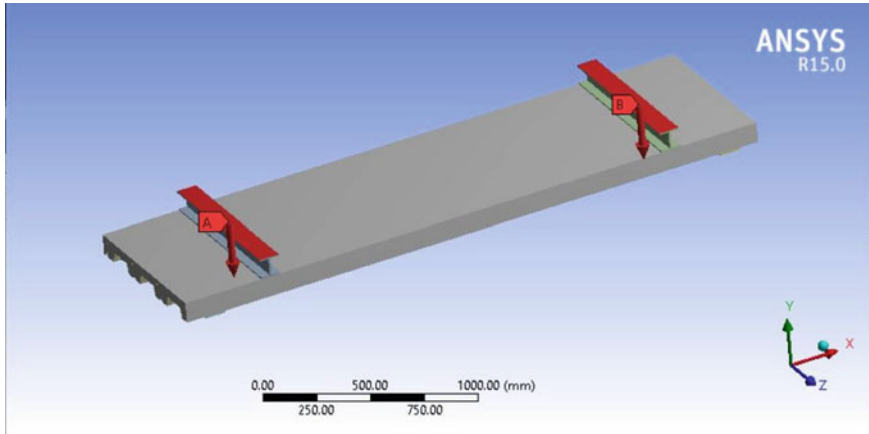


Fig. 31.7 Slab modelled in ANSYS

31.4.2 Variation of Shear Span

The composite slab models considered for finite element analysis and the deformations obtained are listed in Table 31.4. Also, the graph showing deflection with variation in shear span is given in Fig. 31.8. The following slabs are modelled with constant thickness of profile steel sheet as 8 mm. The shear span is defined as the distance between the centres of support at either end to the point of application of the line load in the slab. It is observed that the value of deformation increases with

Table 31.4 Maximum deflection of the models with a varying shear span

Shear span	Max deformation (mm)
Span/10	5.376
Span/7.5	7.457
Span/6	9.265
Span/5	10.972
Span/4.3	12.559

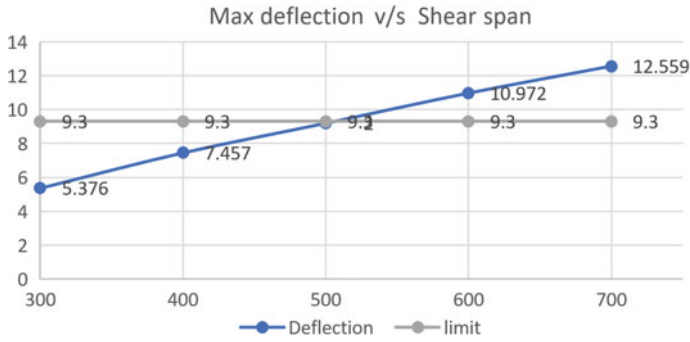


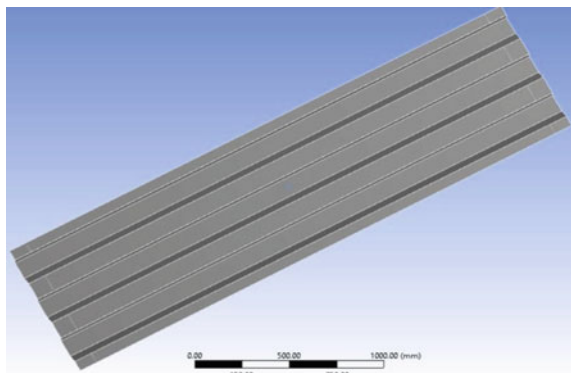
Fig. 31.8 Variation of deformation with shear span

increase in shear span. So it can be concluded that for shear spans below 600 mm ($L/5$), the deflection is within the permissible limits.

31.4.3 Variation of Stiffener Spacing

Stiffeners are plate sections attached to the profiled deck slabs to decrease the out of plane deformations. Here the composite slab modelled is of dimension $3\text{ m} \times 0.82\text{ m}$ and shear span of 600 mm. The slab is modelled with no stiffener, 2 stiffeners, 3 stiffeners, 4 stiffeners, and 5 stiffeners. Figure 31.9 shows the composite slab without stiffeners whereas Fig. 31.10 shows composite slab modelled with 5 stiffeners. The maximum deflection of composite slab with no stiffeners was 10.972 mm which considerably reduced on addition of stiffeners. Maximum deflection with varying number of stiffeners is given in Table 31.5. Also the graph showing deflection with variation in stiffener spacing is given in Fig. 31.11. Here it is seen that deflection of composite slab decreases with increasing number of stiffeners. Also with 3 stiffeners maximum deflection is within the limits.

Fig. 31.9 Arrangement of corrugated metal deck slab without stiffeners



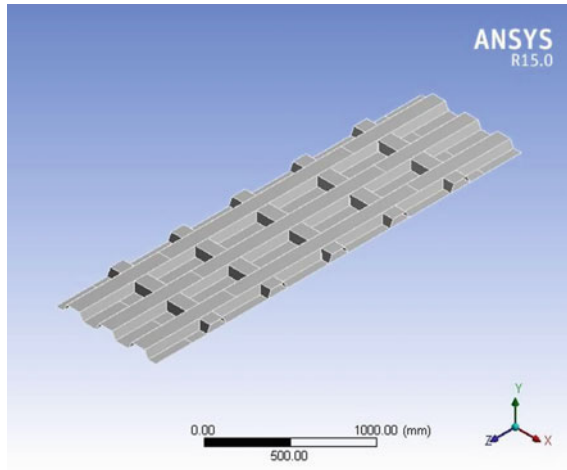


Fig. 31.10 Arrangement of corrugated metal deck slab with 5 stiffeners

Table 31.5 Maximum deflection of the models with varying stiffener spacing

Slab designation	Stiffener spacing	Max deformation (mm)
No stiffener	—	10.972
2 Stiffener	Span/3	10.44
3 Stiffener	Span/4	8.903
4 Stiffener	Span/5	8.085
5 Stiffener	Span/6	7.4155

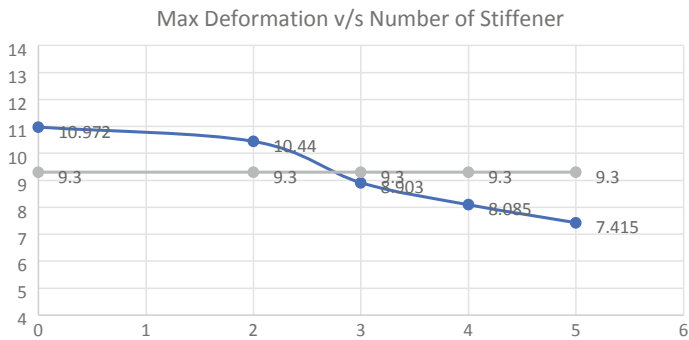


Fig. 31.11 Variation of deformation with stiffener spacing

31.4.4 Variation of Shear Stud Spacing

Shear studs are provided in the troughs of metal deck slabs to prevent the relative slip of concrete and metal deck slab. The spacing of the shear studs in the composite slab is to be fixed by conducting trials with varying spacings. Here composite slabs with shear stud spacing of 150, 300, and 450 mm were modelled and deformations were evaluated. Maximum deflection with varying number of shear studs is given in Table 31.6. Also the graph showing deflection with variation in stud spacing is given in Fig. 31.13 (Fig. 31.12).

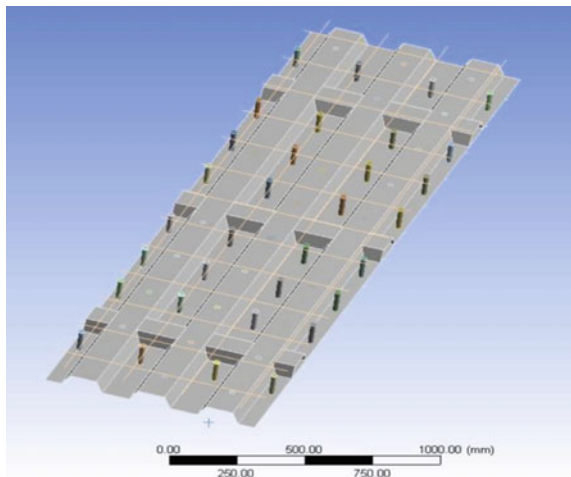
On increasing the shear stud spacing the deflection values also slightly increase. However, even 45 cm spacing of studs keep the deflection within the limits, i.e., 8.399 mm (<8.57 mm). Here the deflection of composite slab modelled with 600 mm shear span with 3 stiffeners and shear stud at 450 mm spacing are within the limits.

SL. No	Type of slab	Deformation (mm)
1	Composite slab without stiffener	10.972
2	Composite slab with 3 stiffeners	8.903
3	Composite slab with 3 stiffeners and shear stud spacing 450 mm	8.399

Table 31.6 Maximum deformation of the models with varying shear stud spacing

Shear stud spacing	Max deformation (mm)
15 cm	7.409
30 cm	7.717
45 cm	8.399

Fig. 31.12 Typical arrangement of with shear studs on corrugated metal deck slab



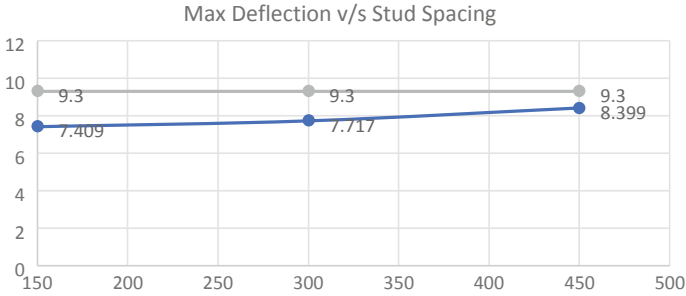


Fig. 31.13 Variation of deformation with shear stud spacing

31.5 Conclusion

The analytical study of composite deck slabs using non-linear finite element analysis is carried out. Results from slab models with varying shear span, stiffener spacing, and number of shear studs are studied. The behaviour of composite slab with varying parameters is represented. The behaviour of the profiled composite sheet deck slab directly depends on the shear span. It is observed that shear span is the factor which governs the longitudinal shear strength. Stiffeners when provided help to reduce the maximum deformations. And shear stud is an effective way to transfer the shear at interface. All the stresses and strains in steel and concrete are checked and found to be within permissible limits.

The maximum deflections are obtained from the analysis is studied and the following conclusions are made:

- As shear span of the slab increases by 100 mm, deflection is observed to increase approximately by 20%.
- For shear spans below span/5, the deflection is within the permissible limits.
- The stiffener spacing has an inverse relationship with the load-carrying capacity of composite slabs.
- When stiffener spacing decreases from span/3 to span/4, the deflection is reduced by 14.7%.
- Also the deflections are within the limit and the optimum number of stiffeners spacing is observed to be span/4.
- The spacing of shear studs has very little effect of load-carrying capacity as studs are intended to transfer longitudinal shear.
- On decreasing the stud spacing from 450 to 300 mm the deflection reduces by 8%.
- And when stud spacing is further reduced to 150 mm the deflection reduces by 3.9%.

References

- Alashker Y et al (2010) Progressive collapse resistance of steel-concrete composite floors. *ASCE J Struct Eng*
- Benmokrane B et al (2006) Designing and testing of concrete bridge decks reinforced with glass fibre bars. *J Bridge Eng ASCE*. <https://doi.org/10.1061/ASCE1084-0702>
- Calixto JM, Lavall AC et al (1998) (1998) Behaviour and strength of composite slabs with ribbed decking. *J Constr Steel Res* 46(1–3):211–212
- EN 1994-1-1 (2004) Eurocode 4: design of composite steel and concrete structures. Part 1.1: general rules and rules for buildings. Brussels: European committee for standardization
- Hedao NA et al (2012) Design of composite slabs with profiled steel decking: a comparison between experimental and analytical studies. *Int J Adv Struct Eng*. Elsevier
- IS 11384 (1985) Code of practice for composite construction in structural steel and concrete [CED 38: special structures]
- Kalamkar SS, Akhare AR (2016a) Analytical study on behaviour of composite slabs with profiled steel decking. *J Eng Res* 14(S1):88–96. ISSN 0972-768X
- Kalamkar SS, Akhare AR (2016b) Analytical study on behaviour of composite slabs with profiled steel decking. *Int J Eng Res* 5(3):654–657
- Liu J, Astaneh-Asl A (2000) Cyclic testing of simple connections including effects of slab. *ASCE J Struct Eng*
- Manjunath TN, Sureshchandra BS (2014) Experimental study on concrete slab with profiled steel decking. *J Eng Res Technol*. ISSN:2278-0181
- Marimuthu V et al (2007) Experimental studies on composite deck slabs to determine the shear-bond characteristic values of the embossed profiled sheet. *J Constr Steel Res* 63 (2007):791–803 ScienceDirect
- Merool V et al (2014) Experimental study on composite deck with different aspect ratio. *J Adv Struct Eng* 9(30). <https://doi.org/10.17485/ijst/2016/v9i30/99216>
- Panchal DR (2014) Advanced design of composite steel-concrete structural element. *Int J Eng Res Appl* 4(7)(Version 2)
- Porter ML, Ekberg CE (1967) Design recommendations for steel deck floor slabs. *J Struct Div ASCE* 1976; 102(ST 11): 2121–2135
- Ranzi, G., Bradford, M. A., Ansourian, P., Filonov, A., Rasmussen, K. J. R., Hogan, T. J., and Uy, B. (2009) Full-scale tests on composite steel-concrete beams with trapezoidal decking. *J Constr Steel Res* 65: 1490–1506. Elsevier
- Siddh SP, Patil YD, Patil HS (2016) Experimental studies on behaviour of composite slab with profiled steel sheeting. *Mater Today Proc* 4(2017):9792–9796 ScienceDirect
- Suthitha S, Lokeshwaran N (2016) Experimental investigation and comparison of composite slab with perpendicular and skew type steel decking. *Int J Struct Eng* 14(S1):88–96. ISSN 0972-768X
- Swaminathan S et al (2016) Experimental investigation on shear connectors in steel-concrete composite deck slabs. *Indian J Sci Technol*
- Tenhovuori AI, Leskela MV (1998) Longitudinal shear resistance of composite slab. *J Constr Steel Res* 46(1–3):228
- Wright HD, Evans HR, Harding PW (1987) The use of profiled steel sheeting in floor construction. *J Constr Steel Res* 7:279–295

Part IV
Environmental Technologies

Chapter 32

Numerical Investigation on the Temperature Distribution of a Steel Reactor with Copper Bottom Surface for Pyrolysis of Polyethylene Terephthalate Waste Plastics



Anandhu Vijayakumar and Jilse Sebastian

32.1 Introduction

Plastic has a tremendous impact on the contemporary lifestyle of mankind. The need for plastic is ever increasing, as a result of this huge amount of waste is generated. The energy recovery from plastic waste through pyrolysis is a promising technique to reduce the threat produced by plastic waste (Kumar et al. 2013). Pyrolysis is a thermal degradation process that is characterized by less or absence of oxygen. The rate of pyrolysis is determined by certain factors such as temperature and time (Chintala et al. 2018). The design and model of pyrolysis reactor are also important because the amount of fuel produced depends on the design of the reactor.

Several investigators have reported the benefits of energy recovery (plastic oil) from plastic waste through pyrolysis and its ability to replace conventional fuels. Kalargaris et al. (2017) conducted pyrolysis of low-density polyethylene (LDPE) plastic and ethylene-vinyl acetate (EVA) plastic at a temperature of 700 °C for low-density polyethylene and 900 °C for ethylene-vinyl acetate. Viswanath et al. (Damodharan et al. 2017) experimentally investigated the potential of HDPE plastic oil as an alternative for diesel fuel. The pyrolysis is conducted at a temperature of 450 °C. Some papers reported that the pyrolysis of waste plastic happened at a temperature range of 350–600 °C (Kaimal and Vijayabalan 2015, 2016; Mani et al. 2009; Rinaldini et al. 2016). But the point of temperature distribution inside the reactor is not considered. The temperature distribution inside the pyrolysis reactor

A. Vijayakumar (✉) · J. Sebastian
Department of Mechanical Engineering, St. Joseph's College of Engineering
and Technology, Palai, Kerala, India
e-mail: anandhuvijayakumar@gmail.com

© Springer Nature Singapore Pte Ltd. 2020
H. Drück et al. (eds.), *Green Buildings and Sustainable Engineering*,
Springer Transactions in Civil and Environmental Engineering,
https://doi.org/10.1007/978-981-15-1063-2_32

397

should be considered as it is essentially important to calculate the region of thermal cracking. The thermal cracking of waste plastic occurs in a region having uniform temperature distribution (Güngör et al. 2015).

The present work is focused to identify the potential of a steel reactor with copper bottom surface for the pyrolysis of waste plastics. The commercial CFD code FLUENT 15.1 was employed to investigate the temperature distribution in the steel reactor with the copper bottom surface.

32.2 Modelling

32.2.1 Geometry

A 3D model of cylindrical steel reactor with copper bottom surface is developed by using SOLID EDGE ST7 with a dimension of 0.40 m diameter at bottom, 0.50 m diameter at top, 0.60 m height and 0.002 m thickness shown in Fig. 32.1. The outlet vent has a dimension of 0.01 m diameter and 0.05 m height. A temperature of 733 K is applied at the copper bottom of the reactor as the heat input. The simulation is done based on the commercial CFD code FLUENT 15.1. After modelling the reactor, it is meshed with different number of elements and the result is compared with the experimental results done by Hartulistiyoso et al. (2015) for selecting the suitable mesh. The mesh size with 362654 number of nodes and 102431 elements is selected.

Fig. 32.1 Model of the pyrolysis reactor

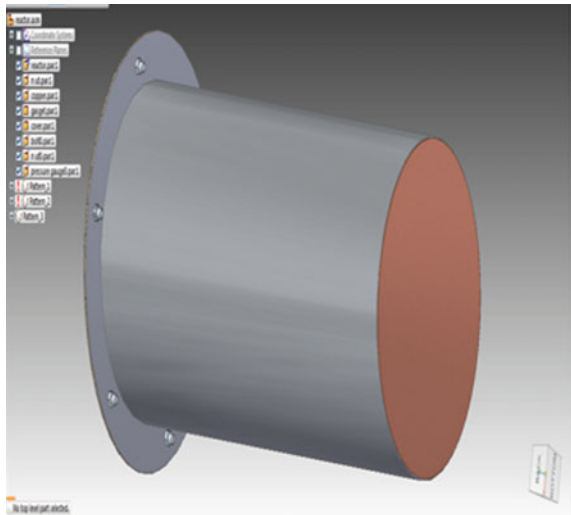


Table 32.1 Boundary conditions

Sl No	Parameter	Type	Condition	Value
1	Operating pressure	–	Absolute	101325 Pa
2	Material	Air	Density	1.225 kg/m ³
			Cp	1006.43 J/kg K
			Thermal conductivity	0.0242 W/m K
			Viscosity	1.789 × 10 ⁻⁵ kg/ms
3	Inlet	Velocity-inlet	Velocity magnitude	0.749 × 10 ⁻³ m/s
			Temperature	733 K
4	Outlet vent	Pressure outlet	Gauge pressure	0 Pa

32.2.2 *Boundary Conditions*

The boundary conditions applied at the different portions of the geometry are shown in Table 32.1. The flow is laminar and the energy equation is utilized in order to solve the temperature. The number of iteration is 10,000.

32.2.3 *Grid Independence Study*

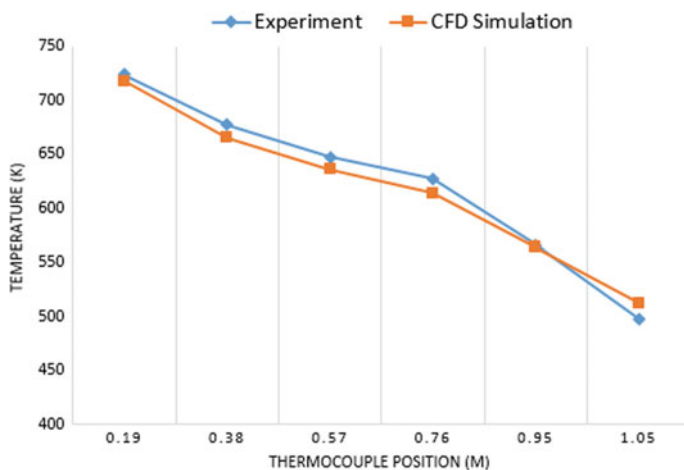
Grid independence study was conducted to investigate the influence of mesh density on the numerical results. The maximum temperature at the outlet vent is measured at different mesh density. Among them, four mesh sizes were selected considering the variation of obtained results from the experimental results. The temperature at the outlet vent with different mesh densities are listed in Table 32.2. The mesh size with 362,654 number of nodes and 102,431 elements is selected on the basis of variation of obtained results from the experimental results (Hartulistiyoso et al. 2015).

32.2.4 *Validation*

The simulation result is compared with the experimental works done by Hartulistiyoso et al. (2015). There is not much difference between the experimental and numerical results. The air properties used in the simulation is the same as that of Hartulistiyoso et al. (2015) and has similar results as that of temperature distribution inside the reactor. The Fig. 32.2 shows the comparison of temperature profile between experimental and numerical results in the axial direction. There is only 2% variation between the results.

Table 32.2 Mesh sizes used for grid independence study

Sl No	Number of nodes	Temperature at outlet vent (K)
1	200,242	542
2	284,986	530
3	362,654	524
4	398,621	526

**Fig. 32.2** Comparison of temperature profile between experimental and CFD simulation

32.3 Result and Discussion

32.3.1 Temperature Contour

The Fig. 32.3 shows the temperature distribution inside the reactor obtained from the simulation results. The maximum temperature inside found is 723 K which is the red region in the result.

The temperature is decreased while moving in the axial direction. This is due to the convection heat transfer from the gas to the wall inside the reactor. The temperature at the outlet vent is 524 K. From the simulation result, it is found that the region of maximum pyrolysis reaction occurs at 3/4th of the total length of the reactor. Uniform temperature distribution is obtained at 3/4th of the total length of the reactor. The lowest temperature is shown in the blue region at the top of the reactor.

The Fig. 32.4 shows the profile of temperature distribution in the heating process up to 90 min. The temperature is gradually increased with time up to 90 min. The temperature distribution is maximum for 0.12 m height in the axial direction. From

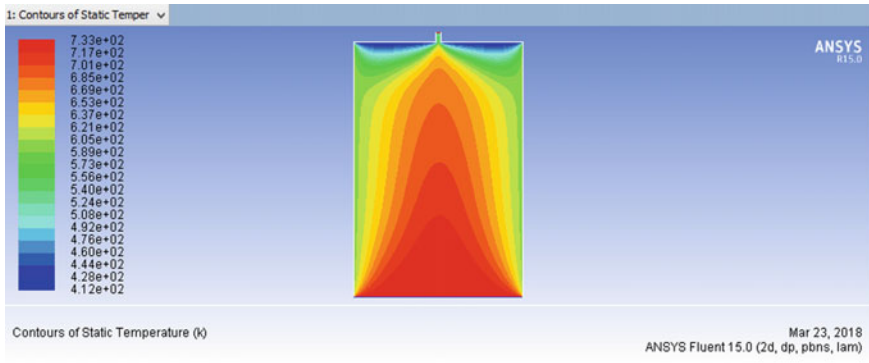


Fig. 32.3 Profile of temperature distribution inside the reactor

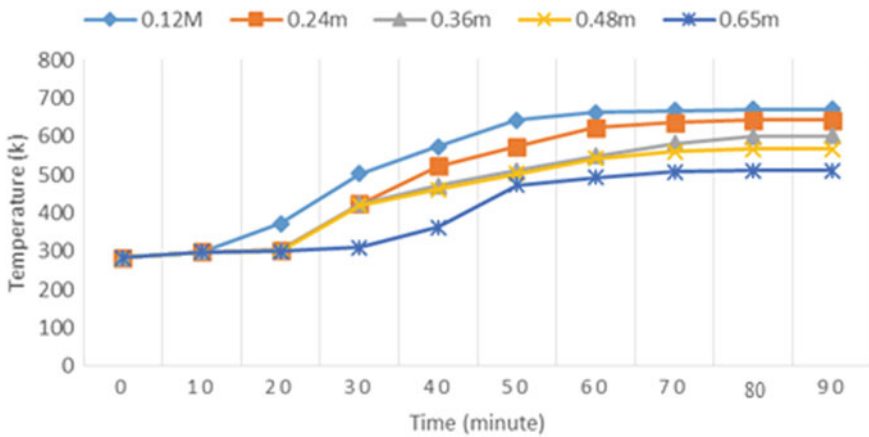


Fig. 32.4 Temperature distribution in the heating process up to 90 min

the simulation result, it is found that the region of maximum pyrolysis reaction occurs at 3/4th of the total length of the reactor.

After 90 min the temperature distribution at all height in the axial direction is reached in a steady state shown in Fig. 32.5. There is a constant temperature difference of about 50 °C that is obtained for all height in the axial direction except for 0.48 m. This is mainly due to the thermal cracking process of plastic. The plastic consumes more heat during the thermal cracking process and this leads to the difference between 0.36 m and 0.48 m at about 20 °C. The thermal cracking occurs at a region having uniform temperature distribution.

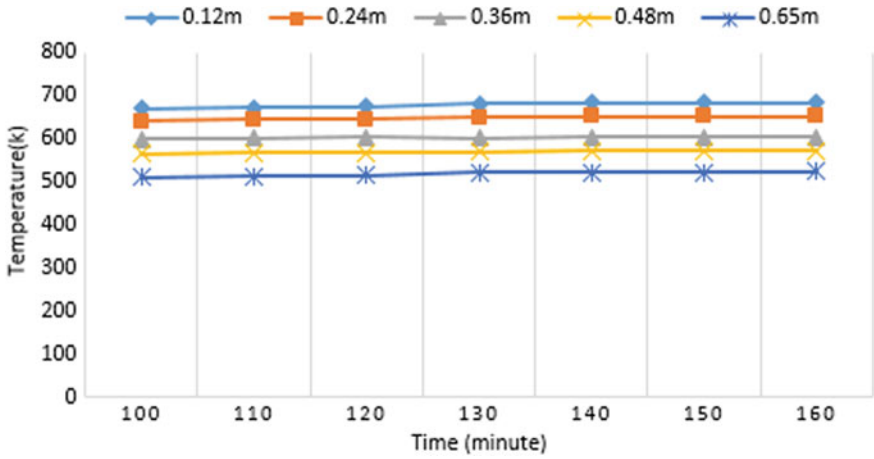


Fig. 32.5 Profile of steady state temperature

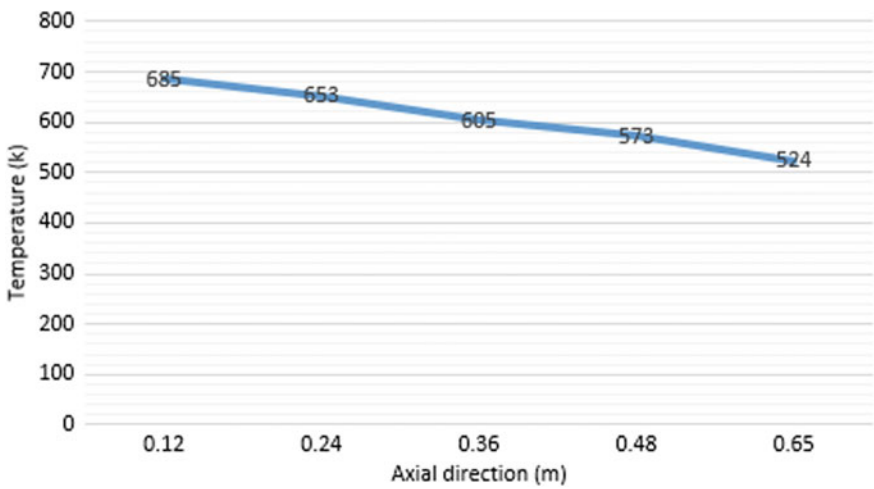


Fig. 32.6 Profile of temperature distribution from below upwards (axial direction)

32.3.2 Temperature Distribution in Axial Direction

Figure 32.6 shows the profile of temperature distribution from below upwards (axial direction) of a pyrolysis reactor. The temperature at 0.12 m from the bottom is 685 K and at the outlet of the reactor is 524 K. The temperature is maximum at the bottom and minimum at the top of the reactor.

32.4 Conclusions

The study of temperature distribution in the steel reactor with the copper bottom surface for the pyrolysis of plastic has been conducted. The temperatures from below upward (Axial Direction) (0.12, 0.24, 0.36, 0.48 and 0.65 m) are 685 K, 653 K, 605 K, 573 K and 524 K, respectively. The thermal cracking of plastic occurs at a region having uniform temperature distribution. From this study, a uniform temperature distribution is obtained in the axial region in the axial direction up to 3/4th of total length of reactor. It is found that the region of maximum pyrolysis reaction occurs up to 3/4th of the total length of the reactor.

References

- Chintala V, Godkhe P, Phadtare S, Tadpatrikar M, Pandey JK, Kumar S (2018) A comparative assessment of single cylinder diesel engine characteristics with plasto-oils derived from municipal mixed plastic waste. *Energy Convers Manag* 166:579–589
- Damodharan D, Sathiyagnanam AP, Rana D, Kumar BR, Saravanan S (2017) Extraction and characterization of waste plastic oil (WPO) with the effect of n-butanol addition on the performance and emissions of a DI diesel engine fueled with WPO/diesel blends. *Energy Convers Manag* 131:117–26
- Güngör C, Serin H, Özcanlı M, Serin S, Aydın K (2015) Engine performance and emission characteristics of plastic oil produced from waste polyethylene and its blends with diesel fuel. *Int J Green Energy* 12(1):98–105
- Hartulistiyoso E, Sigiyo FA, Yulianto M (2015) Temperature distribution of the plastics Pyrolysis process to produce fuel at 450°C. *Environ Sci* 28:234–241
- Kaimal VK, Vijayabalan P (2015) A detailed study of combustion characteristics of a DI diesel engine using waste plastic oil and its blends. *Energy Convers Manag* 105(95):1–6
- Kaimal VK, Vijayabalan P (2016) A Study on synthesis of energy fuel from waste plastic and assessment of its potential as an alternative fuel for diesel engines. *Waste Manag* 51(9):1–6
- Kalargaris I, Tian G, Sai G (2017) Combustion, performance and emission analysis of a DI diesel engine using plastic pyrolysis oil. *Fuel Process Technol* 157:108–115
- Kumar S, Prakash R, Murugan S, Singh RK (2013) Performance and emission analysis of blends of waste plastic oil obtained by catalytic pyrolysis of waste HDPE with diesel in a CI engine. *Energy Convers Manag* 74:323–331
- Mani M, Subash C, Nagarajan G (2009) Performance, emission and combustion characteristics of a DI diesel engine using waste plastic oil. *Appl Therm Eng* 29(13):2738–2744
- Rinaldini CA, Mattarelli E, Savioli T, Cantore G, Garbero M, Bologna A (2016) Performance, emission and combustion characteristics of a IDI engine running on waste plastic oil. *Fuel* 183:292–303

Chapter 33

Soil Organic Carbon Estimation Using Remote Sensing Technique



Akhil Francis, R. Kevin, Girigan Gopi and Rajesh Baby

Abbreviations

NDVI	Normalized Differential Vegetation Index
BSI	Bare Soil Index
OLI	Operational Land Imagery
RS data	Remote Sensing data

33.1 Introduction

Agricultural and forest land together constitute a major role in atmospheric carbon dioxide sequestration (Halliday and McMurtrie 2003). The release of carbon dioxide into atmosphere is through two main processes which are the respiration of plants and decomposition of organic matter. Soil acts as a source or sink of greenhouse gases according to the land use and management pattern adopted (Lal 1999). Soil contains about 70% of above ground carbon on one hand and about 60% of all soil organic carbon on other (Batjes 1996). The amount of soil carbon is estimated to be double the amount in atmosphere. The release of carbon dioxide during decomposition and respiration depends on the amount of carbon in soil (Fung et al. 2007). Thus, determining the spatial distribution of soil carbon can aid measures to reduce greenhouse gas emission.

Soil organic carbon also plays a major role in determining the agricultural productivity. Soil organic carbon is the amount of carbon present in the organic substances of soil. Factors on which SOC formation depends are soil genesis type,

A. Francis · R. Kevin · R. Baby (✉)
St. Joseph's College of Engineering and Technology, Palai, Kerala, India
e-mail: rbaby55@gmail.com

A. Francis
e-mail: akhilfrancisva@gmail.com

G. Gopi
M. S. Swaminathan Research Foundation, Wayanad, Kerala, India

land use data, decomposition of biomass, plant types, etc. It has been shown that SOC plays a major role in maintaining the fertility of soil, aggregating nature of soil, soil structure, water holding capacity and infiltration rate of the soil (Francaviglia et al. 2017); but due to wrong land use and cultivation practices SOC has shown a decreasing trend over years (Francaviglia et al. 2017). The various factors affecting SOC in a negative manner are frequency of soil tillage, reduction of biomass return to soil and the frequency of cultivation.

Through this framework it could be understood that monitoring and estimation of SOC is important to increase productivity, reduce soil loss and preserve its quality. Various statistical approaches have been developed over years for estimation of SOC. Interpolation methods have been widely used where field SOC measurements are made regularly and machine learning predictive models have been used for non-regularly sampled regions (Henderson 2005). Reliable estimates of SOC from the field measurements are difficult to obtain due to pedo-landscape. Lately the scopes of remote sensing covariates have been explored for digital soil mapping (Castaldi 2016). SOC values obtained from normalized differential vegetation index (NDVI) and bare soil index (BSI) data's obtained from RS covariates prove to be an efficient method for the evaluation of spatial and multitemporal SOC (Bhunia et al. 2019).

The present work deals with the estimation of SOC using remote sensing indices (NDVI and BSI), and assesses how SOC is dependent on the RS indices using multivariable regression. Field measurement of SOC involved sample collection and analysis with Walkley-Black method (Walkley 1934). The remote sensing method involved use of different bands obtained from LANDSAT 8 OLI images to calculate NDVI and BSI and evaluate the relationship between the RS data and the field SOC data using multivariable regression analysis and formulate an equation to find SOC from the RS data without any field work.

33.2 Study Area

The study area Meenangadi is an old town situated at E. long $76^{\circ} 38' 23''$ and $76^{\circ} 48' 40''$ and N. Lat $11^{\circ} 9' 08''$ and $11^{\circ} 13' 40''$ and covers an area of 53.52 sq. km in Wayanad district, Kerala, India. Meenangadi in Malabar is one of the border districts of Kerala, forming a continuous plateau with the Nilgris of Tamil Nadu. Meenangadi is surrounded by Kalpetta and Ambalavayal panchayath in west, Gudalur taluk in east and Mananthavady taluk in the west. The Wayanad district in which Meenangadi lies has an altitude of 700 to 2100 m above mean sea level, high velocity winds blow during South-West monsoon and dry winds blow in between March and April. Wayanad has a salubrious climate and one of the highest rainfalls receiving area is Meenangadi. Northern, Southern and Western areas consist of high hills and the Eastern area is flatter and open. Due to this particular type of terrain there are east flowing and west flowing rivers in the district. There are four small draining rivers and 23 streams in Meenangadi. Meenangadi has a table land of 70

and 20% fertile land, in which the total farming area is about 4919 ha. The major crops found in the study area are pepper, coffee, coconut, arecanut, rubber, cocoa, paddy, banana, ginger and elephant yam.

33.3 Soil Sample Collection and Analysis

Soil samples at depth of 0–20 cm were collected randomly from 30 positions from two wards of Meenangadi panchayath. Coordinate positions of each of these positions was pointed and recorded using hand-held smart phones. The positions were selected in such a manner that the number of samples collected constituted a uniform quantity of sample from each type of land use/land cover category. The different land usage type tested were land with several types of cultivation such as paddy, elephant yam, banana, ginger, pepper, arecanut and silver oak. SOC concentration in the soil sample was found out using both Walkley-Black method and modified Mebius procedure (Yeomans 1988).

33.4 Data Collection and Processing

The data used to determine the RS indices were obtained from LANDSAT 8 satellite. The raw satellite image from LANDSAT was rectified and georeferenced using survey of India (SOI) topographical sheet and Google map. Other pre-processing techniques used were geometric distortion removal, atmospheric correction, radiometric calibration, image registration that helped image interpretation. The different bands in the image were used to calculate the RS indices after the pre-processing step. Also ground truthing was done to help identify different features correctly. Linear stretch function was used to enhance the contrast and clarity of the image. All the image pre-processing was done in ERDAS Imagine v15.0 software.

33.4.1 Bare Soil Index and NDVI

Bare soil index indicates the amount or area of soil that is not covered by vegetation, artificial/natural turfs, rocks, gravel and other similar coverings. Bare soil index is calculated using blue, red, green and nearinfrared bands in the image using the following equations (Jamalaba 2004)

Table 33.1 Bands and their wavelengths

Bands (Color)	Wavelength (mm)
Band 1—Ultra Blue	0.435–0.451
Band 2—Blue	0.452–0.512
Band 3—Green	0.533–0.590
Band 4—Red	0.636–0.673
Band 5—Near infrared	0.851–0.879
Band 6—Short wave infrared	1.566–1.651

$$BSI = \left[\frac{[(Red\ band_4 + SWIR_6) - (NIR\ Band_5 + Blue\ band_2)]}{[(Red\ band_5 + SWIR_6) + (NIR\ Band_5 + Blue\ band_2)]} * 100 \right] + 100 \tag{33.1}$$

and the BSI map was plotted using ARCGIS v10.4.1 software.

For estimation of NDVI near infrared (B₅) and red band (B₄) are used. The following equation is used to estimate the NDVI (Yongnian et al. 2010)

$$NDVI = \frac{[(NIR_5 - Red_4)]}{[(NIR_5 + Red_4)]} \tag{33.2}$$

The resulting value of NDVI lies in the range of +1 to -1, with positive values indicating high vegetation and negative values indicating low vegetation (Gbolo et al. 2015). The bands along with their corresponding wavelength are mentioned in Table 33.1.

33.5 Analysis and Mapping

The relationship between the dependent variables (NDVI and BSI) and the independent variable (SOC) is calculated using Pearson’s correlation coefficient, followed by the multivariable regression analysis. The model was based on the coefficient of determination R².

The set of readings with the highest R² and lowest RMSE was considered as valid and was used to formulate equation of regression analysis (Jaber et al. 2012) and this equation was fed to the raster calculator tool in ArcGIS v10.4 for spatial mapping of SOC.

33.6 Results and Discussion

The results of multivariable regression analysis (R² = 0.62) are as shown in Table 33.2.

Table 33.2 Regression analysis for finding the relation between SOC and RS indices

	Coefficients	Standard Error	t Stat	P-value
Intercept	4.24	1.62	2.82	<0.001
X Variable 1	11.90	3.00	3.77	<0.0001
X Variable 2	-0.021	0.01	-3.38	<0.0001

From the above table the relationship between SOC and RS indices can be derived as following

$$SOC = 4.24 + 11.90NDVI - 0.021BSI \quad (33.3)$$

The spatial map of SOC is plotted using the above equation and is shown in Fig. 33.1. The highest SOC was observed in areas of dense forest land and the least in sandy areas. The NDVI and BSI spatial map using ArcGIS v10.4 are as shown in Figs. 33.2 and 33.3. The NDVI value varied from -0.25 to 0.47.

To find the relationship between NDVI and SOC linear regression was carried out as shown in Table 33.3 and the following relationship was obtained.

$$SOC = 0.162 + 0.028 * NDVI \quad (33.4)$$

Similarly, to find the relation between the BSI and SOC, linear regression was repeated as shown in Table 33.4 and the below given relationship was obtained

$$SOC = 10.1 - 0.04 * BSI \quad (33.5)$$

33.7 Conclusion

The study dealt with was spatial mapping of SOC for different types of landscapes in Meenangadi panchayath. Determining and spatial mapping of NDVI and BSI proved to be an efficient way of determining the SOC distribution over a large area. The predicted SOC and observed SOC showed dissimilarity because of the coarse resolution of 30 m used. More accurate result can be obtained using much more fine resolutions and narrow spectral bands. Since observed SOC values was obtained within a small area the SOC mapping showed both regions with highly concentrated SOC and regions with very sparse SOC which does not agree with the observed SOC in those areas. The mapping can be made more accurate if the data are collected from the area of study using stratified random sampling which ensures the data collected uniformly, covers the whole area of study.







Fig. 33.1 Spatial soil organic carbon mapping of Meenangadi



Legend

soc

<VALUE>

	0.418227971 - 0.645927672
	0.645927672 - 0.776041787
	0.776041787 - 0.859170249
	0.859170249 - 0.953141554
	0.953141554 - 1.108555636
	1.108555637 - 1.339869618

Obtaining high resolution images of the area of study proved to be a cumbersome process due to financial difficulties of accessing those images from highly expensive satellites. Hence, future work needs some means of accessing the indices without the help of satellite, instead by sophisticated means that can obtain the indices with high resolution and user controllable variables as done by drones.

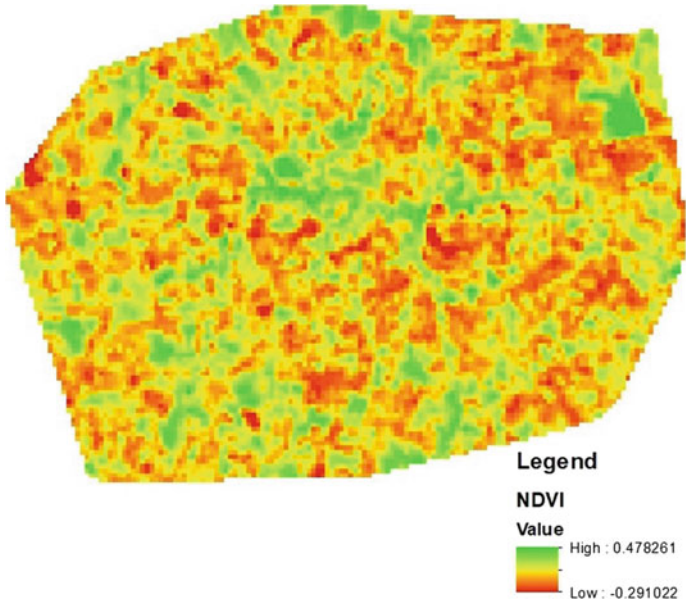


Fig. 33.2 Spatial NDVI mapping of Meenangadi

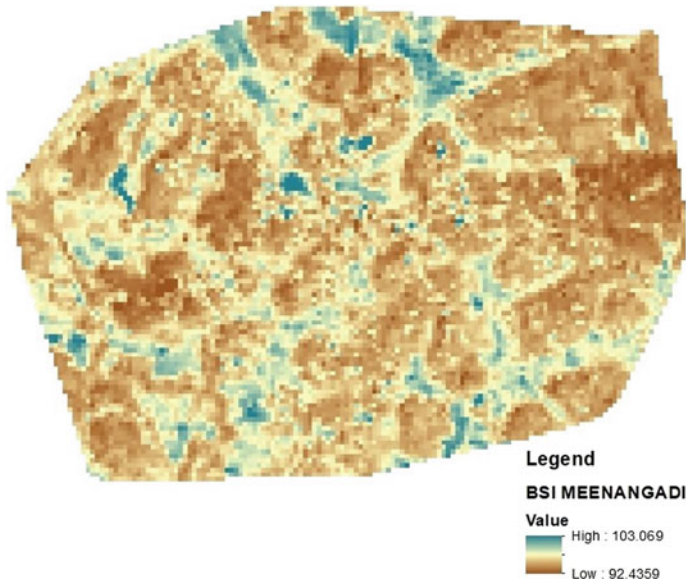


Fig. 33.3 Spatial BSI mapping of Meenangadi

Table 33.3 Linear regression to find the relation between SOC and NDVI

	Coefficients	Standard error	t Stat	P-value
Intercept	0.162	0.020	12.04	<0.001
X Variable 1	0.028	0.005	-1.26	<0.0001

Table 33.4 Linear regression to find the relation between SOC and BSI

	Coefficients	Standard error	t Stat	P-value
Intercept	10.1	0.73	1.09	0.00
X Variable 1	-0.04	0.01	-1.00	0.001

References

- Batjes (1996) Total carbon and nitrogen in the soils of the world. *Eur J Soil Sci* 47:151–163
- Bhunia GS, Kumar Shit P, Pourghasemi HR (2019) Soil organic carbon mapping using remote sensing techniques and multivariate regression model. ISSN: 1010-6049 (Print) 1752-0762 (Online)
- Castaldi F, Castrignanò A, Casa R (2016) A data fusion and spatial data analysis approach for the estimation of wheat grain nitrogen uptake from satellite data. *Int J Remote Sens* 37:4317–4336
- Francaviglia R, Renzi G, Ledda L, Benedetti A (2017) Organic carbon pools and soil biological fertility are affected by land use intensity, vol 600
- Fung IY, Doney SC, John J (2007) Evolution of carbon sinks in a changing climate. *Proc Natl Acad Sci* 102:11201–11206
- Gbolo P, Gerla PJ, Vandeberg GS (2015) Using high resolution, multispectral imagery to assess the effect of soil properties on vegetation reflectance at an abandoned feedlot. *Geocarto Int* 7(1–17)
- Halliday T, McMurtrie S (2003) Mechanisms for changes in soil carbon storage with pasture to *Pinus radiata* land-use change. *Glob Change Biol* 4:1294–1308
- Henderson B., Bui EN, Moran CJ, Simon DA (2005) Australia-wide predictions of soil properties using decision trees. *Geoderma* 124:383–398
- Jaber SM, Lant CL, Al-Qinna MI (2012) Estimating spatial variations in soil organic carbon using satellite hyperspectral data and map algebra. *Int J Remote Sens* 32(18):5077–5103
- Jamalaba A (2004) Forest canopy density monitoring, using satellite images
- Lal (1999) Soil management and restoration for C sequestration to mitigate the accelerated greenhouse effect. *Prog Environ Sci* 1(4):307–326
- Rani M, Tomar V, Patariya P (2016) Estimation of accumulated soil organic carbon stock in tropical forest using geospatial strategy. *Egypt J Remote Sens Space Sci* 109–123
- Walkley B (1934) An examination of DEGTJAREFF method for determining soil organic matter and a proposed modification of the chromic acid titration method. *Soil Sci* 37:29–37
- Yeomans B (1988) A rapid and precise method for routine determination of organic carbon in soil. *Commun Soil Sci Plant Anal* 19:1467–1476
- Yongnian Z, Wei H, Benjamin ZF, Honghui Z, Huimin L (2010) Study on the urban heat island effects and its relationship with surface biophysical characteristics using MODIS imageries. *Geosp Inf Sci* 13(1):1–7

Chapter 34

Assessment of Water Pollution Using GIS: A Case Study in Periyar River at Eloor Region



K. V. Anjusha, Amala Mareena James, Feby Ann Thankachan, John Benny and V. Bibin Hezakiel

34.1 Introduction

Water is one of the most essential elements for the survival of human life and health of the environment. Water quality testing is an important part of environmental monitoring. BOD, DO, pH, Conductivity, Turbidity, Acidity, Alkalinity, TDS etc. are some of the major Water Quality Parameters which needs to be assessed to determine the extent of pollution in a water body. GIS is found to be an effective tool which helped in providing solutions for water sources problems such as to assess water quality and to understand the natural environment. Water Quality Assessment can be done using Spatial Variation Map of Water Quality Parameters using GIS.

The river Periyar, originates from Sivagiri Peaks of Sundaramala in Tamil Nadu. Total length of the river is about 300 km with a catchment area of 5.396 km². During its journey to Arabian Sea, it provides drinking water for several towns including Cochin. Periyar has been performing an important role in shaping the economic prospects of Kerala, as it help in power generation, domestic water supply, irrigation, tourism, industrial activities and fisheries. Due to these reasons the river has been named as “Lifeline of Kerala”. However in recent days due to excess contamination, lower reaches of the river are referred as “a cesspool of toxins”. Many times the Periyar River was found to flow in red colour. This might have occurred because of the ejection of effluents from industries.

Eloor region, about 20 km from where the river Periyar meets the Arabian Sea, is the industrial hub of Kochi, the commercial capital of Kerala and is home to Kerala’s largest industrial cluster. Among 282 industries in Eloor, around 110 are chemical industries. These industries discharge their effluents into the river on

K. V. Anjusha (✉) · A. Mareena James · F. Ann Thankachan · J. Benny · V. Bibin Hezakiel
Rajagiri School of Engineering and Technology, Kakkanad, Kerala, India
e-mail: Anjushakv96@gmail.com

several instances without treatment. Eloor is the 35th toxic hotspot in the world identified by Green Peace in 1999.

34.2 Study Area

Eloor is the industrial hub of Ernakulam, Kerala, belonging to the Alangad Block in Paravur Taluk which is located in between 76° 16' and 76° 20' Eastern Longitude and 10° 05'–10° 02' North Latitude having a population of about 30,092 (according to 2011 census). It is an island of 14.21 km² formed between two distributaries of River Periyar. Location map of study area is shown in Fig. 34.1.

34.3 Methodology

Water quality data collection, spatial variation map creation and analysis were done.

34.3.1 Data Collection

A preliminary questionnaire survey was conducted at Eloor to gather details regarding extend of pollution in the area. The conclusions drawn from the questionnaire survey was that Periyar River water which was the major source of water for domestic purposes in earlier days is currently not depended for any purpose. So, the water is supplied from the Aluva Water Supply which is free of cost. Also, fishing can be seen to be declining due to pollution. Water samples were collected from 12 different locations in Eloor as shown in Fig. 34.2. The sample collection was done in accordance with IS 3025 (Part 1), 1987. Water quality data was



Fig. 34.1 Location map of the study area

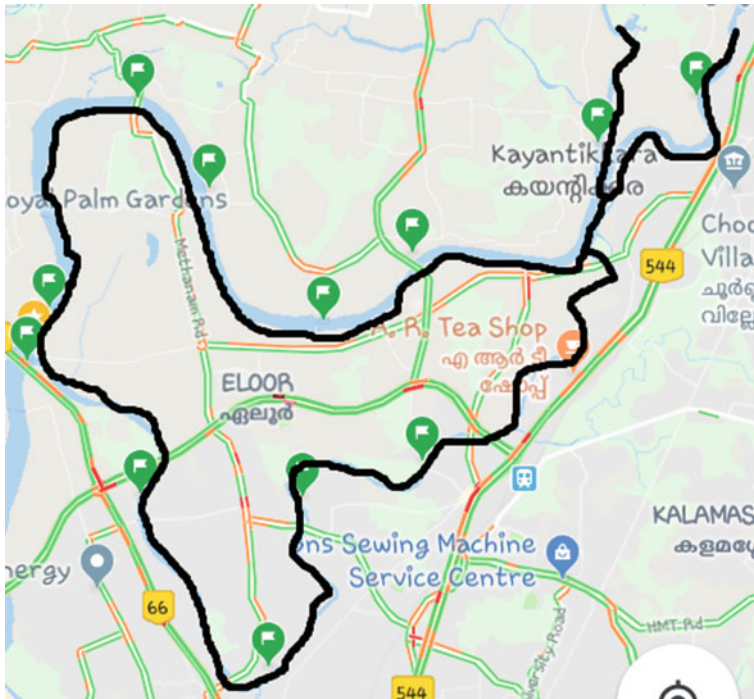


Fig. 34.2 Sampling points

obtained from Laboratory testing and compared with data obtained from Kerala State Pollution Control Board (KSPCB, Gandhi Nagar). Map of the required study area was extracted from Google Earth.

34.3.2 Spatial Variation Map

Spatial variation map of various water quality parameters were prepared in ArcGIS 10.3. The variability of different water quality parameters like BOD, DO, pH, Conductivity, Turbidity, Acidity, Alkalinity, TDS were plotted in the ArcGIS using IDW (Inverse Distance Weighted) interpolation method.

34.4 Results and Discussion

In order to determine the quality of water in Periyar River flowing around Eloor region, spatial variation map of BOD, DO, pH, Conductivity, Turbidity, Acidity, Alkalinity, TDS were generated.

34.4.1 *Spatial Variation Map*

The spatial variation map for different water quality parameter such as BOD, DO, pH, Conductivity, Turbidity, Acidity, Alkalinity, TDS were generated using IDW (Inverse Distance Weighted) interpolation method.

Bio-chemical Oxygen Demand (BOD). BOD is the amount of dissolved oxygen needed by aerobic biological organisms to breakdown organic material present at a specific time and temperature. As per IS 10500:2012, the acceptable limit of BOD for drinking water ranges between 0 and 5 mg/l. High concentration of BOD indicates poor water quality. The spatial variation map for BOD was prepared and is shown in Fig. 34.3a. The minimum and maximum BOD values were obtained as 1.21 mg/l and 70.56 mg/l respectively. It was observed that in the north-eastern side of Eloor, there was a trend of increase in BOD, where the clustering of large number of industries in the north eastern region gave an explanation for the same. Also the BOD level was found to be higher in Northern side which is densely populated area.

Dissolved Oxygen (DO). It is defined as the amount of oxygen essential for aquatic life. According to IS 10500:2012, the acceptable limit of dissolved oxygen for drinking water is 5 mg/l or more. The spatial variation map for Dissolved Oxygen (DO) was prepared and is shown in Fig. 34.3b. The maximum and minimum value for DO was obtained as 11.19 mg/l and 6.70 mg/l respectively.

pH. pH is the logarithm of reciprocal of hydrogen ion concentration and hence becomes an indicator of acidity and alkalinity. According to IS 10500:2012, the acceptable limit of pH for drinking water is between 6.5 and 8.5. The spatial variation map for pH was prepared and is shown in Fig. 34.3c. The maximum and minimum value for pH was observed to be 6.71 and 3.80 respectively. The major portion of Periyar River in Eloor region was found to have a pH ranging from 3.80 to 4.12 which was highly acidic and was not suitable for drinking purposes.

Conductivity. It is the ability to conduct or transmit heat, electricity or sound. It is measured using conductivity meter. According to IS 10500:2012, the acceptable limit of conductivity is 150 $\mu\text{S}/\text{cm}$ and permissible limit is 500 $\mu\text{S}/\text{cm}$ for drinking water. The spatial variation map for conductivity was prepared and is shown in Fig. 34.3d. The maximum and minimum value for conductivity was observed to be 160.37 $\mu\text{S}/\text{cm}$ and 54.56 $\mu\text{S}/\text{cm}$ respectively. The river in north western regions of Eloor had highest conductivity which exhibits a trend of increasing to reach the maximum towards west and then decreasing towards south and south eastern parts of Eloor.

Turbidity. It is the cloudiness or haziness of a fluid caused by large numbers of individual particles that are generally invisible to the naked eye, similar to smoke in air. It is measured by using turbidity meters which works on the principle of measuring the interference caused by the water sample to the passage of light rays. The measurement of turbidity is a key test of water quality. According to IS 10500:2012, the acceptable limit of turbidity is 1 NTU and permissible limit is 5 NTU for drinking water. The spatial variation map for turbidity was prepared and is

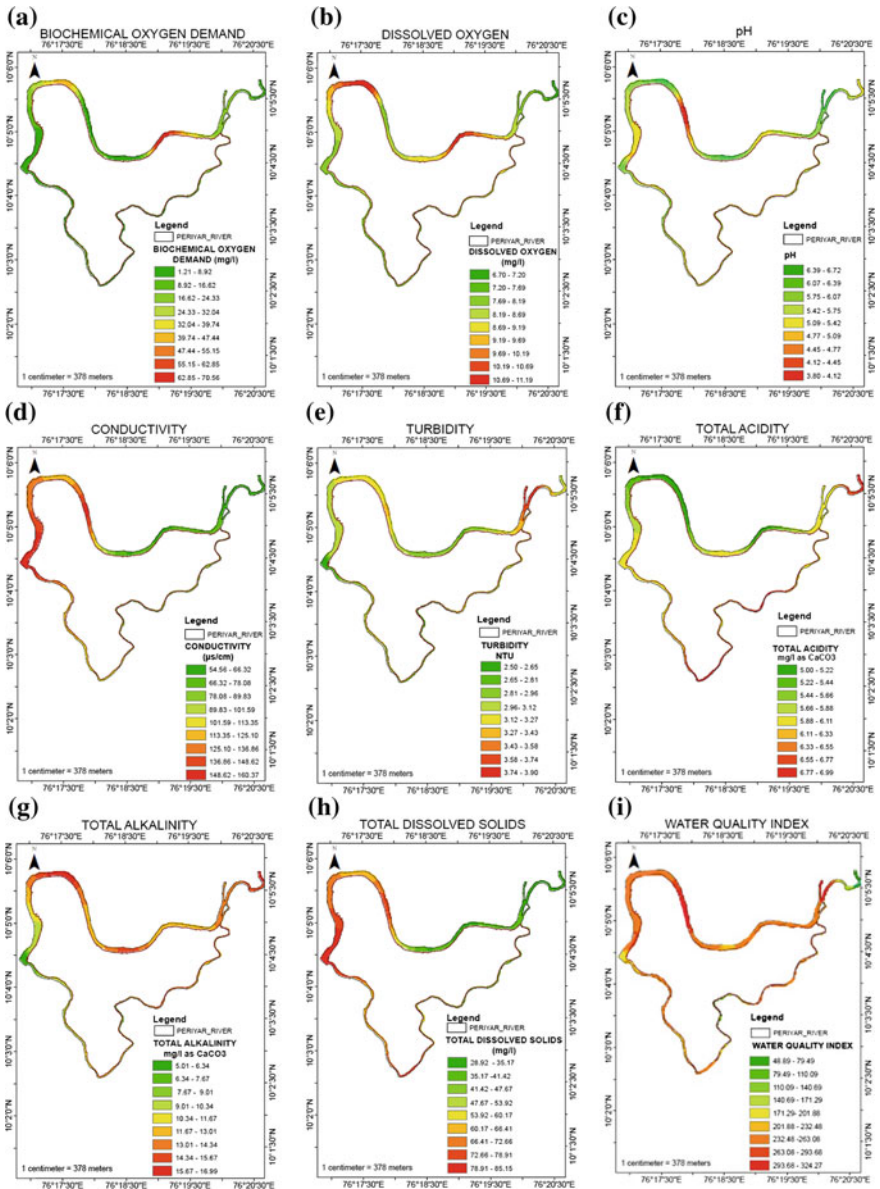


Fig. 34.3 Spatial variation map of **a** BOD, **b** DO, **c** pH, **d** conductivity, **e** turbidity, **f** total acidity, **g** total alkalinity, **h** TDS, **i** WQI

shown in Fig. 34.3e. The maximum and minimum value for turbidity was obtained as 3.89 NTU and 2.50 NTU respectively. The river water in north eastern regions of Eloor had highest turbidity which was the upstream portion which goes on decreasing to the minimum towards west.

Acidity. Acidity is the quantitative expression of water's capacity to neutralize a strong base to a designated pH and an indicator of how corrosive water is. Results of the acidity tests are reported in mg/L CaCO₃. According to IS 10500:2012, there is no specific range for acidity and the maximum value and minimum value observed from the spatial variation map was 6.99 mg/L CaCO₃ and 5 mg/L CaCO₃ respectively. The spatial variation map for acidity was prepared and is shown in Fig. 34.3f. The south eastern regions and upstream portion of Eloor had highest acidity and the northern parts had lowest value.

Alkalinity. Alkalinity is a measure of the capacity of water to neutralize acids. Results of the acidity tests are reported in mg/L CaCO₃. According to IS 10500:2012, the acceptable limit and permissible limit are 200 mg/L CaCO₃ and 600 mg/L CaCO₃ respectively. The maximum value and minimum value observed from the spatial variation map was 16.99 mg/L CaCO₃ and 5.01 mg/L CaCO₃ respectively. The spatial variation map for alkalinity was prepared and is shown in Fig. 34.3g. It was observed that alkalinity was increasing from upstream to downstream and a decrease was observed in the western region of Eloor.

Total Dissolved Solids. The total amount of dissolved solids is measured using conductivity meter in mg/L. The electrical conductivity (μS/cm) of a water sample is converted into approximate concentration of total dissolved solids (ppm), the unit i.e., μS/cm is multiplied by a conversion factor called conductivity factor whose value usually ranges between 0.54 and 0.96. According to IS 10500:2012, the acceptable limit and permissible limit are 500 mg/L and 2000 mg/L respectively. The maximum value and minimum value observed from the spatial variation map was 85.16 mg/L and 28.92 mg/L respectively. The spatial variation map for total dissolved solids was prepared and is shown in Fig. 34.3h. It was observed that total dissolved solids increases from upstream to downstream and reached its maximum at the western region of Eloor region.

Water Quality Index (WQI). Water Quality Index was determined by weighted arithmetic water quality index method.

$$WQI = \frac{\sum Q_i W_i}{\sum W_i} \quad (34.1)$$

$$Q_i = \frac{100(V_i - V_o)}{(S_i - V_o)} \quad (34.2)$$

$$W_i = \frac{K}{S_i} \quad (34.3)$$

Table 34.1 Water quality rating as per weighted arithmetic water quality index method

WQI value	Rating of water quality
0–25	Excellent
26–50	Good
51–75	Poor
76–100	Very poor
>100	Unsuitable for drinking purposes

$$K = \frac{1}{\sum \frac{1}{S_i}} \quad (34.4)$$

where, WQI = Water Quality Index, W_i is Weight for each water quality parameter, V_i is Estimated concentration of i th parameter in the analyzed water, V_o is Ideal value of this parameter in pure water, S_i is Recommended standard value of i th parameter and K is Proportionality constant.

Rating of Water Quality as per weighted arithmetic WQI method is shown in the Table 34.1. The maximum value and minimum value observed from the spatial variation map was 302.05 and 48.25 respectively. The spatial variation map for WQI was prepared and is shown in Fig. 34.3i. It is observed that that river flowing around the Eloor region was completely polluted as the WQI was more than 50 in that region, even exceeding up to 300 which indicated the unsuitability for drinking purposes. While the upper reaches of Eloor region had a water quality index of 48.25 which was good water quality for drinking purposes. From the above statements it is clear that the water entering the Eloor region was pure but as it flows around this region it gets polluted due to the high emission of industrial wastes and the rapid growth of urbanization.

34.5 Conclusion

In this paper, the GIS technology have been thoroughly and successfully utilized in order to assess the water pollution in Periyar River at Eloor Region. Laboratory tests of the water samples from that region gave the necessary data for the preparation of spatial variation map. BOD, DO, pH, Conductivity, Turbidity, Acidity, Alkalinity and TDS were the parameters selected in order to represent the water pollution in the Periyar River and they were used as input criteria in GIS by IDW (Inverse Distance Weighted) interpolation method so as to generate spatial variation map. The results and relevant studies conducted have confirmed that the river flowing around the Eloor region is completely polluted as the water quality index was found to be more than 50 in that region even exceeding up to 300 which indicated the water was inappropriate and unfit for drinking purposes even though the upper reaches of Eloor region has a water quality index of 48.25 which is good water quality for drinking purposes. From the above statements it is evident that the

water entering the Eloor region is pure and harmless but as it flows around this region it gets polluted due to the presence of industries and the rapid growth of urbanization. It could be inferred that application of GIS technologies related with water quality studies, plays an important role in the environmental management and assessment studies of Rivers which are found to be easier and economical than conventional methods. The maps shows the extent of pollution and the vulnerability of water at a particular area which indicates the risk of water contamination. The discussed maps can be used by land use planners, hydrogeologists, water managers or various environmentalists which helps them to identify the rate and extent of pollution of the area.

Chapter 35

Scale Control on Pipe Materials: A Review



Namitha Joshy and V. Meera

35.1 Introduction

Scaling is the deposition of salts having low solubility and often occurs due to changes in pH, temperature and pressure conditions which in turn affects the supersaturation levels and solubility of the salts. Scale formation inside a pipe is shown in Fig. 35.1. Calcium carbonate is the predominant constituent in most of the scale deposits. Moreover magnesium carbonate, calcium sulphate, barium sulphate, iron carbonate, iron sulphide, and iron oxides also contribute to most of the scale problems. When water flows over the rocks and sediments containing ions producing water hardness these scaling species are introduced to water (Alabi et al. 2015).

The buildup of scale deposits is widespread and expensive especially for industrial processes. Energy consumption increases due to scale, for example with scale thickness of 1 mm and 7 mm the energy consumption is greater than 15% and 40% respectively (Dobersek and Goricanec 2007).

In general, the scaling process is categorized into two periods: induction period and scaling period. The time prior to deposition is known as the induction period and is required for the crystal nuclei to arrive at a critical size for further crystal growth. During the scaling period, a compact deposit layer is formed. The steps in scaling process also include transport, during which the scaling substances are transported from the bulk of the fluid to the solid surface. The ageing process consists of crystal structure modification and it initiates as soon as the deposit has been formed on the pipe surface (MacAdam and Jarvis 2015).

N. Joshy (✉) · V. Meera
Government Engineering College, Thrissur, Kerala, India
e-mail: namithathadathil@gmail.com

V. Meera
e-mail: vmeera@gectcr.ac.in

Fig. 35.1 Scale formation on a pipe. *Source* Environmental Science Water Research and Technology 1, p. 408



35.2 Scale Control by Chemical Methods

Acidification, addition of antiscalants and softening by ion exchange processes are the conventionally adopted methods for scale control. The scale exclusion by chemical dissolution is the most preferred, since it is effective for cleaning large surfaces within fairly short times. In addition, due to the non-scratching nature of chemical cleaning, further creations of active sites for scaling on the surfaces are also prevented. The major constituents in scale removing solvents are chelating agents, mineral acids or organic acids. The use of mineral acids are thermally restricted at elevated temperature owing to the high ionization energy at room temperature, while the chelating property of organic acids can be maintained even at high temperature, since they are being much weaker and less ionized (Chauhan et al. 2015).

Generally used commercial scale control agents belongs to polyelectrolytes, organophosphates and condensed polyphosphates with several scale inhibition mechanisms including threshold inhibition, chelation and crystal dispersion. Threshold treatment using phosphates at substoichiometric levels can maintain the solubility of mineral ions beyond its normal limits. Weakening the crystal structure with carboxylic acids, binding the calcium in solution with chelators etc. are some of the inhibition mechanisms adopted with chemical scale inhibitors (MacAdam and Parsons 2004).

Inorganic or organic additives can alter the growth rate and the morphology of the scale deposit crystals. The mechanism of action is as follows: (Hoang 2015)

- Chemically react with the scaling species to alter the scaling potential of water.
- Physically affect the scaling process by surface action and thus inhibits the interaction between material surface and the scale deposit.
- Modify the nature of the scale deposit adhered to the surface and make it more liable to removal processes.
- Annihilate the activity of the scaling species.

The antiscaling agents can delay the induction time and thus enables alteration of scaling potential of water. Sometimes they help to modify the crystal structure of scale deposit by imparting non-sticking properties.

Westin and Rasmuson (2005) studied the effect of four calcium complexing substances such as citric acid (CIT), diethylene triamine pentaacetic acid (DTPA), ethylene diamine tetracetic acid (EDTA) and pyromellitic acid (PMA) on the crystal growth rate of calcium carbonate polymorphs, aragonite and calcite. Even at a concentration of 0.04 mmol/L, CIT was efficiently blocked the growth of aragonite. In case of calcite, the results were almost same for all four substances at 0.5 mmol/L concentration. Hence the polymorph and concentration of calcium complexing substances has an important influence on growth retarding effect.

With increasing shortages of freshwater, secondary treated municipal wastewater can be used as an alternative for power plant cooling system. Li et al. (2011) found that polymaleic acid at a dosage of 10 mg/L can effectively inhibit the scale formation when the makeup water was recirculated four times in a cooling system.

The performance of poly epoxy succinic acid (PESA) and poly aspartic acid (PASP) on scale inhibition is evaluated by static and rapid controlled precipitation methods conducted by Liu et al. (2012). Based on static test results, for the inhibition of calcium carbonate and strontium sulphate the performance of PESA exceeded PASP. However, PASP performed superior to PESA in terms of calcium sulphate and barium sulphate scaling inhibition. With dosages of 0.25 mg/L PESA and 0.3 mg/L PASP total inhibition was achieved within 60 min. These inhibitors could deform the crystal structure of the precipitates by converting their compact and regular lattice into loose and rough ones and thus enabling easy removal by cleaning.

Experimental investigations were carried out by Muryanto et al. (2014) in a study to assess, calcium carbonate scale formation in pipes considering the effect of flow rates, temperature, and malic acid as scale inhibiting agent. The experiments were conducted using synthetically prepared scale-forming solution of calcium carbonate which was allowed to flow in a laminar manner at flow rates of (mL/min): 30, 40 and 50, respectively. Other parameters evaluated were: solution temperature (°C): 25, 30 and 40 as well as concentration of malic acid (ppm): 3 and 5. The results showed an abrupt decrease in conductivity of the solution after certain period. During induction time the conductivity remained steady. The induction period varied from 17 to 34 min, which means that the scale starts forming 17 to 34 min after the mixing of the solution. Also found that fluid flow enhances the scale formation since higher flow rates resulted in more calcium carbonate scale mass. Similarly, with rise in the temperature of the solution, amount of scale deposited also increased. Overall, higher concentrations of malic acid resulted in longer induction time and lesser amount of scale deposit.

Bhuvanewari et al. (2015) conducted experiments to assess the influence of ethylene diamine tetraacetic acid on the morphology and polymorphism of calcium carbonate. Experiments were conducted using EDTA at temperatures (°C): 60, 80 and 100. The study results showed that EDTA was very efficient for stabilizing

aragonite at 80 °C and with rise in temperature, formation of calcite is found to be dominating.

Al-Roomi and Hussian (2015) evaluated the calcium sulphate scale inhibition efficiency of low molecular weight maleic anhydride copolymers. The experiments were conducted in the artificial cooling water and the pipe surfaces used for the study were made of steel and copper. For 0.15 M calcium sulphate solution in copper and steel pipes, 2 ppm concentration of polymers showed inhibition efficiency up to 98.9% at 60 °C and 90–91% at 70 °C. But as the temperature rises to 75 °C, 15–20% reduction in efficiency was observed. Hence these polymers can be effectively used up to a temperature of 70 °C even at very low concentration.

35.3 Scale Control by Magnetic Methods

The mechanisms anticipated to explain the effects of magnetic field on CaCO₃ scaling can be generally categorized into chemical and physical ones. The chemical mechanisms include modifying the crystal nucleation by changing the crystal liquid interface (Barrett and Parsons 1998).

Stuyven et al. (2009) proposed a new explanation for the scale preventive mechanism under magnetic water treatment. When an external magnetic field is applied perpendicular to the turbulent flow, micron size suspended particles would fragment resulting in their size-reduction and hence the surface area increases by four to six orders. Since larger surface area offer more precipitation sites, homogeneous precipitation in the bulk of the solution will increase instead of the heterogeneous precipitation on material surfaces of containers or pipes.

The effect of magnetic water treatment under flowing condition arises from the action of Lorentz force and is developed while ionic species move through the magnetic field. The magnitude of Lorentz force (F_L) thus generated is defined in Eq. (35.1) and it depends on quantity of charged species (q), velocity of particles (v), intensity of magnetic field (B) and angle between v and B vectors (θ). Lorentz force has important influence on crystal nuclei formation, enhancing the crystal particle dissolution and distorting the double layer of crystals (Sohaili et al. 2016).

$$|F_L| = q |v \times B| = qvB \sin\theta \quad (35.1)$$

Anti-scale effect under the magnetic water treatment depends on the composition and physico-chemical characteristics of the scale-forming water. The anti-scale effect on water increases with increase of temperature, calcium and magnesium ions and alkalinity as well as with reduction of the total salinity of water. Also, it depends on strength of magnetic field, flow velocity, residence time of water in the magnetic field and other factors (Mosin and Ignatov 2015).

Chibowski et al. (2003) evaluated the precipitation of calcium carbonate on different substrates such as stainless steel, copper, aluminium and glass in the presence of magnetic field (0.1 T) at different temperatures. The largest magnetic

field effect was found on glass at 60 °C, which accounted 50% reduction of the deposit.

Ionic and particle mechanisms are the two most popularly reported mechanisms to study the effect of magnetic fields on calcium carbonate deposit. Saksono et al. (2008) explored the effects of both mechanisms in CaCO₃ deposit and total CaCO₃ precipitation. The effects of both mechanisms were found to be conflicting to each other. Particle mechanism helps to reduce the calcium ion concentration in solution during magnetization. Ionic mechanism reduced scale formation after magnetization and separation processes. Hence magnetic treatment could be applied for reducing water hardness and for inhibiting scale formation.

Alimi et al. (2009a) conducted a study to investigate the influence of pipe material (PTFE, Tygon, PVC, copper, and stainless steel) on the calcium carbonate precipitation process in the presence of external magnetic field. In their study, 4 mm CaCO₃ solution was exposed to a magnetic field of 0.16 T for 15 min with different flow rates (0.54–0.94 L min⁻¹) and pH (6–7.5). The results of precipitation tests have shown that magnetic treatment increases the total precipitate quantity in the bulk solution instead of adhering on the pipe surface. After magnetic treatment, total and homogeneous precipitation ratios were found to be increasing for all tested pipes and are indicated in Figs. 35.2 and 35.3 respectively. The increase in total precipitation ratio was predominant in the case of PTFE and Tygon where it increased by about 10 and 17% respectively. Homogeneous precipitation ratio increases with flow rate and was about 7% for water in PTFE pipe.

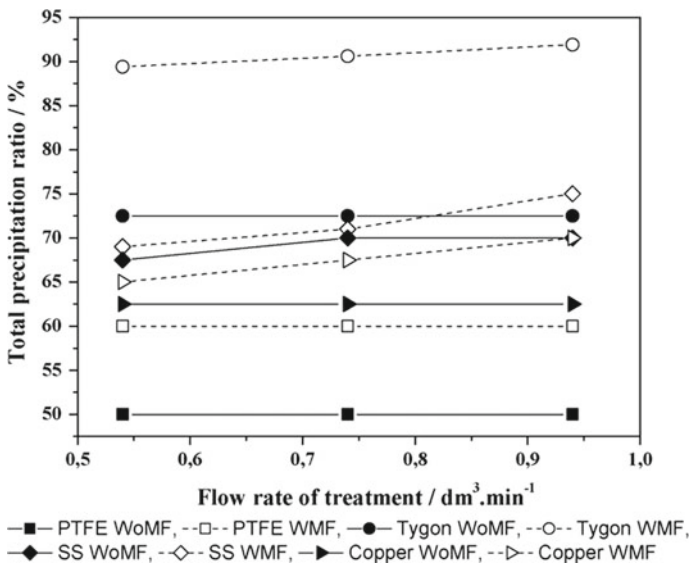


Fig. 35.2 Effect of pipe material on total precipitation rate of calcium carbonate. Source Chemical Engineering and Processing 48, p. 1329

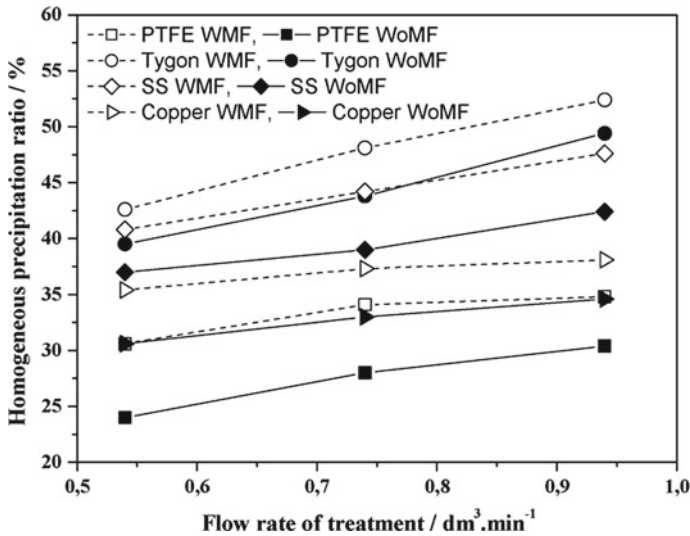


Fig. 35.3 Effect of pipe material on homogeneous precipitation rate of calcium carbonate. *Source* Chemical Engineering and Processing 48, p. 1329

Alimi et al. (2009b) also conducted experiments on calcium carbonate precipitation in the presence of foreign ions (Mg^{2+} , SO_4^{2-} , Na^+ , Cl^-) under external magnetic field conditions. The solutions of Na_2SO_4 , $MgCl_2$ and $NaCl$ of different ionic strength (M): 0.015, 0.0195 and 0.027 is used. Magnetic field of 0.16 T was applied for 15 min and found that total and homogeneous precipitation ratios to be decreasing with increase of ionic strength. The effect was more pronounced for 0.027 M $MgCl_2$ and Na_2SO_4 which inhibited the precipitation of $CaCO_3$ in bulk of the solution by 41.7% and 51.3% respectively.

Sohaili et al. (2016) studied the removal of scale deposition on pipe walls by using magnetic field of different strength. Figure 35.4 provides the schematic illustration of magnetic water treatment. Magnetic strength varying from 0.1 T to 0.4 T was used to examine its effect on scale reduction. The scale removal efficiency was determined based on calcium concentration in the outlet and found an increase of 8% to 15% for an increase of magnetic field strength varying from 0.1 T to 0.4 T.

Bali and Gueddari (2018) studied the consequences of magnetic treatment (0.8 T) on the physico-chemical and microbiological characteristics of hard water. The results of rapid controlled precipitation test revealed a reduction of scaling potential for the magnetically treated water. The precipitation of $CaCO_3$ was belated for 10 min by magnetic treatment. Also, observed a significant enhancement of bacteriological quality of the treated water. Average reductions of 2.02 log Total coliforms, 0.95 log *Escherichia coli* and 1.06 log Faecal streptococci were obtained.

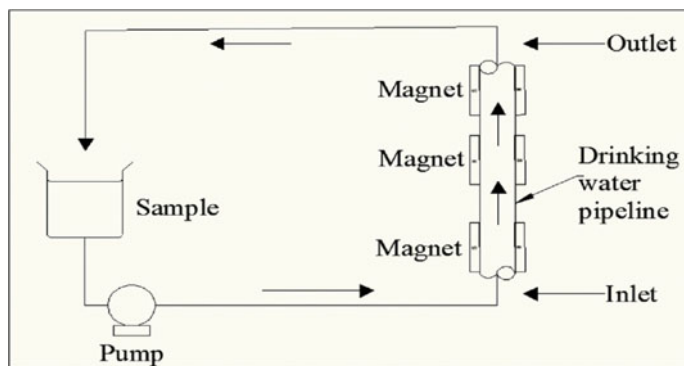


Fig. 35.4 Schematic diagram of magnetic water treatment. *Source* Journal of Cleaner Production 139, p. 1394)

35.4 Scale Control by Surface Modification of Pipe Material

Besides the water chemistry, scale formation is also affected by the physical nature of the surface material of pipe through which water flows and this in turn is related to the surface free energy of the material. The adhesion of calcium carbonate scale deposits to material surfaces can be inhibited by reducing the surface energy (MacAdam and Parsons 2004).

The super-hydrophobic property can be applied to material surfaces and is well related to the lotus-effect in nature. The combined effect of the surface morphology and the chemical composition contributes to this property. Super-hydrophobic surfaces can be fabricated either by modifying rough surfaces with low-surface-energy material or preparing rough structures on low-surface-energy material (Li et al. 2016).

The anti-scaling effect of the modified super-hydrophobic Cupric Oxide (CuO) nanowire surface should attribute to the sluggish CaCO_3 crystal nucleation rate. This is due to the low-surface energy of the material and retention of air film on the super-hydrophobic surface which contributes small adhesion strength of CaCO_3 crystal (Jiang et al. 2015).

Nevertheless, the super-hydrophobic surfaces cannot be preferred for long term uses, due to the gradual reduction of super-hydrophobicity over time when subjected to continuous exposure to fluid. Zhang et al. (2018) designed a super-hydrophilic nanohair coating composed of poly hydroxy ethyl methacrylate (PHEMA) hydrogel and conducted adhesion experiments. The results revealed that, PHEMA hydrogel exhibit high anti-adhesion against mineral crystals even at high temperature, under flow conditions. Hence the mechanical stability can take advantage under extreme environmental conditions where chemical inhibitors cannot work.

35.5 Conclusions

Mineral fouling is a recurrent technological problem encountered in water intensive processes and operations. Scale deposit formation on pipelines reduces the flow capacity, thus necessitating more pumping power. Furthermore when precipitated on heated surfaces such as heat exchangers and water heaters it reduces the heat transfer efficiency due to the insulating effects of the scale deposits. This paper provides a clear idea of the various scale control techniques that can be given for modifying the water chemistry as well as the pipe material, among them chemical treatment is found to have excellent scale inhibition efficiency. Magnetic water treatment is a simple, lucrative and environmental friendly approach with considerable scale removal efficiency. Also, it can encourage the homogeneous nucleation process and alter the crystallization of mineral ions. The fabrication of super-hydrophilic coatings having excellent anti-adhesion property against mineral crystals under dynamic fluid flow can be used as a substitute for super-hydrophobic surfaces. Hence, future research works can be conducted on above mentioned treatment methods to use them as standalone technologies or in combination so as to ensure excellent scale inhibition, low aquatic and human toxicity, high biodegradability and good price to performance ratio.

References

- Alabi A, Chiesa M, Garlisi C, Palmisano G (2015) Advances in anti-scale magnetic water treatment. *Environ Sci Water Res Technol* 1:408–425
- Alimi F, Tlili MM, Amor MB, Maurin G, Gabrielli C (2009a) Effect of magnetic water treatment on calcium carbonate precipitation: Influence of pipe material. *Chem Eng Process* 48:1327–1332
- Alimi F, Tlili M, Amor MB, Maurin G, Gabrielli C (2009b) Influence of magnetic field on calcium carbonate precipitation in the presence of foreign ions. *Surf Eng Appl Electrochem* 45:56–62
- Al-Roomi YM, Hussain KF (2015) Application and evaluation of novel acrylic based CaSO_4 inhibitors for pipes. *Desalination* 335:33–44
- Bali M, Gueddari M (2018) The effect of magnetic treatment on the physico-chemical and microbiological characteristics of hard waters. *Sep Sci Technol* 53(9):1405–1411
- Barrett RA, Parsons SA (1998) The influence of magnetic fields on calcium carbonate precipitation. *Water Res* 32(3):609–612
- Bhuvaneswari S, Subramani K, Subramani VK, Palanisamy K (2015) Influence of EDTA polymorphic and morphological transformation of CaCO_3 under CO_2 atmosphere at different temperature and different combination. *IOSR J Appl Chem* 8(1):36–43
- Chauhan K, Sharma P, Chauhan GS (2015) *Mineral scales and deposits*, 2nd edn. Elsevier, USA
- Chibowski E, Holysz L, Szczes A (2003) Adhesion of in situ precipitated calcium carbonate in the presence and absence of magnetic field in quiescent conditions on different solid surfaces. *Water Res* 37:4685–4692
- Dobersek D, Goricanec D (2007) Influence of water scale on thermal flow losses of domestic appliances. *Int J Math Models Methods Appl Sci* 1(2):55–61
- Hoang TA (2015) *Mineral scales and deposits*, 2nd edn. Elsevier, USA

- Jiang W, He J, Xiao F, Yuan S, Lu H, Liang B (2015) Preparation and antiscaling application of superhydrophobic anodized CuO nanowire surfaces. *Ind Eng Chem Res* 54:6874–6883
- Li H, Hsieh M, Chien S, Monnell JD, Dzombak DA, Vidic RD (2011) Control of mineral scale deposition in cooling systems using secondary-treated municipal wastewater. *Water Res* 45:748–760
- Li H, Yu S, Han X, Zhao Y (2016) A stable hierarchical superhydrophobic coating on pipeline steel surface with self-cleaning, anticorrosion, and anti-scaling properties. *Colloids Surf A Physicochem Eng Asp* 503:43–52
- Liu D, Dong W, Li F, Hui F, Ledion J (2012) Comparative performance of polyepoxysuccinic acid and polyaspartic acid on scaling inhibition by static and rapid controlled precipitation methods. *Desalination* 304:1–10
- MacAdam J, Jarvis P (2015) *Mineral scales and deposits*, 2nd edn. Elsevier, USA
- MacAdam J, Parsons SA (2004) Calcium carbonate scale formation and control. *Environ Sci Biotechnol* 3:159–169
- Mosin O, Ignatov I (2015) Magnetic water treatment for elimination of scaling salts. *J Med Physiol Biophys* 11:86–100
- Muryanto S, Bayuseno AP, Ma'mun H, Usamah M, Jotho (2014) Calcium carbonate scale formation in pipes: effect of flow rates, temperature and malic acid as additives on the mass and morphology of the scale. *Proc Chem* 9:69–76
- Saksono N, Gozan M, Bismo S, Krisanti E, Widaningrum R, Song SK (2008) Effect of magnetic field on calcium carbonate precipitation: Ionic and particle mechanisms. *Korean J Chem Eng* 25(5):1145–1150
- Sohaili J, Shi HS, Baloo L, Zardari NH, Ahmad N, Muniyandi SK (2016) Removal of scale deposition on pipe walls by using magnetic field treatment and the effects of magnetic strength. *J Clean Prod* 139:1393–1399
- Stuyven B, Vanbutsele G, Nuyens J, Vermant J, Martens JA (2009) Natural suspended particle fragmentation in magnetic scale prevention device. *Chem Eng Sci* 64:1904–1906
- Westin KJ, Rasmuson AC (2005) Crystal growth of aragonite and calcite in presence of citric acid, DTPA, EDTA and pyromellitic acid. *J Colloid Interface Sci* 282:359–369
- Zhang T, Wang Y, Zhang F, Chen X, Hu G, Meng J, Wang S (2018) Bio-inspired superhydrophilic coatings with high anti-adhesion against mineral scales. *NPG Asia Mater* 10:1–7

Chapter 36

Smart and Sustainable Urine-Powered Microbial Fuel Cells Eco-Technology



S. Azhar Mohammed Pillai, N. Madhavan and Arun K. Sundaram

36.1 Introduction

Observing the Spontaneous need for clean water and efficient energy throughout the world, pressure on alternative sources are increased to cope up with the requirement of this growing population. Microbial Fuel Cell (MFC) is definitely a sustainable solution that directly converts organic biomass present in Urine (or wastewater) into electric current. Thus, a possible alternative solution for energy and water clean-up is efficiently maintained (Habermann and Pommer 1991). Climate change is adversely affecting the humans and species all over the world. So the initiative of researching clean energy resources has led to Microbial fuel cells. MFCs provide a chance for generating electricity from urine which would eventually treat wastewater and emits zero harmful pollutants. The growing demand for Smart and renewable energy sources arises due to depletion of conventional fossil fuels. MFCs occupy a wide range of substrates that has shown to produce efficient electricity generation and COD removal rates, but one potential fuel, which was ignored and underexploited is urine. Urine is an ample waste product with a production of 6.4 trillion liters of a population of 6.97 billion including average daily urine production of 2.5 L/adult human) (Ieropoulos et al. 2012) (Fig. 36.1).

S. Azhar Mohammed Pillai (✉) · N. Madhavan · A. K. Sundaram
Mar Baselios College of Engineering, Trivandrum 695015, India
e-mail: azharsakkir@gmail.com

N. Madhavan
e-mail: nirmalmsphd@gmail.com

A. K. Sundaram
e-mail: arunksundarama@gmail.com

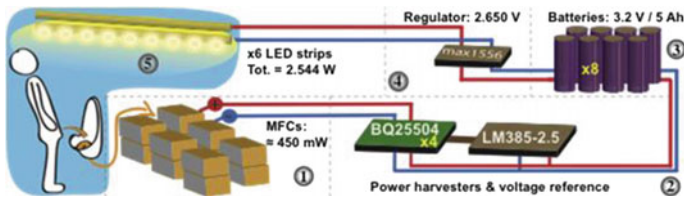


Fig. 36.1 Urine-powered MFC cycle

MFC occupies electric current using microbial metabolism, where the anodic biofilm act as an engine of the process, utilizing urine or biodegradable waste and converting biochemical energy of the fuel to electrical energy (Gajda et al. 2018). The development of MFC into modern commercial product possesses many challenges like the high cost of materials and the low efficiency of the energy produced. Therefore, focus is on the successful scale-up process which uses the optimized materials and design of cost- energy efficient technology (Do et al. 2018). Moreover lab-based and field trial led research proved development of Urine-powered MFC for large-scale applications (Khan et al. 2017). Keeping this whole new idea in mind, recent progress in MFC architecture closer to the real-life implementation resulted in the use of ceramic in MFC (Gajda et al. 2015). Non-platinum catalysts and open to air cathodes (Walter et al. 2018) with improved design of multiple MFC units in the system. This paper focus the work carried out Bristol BioEnergy Centre, and Department of Applied Sciences, the University of the West of England, Bristol, United Kingdom. They constructed modules having several Microbial Fuel cells fluidically and electrically connected in parallel, moreover, the modules could be connected in an electrical array both in series and in parallel, and fluidically connected in a cascade configuration. The Pee Power stack was tested in the field demonstrating its capability to be used in real-life applications by powering the internal lighting of a urinal, only from the urine provided by the users (Ieropoulos et al. 2016). However, the power output generated by the experiment can be improved (Ieropoulos et al. 2016). Hence a new approach is being developed in various researches (Kim et al. 2010) which proved a good method for wastewater treatment plans (Liang et al. 2018). But, large-scale plants proved to have issues like transport limitations, including ionic transport and acidity/alkalinity transport from the electrodes and hence low performance (Popat and Torres 2016). Therefore the improvement in efficiency can be gained using miniaturized, as above mentioned, found to have smaller stacked MFCs exceeded larger reactors in voltage and current of similar geometric foot-print and volume and (Ieropoulos et al. 2010); with the increase in the surface area–volume ratio and reducing the distance between the electrodes (Qian and Morse 2011). For instance, a microscale having flat-plate MFC having high surface area–volume ratio completely enhances the coefficient of mass transfer which eventually improves power density (Ren et al. 2014). Also, the integration (series or parallel or both connections) of stacked

MFCs will possess more efficient wastewater treatment and developed useful electricity levels, such as powering indoor light. However, small-scale reactors have a power output greater than the large-scale MFC with same materials (Logan et al. 2015). Therefore the power density, also described as the actual power of the MFC divided by the volume of the reactor (W/m^3) or the electrode surface area (W/m^2), generally decreases with increasing scale. The variations in power density through scale-up is due to changes in various significant factors, like the volume of the reactor, space between electrodes and surface area of electrode per volume ratio (Cusick et al. 2011) which define internal resistance of MFC (Ieropoulos et al. 2008).

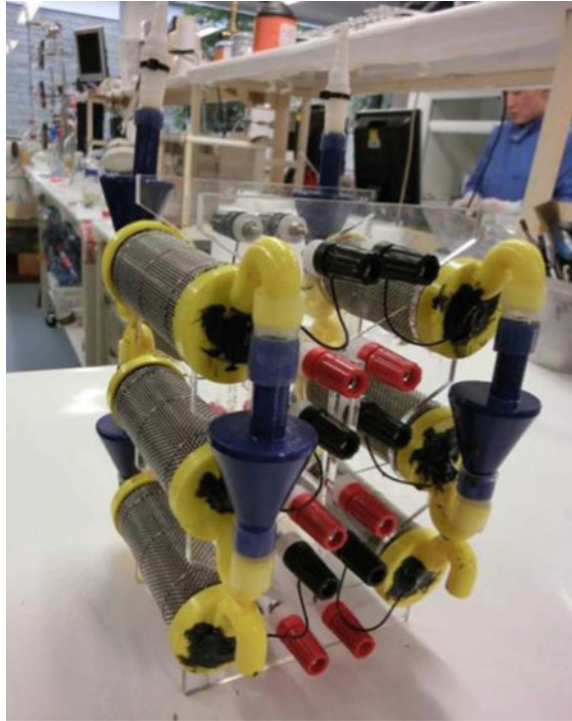
36.1.1 Methodology-Working of Microbial Fuel Cell

An MFC is a type of bioelectrochemical reactor having organic wastes in the feedstock which gets oxidized in the anodic chamber to generate carbon dioxide, protons, and electrons (in the biological form of NADH/NADPH). Feedstock fuel (utilizable substrate here urine) can introduce a wide variety of compounds, like acetate and other low molecular weight monomers, including sugars to particulate macromolecules and complex real-world mixtures such as sludge, under anaerobic conditions in the anode chamber. The utilization of complex macromolecules which could be present in urine (Brooks and Keevil 1997) is the hydrolytic activity around and within the anodic biofilm. The generated electron which flows continuously over the anode and parallel connected protons in the cathode chamber creates charge balance and Current flow from Microbial fuel cells to series of resistors and electronic instruments.

36.1.2 Biological Mechanism Inside the Bacteria

Microbes in the anodic chamber are forced to perform anaerobic respiration and they release electrons protons and carbon dioxides, which are transported outside the cell using nanowires or c-type cytochromes. Electrons produced from the NADH redox reactions inside the bacteria are transported to the anode (via direct electron transfer or via chemical active redox mediators) and then transported through the external circuit to the cathode within the cathodic chamber, while protons generated passes through PEM (proton exchange membrane) that separated two chambers and at the cathode this proton reacts with oxygen to form water (by product) (Lusk et al. 2018).

Fig. 36.2 Two cascades of 3 MFCs, fitted with air gap adaptors (Ieropoulos et al. 2013)



36.1.3 Material Used

- Ceramic cylinder with a volume of 49 mL (Ieropoulos et al. 2013).
- The anode electrodes were made from carbon fiber veil made to form a spiral brush (Fig. 36.2).
- The cathode was made by painting micro-porous layer (MPL) on the outside surface of the ceramic compartment with stainless steel.
- Finally connected to a state of the art energy harvester BQ25504EVM-674 (Farnell, UK) which would eventually maintain voltage and power level to a fixed value (Ieropoulos et al. 2013).

36.1.4 Effect of Various Parameter MFC

Data recorded. Resistor stat tool was employed for the experiments for obtaining the power density of MFCs operated under open circuit condition. The time duration for each resistance was fixed as 5 min, with the limit of 40 k Ω –4 Ω and the total number of resistances employed were 34 (Ieropoulos et al. 2008) (Fig. 36.3).

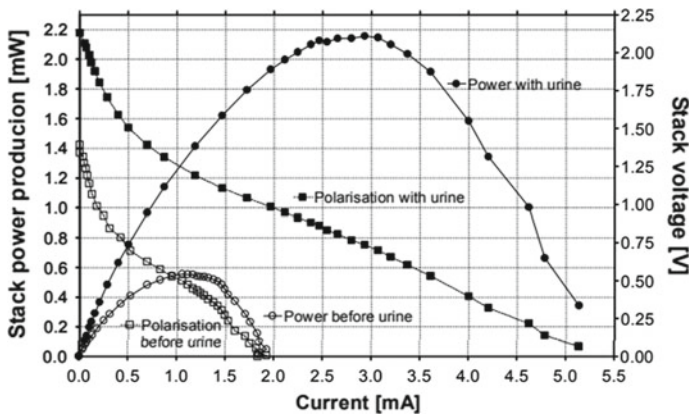


Fig. 36.3 This graph shows the difference of power and polarization curve with urine and without urine (acetate) when power in mW and current in mA and voltage (Ieropoulos et al. 2008)

The power obtained from urine due to the presence of exoelectrogenic bacteria have resulted in the production of peak current output of 5.25 mA and more power than other substrates. In Microbial fuel cells, effective power production is essentially associated with quick microbial metabolic rates, therefore indicating more effective utilization and conversion of the substrate (Ieropoulos et al. 2008). Organic components are broken down by the microbes and the majority of organic carbon is oxidized using electron transfer to CO_2 , whilst a little of it is used as building blocks for newly generated cell material. A proportion of inorganic Nitrogen, Phosphorous, and potassium is also used as a part of new cells, and hence eliminated from the waste-stream, although the majority may be lost by mineralization. An additional pathway for Nitrogen would be changed to Ammonia, which depends on pH (Ieropoulos et al. 2008).

36.2 Effect on pH

The activity of most prokaryotes is governed by pH. The maximum rate microbes perform biological activities of growth and metabolism is at optimum pH. Various studies have shown that the highest power was obtained at pH 8.5 when the enzymes discharged by the microbes are in a conducive form of ionic groups on their active sites for their proper function (Fig. 36.4).

Variation in the pH would result in changes in the ionic form of the active sites, which would further change the enzymatic activity leading to the variation in the reaction rate as well (Parkash et al. 2015). The study also reported that at pH 6 and below, electrochemical and cellulosic activities will be lower when compared to the results obtained at higher pH resulting in lower electricity production. This is due to

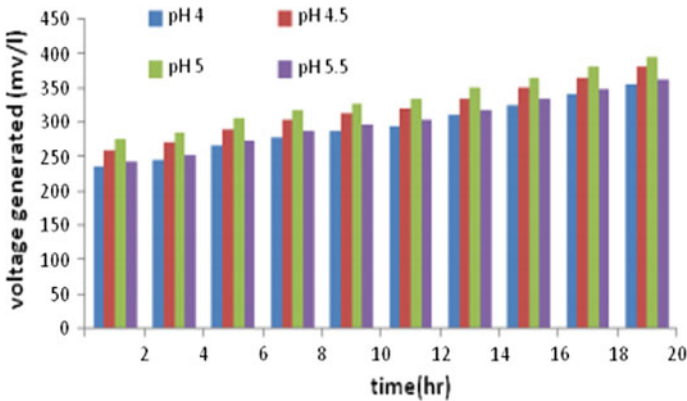


Fig. 36.4 Voltage time relation for pH 4, 5, 4.5, 5.5 (Larrosa-Guerrero et al. 2010)

the denaturation of proteins, celluloses or active sites when maintained under acidic states. When observed the neutral pH was proper for cellulose degradation, as acidic states tend to hinder the growth of most of the cellulose degrading yeasts (Kumar et al. 2012).

36.3 Effects of MCF Design

36.3.1 Small, Medium and Large Scale

Three MFC sizes were used for the study: small, medium and large having 6.3, 29.63 and 652.5 mL of anodic void volumes respectively. The urine completely covered the electrode material. The maximum Power density generated from the large-scale Microbial Fuel Cells was 0.212 mW/m^2 (0.227 W/m^3). But the small-scale Microbial fuel cells power density was 1.8 mA/m^2 (1.83 A/m^3) (Ieropoulos et al. 2008).

From Fig. 36.5 this is evident that there exists a small difference of voltage of small and medium-sized MFC but the current value remains constant. The values of large-scale MFC was nearly half the peak power density values produced from the small- and medium-sized MFCs.

36.3.2 Stacked MFC

Polarization data of 10 identical small-scale Microbial Fuel Cells connected in series, parallel and series/parallel arrangements compared to MFCs arranged in series and the five pairs in parallel. The same amount of urine was fed to the MFCs in

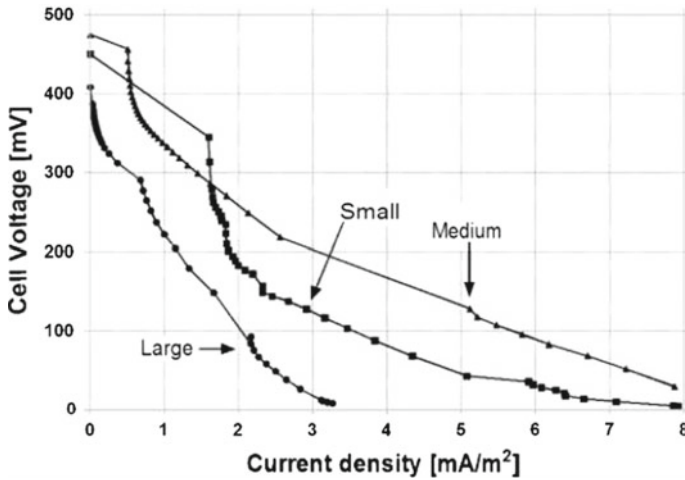


Fig. 36.5 For carious sized MFC polarization curve drawn for interpretation (Ieropoulos et al. 2008)

continuous mode. The peak Power density from the 10 MFCs arranged in series was 0.45 mW/m^2 (0.47 W/m^3) with a corresponding current density of 0.69 mA/m^2 (0.75 A/m^3) (Ieropoulos et al. 2008). Compared with the single small-scale MFC, open circuit voltage noted from this experiment was approximately 3.5 times higher (1500 mV). The value for power level produced from this stacked MFCs was considerably higher than that produced from the single small-scale MFC. When MFCs are stacked the voltage and current are equal to sum of all individual cells respectively so from this it is evident that stacked MFCs produce much more power output than single MFCs (Fig. 36.6).

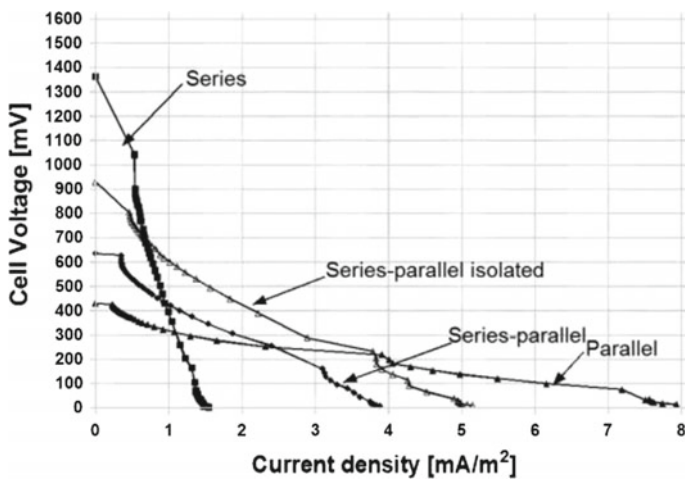


Fig. 36.6 Small MFC stacked and plotted with voltage-current density (Ieropoulos et al. 2008)

36.4 Applications of Urine-Powered MFC

- At the practical level, MFCs could be employed in wastewater treatment plants, conserving enormous energy expenses by efficiently producing energy during the process of treating urine and circulating it back into the fuel cell compartment.
- Urine-powered MFC can be deployed in low energy infrastructure areas of the world.
- Urine-powered MFC can be used in public toilet along with Mobile charging facility.
- And also used any home or offices with cascaded Urine-powered MFC to combine each power output and amplify it.
- Urine-powered MFCs can be used to recover nutrients (N, K, P) uses in fertilizer producing company.
- Floating MFCs coupled to plants that act as independent sensors are used extensively to send a signal in natural water bodies (here microbes use biodegradable organic wastes from plant roots) (Schievano et al. 2017).

36.5 Conclusions

1. Urine-powered MFC is a remarkably future technology for the generation of reliable electricity urine. The most viable way of raising power density is to produce miniaturized MFCs and arrange various units in stacks also called Stacked MFC. Being a sustainable and non-polluting.
2. In this review paper, the current and future prospects of urine-powered Microbial Fuel cells. The experimental glimpse showcased here is the work done by UWE Bristol UK. Microbial fuel cells are the fuel cells of the future promoting a clean and sustainable world. A lot of research under this field is required for the commercial deployment of urine-powered MFC. From this review, it is clear that urine is one of the superior fuel to be used in MFC. Being a sustainable and non-polluting fuel cell it will create a demand for renewable energy sector when the world is growing rapidly and creating a huge demand for energy. Due to the small power density generated from MFCs research and investment in this field can definitely come up with more enhanced power output.
3. It is observed that optimized power output and waste utilization rates of small-scale MFCs provide more benefits rather than large-scale stacks (Ieropoulos et al. 2008). The financial aspects of practical implementation and commercialization lack due to the material, capital, and running costs. The

capital investment for any green and sustainable technology will be the same for any venture. The costs of service and maintenance will be lower due to the built-in longevity and stability. The material cost can be reduced by employing ceramic compartments.

References

- Brooks T, Keevil CWW (1997) A simple artificial urine for the growth of urinary pathogens. *Lett Appl Microbiol* 24:203–206 PMID: 9080700
- Cusick RD, Bryan B, Parker DS, Merrill MD, Mehanna M, Kiely PD et al (2011) Performance of a pilot-scale continuous flow microbial electrolysis cell fed winery wastewater. *Appl Microbiol Biotechnol* 89:2053–2063. <https://doi.org/10.1007/s00253-011-3130-9>
- Do MH, Ngo HH, Guo WS, Liu Y, Chang SW, Nguyen DD et al (2018) Challenges in the application of microbial fuel cells to wastewater treatment and energy production: a mini review. *Sci Total Environ* 639:910–920. <https://doi.org/10.1016/j.scitotenv.2018.05.136>
- Gajda I, Greenman J, Melhuish C, Santoro C, Li B, Cristiani P, et al (2015) Electro-osmotic-based catholyte production by microbial fuel cells for carbon capture. *Water Res* 86:108–115. <https://doi.org/10.1016/j.watres.2015.08.014>; Pasternak G, Greenman J, Ieropoulos I (2016) Comprehensive study on ceramic membranes for low-cost microbial fuel cells. *ChemSusChem* 9:88–96. <https://doi.org/10.1002/cssc.201501320>
- Gajda I, Stinchcombe A, Merino-Jimenez I, Pasternak G, Sanchez-Herranz D, Greenman J, Ieropoulos IA (2018) Microbial fuel cell for efficient power generation from urine and stack development. *Front Energy Res*. <https://doi.org/10.3389/fenrg.2018.00084>
- Habermann W, Pommer EH (1991) Biological fuel cells with sulphide storage capacity. *Appl Microbiol Biotechnol* 35(1)
- Ieropoulos I, Greenman J, Melhuish C (2008) Microbial fuel cells based on carbon veil electrodes: stack configuration and scalability. *Int J Energy Res* 32:1228–1240. <https://doi.org/10.1002/er.1419>
- Ieropoulos I, Greenman J, Melhuish C (2008) Microbial fuel cells based on carbon veil electrodes: stack configuration and scalability. *Int J Energy Res* 32(13):1228–1240. <https://doi.org/10.1002/er.1419>
- Ieropoulos I, Greenman J, Melhuish C (2010) Improved energy output levels from small-scale microbial fuel cells. *Bioelectrochemistry* 78:44–50. <https://doi.org/10.1016/j.bioelechem.2009.05.009>
- Ieropoulos I, Greenman J, Melhuish C (2012) Urine utilisation by microbial fuel cells; energy fuel for the future. *Phys Chem Chem Phys* 14(1):94–98. <https://doi.org/10.1039/c1cp23213d>
- Ieropoulos IA, Ledezma P, Stinchcombe A, Papaharalabos G, Melhuish C, Greenman J (2013) Waste to real energy: the first MFC powered mobile phone. *Phys Chem Chem Phys* 15 (37):15312–15316. <https://doi.org/10.1039/b000000x>
- Ieropoulos IA, Stinchcombe A, Gajda I, Forbes S, Merino-Jimenez I, Pasternak G et al (2016) Pee power urinal—microbial fuel cell technology field trials in the context of sanitation. *Environ Sci Water Res Technol* 2:336–343. <https://doi.org/10.1039/c5ew00270b>
- Kim JR, Premier GC, Hawkes FR, Rodríguez J, Dinsdale RM, Guwy AJ (2010) Modular tubular microbial fuel cells for energy recovery during sucrose wastewater treatment at low organic loading rate. *Bioresour Technol* 101:1190–1198. <https://doi.org/10.1016/j.biortech.2009.09.023>; Dong Y, Qu Y, He W, Du Y, Liu J, Han X, et al (2015) A 90-liter stackable baffled microbial fuel cell for brewery wastewater treatment based on energy self-sufficient mode. *Bioresour Technol* 195:66–72. <https://doi.org/10.1016/j.biortech.2015.06.026>; Ge Z, He Z (2016) Long-term performance of a 200 liter modularized microbial fuel cell system treating

- municipal wastewater: treatment, energy, and cost. *Environ Sci Water Res Technol* 2:274–281. <https://doi.org/10.1039/c6ew00020g>
- Kumar S, Kumar HD, Gireesh Babu K (2012) A study on the electricity generation from the cow dung using microbial fuel cell. *J Biochem Tech* 3(4):44–447
- Khan MD, Khan N, Sultana S, Joshi R, Ahmed S, Yu E et al (2017) Bioelectrochemical conversion of waste to energy using microbial fuel cell technology. *Process Biochem* 57:141–158. <https://doi.org/10.1016/j.procbio.2017.04.001>
- Larrosa-Guerrero A, Scott K, Head IM, Mateo F, Ginesta A, Godinez C (2010) Effect of temperature on the performance of microbial fuel cells. *Fuel* 89(12):3985–3994. <https://doi.org/10.1016/j.fuel.2010.06.025>
- Liang P, Duan R, Jiang Y, Zhang X, Qiu Y, Huang X (2018) One-year operation of 1000-l modularized microbial fuel cell for municipal wastewater treatment. *Water Res* 141:1–8. <https://doi.org/10.1016/j.watres.2018.04.066>
- Logan BE, Wallack MJ, Kim KY, He W, Feng Y, Saikaly PE (2015) Assessment of microbial fuel cell configurations and power densities. *Environ Sci Technol Lett* 2:206–214. <https://doi.org/10.1021/acs.estlett.5b00180>
- Lusk Bradley G, Colin A, Parameswaran P, Rittmann BE, Torres CI (2018) Simultaneous fermentation of cellulose and current production with an enriched mixed culture of thermophilic bacteria in a microbial electrolysis cell. *Microb Biotechnol* 11(1):63–73. <https://doi.org/10.1111/1751-7915.12733>
- Parkash A, Aziz S, Soomro SA (2015) Impact of salt concentrations on electricity generation using hostel sludge based dual chambered microbial fuel cell. *J Bioprocess Biotech*. 27(2):1057–1061
- Popat SC, Torres CI (2016) Critical transport rates that limit the performance of microbial electrochemistry technologies. *Bioresour Technol* 215:265–273. <https://doi.org/10.1016/j.biortech.2016.04.136>
- Qian F, Morse DE (2011) Miniaturizing microbial fuel cells. *Trends Biotechnol* 29:62–69. <https://doi.org/10.1016/j.tibtech.2010.10.003>
- Ren H, Torres CI, Parameswaran P, Rittmann BE, Chae J (2014) Improved current and power density with a micro-scale microbial fuel cell due to a small characteristic length. *Biosens Bioelectron* 61:587–592. <https://doi.org/10.1016/j.bios.2014.05.037>
- Schievano A, Colombo A, Grattieri M, Trasatti SP, Liberale A, Tremolada P, Pino C, Cristiani P (2017) Floating microbial fuel cells as energy harvesters for signal transmission from natural water bodies. *J Power Sources* 340:80–88. <https://doi.org/10.1016/j.jpowsour.2016.11.037>
- Walter XA, Merino-Jiménez I, Greenman J, Ieropoulos I (2018) Pee power urinal II—urinal scale-up with microbial fuel cell scale-down for improved lighting. *J Power Source* 392:150–158

Chapter 37

Gasification of Sawdust in Bubbling Fluidised Bed Gasifier



Jerald Joseph, John Raphael, R. Kevin, Joel George
and Vishnu Sankar

37.1 Introduction

Alternative energy sources are essentially identified for the conventional energy source like the fossil fuel due to its depleting nature and ever increasing energy demand. Biomass is a renewable source of energy which is an alternative to fossil fuel. Biomass is the recently living species like plants and animals, but fossil fuels take millions of years to form. Biomass is a carbon neutral fuel as it does not add extra carbon to the atmosphere.

Main products obtained from the biomass conversion are solid fuel (charcoal), liquid fuel (biodiesel) and gaseous fuel (syngas). Biomass can be converted into useful fuel by biochemical and thermo-chemical conversion methods. The biochemical conversion methods include digestion and fermentation while thermo-chemical conversion methods include pyrolysis, gasification, liquefaction and combustion.

J. Joseph (✉) · J. Raphael · J. George · V. Sankar
Mechanical Engineering, Rajagiri School of Engineering and Technology,
Ernakulam, India
e-mail: geraldj6@gmail.com

J. George
e-mail: joelpull@gmail.com

V. Sankar
e-mail: vishnus@rajagiritech.edu.in

R. Kevin
Mechanical Engineering, St. Joseph's College of Engineering and Technology,
Pala, India
e-mail: rkevin635@gmail.com

Gasification is a thermo-chemical process that converts carbonaceous materials like biomass into useful and convenient gaseous fuels (Prabir 2010). Biomass is gasified in a thermal reactor called gasifier. Different types of gasifiers available are Moving bed type, fluidized bed and entrained flow. Comparison between different gasifiers was made by Warnecke (2000) and it was concluded that fluidised bed gasifier has higher heat and mass transfer, which results in better temperature distribution. The gases produced from gasification process are hydrogen, methane, carbon monoxide, and carbon dioxide. These gases are obtained by reaction of the material at high temperatures of about 700 °C, with a controlled amount of oxygen and/or steam. Hydrogen is the main gaseous fuel that is obtained from gasification, which finds application in internal combustion engines and fuel cells. In addition to being a clean fuel the energy released by it on combustion is higher than any other fuel on mass basis (Marban and Valdes-Solis 2007). Hydrogen yield from biomass gasification depends on several factors like moisture content, feed stock composition, type of gasifier, amount of gasifying agent, and so forth.

37.2 Biomass

Biomass refers to any non-fossilized and biodegradable organic material originating from plants, animals and micro-organisms. Major part of the biomass is made up of ligno-cellulosic stuffs which influence the hydrogen yield during biomass gasification. Most important biomass sources are wood and wood wastes, crops and their waste by-products, municipal solid waste, animal waste, waste from food processing, and aquatic plants and algae.

Biomass can be characterized based on the chemical constituent (cellulose, hemicelluloses and lignin), elemental composition, inherent mineral content, amount of volatile matter, moisture content and physical properties (particle size, shape and density) and recognized their influence in product gas composition and hydrogen yield during biomass gasification. Characterization of different locally available biomasses has been carried out to select appropriate one for air gasification (Table 37.1).

Table 37.1 Results of characterization of biomass

Biomass	Moisture (%)	Volatile (%)	Ash (%)	Fixed carbon (%)
Saw dust	12.8	69	4	14.1
Ground nut	12.5	61	12.7	13.7
Coffee husk	12.4	67	7	12.6
Coconut shell	10.2	77	0.8	12.1
Sugarcane	13.6	72	5	9

37.3 Experimental Investigation

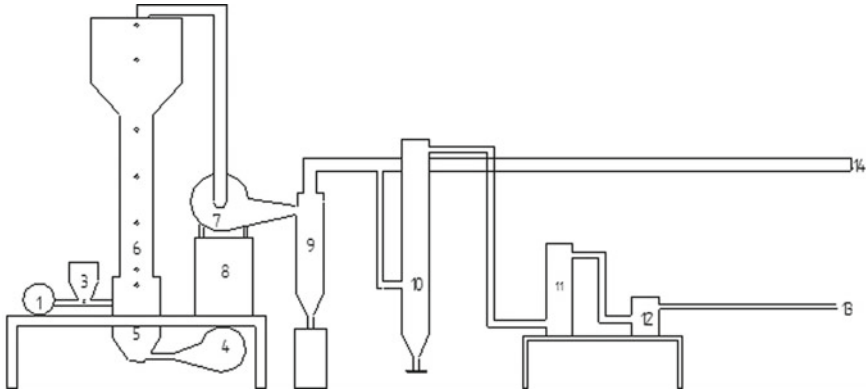
An experimental investigation is carried out in a bubbling fluidised bed gasifier with air as gasifying agent and sawdust as biomass. Investigation is carried out to determine gas yield and composition at different operating conditions.

37.3.1 *Experimental Setup*

The experiment was performed on a lab scale bubbling fluidised bed gasifier. The setup consists of biomass feeder, bubbling fluidised bed reactor, cyclone separator, ash pit, water scrubber, moisture filter and gas outlet. The BFBG has a cylindrical riser of 2300 mm height. The cylindrical chamber of the gasifier is made up of multiple layers of refractory material capable of withstanding temperature of about 1500 °C. The bottom portion is equipped with a heater of 3 kW which is provided for initial heating. The top portion of BFBG is expanded to allow settling of unburnt biomass. A distribution plate is provided at the base of the bed which supports the inert material (sand). An air inlet blower is provided at the bottom of the distribution plate to fluidise the bed. The biomass is supplied to the gasification chamber through the hopper and feed screw assembly and the feed rate can be controlled by controlling the speed of the feed screw through a motor. A suction pump is attached to take out the gases formed in the riser and to reduce the pressure formed in riser due to gas accumulation. The producer gas generated as a result of gasification is passed through the cyclone separator, water scrubber, moisture filter and an oil scrubber in order to remove the impurities and increase the gas quality. The control and monitoring unit consists of a set of thermocouples, U tube manometres, producer gas analysers, flow meters and rpm indicators to measure temperature, pressure head, gas composition, steam rate and feed rate, respectively (Joel et al. 2018). The schematic representation of the experimental setup and the components are shown in Fig. 37.1.

37.3.2 *Experimental Procedure*

Sawdust (250 µm) having moisture content less than 15% is used for gasification purpose. River sand (1 mm particle size) is fed to the bed through the hopper. The heater is turned on and the base of gasifier is brought to a gasification temperature of about 600 °C, which takes about 3–4 h. The biomass is loaded into hopper and fed to the gasification chamber slowly along with the air from inlet blower to increase the rate of partial combustion and hence increase the gasification temperature to about 700 °C. The inlet air supply and feed rate is controlled precisely to maintain the gasification temperature. The suction pump is turned on to maintain



1	Screw feeder	8	Control And Measuring Instrument
2	Feed screw	9	Cyclone Separator
3	Hopper	10	Water Scrubber
4	Air inlet blower	11	Moister Filter
5	Plenum	12	Oil Scrubber
6	Free board	13	Gas sampling point
7	Suction pump	14	Fire torch

Fig. 37.1 Schematic representation of experimental setup

smooth flow of producer gas from the riser to the outlet. Once a stable condition is achieved the feed rate is increased to achieve gasification conditions. The cleaned producer gas is extracted at the sampling point and is fed to the gas analyser which detects the gas composition. Different operating conditions are obtained by varying the feed rate, inlet air quantity and temperature of the heater. The experimental results obtained are used to validate the thermodynamic model developed.

37.4 Thermodynamic Equilibrium Model

37.4.1 Model Development

Many studies have been performed to investigate the influence of operating parameters on producer gas yield. Mathematical and computational approaches

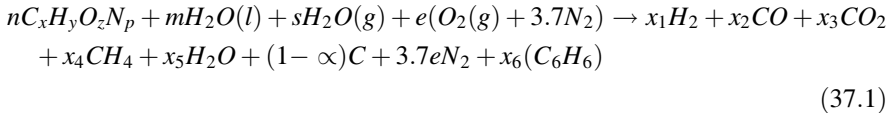
have been applied to conduct these studies due to the extensive range of investigations. Different mathematical models like thermodynamic equilibrium model, kinetic model, phenomenological model, artificial neural network model, etc. were considered to simulate biomass gasification. Stoichiometric thermodynamic equilibrium model (TEM) was selected as it is less computational intensive and hence used as a tool for preliminary comparison (Puig-Arnavat et al. 2010). The second law of thermodynamics applied to chemical systems is the basis of the thermodynamic equilibrium model (Rupesh et al. 2014). Stoichiometric thermodynamic equilibrium models based on specific chemical reactions are used here for the estimation of product gas composition (Janajreh and Al Shrah 2013). A stoichiometric thermodynamic equilibrium model is formulated to assess the producer gas yield from different locally available biomasses.

The major assumptions (Joel et al. 2016) made for formulation are:

- (1) Gasifier is considered as a steady state system with uniform temperature and pressure throughout.
- (2) The reaction time in the gasifier is high enough to attain thermodynamic equilibrium.
- (3) All the gases behave ideally.
- (4) Gases except H_2 , CO , CO_2 , CH_4 and N_2 are considered dilute.
- (5) Nitrogen is considered inert in the entire process.
- (6) Biomass comprises of Carbon, Oxygen, Hydrogen and Nitrogen.

The following equations are used for modelling the gasification process.

General Gasification Equation:



Carbon Balancing:

$$x_2 + x_3 + x_4 + 6x_6 + (1 - \alpha) - n\frac{C}{12} = 0 \quad (37.2)$$

Hydrogen Balancing:

$$2x_1 + 4x_4 + 2x_5 + 6x_6 - nH - 2m - 2s = 0 \quad (37.3)$$

Oxygen Balancing:

$$x_2 + 2x_3 + x_5 - n\frac{O}{16} - m - s - 2e = 0 \quad (37.4)$$

Table 37.2 Results of characterisation of biomass

	Saw dust		Saw dust
Proximate analysis (wt%)		Ultimate analysis (wt%)	
Moisture	0.12	Carbon	44.58
Volatile matter	0.69	Hydrogen	6.2
Ash	0.04	Nitrogen	0.41
Fixed carbon	0.14	Oxygen	48.81
Calorific value (MJ/kg)	15.25		

From methane reaction:

$$(x_{total}) - K_2 x_1^2 = 0 \quad (37.5)$$

From water gas shift reaction:

$$x_3 x_1 - x_2 x_5 K_1 = 0 \quad (37.6)$$

To determine five unknowns there are three linear Eqs. (37.2, 37.3, and 37.4) and two non-linear Eqs. (37.5 and 37.6). Mole fractions of the constituents of the gaseous product can be obtained by simultaneously solving these equations using Newton–Raphson method in MATLAB platform in which the results of ultimate and proximate analyses of biomass as input data Table 37.2 are used. Once the mole fractions are determined the lower heating value of the product gas can also be calculated from the gas composition and is expressed in mole basis.

37.4.2 Model Validation

There are chances of deviation of numerical result from experimental result due to various assumptions considered during model development. Equilibrium models usually over-estimate hydrogen and carbon monoxide and under-estimate carbon dioxide and methane. To reduce the deviations suitable correction factor is introduced to estimate the value of equilibrium constants. The accuracy of the model developed is analysed by comparing the predicted gas yields from the proposed model with experimental results. The developed model is validated with the experimental results obtained by the gasification of coconut shell in the same gasifier. The statistical parameter of root mean square (RMS) value is used in error estimation as shown in Eq. (37.7).

$$\text{RMS} = \sqrt{\frac{\sum (x_e - x_p)^2}{N}} \quad (37.7)$$

x_e, x_p and N is experimental data, predicted value, and number of observations, respectively.

37.5 Results and Discussion

The experimental results of gasification are presented in Table 37.3 and comparison of concentration of gases is represented in Fig. 37.2.

It was observed during the experimental investigation (Fig. 37.2a, b) that as temperature increases percentage of both H₂ and CO increases while CO₂ decreases. This behaviour is attributed to enhancement of char gasification and Boudouard reactions. Hydrogen yield in the range 8.3–10.8 (%V) was obtained in the operating range (T = 680 – 740 °C, ER = 0.26). Comparing Fig. 37.2a, b it is noted that during the experimentation when ER increases the H₂ and CO percentage decreases and CO₂ increases. The decrease in H₂ and CO with increase in ER occurs due to oxidation of H₂ and CO in the presence of excess air.

The numerical results of gasification obtained through the mathematical model programmed in MATLAB are tabulated in Table 37.4. The table presents the model predictions in the temperature range 700–760 °C at different ER (0.26 and 0.3). The

Table 37.3 Experimental results of gasification

BFR	Temperature	ER	H	CO	CO ₂	CH ₄
13.68	760	0.30	8.37	15.4	7.4	0.7
13.68	740	0.30	8.01	15.36	7.63	9.8
13.68	720	0.30	7.78	15.21	7.62	9
13.68	700	0.30	7.15	14.78	7.78	8.9
13.68	680	0.30	6.44	13.5	8.22	8
16.7	740	0.26	10.83	18.41	5.71	10
16.7	720	0.26	10.58	17.94	5.88	9.5
16.7	700	0.26	9.5	16.51	5.7	10.1
16.7	680	0.26	8.73	11.42	6.97	11

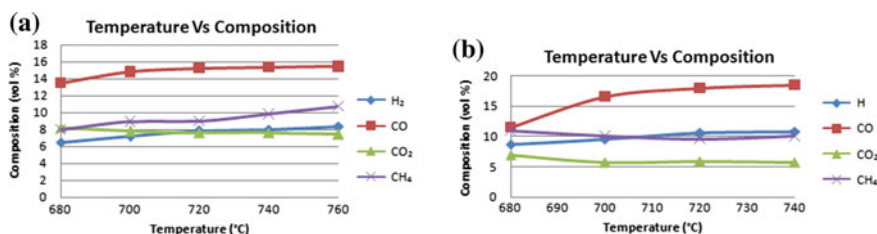


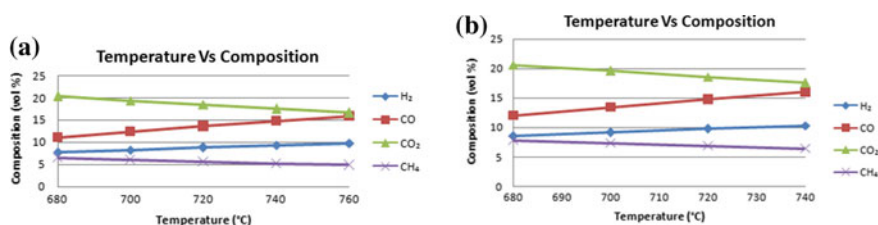
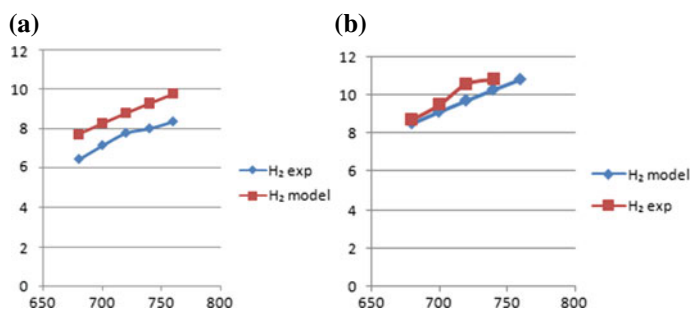
Fig. 37.2 Comparison of gas composition at a ER = 0.3 b ER = 0.26

Table 37.4 Results obtained from mathematical model

Temperature	ER	H	CO	CO ₂	CH ₄
760	0.30	9.79	15.91	16.61	4.85
740	0.30	9.31	14.76	17.49	5.23
720	0.30	8.81	13.57	18.41	5.62
700	0.30	8.28	12.33	19.36	6.02
680	0.30	7.74	11.06	20.33	6.42
740	0.26	10.30	16.00	17.56	6.37
720	0.26	9.73	14.73	18.55	6.82
700	0.26	9.14	13.41	19.58	7.29
680	0.26	8.53	12.06	20.63	7.76

yield predicted by the model is illustrated in Fig. 37.3a, b. Comparison of hydrogen yield obtained from the model and experiment is also displayed in Fig. 37.4a, b.

The numerically obtained results and the experimental results are compared and validated. It is observed from Fig. 37.4a, b that both, experimental and numerical model showed the same trend. However RMS error in the range 6.5–7.5 is observed from that of the experimental results of saw dust (Fig. 37.5). For coconut shell

**Fig. 37.3** Comparison of gases at **a** ER = 0.3 **b** ER = 0.26**Fig. 37.4** Comparison of concentration of H₂ **a** ER = 0.03 **b** ER = 0.26

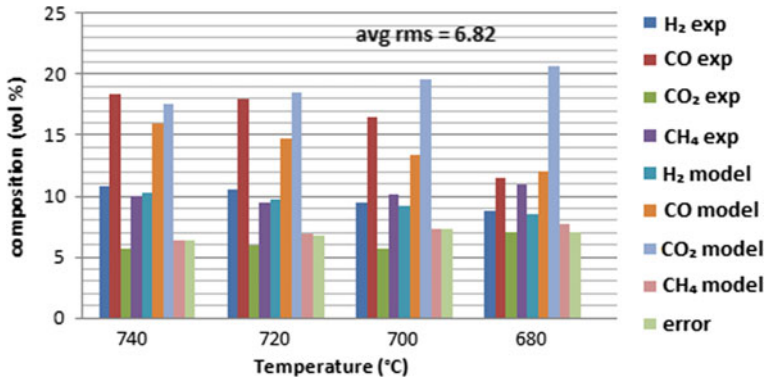


Fig. 37.5 Comparison of different components with temperature of sawdust

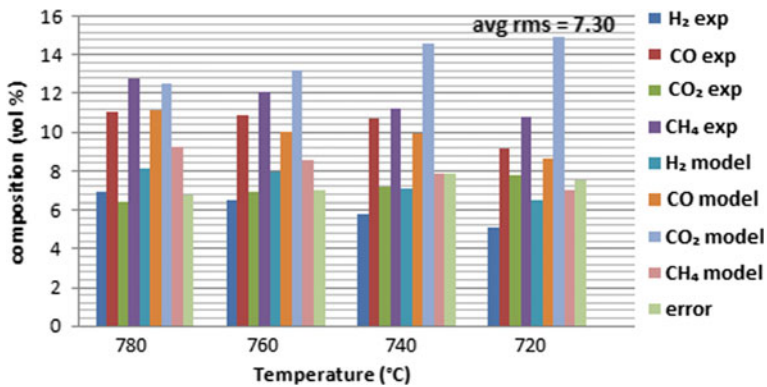


Fig. 37.6 Comparison of different components with temperature of coconut shell

RMS error is in the range 6.5–8.0 as shown in Fig. 37.6. It is noted that the error obtained is within the acceptable range. The numerical model thus can be applied for the gasification of every biomass.

37.6 Conclusion

Energy generation from biomass, a sustainable source has been considered in this study. Among the different methods for energy generation, gasification was found to be one of the effective methods. The different factors affecting biomass gasification were analyzed to study the behaviour of gasification process. Characterization of biomasses was carried out to identify suitable biomass for

gasification, from which saw dust was identified as appropriate one for experimental investigation.

Experimental investigations were carried in a bubbling fluidised bed gasifier to determine the producer gas yield during the air gasification of saw dust. The study was carried out to assess the producer gas composition at different operating conditions (Temperature and ER). A thermodynamic equilibrium model was developed to analyse the air gasification of sawdust. The developed model predictions were compared with the experimental results in terms of the product gases generated. The concentration of hydrogen was found to be increasing with temperature as expected due to the enhancement of endothermic reactions. It was observed that hydrogen yield is influenced by temperature and ER. Maximum hydrogen yield of 10.83% was obtained during the specified operating conditions of the experiment at $T = 760\text{ }^{\circ}\text{C}$ and $ER = 0.26$. The corrected and validated model predicted a hydrogen yield of 10.3% under the same operating condition.

Acknowledgements Authors gratefully acknowledge the guidance and support of Dr. C. Muraleedharan and Dr. P. Arun, Department of Mechanical Engineering, National Institute of Technology, Calicut throughout the project on “Gasification of sawdust in bubbling fluidized bed gasifier”.

References

- Janajreh I, Al Shrah M (2013) Numerical and experimental investigation of downdraft gasification of wood chips. *Energy Convers Manag* 65:783–792
- Joel G, Arun P, Muraleedharan C (2016) Stoichiometric equilibrium model based assessment of hydrogen generation through biomass gasification. *Procedia Technol* 25:982–989
- Joel G, Arun P, Muraleedharan C (2018) Experimental investigation on co-gasification of coffee husk and sawdust in a bubbling fluidised bed gasifier. *J Energy Inst* (in press). <https://doi.org/10.1016/j.joei.2018.10.014>
- Marban G, Valdes-Solis T (2007) Towards the hydrogen economy? *Int J Hydrog Energy* 32 (12):1625–1637
- Prabir B (2010) *Biomass gasification and pyrolysis: practical design and theory*, 1st edn. Academic Press, London, UK
- Puig-Arnavat M, Bruno JC, Coronas A (2010) Review and analysis of biomass gasification models. *Renew Sustain Energy Rev* 14(9):2841–2851
- Rupesh S, Muraleedharan C, Arun P (2014) Analysis of hydrogen generation through thermochemical gasification of coconut shell using thermodynamic equilibrium model considering char and tar. *Int Sch Res Not* 2014, Article ID 654946. Hindawi Publishing Corporation
- Warnecke R (2000) Gasification of biomass: comparison of fixed bed and fluidized bed gasifier. *Biomass Bioenerg* 18(6):489–497

Part V
Digitization of Energy Sector, E-Mobility
and Sustainable Transportation Systems

Chapter 38

Numerical Simulation and Performance Analysis of MLI During Reentry of Hypersonic Vehicles



P. M. Suteesh and Alex Chollackal

38.1 Introduction

Multi-Layer Insulation (MLI) is a passive thermal control system which is mainly used for cryogenic applications and space exploration programs (Suteesh and Chollackal 2018; Krishnaprakas et al. 2000). During ascent and reentry of hypersonic vehicles, very high temperature is developed at the surface due to friction heating between air molecule and vehicle surface. The change in the density and other thermodynamic properties of air column with respect to height from the earth surface, results in uneven heat flux at the vehicle surface. It can maintain large temperature gradient. MLI contain foils with high reflectivity and low thermal conductivity spacers arranged in a continuous manner. Mylar and Kapton are used as the material for spacer while gold or silver is used as the foil material for fabricating MLI (Meseguer et al. 2012; Bapat et al. 1990a).

The high reflectivity of the foil will reflect back the portion of incoming thermal radiation to the surrounding while the spacer is used to separate each foil from one another in order to reduce conduction heat transfer. The possibility of heat transfer by gas convection can be ruled out irrespective of the pressure and temperature distribution in the insulation (Huang and Zhang 2013). The principle of heat transfer in MLI is shown in Fig. 38.1.

Bapat et al. (1990b) used Mylar foil and glass spacer and used collective radiation, conduction and gas conduction model to evaluate the thermal performance of MLI. In this study, an ANSYS model of MLI is used to simulate the transient heating of MLI and mechanical ANSYS parametric design language (APDL) is used to solve the problem.

P. M. Suteesh (✉) · A. Chollackal
Department of Mechanical Engineering, SJ CET Palai, Pala, Kerala, India
e-mail: suteeshpm@gmail.com

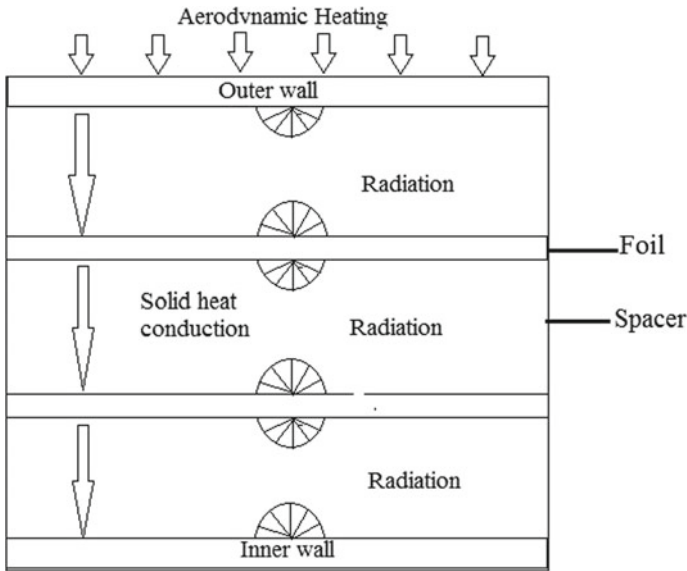


Fig. 38.1 Illustration of combined heat transfer model in MLI. (Solid conduction and thermal radiation is considered)

38.2 Mathematical Modeling

The problem can be assumed to be a composite wall with zero contact resistance. The gas conduction is neglected by assuming the spacer as non-void solid element. Since aerodynamic heating takes place uniformly throughout the surface, conduction heat transfer occurs in the insulation towards inward direction only. Thus the problem can be recognized as unsteady conduction in one dimension only. The 1D heat conduction equation along with radiation term as shown in Eq. (38.1) is solved to find the temperature distribution across the insulation.

$$\rho C \frac{\partial T}{\partial t} = \frac{\partial}{\partial x} \left(k_x \frac{\partial T}{\partial x} \right) - \frac{\partial q_r''}{\partial x} \tag{38.1}$$

q_r'' is the radiation heat flux, ρ is the density of the MLI, C is the specific heat of the MLI, k_x, k_y, k_z are the thermal conductivity in x, y and z directions respectively. The values of C and ρ are taken from reference (Daryabeigi 2001)

$$q_r'' = \epsilon \sigma (T_h^4 - T_c^4) \tag{38.2}$$

where σ is the Stefane-Boltzmann constant ($5.67 \times 10^{-8} \text{ W}/(\text{m}^2 \text{ K}^4)$), ϵ is foil emissivity, T_h and T_c are the hot and cold temperature at the two sides of the layer in kelvin. The temperature applied on the top surface of the present multilayer

insulation is close to the aerodynamic heating temperature. The above Eq. (38.1) is subjected to the boundary conditions:

$$T(x, 0) = T_0 = 298 \text{ K} \tag{38.3}$$

$$T(0, t) = T_1(t) \tag{38.4}$$

$$T(L, t) = T_2(t) \tag{38.5}$$

T_0 is the initial temperature of the MLI, which is equal to atmospheric temperature since aerodynamic heating not yet started. T_2 is the temperature applied on the top side of the layer of MLI (at $x = 0$) and is the temperature at the bottom side of the layer at a distance of L from the top surface, which is to be predicted and kept below safe limit.

Numerical solution of Eq. (38.1) is obtained by using ANSYS 15.0.

38.2.1 Numerical Simulation and Validation

Figure 38.2 shows the MLI specimen used for numerical simulation.

It consists of six layers of spacer separated by five reflective layers. The length and breadth of MLI is 150 mm. The thickness of the foil is 0.1 mm. The thickness of the spacer is 4 mm and the thickness of top and bottom boundaries are 1.75 mm.

The material specification and dimensions of MLI is summarized in Table 38.1. The radiative heat transfer from the spacers is negligible at atmospheric pressure (Haim et al. 2014) and the emissivity of the spacer can be neglected. The above dimensions and material specification is adopted from Tingwu et al. (2014). A cubic portion of the MLI is taken for the study purpose.

Fig. 38.2 A typical multilayer insulation sample

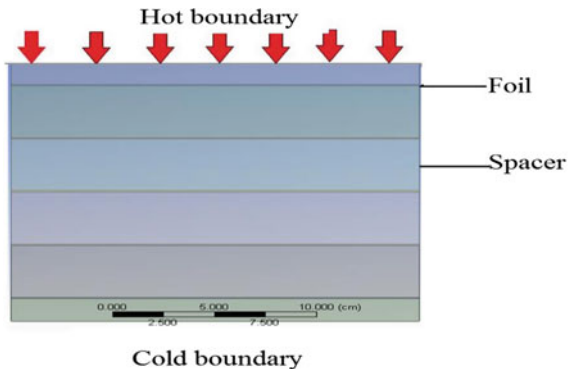


Table 38.1 Specifications of MLI

Sl. no.	Layer	Density (kg/m ³)	Thermal conductivity (W/m K)	Specific heat (J/kg K)	Emissivity	Thickness (mm)
1	Exterior insulation spacer	220	0.03	700	–	1.75
2	Interior insulation spacer	220	0.03	700	–	4
3	Gold-coated foil	1343	100	129	0.02	0.1

38.2.1.1 Boundary Condition and Grid Independence Study

Top boundary condition (temperature) of unsteady nature due to aerodynamic heating is given below as graph (Daryabeigi 2001) (Fig. 38.3).

A grid independence test was conducted before the analysis to check the quality of the mesh and its influence on the simulation. The mesh independence study is carried out in steady state thermal analysis.

Temperature of 1000 K is given at the top upper layer of MLI and the bottom layer temperature is measured at different mesh density. Figure 38.4 presents a typical mesh containing 10,000 elements. Quadrilateral method is used to generate the mesh with different edge sizing. Five mesh sizes were tested. The mesh is changed by giving edge size by 1 mm, 2 mm, 3 mm, 4 mm and 5 mm which results in a mesh with 57,141 nodes, 10,681 nodes, 5536 nodes, 2508 nodes and 1705 nodes respectively. The temperature of the bottom surface of the thermal insulation structure with different mesh densities are listed in Table 38.2. The percentage deviation from the reference point (10,000 element size is taken as reference) is the criteria for the selection of the grid.

It is found that there is a little variation among the mesh quality. Therefore, the mesh with 5 mm edge sizing is adopted for later simulation.

Fig. 38.3 Aerodynamic heating load on top surface

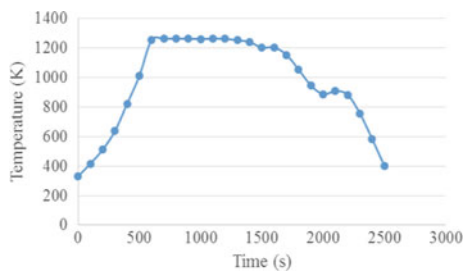
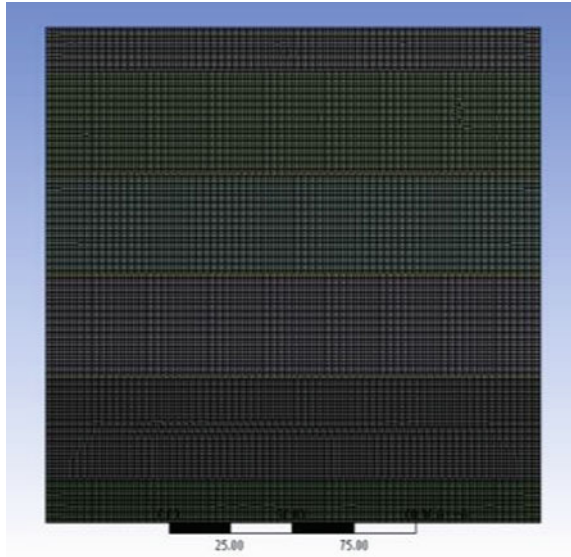


Fig. 38.4 A typical mesh**Table 38.2** Grid independence study

Sl. no.	Edge size (mm)	Number of nodes	Number of elements	Bottom layer temperature (K)	Percentage deviation (%)
1	1	57,141	10,000	542.22	0
2	2	10,681	1500	542.37	0.027
3	3	5536	735	542.32	0.018
4	4	2508	275	542.95	0.13
5	5	1705	176	542.8	0.107

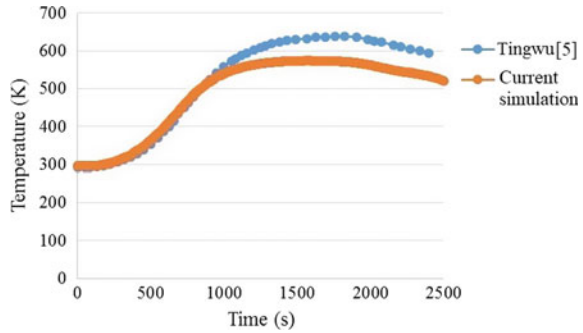
38.2.1.2 Validation

The data obtained by Tingwu et al. (2014) is used to validate the current study. Figure 38.5 is an evaluation of bottom layer temperature between the calculated results and data from literature of Tingwu et al. (2014). The model is a simplified one, which neglect the effect of convection losses to the surrounding. So deviation of result is expected from that of Tingwu et al. (2014).

38.3 Results and Discussions

The current simulation focus on the influence of emissivity of foil and arrangement of foil subjected to non-uniform heating. In real practice the emissivity of a material is a function of temperature. But the variation of emissivity in the applied load

Fig. 38.5 Validation of bottom layer temperature with the data obtained by Tingwu et al. (2014)



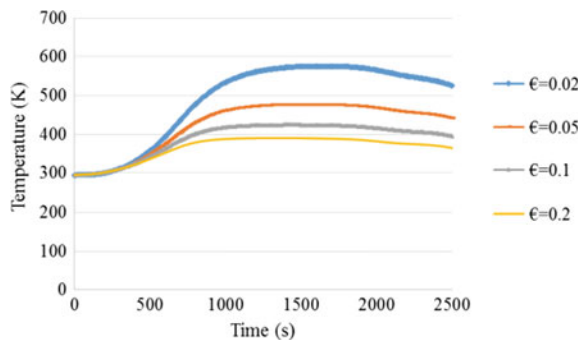
temperature is negligible, thus a constant emissivity is applied to the material for simplification. The variation of emissivity can be achieved by changing the surface finish or by changing the material.

38.3.1 Effect of Emissivity of Foil

While finding the effect of emissivity on bottom layer temperature, the total number of layers used is 6. Boundary condition used for validation is also adopted here. Figure 38.5 presents effect of emissivity of foil on bottom layer temperature. The result shows that the bottom layer temperature is inversely proportional to the emissivity of the foil at elevated temperatures above 350 K, but no evidence of influence at low temperatures. It is observed that when emissivity increases to 10 times, the bottom layer temperature reduces by around 200 K from a peak of 575 K (Fig. 38.6).

During aerodynamic heating, the temperature of the foil will be very large compared to the surrounding gas layer at a distance from the surface. This causes increase in heat transfer to the surrounding through radiation (qr''). And the

Fig. 38.6 Effect of emissivity on bottom layer temperature



radiation heat transfer will increase with increase in emissivity of the foil. So more heat is removed from the surface and lower temperature is attained at higher emissivity.

38.3.2 Effect of Spacer Configuration

Five different arrangements of spacer are studied in this section. The arrangement is obtained by changing the distance between the foils. The foil distance can be changed by varying the spacer thickness. The five layouts are as follows

- Uniform spacer thickness,
- Increasing spacer thickness towards the cold boundary,
- Decreasing spacer thickness towards the cold boundary,
- Increasing spacer thickness towards the center and
- Decreasing the spacer thickness towards the center.

Three different configuration of MLI was studied by Tingwu et al. (2014) and concluded that uniform spacer configuration shows the better resistant to heat flow. In this study, a nine layer configuration of spacer is adopted now which is different from the previous case. The spacer thickness is varied and its effects are studied. The total thickness of the foil is set to 28 mm. In Fig. 38.7a, the foil distance is uniform and the spacer thickness is 3.8 mm. In increasing spacer, the first spacer thickness is 0.35 mm and the last spacer thickness is 7.25 mm as shown in Fig. 38.7b, and the increment follows an arithmetic progression. In Fig. 38.7c, the increasing spacer configuration is reversed to make decreasing spacer configuration. In Fig. 38.7d, e, the spacer thickness is increasing and decreasing towards the center, the total thickness of the MLI is kept same as increasing spacer.

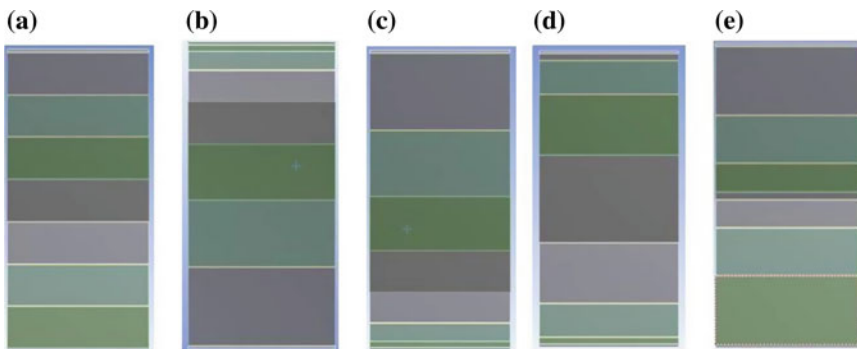
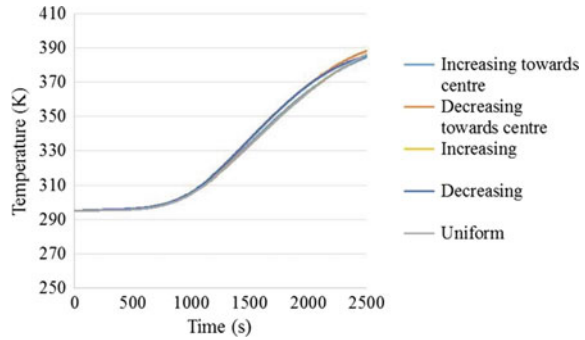


Fig. 38.7 Spacer configuration: **a** uniform, **b** increasing, **c** decreasing, **d** increasing towards center and **e** decreasing towards center

Fig. 38.8 Bottom layer temperature at different foil condition



From Fig. 38.8, it can be seen that, the temperature of all configuration is same before 1000 s. At the final state, the MLI with decreasing spacer thickness towards the center has somewhat higher temperature, while the uniform spacer has the minimum temperature among the configurations. It suggests that the spacer configuration has little effect on the bottom layer temperature. Also uniform spacer is more preferred at high temperatures for better performance.

38.4 Conclusions

In this study a one dimensional numerical model of MLI with transient heat load is studied. Some assumptions are adopted in the study for the simplification of calculations. The major findings in the study are listed below

1. As the emissivity of the foil increases, the bottom layer temperature decreases due to heat rejection to the surrounding by thermal radiation at high temperatures above 350 K.
2. The configuration of spacer or foil does not have any effect on the performance of multilayer insulation at low temperature. At higher temperature, the uniform spacer shows slightly better performance among the spacer configuration.

References

- Bapat S, Narayankhedkar K, Lukose T (1990a) Experimental investigations of multilayer insulation. *Cryogenics* 30(8):711–719
- Bapat S, Narayankhedkar K, Lukose T (1990b) Performance prediction of multilayer insulation. *Cryogenics* 30(8):700–710
- Daryabeigi K (2001) Thermal analysis and design of multi-layer insulation for reentry aerodynamic heating. In: 35th AIAA thermophysics conference. AIAA, pp 2001–2834
- Haim Y, Weiss Y, Letan R (2014) Effect of spacers on the thermal performance of an annular multi-layer insulation. *Appl Therm Eng* 65:418–421

- Huang C, Zhang Y (2013) Calculation of high-temperature insulation parameters and heat transfer behaviors of multilayer insulation by inverse problems method. *J Aeronaut* 27(4):791–796
- Krishnaprakas CK, Narayana KB, Dutta P (2000) Heat transfer correlations for multilayer insulation systems. *Cryogenics* 40:431–435
- Meseguer J, Perez Grande I, Sanz Andres A (2012) Spacecraft thermal control, Chapter 7. Woodhead Publishing Limited, Cambridge, pp 111–118 (2012)
- Sutheesh PM, Chollackal A (2018) Thermal performance of multilayer insulation: a review. In: IOP conference series
- Tingwu J, Ruiping Z, Bengt S, Gongnan X (2014) Investigation on thermal performance of high temperature multilayer insulations for hypersonic vehicles under aerodynamic heating condition. *Appl Therm Eng* 70:957–965

Chapter 39

Detachable Module for Semi-automating a Conventional Wheelchair



Ahmed Harris, Allwyn Francis, Amritha Behanan,
Arnold Fernandez, Vishnu Sankar and John M. George

39.1 Introduction

Mobility is considered one of the most important aspects of human health. However, most of the physically handicapped are dependent on the wheelchair to attain mobility. As per the reports of World Health Organization, this accounts to almost 65 million people of the global population. In majority of the cases, the mobility impaired people depend on a second person to help them manoeuvre the wheelchair. This is a huge setback to their self-confidence. The care-givers too, often, end up having lower back and shoulder injuries and other long-term health issues.

Other concerns of using manual wheelchairs include difficulty in manoeuvring through small doorways and corridors of buildings. Simple daily activities like shopping, and visiting friends grow into a demanding and difficult task and using the manual wheelchairs on rough and uneven terrains becomes close to impossible. The electric or powered wheelchairs are considered a favorable alternative to the conventional manual wheelchair models.

However, the high prices of these wheelchairs (starting INR 1.5 lakhs) make it unaffordable by the common mass. Thus, considering these aspects we introduce this new design concept for a wheelchair which has a much simpler structure compared to the current market complex versions. Automation is done so that it becomes easier for the patient to get control over his chair. Cost is another factor that influences the marketability of the wheelchair. Hence, cost of the product is reduced by using simple materials for its construction. We are planning to develop a

A. Harris · A. Francis · A. Behanan · A. Fernandez · V. Sankar (✉)
Mechanical Engineering, Rajagiri School of Engineering and Technology, Ernakulam, India
e-mail: vishnus@rajagiritech.edu.in

J. M. George (✉)
Rajagiri School of Engineering and Technology, Ernakulam, India
e-mail: johnmg@rajagiritech.edu.in

module that is simple in structure which can be fastened to the conventional wheelchair in order to make itself-propelling. The automated control system will reduce the efforts significantly with the added advantage of lesser production cost than those wheelchairs that are available in the current market.

39.2 Mechanical Design

The work involves attaching a module to a manual wheelchair using a specially designed locking mechanism. Any type of manually propelled wheelchair—even pediatric and bariatric can be made self-propelling by this attached module.

A maximum speed of 1 m/s can be achieved by this module and it consists of

- A 250 W 48 V BLDC hub motor
- A 48 V 20 A lead-acid battery
- A motor controller
- Throttle system
- Drum brake system.

The structure comprises of a wheel with a BLDC hub motor which drives the system. The motor controller controls the motor which is powered by a lead acid battery. The module has a throttle system to vary the speed and a drum brake system attached to the driving wheel. The skeleton is made using Steel alloy, which has a better strength to weight ratio and is durable when compared to lightweight Aluminum alloys. The lock is made of mild steel using CNC lathe and CNC milling machine. Mild steel has better strength to weight ratio than stainless steel, tough and malleable and low cost, but its corrosive. Other components like speedometer, battery charge indicator, head lamp, indicators and horn are also included in the module (Fig. 39.1).

Description:

The lock consists of two parts, one of which is attached to the wheelchair and the other welded to the module. The part fastened to the module is initially hooked onto

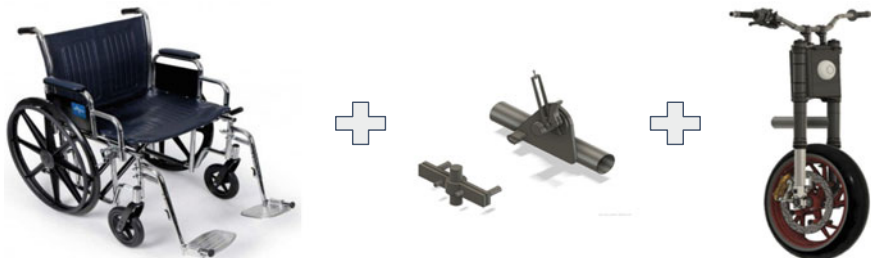


Fig. 39.1 Wheelchair, coupling locks and detachable module

the fixed part of the lock in wheelchair as shown in Fig. 39.2a. On pushing the handle bar, the driving wheel comes closer to the wheelchair and the castor wheels of the wheelchair is lifted to a certain distance so that it does not hinder the propulsion, as in Fig. 39.2b (Figs. 39.3 and 39.4).

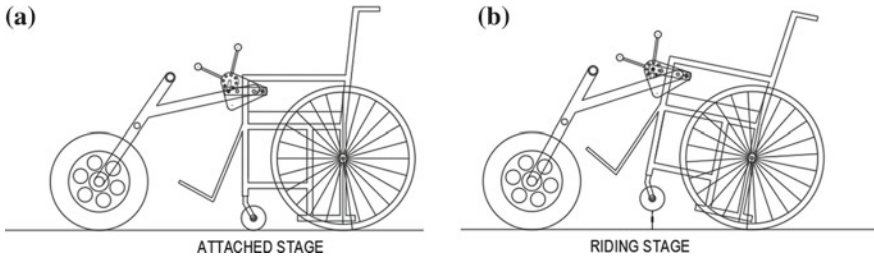


Fig. 39.2 2D sketch of the proposed wheelchair–module system

Fig. 39.3 Isometric view of coupling lock

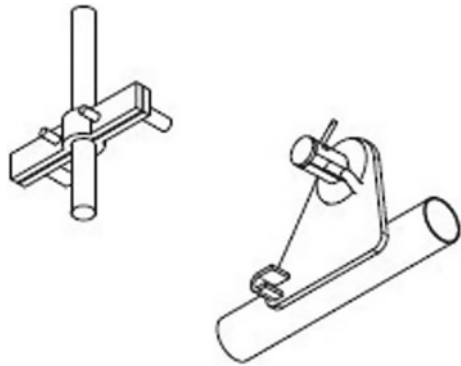
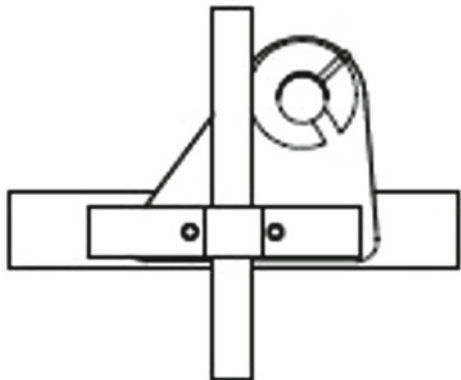


Fig. 39.4 Front view of coupling lock



39.2.1 Material Selection for Coupling Lock

39.2.1.1 Characteristics of Mild Steel

Mild steel is ductile and hard having yield strength of 250 MPa. It is a great conductor of electricity making it suitable for welding process. It has good machinability and can be machined in shaper, lathe, milling or drilling machines. Addition of carbon increases the strength of mild steel. In addition to the above parameters mild steel is comparatively less costly and easily available (Fig. 39.5).

Design Goals:

- The module must be able to propel a conventional wheelchair corresponding to the acceleration given by the user
- Less expensive
- More compact design
- Eco friendly
- Can overcome slight bumps and steepness on road
- More comfort to the user and easy accessibility.

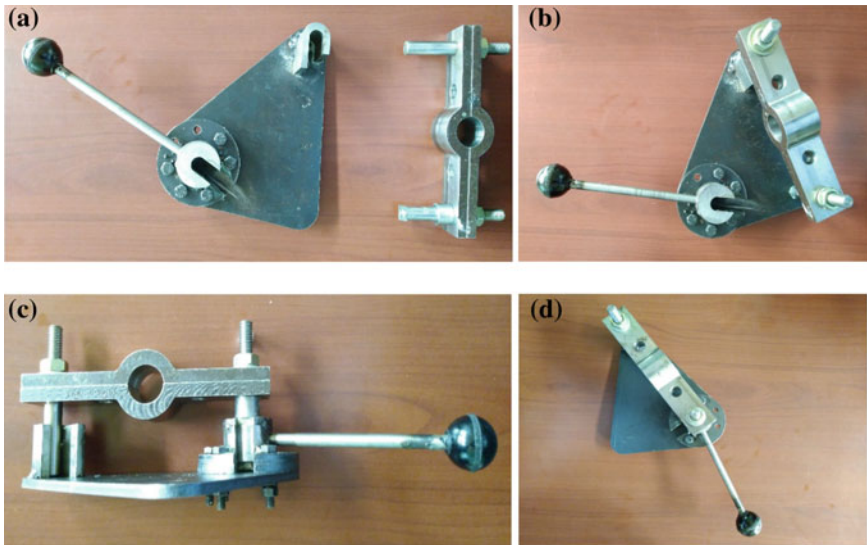


Fig. 39.5 Figure a shows the two coupling locks unattached. Figure b shows the coupling locks partially connected. Figure c is the top view of attached coupling locks and figure d shows the side view of the attached coupling lock

39.3 Electrical Design

39.3.1 Motor Selection

39.3.1.1 Drive Wheel Motor Torque Calculations

For selection of drive wheel motors for wheelchair, we have to consider a number of factors to determine the maximum torque required for propel (Chauhan 2015).

In order to choose motors capable of producing enough torque to propel the wheelchair, it is necessary to determine the total tractive effort (TTE) requirement for the wheelchair:

$$TTE [N] = RR [N] + GR [N] + F_a [N] = 88.30 + 621.88 + 200.00 = 910.18 [N]$$

where:

- TTE total tractive effort [N]
- RR force necessary to overcome rolling resistance [N]
- GR force required to climb a grade [N]
- F_a force required to accelerate to final velocity [N].

1. Rolling Resistance (RR) is the force necessary to propel the wheelchair over a particular surface. The worst possible surface type to be encountered by the wheelchair should be factored into the equation (Table 39.1).

$$RR = W_{GV} \times C_{sf} = 1471.5 \times 0.06 = 88.30 [N]$$

where:

- RR rolling resistance [N]
- W_{GV} gross vehicle weight [N]
- C_{sf} surface friction coefficient.

2. Grade Resistance (GR) is the amount of force necessary to move the wheelchair up a slope or ramp. This calculation must be made using the maximum angle or grade the wheelchair will be expected to climb in normal operation.

Table 39.1 C_{sf} values for different materials

Contact surface	C _{sf}
Concrete (good/fair/poor)	0.010/0.015/0.020
Asphalt (good/fair/poor)	0.012/0.017/0.022
Wood (dry/dusty/wet)	0.010/0.005/0.001
Snow (2 in./4 in.)	0.025/0.037
Dirt (smooth/sandy)	0.025/0.037
Mud (firm/medium/soft)	0.037/0.090/0.150
Grass (firm/soft)	0.055/0.075
Sand (firm/soft/dune)	0.060/0.150/0.300

$$GR = W_{GV} \times \sin(\alpha) = 1471.5 \times \sin(25^\circ) = 621.88 \text{ [N]}$$

where:

- GR grade resistance [N]
 W_{GV} gross vehicle weight [N]
 α maximum incline angle [degrees].

3. Acceleration Force (F_a) is the force necessary to accelerate from a stop to maximum speed in a desired time.

$$F_a = (W_{GV} \times V_{\max}) / (g \times t_a) = (1471.5 \times 4) / (9.81 \times 3) = 200 \text{ [N]}$$

where:

- F_a acceleration force [N]
 W_{GV} gross vehicle weight [N]
 G acceleration due to gravity = 9.81 [m/s^2]
 V_{\max} maximum speed [m/s]
 t_a time required to achieve maximum speed [s].

4. To verify the vehicle will perform as designed in regards to tractive effort and acceleration, it is necessary to calculate the required wheel torque (τ) based on the tractive effort.

$$\tau = \text{TTE} \times R_w \times R_f = 910.18 \times 0.15 \times 1.1 = 150.17 \text{ [N-m]}$$

where:

- τ wheel torque [N-m]
TTE total tractive effort [N]
 R_w radius of the wheel/tire [m]
 R_f friction factor that account for frictional losses between bearings, axles etc.

5. Reality Check

When the required torque has been calculated and it is necessary to check if the wheels of the wheelchair are capable enough to transmit the required amount of torque without slip. The maximum torque is given as:

$$\tau_{\max} = (\mu \times W_w \times R_w) = (0.7 \times 1471.5 \times 0.15) = 154.5 \text{ [N-m]}$$

where:

- μ coefficient of static friction
 W_w weight (normal load) on drive wheel [N]
 R_w radius of the wheel/tire [m].

For satisfactory performance of the wheelchair

$$\tau_{\max} \geq \tau = 154.5 \geq 150.17 \text{ [N-m]}$$

39.3.2 Selection of Drive Motor

The motor selection process begins with evaluating the application and ensuring the motor chosen will properly match the needs of the application. Thus, we have to consider the following factors while selecting the motor:

- Input Power Source: Voltage, frequency, current and control type
- Working Environment: Ingress Protection (IP) Rating and Temperature (indoor/ outdoor)
- Motor Specifications: Size and weight, motor life expectancy, maintenance and noise
- Motor Performance: Speed and torque, starting/stall torque, duty cycle and load profile (Table 39.2).

Characteristics Brushless DC Motors

- Variable speed operation
- High efficiency between 70 and 95% (small to large)
- High starting torque
- Requires a control to operate
- Life 20,000+ h
- Similar speed-torque characteristics to PMDC.

The performance of a BLDC motor and a PMDC (Permanent Magnet DC Motor) motor is similar. The performance curve of both shows linear progressive speed-torque from no load to stall. Although the performance curve looks identical, the efficiency and power density of the BLDC motor is superior to that of its

Table 39.2 Reference guide for motors

	Universal	DC	AC	Brushless
Voltage	AC, DC	DC	AC	AC, DC
Speed	8000–20,000+	350–6000	1200–3400	2300–3800
Horsepower	Very high	Medium	Low-medium	High
Starting torque	High	Very high	Low-medium	Very high
Efficiency	55–70%	60–70%	40–80%	65–80%
Life	Low	Medium	Very low	Very high
Speed regulation	Poor	Fair	Good	Excellent
Maintenance	High	Medium	Very low	Very low
Noise	Noisy	Medium	Quiet	Quiet

counterpart. The brushless motor has become a favorable choice as it combines the benefits of an AC induction motor and the desired speed-torque curve of a PMDC motor. In terms of its power density, the BLDC motor is second just to the Universal motor. In spite of its higher cost per motor compared to UM, PMDC, and AC; there are various applications where the BLDC motor is a cost-effective solution owing to its desirable features.

Advantages of BLDC Motors

- Totally enclosed typical
- Long life
- Low maintenance
- High power levels for size
- Works well with gearboxes
- Could be used in variable speed applications.

39.4 Analysis

In Ansys Workbench the static structural analysis was done. The analysis was done for two conditions

- The strength of the design with self-weight
- The strength of the design when a tensile force is applied.

The testing of self-weight-based analysis was done by mesh convergence test. Mesh convergence test refers to the smallness of the elements required in a model to ensure that the results of an analysis are not affected by changing the size of the mesh.

Here various meshing criteria were chosen and force was constant, which is the self-weight. The lock was fixed and force of gravity in the downward direction was applied. The mesh used were Hexadominant mesh of different density and sizing. The meshing was done with coarse, medium and fine relevance with element size of 1 mm. The results obtained through mesh convergence test prove that the design is strong and will not deform under its self-weight.

The tensile force analysis was done with Hexadominant mesh of fine relevance and element size of 1 mm. The inner faces of the coupling to the wheelchair were made fixed and the force was applied of the rod connecting the lock to the module. Different loads based on the weight of the user, the speed was applied with factor of safety of 2–3.

The maximum equivalent normal stress value from the study was found to be 225.5 MPa when a force of 750 N was applied, which is less than the yield strength of mild steel which is 250 MPa.

The results obtained by this analysis ensured us that the designed lock was strong and will not deform when operated (Figs. 39.6 and 39.7).

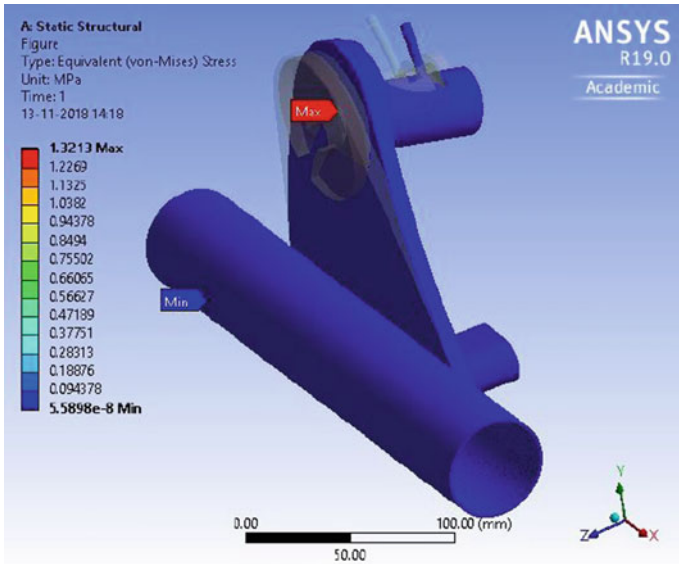


Fig. 39.6 Mesh convergence test—self-weight

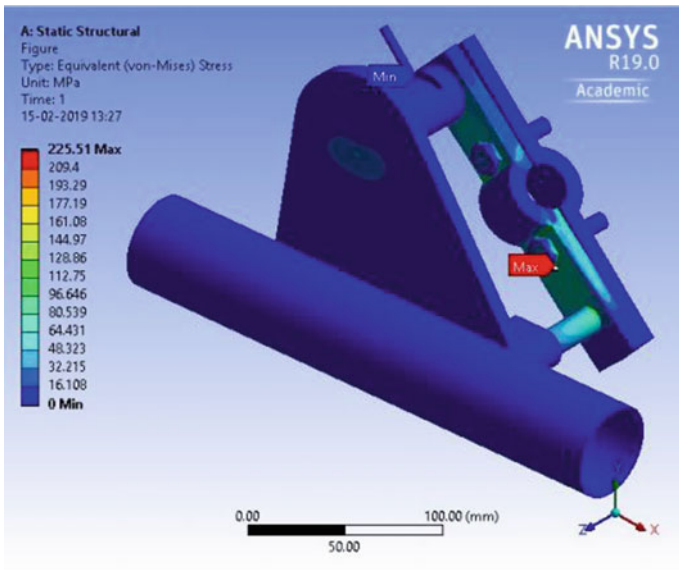


Fig. 39.7 Tensile force analysis—equivalent shear

39.5 Conclusion

The proposed work is a sustainable mode of transportation which can be used in healthcare and other sectors. The disabled need to put in significantly lesser effort to propel the wheelchair compared to a conventional wheelchair. The care-givers are also relieved of any strain in lower back, arms, shoulders and hands due to pushing a wheelchair. This system would enable its users to travel indoor as well as outdoors. However, due to cost considerations, lead-acid batteries were used for development of the prototype. An apt choice would be to make use of Li ion battery as it occupies less space and also provides higher battery power and hence higher run time.

Reference

Chauhan S (2015) Motor torque calculations for electric vehicle. *Int J Sci Technol Res* 4(8): 126–127

Chapter 40

Brainwave-Assisted Drive for Electric Vehicles



Jeffin Francis, Anupama Johnson, N. Aby Biju, Jeswant Mathew, Alan Jones Ukken, P. Jegil Jerson and Vishnu Sankar

40.1 Introduction

Worldwide about one lakh people meet their death in road accidents as a result of drowsy driving. Studies suggest that drivers with sleep duration limited to less than 4 h are far more dangerous than drunken drivers. Most of the drivers are sleep deprived and they tend to sleep off while driving. In order to avoid accidents caused under such situations, a device can be used to detect the state of the brain and enable the car to drive as the situation demands (Li et al. 2008; Yordanov et al. 2017). This is achieved by reading the neural activity of the brain. The brain contains a huge number of neurons. These neurons transfer information amongst themselves through electric charges (Chae et al. 2011). The neurons are charged by the membrane proteins which then transmit ions across the brain. When a metal electrode is placed on the scalp, the electrons perform a push or a pull action. The push or pull action causes a potential difference amidst the ions. The potential difference of the neurons is sensed by a bio-sensor and it is transmitted to the processing unit and thereby to the driving system of the vehicle. The application of this technology was conducted on a electric car (Giese et al. 1979).

40.2 System Design

40.2.1 Electroencephalogram (EEG)

The EEG wave patterns originate from the central nervous system and are classified as Alpha, Beta, Gamma, Theta, Delta waves. These patterns of wave are recognized

J. Francis · A. Johnson · N. A. Biju · J. Mathew · A. J. Ukken · P. J. Jerson · V. Sankar (✉)
Mechanical Engineering, Rajagiri School of Engineering and Technology, Ernakulam, India
e-mail: vishnus@rajagiritech.edu.in

by electrodes on the scalp of the driver as minute electrical signals. These signals are processed by initially enhancing and filtering by Low Pass Filter (LPF) and thereafter by a High Pass Filter (HPF), the differential amplifier is used to eliminate interference signals such as noise in the signal pattern. The voltage span of the signals created during the brain activity is in the range of micro voltage (peak to peak) and frequency in the range of 0.5–60 Hz. After processing the raw data, the analogue signals are converted into digital waveforms by high-resolution analogue to digital converter, thereby the microprocessor algorithm can process the controls analysing the digital waveforms.

40.2.2 Brain Computer Interface (BCI)

The BCI is a mind machine interface which reads the corresponding brainwave signals and interprets the same for the microprocessor to process on. This serves as a pathway to communicate with the car without any physical controls on the throttle and steering. BCI is not used for reading the drivers mind but rather it measures the EEG signals originating in the central nervous system.

The headset in Fig. 40.1 makes use of electroencephalography and electromyography to read the activity of the brain. A bio-sensor is attached to the probe to transmit the signals from the brain to the processor (Yordanov et al. 2017).

40.2.3 Types of Brainwaves

40.2.3.1 Alpha Waves

Alpha waves are rhythmic and repetitive patterns in the frequency range of 7.5–12.5 Hz which arises due to the synchronous electrical activity of the thalamic pacemaker cells in humans (Gupta et al. 2016). These waves connect the conscious and the subconscious mind. These waves promote deep relaxation to the brain. If the user is drunk or is under similar conditions, these waves will be generated and hence, the car will not be started, hence ensuring safety (Fig. 40.2).

40.2.3.2 Beta Waves

They are brainwaves with a frequency range of 12.5 and 30 Hz (Gupta et al. 2016). Beta waves are associated with the normal activity of the brain. Beta waves can be classified into three

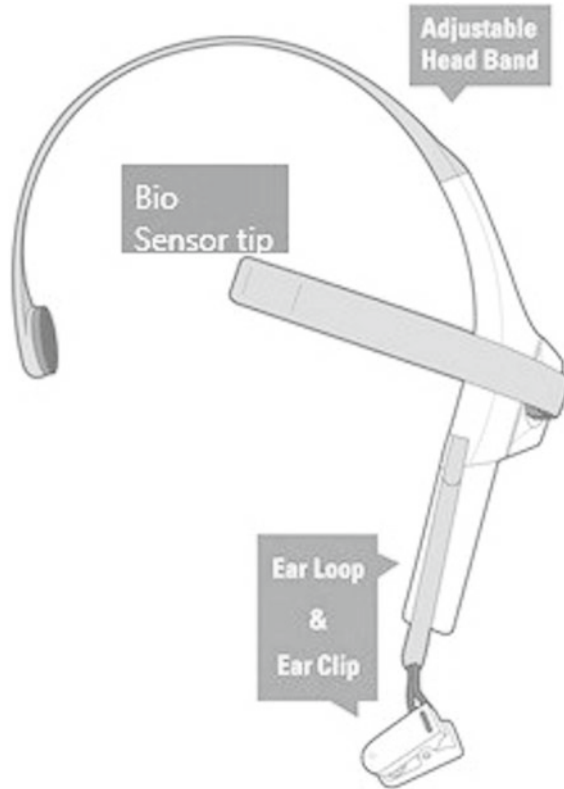
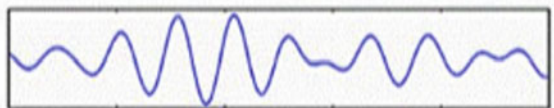


Fig. 40.1 EEG headset

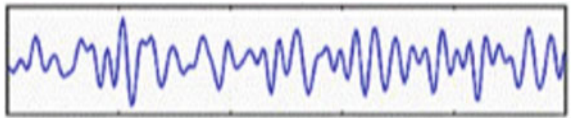
Fig. 40.2 Recording of alpha waves (Gupta et al. 2016)



- i. Low Beta Waves which range from 12.5 to 16 Hz
- ii. Beta Waves ranging from 16.5 to 20 Hz
- iii. High Beta Waves ranging from 20.5 to 28 Hz.

Having the right amount of concentration will promote the generation of beta brainwaves. These waves help the user to focus on the activity done (Fig. 40.3).

Fig. 40.3 Recording of beta waves (Gupta et al. 2016)



40.2.3.3 Gamma Waves

Gamma waves range from 40 to 100 Hz. These waves are important in learning, memory and information processing. Mentally challenged people and students with difficulty in learning tend to have a lower gamma activity in comparison to people without such difficulties.

40.2.3.4 Theta Waves

Theta waves range from 4 to 8 Hz (Gupta et al. 2016). These are rhythmic patterns that arise during sleepy conditions. While the driver is sleepy, theta waves are produced and on sensing this, the drive to the car is cut-off. There are two types of theta waves

- i. Hippocampal theta wave: These are strong oscillations and are observed in the hippocampus and similar structures of the brain in mammals other than humans.
- ii. Cortical theta waves: these waves are comparatively of low frequency. Usually, these are read from human brain cells (Fig. 40.4).

40.2.3.5 Delta Waves

They are high amplitude, low-frequency brain waves that range from 0.5 to 4 Hz (Gupta et al. 2016). They are found very often in infants and small children. Ageing tends to produce low amounts of delta waves even during deep sleep. Delta waves reach maximum during deepest levels of relaxation (Fig. 40.5).

Fig. 40.4 Recording of theta waves (Gupta et al. 2016)

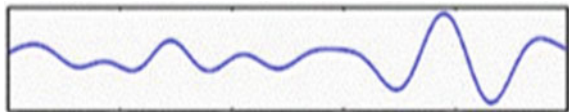
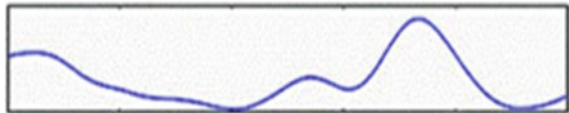


Fig. 40.5 Recording of delta waves (Gupta et al. 2016)



40.2.4 Arduino Mega Microcontroller

See Fig. 40.6.

Microcontroller – ATmega2560
 Flash Memory – 256KB, SRAM – 8KB, EEPROM – 4KB
 Clock Speed – 16MHz

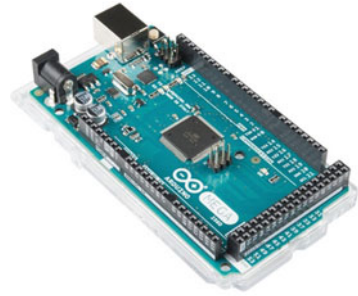


Fig. 40.6 Arduino mega

Microcontroller—ATmega2560
 Flash Memory—256 KB, SRAM—8 KB, EEPROM—4 KB
 Clock Speed—16 MHz.

40.3 Methodology

The brain activity of the driver is detected by a gadget called “Neurosky Mindwave 2 Headset”. It includes an electrode in the front portion of the drivers scalp. The values are detected by the electrode due to the electrical activity of the brain at the rate of 512 samples per seconds (SPS). The values are then transmitted via Bluetooth transmission, to the microcontroller Arduino Mega. The transmitted values are stored and instantaneously applying signal processing and conditioning we obtain the brainwaves related to the drive pattern. Depending on the levels of attention, blink and meditation level, the microprocessor algorithm is executed for different car control commands. The microcontroller recognizes the signal for navigation, sends it to the motor and steering controller as shown in Fig. 40.7.

The microcontroller connects all the wireless systems (Chae et al. 2011). The intensity change in the beta waves of the driver’s brain is used for driving the car. If the driver is sleepy or drunken, the probe will sense alpha waves produced in the brain, and the car is preprogrammed to slow down and alert the user. The signal will enable the driver to park safely, if the intensity of the alpha wave is too high (Giese et al. 1979), then the car will park automatically with the help of sensors and autonomous system drives.

The various parameters such as latency time, error in motor speed control, path/trajectory error in steering control will be analyzed through the paper.

Latency Time—The time delay between consecutive signals from the headset are measured and logged using the system clock of the microcontroller.

Motor Speed Error—The error between the intended speed as controlled using the brainwave headset and the actual motor speed is to be compared at the microcontroller and corrected using a correction factor. The measurement of the

Methodology

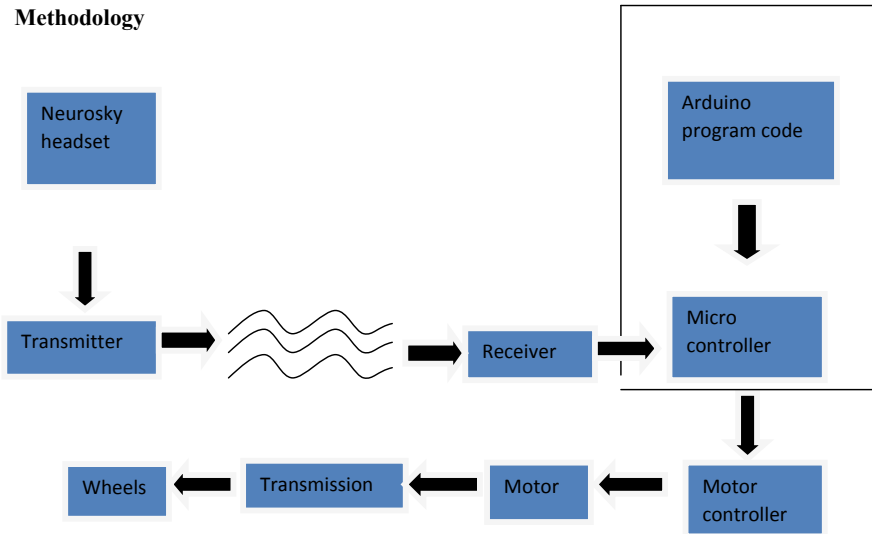


Fig. 40.7 Block diagram of the brainwave controlled electric car

motor speed is done using the hall-effect speed sensor within the motor. The correction voltage value is fed into the motor controller by the microcontroller to correct the speed of the motor.

Path/Trajectory Error—The deviation of the obtained path from the actual intended path is compared and error reduced using correction signals by the motor steering controller.

40.4 Result

The latency time (highest) was found to be 1.65 s, this causes the car controls delayed by 1.65 s causing the error in trajectory and speed of the motor. This error can be reduced by eliminating the electromagnetic interference noises. The error in speed was measured and compared with the reference signal from the microcontroller, a correction voltage value is given to the motor speed controller and the speed is corrected. During the control of an electric car using brainwave the trajectory control is the most important factor in order to avoid collision and parking during the drowsy state of the user. The trajectory error was calculated by setting an actual trajectory in the drive field and the deviation from the actual trajectory is calculated. The correction value in steering motor control is introduced to correct the trajectory. The proposed architecture without correction Figs. 40.8 and 40.9 with correction control is shown below.

Fig. 40.8 Without correction control

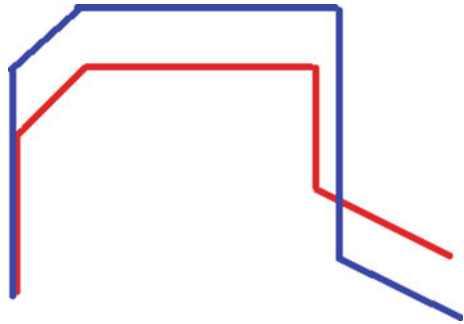
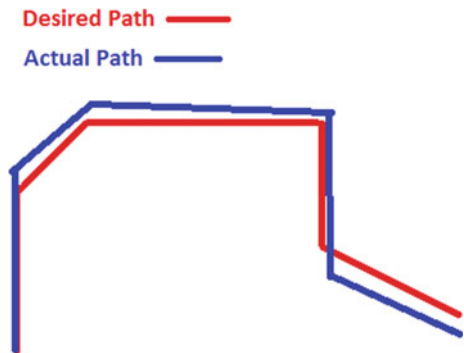


Fig. 40.9 With correction control



40.5 Conclusion

Controlling of EVs using brainwaves showed lesser chances of collision (Bi et al. 2013). During drowsy or drunken conditions of the driver, the probe sensed alpha waves, the user was warned and the necessary steps as mentioned above were completed. Potentially this can be used by drivers during night time for their commutation. The error due to latency time can be reduced by improving the communication devices and reducing the electromagnetic interference. The proposed architecture with correction controls shows potential for future vehicles to be controlled using brainwave technology for reducing accidents and vehicle control for differently abled people.

References

Bi L, Fan X-A, Liu L (2013) EEG based brain-controlled mobile robots: a survey. *IEEE Trans Hum-Mach Syst* 43:161–176. IEEE. <https://doi.org/10.1109/tsmcc.2012.2219046>

Chae Y, Jo S, Jeong J (2011) Brain-actuated humanoid robot navigation control using asynchronous brain-computer interface. In: *Proceedings of the 5th international IEEE EMBS*

- conference on neural engineering. IEEE, pp 519–524. <https://doi.org/10.1109/ner.2011.5910600>
- Eswari C, Ramya SK (2011) Biometrics using headgear to scan brainwaves. In: 2011 national conference on innovations in emerging technology. IEEE. <https://doi.org/10.1109/ncoiet.2011.5738841>
- Giese DA, Bourne JR, Ward JW (1979) Syntactic analysis of the electroencephalogram. IEEE Trans Syst Man Cybern 9:429–435. IEEE. <https://doi.org/10.1109/tsmc.1979.4310255>
- Gupta A, Ramdinmawii E, Mittal VK (2016) Significance of alpha brainwaves in meditation examined from the study of binaural beats. In: 2016 international conference on signal processing and communication (ICSC). IEEE, pp 484–489. <https://doi.org/10.1109/icspc.2016.7980629>
- Isa IS, Zainuddin BS, Hussain Z, Sulaiman SN (2014) Preliminary study on analyzing EEG alpha brainwave signal activities based on visual stimulation. In: International conference on robot PRIDE 2013–2014—medical and rehabilitation robotics and instrumentation, ConfPRIDE 2013–2014, vol 42. IEEE, pp 85–92. <https://doi.org/10.1016/j.procs.2014.11.037>
- Jiang Y, Hau NT, Chung W-Y (2017) Semi-asynchronous BCI using wearable two-channel EEG. IEEE Trans Cogn Dev Syst 10:681–686. IEEE. <https://doi.org/10.1109/tcds.2017.2716973>
- Kerrin ZA, Aunon JI (1990) Man-machine communications through brain—wave processing. IEEE Eng Med Biol Mag 9:55–57. IEEE. <https://doi.org/10.1109/51.62907>
- Leeb R et al (2006) Walking by thinking: the brainwaves are crucial, not the muscles!. Presence 15:500–514. IEEE. <https://doi.org/10.1162/pres.15.5.500>
- Li Y, Wang C, Zhang H, Guan C (2008) An EEG-based BCI system for 2D cursor control. In: 2008 International joint conference on neural networks. IEEE, pp 2215–2220. <https://doi.org/10.1109/ijcnn.2008.4634104>
- Yordanov Y, Tsenov G, Mladenov V (2017) Humanoid robot control with EEG brainwaves. In: The 9th IEEE international conference on intelligent data acquisition and advanced computing systems: technology and applications. IEEE, pp 238–242. <https://doi.org/10.1109/idaacs.2017.8095083>

Chapter 41

Suitability of an LRT Connecting Thoppumpady and Goshree



Hridya Mary Joseph, Megha Jose Kandappassery, K. R. Malavika, Prinu Varkey and Deepthi I. Gopinath

41.1 Introduction

Growing concerns about environment, oil depletion, and traffic congestion call for a fresh look at mass transit systems—specifically non-polluting, low noise, non-oil-consuming, and high-speed electric transit. Indian cities are growing rapidly. There is a need to direct growth in a planned manner with adequate attention to the transport system at early stages in their development. Cities are witnessing fast growth in the number of personal motor vehicles, with severe congestion and pollution being the most visible manifestation of the growth in the number of motor vehicles. Efforts at remedying the situation will need to focus on improving the public transport system. In several cities this would require implementation of Mass Transit systems such as metro rail, bus rapid transit, light rail transit, etc.

Mass Rapid Transit Systems in urban areas not only facilitate easy and quick movement of people but also have a positive impact on the economic growth and quality of life. This results in increased income and various benefits to the society like reduced external cost due to reduction in traffic congestion, road and parking cost, transport cost and per-capita traffic accidents. Mass Rapid Transit Systems tend to reduce per-capita vehicle ownership as well as usage and encourage more compact and walkable development pattern which provide various benefits to the society.

Due to rapid urbanization, trips in growing urban areas have enormously increased. In fact, providing bus transit system as a public transport facility is not sufficient to fulfil this increased demand. To deal with such demand **Light Rail Transit (LRT)** (refer Fig. 41.1) will be a good solution. It is relatively cheap to

H. M. Joseph · M. J. Kandappassery (✉) · K. R. Malavika · P. Varkey · D. I. Gopinath
Rajagiri School of Engineering and Technology, Ernakulam, Kerala, India
e-mail: meghajose2015@gmail.com



Fig. 41.1 Light rail transit (LRT) (https://www.transit.wiki/Sacramento_RT_Light_Rail)

construct and is a pollution free mode. It is flexible and hence can be operated on all types of Right of way (ROW) as per traffic condition. In view of the rising concern over the viability of costly metro rail projects, especially in smaller cities, the Centre is planning to promote Light Rail as an alternative mass rapid transport system (MRTS) in urban areas (Comprehensive Mobility Plan for Greater Kochi Region 2016).

41.2 Existing Scenario in Kochi

Kochi city is blessed with connection to neighboring parts of southern India by all major modes of transportation like road, rail, air and water. The city is linked to other states by strategically placed three National Waterways, an international Airport, and Cochin Port along with the major highways namely NH 17, NH 47, and NH 49. RITES have done a survey in 2001 for the preparation of a report on the comprehensive study for the transport system in Greater Cochin area. Its analysis reveals that

- The buses contribute about 14% of the vehicular traffic and carry 73% of the Passenger traffic;
- The share of cars in terms of vehicular trips is about 38% carrying 15% of passenger trips;
- Two wheelers contribute 35% of vehicular traffic (considering a population of 1 lakh, two wheelers contribute to about 35,000. By assuming a mode shift of

70%, 24,500 two wheelers will shift to public transport) and 8% of passenger traffic;

- Auto rickshaws constitute about 13% of vehicular traffic and 4% of passenger trips.

41.3 Proposed Route

The proposed stretch extends from Thoppumpady to Goshree Chathiyath Road (refer Fig. 41.2). This will connect major centers like Naval Base, Thevara, Jos junction, Ravipuram, MG road, Banerji Road and High Court. It has an intersection with metro at MG road. At present there are 20 bus stops in the stretch from Thoppumpady to Goshree (13 km) which reduces the comfort of the commuters due to the frequent stops. For the purpose of Transportation studies, the route was divided into four stretches namely: Thoppumpady-Thevara (5 km),

Fig. 41.2 Proposed alignment for Light rail transit (LRT)



Thevara-Medical Trust (1.9 km), Kacheripady-High Court (3.5 km) and High court-Goshree (2.6 km)

41.4 Data Collection and Analysis

In transportation planning, data collection is the most important and the very foundation on which the entire project rests. The collected information is used to understand the current state of transportation system and the community's transportation needs (National Transport Development Policy Committee 2012).

Following transportation studies were undertaken to meet the above objectives:

1. Traffic Volume Count (TVC)
2. Road Inventory Survey
3. Population Forecast and Accident Data
4. Boarding and Alighting Survey

41.4.1 Traffic Volume Count (TVC)

The main objective of the survey was to count the number of classified vehicular volumes in order to arrive at an estimate of people per hour per direction which in turn provided a clear picture of existing traffic volume. The scope of the survey was to define the relevant stretches and identifying suitable midblock sections and to count the number of vehicles crossing the midblock section in each direction during the morning and evening peak hour period of 3 h (Data Collection and Analysis for Public Transport 2016).

Traffic Volume Count was carried out at four midblock sections of the stretches namely: Thoppumpady-Thevara, Thevara-Medical Trust, Kacheripady-Highcourt and Highcourt-Goshree (refer Fig. 41.3). Traffic Counts were conducted on normal working days for three hours during the morning and evening peak hours.

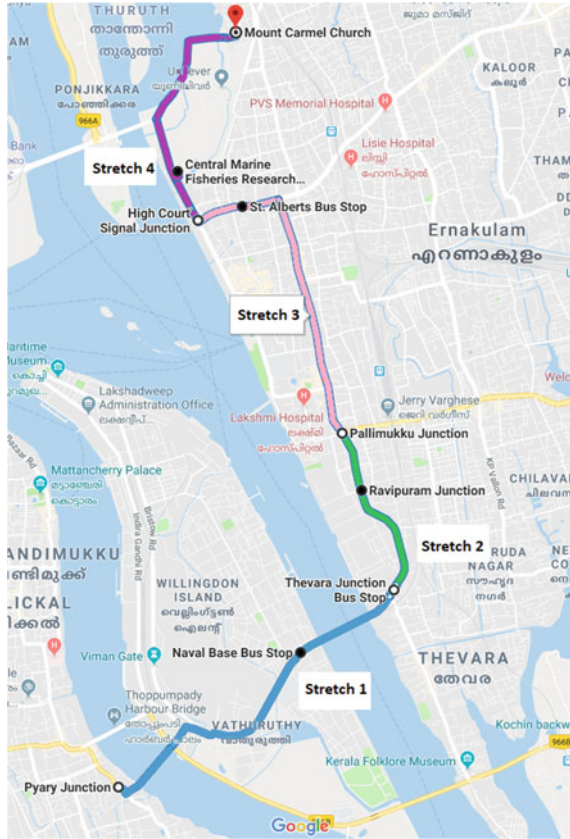
In all locations, bi-directional counts were carried out by vehicle type such as, Cars, Buses, Two wheelers, Bicycles, LCV, MAV, Trucks, Tempo Travelers, Auto Rickshaws, Other types, etc.

After the required data was collected, all types of vehicles were converted into passenger car units by using those recommended by Indian Roads Congress (IRC). The findings are represented in Table 41.1.

The four midblock locations chosen were Naval Base (Thoppumpady- Thevara), Ravipuram (Thevara-Medical Trust), St. Albert's (Kacheripady-Highcourt) and CMFRI (Highcourt-Goshree).

From Table 41.1 the traffic composition for different midblock sections were obtained and the total vehicular traffic for different stretches were identified. The

Fig. 41.3 Map of stretches for Traffic Volume Count Survey



highest traffic flow was observed at Ravipuram. The data obtained TVC survey was used to calculate PPHPD as shown in Table 41.8.

41.4.2 Road Inventory Survey

In this survey details like number of lanes, median lengths, footpath and drain availability and road width, parking provisions, etc., was collected.

Road Inventory survey was carried out through the proposed route while detailing several roadway features which includes pavement width, footpath and drain availability, roadside parking provision, median lengths, number of lanes, etc. (Data Collection and Analysis for Public Transport 2016).

The road under study was found to comprise of mainly two lanes and four lanes, as shown in Table 41.2. Majority of the roads in the proposed routes have medians as shown in Table 41.3.

Table 41.1 Traffic observed at midblock location

Sl. no	Location	Direction	Count		Total	
			Vehicle	PCU	Vehicle	PCU
1	Naval base	Thoppumpady to Thevara	8796	6206.5	13,905	10,505
		Thevara to Thoppumpady	5109	4298.5		
2	Ravipuram	Thevara to Medical Trust	10,333	7709.5	15,401	11,973
		Medical Trust to Thevara	5068	4263.5		
3	St. Albert's	Kacheripady to High Court	6011	5574	12,238	11,069
		High Court to Kacheripady	6227	5495		
4	CMFRI stop	High Court to Goshree	4185	3840.5	12,561	10,398
		Goshree to High Court	8376	6557.5		

Table 41.2 Type of carriageway

No of lanes	Divided/ Undivided	Percentage (%)
Two lane	Undivided	38.64
	Divided	0
Four lane	Undivided	0.16
	Divided	61.19
More than four lanes	Undivided	0
	Divided	0
Total		100

Table 41.3 Availability of median

Median	Percentage (%)
Present	56.65
Absent	43.34
Total	100

Footpaths are available in most roads in the proposed route under study (refer Table 41.4). Table 41.5 shows the percentage of different road width available.

From the road inventory survey, majority of the roads were two lanes undivided and four lane divided and medians comprise of 56.65% of the total length of the route. Around 34% of the roads have a width of 12–18 m which makes land acquisition a priority in these areas. Around 32% of the roads have a width in the range of 18–24 m.

Table 41.4 Availability of footpath

Footpath	Present (%)	Absent (%)
LHS	56.72	43.27
RHS	71.43	28.56

Table 41.5 Percentage of different Road width available

Row (m)	Length (km)	Percentage (%)
<10	2.44	20.04
10 to 12	1.58	12.98
12 to 18	4.18	34.34
18 to 24	3.84	31.55
>24	0.13	1.06
Total		100

Table 41.6 Population forecast

Year	2015	2018	2020	2025	2035
PPHPD (CMP)	9800	10,143	10,483	11,000	13,200
Route ridership	2570	3671	4405	6240	9910

41.4.3 Population Forecast and Accident Data

The population in the year of 2035 was forecasted to obtain 9910 PPHPD in the route under study using the known population in the region of Kochi from the Comprehensive Mobility Plan (CMP 2016). The detailed population forecast is shown in the Table 41.6. It is clear that over the years the ridership in the route will keep increasing. Considering such an increase along with the almost stagnant number of buses due to restrictions in obtaining a route permit, the number of buses proved to be insufficient to meet the demand of the future population. In such a scenario, a fresh look to a new mode of transport is necessary. For this, Mass Rapid Transit systems (MRTS) is a potential solution.

From the accident data, shown in Table 41.7, the number of accidents and deaths have reduced marginally over the years 2015–2017. By introducing a system such as a MRTS which usually has its dedicated right of way, the number of accidents can be reduced further since there is no probability of collision with other vehicles. Moreover, most MRTS are electrically powered and hence, is a more eco-friendly mode of transport.

Table 41.7 Accident data

Year	Total accidents	Total deaths
2015	2561	2889
2016	2573	2764
2017	2503	2737

Table 41.8 Up line and down line sectional load

Vehicles	Up line (T-G)	Down line (G-T)
Two Wheeler	5124.11	3233.3
Auto Rickshaw	1014.3	1102.5
Car	1858.85	2274.8
Bus	1121	1298
Total	9118.26	7908.6
PPHPD (forecasted)	10941.912	9490.32
PPHPD (mode shift)	7659.3384	6643.224

41.4.4 Boarding Alighting Survey

The survey was to estimate the number of people boarding and alighting buses from major bus stops along the proposed route and using the data to analyze the existing ridership and determine locations having greatest transit demand. The survey was conducted for 3 h during morning and evening peak hours at various bus stops on the specified route (Data Collection and Analysis for Public Transport 2016). The information regarding time, vehicle registration number, number of people boarded and alighted, bus occupancy, route and direction were collected. 20 bus stops across the study area are selected for the survey. The Table 41.8 shows the PPHPD calculation from the TVC survey and BAS.

From the Boarding Alighting survey and Traffic Volume count survey, up line sectional load has a volume of 7659 PPHPD and the down line sectional load has a volume of 6643 PPHPD. The design PPHPD is taken as the maximum of both direction, i.e., 7659 which is to be referred in relation to the design PPHPD values for other modes of Mass Rapid Transit Systems as in Table 41.9. For the calculation of PPHPD, a mode shift of 70% of people from private transport to public transport is used as obtained from CMP (2016).

41.5 Preparatory Works for MRTS

A mass rapid transit system (MRTS) that assures on timely arrivals and departures has often been cited as the single most important factor that improves the quality of life of people in cities. The preparatory work includes widening of a few roads and construction of flyovers. The Light Rail Transit is proposed to be aligned through the center of the roads giving sufficient space on either sides for one lane each for to and fro movements of other vehicles. At other major junctions like St. Albert's, Jos Junction, Ravipuram, Cochin Shipyard Thevara, Pyari and Thoppumpady the width is approximately between 14 and 16 m, where the one lane combination is feasible. The Goshree-walkway, High Court Junction road, MG road till metro has a width of about 20–22 m which can be utilized to convert the usual one lane combination with the LRT into a two-lane combination. Currently there are two major bridges

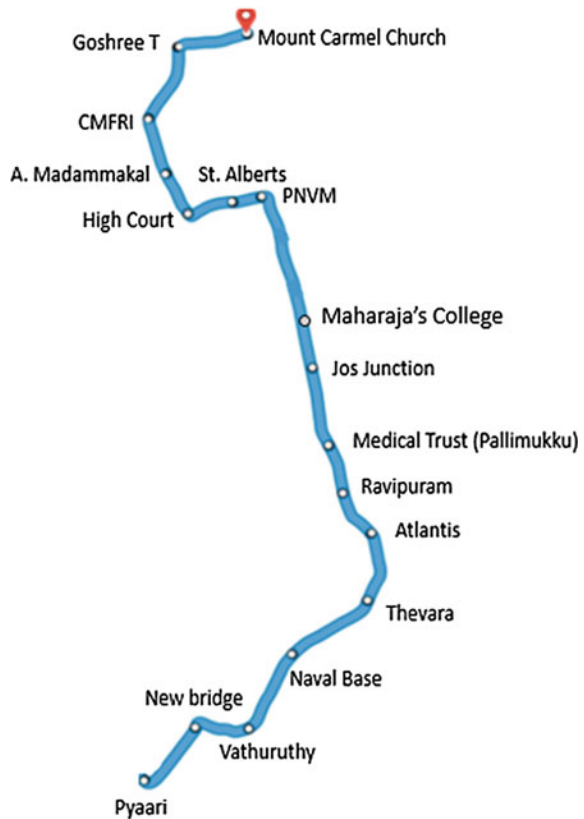
Table 41.9 Design PPHPD for different mode of mass transit

Mode	Design PPHPD
Metro rail	$\geq 15,000$
LRT	$\leq 10,000$
Mono rail	$\leq 10,000$
BRT	≥ 4000 up to 20,000

along the proposed route—The Venduruthy bridge (11 m) and BOT bridge (13 m) both being two lane undivided roads and roads from Thevara junction to Venduruthy Bridge and after the Pyari junction are the smallest with about 8 m width making land acquisition a priority in order to meet the LRT requirement of having a section of at least 22 m.

The stations for the LRT is suggested such that it connects all the bus stops. A map representing the stations is given below in Fig. 41.4. The depot is planned at the Pyary Junction and the various stations from Goshree to Thoppumpady are

Fig. 41.4 Suggested stations for proposed route



planned in consideration to reduce traffic, connect major junction, and provide access to school, college and workers to facilitate proper public transport utilization in Kochi.

41.6 Conclusion

The city has several corridors with demands ranging from a few hundred trips to several thousand trips per hour that need to be served by an MRT. For an economic network, it is necessary that the capacity of chosen mode matches the future project demand level in a corridor. Thus, alternative modes of mass transit may be needed as appropriate to each corridor. The Table 41.9 (National Transport Development Policy Committee (NTDPC) 2012) shows the PHPDT of various MRT.

From the study conducted, the calculated PPHPD is of 7659 and is found to be less than or equal to 10,000 and hence, a Light Rail Transit (LRT) is suitable for the route Goshree Chathiyath road to Thoppumpady. It is also found that there is an overlapping of 1.8 km of Metro with the proposed route for LRT at Jos Junction-Mg Road (Alapatt Heritage), since it overlaps for a distance less than 2 km it is permissible. LRT requires less road space (2–3 lanes) than BRT (three–four lanes) because overtaking facility is not needed and one island platform will suffice against two platform for BRT, one in each direction. Unlike Metro the cost for construction for an LRT is also less. Metro needs approximately Rs. 300 Cr/Km and LRT cost Rs. 100 Cr/km. LRT does not have much waiting time too, people can walk and board through line of sight from street level. Therefore it can be concluded that a Light Rail Transit (LRT) is a mode of mass transit that is suitable for the proposed route from Goshree Chathiyath Road to Thoppumpady that will help to expand Kochi's growing transit system; facilitating smooth travel of large numbers of people comfortably and conveniently.

References

- Comprehensive Mobility Plan for Greater Kochi Region (2016) Urban Mass Transit Company Limited, KMRL
- Data Collection and Analysis for Public Transport (2016) EMBARQ, India
- Institute of Urban Transport (2013) Modern trams (light rail transit)—for cities in India, India
- IRC SP 041 Guidelines for the design of at-grade intersections in rural and urban areas
- National Transport Development Policy Committee (NTDPC) final report (2012)
- Sanghi D, Variya HR (2013) Light rail transit-today's need for developing cities in India. *Int J Sci Res (IJSR)* 4(3):596–601

Chapter 42

Parameter Study of Electric Vehicle (EV), Hybrid EV and Fuel Cell EV Using Advanced Vehicle Simulator (ADVISOR) for Different Driving Cycles



P. K. Prathibha, Elizabeth Rita Samuel and A. Unnikrishnan

42.1 Introduction

In the present scenario of the world, transportation sector is the largest user of energy. At the present usage of oil, on a worst come situation the reserves will last hardly 35 years. Eventually it will give rise to exorbitant price hikes to oil and thus the transportation based on oil and other fossil fuels will not be economically viable. Another major concern is the global warming as a result of release of green house gases when fossil fuels are burnt which leads to myriad of problems like climate change and rising sea levels which could destroy coastal cities of the world. Consequently it prioritizes the necessity to develop clean, efficient and environment friendly urban transportation system. Thus Electric Vehicles (EVs) are attaining great importance and will dominate the clean vehicle market (Larminie 2003).

The major components of an EV are the motor, controller, power source and transmission. Electrochemical batteries are the traditional source of energy in EVs. Alternative energy sources are also being developed for zero emission vehicles. The limited range, limited life cycle as well as high cost of battery-driven EVs prompted the search for fuel cells, ultra capacitors and flywheels.

The development of the HEV was initiated by a number of auto industries to overcome the battery and range problem of pure EVs. An HEV is a combination of gasoline engine with an electric motor. The electric motor is used to improve the energy efficiency and vehicular emissions. The extended range capability is provided by Internal Combustion Engine (ICE). The cost of EVs and HEVs are expected to be high until production volume increases significantly.

P. K. Prathibha (✉) · E. R. Samuel · A. Unnikrishnan
Rajagiri School of Engineering and Technology, Kakkanad, Cochin, Kerala, India
e-mail: prathibhapk@rajagiritech.edu.in

© Springer Nature Singapore Pte Ltd. 2020
H. Drück et al. (eds.), *Green Buildings and Sustainable Engineering*,
Springer Transactions in Civil and Environmental Engineering,
https://doi.org/10.1007/978-981-15-1063-2_42

Depending on the configurations of drive train, HEVs can be classified as

1. Series hybrid
2. Parallel hybrid
3. Series- parallel hybrid and
4. Complex hybrid

The series hybrid drive train is mostly employed in heavy commercial vehicles, military vehicles and buses since large vehicles are having ample space for the huge engine/generator system. But in parallel hybrid vehicle, both engine and electric motor directly supply torque to the driven wheels and no energy form conversion occurs, hence energy loss is less. Also in parallel HEV, generator is not needed and smaller traction motor is used thereby compactness is achieved. Therefore, majority passenger cars use this configuration. In the series-parallel hybrid system, features of both series and parallel HEVs are incorporated. Both series-parallel and complex HEV is having a complex control system (Ehsani et al. 2004). In this paper, parallel HEV configuration is evaluated in ADVISOR.

Fuel cell Evs can be a suitable alternative to battery Evs, serving as Zero Emission Vehicles (ZEVs) without the range problem. A battery storage system is necessary to supply the power during transient and overload conditions and also to absorb the regenerative braking energy.

For any vehicle, the important performance constraints are initial acceleration, cruise speed, gradability and driving range. In this paper, the above-mentioned various parameters of EVs, HEVs and Fuel cell EVs are studied for UDDS (Urban Dynamometer Driving Schedule) and CYC_US06HWY (Highway) driving cycles using Advanced Vehicle Simulator (ADVISOR) software which works in MATLAB platform.

42.2 ADVISOR Simulation Tool

The U.S. Department of Energy (DOE) and the National Renewable Energy Laboratory (NREL) developed ADVISOR in 1994 as an analysis tool for vehicle design. It is a model written in the widely accepted MATLAB/Simulink environment which enables simulation and analysis of conventional as well as advanced vehicles. ADVISOR tests the impact of variations in vehicle components or other changes that might affect vehicle performance parameters. By selecting vehicle component types, sizes, and parameters the user can alter simulation results. It is flexible enough to model specific components and vehicle configurations for the needs of most users (Markel et al. 2002).

The major benefits of ADVISOR are

1. It reduces testing time to evaluate various vehicle power train configurations
2. Provides a shared simulation platform for the government and industry
3. Assists the automobile industry to manufacture fuel efficient vehicles and its components

In ADVISOR there are three main Graphical User Interfaces (GUIs) that guide the user in the simulation process. The GUIs enable interaction with the input and output data available in the MATLAB workspace. The vehicle model is illustrated graphically using block diagrams and the results can be obtained from the results window. In Fig. 42.1, the ADVISOR vehicle input window is shown where the user can build the vehicle of their interest. Drop down menus are utilized to take various vehicle configurations and components. The size of a component can be changed by editing the characteristic value displayed in the boxes on the top right end of the screen. Various vehicle configuration parameters can be saved and the “continue” button leads them to the simulation setup screen. In Fig. 42.2, simulation parameter screen is shown, where the user defines various drive cycle parameters. Major events that can be simulated include various drive cycles, and acceleration and grade tests. Again, at the right side of the window, the user can choose various drive cycles and define the simulation parameters and information about the selections which is provided at the left side of the screen (Saleki et al. 2017).

The vehicle performance can be reviewed in the results window shown in Fig. 42.3, where fuel economy and emissions are displayed. It can choose a large number of output options related to speed and torque, fuel consumption, vehicle

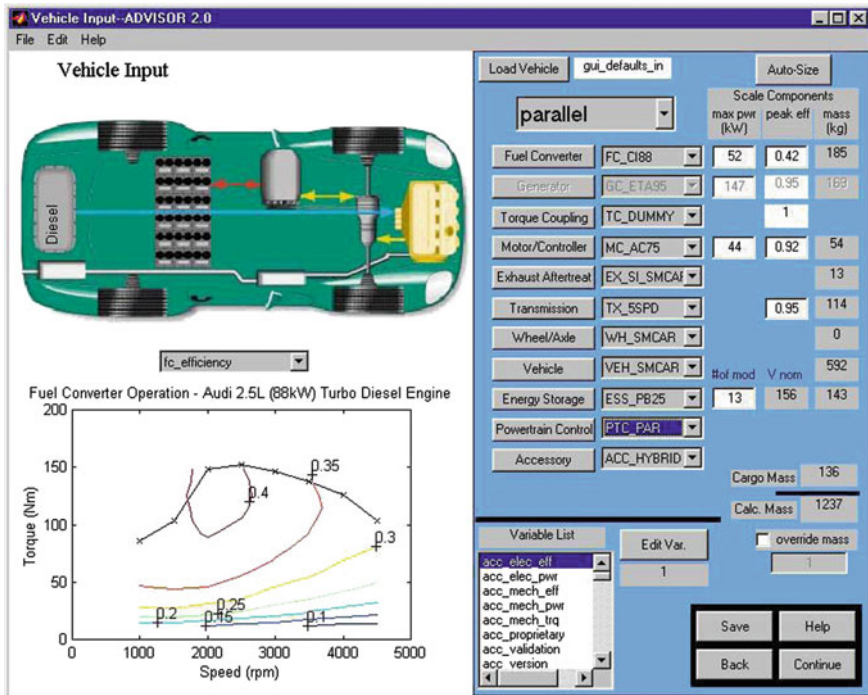


Fig. 42.1 ADVISOR vehicle input screen

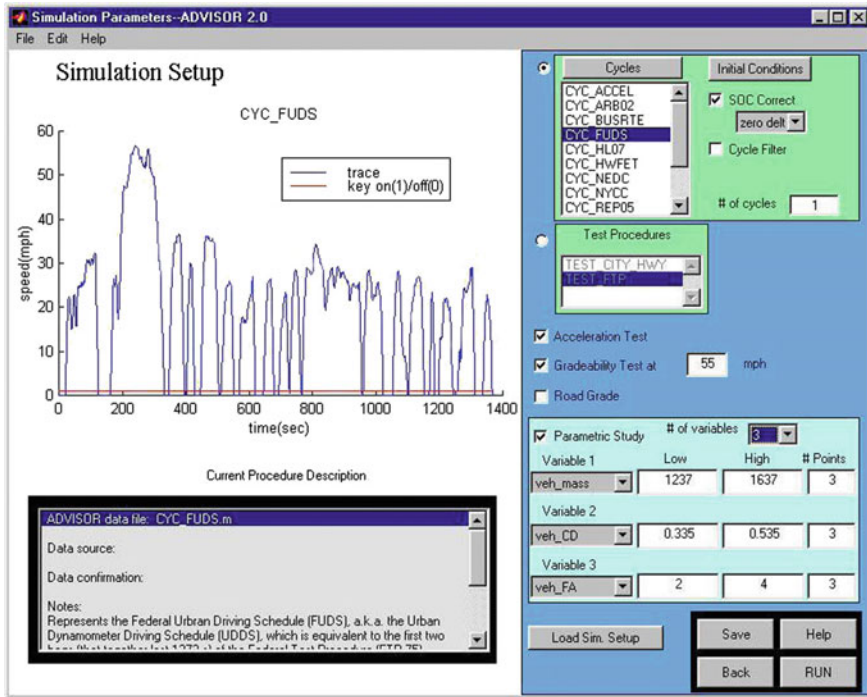


Fig. 42.2 ADVISOR simulation set up screen

emissions, battery State of Charge (SoC) and various other parameters, maximum four parameters can be plotted simultaneously (Wipke et al. 1998).

42.3 Pure EV

Currently, industry and academia are struggling to overcome the challenging barriers that hinder widespread use of electric vehicles. Some of the major concerns to overcome are the lifetime, energy density, power density, weight and cost of battery packs. EVs employ an electric motor for tractive effort and chemical batteries, fuel cells, ultracapacitors, and flywheels for their corresponding energy sources.

The concept of EV is essentially easy to understand and is indicated in Fig. 42.4. The vehicle consists of an energy storage system, an electric motor and controller. The battery is recharged from the electricity mains via a plug and a battery charging unit that can be either carried on board or may be fitted at the charging point. The power supplied to the motor and the vehicle speed is controlled by the motor controller. Figure 42.5 shows pure EV in ADVISOR software and the block diagram representation of EV in ADVISOR is shown in Fig. 42.6.

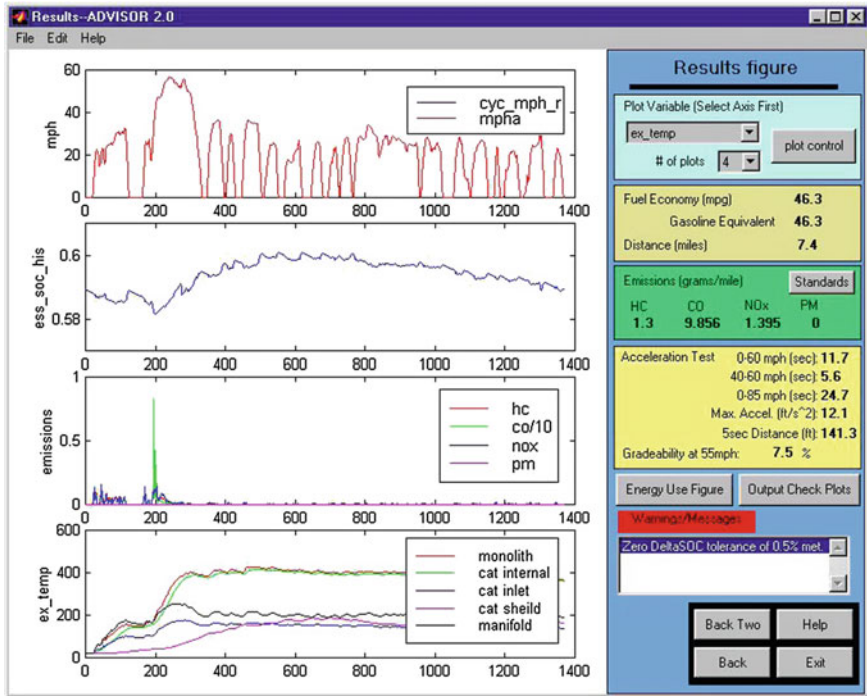
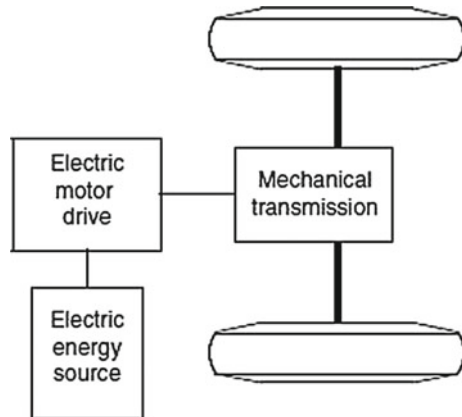


Fig. 42.3 ADVISOR results screen

Fig. 42.4 Primary EV power train



In the result window of ADVISOR for pure EV simulation, the speed in miles per hour (mph), Battery State of Charge (SoC) and emissions for Urban and Highway drive cycles are obtained which are shown in Figs. 42.7 and 42.8.

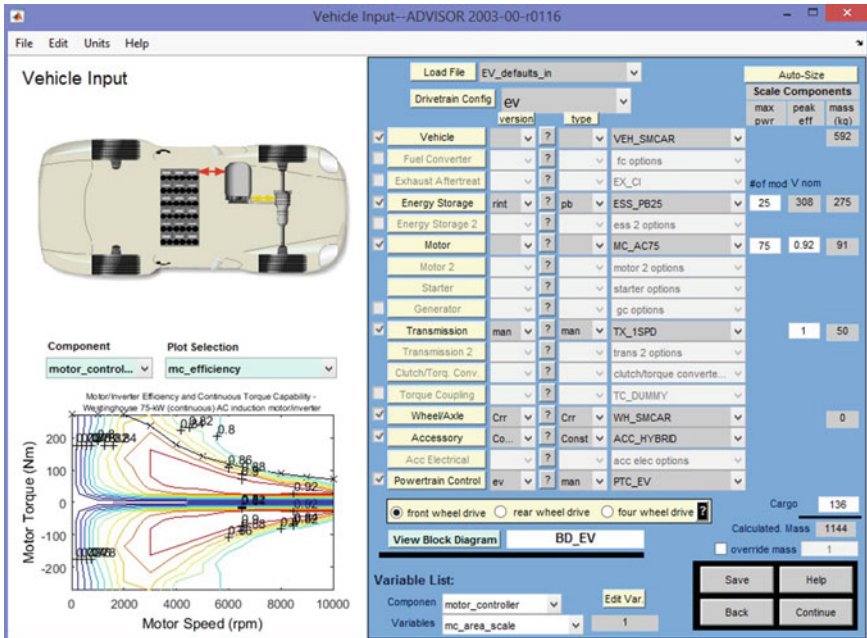


Fig. 42.5 Pure EV in ADVISOR

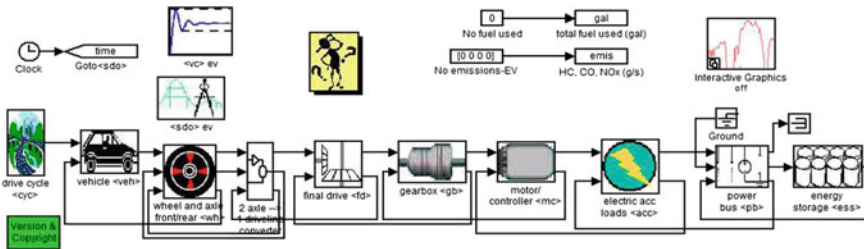


Fig. 42.6 Block diagram representation of EV in ADVISOR software

For urban drive cycle, frequent stop/go operation will be required and from Fig. 42.7 it is clear that totally there are 17 stops and maximum speed achieved is only 56.7 mph. In comparison to the highway drive cycle in Fig. 42.8 there is only single stop for the vehicle and maximum speed is 80.3 mph. State of Charge (SoC) of battery is the ratio of remaining capacity to the fully charged capacity. From SoC curve, it is evident that for highway drive cycle it is poor as the regenerative braking is not that much effective because of lesser number of vehicle stops. EV is shown to be a ZEV as there are no emissions obtained in the analysis and thus it becomes a promising technology.

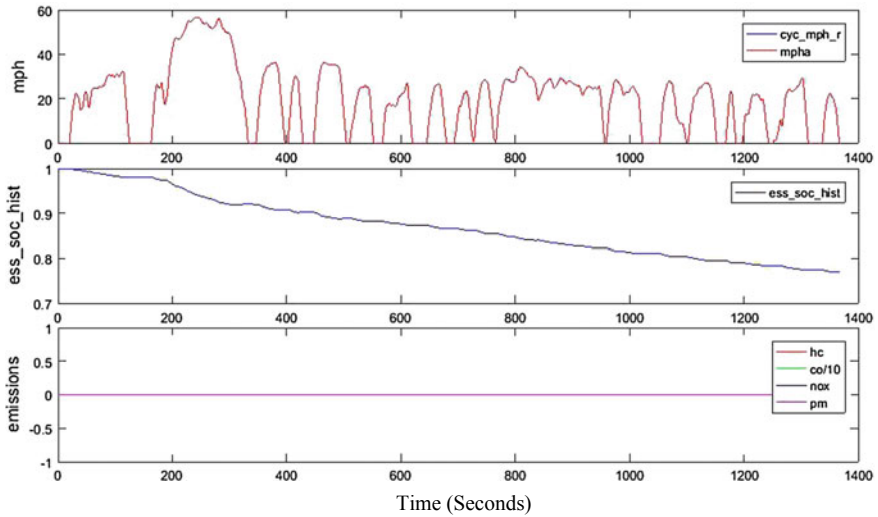


Fig. 42.7 Speed, SoC and emissions of pure EV for **urban** drive cycle

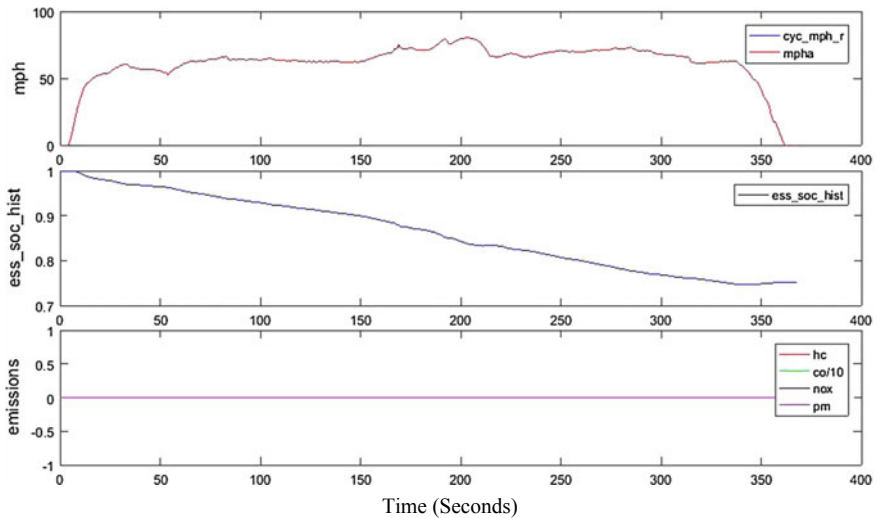
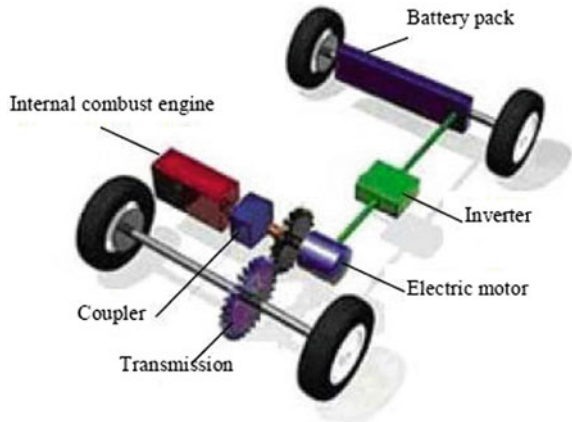


Fig. 42.8 Speed, SoC and emissions of pure EV for **highway drive cycle**

42.4 Parallel HEV

In a parallel hybrid power train, more than one energy source can provide propulsive force. In the parallel hybrid system shown in Fig. 42.9, the Internal Combustion Engine (ICE) and the motor are coupled. The electric motor can act as

Fig. 42.9 Parallel HEV configuration



an electric generator to charge the battery while regenerative braking. Parallel HEV block diagram representation in ADVISOR is shown in Fig. 42.10.

In the result window of ADVISOR for parallel HEV simulation, the speed in miles per hour (mph), Battery State of Charge (SoC) and emissions for Urban and Highway drive cycles are obtained which are shown in Figs. 42.11 and 42.12.

From simulation results it is clear that SoC is not as much diminishing as EV, since tractive effort is also provided by IC engine. For both urban and highway drive cycles, SoC value reduction is almost same but there are emissions like carbon monoxide, nitrous oxide, hydrocarbons, etc., occurring due to the burning of fuel in IC engine.

42.5 Fuel Cell EV

Fuel cell was first developed for space applications as an alternative power sources. There are several types of fuel cells, each with strengths and weaknesses. Low temperature is desirable for vehicle applications. A fuel cell EV consists of fuel

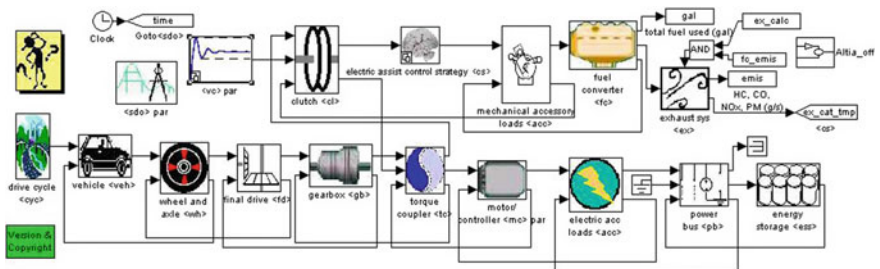


Fig. 42.10 Parallel HEV block diagram in ADVISOR

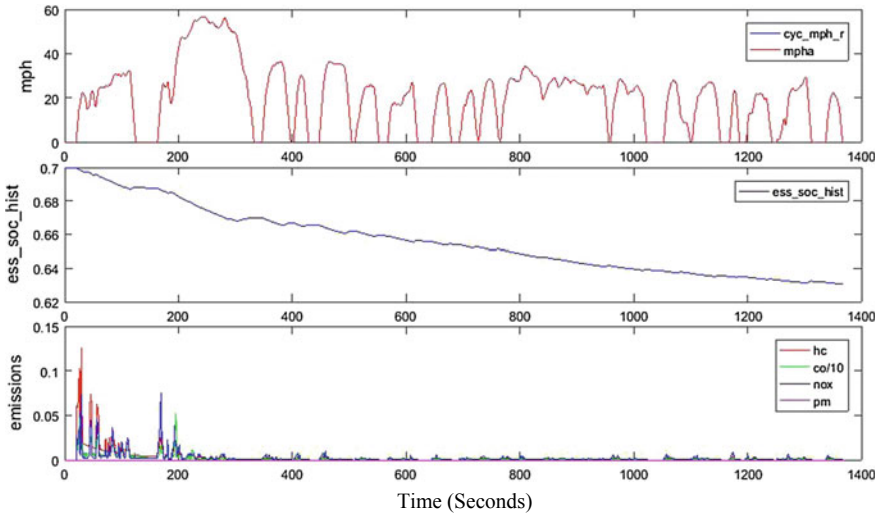


Fig. 42.11 Speed, SoC and emissions of parallel HEV for urban drive cycle

storage system, a fuel cell stack and its control unit, a power processing unit and the propulsion unit. The fuel cell has current source type characteristics and the output of a single cell is very low. Several fuel cells have to be stacked in series to obtain a higher voltage. Figure 42.13 shows the major components in a HONDA 2008 FCX fuel cell car.

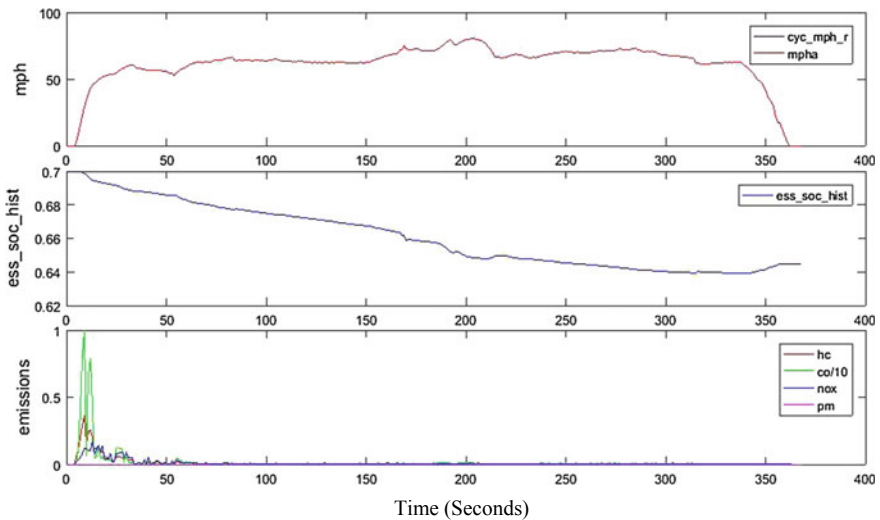


Fig. 42.12 Speed, SoC and emissions of parallel HEV for highway drive cycle

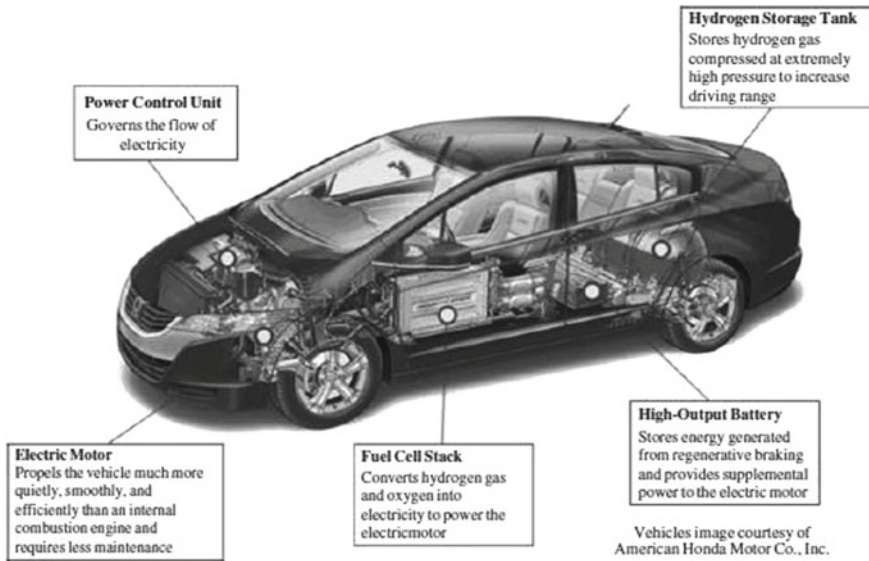


Fig. 42.13 Honda 2008 FCX clarity fuel cell car. Source <http://www.fueleconomy.gov/feg/fuelcell.shtm>. Courtesy American Honda

Block diagram representation of a fuel cell EV in ADVISOR is shown in Fig. 42.14

Present fuel cell systems do not allow the flow of bidirectional energy and thus have the difficulty in achieving regenerative braking energy. Therefore, any kind of hybridization of fuel cells with alternative energy storage devices such as batteries and super-capacitors will be advantageous. In hybrid powertrains, the fuel cell system supplies the base power for constant speed driving, where as other energy storage devices provide additional power demand during acceleration and high-load operation. From Fig. 42.15 it is clear that for urban drive cycle, effective regenerative braking is achieved and battery SoC is increasing even- though there is a dip in SoC while starting. This dip is because at the starting power is drawn from

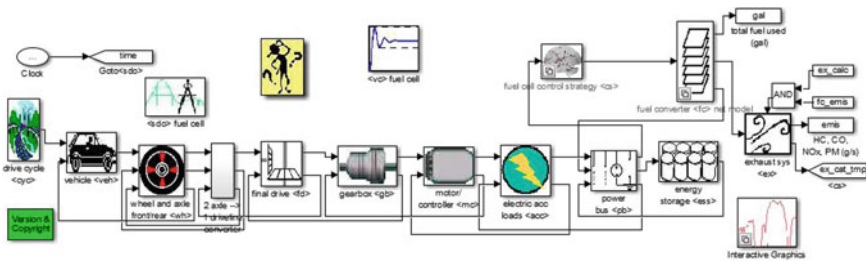


Fig. 42.14 Fuel cell EV block diagram in ADVISOR

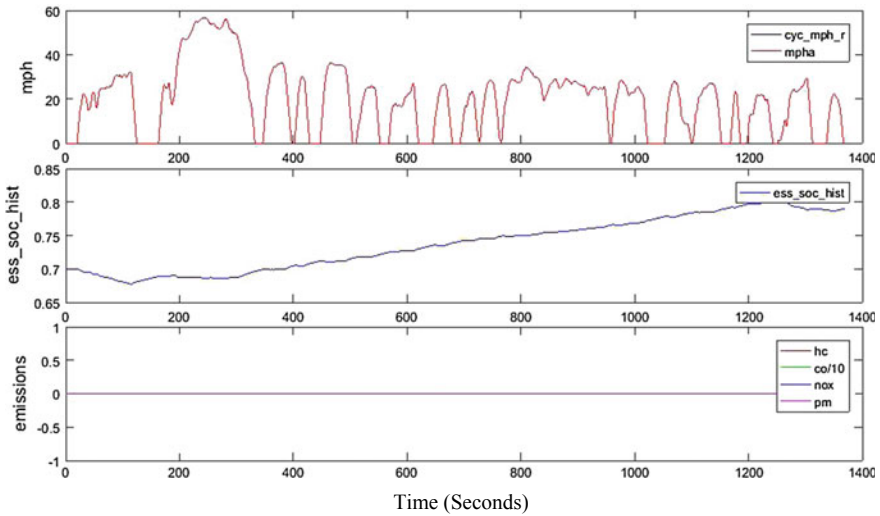


Fig. 42.15 Speed, SoC and emissions of fuel cell EV for urban drive cycle

battery under high load. Whereas in case of highway drive cycle, there is only little scope for regenerative braking as there is only single stop for vehicle and battery SoC is diminishing due to high acceleration. Like EV, FCEV is also promising to be a Zero Emission Vehicle (ZEV) as there are no emissions obtained in the simulation graph of Fig. 42.16.

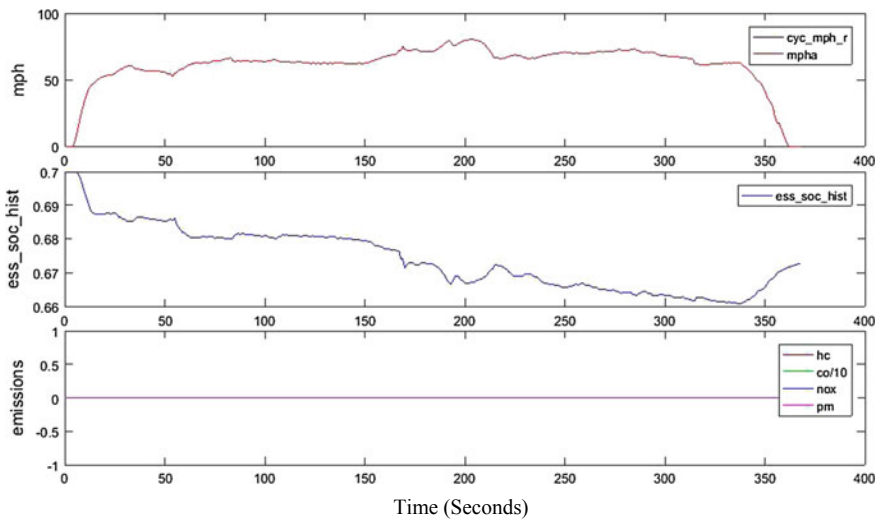


Fig. 42.16 Speed, SoC and emissions of fuel cell EV for highway drive cycle

42.6 Parameter Study of EV, Parallel HEV and FCEV

The major parameters compared for EV, parallel HEV and FCEV are SoC and Emissions for urban and highway drive cycles since they are the crucial factors determining driving range and pollution level of a vehicle. Figure 42.17 shows SoC comparison of EV, HEV and FCEV for CYC_UDDS drive cycle where frequent stop/go operation will be required. From figure it is clear that FCEV is found to be more suitable vehicle for urban driving. This is because a fuel cell will produce electricity until fuel is supplied while batteries can produce electricity only from stored chemical energy. Therefore batteries require frequent recharging for reliable operation. That is why SoC of EV is diminishing on long run; but in a HEV SoC is almost constant because the tractive effort is also provided by the IC engine.

Figure 42.18 shows SoC comparison of EV, HEV and FCEV for CYC_US06_HWY drive cycle, where only single stop of vehicle is occurred. Here also FCEV is superior over HEV, but both are having almost same range of SoC. SoC of FCEV not increasing the case of urban drive cycle because, battery power is used for acceleration also. For EV, SoC is again reducing because of lack of chance of regenerative braking.

Figure 42.19 shows the emissions comparison of EV, HEV and FCEV for urban and highway drive cycles and from figure it is clear that EV and FCEV is having zero emissions and the most promising environment friendly technologies. HEV is having emissions due to the presence of IC engine and pollution level is high in highway driving compared to urban driving because of high acceleration.

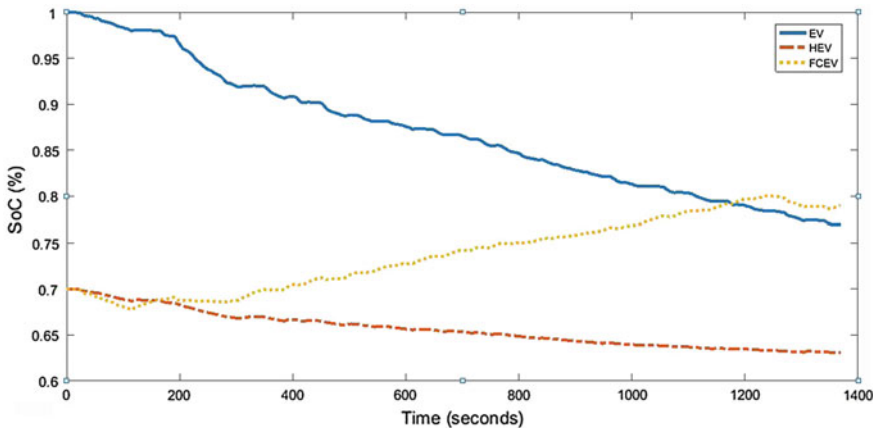


Fig. 42.17 SoC for EV, HEV and FCEV for urban drive cycle

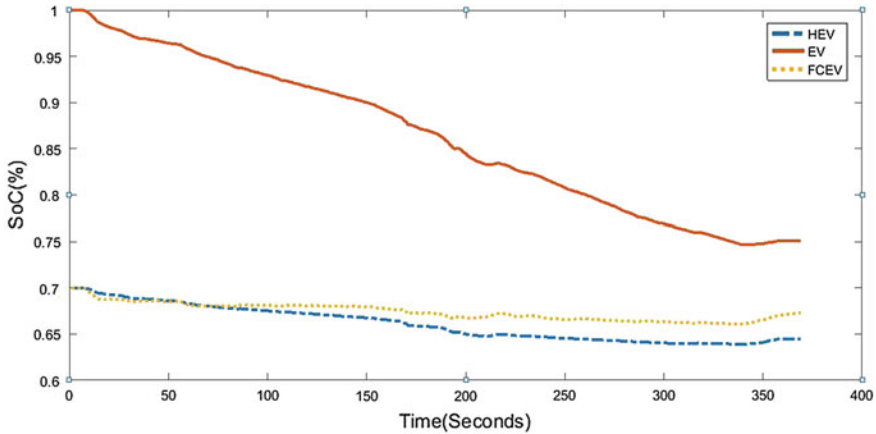


Fig. 42.18 SoC for EV, HEV and FCEV for highway drive cycle

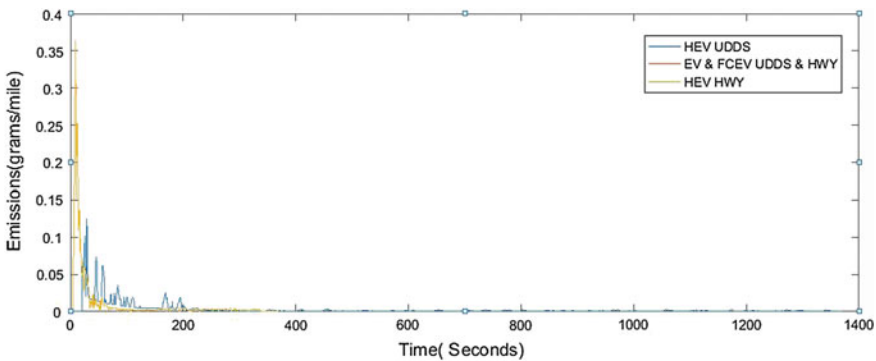


Fig. 42.19 Emission comparison of EV, HEV and FCEV for urban and highway drive cycles

42.7 Conclusion

Simulation of EV, parallel HEV and FCEV has been done in ADVISOR software in MATLAB platform. Parameters like speed, SoC, emissions and overall ratio for different vehicle configurations are obtained. For all configurations, acceleration test has been done with Urban and Highway drive cycles. ADVISOR provides vehicle engineers an easy to use and flexible, yet robust analysis package for vehicle modeling. EV and parallel HEV are having almost similar SoC variations in both cycles, whereas FCEV is having increasing SoC in urban drive cycle. Regarding emissions, both EV and FCEV behaved as Zero Emission Vehicle while HEV is

having emissions in both cases which are high in highway drive cycle. Fuel cell EV is found to be more efficient compared to EV and parallel HEV considering driving range and pollution level. By using hybrid energy storage systems in EV, its performance can be improved especially during uphill or acceleration conditions.

References

- Antoniou A, Komyathi J, Bench J, Emadi A (2005) Modeling and Simulation of various Hybrid Electric Configurations of the High—Mobility Multipurpose Wheeled Vehicle. HMMWV), IEEE
- CHEN D, Li X, CHEN D, CHEN L, YANG L, TIAN F, XU D (2014) Research on simulation of the hybrid electric vehicle based on software ADVISOR. *Sens Transducers* 171(5):68–77
- Ehsani M, Gao Y, Gay SE, Emadi A (2004) Illinois institute of technology modern electric, hybrid electric, and fuel cell vehicles—fundamentals, theory and design
- Hassan A, Mushtaq Z, Rehman A (2015) Performance analysis of drive train configurations using ADVISOR. *Int J Innov Res Adv Eng (IJRAE)* 1(2):306–312
- HOU J, GUO X (2008) Modeling and simulation of hybrid electric vehicles using HEVSIM and ADVISOR. In: IEEE vehicle power and propulsion conference (VPPC)
- Larminie J, Oxford Brookes University, Oxford, UK, John Lowry Acenti Designs Ltd., UK (2003) *Electric vehicle technology explained*, Wiley, The Atrium, Southern Gate, Chichester, West Sussex PO19 8SQ, England
- Markel T, Brooker A, Hendricks T, Johnson V, Kelly K, Kramer B, O’Keefe M, Sprik S, Wipke K (2002) ADVISOR: a systems analysis tool for advanced vehicle modeling. *J Power Sources* 110:255–266
- Saleki A, Rezazade S, Changizian M (2017) Analysis and simulation of hybrid electric vehicles for sedan vehicle. In: 25th Iranian conference on electrical engineering (ICEE2017), vol 978, no 1, pp 1412–1416
- Soylu S (ed) (2011) *Electric vehicles—modelling and simulations*, p. cm. 978-953-307-477-1
- Wipke K, Cuddy M, Bharathan D, Burch S, Johnson V, Markel T, Sprik S (1998) ADVISOR 2.0: a second-generation advanced vehicle simulator for systems analysis. In: North American EV & infrastructure conference and exposition (NAEVI 98)
- YAICH M, HACHICHA MR, GHARIANI M (2015) Modeling and simulation of electric and hybrid vehicles for recreational vehicles. In: 16th International conference on sciences and techniques of automatic control and computer engineering, vol 978, pp 181–187

Chapter 43

Pre-feasibility Study on Light Rail Transit Connecting Kakkanad and Padma Junction



Lalichan Nithya, A. Aathira, B. Abhilash, John Thomas Joel, Joseph Joseena and Sebastian Angel

43.1 Introduction

Kochi, known as “Queen of Arabian Sea”, is considered to be the port city on the south-west coast of India. It is a part of Ernakulum district in the state of Kerala, which has been a port since 1341. Being an international economic zone with comparably high population density, this metropolitan city has a congested road transportation network.

Kochi is enriched with many of those potential driving establishments which enhance its global value. The city stands as a growing center of information technology, with the smart city plan, start-up villages, Infopark, and special economic zones. It also serves as a venue for India’s first global hub terminal—the International Container Transshipment Terminal (ICTT) at Vallarpadam. This city also has an international airport to its pride, the Cochin International Airport Ltd (CIAL) which is increasing by leaps and bounds its international connectivity and business with global companies. Owing the fourth largest cricket stadium, the Jawaharlal Nehru International Stadium, Kochi city is boosting up its development in sports too.

All the abovementioned recent establishments have made Kochi a major attracting center for job opportunities, business, entertainment, and tourism. With its growing population and a handful of development plans, the transportation demand of the city has also increased to an alarming rate. This calls out for enhancement and upgradation in the transportation facilities of the city so as to ensure the sustainability aspect of development.

L. Nithya (✉) · A. Aathira · B. Abhilash · J. T. Joel · J. Joseena · S. Angel
Rajagiri School of Engineering and Technology, Kochi, India
e-mail: nithyalalichan@gmail.com

S. Angel
e-mail: angelsebastian08@gmail.com

At present, the inefficiency and inadequacy of public transport in the city have led the passengers to shift to private transport modes. This has led to more congestion on the roads. Road widening measures and new road infrastructure has only worsened the situation as more and more people shifted to private vehicles. Implementation of an efficient public mode of transport with better amenities and services like Mass Rapid Transit mode which would make the passengers shift from private vehicles to public transport would significantly reduce the congestion and the carbon footage of the region. This paper aims to study the feasibility of Light Rail Transit connecting two important spots in Kochi city.

43.2 Literature Review

43.2.1 Existing Public Transport System in Kochi

Kochi, the Gateway of South India is industrially advanced and one of the fastest developing cities of the nation. Kochi spreads over 94.88 sq. km and has a population of 6 lakh people according to the 2011 census. As per the Comprehensive Mobility Plan (CMP) prepared by the Urban Mass Transit Company Ltd. for Kochi Metro Rail Ltd., Ernakulum district has a population of 30,05,789 persons with an urban population of 14,77,085 and an average density of 1012 persons per sq. km. The population of Cochin Municipal Corporation has increased from 5.64 lakhs in 1991 to 5.98 lakhs in 2001 and eventually reached 6.46 lakhs in 2011. The Kochi city region comprises Cochin Corporation and its immediate influence areas of 369.72 sq. km. The population of Kochi city region increased from 11.28 to 12.23 lakhs from 2001 to 2011 with a decadal growth of 8%. The major public mode of transport in Cochin City has been the bus service. But this mode of public transport does not ensure safe and efficient urban mobility.

CMP data reveals the road network characteristics and traffic characteristics of the Kochi region as indicated below:

1. Private vehicles (two-wheelers and cars) comprise 79% of the users.
2. 75% of roads do not have appropriate road markings and signboards.
3. Absence of cycle tracks discourages the people to cycle along the roads of Kochi.
4. Only 15% of the roads have footpaths on both sides.
5. Public transport(buses) is only 4% of the total vehicles and this 4% of buses carry 49% of motorized trips.
6. 25% of the surveyed roads have on-street parking facility.
7. The emission rate from vehicles in 2015 was 29.98 tons/day. As per forecasts, it would be 49.86 tons/day by 2035. This could cause fatal diseases like ischemic heart diseases, stroke, chronic obstructive pulmonary disease, and lung cancer respiratory infections.

8. The number of road accidents in 2011 was 35,216 which witnessed a rise of 38,470 in 2017.

The rise in the number of vehicles and the resulting traffic congestion have made the life of people in Kochi worsen. People have to spend hours in traffic. Lack of signboards, signals, street lights, medians, etc., makes the problem fatal. Inadequate bus shelters, lack of buses in certain regions, delay in bus timings due to traffic blocks, etc., are some of the problems of passengers who depend upon the public transport system. The increasing bus service adds up to the carbon emission, which is of high concern in the present scenario. Kochi Metro, Phase I, stretching from Aluva (27 km North of Kochi) to Petta, was an initiative to tackle this problem. Kochi Metro connects up the towns lying straight in the route from Aluva to Ernakulum, and the main challenge faced by metro is the absence of an effective feeder system to connect nearby towns to the metro stations.

This has led to the need for an efficient Mass Rapid Transit System that can bring up overall connectivity to the towns and hectic junctions within the city, making out a looping network of integrated transport whereby the accessibility to any part of city can be done with ease. Kakkanad is one of the important residential cum industrial hubs which have been connected to Padma Junction, yet another commercial hub by means of road traffic at present. Proposing a Light Rail Transit along the shortest route connecting Kakkanad and Padma Junction will ensure better connectivity and helps to reduce the road traffic in existing road section.

43.2.2 Mass Rapid Transit System (MRTS)

Mass Rapid Transit Systems are the modes of transport that enable fast, safe, and mass urban mobility with its own exclusive right of way and terminals. Light Rail Transit (LRT), Bus Rapid Transit (BRT), and Metro transit System belong to Mass Rapid Transit. Each of the transit systems varies with its capacity, speed, acceleration, axle load, accessibility, and affordability. High population density always demands the use of rapid transit systems as it reduces the traffic congestion in the cities.

Bus Rapid Transit. Bus Rapid Transit System involves buses running on the exclusive right of way with great accessibility to bus stations and priority signals at intersections. BRTs are the simplest, cheapest, and flexible mode of MRT. They are at grade facility which attracts more passengers. It has comparatively low capacity for transporting passengers. The cost of establishment is also very low and hence it could be widely planned in the cities of India. It could easily reduce the traffic congestion to a great extent and it attracts passengers with its low bus fare compared to other MRTS. The first BRTS in India is Rainbow Bus Transit System in Pune, which started in 2006.

Metro Transit System. Metro transit system is a rapid transit system that consists of trains that run on separated lanes with enhanced amenities and services. The pathways are often elevated with piers that could take approximately 17 tons of

axle load. Among all the MRTS, the metro has the highest capacity and speed. High demand for urban mobility could be easily satisfied with metro system. Passenger comfort, safety, and reliability are the assured features of Metro Rail Transit Systems.

Light Rail Transit. Light Rail Transit, also known as Light Rapid Transit is a modern version of trams. It uses electrified individual tramcars or multiple units. Trams started working even before hundred years ago. The major difference of LRT from trams is that it causes less pollution by using electrically operated units and better amenities. At present, there are no light rails in India, but a few are there in the planning stage.

Features of LRT:

1. Speed—30 km/h;
2. Maximum acceleration—1 m/s²;
3. Capacity in PPHPD—1000–25,000;
4. Interstation distance—600–800 m;
5. Approximate cost—100 cr/km;
6. Project time /20 km—2 yrs;
7. Safe and easy boarding;
8. Off-board ticketing;
9. Low axle load compared to metro;
10. Sharp road bends up to 25 m radius, minimizes the need for property acquisition;
11. Eco-friendly as it works on electricity;
12. Branding and communication;
13. Closed corridor movement;
14. Segregated path;
15. Medium capacity Mass Rapid Transit System; and
16. Low life cycle cost for construction and maintenance.

Requires less road space compared to bus rapid transit (for BRT 3–4 lanes, for LRT 2–3 lanes.)

43.2.3 Study Area

The study area includes the Kakkanad region which houses the Civil Station, Special Economic Zone, Infopark, Smart city, and the MG road stretch which is the hub of trade and commerce. Kakkanad being the upcoming demanding zone lacks a good network of the public mode of transport from the other zones of Kochi.

The proposed project route as shown in Fig. 43.1, extending from Kakkanad to Padma Junction of MG road, about 9.6 km that can help to integrate the entire public transport by connecting important junctions and spots in the city as shown in Fig. 43.2.

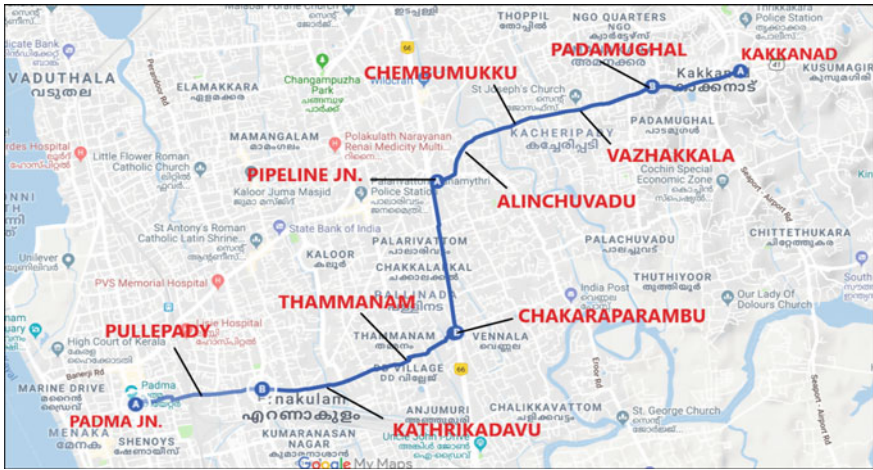


Fig. 43.1 The proposed route from Kakkannad to Padma junction Source Google map

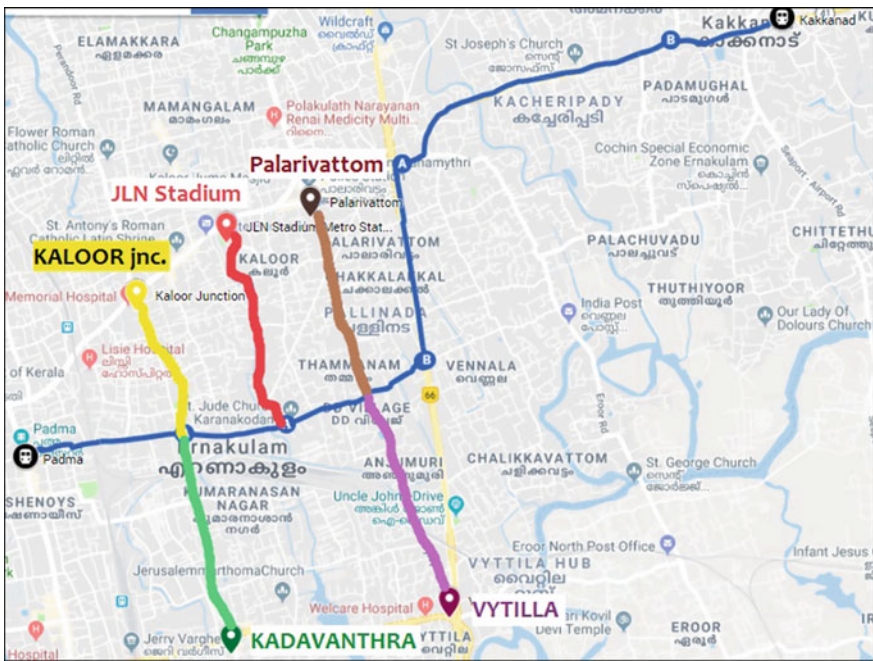


Fig. 43.2 The proposed route provides connectivity to other important centers Source Google map

43.3 Methodology

A reconnaissance survey was conducted to identify a suitable route for this study. Surveys including Road Inventory Survey (RIS), Traffic Volume Count (TVC) survey, Vehicle Occupancy Survey, Boarding Alighting Survey (BAS), and Bus Operator Survey (BOS) were performed. Analyzing the data collected from the survey, results were summarized and the study was carried out to find the viability of LRT in the study route.

Road Inventory survey was conducted with the help of manual inspection and video graphic methods throughout the selected stretch. Figure 43.4 shows the LRT cross section proposed at the LRT station. Inventory studies are tabulated and marked on Autodesk AutoCAD to analyze the existing road conditions and facilities in the proposed cross section. The general methodology of the observational field study involved the following steps.

1. Available right of way at various locations was measured.
2. Presence and width of sidewalks and curbs on these corridors were checked.
3. Presence and width of the median on these corridors were checked.
4. Existing conditions at the proposed area for the LRT track were noted.
5. Obstructions with descriptions were noted.
6. Identified the utilities to be relocated
 - Electric posts, waste bins, buildings, fences, and compound walls.
7. Environmental barriers present were identified
 - Trees and bushes.

The TVC survey counts the peak-hour vehicular traffic along a midblock section. The survey was conducted in five stretches as shown in Fig. 43.3.

The TVC data was collected by counting the vehicles passing through the route in every 5-min interval for 3 h peak time in the morning and evening. Classified volume count was conducted manually as each type is having an influence on the performance of the road in its own way. The average occupancy of each type of vehicle is also found out.

The BAS survey obtains the number of passengers boarding and alighting in buses passing through a particular stop. Thus, the total number of passengers boarding and alighting in the existing bus stops were counted for the 3 h peak time. Since the proposed route has no continuous bus stops, the survey was conducted in consecutive five stops from civil station to pipeline junction. Table 43.1 shows the collected data which gives Passenger per Hour per Direction (PPHPD) using existing bus service.

The BOS survey was conducted from various bus depots to collect the details of the existing buses' routes, average passenger capacity, average number of tickets sold per day and the number of trips of private buses, KSRTC buses and KURTC buses in service through the proposed route. Table 43.2 shows the data obtained from the BOS survey.



Fig. 43.3 Divided midblock sections where the TVC survey was conducted *Source* Google map

43.4 Results and Discussion

Existing conditions in the proposed area for the LRT track were noted by RIS. Thus, suitability of construction of the proposed LRT cross section throughout the study area, stretches where land acquisition is required, and the approximate cost for relocation of utilities were analyzed from it (Fig. 43.4).

TVC survey provides the peak-hour vehicular traffic volume. Knowledge of vehicular volume using a road network is important for understanding the efficiency at which the system works at present. The data obtained from an occupancy survey is combined with vehicle count to get the total number of persons traveling through the proposed stretch. Thus, this survey provides the base for tram design, fleet size calculation, station design, headway calculation, and traffic control system design. Figure 43.5 graphically summarizes the data collected from the TVC survey, with the classified count of vehicles in horizontal axis and the percentage of each type of vehicle in the Y-axis.

Analyzing Fig. 43.5, we can infer that there is no public mode of transport connecting the route from Chakkaraparambu to Padma junction and the whole contribution of traffic solely depends on private vehicles. The percent of two-wheelers occupying the route exceeds 60% at Pullepady–Padma section followed by autorickshaws, cars, and other private vehicles. This data is confirmed from the data obtained from bus operator survey as in Table 43.3 which shows absence of bus service in the proposed region. Hence the analysis concludes that increased private mode of transport due to the absence of efficient public mode of transport is the factor responsible for the traffic congestion occurring in this route.

Table 43.1 BAS data collected at existing bus stops in the proposed route

Existing bus stop location	Kakkanad–Padma stretch			Padma–Kakkanad stretch				
	Boarding	Alighting	Total passengers	PPHPD	Boarding	Alighting	Total passengers	PPHPD
Civil station	404	0	404	404	134	0	134	134
Padamughal	85	55	140	435	43	70	114	161
East Vazhakkala	53	23	75	465	70	113	184	204
Vazhakkala	150	74	224	541	97	186	283	294
Chembumukku	176	37	214	680	39	59	98	314
Alinchuvadu	77	98	175	659	43	70	114	341
Pipeline	115	175	289	599	0	424	424	765

Table 43.2 Proposed LRT stations

Sl. no.	Station name	Chainage (km)	Distance between stations (km)
1	Civil station	0	0.000
2	Padamughal	1.55	1.550
3	Vazhakkala	2.25	0.700
4	Chembumukku	2.764	0.514
5	Pipeline junction	3.974	1.210
6	Ernakulum Medical Center (EMC)	4.597	0.623
7	Chakkaraparambu	5.717	1.120
8	Thammanam	6.4	0.683
9	Kathrikadavu	8.06	1.66
10	Pullepady	8.615	0.555
11	Padma	9.589	0.974

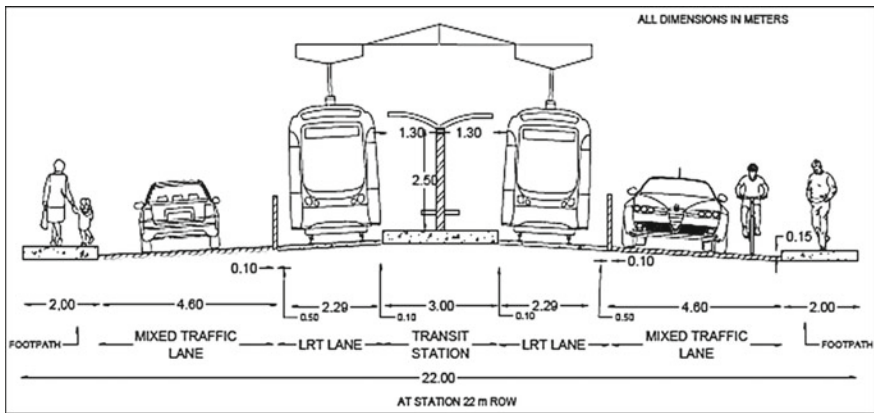


Fig. 43.4 Proposed LRT cross section

Figure 43.5 also highlights the potential of the region for the implementation of MRT mode of transport.

The boarding and alighting counts were used to analyze the demand of passengers or existing bus stop, and to determine the locations in the proposed stretch having the greatest transit demand. Thus, the BAS data can be used for LRT station selection and they are shown in Table 43.2.

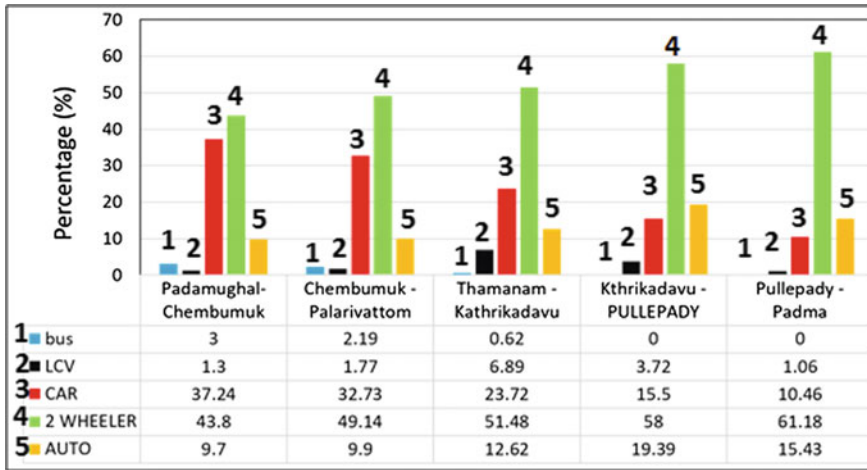


Fig. 43.5 Graphical representation classified volume count of five types of vehicles obtained from TVC survey conducted in five midblock sections

Table 43.3 BOS data collected

Stretch (private buses)	No. of buses	No. of tickets (sold per trip)	Trips	Ridership
Kakkanad-Palarivattom (to different places)	170	35	6	35,700
Palarivattom-Thammanam (Vytila-Vytila city services)	20	70	13	18,200
Total				53,900
Stretch (KSRTC)	No. of buses	No. of tickets (sold per trip)	Trips	Ridership
Kakkanad-MG Road (via Palarivattom)	5	110	11	6050
Total				6050

43.5 Conclusion

LRT is the most viable and sustainable alternative for future road expansion works to meet the increasing travel demand.

There exist a few public transport systems currently connecting Kakkannad and MG road through the Palarivattom-Kaloor route. The project route extends from Palarivattom civil line road to Chakkaraparambu, connecting Thammanam junction, Kathrikadavu junction, Pullepady junction, and finally intersecting up with metro rail station at Padma. A part of the stretch connecting Chakkaraparambu to Padma through the Thammanam-Pullepady road and Kathrikadavu junction has a

missing link of the public transport system in operation. All the road users through this stretch depend solely on private vehicles. Bringing up a suitable MRTS at this route can help and attract more people to public transport.

Another salient feature of the route is its expected potential in the future. The proposed route connects the four main potential junctions of the area like Kadavanthra, Vytilla, JLN Stadium, and Kaloor junction.

From the study and analysis of data collected, it can be highlighted that the main reason behind the road traffic congestion in the route from Kakkanad to Padma can be reduced by introducing an efficient mode of public transport service through the route. Commencing bus service will not prove to be sustainable environmentally. This problem can be tackled by proposing LRT through the route. Being electrically propelled, this will not cause environmental issues and will be cost effective to achieve long-term sustainable goals.

References

- Urban Mass Transit Company Ltd. (2016) Comprehensive Mobility Plan
- Kochi Metro Rail Ltd. (2016) Light Rail Transit to West Kochi Islands
- Institute of Urban Transport (India) (2013) Modern trams (Light Rail Transit)-for cities in India
- EMBARQ India (2015) BUS KARO-A guidebook on bus planning & operations
- EMBARQ India (2016) Data collection and analysis for public transport
- Kadiyali LR (2013) Traffic engineering and transport planning, 8e